Bitlis Eren Üniversitesi
Fen Bilimleri Dergisi

Bitlis Eren University
Journal of Science

BEU FBD

Bitlis Eren Üniversitesi Fen Bilimler Dergisi

Bitlis Eren University Journal of Science
Yıl/*Year:* 2024 - Cilt/*Volume:* 13 - Sayı/*Number:* 1

Dergi Hakkında / *About Journal*

Bitlis Eren Üniversitesi Fen Bilimleri Dergisi, mühendislik ve temel bilimler alanlarındaki gelişmeleri ve yenilikleri takip etmek, meslek kuruluşlarının, araştırmacıların ve bireylerin ulusal ve uluslararası gelişimlerine katkıda bulunmak ve bu alanlarda elektronik bir kaynak oluşturmak amacıyla yayımlanmaktadır. Derginin yazım dili Türkçe veya İngilizcedir. Fen Bilimleri Dergisi, Bitlis Eren Üniversitesi Lisansüstü Eğitim Enstitüsü yayını olup, 2012 yılından bu yana ücretsiz ve açık erişimli olarak yayın hayatına devam etmektedir. Mühendislik ve temel bilimlerin bilgi tabanına ve teknolojik gelişmelere ışık tutması amacıyla bu alanlarda yapılmış deneysel ve teorik ilerlemeleri konu alan özgün araştırma makalelerine yer verilmektedir. Dergiye gönderilen çalışmaların benzerlik oranı %25'i geçmemelidir. Yazım kurallarına uymayan makaleler, hakemlere gönderilmeden önce düzeltilmek üzere yazara geri gönderilir. Bu nedenle, derginin yazım kuralları dikkate alınmalıdır. Ayrıca, editörlerden yazarlara iletilen düzeltmelere veya taleplere 30 gün içerisinde cevap verilmediği takdirde ilgili makaleler reddedilir. Makaleler şekiller ve tablolar dâhil 20 sayfayı geçmemelidir. Dergiye yayın için gönderilen makaleler en az iki hakem tarafından değerlendirilir. Yazarlardan hakem önerisi talep edilmemektedir. Makalelerin dergide yayımlanabilmesi için hakemler tarafından olumlu görüş bildirilmesi gerekmektedir. Dergi Editör Kurulu, hakem raporlarını (*en aziki hakemin değerlendirmeleri geldikten sonra*) dikkate alarak makalelerin yayımlanmak üzere kabul edilip edilmemesine karar verir. Fen Bilimleri Dergisi, yılda dört defa (*Mart*, *Haziran, Eylül, Aralık*) yayımlanmaktadır. **Dergimiz Tübitak-Ulakbim Mühendislik ve Temel Bilimler Veri Tabanı Dergi Listesinde taranmaktadır.**

B.E.Ü. Fen Bilimleri Dergisi 13(1), 2024 / *B.E.U. Journal of Science 13(1), 2024*
İÇİNDEKİLER / *CONTENTS*

A Comparative Analysis of Passenger Flow Forecasting in Trams Using Machine Learning Algorithms

Beyhan ADANUR DEDETURK[1*], Bilge Kagan DEDETURK[2], Ayhan AKBAS[3]

[1]Department of Computer Engineering, Abdullah Gul University, Kayseri, Türkiye
[2]Department of Software Engineering, Erciyes University, Kayseri, Türkiye
[3]Institute for Communication Systems, University of Surrey, Guildford, UK
(ORCID: 0000-0003-4983-2417) (ORCID: 0000-0002-8026-5003) (ORCID: 0000-0002-6425-104X)

Abstract

Forecasting tram passenger flow is an important part of the intelligent transportation system since it helps with resource allocation, network design, and frequency setting. Due to varying destinations and departure times, it is difficult to notice large fluctuations, non-linearity, and periodicity in tram passenger flows. In this paper, the first-order difference technique is used to eliminate seasonal structure from the time series data, and the performance of different machine learning algorithms on passenger flow forecasting in trams is evaluated. Furthermore, the impact of the COVID-19 pandemic on forecasting success is examined. For this purpose, the tram data of Kayseri Transportation Inc. for the years 2018-2021 is used. Different estimation models, including Linear Regression, Support Vector Regression, Random Forest, Artificial Neural Network, Convolutional Neural Network, and Long Short-Term Memory are applied, and the time series forecasting performances of the models are evaluated with MAPE and R^2 metrics.

1. Introduction

With the continuous expansion of the corporate sector in major urban centers, traffic congestion has become increasingly prominent. Among its various challenges, overcrowding is particularly critical, presenting hidden threats to public safety and significant time wastage. A promising solution to this problem is the expansion of public transportation networks, focusing specifically on trams [1].

The rapid proliferation of tram systems and the development of sophisticated information management systems have led to a substantial generation of passenger trip data. This data surge has sparked significant interest in the scientific community, particularly in developing reliable methods to predict tram passenger flow. Accurate forecasting of passenger flows is crucial for efficient transportation management and plays a pivotal role in devising appropriate contingency plans for

emergencies, thus enhancing the city's overall emergency response capabilities [2].

In essence, the growth of corporate activities in urban areas has exacerbated traffic congestion issues, especially overcrowding. This has underscored the need for solutions like expanding tram networks. Leveraging the wealth of data generated by these systems has become a key research focus. Accurate predictions of passenger flow can lead to better urban transportation management and improved emergency preparedness.

The aim of the article is to assess the efficiency of different machine learning algorithms in forecasting tram passenger flow. The study tackles the challenges in forecasting due to significant fluctuations, non-linearity, and periodicity in passenger numbers. Techniques such as log transform and first-order difference are utilized to preprocess the data, and the study investigates the impact of the COVID-19 pandemic on forecasting accuracy. Data

---

*Corresponding author: *beyhan.adanur@agu.edu.tr*

from Kayseri Transportation Inc. for 2018-2021 is analyzed using various models, including Linear Regression, Support Vector Regression, Random Forest, Artificial Neural Network, Convolutional Neural Network, and Long Short-Term Memory (LSTM). These models are evaluated using MAPE and R^2 metrics to establish effective methods for predicting tram passenger flows, which can enhance urban transportation management and emergency preparedness.

In the study, the log transform is applied to daily tram passenger number data from January 1, 2018, to July 1, 2021. Subsequently, the first-order difference of consecutive days' passenger numbers is calculated. Three datasets are prepared: pre-pandemic (799 data points), in-pandemic (445 data points), and the entire dataset (1244 data points). These are divided into training and test sets for the last 30 days' prediction using the previous 10 days' data. The aforementioned models are trained and tested, employing multi-step and multi-output forecasting techniques. The study compares the results and assesses the impact of the pandemic on forecasting success, aiming to contribute to the field with new insights and methodologies. The key contributions of this study can be summarized as follows:

- Creation and public sharing of the Kayseri tram passenger flow dataset.
- Investigation of the COVID-19 pandemic's effects on time series forecasting.
- Application of log transform and first-order difference techniques to reduce noise, linearize the data, and address seasonal patterns.
- Implementation and detailed comparative performance evaluations of various machine learning and deep learning methods.
- Comparison of the performance of multi-step and multi-output techniques.

We believe this will establish a hybrid method for future studies. The remainder of this paper is organized as follows: Section 2 reviews the related works. Section 3 describes the methodologies of LR, SVR, Random Forest, ANN, CNN, and LSTM. Section 4 discusses the experimental results. Finally, Section 5 concludes the paper, explaining the major results and limitations of the current study, their significance, and suggesting future research topics.

2. Related Work

Intelligent computing and machine learning technologies are increasingly being used in various forecasting application scenarios, yielding impressive results. This progress is largely due to advancements in artificial intelligence and the growth of big data [3]-[4]. Forecasting models can be categorized into three types: parametric, non-parametric, and hybrid [5]. Several parametric methods for forecasting transportation demand have been developed, including Box-Jenkins [6], smoothing techniques [7], autoregressive integrated moving average (ARIMA) [8], gray forecasting [9], and state space models [10]. Among these, the ARIMA model [8]-[11] is frequently used. It is a linear function of time-lagged variables and error terms; however, passenger flows are often characterized by high fluctuations, non-linearity, and periodicity. Therefore, traditional parametric models, which assume linear relationships between time-lagged variables, may not effectively represent the structure of non-linear flows.

Similarly, various non-parametric methods for forecasting transportation demand have been developed, including neural networks [14], k-nearest neighbors [15], Kalman filters [16], support vector regression (SVR) [17], and other methods [18]. Neural network models, such as Back Propagation (BP), stacked auto-encoders, and LSTM, often show good performance in trip mode analysis and flow prediction or similar issues [19]-[24]. However, they are susceptible to parameter selection and can be prone to local minima and overfitting [25]. SVM variants are also commonly used [26]-[28]. Unlike neural networks, SVR employs the structural risk minimization principle, aiming to reduce the generalization error upper bound rather than the training error [29], potentially overcoming some fundamental flaws of neural networks [30].

The use of hybrid models to enhance forecasting accuracy has become increasingly popular [31]. Each model constituting a hybrid model has its own set of advantages and disadvantages. The key idea behind hybrid modeling [32], [33] is to combine multiple models while retaining each's benefits. These models have shown promising results in addressing forecasting challenges.

Wang et al. [34] used an integrated model combining multivariate linear regression, K-nearest neighbor, XGBoost, and GRU as four submodels to accurately predict urban public transportation short-term passenger flows. They then integrated these models using a regression algorithm, demonstrating the integrated model's superiority over individual sub-models. Additionally, the popular hybrid forecasting model, the decomposition-integration method, decomposes the original data into several components, processes each component, and integrates them for final predictions [5], [35]-[36]. However, this method is rarely used for short-term bus passenger flow forecasting, and it typically involves only a single decomposition of the original

data. Some components remain highly unstable after initial decomposition, which hinders accurate predictions. Therefore, additional noise reduction for unstable components post-decomposition is necessary.

Li et al. [37] developed a secondary decomposition-integration method for short-term bus route passenger flow prediction, integrating empirical modal decomposition, sample entropy, and kernel extreme learning machines. However, the superficial structure of traditional machine learning methods struggles with the complex nonlinearity of spatial and temporal travel demand patterns [38].

A recent study introduced a new model, ITS-Pro-Flow, for predicting short-term traffic flow in intelligent transportation systems (ITS) [49]. It builds upon the Pro-Energy model, utilizing historical data and current conditions for prediction. ITS-Pro-Flow improves upon Pro-Energy by dynamically adjusting past predictions and current observations, with extensive simulations showing its enhanced accuracy. The model incorporates a dynamic weighting factor and a thresholding strategy, improving adaptability and precision. The study also explores parameter variations for optimal prediction accuracy.

With the advent of the Internet of Things (IoT), numerous devices and software have been developed to assist in prediction tasks. Gao et al. [39] proposed a method to increase the efficacy of software-defined devices, while they also introduced a technology to transform business process execution language (BPEL) into timed automata for formal verification, bridging BPEL and IoT data in support of prediction tasks [40]. Huang et al. [41] optimized virtual machine allocation strategies for cloud data centers, and Ma et al. [42] proposed a real-time multiple workflow scheduling method in a cloud environment, enhancing the processing efficacy of large data sets for passenger flow source data analysis.

Despite the successes of these methods, current passenger flow forecasting faces challenges such as reliance on a single data source and insufficient analysis of influencing factors, leading to low accuracy in existing methodologies and impacting urban traffic management [43]. Often, the performance of a hybrid model is either compared with those in the literature or with a maximum of 2-3 methods.

3. Material and Method

In this section, we briefly talk about the data set and the preprocessing methods used. Following that, we discuss the machine learning models that were utilized, which include LR, SVR, Random Forest,

ANN, CNN, and LSTM architectures. A flow diagram is presented in Figure 1 to demonstrate the research process.
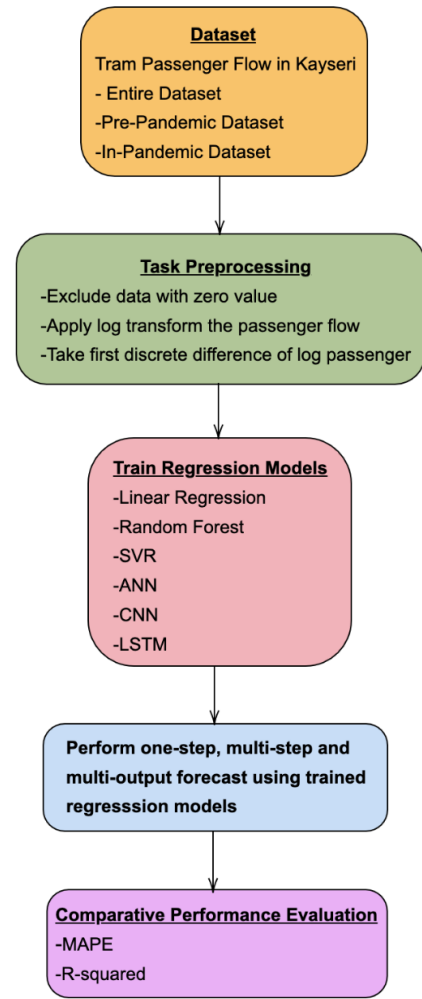
Figure 1. Overall methodology diagram.

3.1. Dataset

The dataset [44] consists of Kayseri tram daily passenger data between January 1, 2018 and July 1, 2021. The daily passenger flow data is shown in Figure 2. Because of eids such as Ramadan Eid, Eid of Sacrifice, and July 15 Democracy and National Unity Day, a free transit system is implemented in the city of Kayseri, and therefore, tram passenger numbers are not available. In addition, the number of passengers remained below fifty on the days when the curfew was performed during the COVID-19 pandemic. For this reason, the number of passengers on some days is seen as close to zero in Figure 2. These days were excluded from the dataset due to the absence of passenger flow data. Therefore, passenger data for 33 days out of 1277 was excluded from the dataset, leaving a total of 1244 passenger data points in the dataset. As seen from Figure 2, there has been a noticeable decrease in passenger numbers since

mid-March 2020 due to the COVID-19 pandemic. The first detected COVID-19 case in Türkiye was announced by the Ministry of Health on March 11, 2020. The first death due to the virus in the country occurred on March 15, 2020. As of March 16, 2020, passenger flow in urban rail transportation in Kayseri started to decrease. In our study, in order to observe the effect of the COVID-19 pandemic, the entire dataset was divided into two parts: pre-pandemic (799 days) and during the pandemic (445 days), and three different datasets were obtained together with the whole dataset.

3.2. Preprocessing

Before being modeled with machine learning techniques, time series analysis often requires some data preparation. In time series forecasting, data transforms can be used to eliminate noise and improve the signal. One of the most frequently used data transformation techniques in time series data analysis is log transformation. By using log transformation, time series data with an exponential distribution can be turned into a linear trend, which is easy to model. Figure 3 shows the data obtained after applying the log transform to the passenger flow data, and, as can be seen, the data is squeezed into a smaller range. After obtaining log passenger data, the first-order difference technique was performed to make the time series data stationary. To simplify the prediction problem, differencing methods can be employed to eliminate trend and seasonal structure from the series. A difference transform is a simple approach to getting rid of a systematic structure in a time series. By subtracting the preceding value from each value in the series, a trend can be removed. The process is known as first-order differencing. After performing the first-order difference on the log transform data, the obtained data are shown in Figure 4.
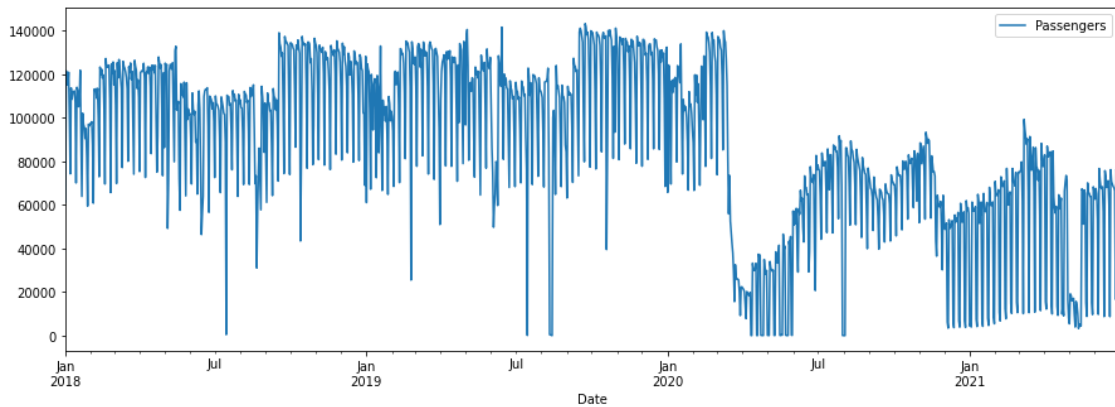
Figure 2. Tram passenger flow data in Kayseri.
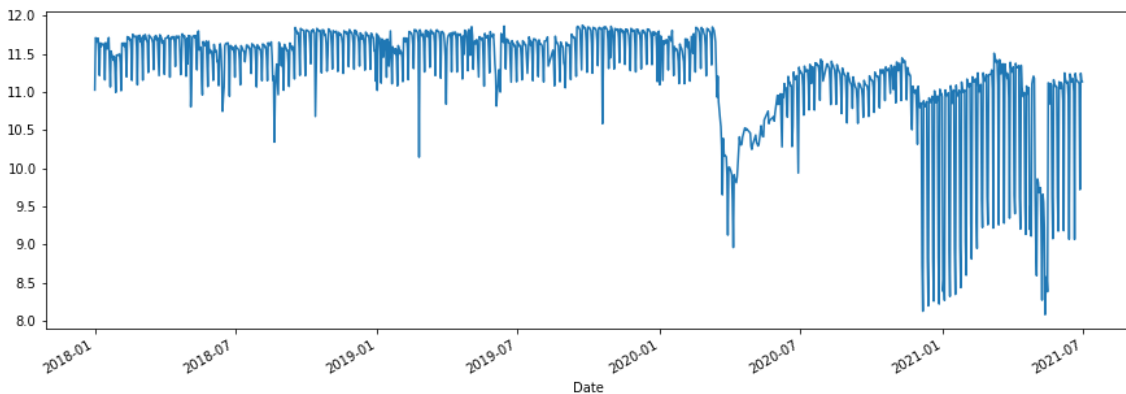
Figure 3. Tram passenger flow data after applying log transformation.
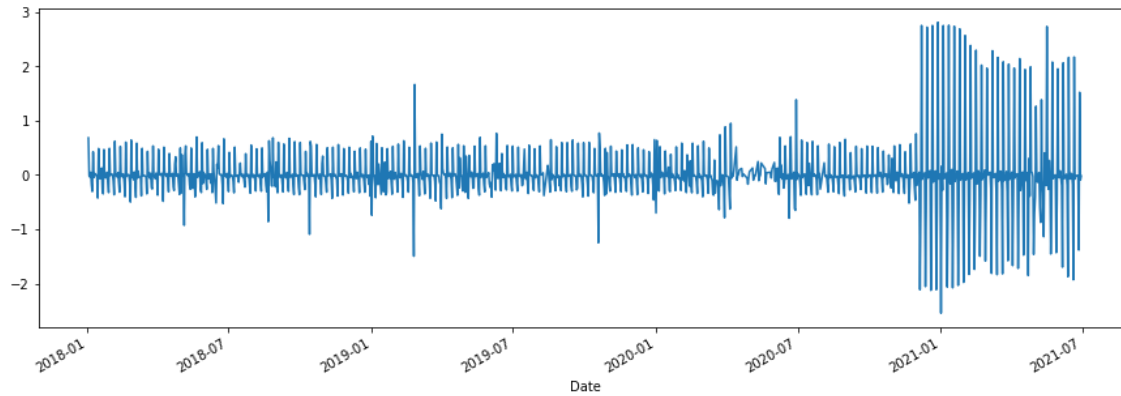
Figure 4. The data obtained after performing first order difference on log passenger data.

3.3. Linear Regression

Linear regression is a statistical technique used for predicting future values based on past data. It's a popular quantitative method for identifying underlying trends and determining if values have deviated significantly. A linear regression trendline uses the least squares method to plot a straight line across data, minimizing the gaps between the values and the trendline. Each data point's trendline value is plotted using this linear regression indicator [45].

In our experiments, two different LR models are trained. The first model, used for one-step forecasting, predicts the passenger flow of a day using first-order difference data from the previous 10 days, resulting in an input vector size of 10. The second model, designed for multi-output forecasting, predicts passenger flow for the next 30 days using the same input data. Both models use the same input layer shape and are trained and tested using the scikit-learn Linear Regression module with default settings.

3.4. Support Vector Regression

Support vector machines (SVM) are a supervised machine learning method based on the Vapnik-Chervonenkis (VC) theory, which identifies characteristics of machine learning conducive to accurate test data predictions. SVM is applicable to both classification and regression problems. Support vector regression (SVR) involves computing a linear regression function in a high-dimensional input space (feature space) where the input data is mapped through a nonlinear function. This transforms a nonlinear regression problem in low-dimensional input space into a linear one in high-dimensional space, where the solution is derived [46].

Two different SVR models are trained in the experiments. The first model, for one-step

forecasting, and the second model, for multi-output forecasting, use the same inputs as the LR models. Both models are trained and tested using the Scikit-learn SVR module with default settings.

3.5. Random Forest

A random forest (RF) is an ensemble of several independent decision trees. Each tree generates a class prediction, and the model's forecast is the one with the most votes. Random forests are effective because they combine many generally uncorrelated trees, outperforming individual constituent models. RF is notable for its application to both regression and classification problems, faster training compared to other methods, higher estimation speed, fewer tuning parameters, and direct applicability to multidimensional problems [47].

Two different RF models are trained in the experiments. The first model is for one-step forecasting, while the second model is for multi-output forecasting. Both models use the same inputs as the previous models and are trained and tested using the Scikit-Learn Random Forest Regressor module with default settings.

3.6. ANN

The ANN (Artificial Neural Network) model is an intelligent system used for solving complex issues in various applications, including optimization and prediction. The ANN structure comprises an input layer for data collection, an output layer for computed information, and one or more hidden layers connecting the input and output. Each neuron, the fundamental processing unit of a neural network, performs two tasks: receiving inputs and generating output. Inputs are multiplied by connection weights,

their products and biases are added, and then an activation function is used to generate output.

Two different ANN models are trained in the experiments. The first model, for one-step forecasting, uses first-order difference data from the previous 10 days, resulting in an input vector size of 10. It is enhanced by adding a dense layer of 24 units activated using the Rectified Linear Unit (ReLU) function and a 1-unit dense output layer for single-day prediction. The second model, for multi-output forecasting, uses the same input data. It includes a 24-unit dense layer and a 30-unit dense output layer, with the hidden layer activated using the ReLU function.

3.7. CNN

A standard CNN (Convolutional Neural Network) design includes an input layer, multiple hidden layers, and an output layer. The hidden layers consist of convolutional layers, an activation layer, pooling, and fully connected dense layers. The convolution layer, critical to the CNN model, accumulates discriminative features from the input using defined convolution filters. The activation layer introduces non-linearity with an activation function (e.g., ReLU, tanh, or sigmoid), helping to resolve the vanishing gradient problem during training. The pooling layer's main goal is to reduce the data representation size, the number of parameters, and the model's computational cost.

Two different CNN models are trained in the experiments. The first model, for one-step forecasting, uses first-order difference data from the previous 10 days with an input layer shape of 10x1. It includes a 16-filter convolutional layer with a 3-kernel and ReLU activation, followed by a max-pooling operation with a pool size of two. A second convolutional layer with a 32-filter and 3-kernel, along with ReLU activation, is added, followed by a GlobalMaxPooling1D operation and a 1-unit dense output layer. The second CNN model is similar but includes a 30-unit output layer for multi-output forecasting.

3.8. LSTM

LSTM (Long Short-Term Memory) is a type of RNN (Recurrent Neural Network) designed to address the problem of vanishing or exploding gradients. Its unique feature is the LSTM cell, which has specific gates: the input gate determines the relevance of incoming data, the forget gate decides what portions of the cell state to discard, and the output gate determines what information to forward to the next hidden state. Compared to traditional RNN models, LSTM can maintain long-term dependencies among

input data items, helping to alleviate the vanishing gradient problem.

Two different LSTM models are trained in the experiments. The first model, for one-step forecasting, uses first-order difference data from the previous 10 days, with an input layer shape of 10x1 and a hidden state dimension of 24. It includes a dense layer with 1 unit. The second model, for multi-output forecasting, uses the same input data. An LSTM layer with 24 internal units is added, followed by a GlobalMaxPooling1D operation and a dense output layer of 30 units.

3.9. Evaluation Criteria

In this research, two popular scale invariant metrics named Mean Absolute Percentage Error (MAPE) and R-squared (R^2) are used to evaluate the performance of forecasting methods. The MAPE is the mean of absolute percentage errors. One disadvantage of this metric is that if there is an actual value that equals zero, then the MAPE value equals infinity, and this makes no sense with regard to percentage. However, the preprocessed data used in this research does not contain zero values.

$$MAPE = \frac{1}{N}\sum_{i=1}^{N}\left|\frac{y_i - p_i}{y_i}\right| \qquad (1)$$

where N is the total number of data values, p_i is the predicted value, and y_i is the actual value for i[th] position. Because the MAPE value corresponds to the error in terms of percentages, the lower the MAPE value is, the better the forecast is. As indicated in Equation (2), the R^2 metric indicates how much variance is accounted for by the fitted model. It is a statistical measure that represents the proportion of the variance for a dependent variable that's explained by an independent variable or variables in a regression model. The higher the R^2 value represents the better the prediction performance [4].

$$R^2 = 1 - \frac{\sum_{i=1}^{N}(y_i - p_i)^2}{\sum_{i=1}^{N}(y_i - \overline{y})^2} \qquad (2)$$

where y_i and p_i correspond to the actual value and predicted value for i[th] position, respectively. $\overline{y}$ is the mean of the actual values.

4. Results and Discussion

In this section, we will first evaluate the forecasting performances of time series forecasting methods on pre-pandemic, in-pandemic, and entire datasets, according to the visuals in Table 1, Table 2, and Table

3. Based on these tables, we will compare the performances of the methods with each other. Additionally, the best performances will be evaluated according to the MAPE and R^2 values presented in Table 4 and Table 5. Then, we will examine the impact of the COVID-19 pandemic on forecasting performance. Finally, the effects of multi-step and multi-output techniques on forecasting performance will be explored, and we will determine which technique is superior.

One-step forecasts are used to predict the next step's observation. In contrast, multi-step forecasts are utilized to predict a series of future values based on observed time series data. The multi-output technique involves creating a single model capable of predicting the entire forecast sequence in one attempt [48].

Table 1. Comparison of actual values and predicted values by LR and SVR.
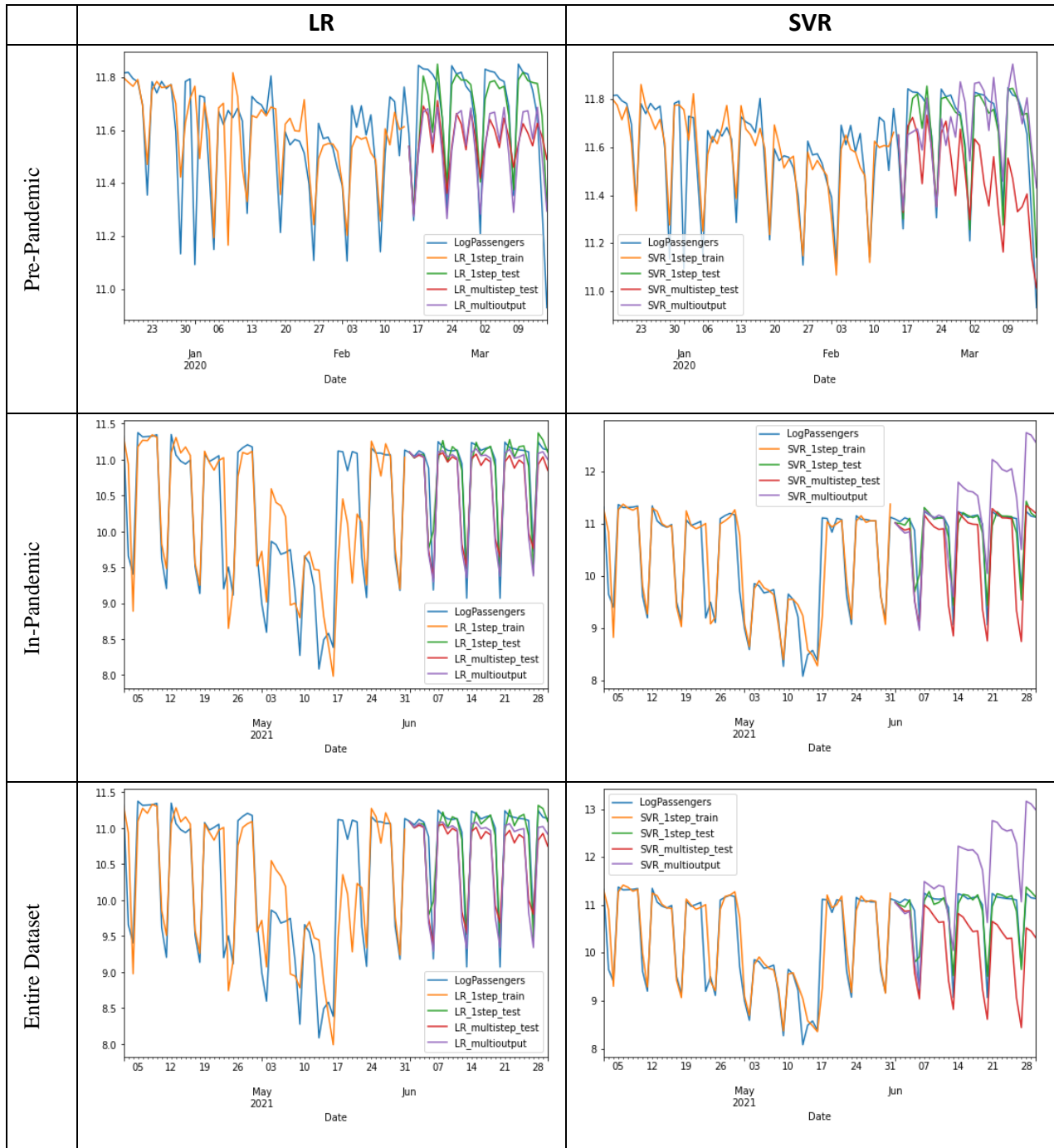
Table 2. Comparison of actual values and predicted values by RF and ANN.
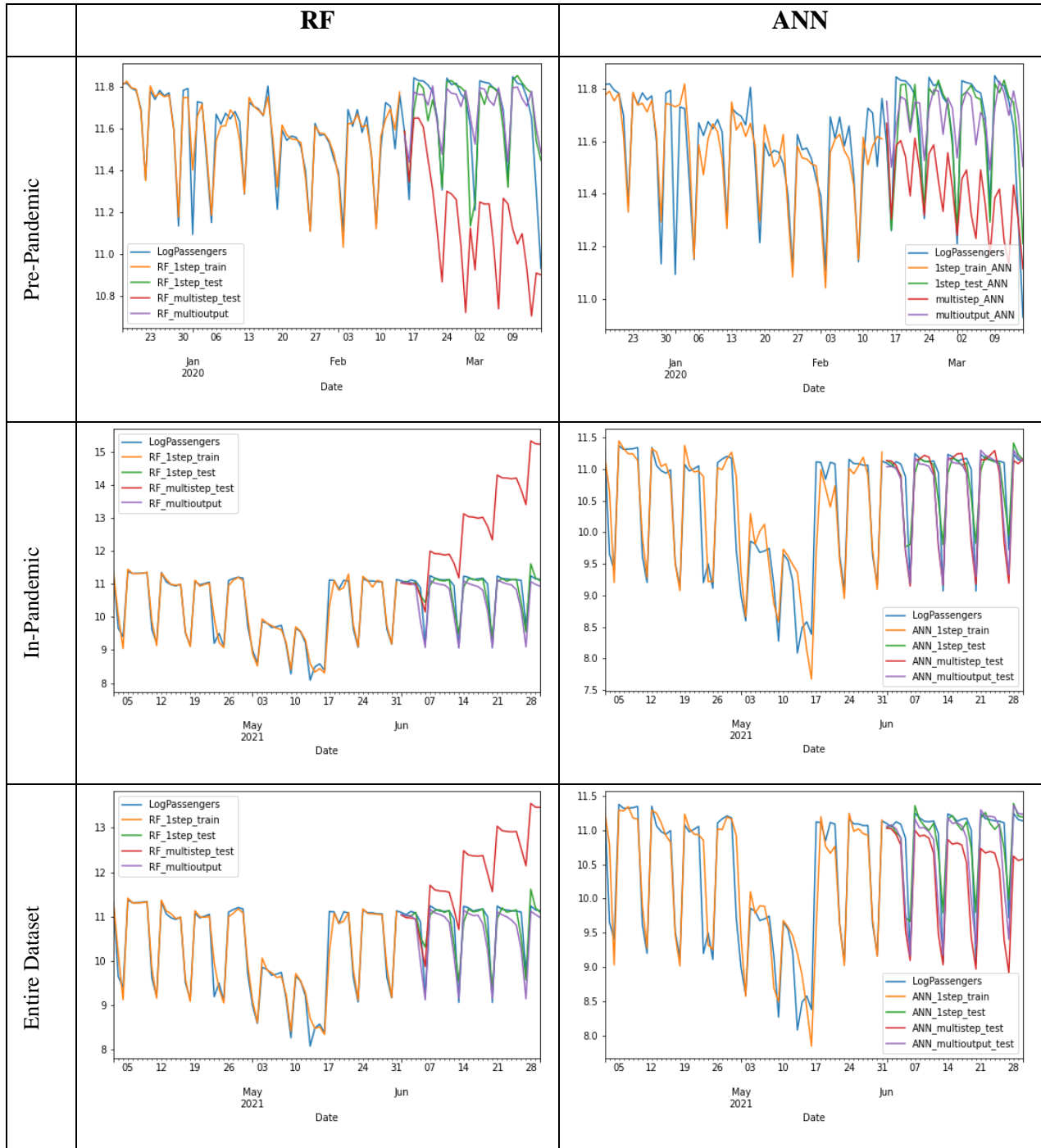
In this study, both multi-step and multi-output forecasting techniques are applied to the models, as they are designed for 30-day time series forecasting.

Upon examining the figures in Table 1, Table 2, and Table 3 for the pre-pandemic dataset, it is evident that the multi-output performances of all models are superior to their multi-step counterparts. In all models except LR, a clear superiority of multi-output performances over multi-step performances is observed. When comparing the visuals in Table 1,

Table 2, and Table 3 in terms of multi-output performance, it is apparent that RF provides the best performance, while LR exhibits the least impressive results.

When comparing the multi-step performances of the methods on the pre-pandemic dataset, it is evident that the LR model demonstrates the best performance, while the RF model exhibits the worst. As shown in Table 4 and Table 5, the LR model

achieved the best MAPE (1.57) and the best R^2 (0.17)
values for multi-step forecasting.

Table 3. Comparison of actual values and predicted values by LSTM and CNN.
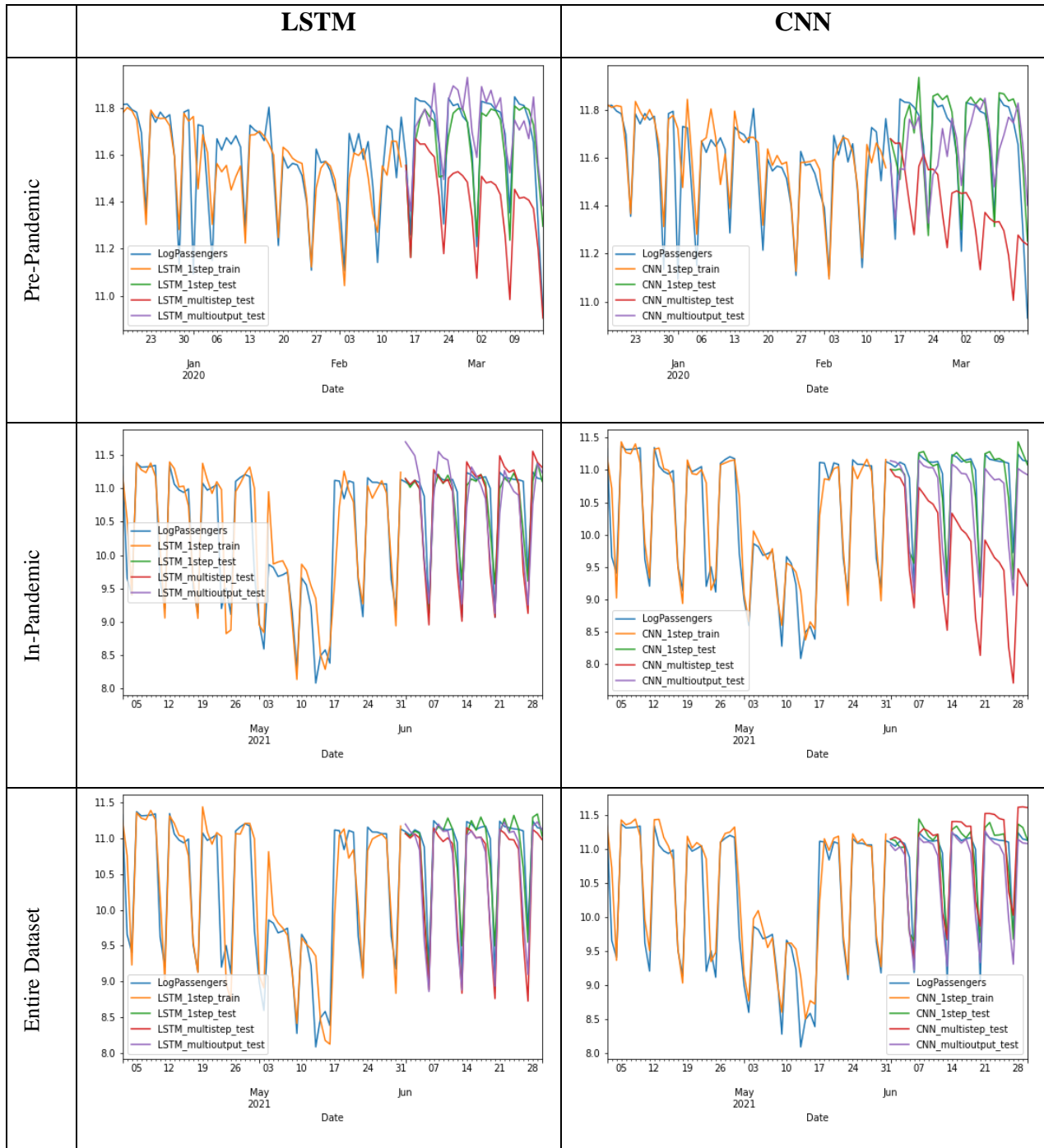
Conversely, the RF model's performance is the poorest, as indicated by its MAPE (4.30) and R^2 (-4.951) values.

Additionally, when considering the multi-output values in Table 4 and Table 5, it is observed that the RF model achieves the best MAPE (0.83) and R^2 (0.616) values, while the LR model shows the worst performance with a MAPE of 1.39 and an R^2 of 0.366.

Upon examining the visuals in Table 1, Table 2, and Table 3 for the in-pandemic dataset, it is noted that the multi-step performance of the SVR model is significantly better than its multi-output performance, whereas the multi-output performances of the RF and CNN models are notably better than their multi-step counterparts.

Analyzing the values in Table 4 and Table 5 reveals that the multi-output performance of the LR

and ANN models is superior to their multi-step performance, while the LSTM model performs better in multi-step forecasting than in multi-output forecasting. For the in-pandemic dataset, the ANN model achieves the best multi-output performance with a MAPE value of 2.11, and the RF model attains an R^2 value of 0.644. The best multi-step performances are achieved by the ANN model with a MAPE of 2.37 and the LR model with an R^2 of 0.498. The SVR model exhibits the worst multi-output performance with a MAPE of 5.39 and an R^2 of -0.35, whereas the RF model shows the poorest multi-step performance with a MAPE of 17.44 and an R^2 of -11.547.

When analyzing the visuals in Table 1, Table 2, and Table 3 for the entire dataset, it is observed that the multi-output performances of all models surpass their multi-step counterparts, except for the SVR model. These tables also indicate that the RF model demonstrates the worst multi-step performance. Upon examining the MAPE and R^2 values in Table 4 and Table 5, it is seen that the LSTM model, with a MAPE of 2.99, and the CNN model, with an R^2 value of 0.55, achieve the best multi-step performance. Conversely, the RF model records the worst multi-step performance, with a MAPE of 10.86 and an R^2 value of -3.696.

It is observed that the CNN model, with a MAPE value of 2.10, and the RF model, with an R^2 value of 0.706, exhibit the best multi-output performance. Conversely, the SVR model shows the worst multi-output performance, with a MAPE value of 8.32 and an R^2 value of -1.816.

MAPE is a suitable metric for benchmarking performance across different datasets. Therefore, performance comparisons of pre-pandemic, in-pandemic, and entire datasets are made based on MAPE values. Table 4 indicates that the best MAPE value for the pre-pandemic dataset is 0.83 for the in-pandemic dataset, it is 2.11; and for the entire dataset, it is 2.10. Evaluating the best MAPE values from these three different datasets suggests that the COVID-19 pandemic has negatively impacted forecasting performance. Additionally, Tables 4 and 5 reveal that all the best results are achieved using the multi-output method. Although the multi-step performance of some models surpasses their multi-output performance, the multi-output method generally performs much better and has achieved the best results. Therefore, choosing the multi-output technique would be a more logical approach.

Table 4. MAPE results of different forecasting methods.

		LR(%)	SVR(%)	RF(%)	ANN(%)	LSTM(%)	CNN(%)
Pre-Pandemic	Multi-step	1.57	1.77	4.30	2.39	2.17	2.99
	Multi-output	1.39	1.09	0.83	1.14	0.95	1.13
In-Pandemic	Multi-step	2.82	3.19	17.44	2.37	2.45	10.53
	Multi-output	2.38	5.39	2.44	2.11	3.41	2.92
Entire Dataset	Multi-step	3.24	6.03	10.86	4.75	2.99	3.15
	Multi-output	2.75	8.32	2.19	2.17	2.80	2.10

Table 5. R^2 results of different forecasting methods.

		LR	SVR	RF	ANN	LSTM	CNN
Pre-Pandemic	Multi-step	0.170	-0.066	-4.951	-0.903	-0.375	-1.787
	Multi-output	0.366	0.518	0.616	0.419	0.597	0.434
In-Pandemic	Multi-step	0.498	0.099	-11.547	0.488	0.467	-3.249
	Multi-output	0.504	-0.350	0.644	0.577	0.430	0.439
Entire Dataset	Multi-step	0.459	-0.584	-3.696	-0.119	0.353	0.550
	Multi-output	0.449	-1.816	0.706	0.617	0.383	0.609

4.1. Benefits and Advantages of the Study

This study presents several significant benefits and advantages in the field of passenger flow forecasting on trams using machine learning algorithms. The key benefits of this research can be summarized as follows:

- **Enhanced Forecasting Accuracy:** By employing a range of machine learning algorithms, including LR, SVR, RF, ANN,

CNN, and LSTM, this study demonstrates improved accuracy in forecasting tram passenger flow. The use of MAPE and R^2 metrics for performance evaluation further substantiates the reliability of the forecasts.

- **Innovative Data Preprocessing Techniques:** The application of log transform and first-order difference techniques for data preprocessing is a novel approach in this field. These methods effectively handle the challenges of large fluctuations, non-linearity, and periodicity in passenger numbers, leading to more accurate forecasting models.
- **Comprehensive Analysis of Pandemic Impact:** The study provides a thorough analysis of the impact of the COVID-19 pandemic on passenger flow forecasting. By dividing the dataset into pre-pandemic, in-pandemic, and entire dataset periods, the research offers valuable insights into how extraordinary events can affect passenger behavior and forecasting accuracy.
- **Practical Implications for Urban Transportation Management:** The findings of this study have practical implications for urban transportation planning and management. Accurate forecasting models can assist in efficient resource allocation, network design, and frequency setting of tram services, contributing to better urban transportation systems.
- **Methodological Contributions:** The study contributes methodologically to the field by comparing multi-step and multi-output forecasting techniques. This comparative analysis not only enhances the understanding of different forecasting methods but also guides future research in selecting appropriate techniques based on specific requirements.
- **Data Set Creation and Sharing:** The creation and public sharing of the Kayseri tram passenger flow dataset is a valuable contribution. It not only facilitates further research in this area but also promotes transparency and reproducibility in scientific studies.
- **Cross-Disciplinary Applicability:** While focused on tram passenger flow, the methodologies and findings of this study have potential applicability in other domains facing similar forecasting challenges, thereby extending its impact beyond the field of urban transportation.

This comprehensive approach to forecasting tram passenger flow using machine learning techniques underscores the study's contribution to both the academic and practical realms of intelligent transportation systems. The advantages highlighted in this section demonstrate the study's relevance, innovation, and applicability in addressing complex challenges in passenger flow forecasting.

5. Conclusion

In this study, daily passenger flow data of the Kayseri tram between January 1, 2018 and July 1, 2021 is used, and three different datasets are created using the pre-pandemic period, the pandemic period, and the entire dataset in order to observe the effects of the COVID-19 pandemic on the forecasting performance. Log transform and first-order difference techniques are applied to the datasets, respectively, in order to clear the noise in the data, obtain a more linear structure, and eliminate the seasonal structure from the data. LR, SVM, RF, ANN, CNN, and LSTM models are trained on three different datasets to estimate the passenger numbers for the next 30 days by looking at the passenger numbers of the previous 10 days. Multi-step and multi-output techniques are used to estimate the last 30 days.

From the results obtained, it is understood that the multi-output technique has superior performance to the multi-step technique and that the COVID-19 pandemic has a negative effect on forecasting performance. According to the R^2 metric, the RF model performs best on all datasets. According to the MAPE metric, RF on the pre-pandemic dataset, ANN on the in-pandemic dataset, and CNN on the entire dataset show the best performances. It is understood that the RF model, which uses the multi-output technique in the normal order, that is, in the pre-pandemic period, can predict the number of 30-day Kayseri passengers with quite high success.

In the future, efforts to develop machine learning methods combined with meta-heuristics and bio-inspired algorithms will be important in terms of both reducing the negative impact of the COVID-19 pandemic on forecasting performance and improving success.

Data availability. The dataset investigated in this study is available at

https://raw.githubusercontent.com/kagandedeturk/TimeSeries/main/Tramvay.csv .

Conflict of Interest Statement

There is no conflict of interest between the authors.

Statement of Research and Publication Ethics

The study is complied with research and publication ethics.

References

[1]   D. Li *et al.*, "Percolation transition in dynamical traffic network with evolving critical bottlenecks," *Proceedings of the National Academy of Sciences*, vol. 112, no. 3, pp. 669–672, 2014. doi:10.1073/pnas.1419185112.

[2]   M. Ni, Q. He, and J. Gao, "Forecasting the subway passenger flow under event occurrences with social media," *IEEE Transactions on Intelligent Transportation Systems*, pp. 1–10, 2016. doi:10.1109/tits.2016.2611644.

[3]   J. Yu, "Short-Term Airline Passenger Flow Prediction Based on the Attention Mechanism and Gated Recurrent Unit Model," *Cognitive Computation*, vol. 14, no. 2, pp. 693–701, 2022. doi:10.1007/s12559-021-09991-x .

[4]   A. Kanavos, F. Kounelis, L. Iliadis, and C. Makris, "Deep Learning Models for Forecasting Aviation Demand Time Series," *Neural Computing and Applications*, vol. 33, no. 23, pp. 16329–16343, 2021. doi:10.1007/s00521-021-06232-y

[5]   C. Li, X. Wang, Z. Cheng, and Y. Bai, "Forecasting Bus Passenger Flows by Using a Clustering-Based Support Vector Regression Approach," *IEEE Access*, vol. 8, pp. 19717–19725, 2020, doi: 10.1109/access.2020.2967867.

[6]   S. Anvari, S. Tuna, M. Canci, and M. Turkay, "Automated Box–Jenkins Forecasting Tool With an Application for Passenger Demand in Urban Rail Systems," *Journal of Advanced Transportation*, vol. 50, no. 1, pp. 25–49, Sep. 2015, doi: 10.1002/atr.1332.

[7]   A. Samagaio and M. Wolters, "Comparative Analysis of Government Forecasts for the Lisbon Airport," *Journal of Air Transport Management*, vol. 16, no. 4, pp. 213–217, Jul. 2010, doi: 10.1016/j.jairtraman.2009.09.002.

[8]   M. Milenković, L. Švadlenka, V. Melichar, N. Bojović, and Z. Avramović, "Sarima Modelling Approach for Railway Passenger Flow Forecasting," *Transport*, pp. 1–8, Mar. 2016, doi: 10.3846/16484142.2016.1139623.

[9]   X. Xiao, J. Yang, S. Mao, and J. Wen, "An Improved Seasonal Rolling Grey Forecasting Model Using a Cycle Truncation Accumulated Generating Operation for Traffic Flow," *Applied Mathematical Modelling*, vol. 51, pp. 386–404, Nov. 2017, doi: https://doi.org/10.1016/j.apm.2017.07.010.

[10]   A. Stathopoulos and M. G. Karlaftis, "A Multivariate State Space Approach for Urban Traffic Flow Modeling and Prediction," *Transportation Research Part C: Emerging Technologies*, vol. 11, no. 2, pp. 121–135, Apr. 2003, doi: https://doi.org/10.1016/s0968-090x(03)00004-4.

[11]   X. Tang and G. Deng, "Prediction of Civil Aviation Passenger Transportation Based on ARIMA Model," *Open Journal of Statistics*, vol. 06, no. 05, pp. 824–834, 2016, doi: https://doi.org/10.4236/ojs.2016.65068.

[12]   N. K. Chauhan and K. Singh, "A Review on Conventional Machine Learning vs Deep Learning," in 2018 *International Conference on Computing, Power and Communication Technologies (GUCON)*, Sep. 2018, doi: https://doi.org/10.1109/gucon.2018.8675097.

[13]   Y. Park, Y. Choi, K. Kim, and J. K. Yoo, "Machine Learning Approach for Study on Subway Passenger Flow," *Scientific Reports*, vol. 12, no. 1, p. 2754, Feb. 2022, doi: https://doi.org/10.1038/s41598-022-06767-7.

[14]   F. Moretti, S. Pizzuti, S. Panzieri, and M. Annunziato, "Urban Traffic Flow Forecasting Through Statistical and Neural Network Bagging Ensemble Hybrid Modeling," *Neurocomputing*, vol. 167, pp. 3–7, Nov. 2015, doi: https://doi.org/10.1016/j.neucom.2014.08.100.

[15]   B. Sun, W. Cheng, P. Goswami, and G. Bai, "Short-Term Traffic Forecasting using Self-Adjusting K-Nearest Neighbours," *IET Intelligent Transport Systems*, vol. 12, no. 1, pp. 41–48, Feb. 2018, doi: https://doi.org/10.1049/iet-its.2016.0263.

[16]   J. Guo, W. Huang, and B. M. Williams, "Adaptive Kalman Filter Approach for Stochastic Short-Term Traffic Flow Rate Prediction and Uncertainty Quantification," *Transportation Research Part C: Emerging Technologies*, vol. 43, pp. 50–64, Jun. 2014, doi: https://doi.org/10.1016/j.trc.2014.02.006.

[17]   Y. Sun, B. Leng, and W. Guan, "A Novel Wavelet-Svm Short-Time Passenger Flow Prediction in Beijing Subway System," *Neurocomputing*, vol. 166, pp. 109–121, Oct. 2015, doi: https://doi.org/10.1016/j.neucom.2015.03.085.

[18]   L. Li, X. Chen, and L. Zhang, "Multimodel Ensemble for Freeway Traffic State Estimations," *IEEE Transactions on Intelligent Transportation Systems*, vol. 15, no. 3, pp. 1323–1336, Jun. 2014, doi: https://doi.org/10.1109/tits.2014.2299542.

[19]   J. Zhang, F. Chen, Z. Cui, Y. Guo, and Y. Zhu, "Deep Learning Architecture for Short-Term Passenger Flow Forecasting in Urban Rail Transit," *IEEE Transactions on Intelligent Transportation Systems*, vol. 22, no. 11, pp. 7004–7014, Nov. 2021, doi: https://doi.org/10.1109/tits.2020.3000761.

[20]   X. Feng, T. Gan, and X. Wang, "Feedback Analysis of Interaction between Urban Densities and Travel Mode Split," *International Journal of Simulation Modelling*, vol. 14, no. 2, pp. 349–358, Jun. 2015, doi: 10.2507/ijsimm14(2)co9.

[21]   Y. Wei and M.-C. Chen, "Forecasting The Short-Term Metro Passenger Flow with Empirical Mode Decomposition and Neural Networks," *Transportation Research Part C: Emerging Technologies*, vol. 21, no. 1, pp. 148–162, Apr. 2012, doi: https://doi.org/10.1016/j.trc.2011.06.009.

[22]   X. Ma, Z. Tao, Y. Wang, H. Yu, and Y. Wang, "Long Short-Term Memory Neural Network for Traffic Speed Prediction Using Remote Microwave Sensor Data," *Transportation Research Part C: Emerging Technologies*, vol. 54, pp. 187–197, May 2015, doi: https://doi.org/10.1016/j.trc.2015.03.014.

[23]   P. He, "Optimization and Simulation of Remanufacturing Production Scheduling under Uncertainties," *International Journal of Simulation Modelling*, vol. 17, no. 4, pp. 734–743, Dec. 2018, doi: https://doi.org/10.2507/ijsimm17(4)co20.

[24]   M. Castro-Neto, Y.-S. Jeong, M.-K. Jeong, and L. D. Han, "Online-Svr for Short-Term Traffic Flow Prediction under Typical and Atypical Traffic Conditions," *Expert Systems with Applications*, vol. 36, no. 3, pp. 6164–6173, Apr. 2009, doi: https://doi.org/10.1016/j.eswa.2008.07.069.

[25]   G. Xie, S. Wang, Y. Zhao, and K. K. Lai, "Hybrid Approaches Based on Lssvr Model for Container Throughput Forecasting: A Comparative Study," *Applied Soft Computing*, vol. 13, no. 5, pp. 2232–2241, May 2013, doi: https://doi.org/10.1016/j.asoc.2013.02.002.

[26]   X. Wang, N. Zhang, Y. Zhang, and Z. Shi, "Forecasting of Short-Term Metro Ridership with Support Vector Machine Online Model," *Journal of Advanced Transportation*, vol. 2018, pp. 1–13, Jun. 2018, doi: https://doi.org/10.1155/2018/3189238.

[27]   A. Singhal, C. Kamga, and A. Yazici, "Impact of Weather on Urban Transit Ridership*," Transportation Research Part A: Policy and Practice*, vol. 69, pp. 379–391, Nov. 2014, doi: https://doi.org/10.1016/j.tra.2014.09.008.

[28]   A. Koesdwiady, R. Soua, and F. Karray, "Improving Traffic Flow Prediction With Weather Information in Connected Cars: A Deep Learning Approach," *IEEE Transactions on Vehicular Technology*, vol. 65, no. 12, pp. 9508–9517, Dec. 2016, doi: https://doi.org/10.1109/tvt.2016.2585575.

[29]   C. Li, R.-V. Sanchez, G. Zurita, M. Cerrada, D. Cabrera, and R. E. Vásquez, "Multimodal Deep Support Vector Classification with Homologous Features and Its Application to Gearbox Fault Diagnosis," *Neurocomputing*, vol. 168, pp. 119–127, Nov. 2015, doi: https://doi.org/10.1016/j.neucom.2015.06.008

[30]   M.-L. Huang, "Intersection Traffic Flow Forecasting Based on N-Gsvr with a New Hybrid Evolutionary Algorithm," *Neurocomputing*, vol. 147, pp. 343–349, Jan. 2015, doi: https://doi.org/10.1016/j.neucom.2014.06.054

[31]   Y. Zhang and Y. Liu, "Analysis of Peak and Non-Peak Traffic Forecasts Using Combined Models," *Journal of Advanced Transportation*, vol. 45, no. 1, pp. 21–37, Sep. 2010, doi: https://doi.org/10.1002/atr.128.

[32]   M. Khashei and M. Bijari, "A Novel Hybridization of Artificial Neural Networks and Arıma Models for Time Series Forecasting," *Applied Soft Computing*, vol. 11, no. 2, pp. 2664–2675, Mar. 2011, doi: https://doi.org/10.1016/j.asoc.2010.10.015.

[33]   T. Pant, C. Han, and H. Wang, "Examination of Errors of Table Integration in Flamelet/Progress Variable Modeling of a Turbulent Non-Premixed Jet Flame," *Applied Mathematical Modelling*, vol. 72, pp. 369–384, Aug. 2019, doi: https://doi.org/10.1016/j.apm.2019.03.016.

[34]   X. Wang, L. Huang, H. Huang, B. Li, Z. Xia, and J. Li, "An Ensemble Learning Model for Short-Term Passenger Flow Prediction," *Complexity*, vol. 2020, pp. 1–13, Dec. 2020, doi: https://doi.org/10.1155/2020/6694186.

[35]   H. Li, J. Bai, and Y. Li, "A Novel Secondary Decomposition Learning Paradigm with Kernel Extreme Learning Machine for Multi-Step Forecasting of Container Throughput," *Physica A: Statistical Mechanics and its Applications*, vol. 534, p. 122025, Nov. 2019, doi: https://doi.org/10.1016/j.physa.2019.122025.

[36]   M. Niu, Y. Hu, S. Sun, and Y. Liu, "A Novel Hybrid Decomposition-Ensemble Model Based on Vmd and Hgwo for Container Throughput Forecasting," *Applied Mathematical Modelling*, vol. 57, pp. 163–178, May 2018, doi: https://doi.org/10.1016/j.apm.2018.01.014.

[37]   Y. Li and C. Ma, "Short-Time Bus Route Passenger Flow Prediction Based on a Secondary Decomposition Integration Method," *Journal of Transportation Engineering, Part A: Systems*, vol. 149, no. 2, Feb. 2023, doi: https://doi.org/10.1061/jtepbs.teeng-7496.

[38]   H. Nguyen, L. Kieu, T. Wen, and C. Cai, "Deep Learning Methods in Transportation Domain: A Review," *IET Intelligent Transport Systems*, vol. 12, no. 9, pp. 998–1004, Jul. 2018, doi: https://doi.org/10.1049/iet-its.2018.0064.

[39]   H. Gao, X. Qin, R. J. D. Barroso, W. Hussain, Y. Xu, and Y. Yin, "Collaborative Learning-Based Industrial IoT API Recommendation for Software-Defined Devices: The Implicit Knowledge Discovery Perspective," *IEEE Transactions on Emerging Topics in Computational Intelligence*, vol. 6, no. 1, pp. 66–76, Feb. 2022, doi: https://doi.org/10.1109/TETCI.2020.3023155.

[40]   H. Gao, Y. Zhang, H. Miao, R. J. D. Barroso, and X. Yang, "SDTIOA: Modeling the Timed Privacy Requirements of IoT Service Composition: A User Interaction Perspective for Automatic Transformation from BPEL to Timed Automata," *Mobile Networks and Applications*, vol. 26, no. 6, pp. 2272–2297, Nov. 2021, doi: https://doi.org/10.1007/s11036-021-01846-x.

[41]   A. A. Amer, I. E. Talkhan, R. Ahmed, and T. Ismail, "An Optimized Collaborative Scheduling Algorithm for Prioritized Tasks with Shared Resources in Mobile-Edge and Cloud Computing Systems," *Mobile Networks and Applications*, Apr. 2022, doi: https://doi.org/10.1007/s11036-022-01974-y.

[42]   X. Ma, H. Xu, H. Gao, and M. Bian, "Real-time Multiple-Workflow Scheduling in Cloud Environment," *Research Square*, Feb. 2021, Published, doi: 10.21203/rs.3.rs-170491/v1.

[43]   K. Peng, W. Bai, and L. WU, "Passenger Flow Forecast of Railway Station Based on Improved Lstm," 2020 *2nd International Conference on Advances in Computer Technology, Information Science and Communications (CTISC)*, Mar. 2020, doi: https://doi.org/10.1109/ctisc49998.2020.00033.

[44]   Dedeturk, B.K.: Dataset. https://raw.githubusercontent.com/kagandedeturk/TimeSeries/main/Tramvay.csv (accessed May 12, 2023).

[45]   W. Xu, H. Peng, X. Zeng, F. Zhou, X. Tian, and X. Peng, "A Hybrid Modelling Method for Time Series Forecasting Based nn a Linear Regression Model and Deep Learning," *Applied Intelligenc*e, vol. 49, no. 8, pp. 3002–3015, Feb. 2019, doi: https://doi.org/10.1007/s10489-019-01426-3.

[46]   Y. Bai et al., "A Comparison of Dimension Reduction Techniques for Support Vector Machine Modeling of Multi-Parameter Manufacturing Quality Prediction," *Journal of Intelligent Manufacturing*, vol. 30, no. 5, pp. 2245–2256, Jan. 2018, doi: https://doi.org/10.1007/s10845-017-1388-1.

[47]   X. Qiu, L. Zhang, P. Nagaratnam Suganthan, and G. A. J. Amaratunga, "Oblique Random Forest Ensemble via Least Square Estimation for Time Series Forecasting," Information Sciences, vol. 420, pp. 249–262, Dec. 2017, doi: https://doi.org/10.1016/j.ins.2017.08.060.

[48]   T. Xiong, Y. Bao, and Z. Hu, "Beyond One-Step-Ahead Forecasting: Evaluation of Alternative Multi-Step-Ahead Forecasting Models for Crude Oil Prices," *Energy Economics*, vol. 40, pp. 405–415, Nov. 2013, doi: https://doi.org/10.1016/j.eneco.2013.07.028.

[49]   H. I. Kazıcı, S. Kosunalp, and M. Arucu, "Its-Pro-Flow: A New Enhanced Short-Term Traffıc Flow Prediction For Intelligent Transportation Systems," *Scientific Journal of Silesian University of Technology. Series Transport*, vol. 120, pp. 117–136, Sep. 2023, doi: 10.20858/sjsutst.2023.120.8.

Advanced Exergy Assessment of an Air Source Heat Pump Unit

Ayşegül GÜNGÖR ÇELİK[1*]

[1]*Manisa Celal Bayar University, Faculty of Hasan Ferdi Turgutlu Technology,*
Department of Mechanical Engineering, Manisa, Turkey
ORCID: 0000-0002-9451-1607

Keywords: Advance exergy, Heat pump, Exergy.

Abstract

Energy conversation systems performance could be assessed by conventional exergy-based analysis methods. Along with the conventional exergy approach, the sources and amounts of the exergy destructions can be determined, and a possible direction for enhancement can be suggested. Nevertheless, interactions between system components (endogenous/exogenous) and technical constraints (avoidable/unavoidable) cannot be identified with any conventional analysis. Therefore, the real potential to improve and optimize can be misdirected. The advanced exergy-based analysis seeks to overcome this limitation. An air-source heat pump unit was assessed using conventional and advanced exergy analysis approaches, respectively. Avoidable/unavoidable and endogenous/exogenous exergy destructions, modified exergy efficiencies, and modified exergy loss ratios were calculated for every single component of the system. The results of the analysis showed that while the evaporator and condenser efficiencies could be improved through design improvements, the internal operating conditions were mainly responsible for the inefficiencies associated with the compressor. The analysis indicated that it was possible to improve evaporator and condenser efficiency by making design improvements. The efficiency of the compressor was mainly determined by the internal conditions in which the compressor operated.

1. Introduction

The two most important problems of the in the not-too-distant past are energy shortages arising from overuse and ecological contamination. Therefore, existing energy resources must be used more effectively and economically; otherwise enhanced exergy approaches should be employed more widely in thermal systems. The largest contributor to household energy consumption is residential space air conditioning, along with the processing of domestic hot water. According to the study of Jung et al. [1], energy demand for heating and cooling buildings is predicted to rise by up to 50% by 2050 as energy consumption grows in many regions.

Heat pumps (HPs) are an emerging technology that is gaining popularity in heating and air conditioning around the world due to their environmentally favorable and efficient use of energy in comparison to standard systems. Exergy analysis is a very powerful method that can be efficiently applied to the design of an energy system. Also, this method provides essential knowledge for selecting the appropriate design parameters of the components and the mode of operation [2]. Conventional exergy-based methodologies are utilized to measure the effectiveness of thermal energy conversion systems. Traditional exergy-based analysis reveals the sources, amounts, and reasons for irreversible losses (exergy losses), costs, and environmental effects and identifies a broad area for enhancement. But interactions between system components and current technical restrictions cannot be identified with any of the conventional analyses. Therefore, a more effective way to improve energy conversion systems is to separate the exergy destruction that occurs in every single component of

the system. This limitation could be removed by implementing advanced exergy-based analyses. A more complex exergy analysis where exergy destruction is separated into avoidable, unavoidable, exogenous, and endogenous parts is called advanced exergy analysis [3].

By implementing the enhanced exergy approach to a military turbojet engine, the types of exergy destruction in the system were determined, and it was found that elements of the jet engine related to ignition should be improved [4]. Chen compared the refrigeration system of the ejector and the vapor compression refrigeration system, performing an enhanced exergy approach [5]. Morosuk and Tsatsaronis [6] investigated the efficiency of an absorption refrigeration machine by implementing the advanced exergy analysis approach. Endogenous avoidable and exogenous avoidable exergy destruction values are remarkable in improving the components in the system one by one. In the study, it is recommended to make an advanced exergoeconomic evaluation by calculating the exergy destruction as well as the initial investment costs by dividing them into sections. The advanced exergy and exergoeconomy analysis methods performed by Vuckovic et al. [7], for a real industrial facility. It was revealed that the performance of the system would be improved by enhancing the operating parameters of the boiler. The natural gas liquefaction and production facilities are evaluated regarding advanced exergoeconomic and exergy analysis, and it is revealed that most of the exergy destruction was exogenous and the exergy destruction in other units was endogenous. The researchers also found that endogenous exergy destruction leads to the greatest costs, according to the results of the exergo-economic analysis [8]. Hepbaşlı and Keçebaş [9] implied an advanced exergy analysis method to assess the improvement potential of a geothermal-sourced central heating system and to reveal the contribution of the system components to this improvement potential rate. The significance of exergy analysis has been increasing in recent years in order to ensure efficient and effective use of energy. With conventional exergy analysis, the location, size, cost, and environmental effects of irreversibility are determined, and general improvements are recommended accordingly. Yet, this information is not sufficient for the presentation of certain insights. In order to identify the realistic potential and to deduce how to improve, advanced exergy analysis based on the splitting of exergy losses should be carried out. The reason for this is that, given the present state of knowledge, some portion of the

exergy destruction could be unavoidable (defined by the division of exergy losses into unavoidable and avoidable fractions), some may be a consequence of exergy losses on the rest of the components of the present thermal system under consideration (exogenous exergy destruction), and therefore, rather than just improving the component with the largest exergy destruction, it may be valuable to enhance the rest of the components [10]. To overcome the above drawbacks, extended exergy analysis has been suggested. The division of exergy destructions into avoidable endogenous, unavoidable endogenous, avoidable exogenous, and unavoidable exogenous in advanced exergy analysis enables it to yield insightful results that conventional exergy analysis cannot. [11].

In the present study, an air source heat pump test unit was installed in the laboratory of Manisa Celal Bayar University, Türkiye, while it was examined through conventional and advanced exergy analysis methods under experimental conditions. First, the exergy destruction rate, the exergy efficiency coefficient, the relative irreversibility, and the enhancement possibility of the individual system components were computed with the conventional exergy analysis approach. After that, advanced exergy analyses were conducted by dividing the exergy destructions into parts. In this regard, the objectives of the current study are to apply advanced exergy analysis to the heat pump unit for further understanding of the exergy destruction rates and then to reveal the possible improvement rate.

2. Material and Method

2.1. Experimental Heat Pump Unit

As the problems associated with energy efficiency and environmental pollution have gradually increased, the number of studies focusing on these issues has also significantly increased in recent years. HP technologies are recognized as important and environmentally friendly and have been used for many years in climate control applications (particularly heating and cooling). In this regard, an experimental setup of an air source heat pump unit has been operated at Manisa Celal Bayar University, Manisa, Türkiye. The conventional exergy and advanced (enhanced) exergy approaches regarding dividing the exergy destructions into unavoidable/avoidable and exogenous/endogenous sections have been performed. The modified illustration of the heat pump system appears in Figure 1.
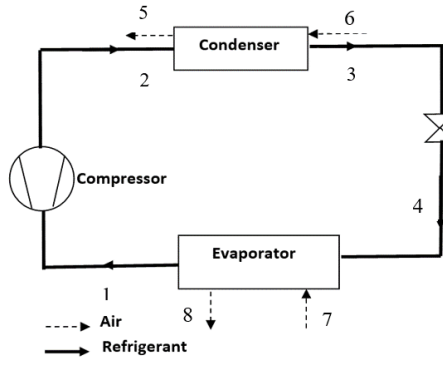
Figure 1. Schematic flow diagram of the air source heat pump system.

Figure 1 shows a schematic diagram of the HP system, which comprising compressor, condenser, expansion valve, and evaporator.

The assumptions used in the analysis are set out below:

(a) As there are no chemical transformations, all processes are in a steady state, and changes in potential and kinetic energy are ignored.

(b) The loss of heat in the heat exchangers is regarded as being of insignificant importance.

(c) The compressor operates adiabatic and irreversibly; the isentropic efficiency is taken as 0.85.

(d) The dead-state temperature is estimated at 10°C, and the pressure is taken at 101.325 kPa for the analysis.

2.2 Conventional Exergy Analysis

In the design and development of systems, exergy analysis is essential as it can indicate the location, type, and amount of exergy destruction and losses. With exergy analysis, the location and size of irreversibility (entropy generation) in a system can be determined, and development and improvement studies can be carried out to reduce irreversibility.

General exergy equations are employed for all system components on a component basis and then for the whole system. At the component level, the exergy product rate ($\dot{E}_{P,k}$) can be defined as the exergy output obtained per unit time, and the exergy fuel rate ($\dot{E}_{F,k}$) can be defined as the input provided to obtain the desired exergy output per unit time. The difference between the exergy fuel rate and the exergy product rate is identified as the exergy destruction rate in the system per time period. The coefficient of exergy efficiency and exergy destruction can be obtained from the standpoint of the exergetic product and the exergetic fuel, while the conventional exergy

balance can be explained as follows for the component kth [12]:

$$\dot{E}_{D,k} = \dot{E}_{F,k} - \dot{E}_{P,k} \tag{1}$$

$$\varepsilon_k = \frac{\dot{E}_{P,k}}{\dot{E}_{F,k}} = 1 - \frac{\dot{E}_{D,k}}{\dot{E}_{F,k}} \tag{2}$$

Other useful concepts such as "improvement potential" (IP), "exergetic factor" (f) and "relative irreversibility" (RI) are used to assess the effects of the system components on the whole system.

$$IP = (1 - \varepsilon)(\dot{E}_g - \dot{E}_ç) \tag{3}$$

$$f = \frac{\dot{E}_{F,k}}{\dot{E}_{F,total}} \cdot 100 \tag{4}$$

$$RI = \frac{\dot{E}_{D,k}}{\dot{E}_{D,total}} \cdot 100 \tag{5}$$

The principle of sustainability is consistent with the management of resources in terms of social, natural, and economic aspects. With environmental and cost control issues, it has become more important. A useful indicator for measuring the sustainability of the framework is the sustainability index. The exergetic sustainability index can be estimated on the basis of [13]:

$$SI = \frac{1}{1 - \varepsilon_k} \cdot 100 \tag{6}$$

2.3 Advanced Exergy Analysis

Conventional exergy analysis can be used to determine the sources, positions, and amounts of irreversibilities in a system and to suggest general improvements to the system. However, none of the conventional exergy analysis methods can be used to calculate the irreversibility resulting from the interaction between system components. Also, conventional exergy analysis is insufficient to reveal the realistic improvement potential due to current technological limitations. Splitting the exergy destruction into parts allows further understanding of the exergy destruction causes. Thereby, the accuracy of the analysis could be enhanced. In advanced exergy analysis, exergy destructions can be split into their endogenous and exogenous and/or avoidable and unavoidable parts [14]. Endogenous exergy destructions ($\dot{E}_{D,k}^{EN}$) for a component of the system are defined as the destructions that are independent of the other components of the system.

In order to estimate endogenous exergy destructions, it is assumed that every component of the system runs under theoretical circumstances, whereas the component under consideration is performing with the same level of efficiency as in the actual system. The inefficiencies caused by the other system components are indicated by the exogenous exergy destruction of one system component. The exogenous exergy destruction ($\dot{E}_{D,k}^{EX}$) of one component of the system indicates irreversibilities that are imposed by the other components of the system.

Endogenous and exogenous exergy destruction is calculated using the following equations:

$$\dot{E}x_{d,k}^{real} = \dot{E}x_{d,k}^{EN} + \dot{E}x_{d,k}^{EX} \tag{7}$$

$$\dot{E}x_{d,k}^{EN} = \dot{E}x_{P,k}^{real} \, x \left(\frac{\dot{E}x_{d,k}}{\dot{E}x_{P,k}}\right)^{EN} \tag{8}$$

Exergy destruction, costs, and environmental impacts that can be prevented by technically appropriate design and/or operational improvements in a system are considered the avoidable part of the exergy destruction. Determining the amount of avoidable exergy destruction in a system plays an important role in emphasizing the steps to be taken for the improvement of efficiency in the whole system. The remaining exergy destruction, which cannot be destroyed by any physical or technological development, is also considered unavoidable exergy destruction [15], [16]. In order to determine the unavoidable exergy destruction, it is assumed that the components of the system are operating at their maximum efficiency according to the current state of technology.

The expressions for the determination of unavoidable and avoidable exergy destructions are given [17]:

$$\dot{E}_{d,k}^{UN} = \dot{E}_{P,k}^{real} \cdot \left(\frac{\dot{E}_{d,k}}{\dot{E}_{P,k}}\right)^{UN} \tag{9}$$

$$\dot{E}x_{d,k}^{real} = \dot{E}x_{d,k}^{UN} + \dot{E}x_{d,k}^{AV} \tag{10}$$

In addition, the modified exergy efficiency coefficient is computed by means of the formula:

$$\varepsilon_k^* = \frac{\dot{E}x_{P,k}^{real}}{\dot{E}x_{F,k}^{real} - \dot{E}x_{D,k}^{UN}} \, x \, 100 \tag{11}$$

Once avoidable/unavoidable and exogenous / endogenous exergy destruction currents are found for all system components, these values are associated with avoidable (AV) and unavoidable (UN) exergy destruction values to obtain useful new terms. One can identify the irreversibility's regarding with the system component itself that can be removed by computing the avoidable endogenous exergy destruction.

$$\dot{E}_{D,k}^{UN,EN} = \dot{E}_{P,k}^{EN} \cdot \left(\frac{\dot{E}_{D,k}}{\dot{E}_{P,k}}\right)^{UN} \tag{12}$$

$$\dot{E}x_{d,k}^{UN,EX} = \dot{E}x_{d,k}^{UN} - \dot{E}x_{d,k}^{UN,EN} \tag{13}$$

Furthermore, the calculation of avoidable exogenous exergy destruction can highlight the irreversibility's that can be eliminated by structural enhancements to the entire system or by enhancing the performance of the residual elements and increasing the performance of the component under consideration.

$$\dot{E}x_{d,k}^{AV,EN} = \dot{E}x_{d,k}^{EN} - \dot{E}x_{d,k}^{UN,EN} \tag{14}$$

$$\dot{E}x_{d,k}^{AV,EX} = \dot{E}x_{d,k}^{AV} - \dot{E}x_{d,k}^{AV,EN} \tag{15}$$

3. Results and Discussion

This study evaluated an air source heat pump system based on the conventional exergy method using advanced exergy analysis and the division of the exergy destruction rates into different parts for the experimental values. Experimental data and calculations of the heat pump unit are shown in Table 1. Conventional exergy analysis parameters such as fuel exergy and product exergy rates for the whole system are shown in Table 2. Also, it shows exergetic parameters such as the exergy efficiency, improvement potential rate, exergy factor, sustainability index, relative irreversibility, and exergy destruction rates for the system components. The evaporator, followed by the compressor and the condenser, had the greatest exergy destruction rates. Moreover, the compressor and the expansion valve exergetic efficiency values demonstrated that these components have the highest value compared to other components. The exergetic improvement potential rate obtained was 1.618 for the whole unit. According to the exergetic factor (*f*) of the heat pump unit, the compressor and evaporator exhibit the greatest quantities of exergetic fuel rate, obtaining 36.97% and 27% of the total exergy fuel rate in the system, respectively. Regarding the relative irreversibility of the air-source heat pump system subcomponents, the condenser has the lowest *RI* rate at 13.84%, and the

evaporator has the highest rate at 57.47% due to its high irreversibility and low efficiency. The exergetic sustainability index (SI) values of the system and components are also given in Table 2. The evaporator has the lowest SI rate at 1.29, followed by the condenser at 1.36, since these components cause more exergy destruction than other components.

Table 1. The thermodynamic specifications determined from experimental data.

State	$\dot{m}$(kg/s)	T (°C)	h (kJ/kg)	s (kJ/kgK)	ex (kj/kg)
1	0.082	24	274.80	1.074	7.602
2	0.082	90.06	326.91	1.096	53.490
3	0.082	38	275.80	0.951	43.316
4	0.082	-5.3	275.80	0.974	36.775
6	0.638	22.1	33.79	-	0.255
7	0.638	25.7	37.44	-	0.425
8	0.638	20.7	31.73	-	0.177

A conventional exergy analysis can show the distribution of exergy destruction and the maximum exergy destruction ratios between individual components. It cannot identify the magnitude of the interactions between system components and the opportunities for improvement. Exergy destructions within a component are divided into categories such as endogenous/exogenous and avoidable/unavoidable in advanced exergy analysis. This method makes it possible to better identify the origins of thermodynamic inefficiency. This also makes it possible to refine and optimize the overall system. This approach specifies the exogenous exergy destruction with the effects of the interactions between the elements while estimating the endogenous exergy destruction with the operational losses within the component. In addition, technological and physical limitations on the efficiency of the system constitute unavoidable exergy destruction. Table 3 summarizes the conclusions of the advanced exergy approach of the present heat pump unit.

Table 2. The calculations of conventional exergy analysis.

Component	$\dot{E}_{F,k}$ (kW)	$\dot{E}_{P,k}$ (kW)	$\dot{E}_{D,k}$ (kW)	ε (%)	$I\dot{P}$ (kW)	RI (%)	SI	f (%)
I Compressor	4.500	3.763	0.737	83.62	0.121	16.61	6.10	36.97
II Condenser	0.834	0.220	0.614	26.38	0.452	13.84	1.36	6.85
III Expansion valve	3.552	3.016	0.536	84.90	0.081	12.08	6.62	29.18
IV Evaporator	3.287	0.736	2.551	22.40	1.979	57.47	1.29	27.00
Overall system	12.173	7.735	4.438	63.54	1.618	100.00	2.74	100.00

Table 3. Advanced exergy approach findings of heat pump unit.

Component	$\dot{E}_{D,k}^{EN}$	$\dot{E}_{D,k}^{EX}$	$\dot{E}_{D,k}^{UN}$	$\dot{E}_{D,k}^{AV}$	$\dot{E}_{D,k}^{UN}$ (kW)		$\dot{E}_{D,k}^{AV}$ (kW)	
	(kW)	(kW)	(kW)	(kW)	$\dot{E}_{D,k}^{UN,EN}$ (kW)	$\dot{E}_{D,k}^{UN,EX}$ (kW)	$\dot{E}_{D,k}^{AV,EN}$ (kW)	$\dot{E}_{D,k}^{AV,EX}$ (kW)
I Compressor	0.511	0.226	0.245	0.491	0.375	-0.134	0.135	0.360
II Condenser	0.117	0.497	0.185	0.428	0.885	-0.532	-0.768	1.029
III Expansion valve	0.458	0.077	0.498	0.037	0.430	0.163	0.027	-0.085
IV Evaporator	0.342	2.208	1.356	1.194	2.00	0.359	-1.666	1.849
Overall system	1.429	3.009	3.059	1.380				

When considering the whole system on the basis of running operation, the unavoidable exergy destruction ($\dot{E}_{D,k}^{UN}$) is calculated to be 3.059 kW. Contrary, the avoidable exergy destruction ($\dot{E}_{D,k}^{AV}$) is estimated to be 1.380 kW for the overall system. Referring to the results for the evaporator, it has the highest unavoidable exergy rate $\dot{E}_{D,k}^{UN}$ with the rates

of 1.356 kW. This rate consist % 44.33 of unavoidable exergy destruction within in the heat pump unit. The maximum $\dot{E}_{D,k}^{AV}$ value is estimated to be 1.194 kW for the evaporator and 0.491 kW for the compressor. Considering the calculation of the endogenous/exogenous exergy destruction rate, the total endogenous exergy destruction is calculated to

be 1.429 kW whereas the overall exogenous exergy destruction ($\dot{E}_{D,k}^{EX}$) is estimated as 3.009 kW. Figure 2 is an illustration of the distribution of exergy destructions in the overall system and its main units.
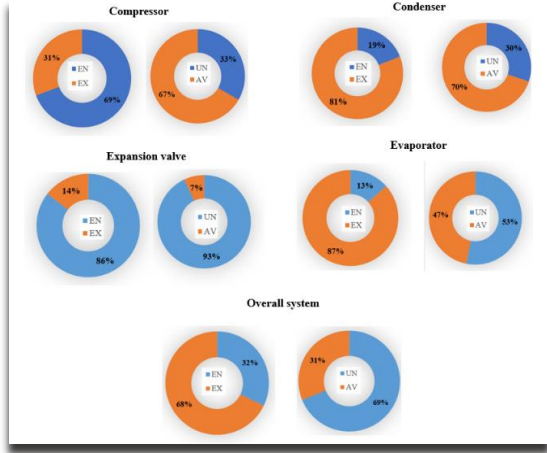
Figure 2. The exergy destruction rates the air source heat pump unit.

Internal exergy destructions so-called endogenous exergy rate at the compressor has substantial 69.0% of sum exergy destructions were considered as endogenous (Fig. 2), meaning that from a design perspective, compressor inefficiency could be autonomously lowered. In addition, more than half (67.0%) of the total avoidable endogenous exergy destruction was attributed to the compressor. Figure 2 shows that both exogenous and avoidable exergy destructions within the condenser were very high. Exogenous and avoidable exergy destructions were in the range of 81.0% and 70.0% of the total exergy destructions, respectively. Therefore, it can be

concluded that the inefficiencies within the condenser are largely affected from the other components of the heat pump unit. From Figure 2 one can notice that three-fourths of the entire exergy destroyed in the evaporator was exogenous. Furthermore, almost half of the total evaporator destruction was avoidable exogenous exergy destruction. All of these results indicate that efforts to reduce evaporator inefficiencies should focus primarily on component interactions.
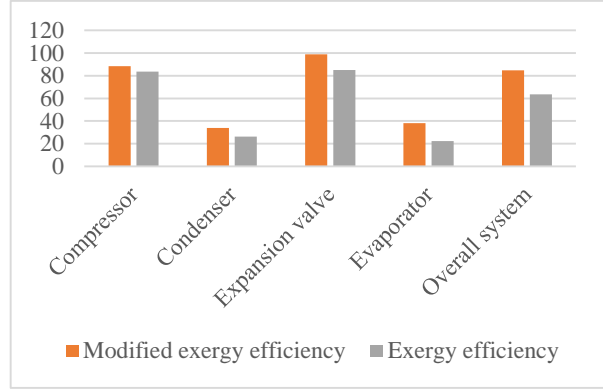
Figure 3. A comparison of the exergy efficiency and the modified exergy efficiency.

While the exergy efficiency of the compressor was 83.61%, the modified exergy efficiency was not increased too much and calculated 88.44%. The conventional exergy efficiencies of the evaporator and condenser were 22.44% and 26.37% when the modified exergy efficiencies were obtained as 38.13% and 33.91%, respectively.

4. Conclusion and Suggestions

The conventional and advanced exergy analyses of an air-source heat pump unit have been performed in this study. The elements of the system were assessed individually, and the following are the main observations that can be derived from the findings of the current study:

- The proportion of unavoidable exergy destruction is found to be highest at 53% for the evaporator, while the condenser has the minimum proportion at 30%. These results show that the range of potential improvements to the evaporator is limited.
- The share of endogenous exergy destruction in total destruction is highest for the compressor (69%). This means that this component is not directly impacted by the operating conditions of the other components.
- The exergy efficiency of the heat pump unit is estimated at 63.54%, according to the experimental data.
- In view of the findings of the advanced exergy analysis, the condenser and compressor components should take priority for the enhancement efforts of the whole system.

For further studies, advanced exergy assessment methods can be used to evaluate other thermal systems, such as trigeneration plants.

Acknowledgment

Statement of Research and Publication Ethics

The study is complied with research and publication ethics.

References

[1]   Y. Jung, J. Oh, U. Han, H. Lee. "A comprehensive review of thermal potential and heat utilization for water source heat pump systems" *Energy and buildings*, vol. 266, pp.112-124, 2022.

[2]   I. Dincer, A.Z. Sahin. "A new model for thermodynamic analysis of a drying process" *International Journal of Heat and Mass Transfer,* vol. 47, pp. 645-652, 2004.

[3]   T. Morosuk, G. Tsatsaronis. "A new approach to the exergy analysis of absorption refrigeration machines" *Energy*, vol. 33, pp. 890–907, 2008.

[4]   O. Balli. "Advanced exergy analysis to evaluate the performance of a military aircraft turbojet engine (TJE) with afterborner system: Splitting exergy destruction into unavoidable/avoidable and endogeneous/exogenous" *Applied Thermal Engineering*, vol. 111, pp. 152-169, 2017.

[5]   J. Chen, "Investigation of vapour ejectors in heat driven ejectors refrigeration system," Ph.D. Thesis, Division of applied thermodynamics and refrigeration department of energy tecnology, Royal Enstitute of technology, KTH , SE-100 44 Stckholm, Sweden, 2014.

[6]   T. Morosuk and G. Tsatsaronis. "A new approach to the exergy analysis of absorption refrigeration machines" *Energy,* vol. 34, pp. 890–907, 2008.

[7]   G.D. Vuckovic, M.V. Vukic, M.M. Stojiljkovic, D.D Vuckovic. "Avoidable and Unavoidable Exergy Destruction and Exergoeconomic Evaluation of the Thermal Processes in a Real Industrial Plant" *Thermal science*, vol. 16, Suppl. 2, pp. 433-446, 2012.

[8]   B. Ghorbani, H. Roshani. "Advanced exergy and exergoeconomic analysis of the integrated structure of simultaneous production of NGL recovery and liquefaction" *Trans Phenom Nano Micro Scales*, vol. 6 (Specials), pp. 8-14, Doi: 0 22111/tpnms, 2018.

[9]   A. Hepbasli and A. Kecebas. "Comparative study on conventional and advanced exergetic analyses of geothermal district heating systems based on actual operational data" *Energy and Buildings*, vol. 61, pp. 193–201, 2013.

[10]   X. Liu, X. Yan, X. Liu, Z. Liu, W. Zhang. "Comprehensive evaluation of a novel liquid carbon dioxide energy storage system with cold recuperator: Energy, conventional exergy and advanced exergy analysis", *Energy Conversion and Management*, vol. 250, 114909, 2021. https://doi.org/10.1016/j.enconman.2021.114909.

[11]   T. Morosuk, G. Tsatsaronis. "Advanced exergy analysis for chemically reacting systems – application to a simple open gas-turbine system" *Int J Therm*, vol.12, no.3, pp.105–111, 2009.

[12]   A. Bejan, G. Tsatsaronis, and M. Moran, *Thermal design and optimization*, Wiley, New York., 542 p., 1996

[13]   O. Balli, H. Caliskan. "On-design and off-design operation performance assessments of an aero turboprop engine used on unmanned aerial vehicles (UAVs) in terms of aviation, thermodynamic, environmental and sustainability perspectives" *Energy Conversion and Management*, Vol. 243, pp. 114403, 2021.

[14]   F. Petrakopoulou, "Comparative evaluation of power plants with Co2 capture: thermodynamic, economic and environmental performance", Ph. D. dissertation, Berlin Technical University, Berlin, 209 p, 2011.

[15]   T. Morosuk, G. Tsatsaronis, C. Zhang. "Conventional thermodynamic and advanced exergetic analysis of a refrigeration machine using a Voorhees' compression process" *Energy Conversion and Management,* vol. 60, pp.143-151, 2012.

[16] T. Morosuk, G. Tsatsaronis. "Understanding and improving energy conversion processes with the aid of exergy-based methods. 1st 492 International Exergy, Life Cycle Assessment, and Sustainability" Workshop and Symposium (ELCAS), 4-6 June, 2009, Nisyros-Greece.

[17] S. Kelly, "Energy systems improvement based on endogenous and exogenous exergy destruction". PhD Thesis, Institut fur Energietechnik, Technische Universtat Berlin, Berlin, Germany, 2008.

Ex vivo UV-C Protective Effect of *Aloe vera*

Isik Didem KARAGOZ[1*], Basak GOKPINAR[1]

[1]*Gaziantep University, Faculty of Arts and Sciences, Department of Biology, Gaziantep/TURKEY*
(ORCID: 0000-0001-6527-2750) (ORCID: 0000-0002-2678-569X)

Abstract

Chronic exposure to UV-C can cause sunburn, skin cancer, oxidative stress as well as photo-aging. Many herbs and plant extracts have recently been recognized as a potential source of sunscreen due to their UV-absorbing properties. *Aloe vera* L., which has been used for therapeutic purposes by humans for centuries, is also among these plants. In this study, it was aimed to reveal the sunscreen properties of the latex and gel parts of *A. vera* and the effect of these properties on cells exposed to UV rays. In this study, primarily, the lethal effect of UV-C rays on healthy cells was observed over time. Then, the latex and gel parts of the obtained *A. vera* plant were separated and spread on the surface of petri dishes as a single and double layer. By adding a determined number of cells of the petri dishes, the protection of *A. vera* against the lethal effect of 1, 1.5 and 2 hours of UV-C exposure was investigated. According to the study findings, in all cells in the control group, an increasing number of deaths occurred as the UV-C exposure time was prolonged and no viable cells remained at the 2nd hour. The double-layered *A. vera* latex and gel groups exhibited less cell death than the control and still had viable cells at 2 hours. From this point of view, it has been shown in this study that a protective product that can be made using *A. vera* can prevent the damages that may develop due to UV-C exposure.

1. Introduction

The World Health Organization defines UV-C rays as the most damaging ray to the skin when compared to other components of sun rays [1]. Even only a small fraction of UV-C rays can penetrate the deep layer of the skin [2]. In addition, due to its UV-C ionization feature, it acts as a strong mutagen and can cause immune-mediated disease and cancer in adverse situations [3]. Given the increasing dangers associated with UV exposure, the use of sunscreen agents in various formulations has increased. Products developed as sunscreens often contain components that can absorb or disperse UV effectively [4]. In protection from the sun and the ultraviolet rays it causes, plants and plant extracts are generally accepted as a potential source of UV protection due to their UV absorbing and antioxidant properties [5-7]. *Aloe vera*, known as one of these plants, is a member of the Liliaceae (Lily) family [8, 9]. There is information on the ancient Egyptian papyrus and Mesopotamian clay tablets that *A. vera* was used in the treatment of infections, solving skin problems, and also as a laxative [10]. At the same time, it is among the data in the literature that *A. vera* suppresses neuroblastoma [11] and glioblastoma/astrocytoma [12] cells by showing anti-inflammatory activity and has anticarcinogenic potential. *A. vera* leaves have two different parts, latex and gel, with different chemical compositions. The latex part is obtained from the pericyclic cells and the gel part is obtained from the parenchyma cells [13].

The outermost large leaves are cut 2-3 times a year for medicinal purposes [10]. The active ingredients in the gel are anti-inflammatory, antioxidant [14], immunoregulatory [15], antidiabetic [16], antiproliferative [17], wound healing [18] and antimicrobial effects [19] were determined. The antioxidant property of *A. vera* is due to the abundant amounts of vitamin A, vitamin C, E, B12, choline and

---

folic acid in its structure. In addition, in an in vitro study using veracylglucan B isolated from the gel, it was demonstrated that it had a significant antiproliferative (cytotoxic) effect on fibroblast culture [17]. *A. vera* is used in medicine, cosmetics, food industry, in many fields as capsules and creams [20]. It is especially preferred in the field of dermatology and it prevents wrinkles by accelerating the formation of collagen and elastin in its content and is used in the treatment of sun-induced burns, especially secondary-degree burns [21, 22].

Within the scope of this study, it was aimed to observe the protective effect of the latex and gel obtained from the *A. vera* plant, which is used as a pharmaceutical raw material in the cosmetic industry and dermatology, against UV-C, which is one of the harmful rays from the sun and kills cells.

2. Material and Method
2.1. Plant Material and Preparation Extract

Healthy and fresh *A. vera* leaves having a length of 30–45 cm were collected from Gaziantep University in Gaziantep/Turkey. The plant material was identified by Dr. H. Tekin, Botanist, University of Gaziantep. Leaves were washed with distilled water to remove dirt. After removing the spikes, the leaves were cut transversely into pieces and the thick

epidermis was carefully separated from the parenchyma (Fig 1). The resulting latex and gel parts were homogenized and freeze-dried.

Figure 1. *A. vera* latex and gel parts

2.2. Preparation of *A. vera* Coated Petri dishes

A. vera latex and gel parts were spread as a thin layer on the top cover of the petri dishes, both on one and both sides (Fig 2). Petri dishes, which were left to dry at room temperature without sunlight, were then stored at room temperature.

Figure 2. Spread of *A. vera* parts on the petri dish

2.3. Cell Culture
2.3.1. Production of Cells

In cell culture studies, human umbilical vein endothelial cells (HUVEC) were used because it is a healthy cell line. The HUVEC cell line obtained from the American Cell Culture Collection (ATCC) cell bank was used. Dulbecco's Modified Eagle Medium (DMEM) medium containing inactivated 10% Fetal Bovine Serum (FBS), L-glutamine, penicillin/streptomycin was used for growth and growth of cells. Cells were produced in flasks in this medium and kept in a 37 °C incubator containing 5%

CO_2. The cells produced were then used for UV studies.

2.3.2. Observation of Morphological Effects of UV-C on Cells

The cells produced and covering the flask base were treated with UV-C for 1, 2 and 3 hours. A UV transluminator (DNR-IS) device, which produces light with a wavelength of 254 nm and an intensity of 8000 µW/cm at room temperature, was used as a UV-C light source (Fig 3). At the end of each hour, cells were observed morphologically under an invert microscope.

Figure 3. UV-C application to cells

2.3.3. Determination of Protective Efficacy of *A. vera* Against UV-C Exposure

For the study, the medium of the cells growing in sufficient quantity was aspirated and washed with PBS (phosphate buffered saline). Afterwards, it was treated with Tris/EDTA and incubated in an environment containing 5% CO_2 at 37 °C, and the cells were separated from the surface. Then, it was centrifuged at 800 rpm for 5 minutes and the pellet part was homogenized with the medium. Viable cells were counted on Thoma slide using Trypan Blue dye.

In order to evaluate the UV-C protective effect of *A. vera* on cells, HUVEC cells were seeded in petri dishes with 500,000 cells. The previously prepared *A. vera* latex and gel-coated petri dishes were closed on the cells and exposed to UV-C at 254 nm for 1 hour. After counting the viable cells at the end of 1 hour, the cells were exposed to UV-C for 1.5 hours, 2 hours and 3 hours and counting was repeated (Fig 4).

Trial groups are as follows;
1. Control Group: 500,000 cells in the medium (petri dish untreated)
2. Latex One Side: 500,000 cells in the medium + the outer surface of the petri dish is covered with shell
3. Gel One Side: 500,000 cells in the medium + the outer surface of the petri dish is coated with gel
4. Latex Double Side: 500,000 cells in the medium + the inner and outer surfaces of the petri dish are covered with shell
5. Gel Double Side: 500,000 cells in the medium + the inner and outer surfaces of the petri dish are coated with gel

Figure 4. UV-C application to *A. vera* coated cell plates

2.4. Statistical Analysis

Each experiment was performed at least in triplicate. Average values are given with standard error of the mean (SEM). Differences between average values were tested for significance using 2way ANOVA and considered as significant for $P < 0.05$. All statistical tests were carried out utilizing the GraphPad Prism program for Windows version 8.4.2

Table 1. Cell counts in groups exposed to UV-C

UV application time	Control	Latex one-side	Gel one-side	Latex double-side	Gel double-side
Number of Cells Before Application (0th hour)	500000	500000	500000	500000	500000
Viable Cell Count After 1 h UV-C	140000	210000	280000	210000	280000
Viable Cell Count After 1.5 h UV-C	70000	90000	140000	100000	140000
Viable Cell Count After 2 h UV-C	0	0	0	25000***	35000***

3. Results and Discussion
3.1. Morphological Observation of UV-C Damage

The morphological structure of the cells that covered the surface of the flask and did not have any UV-C exposure is shown in Figure 5. Here the cells are spread out and appear to be together. After 1 hour of UV-C application, it is seen that the cells start to die and separate from each other as in Figure 6. After the 2nd hour UV-C exposure, the cells were seen to die completely (Fig 7), while at the 3rd hour, it was observed that the cell nuclei were fragmented (Fig 8).
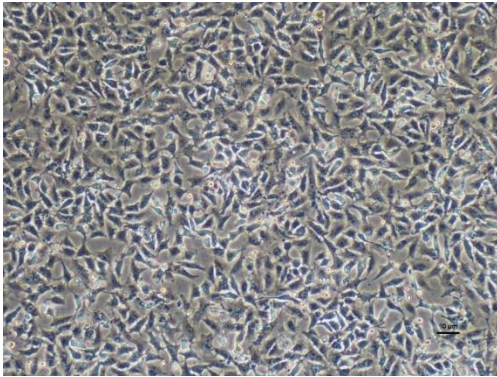
Figure 5. Control group cell image
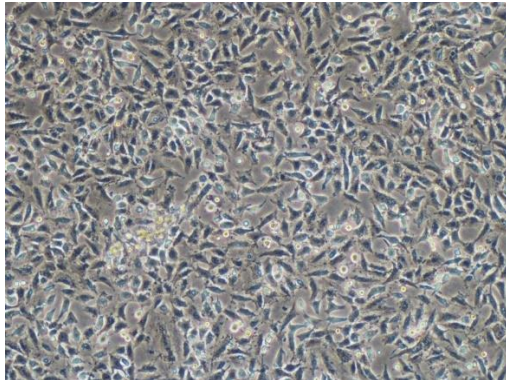
Figure 6. Cell Image Exposed to UV-C for 1 hour
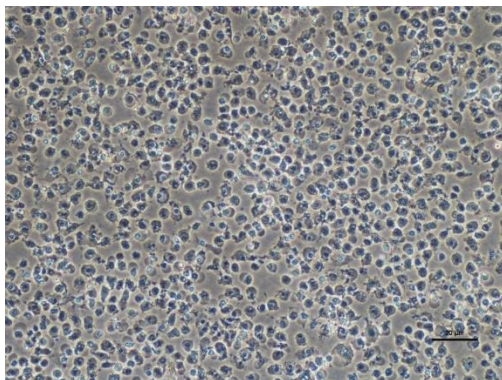
Figure 7. Cell Image Exposed to UV-C for 2 hours
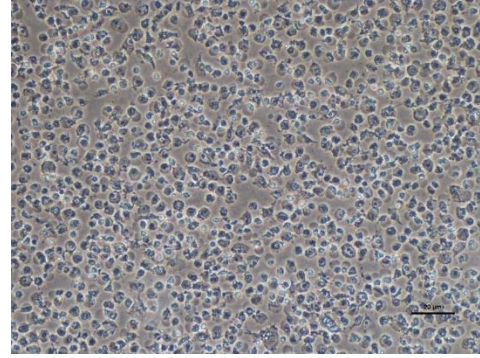
Figure 8. Cell Image Exposed to UV-C for 3 hours

3.2. Determination of Protective Efficacy of *A. vera* Against UV-C Exposure

The numerical differences of the cells in the experimental and control groups as a result of UV-C application are shown in Table 1. When *A. vera* latex and gel layer is added between the cells and the UV-C beam, the change in the situation is remarkable. In the experimental setups formed as a single or double layer with gel, after 1.5 hours of UV application, it was determined that the viability was 2 times higher than the control group, and 1.28 and 1.42 times more viability in the latex single-sided and latex double-sided layer groups, respectively. After 2 hours of UV-C exposure, it was observed that all cells in the control, latex single side and gel single side groups died, while 25000 viable cells were observed in the latex double side group and 35000 live cells on the gel double side.

UV is absorbed by nucleic acids, proteins and cellular membranes. UV absorption leads to the destruction of chemical bonds and free radical formation, initiating a series of oxidative free radical-driven reactions in the presence of oxygen. These reactions cause necrotic and apoptotic cell death [23-24]. It has been found that many plants show protective effects by absorbing UV light in the wavelength range of 300 - 400 nm and activating the antioxidant defense system thanks to their polyphenol content [25-27]. The fact that *A. vera* has a high polyphenol content [28] and has significant antioxidant activity [29] can be considered as the reason why the number of deaths in the *A. vera* containing groups in this study was less than the control. Many similar studies with *A. vera* have also yielded results to support this. When the literature data in which the latex and gel of *A. vera* are evaluated together, it is seen that there are studies that contain the information that UV rays absorption is quite high [30] and that it also has protective properties against UV-A and UV-B damage [31, 32]. The studies on the *A. vera* gel part were examined, it was found that

studies showing the decrease in skin elasticity caused by UV-B [33] and the sterols in the gel prevent skin photo-aging [34]. In addition, when studied in rats and guinea pigs exposed to UV and gamma radiation, it was determined that *A. vera* gel showed wound healing activity in conditions such as cuts, burns and eczema [35-38].

4. Conclusion and Suggestions

According to the findings, it is seen that the leaf and especially the gel parts of *A. vera* are quite effective in protecting healthy cells against UV-C damage. It is thought that this effect may have the potential to be used in many areas. First of all, it is seen that it has the potential to be used as a topical UV-C protective product in the cosmetics industry. In addition, it comes to mind that UV-C protective glasses can be

created with *A. vera* leaf and gel to protect people from damage to their eyes. In conclusion, we think that *A. vera* can be used as a natural source of protection against UV-C and the findings obtained should be supported by further studies on the way to product transformation.

Contributions of the authors
The authors' contributions to the paper are equal.**Conflict of Interest Statement**
There is no conflict of interest between the authors.

Statement of Research and Publication Ethics

The study is complied with research and publication ethics

References

[1] G. P. Pfeifer and A. Besaratinia, "UV wavelength-dependent DNA damage and human non melanoma and melanoma skin cancer," *Photochemical and Photobiological Sciences,* Vol. 11, no.1, pp. 90–97, 2012.

[2] M. Meinhardt, R. Krebs, A. Anders, U. Heinrich, H. Tronnier, "Wavelength-dependent penetration depths of ultraviolet radiation in human skin," *Journal of Biomedical Optics*, Vol. 13, no. 4, pp. 044030, 2008.

[3] D. Mohania, S. Chandel, P. Kumar, V. Verma, K., Digvijay, D. Tripathi, K. Choudhury, S. K. Mitten, D. Shah, "Ultraviolet radiations: Skin defense-damage mechanism," *Advances in Experimental Medicine and Biology*, Vol. 996, pp. 71-87, 2017.

[4] M. S. Latha, J. Martis, V. Shobha, R. Sham Shinde, S. Bangera, B. Krishnankutty, S. Bellary, S. Varughese, P. Rao, B. R. Naveen Kumar, "Sunscreening agents: a review," *The Journal of Clinical and Aesthetic Dermatology*, Vol. 6, no. 1, pp. 16–26, 2013.

[5] A. Takahashi, K. Takeda, T. Ohnishi, "Light-induced anthocyanin reduces the extent of damage to DNA in UV-irradiated Centaurea cyanus cells in culture," *Plant and Cell Physiology*, Vol. 32, no. 4, pp. 541-547, 1991.

[6] J. Rozema, L. O. Björn, J. F. Bornman, A. Gaberščik, D. P. Häder, T. Trošt, B. B. Meijkamp, "The role of UV-B radiation in aquatic and terrestrial ecosystems—an experimental and functional analysis of the evolution of UV-absorbing compounds", *Journal of Photochemistry and Photobiology B: Biology*, Vol. 66, no. 1, pp. 2-12, 2002.

[7] W. Hui-lian, L. Qian-rong, L. Zhao-feng, W. Yu-zhen, "The protective effect and mechanism of soybean oil and its extracts on DNA damage in human ECV304 cells exposed to UV-C," *Biochimica et Biophysica Acta (BBA)-Gene Structure and Expression*, Vol. 1626, no.1-3, pp. 19-24, 2003.

[8] A. Vega-Gálvez, M. Miranda, M. Aranda, K. Henriquez K, J. Vergara, G. Tabilo-Munizaga, M. Pérez-Won, "Effect of high hydrostatic pressure on functional properties and quality characteristics of *Aloe vera* gel (Aloe barbadensis Miller)," *Food Chemistry*, Vol. 129, no. 3, pp. 1060-1065, 2011.

[9] M. H. Radha, and N. P. Laxmipriya, "Evaluation of biological properties and clinical effectiveness of *Aloe vera*: A systematic review," *Journal of Traditional and Complementary Medicine*, Vol. 5, pp. 21-26, 2015.

[10] R. M. Shelton, "*Aloe vera*, Its chemical and therapeutic properties," *International Journal of Dermatology*, Vol. 30, pp. 679-83, 1991.

[11] A. Yonehara, Y. Tanaka, K. Kulkeaw, T. Era, Y. Nakanishi, D. Sugiyama, "*Aloe vera* Extract Suppresses Proliferation of Neuroblastoma Cells *in vitro*," *Anticancer Research*, Vol. 35, no. 8, pp. 4479-85, 2015.

[12] A. Tornero-Martínez, M. Del Carmen Silva-Lucero, E. C. Sampedro, E. Ramón-Gallegos, C. Pérez-Cruz, B. Pérez-Grijalva, R. Mora-Escobedo, "*Aloe vera* and Fermented Extracts Exhibit an Anti-Inflammatory Effect on Human Glioblastoma/Astrocytoma U373 MG Cells," *Plant Foods for Human Nutrition,* Vol 77, no. 1, pp. 37-43, 2022.

[13] F. Capasso, F. Borelli, D. Di Carlo, A. A. Izzo, L. Pinto, N. Mascolo, S. Castaldo, R. Longo, "Aloe and its therapeutic use," *Phytotherapy Research*, Vol. 12, pp. 124–127, 1998.

[14] S. Rajasekaran, K. Sivagnanam, S. Subramanian, "Antioxidant effect of *Aloe vera* gel extract in Streptozotocin-induced diabetes in rats," *Pharmacological Reports*, Vol. 57, no. 1, pp. 90-96, 2005.

[15] F. M. Strickland, R. P. Pelley, M. L. Kripke, "Prevention of ultraviolet radiation-induced suppression of contact and delayed hypersensitivity by *Aloe barbadensis* gel extract," *The Journal of Investigative Dermatology*, Vol. 102, no. 2, pp.197–204, 1994.

[16] A. Can, N. Akev, N. Ozsoy, S. Bolkent, B. P. Arda, R. Yanardag, A. Okyar, "Effect of *Aloe vera* leaf gel and pulp extracts on the liver in type-II diabetic rat models," *Biological & Pharmaceutical Bulletin*, Vol. 27, no. 5, pp. 694–698, 2004.

[17] M. F. Esua, J. W. Rauwald, "Novel bioactive maloyl glucans from *Aloe vera* gel: isolation, structure elucidation and in vitro bioassays," *Carbohydrate Research*, Vol. 341, pp. 355–364, 2006.

[18] J. P. Heggers, R. P. Pelley, D. P. Hill, C. J. Stabenau, W. D. Winters, "Wound healing with aloe substances," *Academic/Industry Joint Conference*, Vol. 41, 1992.

[19] O. O. Agarry, M. T. Olaleye, C. O. Bello-Michael, "Comparative antimicrobial activities of *Aloe vera* gel and leaf," *African Journal of Biotechnology*, Vol. 4, no. 12, pp. 1413-1414, 2005.

[20] D. Vidic, E. Tarić, J. Alagić, M. Maksimović, "Determination of total phenolic content and antioxidant activity of ethanol extracts from Aloe Spp," *Bulletin of the Chemists and Technologists of Bosnia and Herzegovina*, Vol. 42, pp. 5-10, 2014.

[21] N. Mascolo, A. Izzo, F. Borrelli, R. Capasso, G. Di Carlo, L. Sautebin, "Aloes: The Genus Aloe," *United States of America*, Florida, Vol. 391, 2004.

[22] A. Ö. Ağırgan, "*Aloe vera* effects of gel incorporation on mechanical and thermal properties of nanocomposite produced from biopolymer blends," PhD Thesis, Marmara University, Turkey, 2013.

[23] A. Van Laethem, K. Nys, S. Van Kelst, S. Claerhout, H. Ichijo, J. R. Vanderheede, M. Garmyn, P. Agostiniset, "Apoptosis signal regulating kinase-1 connects reactive oxygen species to p38 MAPK-induced mitochondrial apoptosis in UVB-irradiated human keratinocytes," *Free Radical Biology and Medicine,* Vol. 41, pp. 1361-71, 2006.

[24] H. R. Rezvani, F. Mazurier, M. Cario-André, C. Pain, C. Ged, A. Taïeb, A, H. de Verneuil, "Protective effects of catalase overexpression on UVB-induced apoptosis in normal human keratinocytes," *Journal of Biological Chemistry*, Vol. 281, no. 26, pp. 7999-8007, 2006.

[25] V. Kostyuk, A. Potapovich, T. Suhan, C. De Luca, G. Pressi, R. Dal Toso, L. Korkina, "Plant polyphenols against UV-C-induced cellular death," *Planta Medica*, Vol. 74, no. 5, pp. 509-14, 2008.

[26] R. Gomez-Vasquez, R. Day, H. Buschmann, S. Randles, J. R. Beeching, R. M. Cooper, "Phenylpropanoids, phenylalanine ammonia lyase and peroxidases in elicitor-challenged Cassava (Manihot esculenta) suspension cells and leaves," *Annals of Botany*, Vol. 94, pp. 87-97, 2004.

[27] R. A. Dixon, N. L. Paiva, "Stress-induced phenylpropanoid metabolism," *Plant Cell*, Vol. 7, pp. 1085-97, 1995.

[28] World Health Organization, "*Aloe vera* gel," *WHO Monographs on Selected Medicinal Plants*, Malta, Vol. 1, pp. 43-49, 1999.

[29] H. Tariq, M. Zia, U. H. Ihsan, S. A. Muhammad, S. A. Khan, N. Fatima, A. Mannan, A. M. Abbasi, M. Zhang, "Antioxidant, antimicrobial, cytotoxic, and protein kinase inhibition potential in *Aloe vera* L.," *BioMed Research International*, Vol. 28, pp. 6478187, 2019.

[30] M. S. Kumar, P. K. Datta, S. Dutta-Gupta, "In vitro evaluation of UV opacity potential of *Aloe vera* L. gel from different germplasms," *Journal of Natural Medicines*, Vol. 63, no. 2 pp. 195-199, 2008.

[31] E. Misawa, M. Tanaka, M. Saito, K. Nabeshima, R. Yao, K. Yamauchi, F. Abe, Y. Yamamoto, F. Furukawa, "Protective effects of Aloe sterols against UVB-induced photoaging in hairless mice," *Photodermatology, Photoimmunology and Photomedicine*, Vol. 33, no. 2, pp. 101-11, 2017.

[32] K. Subramani, R. Saha, S. Palanisamy, K. S. Balu, S. Rangaraj, V. Murugan, S. Srinivasan, R. Venkatachalam, W. K. Aicher, "Wet chemical preparation of herbal nanocomposites from medicinal

plant leaves for enhanced coating on textile fabrics with multifunctional properties," *SN Applied Sciences*, Vol. 2, pp. 700, 2020.

[33] M. Saito, M. Tanaka, E. Misawa, R. Yao, K. Nabeshima, K. Yamauchi, F. Abe, Y. Yamamoto, F. Furukawa, "Oral administration of *Aloe vera* gel powder prevents UVB-induced decrease in skin elasticity via suppression of overexpression of MMPs in hairless mice," *Bioscience, Biotechnology, and Biochemistry*, Vol. 80, no. 7, pp. 1416-1424, 2016.

[34] R. Yao, M. Tanaka, E. Misawa, M. Saito, K. Nabeshima, K. Yamauchi, F. Abe, Y. Yamamoto, F. Furukawa, "Daily ingestion of *Aloe vera* gel powder containing Aloe sterols prevents skin photoaging in OVX hairless mice," *Journal of Food Science*, Vol. 8, no. 11, pp. 2849-2857, 2016.

[35] J. E. Thompson, "Topical use of *Aloe vera* derived allantoin gel in otolaryngology," *Ear, Nose and Throat Journal*, Vol. 70, pp. 119, 1991.

[36] N. Pugh, S. A. Ross, M. A. Elsohly, D. S. Pasco, "Characterization of aloeride, a new high molecular weight polysaccharide from *Aloe vera* with potent immunostimulatory activity," *Journal of Agricultural and Food Chemistry*, Vol. 49, pp. 1030-1034, 2001.

[37] D. Lalitha-Devi, B. Srinivas, B. Narasinga Rao, "An evaluation antimicrobial activity of Aloe barbadensis Miller (*Aloe vera*) gel extract," *Journal of Pharmaceutical and Biomedical Sciences*, Vol. 21, pp. 1-4, 2012.

[38] R. Rajeswari, M. Umadevi, C. Sharmila Rahale, R. Pushpa, S. Selvavenkadesh, K. P. Sampath Kumar, D. Bhowmik, "*Aloe vera*: the miracle plant its medicinal and traditional uses in India," *Journal of Pharmacognosy and Phytochemistry*, Vol. 1, pp. 118-124, 2012.

Ring Characterizations with Mutually SS-Supplemented Modules

Burcu NİŞANCI TÜRKMEN[1*], Zehra Betül MEŞECİ[2]

[1]*Department of Mathematics, Faculty Art and Science, Amasya University, Amasya, TURKEY.*
[2]*The Institute of Sciences, Amasya University, Amasya, TURKEY.*
(ORCID: 0000-0001-7900-0529) (ORCID: 0009-0007-9714-5183)

Abstract

In this text, the notion of mutually ss-supplemented modules is characterized with the help of semiperfect rings. For this, mutually ss-supplemented modules were first classified according to certain properties. These features can be listed as refinable modules, distributive modules, fully invariant submodules, and (π-) projective modules. It was determined that every submodule of an amply ss-supplemented module is mutually ss-supplemented. It was shown that $C = \oplus_{\varrho \in \Lambda} C_\varrho$ is a mutually ss-supplemented module in which each submodule of C is a fully invariant submodule, for the family of mutually ss-supplemented modules $\{C_\varrho\}_{\varrho \in \Lambda}$.

1. Introduction

In this study, we refer the reader to references [1], [2], [3], and [10] to understand the basic algebraic properties of module theory. We will take all the rings as unitary and associative. We will also use all modules as unitary left S-modules. E is called a *submodule* of C if, for each $c \in E$ and $s \in S$, E is a subgroup of the module C and $sc \in E$. This is denoted as $E \leq C$. Obviously, 0 and C are submodules of C. Here, these submodules are said to be *trivial submodules* of C. Submodules other than trivial are said to be *proper submodules* [2].

If non-zero module C has no submodule except trivial submodules, C is said to be *simple* [3]. A module C is said to be *semisimple* if C is written in the form of a sum of simple modules. The necessary and sufficient condition for semisimple module C is this: each submodule of C is a direct summand in C [3]. The property of semisimplity of a module is preserved under submodules, direct summands and arbitrary sums [3]. Let B be a proper submodule of C. If C has no proper submodule that includes B in C, then B is said to be a *maximal submodule* of C [3]. Let C be a module and B a proper submodule of C. If C has no any proper submodule D of C provided that $B + D = C$, then B is said to be a *small submodule* of C and

denoted as $B \ll C$ [1], [3]. Here, if $B + D = C$, then $D = C$. A module C is said to be *hollow*, if each proper submodule F of C is small. A module C is said to be *local* if C has a proper submodule which includes whole proper submodules of C [1],[3]. The necessary and sufficient condition for a local module C is this: C is hollow and $Rad(C) \neq C$ [1], [3].

Let B, B' be submodules of C. A submodule B' is said to be a *supplement* of B in C, if B' is a minimal element of the submodules D of C with $C = B + D$. Here B' is a supplement of B in C in this case for $C = B + B'$ and $B \cap B' \ll B'$ [1]. An epimorphism $P \xrightarrow{\mu} B \to 0$ is said to be a *projective cover* of B if P is projective and $\ker(\mu) \ll P$. In [7], a submodule U has a supplement in a projective module C, which is a direct summand in C in this case for C/U possesses a projective cover. A module C is said to be *semiperfect* if each factor module of C possesses a projective cover [1]. The set $Soc(C) = \sum \{D \leq C \mid D \text{ is a } \text{simple submodule of } C\}$ is defined in this way that is a submodule of C. A submodule B' is said to be a *mutual supplement* of B in C if, $C = B + B'$, $B \cap B' \ll B$ and $B \cap B' \ll B'$ by [7]. $Rad(C)$ is the intersection of whole maximal submodules of C. The impression $Rad(C)$ is shown by the sum of each submodule of C. If $Rad(C) = C$, then C is said to be a *radical module*. The radical submodule of a

---
* Corresponding author: *burcu.turkmen@amasya.edu.tr*

semisimple module is zero [1]. $Soc_s(C) = \sum\{D \leq C \mid D \ is\ both$ simple and small submodule of $C\}$. So $Soc_s(C) \subseteq Soc(C)$ and $Soc_s(C) \subseteq Rad(C)$ [4]. A module C is said to be *ss-supplemented* if, for each submodule F of C, there is a supplement L of F in C provided that $F \cap L$ is semisimple, termed ss-supplements [4]. A submodule F of a module C has *ample ss-supplements* in C if each submodule L of C such that $C = F + L$ contains an ss-supplement of F in C. A module C is said to be *amply ss-supplemented* provided that each submodule of C has ample ss-supplements in C [4]. A module C is said to be *strongly local* if $Rad(C)$ is semisimple [4]. Following [5], a module C is said to be $\oplus_{ss}$-*supplemented* if every submodule of C is a ss-supplement that is a direct summand of C. It is clear that every $\oplus_{ss}$-supplemented module is ss-supplemented.

2. Material and Method

In [7], the notion of mutually ss-supplemented modules is defined as a strong notion of ss-supplemented modules and is served relevant attributions about these modules.

Following [7], we give the following facts.

Lemma 2.1: [7, Lemma 2.2] Let B, B' be submodules of the module C. Then the following statements are equivalent.
(i) B and B' are mutual ss-supplements in C;
(ii) $C = B + B'$, $B \cap B' \subseteq Rad(B)$, $B \cap B' \subseteq Rad(B')$ and $B \cap B'$ is semisimple;
(iii) $C = B + B'$, $B \cap B' \ll B$, $B \cap B' \ll B'$ and $B \cap B'$ is semisimple;

A module C is said to be *mutually ss-supplemented* if every submodule D of C has an ss-supplement B in C and there exists a submodule B' of C such that B and B' are mutual ss-supplements in C. It is clear that $\oplus_{ss}$-supplemented module is mutually ss-supplemented [7].

Lemma 2.2: [7, Lemma 2.9] Let D and E be submodules of the module C in which D is mutually ss-supplemented. If $D + E$ has a mutual

3. Results and Discussion

In this part, we prove that the notion of mutually ss-supplemented modules is strictly stronger than notion of ss-supplemented modules. We conclude this paper

ss-supplement in C, then E has a mutual ss-supplement in C.

Theorem 2.3: [7, Theorem 2.8] Let C be a module with $Rad(C) \ll C$. Then the following statements are equivalent:
(i) C is mutually ss-supplemented;
(ii) Every submodule of C has a mutual supplement in C and $Rad(C)$ has a ss-supplement in C;
(iii) Every submodule of C has a mutual supplement in C and $Rad(C) \subseteq Soc(C)$.
Proof: (i)$\Rightarrow$(ii) Let C be a mutually ss-supplemented. Then every submodule of C has mutual ss-supplement in C. Then $Rad(C)$ is so.
(ii)$\Rightarrow$(iii) Since $Rad(C) \ll C$, C is a unique ss-supplement of $Rad(C)$ in C by the hypothesis. So $Rad(C) \subseteq Soc(C)$.
(iii)$\Rightarrow$(i) By Lemma 2.1.

Lemma 2.4: [7, Lemma 2.11] Let C be a projective module. Then C is mutually ss-supplemented if and only if every submodule of C has a mutual ss-supplement in C and $Rad(C) \subseteq Soc(C)$.
Proof: ($\Rightarrow$) Let C be a projective module. By [10, 42.3] C is semiperfect. Then we get $Rad(C) \ll C$ by [10, 21.6].
($\Leftarrow$) The proof holds by Theorem 2.3.

Proposition 2.5: [7, Proposition 2.10] Let C be a module which is the sum of the submodules C_1, C_2. If C_1 and C_2 are mutually ss-supplemented, then C is so.

Corollary 2.6: Let $C_1, C_2, \ldots, C_m$ be mutually ss-supplemented submodules of C. Then $C_1 + C_2 + \ldots + C_m$ is mutually ss-supplemented.
Proof: Let us apply induction on m. If $m = 1$, then it is clear that $C = C_1$ is mutually ss-supplemented. Suppose that $C = C_1 + C_2 + \ldots + C_{k-1}$ is mutually ss-supplemented for $m = k - 1$. Let us m= k and D be any submodule of C. Since 0 is a mutual ss-supplement of $C = C_1 + C_2 + \ldots + C_{k-1} + C_k + D$. Since $C_1 + C_2 + \ldots + C_{k-1}$ is mutually ss-supplemented, then $C_m + D$ has a mutual ss-supplement in C. By Lemma 2.2, D has a mutual ss-supplement in C. So $C = C_1 + C_2 + \ldots + C_m$ is mutually ss-supplemented.

by characterizing semiperfect rings thanks to mutually ss-supplemented modules.

Proposition 3.1: Every amply ss-supplemented module is mutually ss-supplemented.

Proof. Let C be an amply ss-supplemented module and $D \leq C$. It follows that D has an ss-supplement in C, say B. So we can write $C = D + B = B + D$. Since C is amply ss-supplemented, there exists a submodule B' of D such that B' is an ss-supplement of B in C. Therefore $B \cap B'$ is semisimple and small in B. Since B is a supplement in C, $B \cap B'$ is small in B' by [9, 41.1(5)]. It means that B and B' are mutual ss-supplements in C. Hence C is mutually ss-supplemented.

Using the above proposition, we get the following implications on modules.

$$\oplus_{ss}\text{-supplemented}$$
$$\Downarrow$$
amply ss-supplemented $\Longrightarrow$ mutually ss-supplemented $\Longrightarrow$ ss-supplemented

Lemma 3.2: Let C be a π-projective and ss-supplemented module. Then C is mutually ss-supplemented.
Proof. It is clear from [4, Proposition 37] and Proposition 3.1.

Corollary 3.3: Let C be an amply ss-supplemented. Then every submodule of C is mutually ss-supplemented.
Proof. It follows from [4, Corollary 36].

Recall from [6] that a module C is called *tg-supplemented* if every submodule D of C has a Rad-supplement, say B, where B is a t-summand of C, that is, $C = D + B$, $D \cap B \ll B$ and B, B' are mutual supplements in C, where B' is a submodule of C.

Theorem 3.4: A module C is mutually ss-supplemented if and only if it is tg-supplemented and $Rad(C)$ is semisimple.
Proof. ($\Rightarrow$) Let D be a submodule of C. Since C is mutually ss-supplemented, there exists submodules B, B' of C such that B is a ss-supplemented of D in C, and, B, B' are mutual ss-supplements in C. Therefore B is a Rad-supplement of D in C, and B, B' are mutual supplements in C. Thus C is tg-supplemented. Now, we will show that $Rad(C)$ is semisimple. Since $Rad(C)$ is the sum of all small submodules of C, it suffices to show that any small submodule of C is semisimple. Let N be a small submodule of C. Since C is ss-supplemented, it follows from [4, Lemma 13] that N is semisimple. So $N \subseteq Soc(C)$, which implies $Rad(C) \subseteq Soc(C)$. It means that $Rad(C)$ is semisimple.

($\Leftarrow$) Let D be a submodule of C. By the assumption, there exist submodules B and B' of C such that B is a Rad-supplement of D in C and B, B' are mutual supplements in C. Therefore $B \cap D \subseteq Rad(C)$ and $B \cap B' \subseteq Rad(C)$. Since $Rad(C)$ is semisimple, $B \cap D$ and $B \cap B'$ are semisimple. It follows from [4, Lemma 3] that B is a ss-supplement of D in C, and B, B' are mutual ss-supplements in C. Hence C is mutually ss-supplemented.

Example 3.5: Let K be a quotient field of a Dedekind domain S. Since K/S is a non-local hollow module, the hollow module K/S is not a strongly local module. From [4, Proposition 16] K/S is not ss-supplemented, and so it is not mutually ss-supplemented.

Theorem 3.6: The following statements are given for a ring S where each left ideal has a mutually supplement:

(i) $_S S$ is mutually ss-supplemented,

(ii) S is semiperfect and $Rad(S) \subseteq Soc(\, _S S)$,

(iii) Every S-module is mutually ss-supplemented.

Proof: By [4, Theorem 41] and Proposition 3.1.

Recall from [10] that a submodule D of C is called characteristic (or fully invariant) if $\theta(D) \leq D$ for each endomorphism θ of C.

Theorem 3.7: Let $\{C_\varrho\}_{\varrho \in \Lambda}$ be a family of mutually ss-supplemented modules $C = \oplus_{\varrho \in \Lambda} C_\varrho$ where each submodule of C is fully invariant. Then C is a mutually ss-supplemented module.

Proof: Let D be any submodule of C. By hypothesis, since $D = \oplus_{\varrho \in \Lambda} (D \cap C_\varrho)$, then $\oplus_{\varrho \in \Lambda} (C_\varrho /(D \cap C_\varrho)) \cong \oplus_{\varrho \in \Lambda} C_\varrho /\oplus_{\varrho \in \Lambda} (D \cap C_\varrho) = C/D$. Since C_ϱ is mutually ss-supplemented for each $\varrho \in \Lambda$, C_ϱ has such submodules K_ϱ and T_ϱ where K_ϱ is an ss-supplement of $D \cap C_\varrho$, and K_ϱ and T_ϱ are mutual ss-supplements of C_ϱ. Hence it is obvious that $(D \cap C_\varrho) \cap K_\varrho = D \cap K_\varrho$ is semisimple for each $\varrho \in \Lambda$. Let $\oplus_{\varrho \in \Lambda} K_\varrho = K$ and $\oplus_{\varrho \in \Lambda} T_\varrho = T$. Let $C = \oplus_{\varrho \in \Lambda} C_\varrho = \oplus_{\varrho \in \Lambda} (D \cap C_\varrho) + \oplus_{\varrho \in \Lambda} K_\varrho = D + K$ and $D \cap K = \oplus_{\varrho \in \Lambda} (D \cap C_\varrho) \cap \oplus_{\varrho \in \Lambda} K_\varrho \subseteq \oplus_{\varrho \in \Lambda} ((D \cap C_\varrho) \cap K_\varrho) = \oplus_{\varrho \in \Lambda} (D \cap K_\varrho) \ll K$. Since $D \cap K_\varrho$

is semisimple for each $\varrho \in \Lambda$, by [3], $D \cap K$ is semisimple. Then $D \cap K \ll K$ and since $D \cap K$ is semisimple, $D \cap K \subseteq Soc_s(K)$. By similar operations, it can be shown that $K \cap T$ are mutual ss-supplemented in C by using K_ϱ and T_ϱ to be mutual ss-supplements in C_ϱ for every $\varrho \in \Lambda$, so C is mutually ss-supplemented.

Recall from [8] that a module C is called *duo* if each submodule is fully invariant.

Corolary 3.8: Let $\left\{C_\varrho\right\}_{\varrho \in \Lambda}$ be the class of mutually ss-supplemented modules and $C = \oplus_{\varrho \in \Lambda} C_\varrho$ where C is a duo-module. Then C is a mutually ss-supplemented module.

Proposition 3.9: Let the module C be π-projective mutually ss-supplemented module, then C is a $\oplus_{ss}$-supplemented module.

Proof: Let D be a submodule of C. According to the hypothesis, C has such submodules L and L' provided that L is a ss-supplement of D and L, L' are mutual supplements of C. Since C is a π-projective module, it follows from [10, 41.14(2)] that $L \cap L' = 0$ and so $C = L \oplus L'$. Then C is a $\oplus_{ss}$-supplemented module.

Proposition 3.10: Let S be a semisimple ring. Then S-module C is mutually ss-supplemented if and only if every submodule of C has a mutual ss-supplement in C.

Proof: Recall from [9, Proposition 4.5] that the ring S is semisimple if and only if every S-module is projective. The proof follows from Lemma 2.4.

Recall from [11, 8.3] that a module C is called *refinable* if for each submodule D, K of C with

$D + K = C$, there exists a direct summand D' of C with $D' \subset D$ and $D' + K = C$.

Proposition 3.11: Every refinable mutually ss-supplemented module is $\oplus_{ss}$-supplemented.

Proof: Let D be any submodule of refinable mutually ss-supplemented module C. Since C is a mutually ss-supplemented module, there is such a submodule K of C with $C = D + K, D \cap K \ll K, D \cap K \ll D$ and $D \cap K$ is semisimple. It is also $D \cap K \ll C$. Since C is refinable, there is a direct summand L of C so that $L \subseteq K$ and $C = D + L$. Then $D \cap L \ll L$. It follows from [3] that $D \cap L \le D \cap K$ is semisimple. Since $C = D + L$, $D \cap L \ll L$ and C has a direct summand L provided that $D \cap L$ is semisimple, as required.

4. Conclusion and Suggestions

Although the module has been made in theory in recent years, it is mentioned in the article named mutually ss-supplemented modules published in the reference [7] in the concept of mutually ss-supplement submodule, which is a special form of the ss-supplement submodule concept in the article in the reference [4], which has led to many studies with many references. Expressed as the characterization of the semiperfect rings of the data. Apart from this, special theorems have been developed to reach amply mutually ss-supplemented modules.

Contributions of the authors
There is no conflict of interest between the authors.

Conflict of Interest Statement
There is no conflict of interest between the authors.

Statement of Research and Publication Ethics

The study is complied with research and publication ethics.

References

[1] F. W. Anderson, K. R. Fuller, *Graduate Texts in Mathematics. Rings and Categories of Modules*, Springer-Verlag, 1992.
[2] T. W. Hungerford, *Algebra.* Springer Verlag, 502, New York, 1973.
[3] F. Kasch, *Modules and Rings*. Published for the London Mathematical Society by Academic Press, 372, Teubner, 1982.
[4] E. Kaynar, E. Türkmen and H. Çalışıcı, SS-supplemented modules. Communications Faculty of Sciences. University of Ankara Series A1 Mathematics and Statistics, vol. 69, no. 1, pp. 473-485, 2020.

[5] E. Kaynar, $\oplus_{ss}$-supplemented modules. *New Trends in Rings and Modules (NTRM 2018)*, Gebze Technical University. Abstract Book, pp. 3 (June 2018).

[6] B. Koşar and C. Nebiyev, "Tg-supplemented modules," *Miskolc Mathematical Notes*, vol. 16, no. 2, pp. 979–986, 2015.

[7] Z. Betül Meşeci, B. Nişancı Türkmen, Mutually SS-Supplemented Modules, 1st Iceans 2022, Proceeding Book, pp 2419-2422, 2022.

[8] A. Ç. Özcan, A. Harmancı, P. F. Smith, "Duo modules," *Glasgow Math. J.*, vol. 48, pp. 533-545, 2006.

[9] J. J. Rotman, *An Introduction to Homological Algebra*. Second Edition. Springer Science+Business Media, LLC, 2009.

[10] R. Wisbauer, *Foundations of Module and Ring Theory*. Gordon and Breach,600, Philadelphia, 1991.

[11] R. Wisbauer, *Modules and Algebras: Bimodule Structure on Group Actions and Algebras* (Vol. 81). CRC Press, 1996.

Dynamic Prediction of Excessive Daytime Sleepiness Through Random Survival Forest: An Application of the PPMI Data

Gonca BUYRUKOĞLU[1*]

[1] *Çankırı Karatekin University, Faculty of Science, Department of Statistics, Çankırı/Türkiye*
(ORCID: 0000-0002-1202-8778)

Abstract
Parkinson's disease (PD) is the second most widespread neurodegenerative disease worldwide. Excessive daytime sleepiness (EDS) significantly correlates with de novo PD patients. Identifying predictors is critical for the early detection of disease. We investigated clinical and biological markers related to time-dependent variables in sleepiness for early detection of PD. Data were obtained from the Parkinson's Progression Markers Initiative study, which evaluates the progression markers in patients. The dataset also includes various longitudinal endogenous predictors. The measures of EDS were obtained through the Epworth Sleepiness Scale (ESS). The random survival forest method, which can deal with multivariate longitudinal endogenous predictors, was used to predict the probability of having EDS in PD. The rate of having EDS among PD patients was 0.452. The OOB rate was 0.186. The VIMP and minimal depth indicated that the most important variables are stai state, JLO, and the presence of the ApoE4 Allele. In early PD, EDS is a good indicator of the diagnosis of the PD and it increases over time and has associations with several predictors.

1. Introduction

Parkinson's disease (PD) is one of the most widespread age-related neurodegenerative diseases worldwide [1]. Although this complex disease is defined by its motor symptoms, non-motor symptoms are quite common and mostly more visible than motor symptoms. Lack of sleep and wakefulness during the day are among the most widespread non-motor symptoms (NMS). Excessive daytime sleepiness (EDS) impacts 16% to 74% of subjects with PD and increases with the duration of the disease and severity [2]–[4]. This symptom has a negative effect on life quality ([2], [5]), and the clinical symptoms of PD differ by disease duration, cognitive impairment, autonomic dysfunction, gender, age, depression,

anxiety, and severe motor symptoms [6]–[8]. EDS is a considerably significant variable, especially in moderate to advanced PD compared to healthy controls (HC) [2], [3].

The existence of EDS has a negative impact on cognitive impairment and the development of a higher risk of dementia [9]. The baseline characteristics regarding EDS in cohort de novo untreated Parkinson patients and HC in the Parkinson Progression Markers Initiative (PPMI) [10] concluded that there was no significant difference between the two groups. EDS was measured with the Epworth Sleepiness Scale (ESS) and defined as true if $ESS \geq 10$. There are few studies to assess EDS in de novo PD patients [11]–[13]. Each of them has very

---

small data, with less than 25 de novo PD patients and one HC. All of them have the same conclusion: EDS does not have a negative impact on untreated PD patients. However, more up-to-date studies indicated that EDS is a part of NMS [14], [15]. Therefore, the uncertainty remains regarding EDS in de novo patients. Abbott et al. [16] stated that EDS is one of the risk factors for developing PD.

So far, there have been very few empirically published accounts of longitudinal change in EDS in PD patients. Tholfsen et al. [17] investigated it in 153 de novo subjects with PD and concluded that the patients with PD had significantly more EDS over time. Breen et al. [7] found that the prevalence of EDS has risen over time. Amara et al. [18] examined the association between clinical, imaging, and biological variables and longitudinal changes in EDS over time with the comparison of HCs. No previous studies have examined the patient-specific risk of PD related to individual longitudinal changes over time. In light of this gap, we aimed to characterize the biological and clinical factors associated with EDS in PD through the investigation of longitudinal trajectories amongst patients in the cohort study.

When the longitudinal and event time processes are associated in the dynamic prediction context, joint modelling is the most effective way to cope with this relationship [19]. Joint models (JM) model the longitudinal and event-time outcomes simultaneously via shared random effects. The method was first developed by Wulfsohn and Tsiatis [20] and extended by Henderson [21]. The method is investigated in detail with the methodological development and advances in [22]. The methodology for the incorporation of multivariate longitudinal data is extended in [23]–[25]. Due to the complexity of the method and the computational burden, the method has been limited to only 2-3 longitudinal biomarkers. Therefore, this brings us to the dynamic prediction with large-dimensional longitudinal predictors: the competing risk random survival forest [26], [27]. Random forest is a common method applied in many disciplines [28], [29]. Random survival forest (RSF) is accurately predicts the event risk and has become widespread since it has the capability of handling a variety of covariates. Nevertheless, this method has been unable to incorporate time-dependent predictors. Thus, Devaux et al. [30] proposed an alternative way to RSF with multivariate longitudinal time-dependent covariates.

This study set out to develop a model for individual dynamic prediction of EDS, associated with clinical and biological factors in the PPMI cohort.

The rest of the paper is organized as follows: Section 2 introduces the material and method, listed under two subheadings: the PPMI data and random forest for time-dependent predictors. Section 3 presents results and discussion, and the final section concludes the study.

2. Material and Method

2.1. The PPMI Data

The PPMI is a comprehensive observational, international, multicenter study that is designed for the identification of PD progression biomarkers for the improvement of understanding the disease etiology and to provide key tools to improve the likelihood of success of PD-modifying therapeutic trials. The PPMI aims to provide a wide research community with a standardized, longitudinal dataset and biosample library. The PPMI cohort includes 168 de novo PD patients, and they were followed up for 2 years [10]. Detailed information regarding the study's procedures and inclusion and exclusion criteria is available at the PPMI website, https://www.ppmi-info.org. The dataset is available upon registering and requesting to access data on the aforementioned website, and downloaded on April 1, 2023.

The data are collected at baseline and annually thereafter. Patients were evaluated with the ESS [31], a measure of EDS, where a maximum score of 24 indicates the worst degree of sleepiness. This test has a significant test-retest correlation [32]. The ESS also has a strong correlation with the sleepiness measures in PD [33], [34] and is sensible to switch due to an intervention [35]. The patients were categorized as having EDS when ESS is greater than or equal to 10 and having severe EDS when ESS is greater than or equal to 17 [31]. In addition to ESS, the patients were assessed with the motor symptoms, Movement Disorders Society – Unified Parkinson's Disease Rating Scale (MDS-UPDRS) [36]. Non-motor symptoms comprise the Montreal Cognitive Assessment (MoCA) [37], the Hopkins verbal learning test (HVLT) [38], the Benton judgment of line orientation test (JLO) [39], the symbol digit modalities test (SDMT) [40], the University of Pennsylvania smell ID test (UPSIT) [41], the REM Sleep Behaviour Disorder Screening Questionnaire

(RBDSQ) [42], and the State-Trait-Anxiety Inventory (STAI) state and trait sub-scores [43].

2.2. Method: Random Forest for Time-Dependent Predictors

We first consider a dataset of N subjects consisting of Y the outcome, $\mathcal{M}_x$ an ensemble of P time-independent covariates, and $\mathcal{M}_y$ an ensemble of Q time-dependent covariates. In principal, random forest includes an ensemble of B trees and aggregated to obtain predictions.

2.2.1. The Tree Building

The tree building aims at the recursive partition of the individuals into the most homogeneous nodes/groups. For each tree, b $(b = 1, 2, \dots, B)$ h a bootstrap sample from N subject is drawn with a replacement. The individuals that are excluded by the bootstrap comprise the out-of-bag (OOB) sample, OOB^b. At each node $d \epsilon \mathcal{D}^b$, the following steps utilizing $N^{(d)}$ are repeated recursively:

1. A random subset of covariates $\mathcal{M}^{(d)} = \left\{ \mathcal{M}_x^{(d)}, \mathcal{M}_y^{(d)} \right\} \subset \{ \mathcal{M}_x, \mathcal{M}_y \}$ is selected to improve accuracy and minimize the correlation between trees. The size of $\mathcal{M}^{(d)}$ is called tuning parameter, mtry.
2. For each time-dependent variable in $\mathcal{M}_y^{(d)}$:
   a. The linear mixed effect model proposed by Laird and Ware [44] is employed at each node d.
   b. An ensemble of $\mathcal{M}_{y\star}^{(d)}$ of subject time-fixed variables is derived.
3. New ensemble of candidate variables $\mathcal{M}_\star^{(d)} = \left\{ \mathcal{M}_x^{(d)}, \mathcal{M}_{y\star}^{(d)} \right\}$ is defined.
4. For each candidate variable $W \in \mathcal{M}_\star^{(d)}$:
   a. A series of splits $c_W^{(d)}$ is built according to the values of the variable that leads each time into two groups.
   b. The distance between two groups is calculated.
5. The subjects are split into two groups: those that maximize the test statistic for survival outcomes or those that minimize the test statistic for categorical and continuous outcomes. The optimal couple is denoted as $\left\{ W_0^d, c_0^d \right\}$ and this represents the left and right daughter nodes, $2d$ and $2d + 1$, respectively.
6. Step 1 to 5 are repeated on the daughter nodes till the stopping criteria are met.

Two stopping criteria to pursue with the stopping of a node are defined: nodesize, a minimal number of individuals in each of the daughter nodes and minsplit, a minimal number of events. Once the stopping criteria is met, the node is counted as a terminal node or leaf $h \in \mathcal{H}$.

In each leaf, a summary $\left(\pi^{h^b} \right)$ is presented utilizing the subjects of the leaf of the tree b.

2.2.2. Out-of-Bag Individual Prediction of the Outcome

The overall OOB prediction $\hat{\pi}_\star$ for an individual $\star$ is found through the tree-based predictions of $\star$ as below:

$$\hat{\pi}_\star = \frac{1}{|\mathcal{O}_\star|} \sum_{b \in \mathcal{O}_\star} \hat{\pi}^{h_\star^b} \qquad (1)$$

where $|\mathcal{O}_\star|$ represents the length of $\mathcal{O}_\star$ and $\hat{\pi}^{h_\star^b}$ denotes the Aalen-Johansen estimator in leaf $h_\star^b$ of the b. Tree.

2.3. Out-of-Bag Error

The OOB error measures the difference between the observed and predicted values. The Integrated Brier score (IBS) between τ_1 and τ_2 is defined as follows:

$$errOOB = \int_{\tau_1}^{\tau_2} \frac{1}{N} \sum_{i=1}^{N} \hat{\omega}_i(t) \left\{ \mathbb{1}_{(T_i \le t, \delta_i = k)} - \hat{\pi}_{ik}(t) \right\}^2 dt \qquad (2)$$

where T is the event time, k is the cause of interest, and $\hat{\omega}$ (t) is the estimated weights, that considers censoring [45].

2.4. Variable Importance

The variable importance (VIMP) quantifies the loss of predictive performance in case of removal of the link between predictor and the response variable [27]. Such a link is broken with the permutation of the predictors at the individual level for time-independent variables and at the observation level for time-dependent variables. Large VIMP value represents good prediction ability for the predictor.

3. Results and Discussion

We aimed to predict the subject probability of having EDS in patients with Parkinson's disease using social, demographic, and clinical variables (sex, presence of the ApoE4 Allele, and baseline count of lymphocytes).

The dataset is split into two: training (2/3 of subjects) and testing (1/3 of subjects) datasets. The random forest is built by specifying the linear mixed models for each longitudinal predictor using the `DynForest` function. The outcome objects were the event indicator and event time data. For the hyperparameters, we chose `mtry=7`, `nodesize=5`, and `minsplit=2`. When the type of outcome is survival, the Fine&Gray statistic test is used as the splitting rule and the cumulative incidence function (CIF) as the leaf statistic. The assessment of the predictive ability of the model is made with the out-of-bag error (OOB). When the outcome of interest is survival, the OOB error is computed using the integrated Brier Score (IBS) [45]. The OOB error for the model is obtained from the mean of the subject-specific OOB error. The computed OOB error from the starting time to the maximum of the time-to-event is 0.186. The rate of having EDS in 168 Parkinson's patients is 0.452. It means that 76 patients have EDS and the rest do not have EDS.
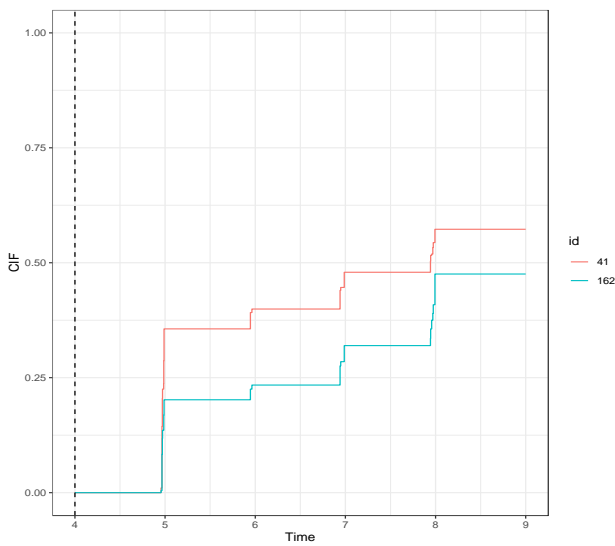
Figure 1. Predicted CIF for individual 41 and 162.

We also predict the outcome for new individuals using the trained random forest. Dynamic prediction can be made by specifying a prediction time, and landmark from which the prediction is made. Only the individuals still at risk at the landmark time (dashed vertical line, at 4 years) are selected for illustration purposes, and subject-specific CIF is predicted using dataframe for those who are at risk at 4 years. Figure 1 displays the CIF of the outcomes of individuals 41 and 162. The risk of having the event for individual 41 had a rapid rise in year 5. After 8 years from landmark time, individual 41 has a higher probability of having EDS than the other.

In order to understand the importance of the predictors, VIMP statistics are presented in Figure 2. Stai state was the most important variable, which has the association with having EDS, with an average gain in IBS of 5.2%, followed by JLO and ApoE4 Allele (gains of 3.8% and 2.5%, respectively). In the case of correlated variables, the variables may be re-grouped into dimensions, and the VIMP can be calculated at the dimension group level. Figure 3 shows that 2 non-motor predictors (stai state and stai trait) in group 2 attained a mean gain of 8.7%.
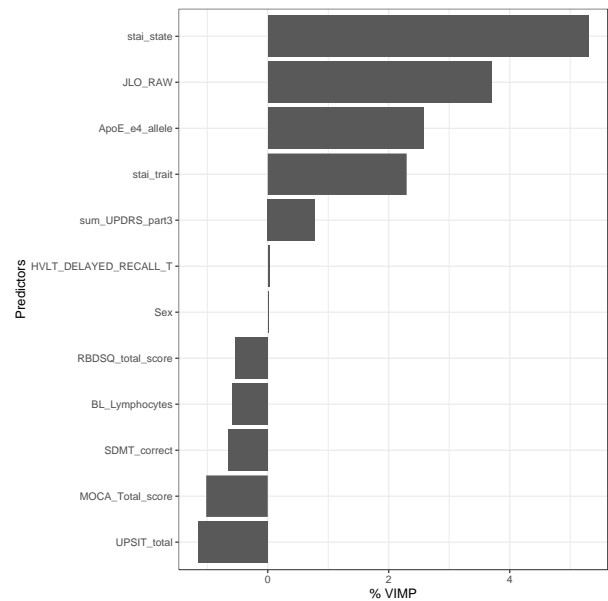
Figure 2. Importance variable.
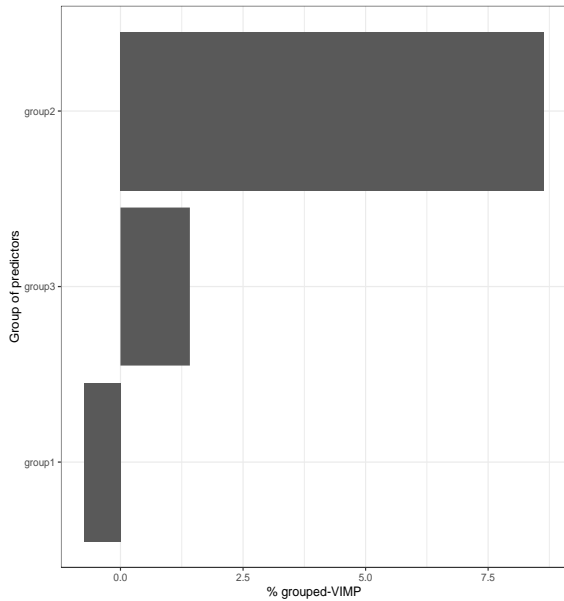
Figure 3. Grouped importance variable (gVIMP), Group1: MOCA, HVLT, JLO, SDMT, UPSIT and RBDSQ; Group2: Stai trait and stai state; Group3: ApoE4 and lymphocyte.

In order to better understand the tree-building process, the minimal depth utilizing large mtry hyper parameter is computed and shown by the predictor and feature in Figure 4. Stai trait has the lowest average minimal depth. The same inference can also be seen for the minimal depth plot regarding features. The lowest average minimal depth belongs to stai trait features. These indicate that the stai predictors are the most efficient predictors for splitting the subjects into homogenous subgroups. These outcomes can also be seen in variable importance plots.
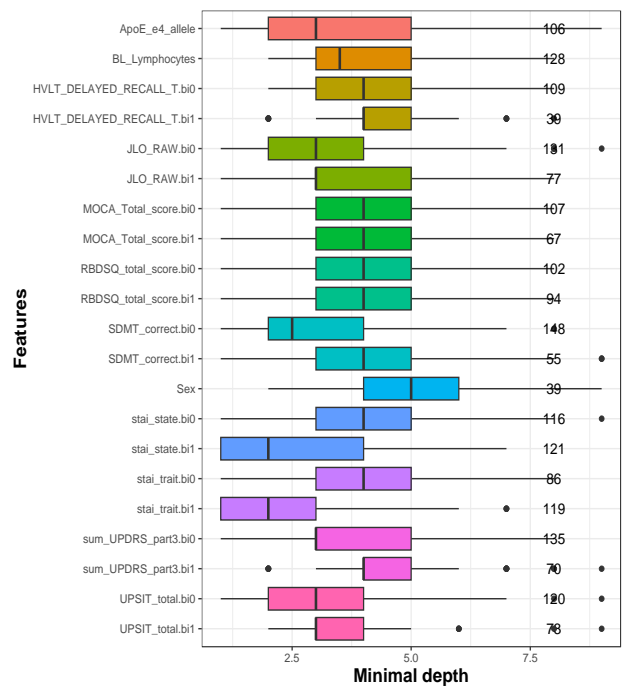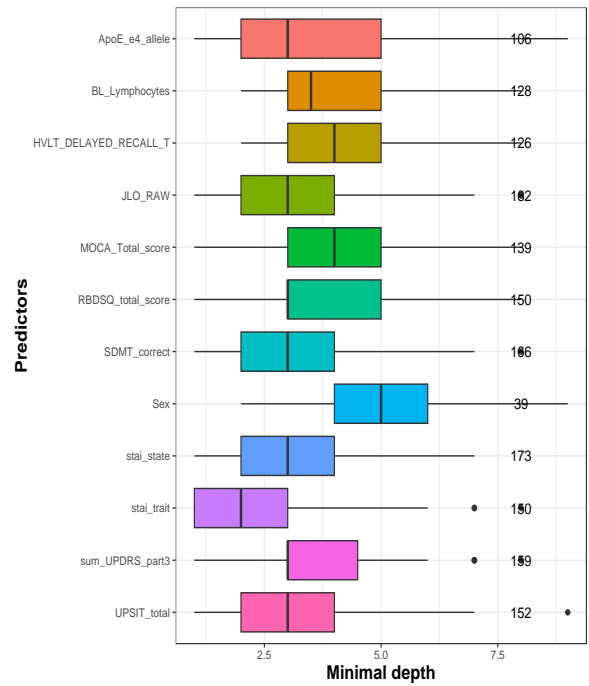
Figure 4. Average minimal depth level by predictor (upper) and feature (lower).

We computed the individual dynamic predictions accounting for multiple longitudinal predictors through the extended random survival forest method in order to deal with time-dependent predictors. The DynForest R package, which is a user-friendly R package and easy-to-use random forest methodology, is utilized to achieve this [46]. Moreover, the importance of the variables using

VIMP, grouped-VIMP and minimal depth are provided.

Some studies have investigated the EDS effect in PD. Feng et al. [47] provided a systematic review and meta-analysis related to EDS in PD. They found that approximately 35.1% of subjects with PD had EDS, and EDS in PD can have association with severe PD. To the best of our knowledge, so far, limited studies have given sufficient consideration to the impact of imaging and biological markers on EDS change over time in PD in Amara et al. [18], Höglund et al. [48], Liu et al. [49], and Pino et al. [50]. They considered the longitudinal change of EDS in patients with PD. Höglund et al. [48] investigated EDS over time associated with PD symptoms. The authors used linear mixed effect models and concluded that EDS did not worsen over the follow-up period and that EDS is a complex nonmotor symptom. This result contradicts ours. On the other hand, Liu et al. [49] and Pino et al. [50] aimed to investigate the effect of sleep problems on longitudinal changes in motor and non-motor symptoms among patients with PD. They both used linear mixed effect, and Liu et al. [49] additionally employed Cox PH models and concluded that patients with PD and have sleep problems progress faster symptoms of more aggressive types of PD. In addition to this, using more advanced methods, Amara et al. [18] implemented the random survival forest method and concluded that EDS had a significant rise over time and had associations with various clinical predictors in early PD. This result is supported by our study. Nonetheless, our study has some advantages (i) it used all available information; (ii) it has a simultaneous analysis of the longitudinal and event time processes; (iii) it allows for complication associations between repeated measurements and event time; (iv) it allows for high-dimensional data.

4. Conclusion and Suggestions

The aim of this study was to investigate individual dynamic prediction of EDS (predict the event - having EDS) with multiple longitudinal time-dependent variables in PD. We identified the most significant clinical markers of rate of progression so that this will benefit clinical care and the testing of new treatments. We also concluded that EDS has a significant effect on patients with PD. Overall, EDS is a clinical manifestation in de novo PD patients. Moreover, this study indicates that many factors, such as stai state, JLO and ApoE4 Allele are the most important variables in EDS in de novo PD patients. Understanding the clinical features of EDS is important to identify early PD and improve life quality.

The prediction model could be improved by considering discrete longitudinal markers (i.e., binary or categorical). Generalized estimated equations can be used instead of generalized mixed models.

Acknowledgment

Statement of Research and Publication Ethics

The study is complied with research and publication ethics

References

[1]   T. Simuni *et al.*, "Longitudinal Change of Clinical and Biological Measures in Early Parkinson's Disease: Parkinson's Progression Markers Initiative Cohort," *Movement Disorders*, vol. 33, no. 5, 2018, doi: 10.1002/mds.27361.

[2]   L. M. Chahine, A. W. Amara, and A. Videnovic, "A systematic review of the literature on disorders of sleep and wakefulness in Parkinson's disease from 2005 to 2015," *Sleep Medicine Reviews*, vol. 35. 2017. doi: 10.1016/j.smrv.2016.08.001.

[3]   M. D. W. Knipe, M. M. Wickremaratchi, E. Wyatt-Haines, H. R. Morris, and Y. Ben-Shlomo, "Quality of life in young- compared with late-onset Parkinson's disease," *Movement Disorders*, vol. 26, no. 11, 2011, doi: 10.1002/mds.23763.

[4]   T. Simuni *et al.*, "Correlates of excessive daytime sleepiness in de novo Parkinson's disease: A case control study," *Movement Disorders*, vol. 30, no. 10, 2015, doi: 10.1002/mds.26248.

[5]   C. Meindorfner, Y. Körner, J. C. Möller, K. Stiasny-Kolster, W. H. Oertel, and H. P. Krüger, "Driving in Parkinson's disease: Mobility, accidents, and sudden onset of sleep at the wheel," *Movement Disorders*, vol. 20, no. 7, 2005, doi: 10.1002/mds.20412.

[6]   K. Zhu, J. J. van Hilten, and J. Marinus, "Course and risk factors for excessive daytime sleepiness in Parkinson's disease," *Parkinsonism Relat Disord*, vol. 24, 2016, doi: 10.1016/j.parkreldis.2016.01.020.

[7]   D. P. Breen, C. H. Williams-Gray, S. L. Mason, T. Foltynie, and R. A. Barker, "Excessive daytime sleepiness and its risk factors in incident Parkinson's disease," *Journal of Neurology, Neurosurgery and Psychiatry*, vol. 84, no. 2. 2013. doi: 10.1136/jnnp-2012-304097.

[8]   D. Verbaan, S. M. Van Rooden, M. Visser, J. Marinus, and J. J. Van Hilten, "Nighttime sleep problems and daytime sleepiness in Parkinson's disease," *Movement Disorders*, vol. 23, no. 1, 2008, doi: 10.1002/mds.21727.

[9]   M. D. Gjerstad, D. Aarsland, and J. P. Larsen, "Development of daytime somnolence over time in Parkinson's disease," *Neurology*, vol. 58, no. 10, 2002, doi: 10.1212/WNL.58.10.1544.

[10]   K. Marek *et al.*, "The Parkinson Progression Marker Initiative (PPMI)," *Progress in Neurobiology*, vol. 95, no. 4. 2011. doi: 10.1016/j.pneurobio.2011.09.005.

[11]   D. Kaynak, G. Kiziltan, H. Kaynak, G. Benbir, and O. Uysal, "Sleep and sleepiness in patients with Parkinson's disease before and after dopaminergic treatment," *Eur J Neurol*, vol. 12, no. 3, 2005, doi: 10.1111/j.1468-1331.2004.00971.x.

[12]   G. Fabbrini, P. Barbanti, C. Aurilia, N. Vanacore, C. Pauletti, and G. Meco, "Excessive daytime sleepiness in de novo and treated Parkinson's disease," *Movement Disorders*, vol. 17, no. 5, 2002, doi: 10.1002/mds.10193.

[13]   J. Buskova *et al.*, "Sleep disturbances in untreated Parkinson's disease," *J Neurol*, vol. 258, no. 12, 2011, doi: 10.1007/s00415-011-6109-7.

[14]   R. Erro *et al.*, "Non-motor symptoms in early Parkinson's disease: A 2-year follow-up study on previously untreated patients," *J Neurol Neurosurg Psychiatry*, vol. 84, no. 1, 2013, doi: 10.1136/jnnp-2012-303419.

[15]   C. Pont-Sunyer *et al.*, "The onset of nonmotor symptoms in parkinson's disease (the onset pd study)," *Movement Disorders*, vol. 30, no. 2, 2015, doi: 10.1002/mds.26077.

[16]   R. D. Abbott *et al.*, "Excessive daytime sleepiness and subsequent development of Parkinson disease," *Neurology*, vol. 65, no. 9, 2005, doi: 10.1212/01.wnl.0000183056.89590.0d.

[17]   L. K. Tholfsen, J. P. Larsen, J. Schulz, O. B. Tysnes, and M. D. Gjerstad, "Development of excessive daytime sleepiness in early Parkinson disease," *Neurology*, vol. 85, no. 2, 2015, doi: 10.1212/WNL.0000000000001737.

[18]   A. W. Amara *et al.*, "Longitudinal assessment of excessive daytime sleepiness in early Parkinson's disease," *J Neurol Neurosurg Psychiatry*, vol. 88, no. 8, 2017, doi: 10.1136/jnnp-2016-315023.

[19]   D. Rizopoulos, *Joint Models for Longitudinal and Time-to-Event Data*. 2012. doi: 10.1201/b12208.

[20]   M. S. Wulfsohn and A. A. Tsiatis, "A Joint Model for Survival and Longitudinal Data Measured with Error," *Biometrics*, vol. 53, no. 1, 1997, doi: 10.2307/2533118.

[21]   R. Henderson, "Joint modelling of longitudinal measurements and event time data," *Biostatistics*, vol. 1, no. 4, 2000, doi: 10.1093/biostatistics/1.4.465.

[22] G. Buyrukoglu, P. Philipson, and N. Lin, "Methodological Development and Advances for Joint Modelling of Longitudinal and Time-To-Event Data," England, 2018. [Online]. Available: https://www.proquest.com/dissertations-theses/methodological-development-advances-joint/docview/2425909057/se-2?accountid=62115

[23] G. L. Hickey, P. Philipson, A. Jorgensen, and R. Kolamunnage-Dona, "Joint modelling of time-to-event and multivariate longitudinal outcomes: Recent developments and issues," *BMC Med Res Methodol*, vol. 16, no. 1, 2016, doi: 10.1186/s12874-016-0212-5.

[24] D. Rizopoulos, "The R package jmbayes for fitting joint models for longitudinal and time-to-event data using MCMC," *J Stat Softw*, vol. 72, 2016, doi: 10.18637/jss.v072.i07.

[25] G. L. Hickey, P. Philipson, A. Jorgensen, and R. Kolamunnage-Dona, "JoineRML: A joint model and software package for time-to-event and multivariate longitudinal outcomes," *BMC Med Res Methodol*, vol. 18, no. 1, 2018, doi: 10.1186/s12874-018-0502-1.

[26] H. Ishwaran, T. A. Gerds, U. B. Kogalur, R. D. Moore, S. J. Gange, and B. M. Lau, "Random survival forests for competing risks," *Biostatistics*, vol. 15, no. 4, 2014, doi: 10.1093/biostatistics/kxu010.

[27] H. Ishwaran, U. B. Kogalur, E. H. Blackstone, and M. S. Lauer, "Random survival forests," *Ann Appl Stat*, vol. 2, no. 3, Sep. 2008, doi: 10.1214/08-AOAS169.

[28] G. Buyrukoğlu, S. Buyrukoğlu, and Z. Topalcengiz, "Comparing Regression Models with Count Data to Artificial Neural Network and Ensemble Models for Prediction of Generic Escherichia coli Population in Agricultural Ponds Based on Weather Station Measurements," *Microb Risk Anal*, vol. 19, 2021, doi: 10.1016/j.mran.2021.100171.

[29] S. Buyrukoğlu, "Early Detection Of Alzheimer's Disease Using Data Mining: Comparison Of Ensemble Feature Selection Approaches," *Konya Journal of Engineering Sciences*, vol. 9, no. 1, 2021.

[30] A. Devaux, C. Helmer, R. Genuer, and C. Proust-Lima, "Random survival forests with multivariate longitudinal endogenous covariates," 2023.

[31] M. W. Johns, "A new method for measuring daytime sleepiness: The Epworth sleepiness scale," *Sleep*, vol. 14, no. 6, 1991, doi: 10.1093/sleep/14.6.540.

[32] P. Hagell and J. E. Broman, "Measurement properties and hierarchical item structure of the Epworth sleepiness scale in Parkinson's disease," *J Sleep Res*, vol. 16, no. 1, 2007, doi: 10.1111/j.1365-2869.2007.00570.x.

[33] C. Monaca *et al.*, "Vigilance troubles in Parkinson's disease: A subjective and objective polysomnographic study," *Sleep Med*, vol. 7, no. 5, 2006, doi: 10.1016/j.sleep.2005.12.002.

[34] R. Poryazova, D. Benninger, D. Waldvogel, and C. L. Bassetti, "Excessive daytime sleepiness in parkinson's disease: Characteristics and determinants," *European Neurology*, vol. 63, no. 3. 2010. doi: 10.1159/000276402.

[35] B. Högl *et al.*, "Scales to assess sleep impairment in Parkinson's disease: Critique and recommendations," *Movement Disorders*, vol. 25, no. 16. 2010. doi: 10.1002/mds.23190.

[36] C. G. Goetz *et al.*, "Movement Disorder Society-Sponsored Revision of the Unified Parkinson's Disease Rating Scale (MDS-UPDRS): Scale presentation and clinimetric testing results," *Movement Disorders*, vol. 23, no. 15, 2008, doi: 10.1002/mds.22340.

[37] Z. S. Nasreddine *et al.*, "The Montreal Cognitive Assessment, MoCA: A brief screening tool for mild cognitive impairment," *J Am Geriatr Soc*, vol. 53, no. 4, 2005, doi: 10.1111/j.1532-5415.2005.53221.x.

[38]   R. H. B. Benedict, D. Schretlen, L. Groninger, and J. Brandt, "Hopkins verbal learning test - Revised: Normative data and analysis of inter-form and test-retest reliability," *Clinical Neuropsychologist*, vol. 12, no. 1, 1998, doi: 10.1076/clin.12.1.43.1726.

[39]   C. E. Qualls, N. G. Bliwise, and A. Y. Stringer, "Short forms of the Benton Judgment of Line Orientation Test: Development and psychometric properties," *Archives of Clinical Neuropsychology*, vol. 15, no. 2, 2000, doi: 10.1016/S0887-6177(98)00043-2.

[40]   R. H. B. Benedict, J. Deluca, G. Phillips, N. LaRocca, L. D. Hudson, and R. Rudick, "Validity of the Symbol Digit Modalities Test as a cognition performance outcome measure for multiple sclerosis," *Multiple Sclerosis*, vol. 23, no. 5. 2017. doi: 10.1177/1352458517690821.

[41]   T. Joseph *et al.*, "Screening performance of abbreviated versions of the UPSIT smell test," *J Neurol*, vol. 266, no. 8, 2019, doi: 10.1007/s00415-019-09340-x.

[42]   K. Stiasny-Kolster, G. Mayer, S. Schäfer, J. C. Möller, M. Heinzel-Gutenbrunner, and W. H. Oertel, "The REM sleep behavior disorder screening questionnaire - A new diagnostic instrument," *Movement Disorders*, vol. 22, no. 16, 2007, doi: 10.1002/mds.21740.

[43]   P. C. Kendall and et al, "The State-Trait Anxiety Inventory: A systematic evaluation," *J Consult Clin Psychol*, vol. 44, no. 3, 1976, doi: 10.1037/0022-006X.44.3.406.

[44]   N. M. Laird and J. H. Ware, "Random-Effects Models for Longitudinal Data," *Biometrics*, vol. 38, no. 4, 1982, doi: 10.2307/2529876.

[45]   T. A. Gerds and M. Schumacher, "Consistent estimation of the expected brier score in general survival models with right-censored event times," *Biometrical Journal*, vol. 48, no. 6, 2006, doi: 10.1002/bimj.200610301.

[46]   A. Devaux, C. Proust-Lima, and R. Genuer, "Random Forests for time-fixed and time-dependent predictors: The DynForest R package," Feb. 2023.

[47]   F. Feng, Y. Y. Cai, Y. B. Hou, R. Ou, Z. Jiang, and H. F. Shang, "Excessive daytime sleepiness in Parkinson's disease: A systematic review and meta-analysis," *Parkinsonism and Related Disorders*, vol. 85. 2021. doi: 10.1016/j.parkreldis.2021.02.016.

[48]   A. Höglund, P. Hagell, J. E. Broman, S. Pålhagen, K. Sorjonen, and S. Fredrikson, "A 10-Year Follow-Up of Excessive Daytime Sleepiness in Parkinson's Disease," *Parkinsons Dis*, vol. 2019, 2019, doi: 10.1155/2019/5708515.

[49]   Y. Liu *et al.*, "Longitudinal Changes in Parkinson's Disease Symptoms with and Without Rapid Eye Movement Sleep Behavior Disorder: The Oxford Discovery Cohort Study," *Movement Disorders*, vol. 36, no. 12, 2021, doi: 10.1002/mds.28763.

[50]   R. Del Pino *et al.*, "Clinical long-term nocturnal sleeping disturbances and excessive daytime sleepiness in Parkinson's disease," *PLoS One*, vol. 16, no. 12 December, 2021, doi: 10.1371/journal.pone.0259935.

Production of Babbitt Metal Thin Film by Thermal Evaporation Method and Investigation of the Change of Thıs Thin Film With Heat Treatment Time

Muhammed Sait KANCA[1*]

[1]msaitkanca@munzur.edu.tr

(ORCID: 0000-0002-2987-4284)

Abstract
In this study, thin films of Babbitt alloy will be investigated. For this purpose, tin (Sn) based Babbitt alloy thin films on glass substrates were produced by thermal evaporation method and these thin films were heat treated at 120°C for different times. The crystal structure of non-heat treated and heat treated babbitt thin films were determined by x-ray measurements. It was observed that the thin films were formed as agglomerations on the crystal structure of tin and crystallization increased as the heat treatment time increased. The grain boundaries on the coating surface can be clearly seen from the SEM images and a decrease in grain size was observed. In addition, it was determined that the oxide layer was deposited on the surface depending on the treatment time applied to the thin films obtained. Finally, it was observed from the AFM images that the roughness value.

1. Introduction

Babbitt metal, invented by Isaac Babbitt in 1839, is a soft alloy of tin (Sn), lead (Pb), copper (Cu), and antimony (Sb). Also known as white metal. tin-based Babbitt alloys, which are among the Babbit alloy types, are highly preferred Babbit alloy types due to their superior corrosion resistance, easy bonding and less dissociation tendency, although they are high cost alloys [1-3]. These metals are the most common classical bearing materials today, especially in engines, compressors, fans, pumps, large turbines, aviation engines and many more rotating machinery [4].

Mechanical wear loss in materials consists of friction caused by the moving contact of the material with another material [5].

Babbitt alloys are used as a primer on surfaces, especially in engine bearings, to minimize the negative effects of this wear [6].

In a study, a new alloy obtained by adding Babbitt alloy to a new alloy, small (0.07 m/s) and high (4.5 m/s) lubrication was applied to the wear test and it was determined that the wear rate decreased and there was a significant decrease in the coefficient of friction [7]. For this reason, compared to other alloys used in bearings, tin-based (Sn-based) Babbitt alloys are widely used in the main components of bearings due to their unique corrosion resistance. Tin-based Babbitt alloys generally contain about 3–8% by weight Cu and 5–8% by weight Sb. Therefore, the microstructures of these alloys also show different properties due to these differences in their compositions [8].

In recent years, gaps in surface engineering research have been identified and this has prompted scientists to conduct further research [9]. With the coatings on the surfaces of the material, it is aimed both to protect the existing properties of the material and to further develop the existing properties [10].

For this reason, depending on the developing technology and this demand (increase in the usage area), especially in the last fifty years, the interest in thin film has increased significantly. The materials produced by the thin film method today have many

---

advantages in terms of both cost, functionality (performance) and aesthetics [11]. In addition, with the recent thin film studies, many new research areas have emerged depending on the thickness, geometry and structure of the produced film. It has led to diversity in usage areas by providing convenience in the integration of materials produced as a result of coating the materials with thin films with various devices. The wear on the surface of the material varies depending on the surface hardness, roughness, grain size, ambient temperature and lubrication regime of the material [12,13]. For this reason, it is of great importance to understand the mechanical properties of the thin film coating on the material surface [14]. Thin films obtained by coating are extremely hard and thermally extremely stable [15]. Babbitt alloys, which are produced with thin film technology, have many uses in cutting tools, drill bits, beds, many electronic devices, decorative coatings, car parts and many more due to their superior resistance to corrosion and ergonomic convenience in technological systems today [11]. The thermal evaporation method, which is one of the thin film production methods, has a wide range of uses and high efficiency. This method has superior properties such as precise control of the thickness of the produced film and obtaining a smooth surface (smooth), flexibility to adjust interfaces, and solvent-free [16,17]. It is known from SEM images in many studies that the surface is homogeneous and the grain size is very small in thin films produced by this method [18]. Therefore, this method is a useful method for improving the friction and wear behavior of a material. Amanov et al. determined that a thin and properly formed saturated nanostructure significantly increased the wear resistance [12]. Paulo Roberto Campos Alcover Junior et al. determined that the coefficient of friction of the coatings produced by the thermal evaporation method is lower than the coatings produced by the traditional methods and their hardness is at an equivalent level [19]. The element that affects the hardness of the material in Babbitt alloys is antimony. As the ratio of the antimony element in the alloy increases, the hardness ratio of the alloy increases and therefore the compressive strength of the alloy also increases [20]. However, this also negatively affects the fragility of the material. The aim of this study is to produce a thin film on the glass surface with Babbitt metal ($Sn_{58}Sb_{35}Cu_7$) by thermal evaporation method. Then, measurements such as crystal structures, optical properties and surface roughness of these thin films will be obtained and evaluations will be made according to these measurement results.

2. Material and Method

The thermal evaporation method is a system formed by melting and evaporating an alloy (or polymer) left in a crucible made of tungsten with the help of electric current under a high vacuum, and adhering these evaporated particles to the coating substrate at a certain distance from the crucible. The two most outstanding features of the thermal evaporation coating method compared to other methods are that a very homogeneous surface coating is obtained in this method and the coating thickness can be interfered with. In order to benefit from these two superior features, factors such as the amount of material placed in the crucible, the distance between the crucible and the coating substrate, the value of the current applied to the crucible for melting the material in the crucible and the application time of this current are very important. Coating processes were carried out in a Leybold brand Univex 300 thermal evaporator. Here, the glass substrate in the form of a sheet of 1 mm in size and 25 mm x 75 mm in size was cleaned first with alcohol and then with the ultrasonic cleaning method. This cleaned glass substrate was placed at a distance of approximately 18 cm from the tungsten crucible and the coating process was carried out in a vacuum environment of 6.4×10^{-5} mbar for 8 minutes. The coating process was carried out by applying a current of 335 A. Finally, the production process was completed by applying heat treatments for one hour, two hours, four hours and six hours at 120 °C, respectively. In order to determine the crystal structure analysis of Babbitt coatings produced by thermal evaporation on glass substrate, XRD analysis measurements were taken at room temperature using Rigaku Miniflex 600 brand X-ray device. AFM images were taken used to determine the surface morphology (roughness) of these coatings. Then, LEO Evo 40 brand SEM-EDX and Mapping measurements were made to determine the surface images and elemental distribution of the existing coating, as well as its qualitative and quantitative properties. The schematic of the experimental procedures is shown in Figure 1. Table 1 shows coding detail of samples and Figure 2 shows image of samples.

Figure 1. Detailed View of the Device of the Thermal Evaporation System
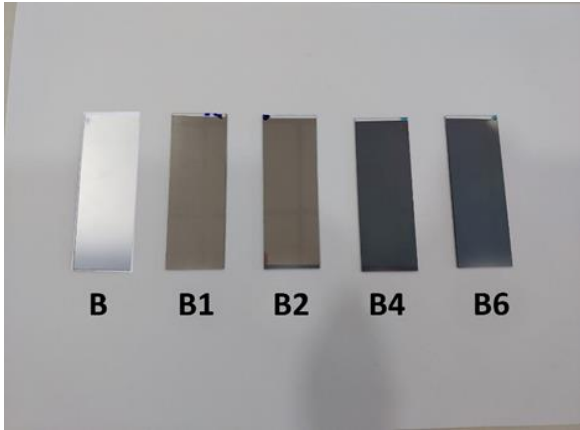
Figure 2. The image of the glass samples that have been coatedand heat treated

Table 1. Coding detail of existing samples

B	B1	B2	B4	B6
Glass specimen coated with Babbitt metal ($Sn_{58}Sb_{35}Cu_7$)	Glass specimen coated with Babbitt metal and heat treated for 1 hour	Glass coated with Babbitt metal Glass specimen heat treated for 2 hours	Glass coated with Babbitt metal Glass specimen heat treated for 4 hours	Glass sample coated with Babbitt metal and heat treated for 6 hours

4. Conclusion and Suggestions

Figures 3-7 show SEM-EDX and mapping images of exist coating. If we pay attention to the mapping image in Figure 3-a, the elements in the alloy are homogeneously distributed in the coating. In the SEM image in Figure 3-b, the grain and grain boundaries formed on the coating surface are clearly visible. Depending on the heat treatment applied to these coatings, oxide began to accumulate on the surface in the form of bubbles due to the tin and antimony elements in the alloy, and the oxide layer on the surface gradually increased in proportion to the duration of the applied heat treatment.

In a study, Kök et al. also determined that the oxide layer on the surface increased when they applied heat treatments at different values to the NiMnGa alloy [21]. This oxide layer accumulated on the surface caused a decrease in the amount of roughness on the surface, and this result is in harmony with the AFM results. In a thin film study conducted by Tasgın et al., they determined that the amount of roughness on the surface decreased significantly with the coating on the glass substrate, using AFM images [22].

In addition, if we pay attention to the SEM images in Figure 3-a - 7-a, respectively, as the duration of the applied heat treatment increases, the copper element in the alloy accumulates in the coating (on the surface) through agglomeration, and this result is also supported by the EDX results.

It was determined that agglomerations occurred on the surface coated with 97Se-3CeO$_2$ thin film due to the heat treatment applied on (100) and (101) planes [22]. The reason for this agglomeration is that the melting point between the copper element (Cu) and the tin and antimony elements (Sn and Sb) in the Babbitt alloy is known.
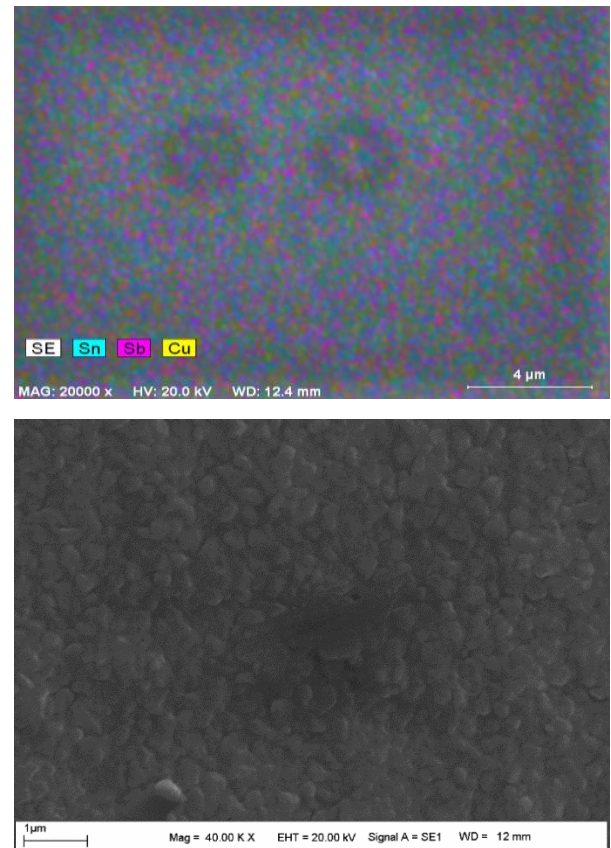
Figure 3. a) mapping image of sample B, **b)** SEM image of sample B
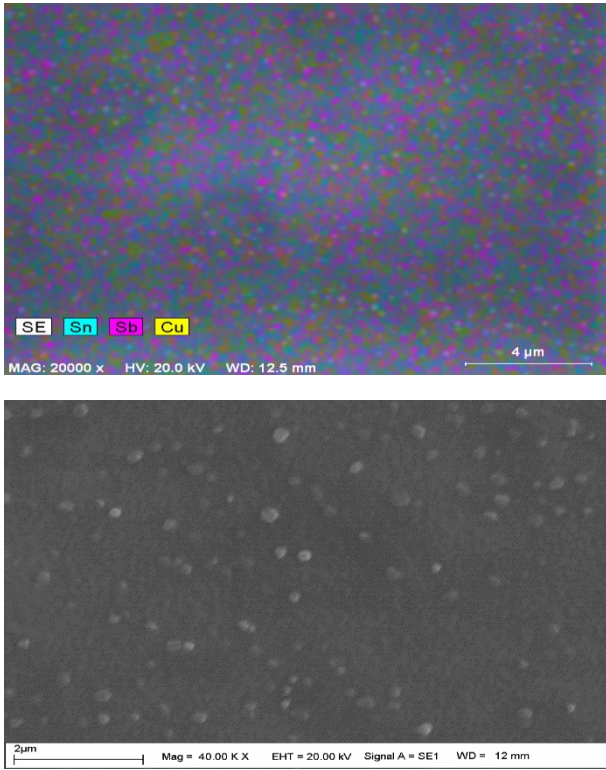
Figure 4. a) mapping image of sample B1, **b)** SEM image of sample B1
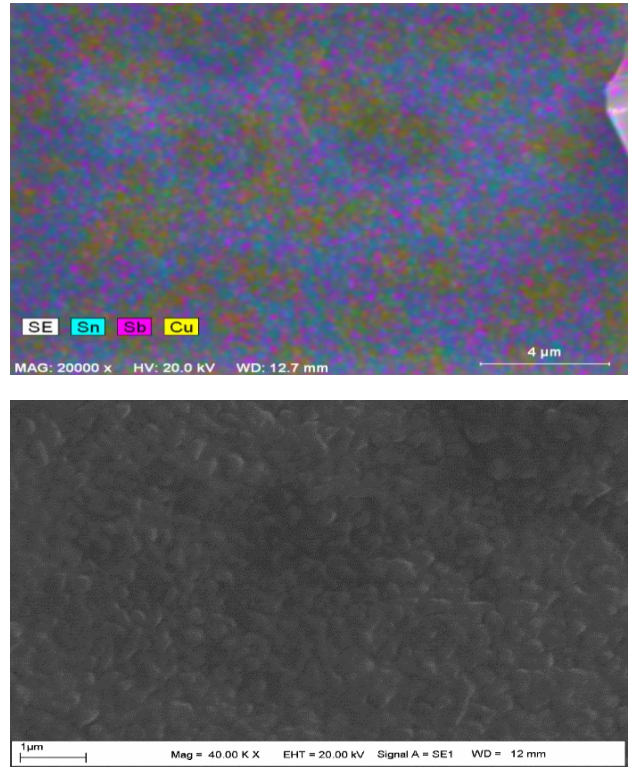
Figure 6. a) Mapping image of B4 sample, **b)** SEM image of B4 sample
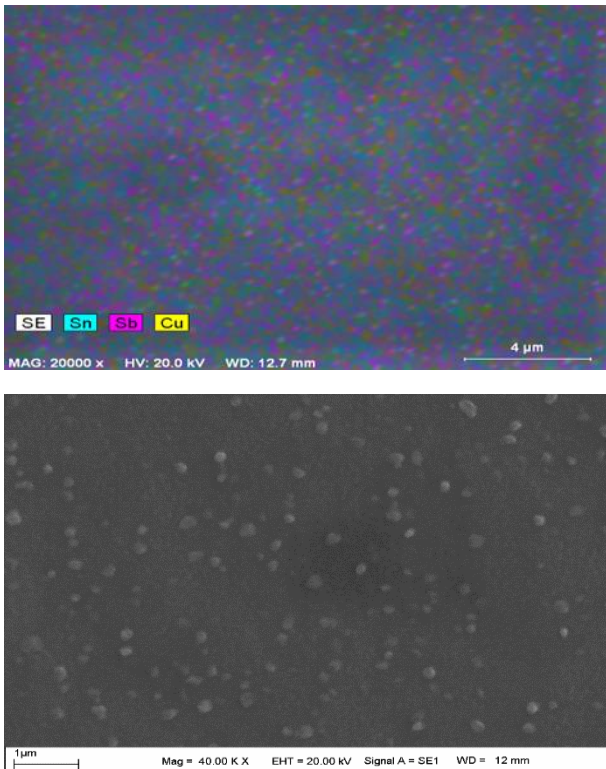
Figure 5. a) mapping image of B2 sample, **b)** SEM image of B2 sample
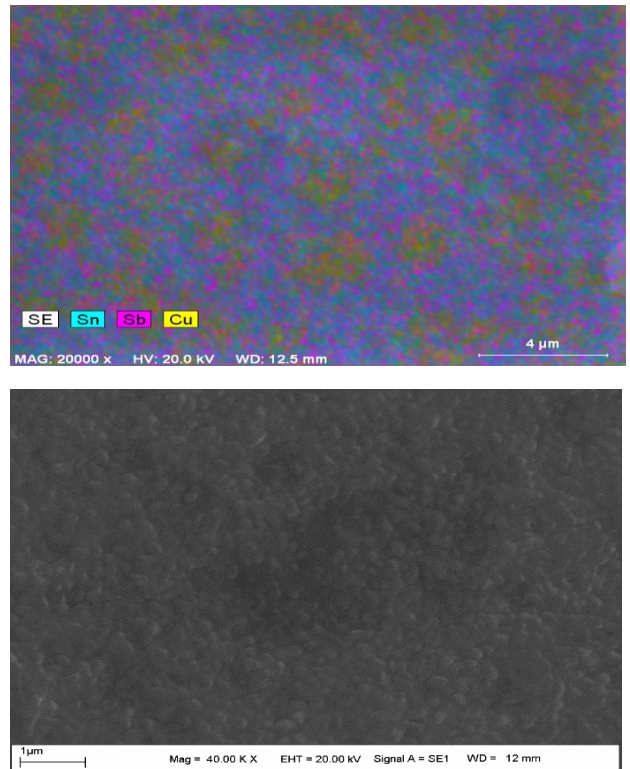
Figure 7. a) mapping image of sample B6, **b)** SEM image of sample
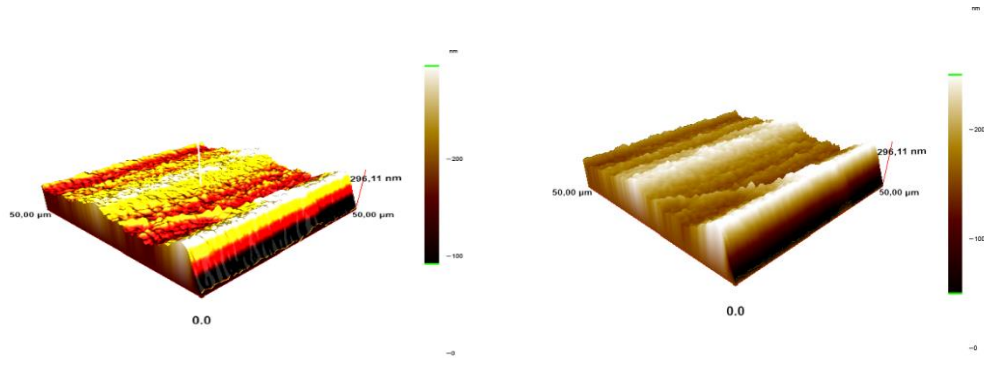
Figure 8. AFM (Surface Spectroscopy) image of sample B
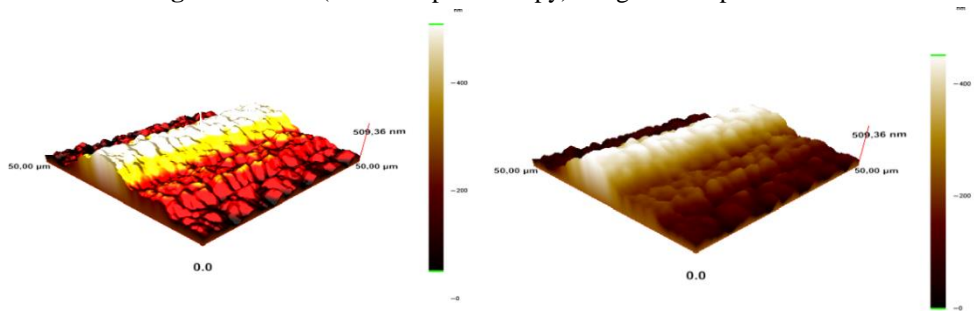
Figure 9. AFM (Surface Spectroscopy) image of B1 Sample
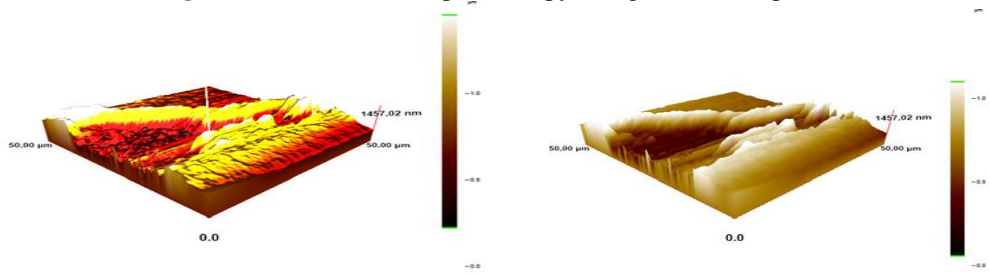
Figure 10. AFM (Surface Spectroscopy) image of B2 sample
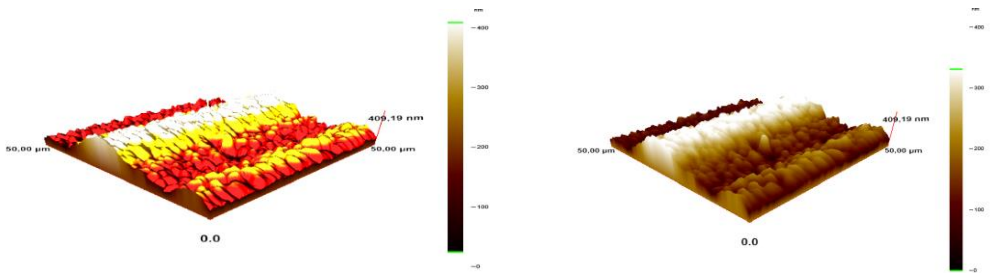
Figure 11. AFM (Surface Spectroscopy) image of B4 sample
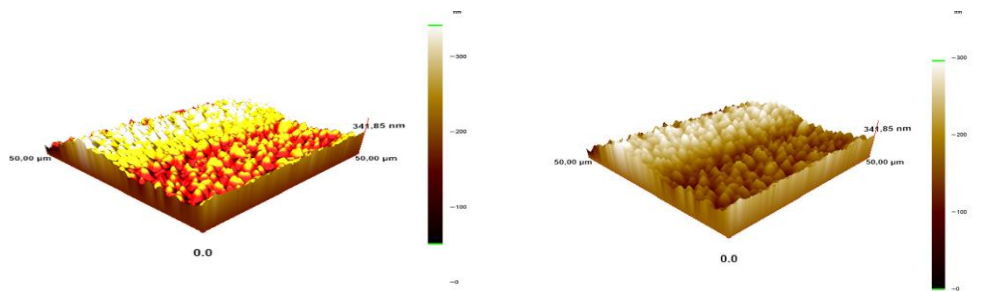
Figure 12. AFM (Surface Spectroscopy) image of B6 sample

Table 2. AFM surface roughness values of existing samples

	B	B1	B2	B4	B6
Average roughness value (Ra) (nm)	29.14	106.37	170	73.2	48.25
Square root of mean roughness value (Rq) (nm)	39.04	126.72	230	87.64	58.80

AFM (Surface Spectroscopy) images and roughness results are given in Table 2 in Figure 8-12 respectively. In Figure 8, the surface image of the B coating without heat treatment is given and the average roughness value was determined as 29.14 nm. If the Ra values of the B1 and B2 coatings given in Figure 9-10 are considered here, an increase in the roughness value on the surface was observed due to the oxide layers that started to form on the surface with the heat treatment applied to the coating, and this value was determined as 170 nm. As the duration of the heat treatment applied to B4 and B6 coatings is increased, an increase is observed in the oxide layer accumulated on the surface, and this increase (deposition) caused the surface to be completely covered with an oxide layer and this caused the roughness value (Ra) of the surface to decrease gradually to 73.2 and 48.25 nm respectively. In Figure 13, x-ray diffractograms of bulk and thin-film Babbitt alloys and of Babbitt thin-film heat-treated at 120 °C at room temperature are given. Obtained x-ray measurements are indexed according to the literature [23-26].

According to the crystal structure investigations, SbSn, Sn and Cu_6Sn_5 compounds were found in the bulk Babbitt alloy, and after it was turned into a thin film, it was observed that crystallization took place in the form of agglomerations on the Sn element [22]. Similarly, in several thin film studies, it has been observed that thin films are formed as agglomerations on a certain crystal layer [27,28]. Peaks at 30° and 43° are also Cu6Sn5 compound phase. When the effects of the heat treatment time on the crystal structure of Babbitt thin film are examined, it is seen that the intensity of the x-ray curve increases and new peaks occur with the heat treatment time.
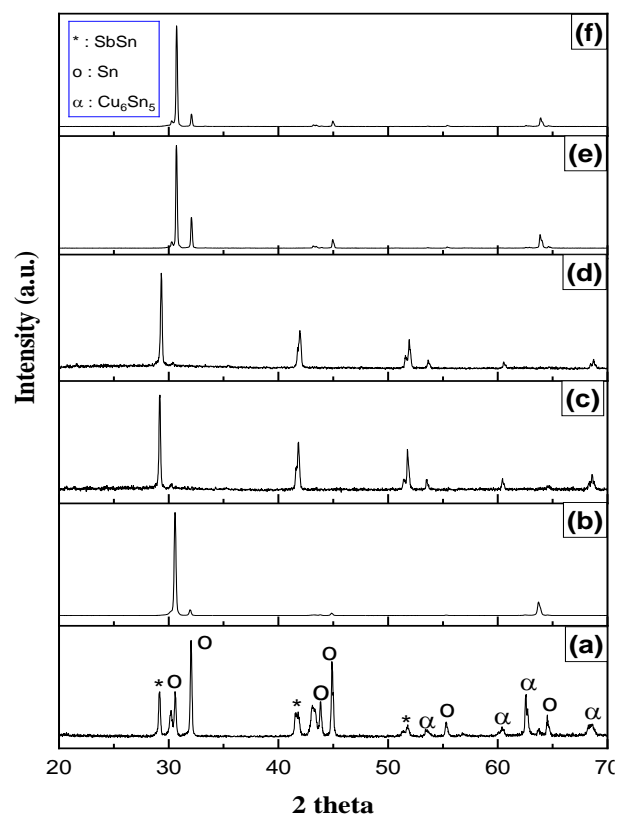
Figure 13. a) Babbitt alloy **b)** thin film Babbitt alloy without heat treatment **c)** Babbitt alloy film subjected to 1 hour heat treatment **d)** Babbitt alloy film subjected to 2 hours heat treatment **e)** Babbitt alloy film subjected to 4 hours heat treatment **f)** Babbitt alloy film subjected to 6 hours heat treatment

As a result of the study, it was determined from the mapping images that the Babbitt thin film coating applied to the glass surface were spread homogeneously on the glass surface. According to the data obtained from the surface spectroscopy (AFM) images, an increase in the oxide layer on the surface was observed in proportion to the heat treatment applied to the coating. This increase also caused a decrease in the roughness value on the surface. In addition, from the SEM images, it is seen that the grain sizes in the coating decrease in proportion to the applied heat treatment and therefore the roughness on the surface decreases. The lowest roughness value on the surface was obtained in the B1 sample, which was not heat treated, while the highest roughness was obtained in the B2 sample, which was heat treated for two hours.

According to the X-ray measurement results, all Babbitt thin films showed that the Sn element was deposited on the main crystal structure, and the intensity of the crystal structure peaks increased with the heat treatment time and indicating that the degree of crystallinity increased.

Acknowledgment   **Statement of Research and Publication Ethics**

References

1. A. Zeren, E. Feyzullahoglu, M. Zeren, "A study on tribological behaviour of tin-based bearing material in dry sliding" *Materials & design*, vol.28, no.1, pp. 318-323, 2007.
2. M.Ö. Bora, O. Coban, T. Sinmazcelik, V. Günay, M. Zeren, "Instrumented indentation and scratch testing evaluation of tribological properties of tin-based bearing materials" *Materials & Design*, vol.31, no.6, pp. 2707-2715, 2010.
3. A. Zeren, "Embeddability behaviour of tin-based bearing material in dry sliding" *Materials & design*, vol.28, no.8, pp. 2344-2350, 2007.
4. X. Zhao, R. Lai, X. Hai, "A study on the microstructures and properties of selective laser melted babbitt metals" *Journal of Materials Engineering and Performance*, vol.28, no.9, pp. 5433-5440, 2019.
5. O. Karpuz, M.V. Akpinar, "İnce Agrega Türünün Kaplama Betonunun Aşınma Direncine Etkisi" *Yapı Teknolojileri Elektronik Dergisi*, vol.5, no.2, pp. 1-8 2009.
6. P. Diouf , A. Jones, "Investigation of bond strength in centrifugal lining of babbitt on cast iron" *Metallurgical and Materials Transactions* A, vol.41, no.3, pp. 603-609, 2010.
7. L. Korshunov, N. Noskova, A. Korznikov, N. Chernenko, N. Vil'Danova, "Effect of severe plastic deformation on the microstructure and tribological properties of a babbit B83" *The Physics of Metals and Metallography*, vol.108, pp. 519-526, 2009.
8. Y. Tasgın, Effect of MgO, "Al2O3 and FeCr2O4 on microstructure and wear resistance of Babbitt metal (Sn–Sb–Cu)" *Materials Research Express*, vol.6, no.4, pp. 046548, 2019.
9. B. Leszczyńska-Madej, M. Madej, J. Hrabia-Wiśnios, A. Węglowska, "Effects of the processing parameters of friction stir processing on the microstructure, hardness and tribological properties of SnSbCu bearing alloy" *Materials*, vol.13, no.24, pp. 5826, 2020.
10. A. Özkartal, D.T. Noori, "Effects of thermal annealing on the characterization of p-NiO/n-GaAs heterojunctions produced by thermal evaporation" *Journal of Materials Science: Materials in Electronics*, vol.32, no.10, pp. 13462-13471, 2021.
11. R. Messier, "Thin film deposition processes" *MRS Bulletin*, vol.13, no.11, pp. 18-21, 1988.
12. A. Amanov, B. Ahn, M.G. Lee, Y. Jeon, Y.-S. Pyun, "Friction and wear reduction of eccentric journal bearing made of sn-based babbitt for ore cone crusher" *Materials*, vol.9, no.11, pp. 950, 2016.
13. M.C. Türküz. "Fiziksel buhar biriktirme yöntemi ile yapılan zirkonyum nitrür ince film kaplamanın kaplama parametrelerinin incelenmesi ve optimizasyonu" *Fen Bilimleri Enstitüsü*, 2006.
14. W.D. Nix, "Mechanical properties of thin films" *Metallurgical transactions A*, vol.20, no.11, pp. 2217-2245, 1989.
15. M. Rao, M. Shekhawat, editors. "A brief survey on basic properties of thin films for device application" *International Journal of Modern Physics: Conference Series*, vol.22, 2013. World Scientific, pp.576-586, 2013.
16. S.-R. Bae, D. Heo, S. Kim, "Recent progress of perovskite devices fabricated using thermal evaporation method: Perspective and outlook" *Materials Today Advances*, vol.14, pp. 100232, 2022.
17. S. Wang, X. Li, J. Wu, W. Wen, Y. Qi, "Fabrication of efficient metal halide perovskite solar cells by vacuum thermal evaporation: A progress review" *Current opinion in Electrochemistry*, vol.11, pp. 130-140, 2018.
18. A.W. Batchelor, "Engineering tribology" *Butterworth-Heinemann*, 1993.

19. P.R.C.A. Junior, A.G.M. Pukasiewicz, "Evaluation of microstructure, mechanical and tribological properties of a Babbitt alloy deposited by arc and flame spray processes" *Tribology International*, vol.131, pp. 148-157, 2019.

20. P. Diouf, A. Jones, "Investigation of bond strength in centrifugal lining of babbitt on cast iron" *Metallurgical and Materials Transactions A*, vol.41, pp. 603-609, 2010.

21. M. Kök, G. Pirge, Y. Aydoğdu, " Isothermal oxidation study on NiMnGa ferromagnetic shape memory alloy at 600–1000° C" *Applied surface science*, vol.268, pp. 136-140, 2013.

22. Y. Taşgin, M.S. Kanca, M. Kök, "Investigation of surface morphology, optical properties and the gamma radiation effect on selenium coated glass substrate containing rare earth oxide" *Optical Materials*, vol.140, pp. 113921, 2023.

23. D. Zhang, F. Zhao, Y. Li, P. Li, Q. Zeng, G. Dong, "Study on tribological properties of multi-layer surface texture on Babbitt alloys surface" *Applied Surface Science,* vol.390, pp. 540-549, 2016.

24. M. Kamal, A. El-Bediwi, A. Lashin, A. El-Zarka, "Copper effects in mechanical properties of rapidly solidified Sn–Pb–Sb Babbitt bearing alloys" *Materials Science and Engineering: A*, vol.530, pp. 327-332, 2011.

25. M. Beger, P. Jurči, P. Grgač, S. Mečiar, M. Kusý, J. Horník, "CrxNy coatings prepared by magnetron sputtering method" *Kovové Materiály-Metallic Materials*, vol.51, no.1, pp. 1-10, 2013.

26. Y. Ni, N. Sun, G. Zhu, S. Liu, J. Liu, G. Dong, "Effect of different Cu6Sn5 morphology on the tribological properties of Babbitt alloy" *Industrial Lubrication and Tribology*, vol.74, no.5, pp. 580-587, 2022.

27. C.R. Dhas, R. Venkatesh, R. Sivakumar, A.M.E. Raj, C. Sanjeeviraja, "Fast electrochromic response of porous-structured cobalt oxide (Co 3 O 4) thin films by novel nebulizer spray pyrolysis technique" *Ionics*, vol.22, pp. 1911-1926, 2016.

28. A. Erlacher, M. Ambrico, V. Capozzi, V. Augelli, H. Jaeger, B. Ullrich, "X-ray, absorption and photocurrent properties of thin-film GaAs on glass formed by pulsed-laser deposition" *Semiconductor science and technology*, vol.19, no.11, pp. 1322, 2004.

Evaluation of the Shielding Properties of Various Water Equivalent Materials Using Different Calculation Methods and Monte Carlo

Turan ŞAHMARAN[1*]

[1]*Hatay Mustafa Kemal University, Kırıkhan Vocational School, Hatay, Turkey*
(ORCID: 0000-0003-3708-6162)

Abstract

In this study, linear attenuation coefficients (LAC), mass attenuation coefficients (MAC), half-valued layer (HVL), and mean free path (MFP) values of various materials such as water equivalent, ABS, Presage, RMI_{457}, RW_3, SW_{557}, Epoxy, A_{150}, Rhizophora spp., and Nylon-12 were found. These values were calculated using Monte Carlo simulation, EpiXS, Phy-X/PSD, and XCOM programs. Additionally, the fast neutron effective removal cross sections (ΣR) have been calculated using the empirical calculation method, Phy-X/PSD, MRCsC program, experimental, and MNCP5 with the help of fast neutron mass removal cross sections. Among all the materials studied, Nylon-12 has the highest ΣR value. The calculated values of HVL, MFP, LAC, and MAC reveal that RW_3, Epoxy, and Presage are the best materials in terms of their shielding properties, respectively.

1. Introduction

In radiation protection, the evaluation of various interaction parameters such as mass attenuation coefficient (μ/ρ), half-value layer (HVL), mean free path (MFP), and total interaction cross-section (σ_t) is crucial for practical applications of protective materials in radiation dosimetry, nuclear medicine, radiation therapy, and radiology fields. Lead and concrete-based materials are currently the most commonly used materials for protecting against X-ray, gamma-ray, and neutron radiation in radiation fields. However, researchers in the field of radiation protective materials are actively seeking alternative material designs due to the environmental toxicity and harmful effects on human health associated with lead (Pb). Furthermore, lead exhibits a blind absorption region for X-rays in the range of 70-90 keV, which has led to the exploration of various alternative materials [1]. Not only X-rays or gamma rays but also radiation from neutrons have led to the design of many new protective materials. Neutron radiation has been used in various fields for many years, such as cancer treatments, the production of radioisotopes, industrial radiography, and the characterization of various materials [2, 3]. However, the use and production of free neutrons entail certain risks. Among these risks, free neutrons can alter the microstructural properties of materials and indirectly cause double-strand breaks in the DNA molecule of biological matter. This can lead to cell mutations and death [4, 5]. Therefore, the shielding design for neutrons is one of the important considerations in radiation safety [6, 7]. In recent years, the shielding properties of many new materials or different materials with modified characteristics have been investigated [8, 9]. For effective neutron radiation shielding, the material structure should consist of hydrogen-rich or low atomic number element combinations [10]. One of the fundamental

---

quantities used for predicting neutron shielding is the fast neutron effective removal cross-section (ΣR) [11]. This empirical cross-section has been derived for hydrogenous systems and utilized in reactor shielding calculation methods. Researchers use experimental measurements, theoretical models, and nuclear data libraries to determine and predict HVL, MFP, MAC, LAC, and fast neutron removal cross-sections for different materials and energy ranges. These data sources are continuously updated and improved to enhance the accuracy of cross-section values and ensure the reliability of nuclear calculations and simulations. The interaction of neutrons with matter is described by parameters such as ΣR,

MFP, and HVL, among others. ΣR is known as a characteristic of materials. To predict the ΣR of any material, a dataset of elemental mass removal cross-sections (Σ_R/ρ) is used [11]. This research involved computing the LAC, MAC, HVL, and MFP measurements for different substances like ABS, presage, RMI_{457}, RW_3, SW_{557}, epoxy, A_{150}, Rhizophora spp. (Rspp), and Nylon-12 within a photon energy span of 0.1-18 MeV. Furthermore, the ΣR values for these materials were assessed using MRCsC, Phy-X/PSD, Monte Carlo N-Particle Transport Code (MCNP5), and empirical calculation approaches.

2. Material and Method

2.1 Theory

The initial intensity of a monoenergetic photon is I_o. The intensity of the photon beam (I is the attenuated photon intensities) passing through the attenuating thickness (x, cm) will decrease. The attenuation of the photon beam is determined using Equation 1, with the help of the Beer-Lambert law [12].

$$I = I_0^{-\mu x} \tag{1}$$

Here, μ (cm^{-1}) represents the LAC. The MAC value for the compound and mixture is defined using Equation 2 [13].

$$\mu_m = \frac{\mu}{\rho} = \sum w_i \left(\frac{\mu_i}{\rho_i}\right) \tag{2}$$

Here, μ_m (cm²/g) represents the MAC. w_i represents the weight fraction of the ith element in the material, and ρ (g/cm³) represents the density of the shielding material. The parameter μ is important for calculating the values that will reduce the initial value of primary radiation to half or one-tenth [14, 15]. MFP represents the average distance traveled by photons before interacting with the absorbing material. Equation 3 provides the formulas for HVL and MFP.

$$HVL = \frac{ln2}{\mu}, \text{MFP} = \frac{1}{\mu} \tag{3}$$

Equations 4, 5, and 6 present the calculations related to materials and neutrons. ΣR represents the probability of neutrons passing through the material without interaction. An empirical approach model was derived for the mass removal cross-section (Σ_R/ρ) [16].

$$\Sigma R = \sum_i \rho_i (\Sigma_R/\rho)i \tag{4}$$

$$\rho_i = \sum_i w_i \rho_s \tag{5}$$

$$\Sigma_{R/\rho} = 0.190\, Z^{-0.743}\, Z \leq 8 \text{ and } \Sigma_{R/\rho} = 0.125\, Z^{-0.565}\, Z > 8 \tag{6}$$

Here, ρi represents the partial density, $(\Sigma_R/\rho)_i$ represents the mass removal cross-section of the ith component, $w i$ is the weight fraction of the constituent, ρs is the sample density, A is the atomic weight, and Z is the atomic number.

2.2 GATE Simulation, MRCsC, EpiXS, and Phy-X/PSD program

The simulation program vGate, version 8.1, was utilized. GATE is an advanced opensource software developed by the international OpenGATE collaboration. All materials used were defined by entering their densities and mass ratios into the *gate.material.db* file. The geometry was designed with a distance of 100 cm between the source and the detector. Initially, with no material present, the simulation was run to obtain the I_o value. Subsequently, by placing a material with dimensions of $10x10x10\ cm^3$ between the source and the detector, the I value was obtained. To determine the Io and I values, a fluence actor was defined in the GATE macro file. This actor counts the fraction of a particle that passes through a volume. MRCsC has been developed to accurately and precisely predict the macroscopic effective removal cross-section, ΣR, for fast neutrons in various shielding materials. The program incorporates the latest data published by the Evaluated Nuclear Data Library 'ENDF/BVIII' [17]. EpiXS is a Windows-based program used for photon

attenuation, dosimetry, and shielding. It includes the EPICS2017 (ENDF/B-VIII) and EPDL97 (ENDF/B-VI.8) data libraries [18]. Phy-X/PSD is the software program of an online tool used for calculating parameters related to radiation shielding and dosimetry [19]. Figure 1 shows the simulation geometry.
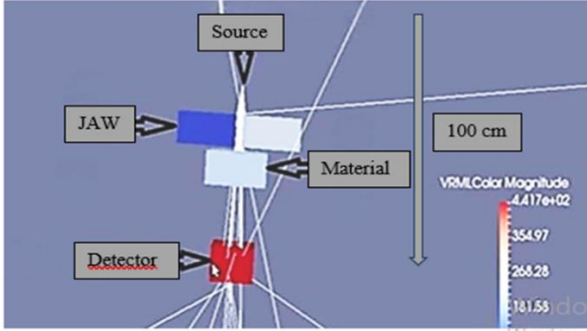
Figure 1. Simulation geometry (not scale)

3. Results and Discussion

In radiotherapy, especially during daily, weekly, or monthly quality control procedures, water-equivalent phantom materials are commonly used. In this study, various photon energies were investigated for the MAC, LAC, HVL, and MFP values of these materials. For these calculations, GATE, EpiXS, and XCOM were respectively employed as simulation, computer program, and theoretical calculation tools. Furthermore, the Σ_R values of these materials were obtained using empirical formulas, MRCsC, Phy-X/PSD, and MNCP5 by utilizing the Σ_R/ρ values found. Table 1 illustrates the elemental composition of the materials used.

Table 1. Density (ρ , g cm^{-3}) and elemental composition of the phantom material

	RW$_3$[20]	SW$_{557}$[21]	ABS[22]	Epoxy[23]	Presage[24]	RMI$_{457}$[21]	Nylon$_{12}$[20]	A$_{150}$[25]	Rspp[26]
H	0.075	0.081	0.081	0.064	0.089	0.080	0.117	0.101	
C	0.904	0.657	0.852	0.642	0.607	0.672	0.730	0.775	0.515
N		0.022	0.066		0.044	0.024	0.070	0.035	
O	0.008	0.193		0.203	0.217	0.199	0.081	0.052	0.422
B		0.001							
F								0.017	0.062
Cl		0.001		0.090	0.033	0.001			
Ca		0.018				0.023		0.018	
Na		0.002							
Mg		0.010							
Al		0.001							
Si		0.011							
S		0.001							
Ti	0.012								
Br					0.008				
ρ	1.045	1.032	1.040	1.110	1.101	1.030	1.010	1.127	1.030

Tables 2 and 3 show that, due to the photoelectric effect, decreases in MAC and LAC values are more pronounced at lower energies compared to higher energies. The reason for this sharp decrease is attributed to the photoelectric cross-section being associated with Z^{4-5} and $E^{-3.5}$ in the low-energy region. As shown in Tables 2 and 3, the data obtained between 0.8 MeV and 10 MeV energies indicate that MAC and LAC values are almost the same for all materials. In these energy ranges, the probability of the photoelectric effect is low, as the photon energy is higher than the energy required for electron

transitions. Another significant interaction process known as Compton scattering becomes more dominant in this range, and in this case, the cross-section is proportional to E^{-1} and Z. After Compton scattering, the pair production process starts to dominate, and this process is proportional to Z^2 in terms of cross-section. As the energy increases, it can be observed that the MAC and LAC values decrease. In Tables 2 and 3, the highest MAC and LAC values were observed in the RW3 material at 0.01 MeV. The RW$_3$ (29.254 cm^2 g^{-1}) material exhibits a sudden

change in MAC values around absorption edges due
to its high Z (Ti) content.

Table 2. The MAC values of materials were compared with the GATE, EpiXS, and XCOM

Energy (MeV)	0.01	0.05	0.08	0.1	0.5	0.8	1	3	6	10	15	18
GATE_RW₃	29.254	0.425	0.229	0.178	0.088	0.070	0.063	0.036	0.024	0.021	0.017	0.016
XCOM_RW₃	31.090	0.465	0.232	0.189	0.089	0.072	0.065	0.037	0.026	0.022	0.020	0.019
EpiXS_RW₃	31.136	0.466	0.232	0.190	0.090	0.072	0.065	0.037	0.027	0.022	0.020	0.020
GATE_SW₅₅₇	4.975	0.219	0.171	0.160	0.090	0.072	0.065	0.035	0.021	0.019	0.017	0.015
XCOM_SW₅₅₇	5.258	0.224	0.179	0.166	0.094	0.076	0.068	0.038	0.026	0.021	0.018	0.017
EpiXS_SW₅₅₇	5.263	0.225	0.179	0.166	0.094	0.076	0.069	0.038	0.027	0.021	0.018	0.017
GATE_ABS	2.146	0.191	0.168	0.165	0.091	0.071	0.060	0.032	0.023	0.020	0.016	0.014
XCOM_ABS	2.312	0.199	0.173	0.163	0.094	0.076	0.068	0.038	0.026	0.021	0.018	0.017
EpiXS_ABS	2.315	0.200	0.173	0.163	0.094	0.076	0.069	0.038	0.026	0.021	0.018	0.015
GATE_Epoxy	7.911	0.238	0.175	0.160	0.086	0.070	0.062	0.030	0.023	0.019	0.016	0.015
XCOM_Epoxy	7.927	0.243	0.181	0.166	0.092	0.075	0.067	0.037	0.026	0.021	0.018	0.017
EpiXS_Epoxy	7.934	0.244	0.182	0.166	0.092	0.075	0.067	0.038	0.026	0.021	0.019	0.018
GATE_Presage	5.138	0.250	0.179	0.165	0.090	0.069	0.065	0.033	0.022	0.018	0.017	0.018
XCOM_Presage	5.273	0.256	0.188	0.171	0.094	0.076	0.069	0.038	0.026	0.021	0.018	0.018
EpiXS_Presage	5.276	0.256	0.188	0.171	0.095	0.077	0.069	0.039	0.027	0.021	0.019	0.017
GATE_RMI₄₅₇	4.983	0.213	0.172	0.162	0.092	0.071	0.063	0.038	0.024	0.020	0.017	0.015
XCOM_RMI₄₅₇	5.065	0.223	0.179	0.166	0.094	0.076	0.068	0.038	0.026	0.021	0.018	0.017
EpiXS_RMI₄₅₇	5.071	0.224	0.179	0.166	0.094	0.076	0.069	0.038	0.027	0.021	0.018	0.017
GATE_Nylon₁₂	2.519	0.201	0.171	0.160	0.092	0.070	0.066	0.034	0.022	0.019	0.016	0.015
XCOM_Nylon₁₂	2.537	0.207	0.179	0.168	0.097	0.079	0.070	0.039	0.027	0.021	0.017	0.018
EpiXS_Nylon₁₂	2.540	0.207	0.179	0.169	0.097	0.079	0.071	0.040	0.027	0.021	0.018	0.017
GATE_A₁₅₀	4.149	0.215	0.175	0.163	0.091	0.072	0.064	0.032	0.022	0.020	0.018	0.016
XCOM_A₁₅₀	4.146	0.219	0.180	0.167	0.095	0.077	0.069	0.039	0.026	0.021	0.018	0.017
EpiXS_A₁₅₀	4.151	0.219	0.181	0.168	0.096	0.078	0.070	0.039	0.027	0.021	0.018	0.017
GATE_*Rspp*	4.299	0.211	0.162	0.151	0.080	0.065	0.061	0.033	0.026	0.018	0.016	0.014
XCOM_*Rspp*	4.250	0.200	0.164	0.152	0.086	0.070	0.063	0.036	0.025	0.020	0.017	0.017
EpiXS_*Rspp*	4.253	0.200	0.164	0.153	0.087	0.071	0.063	0.036	0.025	0.020	0.018	0.017

Table 3. The LAC values of materials were compared with the GATE, EpiXS, and XCOM

Energy (MeV)	0.01	0.05	0.08	0.1	0.5	0.8	1	3	6	10	15	18
GATE_RW₃	30.570	0.444	0.239	0.186	0.092	0.073	0.066	0.038	0.025	0.022	0.018	0.017
XCOM_RW₃	32.480	0.485	0.242	0.197	0.093	0.075	0.067	0.038	0.027	0.022	0.020	0.019
EpiXS_RW₃	32.537	0.487	0.243	0.198	0.094	0.076	0.068	0.039	0.028	0.023	0.021	0.021
GATE_SW₅₅₇	5.134	0.226	0.176	0.165	0.093	0.074	0.067	0.036	0.022	0.020	0.018	0.015
XCOM_SW₅₅₇	5.426	0.231	0.184	0.171	0.097	0.078	0.070	0.039	0.026	0.021	0.018	0.017
EpiXS_SW₅₅₇	5.432	0.232	0.185	0.172	0.097	0.079	0.071	0.040	0.027	0.022	0.019	0.018
GATE_ABS	2.232	0.199	0.175	0.172	0.095	0.074	0.062	0.033	0.024	0.021	0.017	0.015

XCOM_ABS	2.404	0.207	0.180	0.170	0.098	0.079	0.071	0.040	0.027	0.022	0.019	0.018
EpiXS_ABS	2.408	0.208	0.180	0.170	0.098	0.079	0.071	0.040	0.027	0.021	0.018	0.017
GATE_Epoxy	8.781	0.264	0.194	0.178	0.095	0.078	0.069	0.033	0.026	0.021	0.018	0.017
XCOM_Epoxy	8.799	0.270	0.201	0.184	0.102	0.083	0.074	0.041	0.029	0.023	0.020	0.019
EpiXS_Epoxy	8.807	0.271	0.202	0.184	0.103	0.083	0.075	0.042	0.029	0.023	0.021	0.020
GATE_Presage	5.657	0.275	0.197	0.182	0.099	0.076	0.072	0.036	0.024	0.020	0.019	0.020
XCOM_Presage	5.806	0.282	0.207	0.188	0.103	0.085	0.076	0.043	0.030	0.023	0.021	0.017
EpiXS_Presage	5.809	0.282	0.207	0.189	0.104	0.085	0.076	0.043	0.030	0.023	0.020	0.019
GATE_RMI$_{457}$	5.132	0.219	0.177	0.167	0.095	0.073	0.065	0.039	0.025	0.021	0.018	0.015
XCOM_RMI$_{457}$	5.217	0.230	0.184	0.171	0.097	0.078	0.070	0.039	0.027	0.022	0.019	0.018
EpiXS_RMI$_{457}$	5.223	0.231	0.184	0.171	0.097	0.079	0.071	0.040	0.027	0.022	0.019	0.018
GATE_Nylon$_{12}$	2.544	0.203	0.173	0.162	0.093	0.071	0.067	0.034	0.022	0.019	0.016	0.015
XCOM_Nylon$_{12}$	2.562	0.209	0.181	0.170	0.098	0.080	0.071	0.039	0.027	0.021	0.017	0.018
EpiXS_Nylon$_{12}$	2.565	0.210	0.181	0.170	0.098	0.080	0.072	0.040	0.027	0.021	0.018	0.017
GATE_A$_{150}$	4.676	0.242	0.197	0.184	0.103	0.081	0.072	0.036	0.025	0.023	0.020	0.018
XCOM_A$_{150}$	4.673	0.247	0.203	0.188	0.107	0.087	0.078	0.044	0.029	0.024	0.020	0.019
EpiXS_A$_{150}$	4.678	0.247	0.202	0.189	0.107	0.088	0.079	0.044	0.034	0.023	0.021	0.019
GATE_*Rspp*	4.428	0.217	0.167	0.156	0.082	0.067	0.063	0.034	0.027	0.019	0.016	0.014
XCOM_*Rspp*	4.378	0.206	0.169	0.157	0.089	0.072	0.065	0.037	0.026	0.021	0.018	0.018
EpiXS_*Rspp*	4.381	0.203	0.167	0.154	0.087	0.073	0.064	0.035	0.024	0.022	0.017	0.016

HVL and MFP characterize the photon attenuation performance of the materials (Tables 4 and 5). A low HVL and MFP values represent the need for a thinner material to absorb photons. The density of the material is inversely proportional to the HVL and MFP values. The presence of low Z elements (H, C, N, and O) within the material ensures higher HVL and MFP values are achieved. For a sample to be considered a shielding material, it is required to have maximum MAC and minimum HVL and MFP values within the selected range of photon energies. According to Table 4, the RW$_3$ (0.023 cm) material has a lower HVL value compared to the other materials. Following the RW3 material, epoxy (0.079 cm) and presage (0.123 cm) exhibit the best shielding properties, respectively. According to Table 4, it is observed that as the photon energy increases, the HVL value also increases. MFP is defined as the average distance a photon can travel in the target material before interacting with its atoms. According to Table 5, among the investigated materials, RW$_3$ (0.033 cm), epoxy (0.114 cm), and presage (0.177 cm) were found to have the lowest MFP values, respectively. Figure 2 shows HVL values according to energy variation.

Table 4. The HVL values of materials were compared with the GATE, EpiXS, and XCOM

Energy (MeV)	0.01	0.05	0.08	0.1	0.5	0.8	1	3	6	10	15	18
GATE_RW$_3$	0.023	1.560	2.896	3.726	7.536	9.474	10.526	18.421	27.632	31.579	39.009	41.447
XCOM_RW$_3$	0.021	1.426	2.858	3.509	7.451	9.211	10.202	17.923	25.506	30.144	33.158	34.903
EpiXS_RW$_3$	0.021	1.422	2.853	3.493	7.410	9.152	10.191	17.948	24.845	27.700	32.575	33.452
GATE_SW$_{557}$	0.135	3.066	3.927	4.197	7.461	9.327	10.331	19.186	31.977	35.343	39.501	44.767
XCOM_SW$_{557}$	0.128	2.998	3.751	4.045	7.144	8.836	9.875	17.671	25.827	31.977	37.306	39.501
EpiXS_SW$_{557}$	0.128	2.895	3.744	4.039	7.138	8.792	9.783	17.484	25.240	31.794	36.681	38.560
GATE_ABS	0.311	3.489	3.966	4.038	7.322	9.385	11.106	20.823	28.972	33.317	41.647	47.596
XCOM_ABS	0.288	3.348	3.852	4.088	7.089	8.768	9.799	17.535	25.629	31.731	37.019	39.197

	0.01	0.05	0.08	0.1	0.5	0.8	1	3	6	10	15	18
EpiXS_ABS	0.285	3.334	3.849	4.088	7.088	8.728	9.711	17.407	25.349	32.305	37.719	39.885
GATE_Epoxy	0.079	2.623	3.568	3.902	7.260	8.919	10.070	20.811	27.145	32.859	39.020	41.622
XCOM_Epoxy	0.079	2.569	3.449	3.761	6.786	8.324	9.318	16.874	24.012	29.730	34.685	36.725
EpiXS_Epoxy	0.077	2.562	3.436	3.759	6.760	8.329	9.268	16.520	23.662	29.504	33.693	35.245
GATE_Presage	0.123	2.518	3.516	3.815	6.994	9.122	9.684	19.074	28.610	34.968	37.025	34.968
XCOM_Presage	0.119	2.459	3.348	3.681	6.696	8.196	9.109	16.264	23.486	29.551	34.023	35.763
EpiXS_Presage	0.118	2.455	3.345	3.675	6.652	8.176	9.120	16.293	23.480	29.540	34.012	35.737
GATE_RMI$_{457}$	0.135	3.159	3.912	4.153	7.313	9.476	10.680	17.706	28.034	33.641	39.577	44.854
XCOM_RMI$_{457}$	0.133	3.017	3.759	4.053	7.158	8.853	9.894	17.706	25.878	32.039	37.379	39.577
EpiXS_RMI$_{457}$	0.132	3.007	3.758	4.053	7.158	8.817	9.811	17.539	25.343	31.964	36.924	38.840
GATE_Nylon$_{12}$	0.272	3.414	4.013	4.288	7.458	9.802	10.396	20.181	31.188	36.113	42.884	45.743
XCOM_Nylon$_{12}$	0.270	3.315	3.833	4.084	7.074	8.685	9.802	17.593	25.413	32.673	40.361	38.119
EpiXS_Nylon$_{12}$	0.271	3.308	3.821	4.072	7.064	8.697	9.677	17.358	25.326	32.360	37.887	40.118
GATE_A$_{150}$	0.148	2.860	3.514	3.772	6.757	8.540	9.608	19.216	27.950	30.745	34.161	38.432
XCOM_A$_{150}$	0.148	2.808	3.416	3.682	6.473	7.986	8.912	15.767	23.650	29.281	34.161	36.171
EpiXS_A$_{150}$	0.147	2.841	3.416	3.666	6.437	7.921	8.813	15.774	22.935	29.141	33.930	35.830
GATE_*Rspp*	0.157	3.189	4.153	4.456	8.410	10.351	11.030	20.388	25.878	37.379	42.051	48.058
XCOM_*Rspp*	0.158	3.364	4.103	4.426	7.823	9.612	10.680	18.689	26.913	33.641	39.577	39.577
EpiXS_*Rspp*	0.157	3.357	4.102	4.404	7.746	9.541	10.616	18.894	26.947	33.414	37.941	39.579

Table 5. The MFP values of materials were compared with the GATE, EpiXS, and XCOM

Energy (MeV)	0.01	0.05	0.08	0.1	0.5	0.8	1	3	6	10	15	18
GATE_RW$_3$	0.033	2.252	4.179	5.376	10.874	13.671	15.189	26.582	39.872	45.568	56.290	59.809
XCOM_RW$_3$	0.031	2.058	4.125	5.063	10.752	13.291	14.722	25.863	36.805	43.497	47.847	50.365
EpiXS_RW$_3$	0.031	2.052	4.117	5.039	10.691	13.204	14.702	25.893	35.844	42.847	46.966	48.261
GATE_SW$_{557}$	0.195	4.425	5.667	6.056	10.767	13.458	14.908	27.685	46.142	51.000	57.000	64.599
XCOM_SW$_{557}$	0.184	4.326	5.413	5.837	10.308	12.750	14.250	25.500	37.269	46.142	53.833	57.000
EpiXS_SW$_{557}$	0.184	4.307	5.401	5.827	10.299	12.684	14.115	25.225	36.414	4.869	52.920	55.631
GATE_ABS	0.448	5.034	5.723	5.828	10.566	13.543	16.026	30.048	41.806	48.077	60.096	68.681
XCOM_ABS	0.416	4.832	5.558	5.899	10.229	12.652	14.140	25.304	36.982	45.788	53.419	56.561
EpiXS_ABS	0.415	4.81	5.553	5.898	10.226	12.591	14.01	25.113	36.571	46.607	54.417	57.542
GATE_Epoxy	0.114	3.785	5.148	5.631	10.476	12.870	14.531	30.030	39.170	47.416	56.306	60.060
XCOM_Epoxy	0.114	3.707	4.977	5.427	9.792	12.012	13.446	24.349	34.650	42.900	50.050	52.994
EpiXS_Epoxy	0.114	3.695	4.958	5.423	9.753	12.016	13.372	23.833	34.137	42.566	48.608	50.848
GATE_Presage	0.177	3.633	5.074	5.505	10.092	13.163	13.973	27.523	41.285	50.459	53.427	50.459
XCOM_Presage	0.172	3.548	4.831	5.311	9.662	11.826	13.144	23.469	33.890	42.642	49.095	51.606
EpiXS_Presage	0.172	3.541	4.826	5.302	9.597	11.824	13.158	23.505	33.888	42.617	49.894	51.557
GATE_RMI$_{457}$	0.195	4.558	5.645	5.993	10.553	13.674	15.411	25.549	40.453	48.544	57.110	64.725
XCOM_RMI$_{457}$	0.192	4.354	5.424	5.849	10.328	12.775	14.278	25.549	37.341	46.232	53.937	57.110
EpiXS_RMI$_{457}$	0.191	4.338	5.424	5.848	10.327	12.72	14.154	25.303	36.562	46.114	53.27	56.034
GATE_Nylon$_{12}$	0.393	4.926	5.790	6.188	10.762	14.144	15.002	29.121	45.005	52.110	61.881	66.007

|											
XCOM_ Nylon₁₂	0.390	4.783	5.531	5.893	10.207	12.533	14.144	25.387	36.670	47.148	58.241	55.006
EpiXS_ Nylon₁₂	0.391	4.772	5.528	5.875	10.191	12.548	13.961	25.042	36.537	46.686	54.660	57.879
GATE_ A₁₅₀	0.214	4.127	5.070	5.444	9.751	12.324	13.864	27.728	40.332	44.366	49.295	55.457
XCOM_A₁₅₀	0.214	4.052	4.930	5.313	9.340	11.524	12.860	22.752	34.127	42.253	49.295	52.195
EpiXS_A₁₅₀	0.213	4.042	4.930	5.292	9.271	11.421	12.844	22.763	33.081	42.044	48.953	51.693
GATE_ Rspp	0.226	4.601	5.993	6.430	12.136	14.937	15.916	29.420	37.341	53.937	60.680	69.348
XCOM_ Rspp	0.228	4.854	5.920	6.387	11.289	13.870	15.411	26.969	38.835	48.544	57.110	57.110
EpiXS_ Rspp	0.228	4.844	5.918	6.354	11.175	13.764	15.316	27.258	38.877	48.206	54.377	57.100
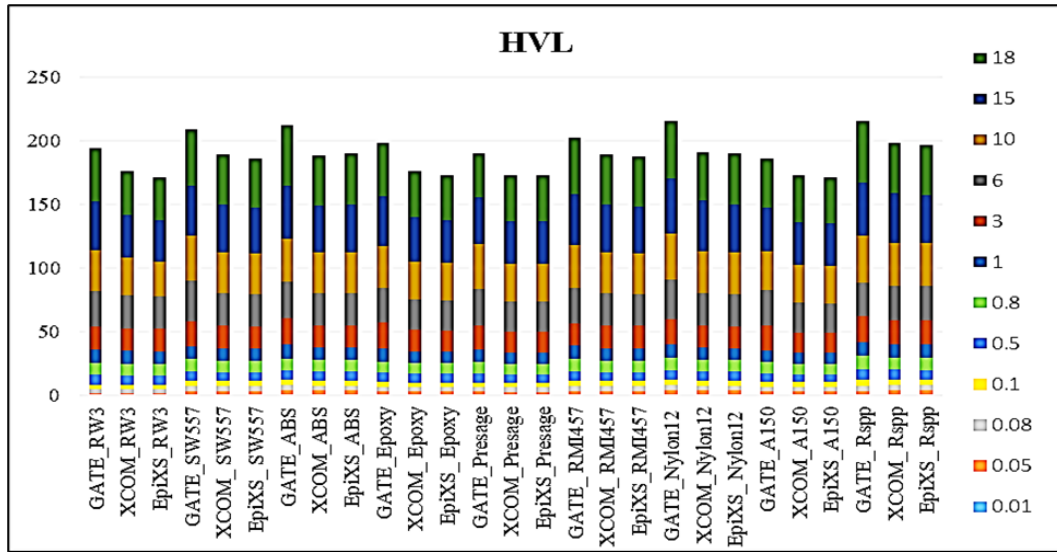
Figure 2. HVL values according to energy variation

Table 6 presents the ΣR values of the selected materials. These values were obtained using empirical formulas from equations 4, 5, and 6, as well as MCNP5 Monte Carlo simulation, MRCsC, and Phy-X/PSD software programs. In the study conducted by Hila et al. [11], they numerically generated fast neutron mass removal cross-sections (Σ_R/ρ, cm²/g) based on ENDF/B-VIII.0 using a sliced spherical shell Monte Carlo model under different neutron source spectra. Using the generated Σ_R/ρ values in this study, Σ_R values for various materials were determined. For effective neutron shielding, materials with high Σ_R values are desired. According to Table 6, the material with the highest ΣR value is Nylon₁₂ (0.131 cm⁻¹). Generally, as the content of low Z elements increases, the ΣR value also increases. In Table 6, the material with the highest hydrogen (H) content is Nylon₁₂. Therefore, it is thought that the highest Σ_R value is observed in this material. The lowest ΣR value was observed in Rspp (0.048 cm⁻¹). This is due to the absence of hydrogen (H) content in

this material. This is because the fast neutron mass removal cross-section of hydrogen is much higher than that of many other elements. In their study, Elwahab et al. [27] stated that hydrogen atoms play a significant role in the slowing-down mechanisms of fast neutrons, implying that the slowing-down process would be maximized when the hydrogen atoms are at their maximum. After Nylon₁₂ material, the best ΣR values are found in the following order: Presage, ABS, A₁₅₀, SW₅₅₅, RMI₄₅₇, RW₃, epoxy, and Rspp, respectively. The lower ΣR value of Rspp compared to other materials is thought to be due to the absence of hydrogen element in its structure. The ΣR values of materials such as Nylon₁₂, presage, ABS, A₁₅₀, SW₅₅₅, RMI₄₅₇, RW₃ and epoxy were found to be close to the ΣR values of paraffin, water, Hematite-serpentine, and concrete. It was observed that the ΣR values obtained for epoxy using the MRCsC program are larger than those of presage, water, concrete, and Hematite-serpentine.

Table 6. Values of ΣR for different calculation

Materials	Σ_R (cm^{-1})				
	MNCP5	MRCsC	Phy-X/PSD	Estimation using $\Sigma R/\rho$ of elements	Experiments
RW$_3$	0.084	0.106	0.095	0.096	-
SW$_{557}$	0.085	0.108	0.095	0.094	-
ABS	0.088	0.113	0.097	0.098	-
Epoxy	0.081	0.103	0.091	0.090	-
Presage	0.095	0.119	0.106	0.105	-
RMI$_{457}$	0.085	0.107	0.094	0.094	-
Nylon$_{12}$	0.105	0.131	0.113	0.114	-
A$_{150}$	0.097	0.111	0.117	0.107	-
Rspp	0.038	0.048	0.046	0.047	-
H$_2$O	0.100	0.110	0.103	0.103	-
Paraffin, C$_{25}$H$_{52}$	0.119	0.141	0.122	0.122	0.109 [29]
Concrete, Dry	0.086	0.102	0.093	0.085	0.087 [29]
Fluorothene, C$_2$F$_3$Cl	0.080	0.096	0.078	0.079	0.075 [29]
Perfluoroheptane, C$_7$F$_{16}$	0.071	0.080	0.067	0.068	0.070 [29]
Hematite–serpentine [28]	0.101	0.103	0.103	0.100	-

4. Conclusion and Suggestions

In this study, the LAC, MAC, HVL, MFP, and ΣR values of various water-equivalent materials, especially those used for quality control in radiotherapy, were obtained using Monte Carlo simulation, MRCsC, Phy-X/PSD, EpiXS computer programs, and XCOM. For daily and weekly quality control procedures in radiotherapy, RW$_3$ exhibited better MAC, LAC, HVL, and MFP values compared to other materials. However, upon examining the ΣR values, it was found that Nylon$_{12}$ is the best material for neutron shielding. The results obtained from this study can serve as a database for researchers and designers working on both photon and neutron shielding. Additionally, these materials offer advantages over existing shielding materials, such as low thickness, lightweight, durability, and non-toxicity. Moreover, these materials can be used in various applications, including radiation therapy rooms, the transportation of chemical isotopes, and other diverse radiation sources.

Statement of Research and Publication Ethics
The study is complied with research and publication ethics.

References

[1] M. G. Dong, M. I. Sayyed, G. Lakshminarayana, M. Ç. Ersundu, A. E. Ersundu, P. Nayar, and M.A. Mahdi, "Investigation of gamma radiation shielding properties of lithium zinc bismuth borate glasses using XCOM program and MCNP5 code", *Journal of Non-Crystalline Solids*, vol. 468, pp. 12-6, 2017.

[2] M. Schulc, M. Kostal, E. Novak, R. Kubín, and J. Simon, "Application of 252Cf neutron source for precise nuclear data experiments", *Applied Radiation and Isotopes*, vol. 151, pp. 187–195, 2019.

[3] F. C. Hila, C. A. M. Dingle, A. Asuncion-Astronomo, C. V. Balderas, M. L. Grande, K. M. D. Romallosa, N. R. D. Guillermo, "Evaluation of time-dependent strengths of californium neutron sources by decay of 252Cf, 250Cf, and 248Cm: uncertainties by Monte Carlo method", *Applied Radiation and Isotopes*, vol. 167, 2021a.

[4] J. Biau, E. Chautard, P. Verrelle, and M. Dutreix, "Altering DNA repair to improve radiation therapy: specific and multiple pathway targeting", *Frontiers in oncology*, vol. 9, pp.1009, 2019.

[5] R. E. Stoller, "Radiation damage correlation. In: Comprehensive Nuclear Materials", *Elsevier,* pp. 456–467, 2020.

[6] M. K. A. Roslan, M. Ismail, A. B. H. Kueh, and M. R. M. Zin, "High-density concrete: exploring Ferro boron effects in neutron and gamma radiation shielding", *Construction and Building Materials*, vol. 215, pp.718-725, 2019.

[7] M. G. Dong, X. X. Xue, Y. Elmahroug, M. I. Sayyed, and M. H. M. Zaid, "Investigation of shielding parameters of some boron containing resources for gamma ray and fast neutron", *Results in Physics*, vol. 13, pp. 1-7, 2019.

[8] C. V. More, R. R. Bhosale, and P. P. Pawar, "Detection of new polymer materials as gamma-ray-shielding materials", *Radiation Effects and Defects in Solids*, vol. 172, pp.469-484, 2017.

[9] M. Büyükyıldız, M. A. Taşdelen, Y. Karabul, M. Çağlar, O. İçelli, and E. Boydaş, "Measurement of photon interaction parameters of high-performance polymers and their composites", *Radiation Effects and Defects in Solids*, vol. 173, pp.474-488, 2018.

[10] N. R.Abd Elwahab, N. Helal, T. Mohamed, F. Shahin, and F. M. Ali, "New shielding composite paste for mixed fields of fast neutrons and gamma rays", *Materials Chemistry and Physics*, vol. 233, pp.249-253, 2019.

[11] F. C. Hila, J. F. M. Jecong, C. A. M., Dingle, A. J. Asuncion-Astronomo, C. V. Balderas, J. A. Sagum, and N. R. D. Guillermo, "ENDF/B-VIII. 0-based fast neutron removal cross sections database in Z= 1 to 92 generated via multi-layered spherical geometry", *Radiation Physics and Chemistry*, vol. 206, p.110770, 2023.

[12] O, Agar, "Study on gamma ray shielding performance of concretes doped with natural sepiolite mineral" *Radiochim. Acta*, vol. 106, pp. 1009–16, 2018.

[13] H. O. Tekin, E. Kavaz, A. Papachristodoulou, M. Kamislioglu, O. Agar, E. A. Guclu, O. Kilicoglu, and M. I. Sayyed, "Characterization of SiO2–PbO–CdO–Ga2O3 glasses for comprehensive nuclear shielding performance: Alpha, proton, gamma, neutron radiation", *Ceramics International,* vol. 45, pp.19206-19222, 2019.

[14] M. I. Sayyed, A. Kumar, H. O. Tekin, R. Kaur, M. Singh, O. Agar, and M. U. Khandaker, "Evaluation of gamma-ray and neutron shielding features of heavy metals doped Bi2O3-BaO-Na2O-MgO-B2O3 glass systems", *Progress in Nuclear Energy*, vol. 118, p.103118, 2020.

[15] Y. Al-Hadeethi, and M. I. Sayyed, "Radiation attenuation properties of Bi2O3–Na2O–V2O5–TiO2–TeO2 glass system using Phy-X/PSD software" *Ceramics international*, vol. 46, pp.4795-4800, 2020.

[16] L. K. Zoller, "Fast-neutron removal cross sections", *Nucleonics*, vol. 22, 1964.

[17] M.G. El-Samrah, A. M. El-Mohandes, A. M. El-Khayatt, and S. E. Chidiac, "MRCsC: A user-friendly software for predicting shielding effectiveness against fast neutrons", *Radiation Physics and Chemistry,* vol. 182, 2021.

[18] F. C. Hila, A. Asuncion-Astronomo, C. A. M. Dingle, J. F. M. Jecong, A. M. V. Javier-Hila, M. B. Z. Gili, C. V. Balderas, G. E. P. Lopez, N. R. D. Guillermo, and A. V. Amorsolo Jr, "EpiXS: A Windows-based program for photon attenuation, dosimetry and shielding based on EPICS2017 (ENDF/B-VIII) and EPDL97 (ENDF/B-VI. 8)", *Radiation Physics and Chemistry*, vol. 182, 2021b.

[19] Şakar, E., Özpolat, Ö.F., Alım, B., Sayyed, M.I. and Kurudirek, M., 2020. Phy-X/PSD: development of a user-friendly online software for calculation of parameters relevant to radiation shielding and dosimetry", *Radiation Physics and Chemistry*, 166, p.108496.

[20] N. Ade, D. Eeden, and F. C. P. van, Plessis, "Characterization of Nylon-12 as a water-equivalent solid phantom material for dosimetric measurements in therapeutic photon and electron beams", *Applied Radiation and Isotopes*, vol. 155, p.108919, 2020.

[21] F. Araki, "Dosimetric properties of a Solid Water High Equivalency (SW557) phantom for megavoltage photon beams", *Physica Medica*, vol. 39, pp. 132–136, 2017.

[22] R. Kumar, S. D. Sharma, S. Desphande, Y. Ghadi, V. S. Shaiju, H. I. Amols, and Y. S. Mayya, "Acrylonitrile Butadiene Styrene (ABS) plastic-based low-cost tissue equivalent phantom for verification dosimetry in IMRT", *Journal of Applied Clinical Medical Physics*, vol. 11, no. 1, pp. 24-32, 2009.

[23] V. P. Singh, N. M. Badiger, and N. Kucuk, "Assessment of methods for estimation of effective atomic numbers of common human organ and tissue substitutes: waxes, plastics and polymers", *Radioprotection*, vol 49, no. 2, pp.155-21, 2014.

[24] S. Brown, A. Venning, Y. De Deene, P. Vial, L. Oliver, J. Adamovics, and C. Baldock, "Radiological properties of the PRESAGE and PAGAT polymer dosimeters", *Applied Radiation and Isotopes*, vol 66, pp. 1970–74, 2008.

[25] T. Şahmaran, and A. Kaşkaş, "Comparisons of various water-equivalent materials with water phantom using the Geant4/GATE simulation program", *International Journal of Radiation Research*, vol 20, no. 3, pp.709-714, 2022.

[26] M. M. Mohd Yusof, R. Hashim, A. A. Tajuddin, S. Bauk, and O. Sulaiman, "Characterization of Rhizophora spp. particleboards as phantom for photon beams", *Ind. Crop. Prod.*, vol. 965, 467-474, 2017.

[27] N. R. Abd Elwahab, N. Helal, T. Mohamed, F. Shahin, and F. M. Ali, "Calculation of Fast neutron Removal Cross-section and Gamma ray Attenuation for New composite Paste Shields", *Interciencias Journal*, vol 44, no. 8, 2019.

[28] A. M. S. Issa, K. Ashok, M. I. Sayyed, M. G. Dong, and Y. Elmahroug, "Mechanical and gamma-ray shielding properties of TeO2-ZnO-NiO glasses", *Mater. Chem. Phys*, vol. 212, pp. 12-20, 2018.

[29] G. T. Chapman, and C. T. Storrs, Effective Neutron Removal Cross Sections for Shielding. USAEC Report ORNL-1843 (AECD-3978). Oak Ridge National Laboratory, Oak Ridge, Tennessee, 1995.

Imidazole Based Novel Schiff Base: Synthesis, Characterization, Quantum Chemical Calculations, In Silico Investigation of ADMEt Properties and Molecular Docking Simulations against VEGFR2 Protein

Ömer DİLEK*

Isparta University of Applied Sciences, Central Research Laboratory Application and Research Center, 32200, Isparta, Turkey
(ORCID: 0000-0003-1409-782X)

Abstract

The potential drug candidate novel Schiff base, 2-(((3-(4-methyl-1H-imidazol-1-yl)-5-(trifluoromethyl)phenyl)imino)methyl)phenol (MITPIM) was synthesized by using salicylaldehyde and 1-[3-Amino-5-(trifluoromethyl)phenyl]-4-methylimidazole, the precursor of nilotinib used in cancer treatment. It was characterized by using spectroscopic techniques such as ^{1}H-NMR, ^{13}C-NMR, ^{19}F-NMR, FT-IR, and UV-Vis. DFT computational technique was used for further investigation. DFT/B3LYP method and the 6-311G(d,p) basis set were used to determine optimized geometry. Then by using optimized geometry and DFT approach three-dimensional molecular electrostatic potential (MEP), vibration frequencies, NMR chemical shift values, HOMOs-LUMOs, and molecular orbital energies were calculated. It was noted that there was good agreement between the experimental and theoretical findings. The ADME and toxicity properties were investigated by using online servers. It was determined from the findings that the MITPIM had good oral bioavailability and minimal toxicity. By using 2XIR protein, the molecular docking simulations of MITPIM were also investigated. The binding energy of the MITPIM-2XIR complex was determined as −9.34 kcal/mol. It was close to nilotinib's binding energy which was −9.69 kcal/mol. Molecular docking and ADMEt results show that the newly synthesized MITPIM has the potential to be a drug.

1. Introduction

Cancer is a type of disease that is caused by cells with the ability to divide uncontrollably, has the potential to spread to other tissues of the body, is the second leading cause of death [1], and is responsible for one out of every 6 deaths worldwide [2], which profoundly affects the individual materially and spiritually. Current treatment methods are surgery, radiotherapy, chemotherapy, hormonal, and targeted drug therapy [2] Due to the undesirable side effects of existing chemotherapeutic drugs and radiotherapy methods, studies on the synthesis of new, easy-to-access, low-cost, targeted anticancer drugs and investigation of their antiproliferative properties have increased [3] nowadays.

When the structures of drug molecules used in cancer treatments in recent years are examined, it is seen that these molecules contain heterocyclic units in their structures. Heterocyclic compounds are structures that have an important place in organic chemistry, containing at least one heteroatom such as nitrogen (N), oxygen (O), or sulfur (S) unlike the carbon atom in their structure. These structures contribute greatly to medicinal chemistry because of their wide application in drug discovery and development [4–6]. The heterocyclic imidazole ring has an aromatic structure containing two nitrogen atoms in its structure, showing polar properties, being

easily ionizable, soluble in water and other polar solvents, and showing amphoteric properties. Because of these properties, the imidazole ring increases the pharmacokinetic properties of the molecule it is found in and is therefore used to optimize the solubility and bioavailability parameters of the molecules [7]. Fluorine (F) is the smallest substituent that can replace the hydrogen atom in organic chemistry. The replacement of hydrogen atoms with fluorine atoms is widely used in medicinal chemistry. The main reasons for this are fluorine has strong electron-withdrawing properties, electrostatic interactions, small atomic size, and high lipophilicity. Additionally, electrostatic interactions of fluorine atoms with proteins, facilitate the binding of ligands to proteins. Synthesis of fluorine-containing molecules and biological applications of them, primarily those with the -CF$_3$ group, are growing daily. [8–10]. Phenolic compounds with OH functional groups have an important place in medicinal chemistry because they have antioxidant, anticancer, antiviral, insecticidal, antimicrobial, and antiparasitic activities [6], [11–13]. Schiff bases are substances that have an imine or azomethine functional group. In the design and development of numerous bioactive lead compounds, it has been discovered that Schiff bases are flexible pharmacophores. Schiff bases have biological activities such as anti-inflammatory, analgesic, antimicrobial, anticonvulsant, antitubercular, anticancer, antioxidant, anthelmintic, antiglycation, and antidepressant activities [14].

The low availability, high cost, and low number of drug agents used in cancer treatment have encouraged researchers to work towards finding new anticancer drugs that are easy to access and low in cost. For this purpose, computer-aided drug design methods have gained importance recently and studies on the design of new drugs with *in silico* techniques have increased. Because this technique not only examines the interaction of drugs with target proteins but also eliminates a large number of molecules and reduces the number of molecules to a minimum. It also shortens the molecule's time to become a drug. In addition, establishing of physicochemical, lipophilicity, water solubility, pharmacokinetic, and drug-likeness properties of new drug candidates by using *in silico* techniques have a crucial role. For example, topological polar surface area (TPSA), Log P$_{o/w}$, Lipinski's rule of five, water solubility, gastrointestinal absorption, and some other properties are criteria sought in drug candidate molecules. These properties of new drug candidates can be learned in advance using *in silico* techniques.

The compound 1-[3-Amino-5-(trifluoromethyl)phenyl]-4-methylimidazole is the precursor of the nilotinib molecule used in cancer treatment. Additionally, this aniline and the compounds produced from it make it a viable substance for additional research and development in the field of pharmaceuticals [15–24]. Based on all of this knowledge, in this work the novel potential bioactive compound, 2-(((3-(4-methyl-1H-imidazol-1-yl)-5-(trifluoromethyl)phenyl)imino) methyl)phenol (MITPIM) which was derived from 1-[3-Amino-5-(trifluoromethyl)phenyl]-4-methylimidazole, was containing imidazole ring, a fluorine atom, imine, and the phenolic functional group was designed and then synthesized.

Spectroscopic techniques were used to identify MITPIM. All quantum chemical calculations were done by using 6-311G(d,p) basis set and DFT/B3LYP method. As a result of quantum chemical calculations. the theoretical vibrational frequencies, NMR chemical shifts, maximum absorption wavelengths, frontier orbitals and MEP surface diagram were obtained. By using VEGFR2 protein (PDB ID: 2XIR), the molecular docking simulations of MITPIM were investigated. ADME and toxicity properties of MITPIM were determined using the SwissADME and ProTox-II online servers.

2. Material and Method

2.1. Physical measurements

The chemicals were supplied by Merck and Aldrich Chemical Company. Chemicals were used without further purification. Aluminum sheets pre-coated with silica gel SIL G/UV254 from MN GmbH & Co., were used to follow reactions. The spots were made visible in UV light (254 nm). Melting point was measured in an open glass capillary tube by using an Electro-thermal 9100 apparatus. The values are not corrected. A Bruker NMR spectrometer (700 MHz) was used to record the ^{1}H and ^{13}C NMR spectra while a Varian NMR spectrometer (600 MHz) was used to record ^{19}F NMR spectrum. Chemical shifts are expressed as parts per million (ppm) in relation to the solvent's residual protons (CHCl$_3$: 7.26 ppm) and carbon resonance (CDCl$_3$: 77.00 ppm). The NMR peak multiplicities were as follows: s for singlet, d for doublet, t for triplet, q for quartet, m for multiplet. 1×10^{-4} M solution compound and PG T80+ double beam spectrophotometer were used to record UV-Vis spectra. The infrared (FT-IR) spectrum was recorded by using the Thermo Nicolet i10, v_{max} in cm^{-1}.

2.2. Synthesis of 2-(((3-(4-methyl-1H-imidazol-1-yl)-5-(trifluoromethyl)phenyl)imino) methyl) phenol (3)

The route of synthesis is depicted in **Figure 1**. Round-bottomed and two necked flask was charged with 1-[3-Amino-5-(trifluoromethyl)phenyl]-4-methylimidazole [25] (**1**, 965.0 mg; 4.0 mmol; 1.0 eq) and salicylaldehyde (**2**, 489.0 mg; 4.0 mmol; 1.0 eq). A magnetic stirring bar and absolute ethanol (20 mL) were added into the flask, the reflux condenser was equipped and the neck was capped with the glass stopper. The mixture was heated up to 80 ˚C and was stirred overnight at this temperature under N_2. TLC technique was used to follow reaction convertion. After completion of the reaction, approximately half of the solvent was evaporated under nitrogen. The mixture was cooled to ambient temperature. The mixture was poured into the beaker containing 50 mL *n*-heptane and the beaker was left in a refrigerator at 4 °C overnight. The solids were filtered, cake was

dried under a vacuum. The aimed title product **3** was synthesized by 80% yield (1.1 g, 3.19 mmol) as a white solid. **Mp:** 108-110 °C. **FT-IR** (KBr): ν_{max} (cm^{-1}) = 3360 (br), 2926 (w), 1610 (s), 1495 (s), 1468 (s), 1320 (s), 1287 (s), 1175 (s). **^{1}H NMR (700 MHz, CDCl$_3$):** δ = 12.50 (s, 1H), 8.66 (s, 1H), 7.85 (s, 1H), 7.51 (s, 1H), 7.47 − 7.38 (m, 4H), 7.09 (s, 1H), 7.05 (dd, J = 8.7, 0.6 Hz, 1H), 6.99 (td, J = 7.5, 1.0 Hz, 1H), 2.31 (d, J = 0.9 Hz, 3H). **^{13}C{^{1}H} NMR (176 MHz, CDCl$_3$):** δ = 165.34 (CH), 161.18 (C), 151.01 (C), 140.51 (C), 138.90 (C), 134.49 (CH), 134.42 (CH), [133.81, 133.62, 133.43, 133.24, (C, J^2_{C-F} = 33.4 Hz)], 132.94 (CH), [125.44, 123.89, 122.34, 120.79, (C, J^1_{C-F} = 273.2 Hz)], 119.54 (CH), 118.55 (C), 117.49 (CH), 117.10 (CH), [116.03, 116.00, (CH, J^3_{C-F} = 3.7 Hz)], [115.35, 115.34, (CH, J^3_{C-F} = 3.3 Hz)], 114.28 (CH), 13.65 (CH$_3$). **^{19}F NMR (CPD, 564 MHz, CDCl$_3$):** δ = -57.85. **UV-Vis (CHCl$_3$):** λ_1 = 248 nm, λ_2 = 272 nm, λ_3 = 344 nm.
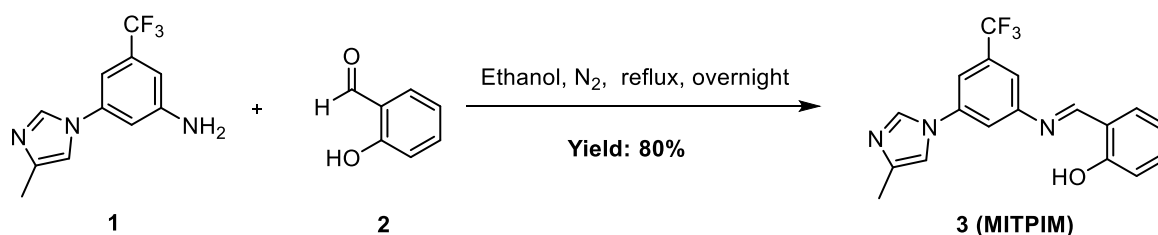

Figure 1. Synthesis of the compound MITPIM

2.3. Computational methods

Quantum chemical calculations were done by using Gaussian 09 package program [26]. Avogadro and Chemcraft were used for all visualizations of quantum chemical calculations [27], [28]. Optimized geometry of MITPIM was determined by using DFT/B3LYP/6-311G(d,p) approach [29], [30]. Calculated vibrational frequencies from optimized geometry of MITPIM were scaled [31] by using 0.9682 factor for frequencies above 1700 cm^{-1} and by using 1.0119 factor for frequencies below 1700 cm^{-1}. TD-DFT [32], [33] approach was used to determine UV-Vis properties while GIAO approach was used to determine chemical shields for ^{1}H, ^{13}C and ^{19}F-NMR [34], [35].

2.4. *In silico* studies

2.4.1. Molecular docking simulations

Molecular docking simulations of the MITPIM and nilotinib compounds were performed by using the SwissDock online web server [36]. UCSF Chimera [37] was used for visualization of images. VEGFR2 protein (PDB ID: 2XIR) was used in the molecular docking studies. Protein Data Bank [38] was used to supply the crystal structure of the 2XIR. After the water was removed and the other residues that were not standart were eliminated from 2XIR, polar hydrogens and Kollman charges were added to 2XIR. A grid box was used to surround 2XIR's active site residues. The 3D coordinates that was binding side of protein were determined by using DeepSite module [39]. By also adding Gasteiger charges to MITPIM and nilotinib which were calculated optimized geometries, were used in the moleculer docking studies.

2.4.2. ADMEt predictions

Physicochemical, pharmacokinetic, lipophilicity, and drug similarity properties of newly synthesized MITPIM were calculated using the SwissADME

online platform [40]. The toxicity parameters such as LD50 and the acceptable usage range of MITPIM were identified using the ProTox-II online server [41].

3. Results and Discussion

3.1. NMR spectra

To make it simpler to compare experimental and computed chemical shifts of the MITPIM, all acquired values are shown collectively in **Table 1**. The computed chemical shift value of the hydroxyl proton of MITPIM was lower as compared to the experimental result (experimental value: 12.50 ppm, theoretical value: 4.53 ppm). While the protons of the methyl group as a doublet peak were at 2.31 ppm experimental, they were at 2.26-2.08 ppm theoretical. Whilst chemical shift values of aromatic protons were observed experimentally in the range of 6.99-8.66 ppm, the DFT technique predicted that they would be in the range of 6.83-9.03 ppm. The results show that the theoretical analysis accurately discloses the characteristics of the MITPIM compound and confirms the spectrum data quite well. **Figures 2** and **3** show, respectively, the compound's experimentally obtained and theoretically predicted ^{1}H-NMR spectra.

Table 1. Experimentally and theoretically obtained ^{1}H-NMR (CDCl$_3$) chemical shifts (CDCl$_3$)

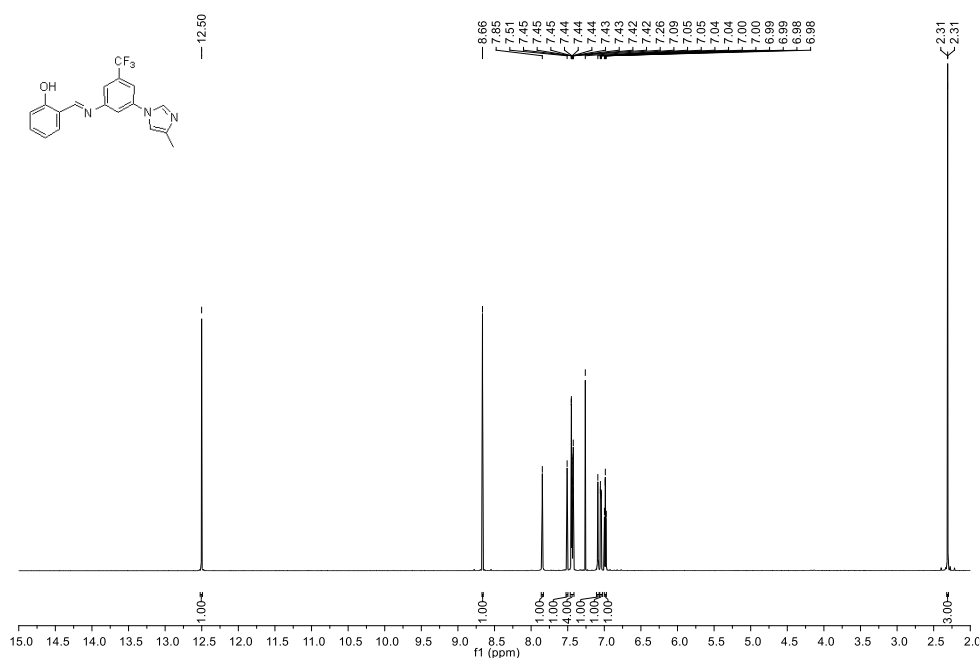| Proton Number	Experimental chemical shift (ppm)	Theoretical chemical shift (ppm)
H9	8.66 (s, 1H)	9.03
H13	7.85 (s, 1H)	8.50
H4	7.51 (s, 1H)	8.10
H6		7.76
H7	7.47 – 7.38 (m, 4H)	7.58
H11		7.52
H5		7.40
H12, H8	7.05 (dd, J = 8.7, 0.6 Hz, 1H) 7.09 (s, 1H)	7.11
H10	6.99 (td, J = 7.5, 1.0 Hz, 1H)	6.83
H14	12.50 (s, 1H)	4.53
H2, H3		2.26 2.08
H1	2.31 (d, J = 0.9 Hz, 3H)	

Figure 2. Experimental ^{1}H-NMR spectrum taken in CDCl$_3$ of the MITPIM
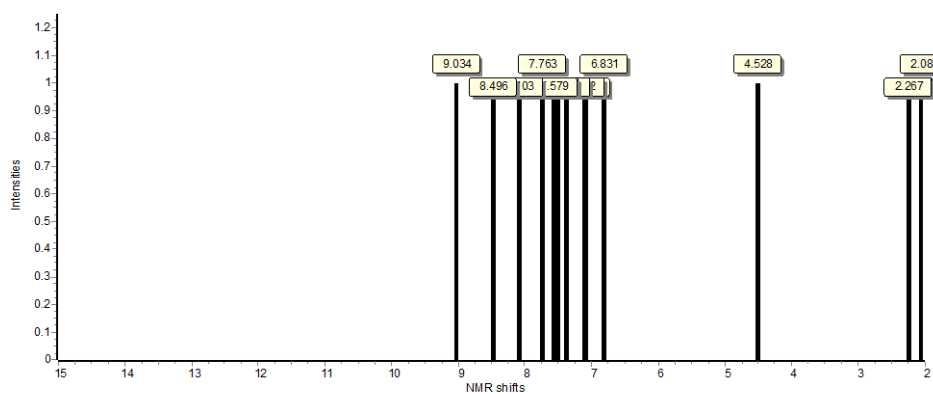

Figure 3. Theoretical ^{1}H-NMR spectrum taken in CDCl$_3$ of the MITPIM

In the ^{13}C-NMR spectrum, the C13 atom associated with the O-H group was measured and recorded at 161.18, however in the theoretical spectrum, this signal was discovered at 164.0 ppm. The signal for the methyl group's carbon atom C1 was identified at 13.65 ppm, while the calculated chemical shift for it appeared at 14.07. The carbon atom C18 of the trifluoromethyl group gave the quartet signals at 125.44, 123.89, 122.34, and 120.79 ppm, and this

carbon atom signal was discovered at 132.80 ppm in the theoretical spectrum. The Schiff base's carbon atom C11 produced a signal at 165.34 ppm, and this carbon atom signal was found in the theoretical spectrum at 161.10 ppm. The expected region was where all other carbon atoms were seen, and **Table 2** was given a detailed breakdown of the values that resulted. **Figures 4** and **5** show the compound's theoretically predicted and experimentally acquired ^{13}C-NMR spectra.

Table 2. Experimentally and theoretically obtained ^{13}C-NMR (CDCl$_3$) chemical shifts

Carbon Number	Group	Experimental chemical shift (ppm)	Theoretical chemical shift (ppm)
C1	CH$_3$	13.65	14.07
C2	CH	134.42	135.84
C3	C	140.51	146.09

C4	CH	114.28	114.65
C5	C	133.81 133.62 133.43 133.24	138.14
C6	CH	115.35 115.34	112.01
C7	C	138.90	142.15
C8	CH	117.49	119.77
C9	C	151.01	161.21
C10	CH	116.03, 116.00	114.58
C11	CH	165.34	161.10
C12	C	118.55	125.78
C13	C	161.18	164.00
C14	CH	117.10	117.69
C15	CH	134.49	138.97
C16	CH	119.54	123.87
C17	CH	132.94	132.12
C18	CF$_3$	125.44 123.89 122.34 120.79	132.80
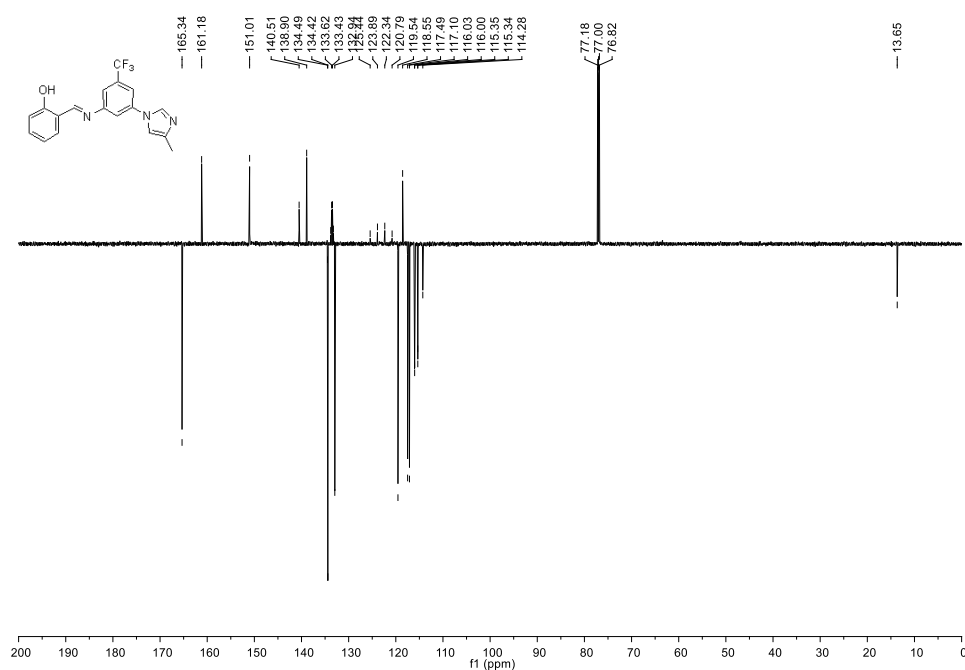
Figure 4. Experimental ^{13}C-NMR spectrum taken in CDCl$_3$ of the MITPIM
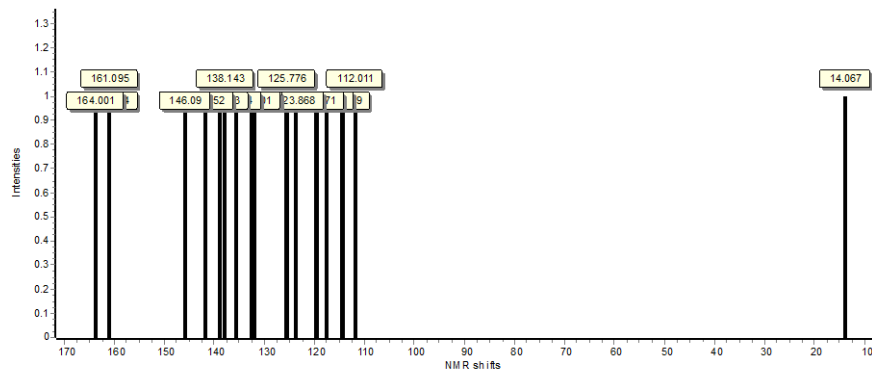
Figure 5. Theoretical ^{13}C-NMR spectrum taken in CDCl$_3$ of the MITPIM

67

In order to confirm MITPIM's structure ^{19}F-NMR analyses was also done. Experimental measurements at -57.85 ppm revealed the fluorine atoms as singlet peak. Theoretically, the relevant atoms were calculated to range between -66.77 and -99.08 ppm using C_6F_6 as a reference. To calculate theoretical chemical shifts of MITPIM, $\delta = \sigma_{ref} - \sigma + \delta_{ref}$ ($\sigma_{ref} = 333.6$ ppm, $\delta_{ref} = -164.9$ ppm, σ = calculated shift) equation was used [42]. The data were shown in Table **3**, experimental and theoretical spectra were given in **Figures 6** and **7**

Table 3. Experimentally and theoretically obtained ^{19}F-NMR chemical shifts

Fluorine Number	Experimental chemical shift (ppm)	Theoretical chemical shift (ppm)
F1		-66.77
F2	-57.85 (CF$_3$)	-68.91
F3		-99.08
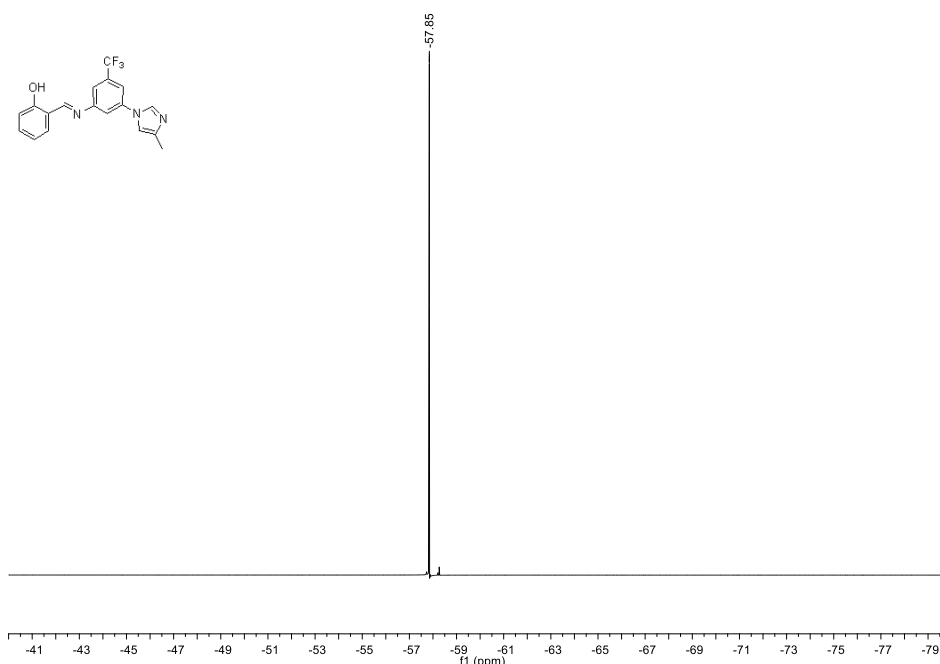
Figure 6. Experimental ^{19}F-NMR (CDCl$_3$) spectrum of the MITPIM
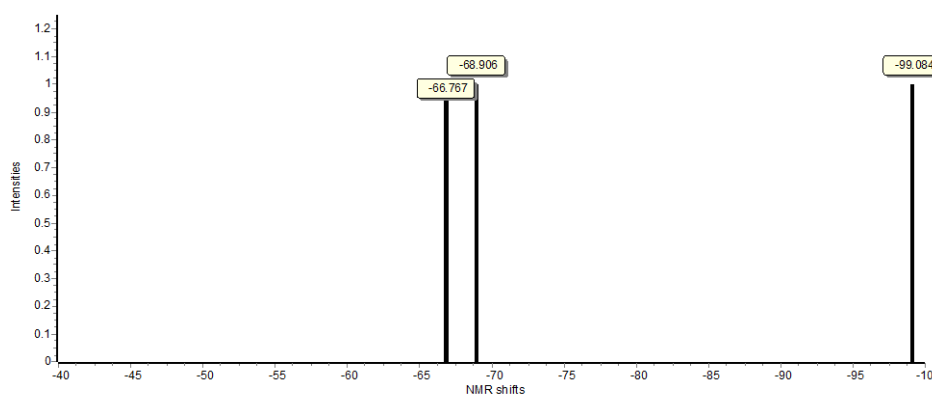
Figure 7. Theoretical ^{19}F-NMR (CDCl$_3$) spectrum of the MITPIM

A correlation between theoretical and experimental NMR chemical shift values was examined, and it was found that theoretical predictions and experimental data showed a good agreement [25], [43–45].

3.2. FT-IR spectra

Table 4 displayed all FT-IR frequency comparisons between the observed and predicted values for each constituent. The C=N double bond stretching vibration was discovered at 1600/1646 cm⁻¹ in the experimental/theoretical FT-IR spectra of the molecule that were captured on the KBr disc. The compound showed the stretching vibration of the -OH group as a broad band at 3360 cm⁻¹, which is consistent with the estimated vibrational frequency of 3350 cm⁻¹.

Table 4. Experimentally and theoretically Vibration frequencies ($\tilde{\nu}_{max}$ (cm⁻¹)) of MITPIM

	Vibration frequencies ($\tilde{\nu}_{max}$ (cm⁻¹))	
Vibrational band	**Theoretical**	**Experimental**
O-H stretching	3350	3360
C-H stretching	3185	3191
C-H stretching	3120	3117
C-H stretching	2934	2926
C=N stretching	1646	1600
C-N stretching	1323	1323
C-N stretching	1287	1284
C-F stretching	1186	1175
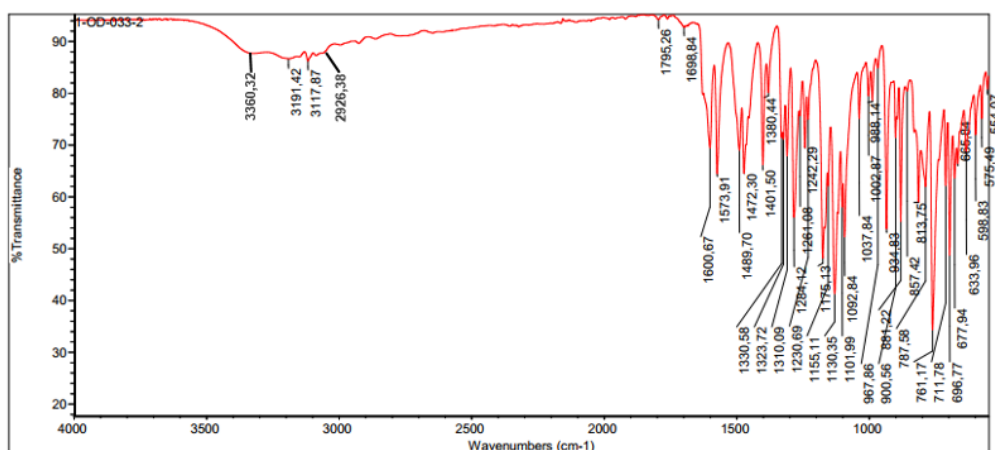
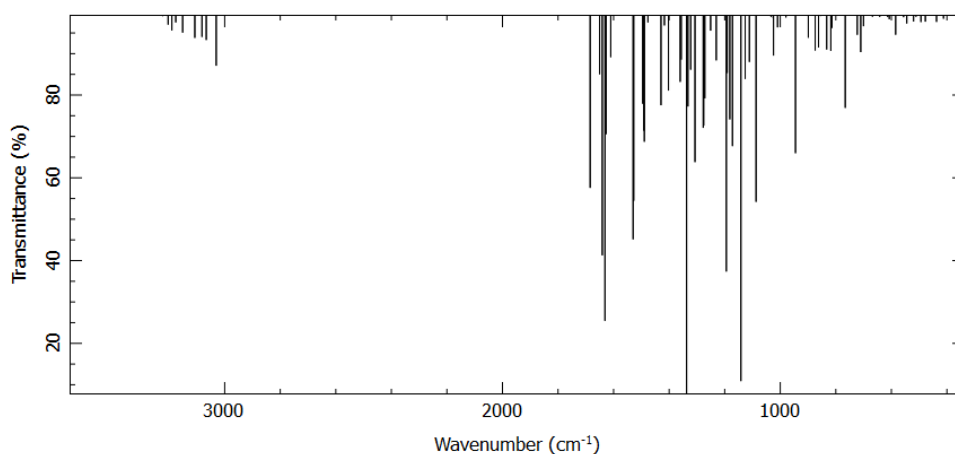**Figure 8.** Experimental FT-IR spectrum of the MITPIM

Figure 9. Theoretical FT-IR spectrum of the MITPIM

Figure 10 showed the linearity between the theoretical and experimental frequency of the compound and the equality of y = 1.0078x – 24.352 (R^2 = 0.9997) was discovered. These results showed that there was agreement between the theoretically and empirically established frequency values [25].
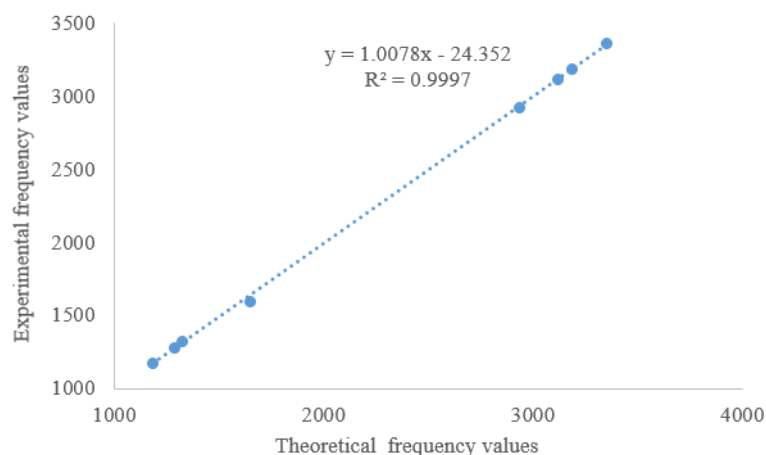
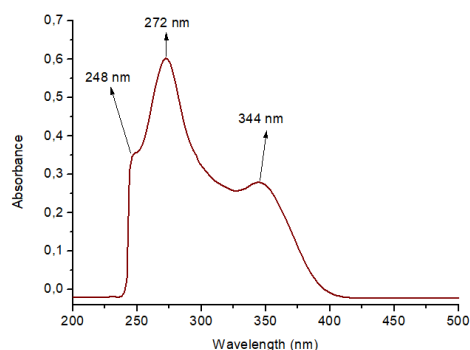**Figure 10.** The linearity of frequency values (cm^{-1})

3.3. UV-Vis spectrum and frontier molecular orbitals

The UV-Vis spectra of MITPIM in CHCl₃ were taken between 200 and 700 nm. We computed the electronic transition wavelengths of the compounds using the TD-DFT method and the B3LYP/6-311G(d,p) level. **Figure 11** displays the UV-Vis spectra of the compounds in both experimental and theoretical forms. Also frontier molecular orbital parameters of the MITPIM (electronic transitions, excitation energies (eV) and oscillator strengths (f)) were shown in **Table 5.** It is shown that in **Table 5,** MITPIM had three maximum absorbance (λ) bands experimentally. These were 344 nm, 272 nm, and 248 nm while theoretical ones were 343 nm, 293 nm, and 277 nm. The responsible band from n→π* was at 344 nm in experimental spectra while this was at 343 nm theoretically one. π→π* transition band originating from the imine group was detected at 272 nm in the experimental UV-Vis spectrum whereas it was at 293 nm in the theoretical one. The other π→π* transitions band sourced from aromatic rings of the MITPIM was at 248 nm in the experimental spectrum, while this was at 277 nm in the theoretical one.

Table 5. Experimental and theoretical electronic transitions, excitation energies (eV), oscillator strengths (f)

Compound	Transitions	Experimental		TD-DFT/B3LYP/6-311G(d,p)		
		λ (nm)	E (eV)	λ (nm)	E (eV)	f
MITPIM	n→π*	344	3.60	343	3.62	0.3311
				326		0.2860
				309		0.0139
	π→π* (imin)	272	4.56	293	4.23	0.0429
	π→π*	248	5.00	277	4.48	0.3977

Experimental UV-Vis Spectrum
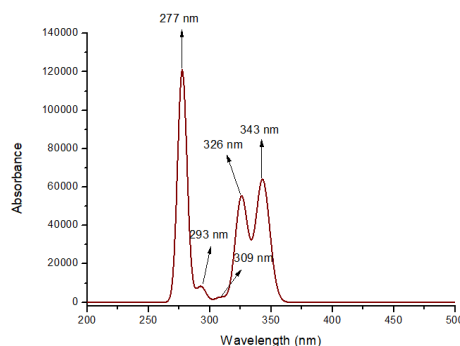
Theoretical UV-Vis Spectrum

Figure 11. Experimental (left) and theoretical (right) UV-Vis spectra of the MITPIM in CHCl₃

The HOMO (Highest Occupied Molecular Orbital) and LUMO (Lowest Unoccupied Molecular Orbital) abbreviations are used to refer to the frontier orbitals of MITPIM. In most cases, HOMO regulates nucleophilic reactions in molecules, while LUMO regulates electrophilic reactions. The HOMOs and LUMOs of MITPIM were calculated using the DFT approach. The information in **Figure 12** related to MITPIM's molecule orbital energies, surfaces, and the energy difference between HOMO and LUMO. Analysis of the compound's HOMO-LUMO graphs revealed that HOMOs were clustered over the whole structure, whilst LUMOs were grouped on the benzene skeletons. The estimated HOMO/LUMO energy for the compound was calculated to be -6.119/-2.196 eV and the energy value for the HOMO-LUMO gap was obtained to be 4.003 eV.
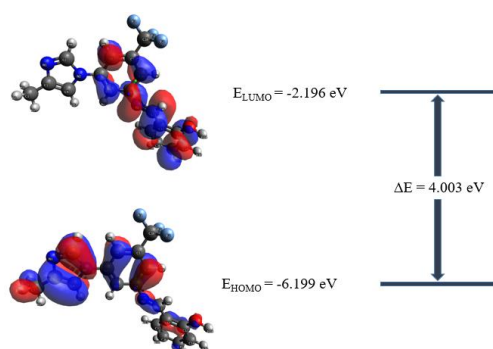

Figure 12. Surfaces of Molecular orbital, energies (E), and energy gap (ΔE) between HOMO and LUMO of the MITPIM

3.4. Computational details

3.4.1. Molecular structure

To achieve the optimized geometry for the MITPIM, a B3LYP method and 6-311G(d,p) basis set was used. The complete optimized geometry of MITPIM, including atom numbering, is shown in **Figure 13**.
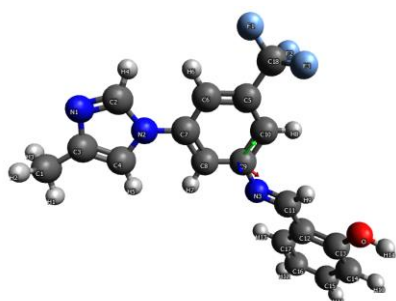

Figure 13. Optimized geometry of MITPIM by using DFT

3.4.2. Molecular electrostatic potential (MEP) diagram

Figure 14 displays the MEP surface diagram for the MITPIM computed at the DFT/B3LYP/6-311G(d,p) level. On the nitrogen atom of the imidazole moiety, the synthesized compound's MEP surface diagram showed an electron-rich area. A negative electrostatic potential was created on the nitrogen atom due to its electronegativity. These regions might be the locations of nucleophilic assaults on molecules if the synthesized molecule were to react with another molecule. The proton in the hydroxyl group, however, was the area of MITPIM electron-poor. The oxygen's high electronegativity in the hydroxyl group loosened its connection with the hydrogen atom and made the proton looser. The chemicals might behave electrophilically in these regions.

Figure 15 depicted the Mulliken atomic charge distribution for the MITPIM molecule determined by the B3LYP method using the 6-311G(d,p) basis set. It was seen that all heteroatoms have a negative charge. Due to fluorine atoms' strong electronegativity, the C18 atom was the highest positive charge (0.72681 a.u.).
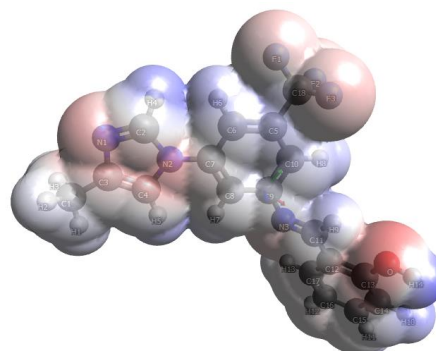

Figure 14. Calculated Molecular electrostatic potential diagram of MITPIM

After the C18 atom, H14 (0.2558 a.u.) atom was also the highest positive charge among the hydrogens due to the electronegative oxygen atom. The most negative atoms were N2 atom (-0.4373 a.u.) in imidazole and O (-0.3651 a.u.) atom in the phenol functional group. As well as N2 and O atoms, N3 (-0.3296 a.u.) atom responsible for the imin group, N1 (-0.3189 a.u.) atom in the imidazole and C5 (-0.3125 a.u.) atom in the benzene which is close to -CF₃ functional group had negative charges. From Mulliken charges, it was concluded that locations with high and low electron density in the MITPIM compound were compatible with the MEP diagram.
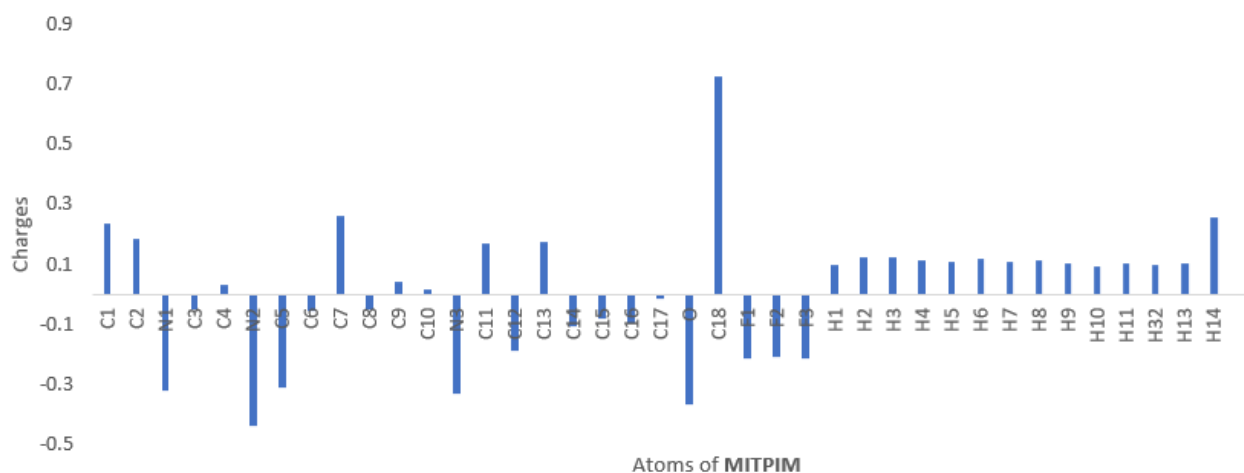
Figure 15. Calculated Mulliken atomic charges of the MITPIM

3.5. *In silico* studies

3.5.1. ADMET predictions

ADME properties of pharmacological substances are crucial in drug discovery. Physicochemical, lipophilicity, water solubility, pharmacokinetic and drug-likeness properties of new substances are important criteria in drug discovery.

Physicochemical and lipophilicity properties of substances like molecular weight, MLOGP, number of H-bond acceptors and donor atoms are the searched properties in Lipinski's rule of five. The molecular weight value of substances must be greater than 150 and less than 500. MLOGP value must be less than 4.15. The number of hydrogen bond acceptor atoms must be less than 10, Number of hydrogen bond donor atom must be less than 5. When Lipinski's rule of five was investigated in MITPIM, it was concluded that the compound has the all criteria (**Table 6**). TPSA value is also important as gets through of substances from cell membranes. The TPSA value of the substance should be less than 140 Å^2.

Lipophilicity is the dispersion of substances between lipids and water at specific rates. To get to their target sites, drug molecules must cross several biological membranes, including the blood-brain barrier, the skin, and the gut. So the dispersion rate is important. The consensus lipophilicity (CLogP$_{o/w}$) value of MITPIM was calculated to be 3.98.

Pharmacokinetic properties also have a crucial role in ADME properties. The Boiled-Egg model is taken part in **Figure 16** which the x-axis is TPSA and y-axis is WLOGP. While white region in the model is responsible for gastrointestinal absorption, yellow region in the model is responsible for whether the compound being crossed the blood-brain barrier or not. When the Boiled-Egg model in **Figure 16** was examined, It was concluded that the red dot was in the white region, The gastrointestinal system can easily absorb the MITPIM and the MITPIM compound did not pass the blood-brain barrier. In the pharmacokinetic properties, Cytochrome P450 enzyme systems also have a crucial role in the metabolism of taken medicines. When **Table 6** was examined, it was estimated that MITPIM is likely to be inhibited by CYP1A2, CYP2C19 and CYP2D6, while is not to be inhibited by CYP2C9 and CYP3A4.

As well as other properties, Druglikeness properties were also investigated. Lipinski (Pfizer), Ghose (Amgen), Veber (GSK), Egan (Pharmacia), and Muegge (Bayer) are the drug companies and these have various rules which are searched criteria in druglikeness properties. When **Table 6** is examined related to this field, The MITPIM compound has had all criteria except Ghose's rule because the WLogP value is greater than 5.6.

The water solubility (LogS) of a substance to reach its target is an important feature. When **Table 6** examined, LogS values of MITPIM according to various mathematical equations which were calculated by researchers are -4.68 (ESOL, Moderately soluble), -4.66 (Ali, Moderately soluble), -6.20 (SILICOS-IT, Poorly soluble) respectively.

Table 6. Physicochemical, lipophilicity, solubility, pharmacokinetics and drug-likeness properties of the MITPIM

Physicochemical Properties		Druglikeness Properties		
Properties	**Value** **MITPIM**	**Requirement**	**Value** **MITPIM**	**Compatible** **MITPIM**
		Lipinski's Rule		
Molecular Formula	$C_{18}H_{14}F_3N_3O$	MW ≤ 500	345.32	
Molecular weight (MW, g/mol)	345.32	M LOGP ≤ 4.15	2.83	Yes
Number of heavy atoms	25	HBA Atoms ≤ 10	6	
Number of aromatic heavy atoms (AHA)	17	HBD Atoms ≤ 5	1	
Number of rotatable bonds (RB)	4	**Ghose's Rule**		
Number of H-bond acceptors (HBA)	6	160 ≤ MW ≤ 480	345.32	
Number of H-bond donors (HBD)	1	-0.4 ≤ WLOGP ≤ 5.6	5.81	
Molar Refractivity (MR)	89.25	40 ≤ MR ≤ 130	89.25	No
TPSA (Å²)	50.41	20 ≤ atoms ≤ 70	39	
Lipophilicity		**Veber's Rule**		
Log $P_{o/w}$ (iLOGP)	2.93	RB ≤ 10	4	Yes
Log $P_{o/w}$ (XLOGP3)	3.90	TPSA ≤ 140	50.41	
Log $P_{o/w}$ (WLOGP)	5.81	**Egan's Rule**		
Log $P_{o/w}$ (MLOGP)	2.83	WLOGP ≤ 5.88	5.81	Yes
Consensus Log $P_{o/w}$	3.98	TPSA ≤ 131.6	50.41	
Pharmacokinetics		**Muegge's Rule**		
GI absorption	High	200 ≤ MW ≤ 600	345.32	
BBB permeant	No	-2 ≤ XLOG3 ≤ 5	3.90	
P-gp substrate	No	TPSA ≤ 150	50.41	
CYP1A2 inhibitor	Yes	Number of rings ≤ 7	3	
CYP2C19 inhibitor	Yes	Number of carbon > 4	18	
CYP2C9 inhibitor	No	Number of heteroatoms > 1	4	Yes
CYP2D6 inhibitor	Yes	RB ≤ 15	4	
CYP3A4 inhibitor	No	HBA ≤ 10	6	
Log K_p (skin permeation, cm/s)	-5.64	HBD ≤ 5	1	
Water Solubility				
Log S (ESOL) Class	-4.68 Moderately soluble			
Log S (Ali) Class	-4.66 Moderately soluble			

Log S (SILICOS-IT) Class	-6.20 Poorly soluble			
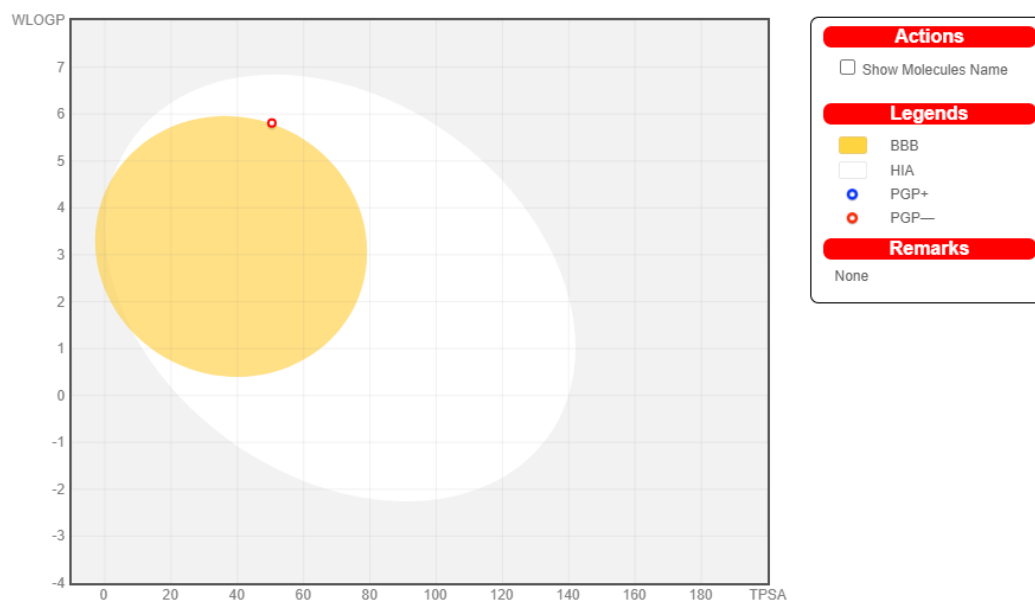
Figure 16. BOILED-Egg model of the MITPIM

The toxicity properties of MITPIM were investigated using the Protox-II online server, which is a widely used tool for predicting toxicity in chemical compounds. The lethal dose (LD50) value was determined 1000 mg/kg, based on the analysis of **Table 7**. These values were found to be lower than the corresponding value (2319.9 mg/kg) in the online server dataset. From the calculated result, It was

concluded that MITPIM exhibits some level of toxicity. Furthermore, the estimated toxicity classes for the substances were established on the Protox-II web server, which ranks compounds from the worst (class 1) to the best (class 6) based on their predicted toxicity. MITPIM was classified into the fourth

toxicity class, which indicates moderate toxicity levels. Notably, neither compound was found to exhibit any carcinogenic or mutagenic properties (**Table 7**).

Table 7. Toxicity properties of the MITPIM

Toxicity Properties	
	MITPIM
Predicted LD50	1000 mg/kg
Predicted Toxicity Class	4
Carcinogenicity	Inactive
Mutagenicity	Inactive
Lethal Dose	Low from dataset

(dataset: 2319.9 mg/kg, MITPIM: 1000 mg/kg)

3.5.2. Molecular Docking Simulations

By using the VEGFR2 protein (PDB ID: 2XIR), the molecular docking simulations of MITPIM were investigated. The 3D coordinates that was binding site of the 2XIR were used as x = 21.0, y = 26.2, and z = 38.8. To create a meaningful comparison, the commercially used drug nilotinib which is a VEGFR2 inhibitor, was used. Optimized geometries of MITPIM and nilotinib were individually docked to the selected region of the 2XIR. The ligand-protein complex which has the lowest docking scores were chosen to investigate the binding modes for MITPIM and nilotinib. From molecular docking studies, valuable information such as binding energy, full fitness score, hydrogen bond location, and length values for each ligand-protein pair were obtained. These detailed findings can be found in **Table 8**.

When the binding energies of MITPIM-2XIR and Nilotinib-2XIR complexes were examined, MITPIM-2XIR binding energy was -9,34 kcal/mol and Nilotinib-2XIR binding energy was -9.69 respectively. From the results it was concluded that the bindings between ligand and proteins were exothermic, Binding energy of MITPIM-2XIR is very close to Nilotinib-2XIR.

Interactions between ligand and protein can be different types such as Van der Waals, Hydrogen bonding, etc. When the docking simulations were

examined, it was concluded that both MITPIM and nilotinib binded to ARG 1027 of 2XIR with a hydrogen bond. It was seen that the most stable interaction was between ARG 1027 HH and LIG 1 N on MITPIM-2XIR complex with 2.113 Å while to be between ARG 1027 HH and LIG 1 N on Nilotinib-

2XIR complex with 2.423 Å in **Table 8**. The optimal binding positions of MITPIM-2XIR and Nilotinib-2XIR were given in **Figures 17** and **18**. Also, the hydrogen binding positions of MITPIM-2XIR and Nilotinib-2XIR were given in **Figure 19.**

Table 8. Molecular docking parameters within the ligand-target molecule couples.

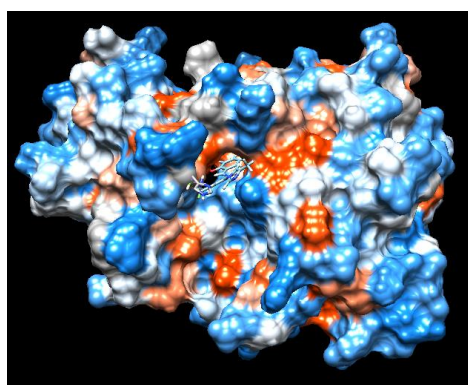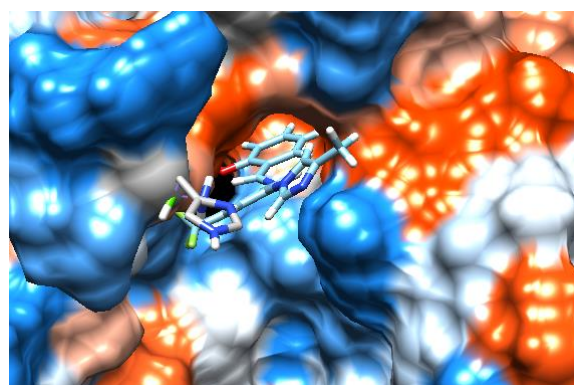| Ligand-Target	ΔG (kcal/mol)	H bond Location (Length, Å)	Fullfitness score
MITPIM-2XIR	-9.34	ARG 1027 HH & LIG 1 <u>N</u> (2.113 Å)	-1700.32
Nilotinib-2XIR	-9.69	ARG 1027 HH & LIG 1 <u>N</u> (2.423 Å)	-1716.68
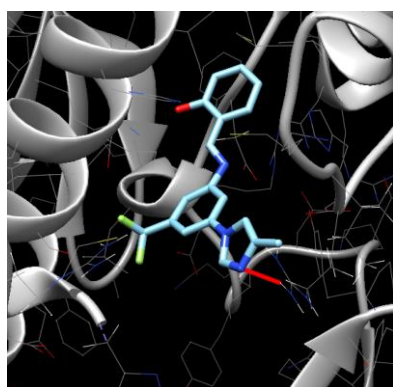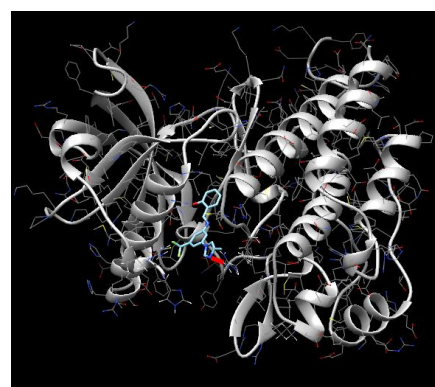
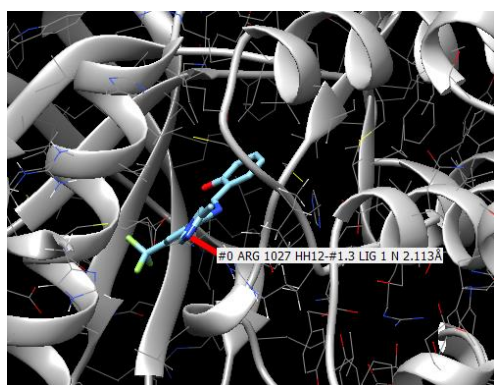**Figure 17.** Visualization of MITPIM-2XIR complex (**a**: zoom in, **b**: zoom out)
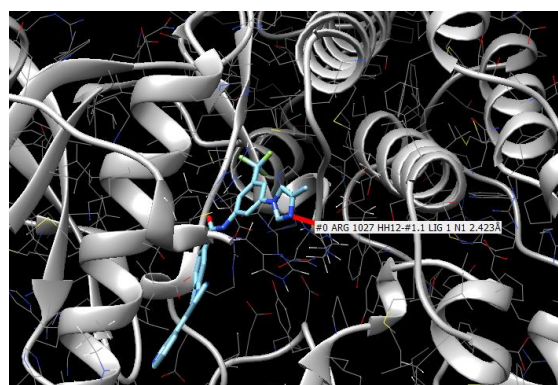

Figure 18. The binding of the MITPIM in the cavity of 2XIR (**a**) and closer views of the hydrophobicity surface (**b**)

Figure 19. H bond visulization of MITPIM (**a**) and nilotinib (**b**) to arginine aminoacid of 2XIR protein

4. Conclusion and Suggestions

Within the scope of the study 2-(((3-(4-methyl-1H-imidazol-1-yl)-5-(trifluoromethyl)phenyl)imino)methyl)phenol (MITPIM) was synthesized and characterized with spectroscopic techniques such as ^{1}H-NMR, ^{13}C-NMR, ^{19}F-NMR, UV-Vis and FT-IR. The DFT/B3LYP method and 6-311G(d,p) basis set were used to calculate all of MITPIM's spectral information. As a result of theoretical calculations, it has been seen that the values are compatible with experimental ones. The findings of *in silico* experiments that included ADME, toxicity, and molecular docking simulations revealed that the synthesized MITPIM had the potential to be a drug. Given that the mean LD50 for the MITPIM in the ProTox-II dataset was 1000 mg/kg, it is clear that this substance is either non-toxic or has very low oral toxicity. In order to forecast the possible anticancer effect of the MITPIM, molecular docking experiments were also carried out. It was shown that MITPIM and VEGFR2 (PDB ID: 2XIR) had a favorable interaction, with a binding energy of about -9.34 kcal/mol, which was near to nilotinib's binding energy of -9.69 kcal/mol. The successful outcomes show that deeper research in related fields is required for MITPIM.

The conclusion section should be stand alone. The aim of the study and its significant results should be given briefly in a concrete way. In addition, suggestions and opinions that are requested to be conveyed to the readers regarding the results of the study can be stated.

Acknowledgment

Contributions of the authors

Conflict of Interest Statement

Statement of Research and Publication Ethics

The study is complied with research and publication ethics

References

[1] R. L. Siegel, K. D. Miller, H. E. Fuchs, and A. Jemal, "Cancer statistics, 2022," *CA Cancer J Clin*, vol. 72, no. 1, pp. 7–33, Jan. 2022.

[2] D. T. Debela, S. G. Muzazu, K. D. Heraro, M. T. Ndalama, B. W. Mesele, D. C. Haile, S. K. Kitui, T. Manyazewal, "New approaches and procedures for cancer treatment: Current perspectives," *SAGE Open Med*, vol. 9, p. 205031212110343, Aug. 2021.

[3] V. V. Padma, "An overview of targeted cancer therapy," *Biomedicine (Taipei),* vol. 5, no. 4, p. 19, Nov. 2015.

[4] P. Martins, J. Jesus, S. Santos, L. R. Raposoi, C. Roma-Rodrigues, P. V. Baptista, A. R. Fernandes, "Heterocyclic Anticancer Compounds: Recent Advances and the Paradigm Shift towards the Use of Nanomedicine's Tool Box," *Molecules*, vol. 20, no. 9, pp. 16852–16891, Sep. 2015.

[5] S. Kakkar, S. Kumar, B. Narasimhan, S. M. Lim, K. Ramasamy, V. Mani, S. A. A.Shah, "Design, synthesis and biological potential of heterocyclic benzoxazole scaffolds as promising antimicrobial and anticancer agents," *Chem Cent J*, vol. 12, no. 1, p. 96, Sep. 2018.

[6] T. Tahir, M. Ashfaq, M. Saleem, M. Rafiq, M. I. Shahzad, K. K. Mojzych, M. Mojzych, "Pyridine Scaffolds, Phenols and Derivatives of Azo Moiety: Current Therapeutic Perspectives," *Molecules*, vol. 26, no. 16, p. 4872, Aug. 2021.

[7] A. Verma, S. Joshi, and D. Singh, "Imidazole: Having Versatile Biological Activities," *J Chem*, vol. 2013, p. 329402, Oct. 2013.

[8] A. Abula, Z. Xu, Z. Zhu, C. Peng, Z. Chen, W. Zhu, H. A. Aisa, "Substitution Effect of the Trifluoromethyl Group on the Bioactivity in Medicinal Chemistry: Statistical Analysis and Energy Calculations," *J Chem Inf Model*, vol. 60, no. 12, pp. 6242–6250, Dec. 2020.

[9] J. B. I. Sap, N. J. W. Straathof, T. Knauber, C. F. Meyer, M. Médebielle, L. Buglioni, C. Genicot, A. A. Trabanco, T. Noël, C.W. A. Ende, and V. Gouverneur, "Organophotoredox Hydrodefluorination of Trifluoromethylarenes with Translational Applicability to Drug Discovery," *J Am Chem Soc*, vol. 142, no. 20, pp. 9181–9187, May 2020.

[10] A. S. Nair, A. K. Singh, A. Kumar, S. Kumar, S. Sukumaran, V. P. Koyiparambath, L. K. Pappachen, T. M. Rangarajan, H. Kim, and B. Mathew, "FDA-Approved Trifluoromethyl Group-Containing Drugs: A Review of 20 Years," *Processes*, vol. 10, no. 10, p. 2054, Oct. 2022.

[11] Y. Zhang, P. Cai, G. Cheng, and Y. Zhang, "A Brief Review of Phenolic Compounds Identified from Plants: Their Extraction, Analysis, and Biological Activity," *Nat Prod Commun*, vol. 17, no. 1, Jan. 2022.

[12] A. Basli, N. Belkacem, and I. Amrani, "Health Benefits of Phenolic Compounds Against Cancers," *in Phenolic Compounds - Biological Activity, InTech*, 2017, pp. 193–210, March 2017.

[13] P. G. Anantharaju, P. C. Gowda, M. G. Vimalambike, and S. V. Madhunapantula, "An overview on the role of dietary phenolics for the treatment of cancers," *Nutr J*, vol. 15, no. 1, p. 99, Dec. 2016.

[14] A. Kajal, S. Bala, S. Kamboj, N. Sharma, and V. Saini, "Schiff Bases: A Versatile Pharmacophore," *Journal of Catalysts*, vol. 2013, p. 893512, Aug. 2013.

[15] A. P. Hnatiuk, A. A. N. Bruyneel, D. Tailor, M. Pandrala, A. Dheeraj, W. Li, R. Serrano, D. A. M. Feyen, M. M. Vu, P. Amatya, S. Gupta, Y. Nakauchi, I. Morgado, V. Wiebking, R. Liao, M. H. Porteus, R. Majeti, S. V. Malhotra, M. Mercola, "Reengineering Ponatinib to Minimize Cardiovascular Toxicity," *Cancer Res*, vol. 82, no. 15, pp. 2777–2791, Aug. 2022.

[16] H. Jung, J. Kim, D. Im, H. Moon, and J.-M. Hah, "Design, synthesis, and in vitro evaluation of N-(3-(3-alkyl-1H-pyrazol-5-yl) phenyl)-aryl amide for selective RAF inhibition," *Bioorg Med Chem Lett*, vol. 29, no. 4, pp. 534–538, Feb. 2019.

[17] D. Zhu, H. Huang, D. M. Pinkas, J. Luo, D. Ganguly, A. E. Fox, E. Arner, Q. Xiang, Z. C. Tu, A. N. Bullock, A. R. Brekken, K. Ding, X. Lu, "2-Amino-2,3-dihydro-1 H -indene-5-carboxamide-Based Discoidin Domain Receptor 1 (DDR1) Inhibitors: Design, Synthesis, and in Vivo Antipancreatic Cancer Efficacy," *J Med Chem*, vol. 62, no. 16, pp. 7431–7444, Aug. 2019.

[18] H. G. Choi, P. Ren, F. Adrian, F. Sun, H. S. Lee, X. Wang, Q. Ding, G. Zhang, Y. Xie, J. Zhang, Y. Liu, T. Tuntland, M. Warmuth, P. W. Manley, J. Mestan, N. S. Gray, T.Sim "A Type-II Kinase Inhibitor Capable of Inhibiting the T315I 'Gatekeeper' Mutant of Bcr-Abl," *J Med Chem*, vol. 53, no. 15, pp. 5439–5448, Aug. 2010.

[19] M. Pandrala, A. A. N. Bruyneel, A. P. Hnatiuk, M. Mercola, and S. V. Malhotra, "Designing Novel BCR-ABL Inhibitors for Chronic Myeloid Leukemia with Improved Cardiac Safety," *J Med Chem*, vol. 65, no. 16, pp. 10898–10919, Aug. 2022.

[20] E. Kalinichenko, A. Faryna, T. Bozhok, and A. Panibrat, "Synthesis, In Vitro and In Silico Anticancer Activity of New 4-Methylbenzamide Derivatives Containing 2,6-Substituted Purines as Potential Protein Kinases Inhibitors," *Int J Mol Sci*, vol. 22, no. 23, p. 12738, Nov. 2021.

[21] X. Lu, Z. Zhang, X. Ren, X. Pan, D. Wang, X. Zhuang, J. Luo, R. Yu, K. Ding, "Hybrid pyrimidine alkynyls inhibit the clinically resistance related Bcr-AblT315I mutant," *Bioorg Med Chem Lett*, vol. 25, no. 17, pp. 3458–3463, Sep. 2015.

[22] E. Kalinichenko, A. Faryna, V. Kondrateva, A. Vlasova, V. Shevchenko, A. Melnik, O. Avdoshko and Alla Belko, "Synthesis, Biological Activities and Docking Studies of Novel 4-(Arylaminomethyl)benzamide Derivatives as Potential Tyrosine Kinase Inhibitors," *Molecules*, vol. 24, no. 19, p. 3543, Sep. 2019.

[23] E. Kalinichenko, A. Faryna, T. Bozhok, A. Golyakovich, and A. Panibrat, "Novel Phthalic-Based Anticancer Tyrosine Kinase Inhibitors: Design, Synthesis and Biological Activity," *Curr Issues Mol Biol*, vol. 45, no. 3, pp. 1820–1842, Feb. 2023.

[24] G. Faudone, R. Zhubi, F. Celik, S. Knapp, A. Chaikuad, J. Heering, D. Merk, "Design of a Potent TLX Agonist by Rational Fragment Fusion," *J Med Chem*, vol. 65, no. 3, pp. 2288–2296, Jan. 2022.

[25] Ç. K. Atay, Ö. Dilek, T. Tilki, and B. Dede, "A novel imidazole-based azo molecule: synthesis, characterization, quantum chemical calculations, molecular docking, molecular dynamics simulations and ADMET properties," *J Mol Model*, vol. 29, no. 8, p. 226, Aug. 2023.

[26] Frisch, M. J., G. W., Trucks, H. B., Schlegel, G. E., Scuseria, M. A., Robb, J. R., Cheeseman, G., Scalmani, V., Barone, G. A., Petersson, H., Nakatsuji, X., Li, M., Caricato, A., Marenich, J., Bloino, B. G., Janesko, R., Gomperts, B., Mennucci, H. P., Hratchian, J. V., Ortiz, A. F I., D. J. F. 2016. Gaussian 09, Revision E.01. Gaussian, Inc.

[27] M. D. Hanwell, D. E. Curtis, D. C. Lonie, T. Vandermeersch, E. Zurek, and G. R. Hutchison, "Avogadro: an advanced semantic chemical editor, visualization, and analysis platform," *J Cheminform*, vol. 4, no. 1, p. 17, Aug. 2012.

[28] Chemcraft - graphical software for visualization of quantum chemistry computations. Version 1.8, build 654. https://www.chemcraftprog.com [Accessed: July. 25, 2023].

[29] A. D. Becke, "Density-functional exchange-energy approximation with correct asymptotic behavior," *Phys Rev* A (Coll Park), vol. 38, no. 6, pp. 3098–3100, Sep. 1988.

[30] C. Lee, W. Yang, and R. G. Parr, "Development of the Colle-Salvetti correlation-energy formula into a functional of the electron density," *Phys Rev B*, vol. 37, no. 2, pp. 785–789, Jan. 1988.

[31] J. P. Merrick, D. Moran, and L. Radom, "An Evaluation of Harmonic Vibrational Frequency Scale Factors," *J Phys Chem A*, vol. 111, no. 45, pp. 11683–11700, Oct. 2007.

[32] R. Bauernschmitt and R. Ahlrichs, "Treatment of electronic excitations within the adiabatic approximation of time dependent density functional theory," *Chem Phys Lett*, vol. 256, no. 4–5, pp. 454–464, Jul. 1996.

[33] M. E. Casida, C. Jamorski, K. C. Casida, and D. R. Salahub, "Molecular excitation energies to high-lying bound states from time-dependent density-functional response theory: Characterization and correction of the time-dependent local density approximation ionization threshold," *J Chem Phys*, vol. 108, no. 11, pp. 4439–4449, Mar. 1998.

[34] R. Ditchfield, "Molecular Orbital Theory of Magnetic Shielding and Magnetic Susceptibility," *J Chem Phys*, vol. 56, no. 11, pp. 5688–5691, Jun. 1972.

[35] K. Wolinski, J. F. Hinton, and P. Pulay, "Efficient implementation of the gauge-independent atomic orbital method for NMR chemical shift calculations," *J Am Chem Soc*, vol. 112, no. 23, pp. 8251–8260, Nov. 1990.

[36] A. Grosdidier, V. Zoete, and O. Michielin, "SwissDock, a protein-small molecule docking web service based on EADock DSS," *Nucleic Acids Res*, vol. 39, no. suppl, pp. W270–W277, Jul. 2011.

[37] E. F. Pettersen et al., "UCSF Chimera--A visualization system for exploratory research and analysis," *J Comput Chem*, vol. 25, no. 13, pp. 1605–1612, Oct. 2004.

[38] H. M. Berman, J. Westbrook, Z. Feng, G. Gilliland, T. N. Bhat, H. Weissig, I. N. Shindyalov, P. E. Bourne, "The Protein Data Bank," *Nucleic Acids Res*, vol. 28, no. 1, pp. 235–242, Jan. 2000.

[39] J. Jiménez, S. Doerr, G. Martínez-Rosell, A. S. Rose, and G. De Fabritiis, "DeepSite: protein-binding site predictor using 3D-convolutional neural networks," *Bioinformatics*, vol. 33, no. 19, pp. 3036–3042, Oct. 2017.

[40] A. Daina, O. Michielin, and V. Zoete, "SwissADME: a free web tool to evaluate pharmacokinetics, drug-likeness and medicinal chemistry friendliness of small molecules," *Sci Rep*, vol. 7, no. 1, p. 42717, Mar. 2017.

[41] P. Banerjee, A. O. Eckert, A. K. Schrey, and R. Preissner, "ProTox-II: a webserver for the prediction of toxicity of chemicals," *Nucleic Acids Res*, vol. 46, no. W1, pp. W257–W263, Jul. 2018.

[42] B. Raimer, P. G. Jones, and T. Lindel, "Quantum chemical calculation of ^{19}F NMR chemical shifts of trifluoromethyl diazirine photoproducts and precursors," *J Fluor Chem*, vol. 166, pp. 8–14, Oct. 2014.

[43] Ç. K. Atay, Y. Kara, M. Gökalp, I. Kara, T. Tilki, and F. Karci, "Disazo dyes containing pyrazole and indole moieties: Synthesis, characterization, absorption characteristics, theoretical calculations, structural and electronic properties," *J Mol Liq*, vol. 215, pp. 647–655, Mar. 2016.

[44] M. Gökalp, T. Tilki, and Ç. K. Atay, "Newly Synthesized Aminothiazole Based Disazo Dyes and Their Theoretical Calculations," *Polycycl Aromat Compd*, pp. 1–23, Feb. 2023.

[45] B. Sezgin, T. Tilki, Ç. K. Atay, and B. Dede, "Comparative in vitro and DFT antioxidant studies of phenolic group substituted pyridine-based azo derivatives," *J Biomol Struct Dyn*, vol. 40, no. 11, pp. 4921–4932, Jul. 2022.

Bishop Frames of Salkowski Curves in E^3

Sümeyye GÜR MAZLUM[1*]

[1] *Gümüşhane University Kelkit Aydın Doğan Vocational School Department of Computer Technology, Gümüşhane, Türkiye.*
(*ORCID:* 0000-0003-2471-1627)

Abstract

In this study, alternative, type-1 Bishop, type-2 Bishop and N-Bishop frames of Salkowski curves in E^3 are calculated. Moreover, curvatures, Darboux and pol vectors of these frames are found. Also, relationships between the Bishop frames, Darboux vectors and pole vectors are given.

1. Introduction

By defining a moving frame at every point on any curve, it is possible to examine the characteristic and kinematic properties of the curve. Therefore, defining a new and useful frame on any curve is always a current and interesting field of study, especially for geometers. One of the best known of the frames defined on any curve is the Frenet frame. This frame consists of three linearly independent orthonormal vectors obtained from derivatives of the curve, [1]. Alternative frame is produced from the elements of the Frenet frame, [2]. Another well-known frame, the Bishop frame, is a relatively parallel frame obtained by rotating the Frenet frame around the T vector by an angle, [3]. This frame is known to be more advantageous than the Frenet frame, which works well even when the second derivative of the curve has vanishing. Therefore, it is a subject that not only geometry but also biology and computer graphics, [4,5]. Based on this frame, type-2 Bishop frame was introduced in [6] and N-Bishop frame was introduced in [7]. The Type-2 Bishop frame is obtained by rotating the Frenet frame of the curve around the B vector by a certain angle, while the N-Bishop frame is obtained by rotating the alternative frame of the curve around N by a certain angle. Some other studies on these frames are [8-21]. On the other hand, Salkowski curves in E^3 are slant helix type curves introduced by Salkowski, [22]. The

Frenet vectors and curvatures of these curves with constant curvature but not constant torsion were found by Monterde, [23]. The Darboux and pole vectors belonging to the Frenet frame and modified frames of Salkowski curves E^3 are studied in [24]. Other some studies on Salkowski curves in E^3 can be looked at from [25-28]. In this study, alternative, type-1, type-2 and N-Bishop frames of Salkowski curves are calculated and curvatures, Darboux and pole vectors belonging to the frames are investigated. Besides, the relations between these elements are given. The aim of this study is to define new frames on Salkowski curves. Although the Frenet frame of the Salkowski curve works smoothly, the literature richness of the curve has been increased with new frames defined on it.

2. Material and Method

Frenet frame $\{T, N, B\}$ of any non-unit speed (with an arbitrary parameter t) regular curve ψ in E^3 is

$$T = \frac{\psi'}{\|\psi'\|}, \qquad N = B \wedge T, \qquad B = \frac{\psi' \wedge \psi''}{\|\psi' \wedge \psi''\|}$$

and curvature $\aleph$ and torsion $\Im$ of ψ are

$$\aleph = \frac{\|\psi' \wedge \psi''\|}{\|\psi'\|^3}, \qquad \Im = \frac{\langle \psi', \psi'', \psi''' \rangle}{\|\psi' \wedge \psi''\|^2}$$

---
* Corresponding author: *sumeyyegur@gumushane.edu.tr*

[1]. Darboux vector and pole vector belonging to the Frenet frame of ψ are

$$\begin{cases} \mathcal{F} = N \wedge N' = \|\psi'\|\left(\Im T + \aleph B\right), \\ \mathcal{C} = \dfrac{\Im}{\sqrt{\aleph^2 + \Im^2}} T + \dfrac{\aleph}{\sqrt{\aleph^2 + \Im^2}} B, \end{cases}$$

where

$$T' = \mathcal{F} \wedge T, \quad N' = \mathcal{F} \wedge N, \quad B' = \mathcal{F} \wedge B.$$

Type-1 Bishop frame $\{T, N_1, B_1\}$ of any non-unit speed regular curve ψ in E^3 is [3]

$$\begin{cases} T = \dfrac{\psi'}{\|\psi'\|}, \\ N_1 = \cos\Theta N - \sin\Theta B, \\ B_1 = T \wedge N_1 = \sin\Theta N + \cos\Theta B, \\ \Theta = \int \|\psi'\| \Im \, dt, \end{cases} \tag{1}$$

curvature $\aleph_1$ and torsion $\Im_1$ of ψ are

$$\aleph_1 = \aleph\cos\Theta, \quad \Im_1 = \aleph\sin\Theta. \tag{2}$$

The matrix representation of type-1 Bishop derivative formulas of ψ is

$$\begin{bmatrix} T' \\ N_1' \\ B_1' \end{bmatrix} = \begin{bmatrix} 0 & \|\psi'\|\aleph_1 & \|\psi'\|\Im_1 \\ -\|\psi'\|\aleph_1 & 0 & 0 \\ -\|\psi'\|\Im_1 & 0 & 0 \end{bmatrix} \begin{bmatrix} T \\ N_1 \\ B_1 \end{bmatrix}. \tag{3}$$

Darboux vector belonging to the type-1 Bishop frame of ψ is [8]

$$\mathcal{F}_1 = T \wedge T' = \|\psi'\|\left(-\Im_1 N_1 + \aleph_1 B_1\right), \tag{4}$$

where

$$T' = \mathcal{F}_1 \wedge T, \quad N_1' = \mathcal{F}_1 \wedge N_1, \quad B_1' = \mathcal{F}_1 \wedge B_1.$$

Type-2 Bishop frame $\{N_2, B_2, B\}$ of any non-unit speed regular curve ψ in E^3 is [6]

$$\begin{cases} N_2 = \sin\Phi T + \cos\Phi N, \\ B_2 = B \wedge N_2 = -\cos\Phi T + \sin\Phi N, \\ B = T \wedge N, \\ \Phi = \int \|\psi'\| \aleph \, dt, \end{cases} \tag{5}$$

curvature $\aleph_2$ and torsion $\Im_2$ of ψ are

$$\aleph_2 = -\Im\cos\Phi, \quad \Im_2 = -\Im\sin\Phi. \tag{6}$$

The matrix representation of type-2 Bishop derivative formulas of ψ is

$$\begin{bmatrix} N_2' \\ B_2' \\ B' \end{bmatrix} = \begin{bmatrix} 0 & 0 & -\|\psi'\|\aleph_2 \\ 0 & 0 & -\|\psi'\|\Im_2 \\ \|\psi'\|\aleph_2 & \|\psi'\|\Im_2 & 0 \end{bmatrix} \begin{bmatrix} N_2 \\ B_2 \\ B \end{bmatrix}. \tag{7}$$

Darboux vector belonging to the type-2 Bishop frame of ψ is [17]

$$\mathcal{F}_2 = B \wedge B' = \|\psi'\|\left(-\Im_2 N_2 + \aleph_2 B_2\right), \tag{8}$$

where

$$N_2' = \mathcal{F}_2 \wedge N_2, \quad B_2' = \mathcal{F}_2 \wedge B_2, \quad B' = \mathcal{F}_2 \wedge B.$$

Alternative frame $\{N, C, W\}$ of any non-unit speed regular curve ψ in E^3 is [2]

$$\begin{cases} N = B \wedge T, \\ C = \dfrac{N'}{\|N'\|} = -\dfrac{\aleph}{\sqrt{\aleph^2 + \Im^2}} T + \dfrac{\Im}{\sqrt{\aleph^2 + \Im^2}} B, \\ W = N \wedge C = \dfrac{\Im}{\sqrt{\aleph^2 + \Im^2}} T + \dfrac{\aleph}{\sqrt{\aleph^2 + \Im^2}} B, \end{cases} \tag{9}$$

curvature F and torsion G are

$$F = \sqrt{\aleph^2 + \Im^2}, \quad G = \dfrac{\aleph\Im' - \aleph'\Im}{F^2}. \tag{10}$$

The matrix representation of alternative derivative formulas of ψ is

$$\begin{bmatrix} N' \\ C' \\ W' \end{bmatrix} = \begin{bmatrix} 0 & \|\psi'\|F & 0 \\ -\|\psi'\|F & 0 & G \\ 0 & -G & 0 \end{bmatrix} \begin{bmatrix} N \\ C \\ W \end{bmatrix}. \tag{11}$$

Darboux vector belonging to the alternative frame of ψ is [19]

$$\overline{\mathcal{F}} = C \wedge C' = GN + \|\psi'\|FW, \tag{12}$$

where

$$N' = \overline{\mathcal{F}} \wedge N, \quad C' = \overline{\mathcal{F}} \wedge C, \quad W' = \overline{\mathcal{F}} \wedge W.$$

N-Bishop frame $\{N, N_3, B_3\}$ of any non-unit speed regular curve ψ in E^3 is [7]

$$\begin{cases} N = B \wedge T \\ N_3 = \cos\Omega C - \sin\Omega W, \\ B_3 = N \wedge N_3 = \sin\Omega C + \cos\Omega W, \\ \Omega = \int G \, dt, \end{cases} \tag{13}$$

curvature $\aleph_3$ and torsion $\Im_3$ of ψ are

$$\aleph_3 = F\cos\Omega, \quad \Im_3 = F\sin\Omega. \tag{14}$$

The matrix representation of N-Bishop derivative formulas of ψ is

$$\begin{bmatrix} N' \\ N_3' \\ B_3' \end{bmatrix} = \begin{bmatrix} 0 & \|\psi'\|\aleph_3 & \|\psi'\|\Im_3 \\ -\|\psi'\|\aleph_3 & 0 & 0 \\ -\|\psi'\|\Im_3 & 0 & 0 \end{bmatrix} \begin{bmatrix} N \\ N_3 \\ B_3 \end{bmatrix}. \tag{15}$$

Darboux vector belonging to the N-Bishop of ψ is

$$\mathcal{F}_3 = N \wedge N' = \|\psi'\|\left(-\Im_3 N_3 + \aleph_3 B_3\right), \tag{16}$$

[17], where

$$N' = \mathcal{F}_3 \wedge N, \quad N_3' = \mathcal{F}_2 \wedge N_3, \quad B_3' = \mathcal{F}_2 \wedge B_3.$$

Definition 2.1. For $m \neq \pm\dfrac{\sqrt{3}}{3}, 0 \in R$ and

$$n = \frac{m}{\sqrt{m^2 + 1}},$$

$$\psi_m = \frac{n}{4m}\left(\frac{n-1}{1+2n}\sin\left((1+2n)t\right)\right.$$

$$-\frac{1+n}{1-2n}\sin\left((1-2n)t\right) - 2\sin t,$$

$$\frac{1-n}{1+2n}\cos\left((1+2n)t\right)$$

$$\left.+\frac{1+n}{1-2n}\cos\left((1-2n)t\right) + 2\cos t, \frac{1}{m}\cos(2nt)\right)$$

is the parametric equation of Salkowski curves in E^3, Figure 1, [22]. The curves are regular in the interval of $\left]-\dfrac{\pi}{2n}, \dfrac{\pi}{2n}\right[$ and

$$\left\|\psi_m'\right\| = \frac{n}{m}\cos(nt). \tag{17}$$
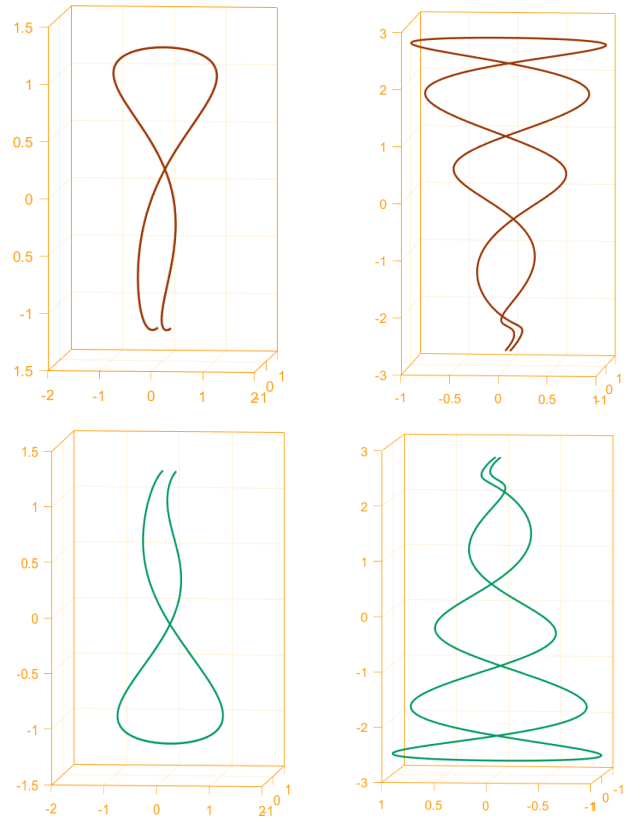

Figure 1. Salkowski curves for $m = \dfrac{1}{5}, \dfrac{1}{11}, -\dfrac{1}{5} - \dfrac{1}{11}$, respectively

Frenet frame $\{T, N, B\}$ of ψ_m is [23]

$$\begin{cases} T = \left(-\cos t\cos(nt) - n\sin t\sin(nt),\right. \\ \quad -\sin t\cos(nt) + n\cos t\sin(nt), \\ \quad \left.-\dfrac{n}{m}\sin(nt)\right), \\ N = \left(\dfrac{n}{m}\sin t, -\dfrac{n}{m}\cos t, -n\right), \\ B = \left(-\cos t\sin(nt) + n\sin t\cos(nt),\right. \\ \quad -\sin t\sin(nt) - n\cos t\cos(nt), \\ \quad \left.\dfrac{n}{m}\cos(nt)\right), \end{cases} \tag{18}$$

curvature $\aleph$ and torsion $\Im$ of ψ_m are [23, 24]

$$\aleph = 1, \quad \Im = -\tan(nt). \tag{19}$$

Darboux vector $\mathcal{F}$ and pole vector $\mathcal{C}$ (or unit vector in the direction of Darboux vector) belonging to the Frenet frame of ψ_m are [24]

$$\begin{cases} \mathcal{F} = \left(\dfrac{n^2}{m}\sin t, -\dfrac{n^2}{m}\cos t, \dfrac{n^2}{m^2} \right), \\[2mm] \mathcal{C} = \left(n\sin t, -n\cos t, \dfrac{n}{m} \right). \end{cases} \qquad (20)$$

3. Bishop Frames of Salkowski Curves in E^3

In this section, type-1 Bishop, type-2 Bishop, alternative and N-Bishop frames of Salkowski curves ψ_m in E^3 will be examined, respectively. Besides, Darboux and pole vectors belonging to these frames of ψ_m will be computed.

3.1. Type-1 Bishop Frame of Salkowski Curves in E^3

Theorem 3.1. For $m \neq \pm\dfrac{\sqrt{3}}{3}, 0 \in R$ and $n = \dfrac{m}{\sqrt{m^2+1}}$, type-1 Bishop frame $\{T, N_1, B_1\}$ of ψ_m obtained by rotating Frenet frame of ψ_m around T by an angle Θ is as follows:

$$\begin{cases} T = \Big(-\cos t\cos(nt) - n\sin t\sin(nt), \\ \qquad -\sin t\cos(nt) + n\cos t\sin(nt), \\ \qquad -\dfrac{n}{m}\sin(nt) \Big), \\[2mm] N_1 = \Big(\dfrac{n}{m}\cos\Theta\sin t + \sin\Theta\cos t\sin(nt) \\ \qquad -n\sin\Theta\sin t\cos(nt), \\ \qquad -\dfrac{n}{m}\cos\Theta\cos t + \sin\Theta\sin t\sin(nt) \\ \qquad +n\sin\Theta\cos t\cos(nt), \\ \qquad -n\cos\Theta - \dfrac{n}{m}\sin\Theta\cos(nt) \Big), \\[2mm] B_1 = \Big(\dfrac{n}{m}\sin\Theta\sin t - \cos\Theta\cos t\sin(nt) \\ \qquad +n\cos\Theta\sin t\cos(nt), \\ \qquad -\dfrac{n}{m}\sin\Theta\cos t - \cos\Theta\sin t\sin(nt) \\ \qquad -n\cos\Theta\cos t\cos(nt), \\ \qquad -n\sin\Theta + \dfrac{n}{m}\cos\Theta\cos(nt) \Big). \end{cases} \qquad (21)$$

Proof: The proof is obvious that from (1) and (18).

Corollary 3.1. For $m \neq \pm\dfrac{\sqrt{3}}{3}, 0 \in R$ and $n = \dfrac{m}{\sqrt{m^2+1}}$, type-1 Bishop frame of ψ_m is obtained by rotating Frenet frame of ψ_m around T by an angle Θ:

$$\Theta = \dfrac{1}{m}\cos(nt) + c_1, \qquad c_1 \in R. \qquad (22)$$

Proof: From (1), (17) and (19),

$$\Theta = \int \|\psi_m'\| \, \mathfrak{I} \, dt = -\dfrac{n}{m}\int \sin(nt)dt$$
$$= \dfrac{1}{m}\cos(nt) + c_1, \qquad c_1 \in R$$

is obtained.

Corollary 3.2. For $m \neq \pm\dfrac{\sqrt{3}}{3}, 0 \in R$ and $n = \dfrac{m}{\sqrt{m^2+1}}$, there is the following matrix relation between of type-1 Bishop frame $\{T, N_1, B_1\}$ and Frenet frame $\{T, N, B\}$ of ψ_m:

$$\begin{bmatrix} T \\ N_1 \\ B_1 \end{bmatrix} = \begin{bmatrix} 1 & 0 & 0 \\ 0 & \cos\left(\dfrac{1}{m}\cos(nt)+c_1\right) & -\sin\left(\dfrac{1}{m}\cos(nt)+c_1\right) \\ 0 & \sin\left(\dfrac{1}{m}\cos(nt)+c_1\right) & \cos\left(\dfrac{1}{m}\cos(nt)+c_1\right) \end{bmatrix} \begin{bmatrix} T \\ N \\ B \end{bmatrix}.$$

Proof: The proof is obvious that from (1) and (22).

Theorem 3.2. For $m \neq \pm\dfrac{\sqrt{3}}{3}, 0 \in R$ and $n = \dfrac{m}{\sqrt{m^2+1}}$, curvature $\aleph_1$ and torsion $\mathfrak{I}_1$ of type-1 Bishop frame $\{T, N_1, B_1\}$ of ψ_m obtained by rotating Frenet frame of ψ_m around T by an angle Θ are as follows:

$$\begin{cases} \aleph_1 = \cos\Theta = \cos\left(\dfrac{1}{m}\cos(nt)+c_1\right), \\[2mm] \mathfrak{I}_1 = \sin\Theta = \sin\left(\dfrac{1}{m}\cos(nt)+c_1\right). \end{cases} \qquad (23)$$

Proof: The proof is obvious that from (2), (19) and (22).

Corollary 3.3. For $m \neq \pm \dfrac{\sqrt{3}}{3}, 0 \in R$ and $n = \dfrac{m}{\sqrt{m^2+1}}$, derivative vectors of Bishop frame $\{T, N_1, B_1\}$ of ψ_m are as follows:

$$
\left\{
\begin{aligned}
T' ={}& \frac{n^2}{m^2}\cos(nt)(\sin t, -\cos t, -m), \\
N_1' ={}& \left(\frac{n}{m}\cos\Theta\cos t\cos^2(nt) \right. \\
& + \frac{n^2}{m}\cos\Theta\sin t\cos(nt)\sin(nt), \\
& \frac{n}{m}\cos\Theta\sin t\cos^2(nt) \\
& - \frac{n^2}{m}\cos\Theta\cos t\cos(nt)\sin(nt), \\
& \left. \frac{n^2}{m^2}\cos\Theta\cos(nt)\sin(nt) \right), \\
B_1' ={}& \left(\frac{n}{m}\sin\Theta\cos t\cos^2(nt) \right. \\
& + \frac{n^2}{m}\sin\Theta\sin t\cos(nt)\sin(nt), \\
& \frac{n}{m}\sin\Theta\sin t\cos^2(nt) \\
& - \frac{n^2}{m}\sin\Theta\cos t\cos(nt)\sin(nt), \\
& \left. \frac{n^2}{m^2}\sin\Theta\cos(nt)\sin(nt) \right).
\end{aligned}
\right. \tag{24}
$$

Proof: From (3), (17), (21) and (23), the vectors

$$ N_1' = -\left\| \psi_m' \right\| \aleph_1 T, $$

$$ B_1' = -\left\| \psi_m' \right\| \Im_1 T, $$

$$ T' = \left\| \psi_m' \right\| \aleph_1 N_1 + \left\| \psi_m' \right\| \Im_1 B_1 $$

are obtained as in (24). These vectors can be obtained in the same way by taking the derivatives of the vectors in (22).

Theorem 3.3. For $m \neq \pm \dfrac{\sqrt{3}}{3}, 0 \in R$ and $n = \dfrac{m}{\sqrt{m^2+1}}$, the matrix representation of type-1 Bishop derivative formulas of ψ_m:

$$
\begin{bmatrix} T' \\ N_1' \\ B_1' \end{bmatrix} = \frac{n}{m}\cos(nt)
\begin{bmatrix} 0 & \cos\Theta & \sin\Theta \\ -\cos\Theta & 0 & 0 \\ -\sin\Theta & 0 & 0 \end{bmatrix}
\begin{bmatrix} T \\ N_1 \\ B_1 \end{bmatrix}.
$$

Proof: The proof is obvious that from (3), (17) and (23). Also, it is also obtained by comparing expressions (21) and (24).

Theorem 3.4. For $m \neq \pm \dfrac{\sqrt{3}}{3}, 0 \in R$ and $n = \dfrac{m}{\sqrt{m^2+1}}$, Darboux vector $\mathcal{F}_1$ belonging to the type-1 Bishop frame of ψ_m is as follows:

$$
\begin{aligned}
\mathcal{F}_1 ={}& \left(-\frac{n}{m}\cos t\cos(nt)\sin(nt) + \frac{n^2}{m}\sin t\cos^2(nt), \right. \\
& -\frac{n}{m}\sin t\cos(nt)\sin(nt) - \frac{n^2}{m}\cos t\cos^2(nt) \\
& \left. \frac{n^2}{m^2}\cos^2(nt) \right).
\end{aligned} \tag{25}
$$

Proof: If (17), (21) and (23) are substituted in (4), (25) is obtained.

Theorem 3.5. For $m \neq \pm \dfrac{\sqrt{3}}{3}, 0 \in R$ and $n = \dfrac{m}{\sqrt{m^2+1}}$, pole vector $\mathcal{C}_1$ belonging to the type-1 Bishop frame of ψ_m is as follows:

$$
\begin{aligned}
\mathcal{C}_1 ={}& \left(-\cos t\sin(nt) + n\sin t\cos(nt), \right. \\
& -\sin t\sin(nt) - n\cos t\cos(nt), \\
& \left. \frac{n}{m}\cos(nt) \right).
\end{aligned} \tag{26}
$$

Proof: From (4) and (23), pole vector (unit vector in the direction of Darboux vector) belonging to the type-1 Bishop frame of ψ_m is

$$
\begin{aligned}
\mathcal{C}_1 &= \frac{\mathcal{F}_1}{\|\mathcal{F}_1\|} = -\frac{\Im_1}{\sqrt{\aleph_1^2 + \Im_1^2}}N_1 + \frac{\aleph_1}{\sqrt{\aleph_1^2 + \Im_1^2}}B_1 \\
&= -\Im_1 N_1 + \aleph_1 B_1 \\
&= -\sin\Theta N_1 + \cos\Theta B_1,
\end{aligned}
$$

Figure 2. Here, it is obvious that from (21). Also, it is also obtained by dividing the vector $\mathcal{F}_1$ by its norm

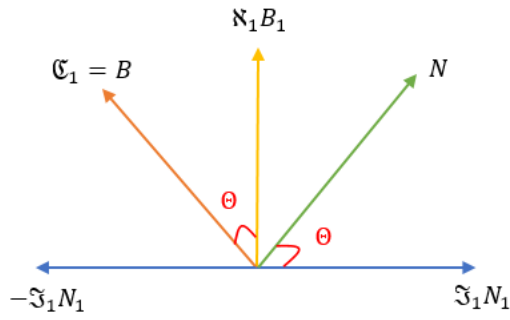$$ \|\mathcal{F}_1\| = \frac{n}{m}\cos(nt). $$

Figure 2. Pole vector $\mathfrak{C}_1$ belonging to the type-1 Bishop frame of ψ_m

Corollary 3.4. Binormal vector B and pole vector $\mathfrak{C}_1$ belonging to the type-1 Bishop frame of ψ_m are the same.

Proof: The proof is obvious that from (18) and (27).

3.2. Type-2 Bishop Frame of Salkowski Curves in E^3

Theorem 3.6. For $m \neq \pm\frac{\sqrt{3}}{3}, 0 \in R$ and $n = \frac{m}{\sqrt{m^2+1}}$, type-2 Bishop frame $\{N_2, B_2, B\}$ of ψ_m obtained by rotating Frenet frame around B by an angle Φ is as follows:

$$
\begin{cases}
N_2 = \Big(-\sin\Phi\cos t\cos(nt) \\
\quad -n\sin\Phi\sin t\sin(nt) + \frac{n}{m}\cos\Phi\sin t, \\
\quad -\sin\Phi\sin t\cos(nt) \\
\quad +n\sin\Phi\cos t\sin(nt) - \frac{n}{m}\cos\Phi\cos t, \\
\quad -\frac{n}{m}\sin\Phi\sin(nt) - n\cos\Phi\Big) \\
B_2 = \Big(\cos\Phi\cos t\cos(nt) \\
\quad +n\cos\Phi\sin t\sin(nt) + \frac{n}{m}\sin\Phi\sin t, \\
\quad \cos\Phi\sin t\cos(nt) \\
\quad -n\cos\Phi\cos t\sin(nt) - \frac{n}{m}\sin\Phi\cos t, \\
\quad \frac{n}{m}\cos\Phi\sin(nt) - n\sin\Phi\Big), \\
B = \Big(-\cos t\sin(nt) + n\sin t\cos(nt) \\
\quad -\sin t\sin(nt) - n\cos t\cos(nt), \frac{n}{m}\cos(nt)\Big).
\end{cases}
\tag{27}
$$

Proof: The proof is obvious that from (5) and (18).

Corollary 3.5. For $m \neq \pm\frac{\sqrt{3}}{3}, 0 \in R$ and $n = \frac{m}{\sqrt{m^2+1}}$, type-2 Bishop frame of ψ_m is obtained by rotating Frenet frame around B by an angle Φ:

$$
\Phi = \frac{1}{m}\sin(nt) + c_2, \quad c_2 \in R. \tag{28}
$$

Proof: From (5), (17) and (30),

$$
\begin{aligned}
\Phi &= \int \|\psi_m{}'\| \aleph \, dt = \int \frac{n}{m}\cos(nt)\,dt \\
&= \frac{1}{m}\sin(nt) + c_2, \quad c_2 \in R
\end{aligned}
$$

is obtained.

Corollary 3.6. For $m \neq \pm\frac{\sqrt{3}}{3}, 0 \in R$ and $n = \frac{m}{\sqrt{m^2+1}}$, there is the following matrix relation between of type-2 Bishop frame $\{N_2, B_2, B\}$ and Frenet frame $\{T, N, B\}$ of ψ_m:

$$
\begin{bmatrix} N_2 \\ B_2 \\ B \end{bmatrix} = \begin{bmatrix} \sin\left(\frac{1}{m}\sin(nt)+c_2\right) & \cos\left(\frac{1}{m}\sin(nt)+c_2\right) & 0 \\ -\cos\left(\frac{1}{m}\sin(nt)+c_2\right) & \sin\left(\frac{1}{m}\sin(nt)+c_2\right) & 0 \\ 0 & 0 & 1 \end{bmatrix} \begin{bmatrix} T \\ N \\ B \end{bmatrix}.
$$

Proof: The proof is obvious that from (5) and (28).

Theorem 3.7. For $m \neq \pm\frac{\sqrt{3}}{3}, 0 \in R$ and $n = \frac{m}{\sqrt{m^2+1}}$, curvature $\aleph_2$ and torsion $\mathfrak{I}_2$ of type-2 Bishop frame $\{N_2, B_2, B\}$ of ψ_m obtained by rotating Frenet frame around B by an angle Φ are as follows:

$$
\begin{cases}
\aleph_2 = \tan(nt)\cos\Phi = \tan(nt)\cos\left(\frac{1}{m}\sin(nt)+c_2\right), \\
\mathfrak{I}_2 = \tan(nt)\sin\Phi = \tan(nt)\sin\left(\frac{1}{m}\sin(nt)+c_2\right).
\end{cases}
\tag{29}
$$

Proof: The proof is obvious that from (6), (19) and (28).

Corollary 3.7. For $m \neq \pm \dfrac{\sqrt{3}}{3}, 0 \in R$ and $n = \dfrac{m}{\sqrt{m^2+1}}$, the derivative vectors of type-2 Bishop frame $\{N_2, B_2, B\}$ of ψ_m are as follows:

$$
\begin{cases}
N_2' = \left(\dfrac{n}{m} \cos\Phi \cos t \sin^2(nt) \right. \\
\qquad - \dfrac{n^2}{m} \cos\Phi \sin t \cos(nt) \sin(nt) \\
\qquad \dfrac{n}{m} \cos\Phi \sin t \sin^2(nt) \\
\qquad + \dfrac{n^2}{m} \cos\Phi \cos t \cos(nt) \sin(nt), \\
\qquad \left. - \dfrac{n^2}{m^2} \cos\Phi \cos(nt) \sin(nt) \right), \\
B_2' = \left(\dfrac{n}{m} \sin\Phi \cos t \sin^2(nt) \right. \\
\qquad - \dfrac{n^2}{m} \sin\Phi \sin t \cos(nt) \sin(nt), \\
\qquad \dfrac{n}{m} \sin\Phi \sin t \sin^2(nt) \\
\qquad + \dfrac{n^2}{m} \sin\Phi \cos t \cos(nt) \sin(nt), \\
\qquad \left. - \dfrac{n^2}{m^2} \sin\Phi \cos(nt) \sin(nt) \right), \qquad (30) \\
B' = \dfrac{n^2}{m^2} \sin(nt)(\sin t, -\cos t, -m).
\end{cases}
$$

Proof: From (7), (17), (27) and (29), the vectors

$$N_2' = -\left\| \psi_m' \right\| \aleph_2 B,$$

$$B_2' = -\left\| \psi_m' \right\| \Im_2 B,$$

$$B' = \left\| \psi_m' \right\| \aleph_2 N_2 + \left\| \psi_m' \right\| \Im_2 B_2$$

are obtained as in (30). These vectors can be obtained in the same way by taking the derivatives of the vectors in (27).

Theorem 3.8. For $m \neq \pm \dfrac{\sqrt{3}}{3}, 0 \in R$ and $n = \dfrac{m}{\sqrt{m^2+1}}$, the matrix representation of type-2 Bishop derivative formulas of ψ_m:

$$
\begin{bmatrix} N_2' \\ B_2' \\ B' \end{bmatrix} = \dfrac{n}{m} \sin(nt) \begin{bmatrix} 0 & 0 & -\cos\Phi \\ 0 & 0 & -\sin\Phi \\ \cos\Phi & \sin\Phi & 0 \end{bmatrix} \begin{bmatrix} N_2 \\ B_2 \\ B \end{bmatrix}.
$$

Proof: The proof is obvious that from (7), (17) and (29). Also, it is also obtained by comparing expressions (27) and (30).

Theorem 3.9. For $m \neq \pm \dfrac{\sqrt{3}}{3}, 0 \in R$ and $n = \dfrac{m}{\sqrt{m^2+1}}$, Darboux vector $\mathcal{F}_2$ belonging to the type-2 Bishop frame of ψ_m is as follows:

$$
\begin{aligned}
\mathcal{F}_2 = &\left(\dfrac{n}{m} \cos t \cos(nt) \sin(nt) + \dfrac{n^2}{m} \sin t \sin^2(nt), \right. \\
&\dfrac{n}{m} \sin t \cos(nt) \sin(nt) - \dfrac{n^2}{m} \cos t \sin^2(nt), \quad (31) \\
&\left. \dfrac{n^2}{m^2} \sin^2(nt) \right)
\end{aligned}
$$

Proof: If (17), (21) and (23) are substituted in (4), (31) is obtained.

Theorem 3.10. For $m \neq \pm \dfrac{\sqrt{3}}{3}, 0 \in R$ and $n = \dfrac{m}{\sqrt{m^2+1}}$, pole vector $\mathcal{C}_2$ belonging to the type-2 Bishop frame of ψ_m is as follows:

$$
\begin{aligned}
\mathcal{C}_2 = &\left(\cos t \cos(nt) + n \sin t \sin(nt), \right. \\
&\sin t \cos(nt) - n \cos t \sin(nt), \quad (32) \\
&\left. \dfrac{n}{m} \sin(nt) \right).
\end{aligned}
$$

Proof: From (8) and (29), pole vector belonging to the type-2 Bishop frame of ψ_m is

$$
\begin{aligned}
\mathcal{C}_2 = \dfrac{\mathcal{F}_2}{\|\mathcal{F}_2\|} &= -\dfrac{\Im_2}{\sqrt{\aleph_2^2 + \Im_2^2}} N_2 + \dfrac{\aleph_2}{\sqrt{\aleph_2^2 + \Im_2^2}} B_2 \\
&= -\dfrac{\Im_2}{\tan(nt)} N_2 + \dfrac{\aleph_2}{\tan(nt)} B_2 \\
&= \sin\Phi N_2 - \cos\Phi B_2,
\end{aligned}
$$

Figure 3. Here, from (27), it is done. Also, it is also obtained by dividing the vector $\mathcal{F}_2$ by its norm

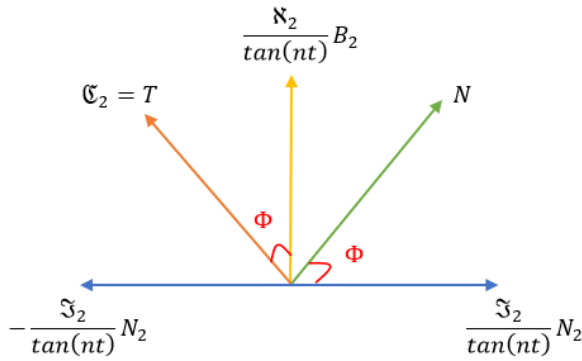$$\|\mathcal{F}_2\| = \dfrac{n}{m} \sin(nt).$$

Figure 3. Pole vector $\mathfrak{C}_2$ belonging to the type-2 Bishop frame of ψ_m

Corollary 3.8. Tangent vector T and pole vector $\mathfrak{C}_2$ belonging to the type-2 Bishop frame of ψ_m are the same.

Proof: From (18) and (34), it is clear.

3.3. Alternative Frame of Salkowski Curves in E^3

Theorem 3.11. For $m \neq \pm\dfrac{\sqrt{3}}{3}, 0 \in R$ and $n = \dfrac{m}{\sqrt{m^2+1}}$, alternative frame $\{N,C,W\}$ of ψ_m is as follows:

$$\begin{cases} N = \left(\dfrac{n}{m}\sin t, -\dfrac{n}{m}\cos t, -n\right), \\ C = (\cos t, \sin t, 0), \\ W = \left(n\sin t, -n\cos t, \dfrac{n}{m}\right). \end{cases} \tag{33}$$

Proof: The proof is obvious that from (9), (18) and (19).

Corollary 3.9. For $m \neq \pm\dfrac{\sqrt{3}}{3}, 0 \in R$ and $n = \dfrac{m}{\sqrt{m^2+1}}$, there is the following matrix relation between of alternative frame $\{N,C,W\}$ and Frenet frame $\{T,N,B\}$ of ψ_m:

$$\begin{bmatrix} N \\ C \\ W \end{bmatrix} = \begin{bmatrix} 0 & 1 & 0 \\ -\cos(nt) & 0 & -\sin(nt) \\ -\sin(nt) & 0 & \cos(nt) \end{bmatrix} \begin{bmatrix} T \\ N \\ B \end{bmatrix}. \tag{34}$$

Proof: The proof is obvious that from (9) and (19).

Theorem 3.12. For $m \neq \pm\dfrac{\sqrt{3}}{3}, 0 \in R$ and $n = \dfrac{m}{\sqrt{m^2+1}}$, curvature and torsion of alternative frame $\{N,C,W\}$ of ψ_m are as follows:

$$\begin{cases} F = \dfrac{1}{\cos(nt)}, \\ G = -n. \end{cases} \tag{35}$$

Proof: The proof is obvious that from (10) and (31). Here, from Definition 2.1, it is seen that $\cos(nt) > 0$.

Corollary 3.10. For $m \neq \pm\dfrac{\sqrt{3}}{3}, 0 \in R$ and $n = \dfrac{m}{\sqrt{m^2+1}}$, the derivative vectors of alternative frame $\{N,C,W\}$ of ψ_m are as follows:

$$\begin{cases} N' = \left(\dfrac{n}{m}\cos t, \dfrac{n}{m}\sin t, 0\right), \\ C' = (-\sin t, \cos t, 0), \\ W' = (n\cos t, n\sin t, 0). \end{cases} \tag{36}$$

Proof: From (11), (17), (33) and (35), the vectors

$$N' = \|\psi_m'\| FC,$$
$$W' = -GC,$$
$$C' = GW - \|\psi_m'\| FN$$

are obtained as in (36). These vectors can be obtained in the same way by taking the derivatives of the vectors in (33).

Theorem 3.13. For $m \neq \pm\dfrac{\sqrt{3}}{3}, 0 \in R$ and $n = \dfrac{m}{\sqrt{m^2+1}}$, the matrix representation of alternative derivative formulas of ψ_m is as follows:

$$\begin{bmatrix} N' \\ C' \\ W' \end{bmatrix} = \begin{bmatrix} 0 & \dfrac{n}{m} & 0 \\ -\dfrac{n}{m} & 0 & n \\ 0 & -n & 0 \end{bmatrix} \begin{bmatrix} N \\ C \\ W \end{bmatrix}.$$

Proof: From (11), (17) and (35), it is obtained. Also, it is also obtained by comparing expressions (33) and (36).

Theorem 3.14. For $m \neq \pm \dfrac{\sqrt{3}}{3}, 0 \in R$ and $n = \dfrac{m}{\sqrt{m^2 + 1}}$, Darboux vector $\overline{\mathcal{F}}$ belonging to the alternative frame of ψ_m is as follows:

$$\overline{\mathcal{F}} = (0,0,1). \tag{37}$$

Proof: If (17), (33) and (35) are substituted in (12), (37) is obtained.

Theorem 3.15. For $m \neq \pm \dfrac{\sqrt{3}}{3}, 0 \in R$ and $n = \dfrac{m}{\sqrt{m^2 + 1}}$, pole vector $\overline{\mathcal{C}}$ belonging to the alternative frame of ψ_m is as follows:

$$\overline{\mathcal{C}} = (0,0,1).$$

Proof: From (12), (17) and (35), pole vector belonging to the alternative frame of ψ_m is

$$\overline{\mathcal{C}} = \frac{\overline{\mathcal{F}}}{\left\|\overline{\mathcal{F}}\right\|} = \frac{G}{\sqrt{G^2 + \left\|\psi_m'\right\|^2 F^2}} N + \frac{\left\|\psi_m'\right\| F}{\sqrt{G^2 + \left\|\psi_m'\right\|^2 F^2}} W$$

$$= GN + \left\|\psi_m'\right\| FW$$

$$= -nN + \frac{n}{m} W,$$

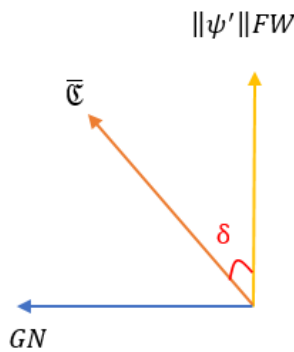Figure 4. Here, it is obvious that from (33). Also, it is also obtained by dividing the vector $\overline{\mathcal{F}}$ by its norm $\left\|\overline{\mathcal{F}}\right\| = 1$.

Figure 4. Pole vector $\overline{\mathcal{C}}$ belonging to the alternative frame of ψ_m

Corollary 3.11. For $m \neq \pm \dfrac{\sqrt{3}}{3}, 0 \in R$ and $n = \dfrac{m}{\sqrt{m^2 + 1}}$, the angle between of the vectors W and $\overline{\mathcal{C}}$ belonging to the alternative frame of ψ_m is $\delta = arc \tan(m)$.

Proof: From Figure 4, (17) and (35), $\tan \delta = m$. So, the proof is completed.

3.4. N-Bishop Frame of Salkowski Curves in E^3

Theorem 3.16. For $m \neq \pm \dfrac{\sqrt{3}}{3}, 0 \in R$ and $n = \dfrac{m}{\sqrt{m^2 + 1}}$, N-Bishop frame $\{N, N_3, B_3\}$ of ψ_m obtained by rotating alternative frame around N by an angle Ω is as follows:

$$\begin{cases} N = \left(\dfrac{n}{m} \sin t, -\dfrac{n}{m} \cos t, -n \right), \\ N_3 = \big(\cos \Omega \cos t - n \sin \Omega \sin t, \\ \qquad \cos \Omega \sin t + n \sin \Omega \cos t, -\dfrac{n}{m} \sin \Omega \big), \\ B_3 = \big(\cos \Omega \cos t - n \sin \Omega \sin t, \\ \qquad \cos \Omega \sin t + n \sin \Omega \cos t, -\dfrac{n}{m} \sin \Omega \big). \end{cases} \tag{38}$$

Proof: The proof is obvious that from (13) and (18).

Corollary 3.12. For $m \neq \pm \dfrac{\sqrt{3}}{3}, 0 \in R$ and $n = \dfrac{m}{\sqrt{m^2 + 1}}$, N-Bishop frame of ψ_m is obtained by rotating alternative frame around N by an angle Ω:

$$\Omega = -nt + c_3, \quad c_3 \in R. \tag{39}$$

Proof: From (13) and (35),

$$\Omega = \int G \, dt = -\int n \, dt = -nt + c_3, \quad c_3 \in R$$

is obtained.

Corollary 3.13. For $m \neq \pm \dfrac{\sqrt{3}}{3}, 0 \in R$ and $n = \dfrac{m}{\sqrt{m^2 + 1}}$, there is the following matrix relation

between of N-Bishop frame $\{N, N_3, B_3\}$ and alternative frame $\{N, C, B\}$ of ψ_m:

$$\begin{bmatrix} N \\ N_3 \\ B_3 \end{bmatrix} = \begin{bmatrix} 1 & 0 & 0 \\ 0 & \cos(-nt+c_3) & -\sin(-nt+c_3) \\ 0 & \sin(-nt+c_3) & \cos(-nt+c_3) \end{bmatrix} \begin{bmatrix} N \\ C \\ W \end{bmatrix}.$$

(40)

Proof: The proof is obvious that from (13) and (38).

Theorem 3.17. For $m \neq \pm\dfrac{\sqrt{3}}{3}, 0 \in R$ and $n = \dfrac{m}{\sqrt{m^2+1}}$, curvature $\aleph_3$ and torsion $\Im_3$ of N-Bishop frame $\{N, N_3, B_3\}$ of ψ_m obtained by rotating alternative frame around N by an angle Ω are as follows:

$$\begin{cases} \aleph_3 = \dfrac{\cos\Omega}{\cos(nt)} = \dfrac{\cos(-nt+c_3)}{\cos(nt)}, \\ \Im_3 = \dfrac{\sin\Omega}{\cos(nt)} = \dfrac{\sin(-nt+c_3)}{\cos(nt)}. \end{cases}$$

(41)

Proof: The proof is obvious that from (14) and (35).

Corollary 3.14. For $m \neq \pm\dfrac{\sqrt{3}}{3}, 0 \in R$ and $n = \dfrac{m}{\sqrt{m^2+1}}$, the derivative vectors of N-Bishop frame $\{N, N_3, B_3\}$ of ψ_m are as follows:

$$\begin{cases} N' = \left(\dfrac{n}{m}\cos t, \dfrac{n}{m}\sin t, 0\right), \\ N_3' = \dfrac{n^2}{m^2}\cos\Omega(-\sin t, \cos t, -m), \\ B_3' = \dfrac{n^2}{m^2}\sin\Omega(-\sin t, \cos t, m). \end{cases}$$

(42)

Proof: From (15), (17), (38) and (41), the vectors

$$N_3' = -\left\|\psi_m'\right\|\aleph_3 N,$$

$$B_3' = -\left\|\psi_m'\right\|\Im_3 N,$$

$$N' = \left\|\psi_m'\right\|\aleph_3 N_3 + \left\|\psi_m'\right\|\Im_3 B_3$$

are obtained as in (42). These vectors can be obtained in the same way by taking the derivatives of the vectors in (38).

Theorem 3.18. For $m \neq \pm\dfrac{\sqrt{3}}{3}, 0 \in R$ and $n = \dfrac{m}{\sqrt{m^2+1}}$, the matrix representation of N-Bishop derivative formulas of ψ_m:

$$\begin{bmatrix} N' \\ N_3' \\ B_3' \end{bmatrix} = \dfrac{n}{m}\begin{bmatrix} 0 & \cos\Omega & \sin\Omega \\ -\cos\Omega & 0 & 0 \\ -\sin\Omega & 0 & 0 \end{bmatrix}\begin{bmatrix} N \\ N_3 \\ B_3 \end{bmatrix}.$$

Proof: The proof is obvious that from (15), (17) and (41). Also, it is also obtained by comparing expressions (38) and (41).

Theorem 3.19. For $m \neq \pm\dfrac{\sqrt{3}}{3}, 0 \in R$ and $n = \dfrac{m}{\sqrt{m^2+1}}$, Darboux vector $\mathcal{F}_3$ belonging to the N-Bishop frame of ψ_m is as follows:

$$\mathcal{F}_3 = \left(\dfrac{n^2}{m}\sin t, -\dfrac{n^2}{m}\cos t, \dfrac{n^2}{m^2}\right).$$

(43)

Proof: If (17), (38) and (41) are substituted in (16), (43) is obtained.

Theorem 3.20. For $m \neq \pm\dfrac{\sqrt{3}}{3}, 0 \in R$ and $n = \dfrac{m}{\sqrt{m^2+1}}$, pole vector $\mathcal{C}_3$ belonging to the N-Bishop frame of ψ_m is as follows:

$$\mathcal{C}_3 = \left(n\sin t, -n\cos t, \dfrac{n}{m}\right).$$

(44)

Proof: From (16) and (41), pole vector belonging to the N-Bishop frame of ψ_m is

$$\mathcal{C}_3 = \dfrac{\mathcal{F}_3}{\|\mathcal{F}_3\|} = -\dfrac{\Im_3}{\sqrt{\aleph_3^2 + \Im_3^2}}N_3 + \dfrac{\aleph_3}{\sqrt{\aleph_3^2 + \Im_3^2}}B_3$$

$$= -\cos(nt)\Im_3 N_3 + \sin(nt)\aleph_3 B_3$$

$$= -\sin\Omega N_3 + \cos\Omega B_3$$

Figure 5. Here, from (38), it is done.

Also, it is also obtained by dividing the vector $\mathcal{F}_3$ by
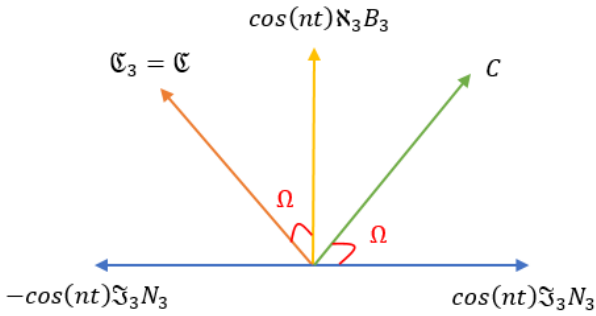
its norm $\|\mathcal{F}_3\| = \dfrac{n}{m}$.

Figure 5. Pole vector $\mathcal{C}_3$ belonging to the type-2 Bishop frame of ψ_m

Corollary 3.15. Pole vector $\mathcal{C}$ and pole vector $\mathcal{C}_3$ belonging to the type-2 Bishop frame of ψ_m are the same.

Proof: From (20) and (44), it is clear.

Corollary 3.16. For $m \neq \pm\dfrac{\sqrt{3}}{3}, 0 \in R$ and

$n = \dfrac{m}{\sqrt{m^2 + 1}}$, there is the following matrix relation

between of N-Bishop frame $\{N, N_3, B_3\}$ and Frenet frame $\{T, N, B\}$ of ψ_m:

$$\begin{bmatrix} N \\ N_3 \\ B_3 \end{bmatrix} = \begin{bmatrix} 0 & 1 & 0 \\ -A(t) & 0 & B(t) \\ B(t) & 0 & A(t) \end{bmatrix} \begin{bmatrix} T \\ N \\ B \end{bmatrix},$$

here,

$A(t) = \cos\Omega\cos(nt) - \sin\Omega\sin(nt),$

$B(t) = -\sin\Omega\cos(nt) - \cos\Omega\sin(nt).$

Proof: The proof is obvious that from (18), (34) and (40).

4. Conclusion and Suggestions

i. The relationship between type-1 Bishop frame $\{T, N_1, B_1\}$ and type-2 Bishop frame $\{N_2, B_2, B\}$ of ψ_m is as follows:

$$\begin{cases} N_2 = \sin\Phi T + \cos\Phi\cos\Theta N_1 + \cos\Phi\sin\Theta B_1, \\ B_2 = -\cos\Phi T + \sin\Phi\cos\Theta N_1 + \sin\Phi\sin\Theta B_1, \\ B = -\sin\Theta N_1 + \cos\Theta B_1. \end{cases}$$

ii. The relationship between type-1 Bishop frame $\{T, N_1, B_1\}$ and N-Bishop frame $\{N, N_3, B_3\}$ of ψ_m is as follows:

$$\begin{cases} N = \cos\Theta N_1 + \sin\Theta B_1, \\ N_3 = \left(-\cos\Omega\cos(nt) + \sin\Omega\sin(nt)\right)T \\ \quad + \left(\sin\Omega\sin\Theta\cos(nt) + \cos\Omega\sin\Theta\sin(nt)\right)N_1 \\ \quad - \left(\sin\Omega\cos\Theta\cos(nt) - \cos\Omega\cos\Theta\sin(nt)\right)B_1, \\ B_3 = -\left(\sin\Omega\cos(nt) + \cos\Omega\sin(nt)\right)T \\ \quad - \left(\cos\Omega\sin\Theta\cos(nt) + \sin\Omega\sin\Theta\sin(nt)\right)N_1 \\ \quad - \left(\sin\Omega\cos\Theta\cos(nt) - \cos\Omega\cos\Theta\sin(nt)\right)B_1. \end{cases}$$

iii. The relationship between type-1 Bishop frame $\{N_2, B_2, B\}$ and N-Bishop frame $\{N, N_3, B_3\}$ of ψ_m is as follows:

$$\begin{cases} N = \cos\Phi N_2 + \sin\Phi B_2, \\ N_3 = \left(-\cos\Omega\cos(nt) + \sin\Omega\sin(nt)\right)N_2 \\ \quad + \left(\cos\Omega\cos(nt) - \sin\Omega\sin(nt)\right)B_2 \\ \quad - \left(\sin\Omega\cos(nt) + \cos\Omega\sin(nt)\right)B, \\ B_3 = -\left(\sin\Omega\cos(nt) + \cos\Omega\sin(nt)\right)N_2 \\ \quad + \left(\sin\Omega\cos(nt) + \cos\Omega\sin(nt)\right)B_2 \\ \quad + \left(\cos\Omega\cos(nt) - \sin\Omega\sin(nt)\right)B. \end{cases}$$

In this study, alternative, type-1 Bishop, type-2 Bishop and N-Bishop frames of Salkowski curves in Euclidean 3-space are defined and the theorems and corollaries throughout the paper are obtained through these frames. Thus, it is possible to carry out new studies on these current frames related to the Frenet frame of Salkowski curves. Moreover, similar studies for anti-Salkowski curves or Salkowski curves in Minkowski 3-space are still an open problem.

References

[1] H. H. Hacısalihoğlu, *Diferansiyel Geometri*. İnönü Üniversitesi Yayınları, Malatya, 1983.

[2] P. D. Scofield, "Curves of constant precessions," *The American mathematical monthly*, vol. 102, pp. 531–537, 1995.

[3] R.L. Bishop, "There is more than one way to frame a curve," *The American Mathematical Monthly*, vol. 82, pp. 246–251, 1975.

[4] N. Clauvelin, W. K. Olson and I. Tobias, "Characterizations of the geometry and topology of DNA pictured as a discrete collection of atoms," *Journal of Chemical Theory and Computation*, vol. 8, pp. 1092–1107, 2012.

[5] C. Y. Han, "Nonexistence of rational rotation-minimizing frames on cubic curves," *Computer Aided Geometric Design*, vol. 25, pp. 298–304, 2008.

[6] S. Yılmaz and M. Turgut, "A new version of Bishop frame and an application to spherical images," *Journal of Mathematical Analysis and Applications*, vol. 371, pp. 764–776, 2010.

[7] O. Keskin and Y. Yaylı, "An application of N-Bishop frame to spherical images for direction curves," *International Journal of Geometric Methods in Modern Physics*, vol. 14, pp. 1750162, 2017.

[8] B. Bükcü and M. K. Karacan, "Special Bishop motion and Bishop Darboux rotation axis of the space curve," *Journal of Dynamical Systems and Geometric Theories*, vol. 6, pp. 27–34, 2008.

[9] B. Bükcü and M. K. Karacan, "The slant helices according to Bishop frame," *International Journal of Computational and Mathematical Sciences*, vol. 3, pp. 67–70, 2009.

[10] E. Damar, N. Yüksel and A. T. Vanlı, "The ruled surfaces according to the type-2 Bishop frame in E^3, " *International Mathematical Forum*, vol. 12, pp. 133–143, 2017.

[11] A. Kelleci, M. Bektaş and M. Ergüt, "The Hasimoto surface according to bishop frame," *Adıyaman Üniversitesi Fen Bilimleri Dergisi*, vol. 9, pp. 13–22, 2019.

[12] S. Kızıltuğ, S. Kaya and O. Tarakcı, "The slant helices according to the type-2 Bishop frame in Euclidean 3-space," *International Journal of Pure and Applied Mathematics*, vol. 2, pp. 211–222, 2013.

[13] A. Çakmak and V. Şahin, "Characterizations of Adjoint Curves According to the alternativeMoving Frame", *Fundamental Journal of Mathematics and Applications*, vol. 5, pp. 42-50, 2022.

[14] M. Masal and A. Azak, "The Ruled Surfaces According to the type-2 Bishop Frame in the Euclidean 3-Space E^3 ," *Mathematical Sciences and Applications E-Notes*, vol. 3, pp. 74–83, 2015.

[15] M. Masal and A. Azak, "Ruled surfaces according to Bishop frame in the Euclidean 3 –spaces," *Proceedings of the National Academy of Sciences, India Section A: Physical Sciences*, vol. 89, pp. 415–424, 2019.

[16] S. Ouarab, A. Ouazzani and M. Izıd, "Ruled surfaces with alternative moving frame in Euclidean 3-space," *International Journal of Mathematical Sciences and Engineering Applications*, vol. 12, pp. 43–58, 2018.

[17] H. K. Samancı and M. İncesu, "Investigating a quadratic Bezier curve due to NCW and N-Bishop frames," *Turkish Journal of Mathematics and Computer Science*, vol. 12, pp. 120–127, 2020.

[18] H. K. Samancı and M. Sevinç, "N-Bishop Çatısına Göre Regle Yüzeylerin Bazı Karakterizasyonları," *Karadeniz Fen Bilimleri Dergisi*, vol. 12, pp. 113–134, 2022.

[19] B. Uzunoğlu, İ. Gök, and Y. Yaylı, "A New approach on curves of constant precession," *Applied Mathematics and Computation*, vol. 275, pp. 317–323, 2016.

[20] S. Yılmaz and Ü. Z. Savcı, "A New Version Darboux Vector and Characterization Some Special Curves According to the type-2 Bishop Frame in E^3," *Proceedings of the National Academy of Sciences, India Section A: Physical Sciences*, vol. 87, pp. 355–362, 2017.

[21] S. Şenyurt, S. Gür Mazlum, D. Canlı and E. Çan, "Some special Smarandache ruled surfaces according to the alternativeframe in E^3," Maejo International Journal of Science and Technology, vol. 17, pp. 138–153, 2023.

[22] E. Salkowski, "Zur transformation von raumkurven," *Mathematische Annalen*, vol. 66, pp. 517–557, 1909.

[23] J. Monterde, "Salkowski curves revisited: A family of curves with constant curvature and non-constant torsion, "*Computer Aided Geometric Design*, vol. 26, pp. 271–278, 2009.

[24] S. Gür Mazlum, S. Şenyurt and M. Bektaş, "Salkowski Curves and Their Modified Orthogonal Frames in E^3," *Journal of New Theory*, vol. 40, pp. 12–26, 2022.

[25] S. Şenyurt and B. Öztürk, "Smarandache curves according to the Sabban frame belonging to spherical indicatrix curve of the Salkowski curve," *Tbilisi Mathematical Journal*, vol. 13, pp. 111–131, 2020.

[26] S. Gür and S. Şenyurt, "Frenet vectors and geodesic curvatures of spheric indicatrix curves of Salkowski curve in E^3," *Hadronic Journal*, vol. 33, pp. 485–512, 2010.

[27] J. Monterde, "The Bertrand curve associated to a Salkowski curve," *Journal of Geometry*, vol. 111, pp. 21, 2020.

[28] S. Deshmukh, A. Alghanemi and R. T. Farouki, "Space curves defined by curvature–torsion relations and associated helices," *Filomat*, vol. 33, pp. 4951–4966, 2019.

Seasonal Variations of Radioactivity Concentrations in Soil and Sediment of Meriç River, Turkey

Selin ÖZDEN[1*], Serpil AKÖZCAN PEHLİVANOĞLU[1]

[1]*Kirklareli University, Faculty of Arts and Sciences, Department of Physics, Kirklareli, Turkey*
(ORCID: 0000-0003-3860-8444) (ORCID: 0000-0001-6661-5540)

Abstract

In this study, the activity concentrations of ^{226}Ra, ^{232}Th, ^{40}K, and ^{137}Cs radionuclides were determined for spring, summer, autumn and winter in soil and sediment samples collected from different sites in the Meriç River using a gamma spectrometer with an HPGe detector. The results showed that the mean activity concentrations in the soil samples were 45.26±1.80 Bq kg^{-1}, 56.24±1.87 Bq kg^{-1}, 704.32±10.82 Bq kg^{-1}, and 2.41±0.54 Bq kg^{-1} for ^{226}Ra, ^{232}Th, ^{40}K, and ^{137}Cs, respectively. The mean ^{226}Ra, ^{232}Th, ^{40}K, and ^{137}Cs activities in the sediment samples were 25.99±0.73 Bq kg^{-1}, 31.05±0.79 Bq kg^{-1}, 658.03±6.27 Bq kg^{-1}, and 2.71±0.24 Bq kg^{-1}, respectively. The mean radioactivity levels in this study were compared with other activity concentrations in various regions' soils and sediments and also with the world mean values. The mean activity concentrations of ^{40}K were found to be higher than the world mean value in both soil and sediment samples. To estimate the potential health risk in samples, radiological hazard parameters such as the radium equivalent activity, the absorbed dose rate, the annual effective dose equivalent, and the external hazard index were calculated for samples and compared with the recommended values.

1. Introduction

All living organisms are continually exposed to background radiation that comes from radioactive sources [1]. Background radiation is natural ionizing radiation from different sources in the environment. There are various sources of background radiation, including food and drinks, rocks in the ground, radon gas and cosmic rays. The composition of the earth's crust is a major source of natural radiation. The natural sources are mainly due to the primordial radionuclides such as ^{238}U and ^{232}Th and their decay products, as well as ^{40}K [2]. Rock, sand, sediments, soil, water, quarry products and other materials used in building constructions contain various concentrations of radioactivity. Natural radioactivity concentrations differ for each region depending on the geological structure. Since natural radionuclides are not homogeneously distributed across regions, their concentration and analysis of their distribution in

materials play an important role in radiation protection [3]. Major routes of exposure to radionuclides include external exposure from radionuclide deposits in river and marine sediments and consumption of foodstuffs [4].

In addition to natural radionuclides, artificial radionuclides are released into the atmosphere due to anthropogenic activities such as nuclear power plant accidents, nuclear weapon tests, medical applications, and industrial activities [5]. One of the most important artificial radionuclides is the anthropogenic radionuclide ^{137}Cs (half-life 30.2 years) which is a product of radioactive fallout. ^{137}Cs radionuclide reached Turkey with radioactive clouds as a result of the Chernobyl disaster in 1986. The Thrace and Black Sea regions of Turkey were highly contaminated after the Chernobyl nuclear power plant accident. ^{137}Cs radionuclide is strongly absorbed and retained in the soil and is soluble in water [5]. Knowledge of the level of natural and artificial radioactivity in river and

coastal ecosystems is important because rivers transport particulate materials and dissolved species from land to sea. Natural and artificial radionuclides migrate from the lithosphere to wider natural ecosystems in a variety of ways, including erosion of terrestrial rocks and subsequent transport by water, wind, and gravity [4], [6]. Long-term exposure to radionuclides has several health problems such as lung diseases, acute leucopenia, anemia, and cancers [7].

The objective of this study is to obtain seasonal radioactivity levels of ^{226}Ra, ^{232}Th, ^{40}K, and ^{137}Cs in soil samples collected from different sites across the Meriç River and in the sediment samples collected from various sites within the Meriç River. Radiological parameters were calculated to evaluate potential health hazards. The data in this study will provide background data on environmental pollution.

2. Material and Method
2.1. Study Area

The samples were collected seasonally from different sites in the Meriç River. The Meriç River is the longest river in the Balkans (about 480 km long) and also has an important aquatic ecosystem in the Thrace region in Turkey [8], [9]. The Meriç River Basin covers an area of approximately 14.600 km^2 in Turkey [8]. The Meriç River comes from Bulgaria and flows along the border between Greece and Turkey. 187 km of the Meriç River is located in Turkey [10]. The samples were collected in the areas of the Meriç River in Edirne, Turkey. The location of Edirne province in Turkey and also the Meriç River is shown in Figure 1.

2.2. Sample Preparation and Activity Analysis

20 measurement sites were selected along the Meriç River, where measurements were carried out for one year. The survey of terrestrial gamma radiation was performed once during each season: autumn, winter, spring and summer. One soil and sediment sample was collected from each point in one season. The samples were collected from the surface layer (8-10 cm). At each sampling point, approximately 1 kg of sediment and 500 g of soil were collected. The soil and sediment samples were dried at 105 °C for more than a day. Impurities such as stones, grass, and weeds in the samples were removed and passed through a 2 mm mesh. The samples were finally placed in 250 ml Marinelli containers for more than 4 weeks to achieve secular equilibrium between ^{226}Ra and its decay products [12]. Sample preparation pictures are given in Figure 2. The net masses of the soil and sediment

samples in the Marinelli containers were about 200-250 g.

Figure 1. Meriç Basin Map [11]

Radionuclide analysis was obtained using a gamma-ray spectrometer equipped with a high-purity germanium (HPGe) detector (Ortec GEM70P4-95, 70% relative efficiency) in Kırklareli University Central Research Laboratory. A solid nuclide mixture of gamma reference calibration source from Isotope Product Laboratories (Eckert&Ziegler, Berlin, Germany) containing the radionuclides ^{241}Am, ^{109}Cd, ^{57}Co, ^{123m}Te, ^{51}Cr, ^{113}Sn, ^{85}Sr, ^{137}Cs, ^{88}Y and ^{60}Co was used for the energy and efficiency calibrations. The spectra collection and the analysis of the spectra were obtained by GammaVision-32 software and Maestro software, respectively. The activity concentrations of ^{232}Th, ^{226}Ra and ^{40}K were determined using the gamma-ray peaks of the 911.2 keV (^{228}Ac) and 583.1 keV (^{208}Tl), 351.9 keV (^{214}Pb) and 609.3 keV (^{214}Bi), and 1460.8 keV, respectively. The activity concentration of ^{137}Cs was evaluated from the gamma-ray peak at 661.66 keV.

The activity concentrations in the samples were calculated by Eq. 1.

$$A = \frac{C}{\varepsilon x I_\gamma x m} \qquad (1)$$

In Eq. 1, A is the activity in Bq kg^{-1}, C is counts (per second), ε is the detector efficiency, Iγ is the gamma-ray emission probability, and m is the mass of the soil and sediment sample in kg [13], [14].
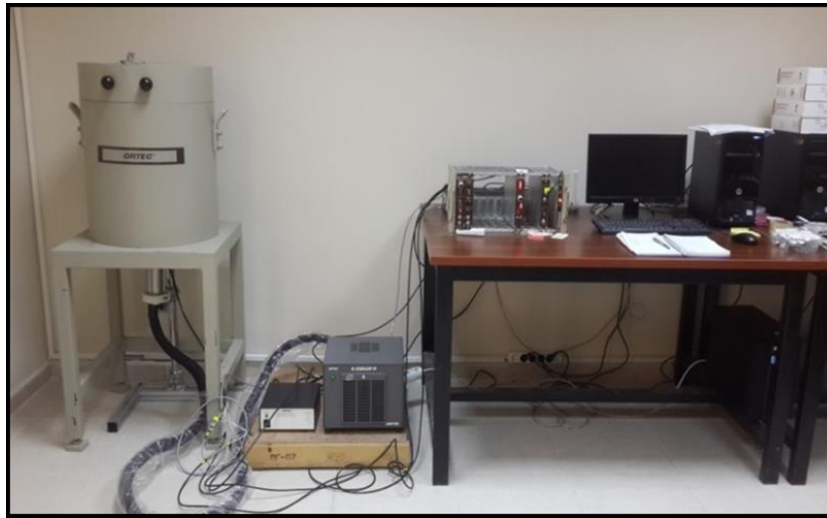
Figure 2. Sample preparation pictures

Figure 3. Gamma spectrometer with High Purity Germanium (HPGe) detector in Kırklareli University Central Research Laboratory

2.3. Calculation of Radiological Hazards

Radiological hazard parameters were determined using Eq. 2, 3, 4, and 5. In equations, Ra_{eq} is radium equivalent activity, C_{Ra} is activity concentration of ^{226}Ra, C_{Th} is activity concentration of ^{232}Th, C_K is activity concentration of ^{40}K, C_{Cs} is activity concentration of ^{137}Cs, D is the total absorbed dose rate in air at l m above ground level, AEDE is the annual effective dose equivalent, and H_{ex} is the external hazard index [15], [16].

$$Ra_{eq}(Bq\ kg^{-1}) = C_{Ra} + 1.43C_{Th} + 0.077C_K \quad (2)$$

$$D\ (nGy\ h^{-1}) = 0.462C_{Ra} + 0.604C_{Th} + 0.0417C_K + 0.03C_{Cs} \quad (3)$$

$$AEDE\ (\mu Sv\ y^{-1}) = D\ (nGy\ h^{-1}) \times 8760\ (h\ y^{-1}) \times 0.2 \times 0.7\ (SvGy^{-1}) \times 10^{-3} \quad (4)$$

$$H_{ex} = \frac{C_{Ra}}{370} + \frac{C_{Th}}{259} + \frac{C_K}{4810} \quad (5)$$

3. Results and Discussion

Activity concentrations in soil and sediments of the Meriç River were measured for four seasons and the mean activity concentrations of radionuclides are summarized in Table 1.

The seasonal variations of the mean activity concentrations of ^{226}Ra and ^{232}Th in samples are given in Figure 4. The mean activity concentrations of ^{226}Ra in soil samples were determined as 43.64±0.70, 35.87±0.77, 41.78±0.62 and 45.26±1.80 Bq kg^{-1} in spring, summer, autumn and winter, respectively. The mean values of ^{232}Th in soil were found as 40.76±1.01 Bq kg^{-1} (in spring), 47.34±0.46 Bq kg^{-1} (in summer), 57.83±2.37 Bq kg^{-1} (in autumn) and 56.24±1.87 Bq kg^{-1} (in winter).

The mean values of ^{226}Ra and ^{232}Th activity concentrations in soil samples were found to be higher than those of the worldwide mean values (35 Bq kg^{-1} for ^{226}Ra and 30 Bq kg^{-1} for ^{232}Th) as reported by UNSCEAR [15]. When we examine the seasonal analysis results of the sediment samples, the mean values of ^{226}Ra activity concentrations were 19.85±0.44, 22.36±0.41, 33.51±1.27 and 28.26±0.79 Bq kg^{-1} in spring, summer, autumn and winter, respectively.

The mean activity concentrations of ^{232}Th in sediment samples were determined as 25.48±0.25 Bq kg^{-1} (in spring), 18.59±0.76 Bq kg^{-1} (in summer), 37.18±1.19 Bq kg^{-1} (in autumn) and 42.95±0.94 Bq kg^{-1} (in winter). The mean activity concentrations of ^{226}Ra in sediment samples were lower than the world average value in all seasons. The mean values of ^{232}Th activity concentrations in sediment samples calculated for the autumn and winter seasons were found to be higher than worldwide mean values [15].
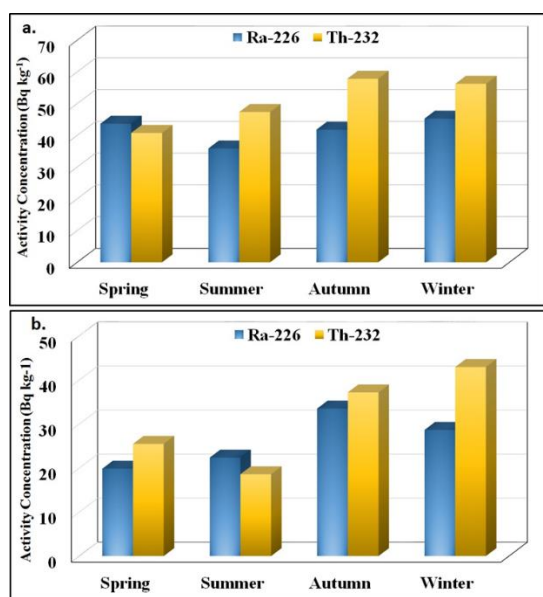

Figure 4. The mean activity concentrations of ^{226}Ra and ^{232}Th in a. soil samples and b. sediment samples

The seasonal variations of the mean activity concentrations of ^{40}K and ^{137}Cs emitted from the samples are presented in Figure 5 and Figure 6, respectively. The highest mean of ^{40}K was found in spring (719.93±5.44 Bq kg^{-1}) in the soil sample. The lowest mean concentration of ^{40}K was obtained in spring (647.23±4.32 Bq kg^{-1}) in the sediment sample. The mean activity concentrations of ^{40}K were found to be higher than the world mean value of 400 Bq kg^{-1} in both soil and sediment samples [15]. Artificial fertilization processes, especially potassium-

containing fertilizers, are known to increase radioactivity. In addition, the transport of fertilized soil from one place to another by rivers also increases radioactivity [17-19]. The high activity concentrations of ^{40}K and ^{226}Ra in these areas of the Meriç River Basin may have resulted from over-fertilization.

The highest mean of artificial ^{137}Cs was obtained in autumn (4.34±0.35 Bq kg^{-1}) in the sediment sample. The lowest mean value of ^{137}Cs was found as 1.38±0.25 Bq kg^{-1} (winter) in the sediment sample. Since the Chernobyl accident affected the Thrace region in Turkey, ^{137}Cs radionuclide have been found in both soil and sediment samples.
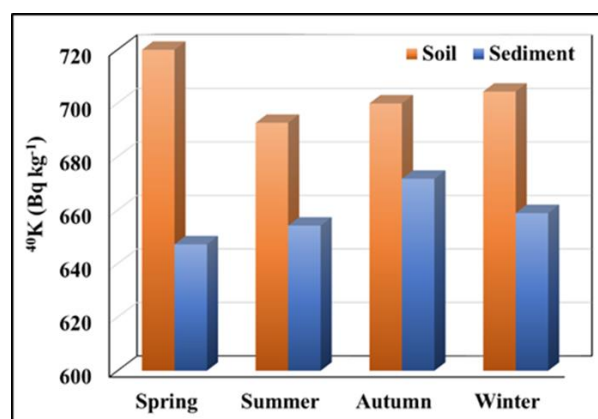

Figure 5. Seasonal variations of the mean activity concentration of ^{40}K

Although soil and sediment gamma activity at some sampling points shows similar activity concentration changes, there are significant variations between winter and summer measurements. As shown in Figures 4a and 5, maximum activity concentrations in soils were generally determined in spring and winter. The frequency and magnitude of floods in the region have increased in recent years. Therefore, the main reason for seasonal variation of radionuclide concentrations in the study area is floods and rainfall regimes. Floods caused the displacement of soils in the study area and the concentrations of radionuclides varied significantly from season to season. It is also thought that potassium fertilizer was used for the soils in the study area and this may have increased the phosphate content of the soil and as a result, disproportionately ^{238}U, ^{226}Ra, ^{232}Th and ^{40}K levels may have accumulated in the soil [20].

Higher values for ^{137}Cs were determined in summer and autumn as a result of dry deposition [21]. Water erosion contributes to the redistribution of washed soil particles in river basins with ^{137}C fixed on them. Therefore, areas of secondary pollution are

formed in river basins where the total inventory of ^{137}Cs exceeds the initial accumulation levels [22]. Humid climates cause the leaching of alkaline metals and soil acidification and can also affect U and Th mobility. Depending on the environmental characteristics (geological factors, climate, human activities, etc.), coprecipitation and sorption in organic matter, clays and oxides may hold radionuclides in soils [23].

Table 1. The mean activity concentrations (Bq kg^{-1}) of radionuclides in soil and sediments of the Meriç River

Sample Type	Season	[226]Ra	[232]Th	[40]K	[137]Cs
Soil	Spring	43.64±0.70	40.76±1.01	719.93±5.44	1.24±0.12
	Summer	35.87±0.77	47.34±0.46	692.67±7.55	3.98±0.35
	Autumn	41.78±0.62	57.83±2.37	699.90±5.86	2.50±0.31
	Winter	45.26±1.80	56.24±1.87	704.32±10.82	2.41±0.54
	Mean	41.64±0.97	50.54±1.43	704.21±7.42	2.53±0.33
Sediment	Spring	19.85±0.44	25.48±0.25	647.23±4.32	2.25±0.11
	Summer	22.36±0.41	18.59±0.76	654.25±4.38	2.86±0.26
	Autumn	33.51±1.27	37.18±1.19	671.73±8.84	4.34±0.35
	Winter	28.26±0.79	42.95±0.94	658.91±7.54	1.38±0.25
	Mean	25.99±0.73	31.05±0.79	658.03±6.27	2.71±0.24

Table 2. Mean activity concentrations of the radionuclides (Bq kg^{-1}) in soil samples from various studies in the literature compared with those of this study

Region	[226]Ra	[232]Th	[40]K	[137]Cs	Reference
Jordan	42	42	23	3.7	[24]
Russia	35	30	400	48.9	[25]
Pakistan	32.9	53.6	647.4	1.5	[26]
Botswana	34.8	41.8	432.7	-	[27]
China	75.1	101.0	535.8	-	[28]
India	60.3	64.5	481.0	-	[29]
North Cyprus	83.7	53.6	593.9	7.1	[30]
Bolu (Turkey)	18.2	17.3	258.3	7.5	[31]
Bartın (Turkey)	8	7	136	2	[32]
Nevşehir(Turkey)	49.45	54.08	698.4	8.26	[33]

Table 3. Mean activity concentrations of the radionuclides (Bq kg^{-1}) in sediment samples from various studies in the literature compared with those of this study

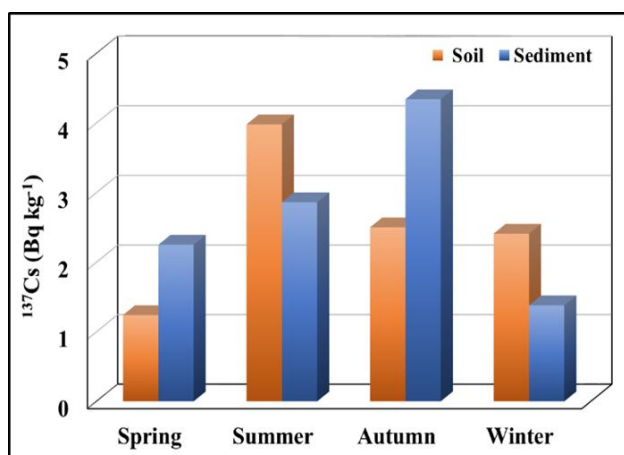| Region	[226]Ra	[232]Th	[40]K	[137]Cs	Reference
Mediterranean Sea coast	20.1	18.4	467.3	-	[35]
Egypt	23.8	19.6	374.9	-	[36]
Iraq	15.48	-	418.47	2.88	[37]
Boka Kotorska Bay	20	35	580	6.1	[38]
Barents Sea	14.2	21.1	439.1	3.2	[39]
Nigeria	-	35.2	501.0	-	[40]
Calabria	21.3	30.3	849	-	[41]
Borçka Black Lake (Turkey)	-	13.85	473.67	35.06	[42]
Izmit Bay (Turkey)	18	-	568	21	[43]
Aegean Sea (Turkey)	21.50	23.13	541.88	-	[44]

Figure 6. Seasonal variations of the mean activity concentration of artificial ^{137}Cs

The mean activity concentrations calculated in this study were compared with the results obtained in other studies in the literature (Tables 2 and 3). The mean of the activity concentrations for ^{226}Ra, ^{232}Th, ^{40}K, and ^{137}Cs in soil samples were found as 41.64, 50.54, 704.21, and 2.53 Bq kg^{-1} in this study, respectively. The mean value of the activity concentration of ^{226}Ra in soil samples is less than the values obtained in China, India, North Cyprus, and Nevşehir (Turkey), as illustrated in Table 2. The mean of the activity concentration of ^{232}Th in soil samples is less than Pakistan, China, India, North Cyprus, and Nevşehir (Turkey) and higher than Jordan, Russia, Botswana, Bolu (Turkey) and Bartın (Turkey). Soil and rock characteristics in a region are the most important factors affecting radioactivity.

In Nevşehir (Turkey), there are metamorphic, sedimentary and volcanic rocks. Higher activity concentrations were observed due to the dominance of volcanic rocks in Nevşehir province. The mean of the activity concentrations of ^{40}K in the soil and sediment samples are higher than in the other regions. The mean activity concentration for ^{137}Cs in soil samples in this study is higher than in Pakistan and Bartın (Turkey). The mean concentrations of ^{226}Ra, ^{232}Th, ^{40}K, and ^{137}Cs in sediment samples were in Meriç River (Turkey) obtained as 25.99, 31.05, 685.03, and 2.71 Bq kg^{-1}, respectively. The mean of the activity concentrations of ^{226}Ra and ^{232}Th in sediment samples are higher than Mediterranean Sea coast, Egypt, Iraq, Boka Kotorska Bay, Barents Sea, Izmit Bay (Turkey), and Aegean Sea (Turkey). The mean activity concentration for ^{137}Cs in sediment samples in the present study is less than Iraq, Boka Kotorska Bay, Barents Sea, Borçka Black Lake (Turkey), and Izmit Bay (Turkey). Izmit Bay is located in the most industrialized region of the Marmara region. In Izmit Bay (Turkey), the highest

activity concentrations of ^{40}K and ^{226}Ra were found near phosphate, fertilizer and petrochemical industrial facilities and are higher than the values in this study. Borçka Lake (Turkey) has been highly contaminated due to the Chernobyl accident and ^{137}Cs concentrations are very high compared to other lakes in Turkey [42]. The variation of obtained values is due to some factors such as the geology of the region, the area (agricultural or industrial), soil and rock type or other characteristic factors [34].

The Meriç River is a transboundary river and industrial wastes, sewage wastes, and radioactive pollution resulting from agricultural activities are transported by water along this long river. The Bulgarian part of the Meriç River Basin has been used for agricultural activities and uranium mining [45]. These radioactive pollutants, especially those coming to Turkey via the river from Bulgaria, cause an increase in the natural and artificial radionuclides in the soil and sediment along the river in Turkey. Therefore, activity concentrations in soil and sediment samples collected along the Meriç River were observed to be higher than in some regions in Turkey.

Figure 7 shows the variation of radiological hazard parameters in samples. The mean values of Ra$_{eq}$ in sediment samples were found to be 101.59, 94.74, 133.69, and 135.80 Bq kg^{-1} in spring, summer, autumn and winter, respectively. In soil samples, the mean values of Ra$_{eq}$ were 152.32, 152.05, 173.47, and 174.99 Bq kg^{-1} in spring, summer, autumn and winter, respectively. All the values of Ra$_{eq}$ in samp1es were lower than the recommended maximum value of 370 Bq kg^{-1} [16]. The mean values of D in sediment samples were 51.62, 48.93, 66.08, and 66.52 nGy h^{-1} in spring, summer, autumn and winter, respectively. In soil samples, the mean values of D were calculated as 74.84, 74.17, 83.49, and 84.32 nGy h^{-1} in spring, summer, autumn and winter, respectively. The mean values of D in autumn and winter for sediment samples were higher than the world average value (57 nGy h^{-1}) [15]. All the values of D in soil samples were found to be higher than the world average. The obtained values of AEDE due to natural and artificial radioactivity in soil samples ranged from 90.96 to 103.41 µSv y^{-1} with a mean value of 97.14 µSv y^{-1}, which is higher than the world average of 70 µSv y^{-1} [15]. In addition, all the calculated values of H$_{ex}$ for soil and sediment samples were found to be lower than unity which does not cause any harm to the human beings in the studied area.
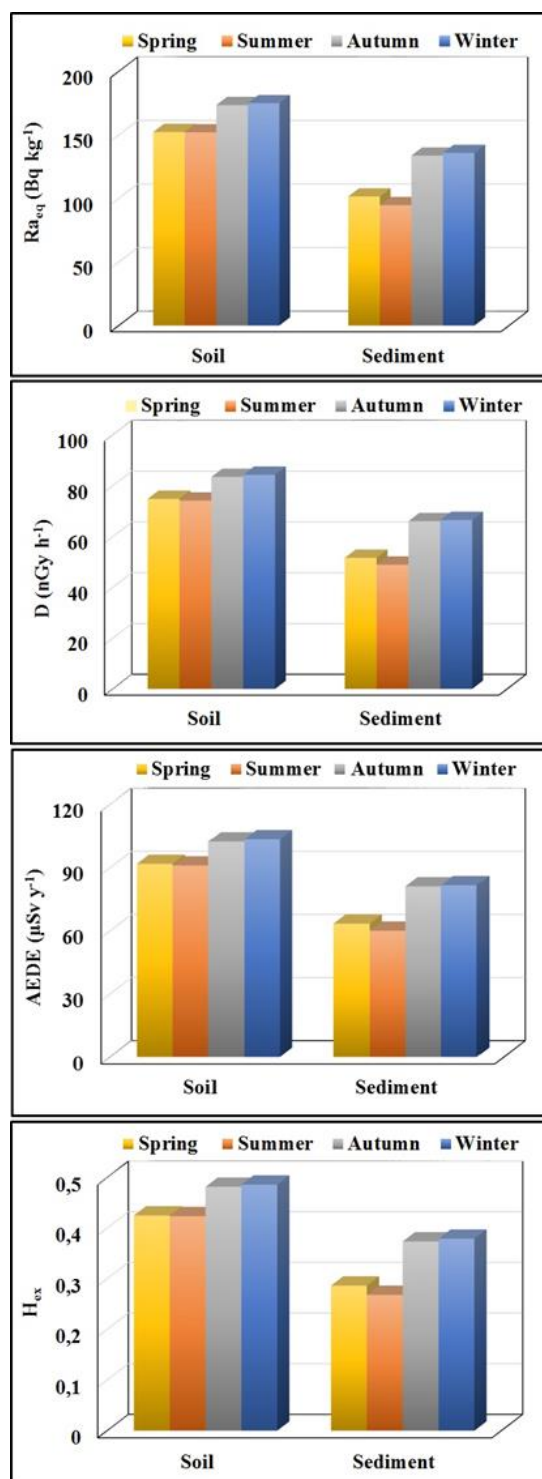
Figure 7. Radiological hazard parameters in soil and sediment samples

4. Conclusion

This study provides a baseline for radioactivity levels in both soil and sediment samples in the Meriç River Basin for spring, summer, autumn and winter. The mean activity concentrations of ^{226}Ra in sediment samples were lower than the world average value for all seasons. The radioactivity concentrations of ^{232}Th in sediment samples for the autumn and winter seasons were higher than in summer and spring. The differences between activity concentrations may be a consequence of variations in meteorological conditions and soil moisture. In addition, the mean activity concentrations of ^{40}K were higher than the world mean value in both soil and sediment samples. The use of artificial fertilizers and their transport via rivers increases radioactivity. ^{137}Cs radionuclide detected in the study area. Since the Chernobyl disaster in 1986 affected the Thrace region of Turkey, ^{137}Cs radionuclide continues to exist in both soil and sediment. To estimate the potential health risk, radiological hazard parameters were calculated. ELCR and D were found higher than the recommended values for some samples. This implies that the population near these areas is likely to receive some radiation dose. Radiological hazard parameters for soil samples were higher than sediment samples. The high-level radiological hazard parameters were due to the high level of radioactivity concentrations of radionuclides in both soil and sediment samples. However, all the calculated values of H_{ex} for samples were found to be lower than unity which does not cause any harm to the human beings in the studied area.

Contributions of the authors

The authors' contributions to the paper are equal

Conflict of Interest Statement

There is no conflict of interest between the authors.

Statement of Research and Publication Ethics

The study is complied with research and publication ethics

References

[1] O. El Samad, R. Baydoun, B. Nsouli, and T. Darwish, "Determination of natural and artificial radioactivity in soil at North Lebanon province," *J. Environ. Radioact*., vol. 125, pp. 36–39, 2013.

[2] O. Belyaeva, N. Movsisyan, K. Pyuskyulyan, L. Sahakyan, G. Tepanosyan, and A. Saghatelyan, "Yerevan soil radioactivity: Radiological and geochemical assessment," *Chemosphere*, vol. 265, no. 129173, p.

129173, 2021.

[3] T. E. Attia, E. H. Shendi, and M. A. Shehata, "Assessment of natural and artificial radioactivity levels and radiation hazards and their relation to heavy metals in the industrial area of Port Said city, Egypt," *Environ. Sci. Pollut. Res. Int.*, vol. 22, no. 4, pp. 3082–3097, 2015.

[4] B. Kücükömeroglu et al., "Radioactivity in sediments and gross alpha–beta activities in surface water of Fırtına River, Turkey," *Environ. Geol.*, vol. 55, no. 7, pp. 1483–1491, 2008.

[5] P. İsel, L. Sahin, N. Hafızoğlu, E. Ganioğlu, and A. Mülayim, "Natural and artificial radioactive pollution in sediment and soil samples of the Bosphorus, Istanbul," *Environ. Sci. Pollut. Res. Int.*, vol. 30, no. 27, pp. 70937–70949, 2023.

[6] M. Fallah, S. Jahangiri, H. Janadeleh, and M. A. Kameli, "Distribution and risk assessment of radionuclides in river sediments along the Arvand River, Iran," *Microchem. J.*, vol. 146, pp. 1090–1094, 2019.

[7] W. M. Abdellah, H. M. Diab, S. U. El-Kameesy, E. Salama, and S. El-Framawy, "Natural radioactivity levels and associated health hazards from the terrestrial ecosystem in Rosetta branch of the River Nile, Egypt," *Isotopes Environ. Health Stud.*, vol. 53, no. 4, pp. 427–439, 2017.

[8] C. tokatlı, "Assessment of water quality in the meriç river as an ecosystem element in turkey's Thrace region," *Pol. J. Environ. Stud.*, vol. 24, pp. 2205–2211, 2015.

[9] C. Tokatlı, "Water and sediment quality assessment of the lifeblood of Thrace Region (Turkey): Meriç River basin," *Fresenius Environmental Bulletin*, vol. 28, no. 5, pp. 4131–4140, 2019.

[10] C. Tokatlı and M. Varol, "Impact of the COVID-19 lockdown period on surface water quality in the Meriç-Ergene River Basin, Northwest Turkey," *Environ. Res.*, vol. 197, no. 111051, p. 111051, 2021.

[11] C. Tokatli and F. Ustaoğlu, "Health risk assessment of toxicants in Meriç River Delta Wetland, Thrace Region, Turkey," *Environ. Earth Sci.*, vol. 79, no. 18, 2020.

[12] S. Özden and S. Aközcan, "Natural radioactivity measurements and evaluation of radiological hazards in sediment of Aliağa Bay, İzmir (Turkey)," *Arab. J. Geosci.*, vol. 14, no. 1, 2021.

[13] S. Özden, S. Aközcan, and O. Günay, "137cs in soils from İstanbul (turkey) sampled 35 years after Chernobyl," *Environ. Forensics*, pp. 1–7, 2023.

[14] S. Özden, "Assessment of natural radioactivity levels and radiological hazard parameters of soils collected from Bulgaria–Turkey border region," *Eur. Phys. J. Plus*, vol. 137, no. 12, 2022.

[15] UNSCEAR, "Sources and biological effects of ionizing radiation," Report to general assembly, with scientific annexes, United Nations, New York, 2000.

[16] J. Beretka and P. J. Matthew, "Natural radioactivity of Australian building materials, industrial wastes and by-products," *Health Phys.*, vol. 48, no. 1, pp. 87–95, 1985.

[17] S. Aközcan, "Distribution of natural radionuclide concentrations in sediment samples in Didim and Izmir Bay (Aegean Sea-Turkey)," *J. Environ. Radioact.*, vol. 112, pp. 60–63, 2012.

[18] S. Aközcan, "Annual effective dose of naturally occurring radionuclides in soil and sediment," *Toxicol. Environ. Chem.*, vol. 96, no. 3, pp. 379–386, 2014.

[19] E. Tabar, H. Yakut, M. M. Saç, C. Taşköprü, M. İçhedef, and A. Kuş, "Natural radioactivity levels and related risk assessment in soil samples from Sakarya, Turkey," *J. Radioanal. Nucl. Chem.*, vol. 313, no. 1, pp. 249–259, 2017.

[20] S. Aközcan, M. Yılmaz, and F. Külahcı, "Dose rates and seasonal variations of 238 U, 232 Th, 226 Ra 40 K and 137 Cs radionuclides in soils along Thrace, Turkey," *Journal of Radioanalytical and Nuclear Chemistry*, vol. 299, pp. 95–101, 2014.

[21] F. Noli, P. Tsamos, and S. Stoulos, "Spatial and seasonal variation of radionuclides in soils and waters near a coal-fired power plant of Northern Greece: environmental dose assessment," *J. Radioanal. Nucl. Chem.*, vol. 311, no. 1, pp. 331–338, 2017.

[22] V. N. Golosov et al., "Erosion as a factor of transformation of soil radioactive contamination in the basin of the Shchekino Reservoir (Tula region)", *Eurasian Soil Science*, vol. 54, pp. 291–303, 2021.

[23] F. C. A. Ribeiro, J. I. R. Silva, E. S. A. Lima, N. M. B. Sobrinho, D. V. Perez, and D. C. Lauria, "Natural radioactivity in soils of the state of Rio de Janeiro (Brazil): Radiological characterization and relationships to geological formation, soil types and soil properties", *Journal of environmental radioactivity*, vol. 182, pp. 34–43, 2018.

[24] A. H. Alomari, M. A. Saleh, S. Hashim, A. Alsayaheen, and A. Abukashabeh, "Statistical relationship between activity concentrations of radionuclides 226Ra, 232Th, 40K, and 137Cs and geological

formations in surface soil of Jordan," *Isotopes Environ. Health Stud.*, vol. 55, no. 2, pp. 211–226, 2019.

[25] E. Mingareeva et al., "Content of radionuclides (226Ra, 232Th, 40K, 137Cs) in soils of the North-West region of Russia formed on three types of soil forming rocks," *E3S Web Conf.*, vol. 175, p. 09018, 2020.

[26] Matiullah, "Measurement of radioactivity in the soil of Bahawalpur division, Pakistan," *Radiat. Prot. Dosimetry*, vol. 112, no. 3, pp. 443–447, 2004.

[27] V. R. K. Murty and N. Karunakara, "Natural radioactivity in the soil samples of Botswana," *Radiat. Meas.*, vol. 43, no. 9–10, pp. 1541–1545, 2008.

[28] J. Yang and Y. Sun, "Natural radioactivity and dose assessment in surface soil from Guangdong, a high background radiation province in China," *J. Radiat. Res. Appl. Sci.*, vol. 15, no. 1, pp. 145–151, 2022.

[29] M. Zubair and Shafiqullah, "Measurement of natural radioactivity in several sandy-loamy soil samples from Sijua, Dhanbad, India," *Heliyon*, vol. 6, no. 3, p. e03430, 2020.

[30] A. Abbasi, A. Kurnaz, Ş. Turhan, and F. Mirekhtiary, "Radiation hazards and natural radioactivity levels in surface soil samples from dwelling areas of North Cyprus," *J. Radioanal. Nucl. Chem.*, vol. 324, no. 1, pp. 203–210, 2020.

[31] S. Dizman, F. K. Görür, R. Keser, and O. Görür, "The assessment of radioactivity and radiological hazards in soils of Bolu province, Turkey," *Environ. Forensics*, vol. 20, no. 3, pp. 211–218, 2019.

[32] T. Özdemir Öge, F. B. Özdemir, and M. Öge, "Assessment of environmental radioactivity in soil samples from Bartın Province, Turkey," *J. Radioanal. Nucl. Chem.*, vol. 328, no. 1, pp. 149–162, 2021.

[33] N. Bingöldağ and P. Otansev, "Spatial distribution of natural and artificial radioactivity concentrations in soil samples and statistical approach, Nevşehir, Turkey," *Radiochim. Acta*, vol. 108, no. 11, pp. 913–921, 2020.

[34] A. A. Abojassim and L. H. Rasheed, "Natural radioactivity of soil in the Baghdad governorate," *Environ. Earth Sci.*, vol. 80, no. 1, 2021.

[35] A. Abbasi and F. Mirekhtiary, "Heavy metals and natural radioactivity concentration in sediments of the Mediterranean Sea coast," *Mar. Pollut. Bull.*, vol. 154, no. 111041, p. 111041, 2020.

[36] H. M. H. Zakaly et al., "An extended assessment of natural radioactivity in the sediments of the mid-region of the Egyptian Red Sea coast," *Mar. Pollut. Bull.*, vol. 171, no. 112658, p. 112658, 2021.

[37] S. Khudair, A. Ali, and N. Tawfiq, "Assessment of natural and industrial radioactivity and radiological hazard in sediments of Tigris river of dhuluiya city, Iraq," *Rafidain Journal of Science*, vol. 29, no. 4, pp. 14–22, 2020.

[38] M. Radomirović et al., "Spatial distribution, radiological risk assessment and positive matrix factorization of gamma-emitting radionuclides in the sediment of the Boka Kotorska Bay," *Mar. Pollut. Bull.*, vol. 169, no. 112491, p. 112491, 2021.

[39] E. Yakovlev and A. Puchkov, "Assessment of current natural and anthropogenic radionuclide activity concentrations in the bottom sediments from the Barents Sea," *Mar. Pollut. Bull.*, vol. 160, no. 111571, p. 111571, 2020.

[40] O. Maxwell et al., "Spatial distribution of gamma radiation dose rates from natural radionuclides and its radiological hazards in sediments along river Iju, Ogun state Nigeria," *MethodsX*, vol. 7, no. 101086, p. 101086, 2020.

[41] F. Caridi et al., "Assessment of natural radioactivity and radiological risks in river sediments from Calabria (southern Italy)," *Appl. Sci. (Basel)*, vol. 11, no. 4, p. 1729, 2021.

[42] S. Dizman, T. Akdemir, C. M. Yeşilkanat, V. Nevruzoglu, E. Bal, and R. Keser, "Investigation and mapping of natural and artificial radioactivity in sediment samples from Borçka Black Lake, Artvin-Turkey," *Int. J. Environ. Anal. Chem.*, pp. 1–15, 2022.

[43] H. A. Ergül, M. Belivermiş, Ö. Kılıç, S. Topcuoğlu, and Y. Çotuk, "Natural and artificial radionuclide activity concentrations in surface sediments of Izmit Bay, Turkey," *J. Environ. Radioact.*, vol. 126, pp. 125–132, 2013.

[44] S. Aközcan et al., "Comparison of radioactivity and metal pollution concentrations in marine sediment samples obtained from the Aegean sea (turkey) and the Calabria region (Italy)," *WSEAS Trans. Environ. Dev.*, vol. 19, pp. 591–596, 2023.

[45] S. Aytas et al., "Natural radioactivity of riverbank sediments of the Maritza and Tundja Rivers in Turkey", *Journal of Environmental Science and Health, Part A*, vol. 47, no. 13, pp. 2163–2172, 2012.

Acute and Chonic Effects of Silver Nanoparticles (AgNPs) on *Unio delicatus*

İlker ŞİMŞEK[1*], Pınar ARSLAN[2], Aysel Çağlan GÜNAL[3], Özgür KUZUKIRAN[4],
Ayhan FİLAZİ[5]

1 Çankırı Karatekin University, Eldivan Vocational School of Health Services,
 Environmental Health Program, Department of Medical Services and Techniques, Çankırı, Turkey
2 Çankırı Karatekin University, Faculty of Science, Department of Biology, Çankırı, Turkey
3 Gazi University, Faculty of Gazi Education, Department of Biology Education, Ankara, Turkey
4 Çankırı Karatekin University, Eldivan Vocational School of Health Services, Veterinary Department,
Çankırı, Turkey
5 Ankara University, Faculty of Veterinary Medicine, Department of Pharmacology and Toxicology,
Ankara, Turkey
(ORCID: 0000-0001-9181-9879) (ORCID: 0000-0001-5910-2835) (ORCID: 0000-0002-9072-543X) (ORCID:
0000-0001-9294-2801) (ORCID: 0000-0002-2800-6215)

Abstract
The widespread use of silver nanoparticles (AgNPs) including water filters, paints, cosmetics, deodorants, clothing, textiles, food packaging, electrical appliances and medical devices inevitably leads to their release into the natural environment, bioaccumulation in organisms and persistent accumulation in natural aquatic systems. The aim of this study is to investigate the acute and chronic effects of silver nanoparticles, which can contaminate aquatic ecosystems, in freshwater mussels, one of the aquatic invertebrate organisms. The model organism of the study, *Unio delicatus*, was obtained from Gölbaşı Lake (Hatay). After that acclimation was performed in the laboratory for two weeks. The mussels were then exposed to 1 and 10 mg/L AgNPs for 7 and 21 days. At the end of the exposure period, hemolymph and tissue samples of the mussels were taken. Total hemocyte count from hemolymph samples, lipid peroxidation and glutathione levels from tissue samples (digestive gland and gill) were investigated. Acute exposure resulted in an increase in the total hemocyte counts, while chronic exposure resulted in a significant decrease (P<0.05). Changes in lipid peroxidation and glutathione levels in gill and digestive gland tissues of mussels also occurred but not significantly. In conclusion, AgNPs caused changes in physiological and biochemical parameters of freshwater mussels.

1. Introduction

Of all commercial goods using nanomaterials, silver nanoparticles (AgNPs) account for 24% of the total. The AgNPs are most frequently found in water filters, cosmetics, textiles, food packaging, electrical appliances, and medical devices [1]. The common use of AgNPs inevitably results in their discharge into the environment, bioaccumulates in the organisms and persistent accumulation in natural aquatic systems [2]. Once in the aquatic environment, AgNPs can go through various alteration processes (oxidation, dispersion, solubilization, adsorption with soluble and particulate organic matter, agglomeration /aggregation) [3]. AgNPs that accumulate in sediment can be transferred to aquatic organisms through environmental exposure. AgNPs taken up by aquatic organisms through the aquatic food chain pose a risk to human health [2].

Mussels have advantages such as the ability to make comparisons during the evaluation of information obtained from the aquatic environment,

to collect information about pollutants in the same area for a long time and to be widely used to quickly assess the current status of many pollutants [4]. For this reason, mussels are one of the leading biological indicators used in the measurement and evaluation of pollution in water. A mussel with an average size of 7-8 cm has the ability to filter 10-15 liters of water per hour. They filter and feed on all kinds of organic and inorganic particles [5]. In addition, freshwater mussels take part in the natural purification function of the water in their environment due to their filter feeding and thus play a decisive role on the ecological balance of the environment [6]. Mussels are particularly at risk of environmental contamination by nanoparticles because they are immobile and feed on suspended matter. Particles trapped in the gills during feeding and respiration are lowered down the digestive tube and accumulate in the "stomach" (digestive gland) where they are broken down. Therefore, nanoparticles can easily accumulate in mussels with aggregation and cause negative effects [7]. The freshwater mussel *Unio delicatus* Lea, 1863 is one of the most common mussel species in large river basins in southwest-eastern Anatolia. Due to its distribution areas, it is an indicator species in biomonitoring, ecotoxicological and phylogenetic studies [8], [9].

Nanoparticles have the potential to affect the physiology and behavior of aquatic organisms, including mussels. Several studies have shown that exposure to nanoparticles can lead to various physiological changes in marine mussels, including changes in the immune system, metabolism, and oxidative stress response [1], [10], [11]. Conversely, freshwater mussels have been used in few studies to investigate the effects of nanoparticles. A study with freshwater mussels showed that acute exposure to nanoparticles did not change the filtering capacity of mussels but had an effect on biomolecules [12]. In the literature review, no chronic exposure to silver nanoparticles at freshwater mussels were found. The aim of this study is investigate the acute and chronic effects of silver nanoparticles on freshwater mussels *Unio delicatus* in terms of total hemocyte count (THC), lipid peroxidation and glutathione.

2. Material and Method

2.1. Test Organisms and Acclimation to Laboratory

Freshwater mussels *Unio delicatus* (mean weight 36.3±4.8 g, mean length 5.2±0.1 cm, mean thickness 2.2±0.2 cm, mean height 1.5±0.1 cm; N=60) acquired from local fishermen in Gölbaşı Lake (Hatay) were used in this study. Freshwater mussels were transported in aerated water and placed in 15 L aquaria containing 10 L of pre-rested tap water without chlorine (1 mussel/L) in the laboratory. Mussels were acclimatized to laboratory conditions for 2 weeks. During this period, the aquarium water was altered by siphoning 50% every two days and the mussels were fed with Spirulina sp. The aquaria water was measured by YSI Professional Plus Multiparameter Instrument (USA) in terms of water quality during the acclimation period. The mean values (mean±SEM) of physicochemical parameters of water are as follows: temperature 21.9±0.25ºC; dissolved oxygen 6.2±0.56 mg/L; pH 7.5±0.2; conductivity: 201.04±0.4 mS/cm; salinity; 0.19±0.02. This study is not subject to HADYEK permission in accordance with Article 8 (k) of the "Regulation on Working Procedures and Principles of Animal Experiments Ethics Committees".

2.2. Exposure to AgNPs

Metal based AgNPs were obtained from Nanografi (Turkey) with the particle size specified as: 18 nm and >99.995% purity. Shape of AgNPs were spherical and crystal structure was cubic. The application concentrations of AgNPs were determined as 1 and 10 mg/L by reviewing literature studies [13], [14]. After freshwater mussels were placed in aquaria (10 mussels/L), 500 mL of aquarium water was taken, AgNPs were added at the determined concentrations and sonicated. After sonication by Ultasons (J.P. Selecta, Spain), AgNPs were added to the aquaria. The mussels were exposed to 1 and 10 mg/L AgNPs for 7 and 21 days [15]. There was one control group (aquarium water and mussels) in the experiments. Aquarium water quality parameters were measured during the experimental period (temperature 22±0.3ºC; dissolved oxygen 6.4±0.2 mg/L; pH 7.8±0.5; conductivity: 200.05±0.6 mS/cm; salinity; 0.20±0.01). After each treatment period, 10 mussel samples were taken and hemolymph tissues were removed with a 2.5 mL syringe after measuring biological data. Then, the gill (G) and digestive gland (DG) tissues of mussels were removed. The tissues were stored at -80ºC (Wisd Simplified Freezing System, WiseCryo Daihan, South Korea) until biochemical analysis.

2.3. Total Hemocyte Counts (THCs)

Hemolymph tissue was collected from freshwater mussels according to the method of [16]. The THCs were counted using a light microscope.

2.4. Biochemical Analysis

The lipid peroxidation was measured based on malondialdehyde (MDA) production in gills and digestive glands, the method of [17] was applied and the MDA levels were determined by reading at 535 and 520 nm using spectrophotometer (Biochrom Libra S22, UK). Briefly, following homogenization of 100 mg of tissue with 1/5 of 1.15% KCl buffer, 500 µL of homogenate sample was taken. The homogenate mixed with 3 mL of 1% phosphoric acid and 1 mL of 0.6% thiobarbutic acid was kept in a hot water bath for 45 minutes. Then, 4 mL of butanol was added and centrifuged at 3000 rpm for 5 minutes. The supernatant portion was read by spectrophotometer. The measurement of the glutathione levels in gills and digestive glands, the method of [18] was applied and the glutathione levels were determined by reading at 410 and 420 nm using spectrophotometer (Biochrom Libra S22, UK).

2.5. Statistical Analysis

To evaluate the experimental results obtained; total hemocyte count, glutathione and MDA determination results were subjected to normal distribution according to Kolmogorov-Smirnov normality test and homogeneity of variances tests to determine the differences between the experimental groups. After all samples met these conditions, one-way ANOVA test was performed and significance levels were determined with GraphPad 5 statistical data analysis program.

3. Results and Discussion

The acute and chronic effects of AgNPs on freshwater mussels was evaluated in the present study. Within the scope of the study, total hemocyte counts, which are physiological parameters, and lipid peroxidation and glutathione levels, which are biochemical parameters, were examined in freshwater mussels exposed to 1 and 10 mg/L silver nanoparticles for 7 and 21 days. The alterations in total hemocyte counts of freshwater mussels exposed to AgNPs for 7 and 21 days are shown in Figure 1. There was an increase in the THCs in the mussels exposed to AgNPs for 7 days compared to the control group (p>0.05). At 21 days of exposure, a decrease in total hemocyte count was observed in the experimental groups compared to the control group. There was a 1.7-fold decrease between the control group and the 10 mg/L AgNPs exposed group (p=0.035).
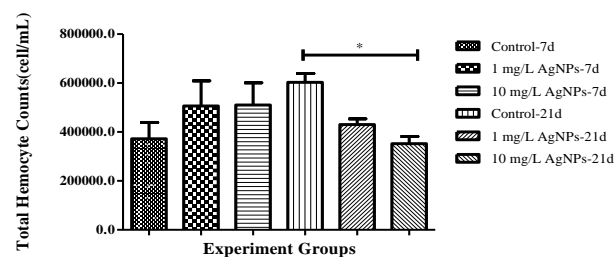

Figure 1. Changes in total hemocyte counts of freshwater mussels after exposure to silver nanoparticles.

The effect of silver nanoparticles on lipid peroxidation levels in gill and digestive gland tissues is shown in Figure 2. As a result of exposure of mussels to 1 and 10 mg/L silver nanoparticles for 7 days, gill and digestive gland MDA levels decreased compared to the control group (p>0.05). In 21-day exposure, an increase in MDA levels occurred in the digestive gland tissues exposed to both 1 mg/L AgNPs and 10 mg/L AgNPs (p>0.05).
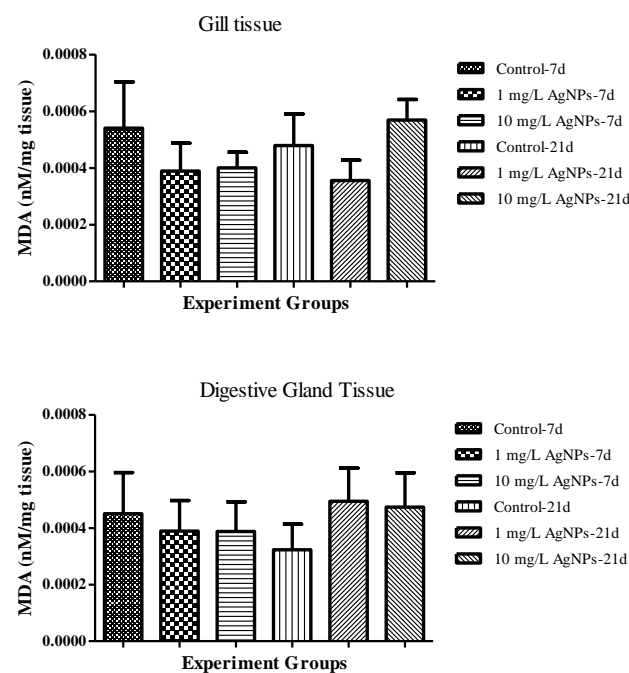

Figure 2. Changes in MDA levels in gill and digestive gland tissues of freshwater mussels after exposure to silver nanoparticles.

The effect of silver nanoparticles on glutathione levels in gill and digestive gland tissues of freshwater mussels is shown in Figure 3. As a result of exposure of mussels to 1 and 10 mg/L AgNPs for 7 days, gill glutathione levels increased 3.3 and 4.1 times compared to the control group. In 21-day exposure, a decrease was observed in the 1 mg/L group compared to the control group and an increase was observed in the 10 mg/L group. The glutathione

levels of digestive gland tissues were decreased in 7-day exposure and increased in 21-day exposure.
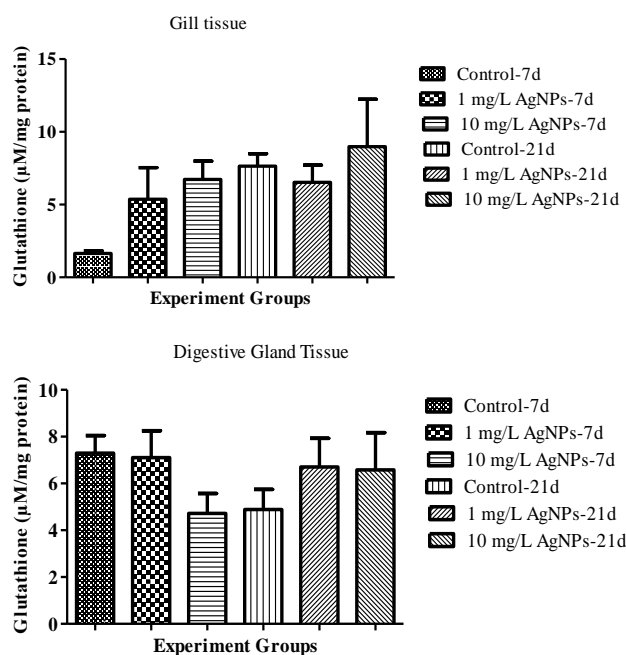

Figure 3. Changes in glutathione levels in gill and digestive gland tissues of freshwater mussels after exposure to silver nanoparticles.

THCs are commonly used physiological/immunological parameter to assess the health status of mussels and indicator of the mussels to stressors such as pollutants, disease, and changes in environmental conditions [8], [9], [16], [19], [20]. In the current study, significant decreases in the THCs occurred with increasing exposure time to nanoparticles. Similar decreases in the THCs were observed in bivalves *Mytilus coruscus* under TiO NPs [21], [22]. These results demonstrate the immunological effects induced by mussels and nanoparticles.

MDA is a reactive compound that is commonly used as a marker of lipid peroxidation and are often used as an indicator of the extent of lipid peroxidation in tissues exposed to oxidative stress [23]. In the context of mussels, measuring MDA levels can provide valuable information on the health of these organisms and the potential impacts of environmental stressors, such as pollution or exposure to nanoparticles, on their cellular and physiological functions [24]. The gill and digestive gland tissues are particularly vulnerable to the damaging effects of oxidative stress caused by pollutants including

nanoparticles [25], [26]. In this study, it was observed that there was a change in MDA levels in the gill and digestive gland tissues from the groups treated with AgNPs. Studies have shown that exposure to nanoparticles indicates similar increase or decrease on lipid peroxidation in gill and digestive gland tissues of mussels, which may lead to cellular damage and dysfunction [24], [26], [27], [28]. A significant increase in MDA levels were observed at 10 μg/L AgNPs in *Mytilus galloprovincialis* [1].

One potential mechanism by which NPs can induce toxicity is through the modulation of glutathione (GSH) levels. GSH is an important antioxidant and detoxification molecule in the organisms, and changes in its levels can have significant impacts on cellular functions [29], [30]. Researches shown that exposure to NPs caused the changes in GSH levels in the mussel tissues including gills and digestive gland [29], [31], [32].

4. Conclusion and Suggestions

In this study, the first response to exposure to AgNPs was alterations in physiological parameter of the mussels. Acute exposure to AgNPs caused increase in the THCs, while chronic exposure to AgNPs caused a significant decrease. Changes in MDA and GSH levels are not significant in the different tissues of AgNPs exposed mussels. As a result of the study, AgNPs caused alterations in the physiological and biochemical parameters of freshwater mussels.

Contributions of the authors

Plan and design of the study: İlker Şimşek, Pınar Arslan ; Materials, methods and data collection: Pınar Arslan, Aysel Çağlan Günal ; Data analysis and interpretation: Özgür Kuzukıran, Ayhan Filazi ; Writing and critical evaluation: İlker Şimşek, Pınar Arslan, Aysel Çağlan Günal, Özgür Kuzukıran, Ayhan Filazi.

Conflict of Interest Statement

There is no conflict of interest between the authors.

Statement of Research and Publication Ethics

The study is complied with research and publication ethics

References

[1] A. Ale, G. Liberatori, M. L. Vannuccini, E. Bergami, S. Ancora, G. Mariotti, N. Bianchi, J. M.Galdopórpora, M. F. Desimone, J. Cazenave, and I. Corsi, ''Exposure to a nanosilver-enabled consumer product results in similar accumulation and toxicity of silver nanoparticles in the marine mussel *Mytilus galloprovincialis*,'' *Aquatic Toxicology*, vol. 211, pp. 46–56, March 2019.

[2] J. Zhao, X. Wang, S. A. Hoang, N. S. Bolan, M. B. Kirkham, J. Liu, X. Xia, and Y. Li, ''Silver nanoparticles in aquatic sediments: Occurrence, chemical transformations, toxicity, and analytical methods,'' *Journal of Hazardous Materials*, vol. 418, p. 126368, September 2021.

[3] M. Auguste, C. Ciacci, T. Balbi, A. Brunelli, V. Caratto, A. Marcomini, R. Cuppini, and L. Canesi, ''Effects of nanosilver on *Mytilus galloprovincialis* hemocytes and early embryo development,'' *Aquatic Toxicology*, vol. 203, pp. 107–116, August 2018.

[4] A. G. Şahin, and M. Karatepe, 2022: ''Vitamins A, E, C, β -carotene contents and MDA level of freshwater mussel, (*Unio elongatulus eucirrus* Bourguignat 1860) in the Karakaya Dam Lake,'' *Ege Journal of Fisheries and Aquatic Sciences*, vol. 39, no. 2, pp. 120-124, June 2022.

[5] A. G. Şahin, M. R. Gül, and M. Küçükyılmaz, ''Karakaya Baraj Gölü'ndeki Tatlı Su Midyesi (*Unio elongatulus eucirrus* Bourguignat 1860)'nin Ağır Metal Düzeylerinin Belirlenmesi,'' *Fırat Üniversitesi Fen Bilimleri Dergisi*i, vol. 28, no. 1, pp. 13-19, January 2016.

[6] M. Güler, D. Çoban, and B. Kırım, ''*Unio terminalis* (Bivalvia: Unionidae)' in üreme biyolojisi üzerine gözlemler,'' *Ege Journal of Fisheries and Aquatic Sciences*, vol. 34, no. 3, pp. 303-309, June 2017.

[7] F. Gagne, J. Auclair, P. Turcotte, and C. Gagnon, ''Sublethal Effects of Silver Nanoparticles and Dissolved Silver in Freshwater Mussels,'' *Journal of Toxicology and Environmental Health, Part A*, vol. 76, no. 8, pp. 479–490, February 2013.

[8] P. Arslan, ''Determinations of the effects of cyfluthrin on the hemocytes parameters of freshwater mussel (*Unio delicatus*),'' *Ege Journal of Fisheries and Aquatic Sciences*, vol. 39, no. 1, pp. 39-45, January 2022.

[9] P. Arslan, and A. Ç. Günal, ''Does Fipronil Affect on Aquatic Organisms? Physiological, Biochemical, and Histopathological Alterations of Non-Target Freshwater Mussel Species,'' *Water*, vol. 15, no. 2, p. 334, January 2023.

[10] T. Gomes, J. P. Pinheiro, I. Cancio, C. G. Pereira, C. Cardoso, and M. J. Bebianno, ''Effects of copper nanoparticles exposure in the mussel *Mytilus galloprovincialis*,'' *Environmental science & technology*, vol. 45, no. 21, pp. 9356-9362, October 2011.

[11] T. Gomes, O. Araújo, R. Pereira, A. C. Almeida, A. Crav, and M. J. Bebianno, ''Genotoxicity of copper oxide and silver nanoparticles in the mussel *Mytilus galloprovincialis*,'' *Marine environmental research*, vol. 84, pp. 51-59, March 2013.

[12] E. G. Canli, A. Baykose, L. H. Uslu, and M. Canli, ''Changes in energy reserves and responses of some biomarkers in freshwater mussels exposed to metal-oxide nanoparticles,'' *Environmental Toxicology and Pharmacology*, vol. 98, p.104077, March 2003.

[13] A. Katsumiti, D. Gilliland, I. Arostegui, and M. P. Cajaraville, ''Mechanisms of toxicity of Ag nanoparticles in comparison to bulk and ionic Ag on mussel hemocytes and gill cells,'' *PLoS One*, vol. 10, no. 6, p. e0129039, June 2015.

[14] M. Munari, J. Sturve, G. Frenzilli, M. B. Sanders, P. Christian, M. Nigro, and B. P. Lyons, ''Genotoxic effects of Ag2S and CdS nanoparticles in blue mussel (*Mytilus edulis*) haemocytes,'' *Chemistry and Ecology*, vol. 30, no. 8, pp. 719-725, March 2014.

[15] REACH, ''Guidance on Information Requirements and Chemical Safety Assessment,'' Chapter R.7b: Endpoint specific guidance Retrieved from https://echa.europa.eu/documents/10162/17224/information_requirements_r7b_en.pdf/1a551efc-bd6a-4d1f-b719-16e0d3a01919?t=1498476047712, 2017.

[16] H. Y. Yavuzcan, A. Ç. G. Benli, ''Nitrite toxicity to crayfish, *Astacus leptodactylus*, the effects of sublethal nitrite exposure on hemolymph nitrite, total hemocyte counts, and hemolymph glucose,'' *Ecotoxicology and Environmental Safety*, vol. 59, no. 3, pp. 370–375, November 2004.

[17] M. Mihara, and M. Uchiyama, ''Determination of malonaldehyde precursor in tissues by thiobarbituric acid test,'' *Analytical Biochemistry*, vol. 86, no. 1, pp. 271-278, May 1978.

[18] G. L. Ellman, ''Tissue sulfhydryl groups,'' *Archives of Biochemistry and Biophysics*, vol. 82, pp. 70-77, May 1959.

[19] H. E. Parry, and R. K. Pipe, ''Interactive effects of temperature and copper on immunocompetence and disease susceptibility in mussels (*Mytilus edulis*),'' *Aquatic toxicology*, vol. 69, no. 4, pp. 311-325, September 2004.

[20] Y. Sui, H. Kong, Y. Shang, X. Huang, F. Wu, M. Hu, and Y. Wang, ''Effects of short-term hypoxia and seawater acidification on hemocyte responses of the mussel *Mytilus coruscus*,'' *Marine pollution bulletin*, vol. 108, no. 1-2, pp. 46-52, July 2016.

[21] X. Huang, D. Lin, K. Ning, Y. Sui, M. Hu, W. Lu, and Y. Wang, ''Hemocyte responses of the thick shell mussel *Mytilus coruscus* exposed to nano-TiO2 and seawater acidification,'' *Aquatic Toxicology*, vol. 180, pp. 1-10, September 2016.

[22] T. Wang, X. Huang, X. Jiang, M. Hu, W. Huang, and Y. Wang, ''Differential in vivo hemocyte responses to nano titanium dioxide in mussels: Effects of particle size,'' *Aquatic Toxicology*, vol. 212, pp. 28-36, July 2019.

[23] D. Tsikas, ''Assessment of lipid peroxidation by measuring malondialdehyde (MDA) and relatives in biological samples: Analytical and biological challenges,'' *Analytical biochemistry*, vol. 524, pp. 13-30, October 2017.

[24] F. Gagne, J. Auclair, P. Turcotte, and C. Gagnon, ''Sublethal Effects of Sılver Nanopartıcles and Dıssolved Silver in Freshwater Mussels,'' *Journal of Toxicology and Environmental Health, Part A*, vol. 76, pp.479–490, February 2013.

[25] E.A. Almeida, A. C. D. Bainy, A. L. Dafre, O. F. Gomes, M. H. Medeiros, and P. Di Mascio, ''Oxidative stress in digestive gland and gill of the brown mussel (*Perna perna*) exposed to air and re-submersed,'' *Journal of Experimental Marine Biology and Ecology*, vol. 318, no.1, pp. 21-30, May 2005.

[26] S. Tedesco, H. Doyle, J. Blasco, G. Redmond, and D. Sheehan, ''Oxidative stress and toxicity of gold nanoparticles in *Mytilus edulis*,'' *Aquatic toxicology*, vol. 100, no. 2, pp. 178-186, March 2010.

[27] M. Dellali, A. Khallouli, A. H. Harrath, F. Falodah, S. Alwasel, H. Beyrem, and F. Boufahja, ''Effects of Au/TiO 2 metallic nanoparticles on *Unio ravoisieri*: Assessment through an oxidative stress and toxicity biomarkers,'' *Environmental Science and Pollution Research*, vol. 28, pp. 18176-18185, January 2021.

[28] S. E. Gürkan, ''Impact of nickel oxide nanoparticles (NiO) on oxidative stress biomarkers and hemocyte counts of *Mytilus galloprovincialis*,'' *Biological Trace Element Research*, vol. 200, no. 7, pp. 3429-3441, March 2022.

[29] L. Canesi, A. Viarengo, C. Leonzio, M. Filippelli, and G. Gallo, ''Heavy metals and glutathione metabolism in mussel tissues,'' *Aquatic Toxicology*, vol. 46, no. 1, pp. 67-76, June 1999.

[30] F. Regoli, and G. Principato, ''Glutathione, glutathione-dependent and antioxidant enzymes in mussel, *Mytilus galloprovincialis*, exposed to metals under field and laboratory conditions: implications for the use of biochemical biomarkers,'' *Aquatic toxicology*, vol. 31, no. 2, pp. 143-164, February 1995.

[31] H. Falfushynska, L. Gnatyshyna, I. Yurchak, I. Sokolova, and O. Stoliar, ''The effects of zinc nanooxide on cellular stress responses of the freshwater mussels *Unio tumidus* are modulated by elevated temperature and organic pollutants,'' *Aquatic Toxicology*, vol. 162, pp. 82-93, May 2015.

[32] X. Huang, Z. Liu, Z. Xie, S. Dupont, W. Huang, F. Wu, and Y. Wang, ''Oxidative stress induced by titanium dioxide nanoparticles increases under seawater acidification in the thick shell mussel *Mytilus coruscus*,'' *Marine environmental research*, vol. 137, pp. 49-59, June 2018.

Optimization of Hybrid Composite Laminates with Various Materials using the GA/GPSA Hybrid Algorithm for Maximum Dimensional Stability

Hacer GEÇMEZ[1], Hamza Arda DEVECİ[2*]

[1] Department of Mechanical Engineering, Graduate School of Natural and Applied Sciences, Erzincan Binali Yıldırım University, Yalnızbağ Yerleşkesi, 24002, Erzincan, Turkey.
[2] Department of Mechanical Engineering, Faculty of Engineering and Architecture, Erzincan Binali Yıldırım University, Yalnızbağ Yerleşkesi, 24002, Erzincan, Turkey.
(ORCID: 0000-0003-3255-1504) (ORCID: 0000-0001-9926-8768)

Abstract

In this study, it is aimed at obtaining the highest dimensional stability against temperature changes in fiber-reinforced hybrid composite laminates considering eight different composite materials: Aramid/Epoxy, AS4/Epoxy, Boron/Epoxy, E-Glass/Epoxy, IM6/Epoxy, GY70/Epoxy, Kevlar49/Epoxy, and Spectra/Epoxy. The study focuses on finding the optimum continuous and traditional fiber angle orientations for the hybrid composite plates that would provide the lowest coefficients of thermal expansion. For this purpose, two different laminate sequences were investigated, each including two materials. A hybrid algorithm combining a genetic algorithm and a generalized pattern search algorithm was used in the optimization. A great number of hybrid design problems were solved repeatedly, and their results were compared both within themselves and to the optimum non-hybrid laminate results. Furthermore, the thermal durability of the selected optimum hybrid designs was evaluated using Tsai-Wu failure and Hashin-Rotem criteria. The results reveal that a substantial increase in dimensional stability can be achieved by stacking sequence optimization of hybrid composite laminates with multiple material selections, and this hybrid design approach can offer the desired laminated composite structures for aerospace applications required to withstand extreme temperature changes.

1. Introduction

Fiber-reinforced composites have become indispensable materials in many engineering applications, including on land, at sea, and in the air, as well as providing many advantages over other traditional materials. With the development of technology, the use of these alternative materials has been an important subject in line with the different needs and expectations of industry. In this regard, it can be said that dimensionally stable composite materials are those materials desired to meet the expectations in satellite applications today. Fiber-reinforced composite materials have the best potential to meet the need for dimensional stability since their tailorability properties give them a chance to obtain very small geometrical changes when exposed to environmental influences such as humidity and temperature.

Dimensional stability is directly related to the material properties, including the coefficient of thermal expansion (CTE) and the coefficient of moisture expansion. Besides, thermal and moisture effects are parameters that should not be disregarded for the dimensional stability of polymer matrix composites and change the mechanical properties of the materials significantly. Unexpected results may emerge during service when these parameters are not

---

considered in the design of composite material applications in engineering. For this reason, there is much ongoing research that investigates the thermal and moisture effects on laminated composite structures in the literature. For instance, Lim and Hong [1] used a modified shear delay analysis to examine the effects of the stiffness reduction and thermal expansion coefficient variation caused by transverse cracks in cross-layer laminate composites. The results showed that transverse cracks reduce the effective stiffness and coefficient of thermal expansion of composite laminates; at the same time, the stiffness reduction and change in the laminate thermal expansion coefficient due to transverse cracks were deeply affected by the laminate configuration. Yoon and Ki [2] studied the estimation of the coefficients of thermal expansion to determine the temperature variation of Carbon/Epoxy laminate materials. For this purpose, a computational method is proposed to estimate the variation of the coefficients of thermal expansion of an overall laminate for temperature variation. In the research, elastic properties and coefficients of thermal expansion in the material's main directions were measured in the range from room temperature to curing temperature and characterized as temperature functions. The coefficients of thermal expansion of laminates with different angles were measured and compared with the predicted ones. Experimental results show that changes in the coefficients of thermal expansion of an overall laminate for temperature change can be well estimated using the proposed method. Kim and Crasto [3] considered aerospace structural materials and investigated the changes in coefficients of thermal expansion using two representative materials. It was aimed at accurately determining low CTE values in the study. The results show that the change in coefficients of thermal expansion due to ply cracking in the cross-ply laminates can be quantitatively predicted under thermal cycling and mechanical loadings.

On the other hand, optimum stacking sequence design for dimensionally stable composite structures has been considered in the literature to prevent and minimize the negative effects of thermal and moisture factors. However, there are limited studies on optimum stacking sequence design for dimensionally stable composite structures. As pioneers in this field, Riche and Gaudin [4] studied the effectiveness of optimizing fiber orientation angles to minimize plate bending problems and achieve dimensional stability in composite structures. By optimizing the stacking sequences, the researchers could deliver the desired performance

and reduce the negative effects of production-related issues. Khalil et al. [5] investigated the effect of hygrothermal residual stresses on the optimum design of laminated composite materials, which was analyzed theoretically. In this study, composite materials exposed to different mechanical, thermal, and humidity loads were investigated. The results showed that among the selected materials, E-glass/epoxy and Kevlar/epoxy have greater moisture absorption capacity compared to other materials when designing optimum composite laminates under thermal and moisture loadings. In addition, the optimum material properties based on the thermal expansion coefficient of the selected composite laminates were investigated by Zhu and Sun [6] using an evolution algorithm. As a result of the research, it was determined that the ratio of plane shear modulus to fiber directional modulus of elasticity has a significant effect on the thermal expansion coefficient. Diaconu and Sekine [7] considered the temperature and moisture parameters affecting the composite materials and suggested an optimization problem to provide minimum displacement in terms of transverse characteristics. In the study of Aydin and Artem [8], it was aimed at finding the optimum stacking sequences of symmetric and balanced laminated carbon/epoxy composites with different numbers of layers. Both single-objective and multi-objective optimization approaches were utilized in the design process. The results show that stacking sequences with lower thermal expansion coefficients and higher elastic modulus can be obtained by continuous laminate designs rather than conventional ones.

Besides the optimization for dimensionally stable composites using a single composite material in laminates, this process may include designing the composite material to have more than one fiber or matrix material. In this regard, optimization studies of hybrid composite laminates constituted using numerous composite materials to ensure maximum dimensional stability have been present in the literature. For instance, in the study of Zhang et al. [9], an optimization was conducted to estimate the thermal expansion coefficients and mechanical properties of hybrid composites used in aerospace. As a result of the dimensional stability optimization, both the optimal design of hybrid composites with zero thermal expansion coefficient and the optimum design of hybrid composite plates with minimum thermal expansion coefficient were found. Bressan et al. [10] addressed the issue of hybrid material component optimization and design patterns made of carbon-epoxy laminates with low thermal expansion. The effects of selected hybrid materials on the

behavior of the composite, such as structural and thermo-elastic mismatches, were investigated using evolutionary strategy algorithms. They reported that hybrid composite materials used in satellite equipment are optimal in terms of minimum mass and high resonance.

Hybridization of laminates can also provide improvements for the other objectives of composite materials. For example, Adali and Duffy [11], with a single-purpose approach, optimized the fiber orientation of antisymmetric and angle-ply hybrid layer structures to further increase cost-effectiveness with a natural frequency constraint. Adali and Verijenko [12] presented a study in which natural frequency, frequency separation, and cost factors were discussed for hybrid graphite-glass/epoxy inter-ply hybrid layer structures, and at the end, optimum fiber orientations of the hybrid composites were obtained. Abachizadeh and Tahani [13] proposed a procedure that covers the design and optimization of a graphite-glass/epoxy hybrid composite with a symmetrical inter-ply hybrid layer structure. Both the maximum natural frequency and minimum cost objectives based on the multi-objective optimization approach have been successfully carried out. It was reported that hybridization provides a reasonable reduction in fundamental frequency for a remarkable reduction in material cost. Aydin and Savran [14] aimed to find the number of high-hardness and cheaper laminates that maximize the fundamental frequency and minimize the cost with the multi-objective optimization approach of stacking sequence design and optimization in inter-ply hybrid composite structures. The results show that the proposed optimum graphite-flax/epoxy composite structure outperforms in terms of maximum fundamental frequency and minimum cost.

As seen in the literature, the studies generally consider a limited number of composite materials in the hybridization process and conventional fiber angles in the stacking sequence designs. Furthermore, these studies did not propose a general, comprehensive, and optimum hybrid design

procedure using many different composite materials using a novel hybrid algorithm not utilized in the field. In this respect, in the present study, the optimum stacking sequence designs of 16-layered symmetric hybrid composite laminates considering various materials were investigated to obtain the lowest thermal expansion coefficients. Aramid/Epoxy, AS4/Epoxy, Boron/Epoxy, E-Glass/Epoxy, IM6/Epoxy, GY70/Epoxy, Kevlar49/Epoxy, and Spectra/Epoxy composite materials were used to hybridize the laminates. Numerous optimization problems were constituted considering continuous, discrete fiber angles and two different material sequences in laminates. These optimum design problems were solved by a powerful hybrid algorithm that is a combination of a genetic algorithm and a generalized pattern search algorithm. Afterward, by selecting the best dimensionally stable designs among all the optimum designs, it was checked whether the thermal stresses that will occur under certain positive and negative temperature changes are in the safe zone with two different composite failure theories.

Considering the studies in the literature, it can be said that the effect of hybridization of multiple materials in specific material sequences and optimization of stacking sequences on the dimensional stability of composite laminates was not thoroughly considered. In this regard, this study proposes a reliable optimum hybrid composite design procedure for maximum dimensional stability in applications that require minimum thermal stresses, including a verification study of the optimum design procedure by testing the designs under thermal loading.

In this study, objective functions in the optimization problems concerning dimensionally stable composite laminates were constituted based on classical lamination theory. Figure 1 shows a representative laminated composite plate with global and local coordinates subjected to thermal loading, ΔT.
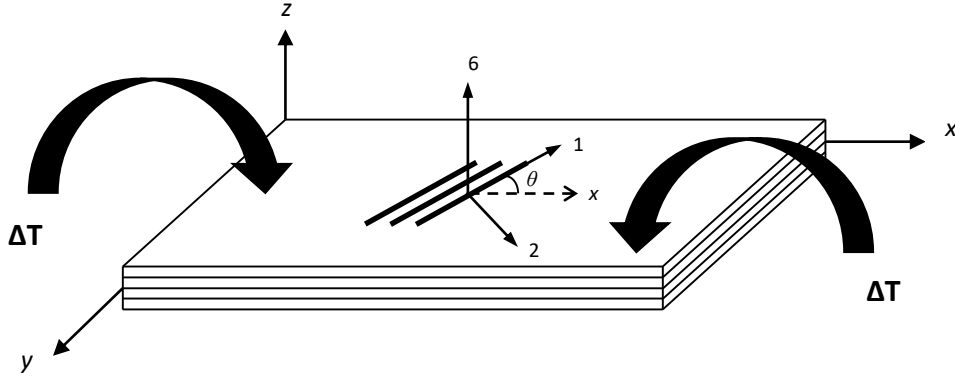
Figure 1. Layered composite plate with global and local coordinates [16]

2. Mechanics of Dimensional Stability

In this study, objective functions in the optimization problems concerning dimensionally stable composite laminates were constituted based on classical lamination theory (CLT) [15]. Figure 1 shows a representative laminated composite plate with global and local coordinates subjected to thermal loading, ΔT.

According to the CLT, the relation between stress and strain of an angled composite layer (k) can be given as follows:

$$\begin{bmatrix} \sigma_x \\ \sigma_y \\ \tau_{xy} \end{bmatrix}_k = \begin{bmatrix} \bar{Q}_{11} & \bar{Q}_{12} & \bar{Q}_{16} \\ \bar{Q}_{12} & \bar{Q}_{22} & \bar{Q}_{26} \\ \bar{Q}_{16} & \bar{Q}_{26} & \bar{Q}_{66} \end{bmatrix}_k \begin{bmatrix} \varepsilon_x \\ \varepsilon_y \\ \gamma_{xy} \end{bmatrix}_k \qquad (1)$$

where $[\bar{Q}_{ij}]$ (i, j = x, y) is transformed reduced stiffness matrix and $[\varepsilon_{ij}]$ (i, j = x, y) indicates mid-plane strains.

In-plane normal resultant forces, N_x, N_y, and shear resultant force, N_{xy} applied on composite plates can be defined as

$$\begin{bmatrix} N_x \\ N_y \\ N_{xy} \end{bmatrix}_k = \begin{bmatrix} A_{11} & A_{12} & A_{16} \\ A_{12} & A_{22} & A_{26} \\ A_{16} & A_{26} & A_{66} \end{bmatrix}_k \begin{bmatrix} \varepsilon_x^0 \\ \varepsilon_y^0 \\ \gamma_{xy}^0 \end{bmatrix} \qquad (2)$$

in which [A] corresponds to the extensional stiffness matrix and [ε^0] is the mid-plane strain matrix of the plate. The elements of [A] matrix are expressed as

$$A_{ij} = \sum_{k=1}^{n} [\bar{Q}_{ij}]_k (h_k - h_{k-1}) \qquad (3)$$

The behavior of laminated composite plates under thermal effects is considered in this study. In this regard, in-plane thermal loads per unit length that occur in a lamina can be expressed as

$$\begin{bmatrix} N_x \\ N_y \\ N_{xy} \end{bmatrix}_k = \Delta T \sum_{k=1}^{n} \begin{bmatrix} \bar{Q}_{11} & \bar{Q}_{12} & \bar{Q}_{16} \\ \bar{Q}_{12} & \bar{Q}_{22} & \bar{Q}_{26} \\ \bar{Q}_{16} & \bar{Q}_{26} & \bar{Q}_{66} \end{bmatrix}_k \begin{bmatrix} \alpha_x \\ \alpha_y \\ \alpha_{xy} \end{bmatrix} \qquad (4)$$

where ΔT is temperature change and $[\alpha]_k$ is the coefficient matrix of thermal expansion. The coefficients of thermal expansion (CTEs) of a composite laminate can be calculated by the following expression.

$$\begin{bmatrix} \alpha_x \\ \alpha_y \\ \alpha_{xy} \end{bmatrix} = \begin{bmatrix} \alpha_x \\ \alpha_y \\ \alpha_{xy} \end{bmatrix}_{\Delta T=1} \begin{bmatrix} A_{11}^* & A_{12}^* & A_{16}^* \\ A_{12}^* & A_{22}^* & A_{26}^* \\ A_{16}^* & A_{26}^* & A_{66}^* \end{bmatrix} \begin{bmatrix} N_x^T \\ N_y^T \\ N_{xy}^T \end{bmatrix} \qquad (5)$$

in which [A^*] =[A]$^{-1}$.

It can be noted that the coefficient of thermal expansion must be 10^{-6} or less to achieve high dimensional stability in laminated composite structures.

3. Failure Criteria

In our study, several optimum laminate designs were selected at the end of the optimization to assess their dimensional stability considering the first ply failure under thermal loading conditions. For this purpose, Tsai-Wu and Hashin-Rotem failure criteria were used to analyze the strength of optimum stacking sequence designs subjected to thermal [17], [18].

110

3.1. Tsai-Wu Failure Criterion

The Tsai-Wu failure criterion based on total strain energy was derived from the von Mises yield criterion for laminated composite materials. According to the criterion, a lamina of a composite plate is considered to have failed if the following condition is satisfied:

$$F_1\sigma_1 + F_2\sigma_2 + F_6\tau_{12} + F_{11}\sigma_1^2 + F_{22}\sigma_2^2 \\ + F_{66}\tau_{12}^2 + 2F_{12}\sigma_1\sigma_2 < 1 \tag{6}$$

where σ_1 and σ_2 are maximum normal stresses in fiber and transverse directions, respectively. τ_{12} is maximum shear stress.

Failure tensor expressions, F_{ij} $(i,j=1,2,6)$ denoted in the equation are also given below.

$$F_1 = \frac{1}{(\sigma_1^T)_{ult}} - \frac{1}{(\sigma_1^C)_{ult}}, F_2 = \frac{1}{(\sigma_2^T)_{ult}} - \frac{1}{(\sigma_2^C)_{ult}},$$
$$F_{11} = \frac{1}{(\sigma_1^T)_{ult}} - \frac{1}{(\sigma_1^C)_{ult}},$$
$$F_{12} = -\frac{1}{2}\sqrt{\frac{1}{(\sigma_1^T)_{ult}\cdot(\sigma_1^C)_{ult}}\cdot\frac{1}{(\sigma_2^T)_{ult}\cdot(\sigma_2^C)_{ult}}}, \tag{7}$$
$$F_{22} = \frac{1}{(\sigma_2^T)_{ult}(\sigma_2^C)_{ult}},$$
$$F_{66} = \frac{1}{(\tau_1)_{ult}^2}$$

where $(\sigma_1^T)_{ult}$ is ultimate tensile strength in longitudinal direction, $(\sigma_1^C)_{ult}$ is compressive strength in longitudinal direction, $(\sigma_2^T)_{ult}$ is tensile strength in transverse direction, $(\sigma_2^C)_{ult}$ is compressive strength in transverse direction, and $(\tau_1)_{ult}^2$ is ultimate shear strength.

3.2. Hashin-Rotem Failure Criterion

Fiber failure of tensile stress in unidirectional lamina $(\sigma_1 > 0)$

$$\sigma_1 = (\sigma_1^T)_{ult} \tag{8}$$

Fiber failure of compressive stress in unidirectional lamina $(\sigma_1 < 0)$

$$-\sigma_1 = (\sigma_1^C)_{ult} \tag{9}$$

Matrix failure of tensile stress in unidirectional lamina $(\sigma_2 > 0)$

$$\left(\frac{\sigma_2}{(\sigma_2^T)_{ult}}\right)^2 + \left(\frac{\tau_{12}}{(\tau_{12})_{ult}}\right)^2 = 1 \tag{10}$$

Matrix failure of compressive stress in unidirectional lamina $(\sigma_2 < 0)$

$$\left(\frac{\sigma_2}{(\sigma_2^C)_{ult}}\right)^2 + \left(\frac{\tau_{12}}{(\tau_{12})_{ult}}\right)^2 = 1 \tag{11}$$

4. Optimization

Stochastic optimization algorithms are generally preferred to solve the optimization problems of composite laminates since they are very capable of finding global optima in the problems, despite the more complex mathematical nature of composite materials than conventional materials. In this study, a hybrid algorithm consisting of a genetic algorithm (GA) and a generalized pattern search algorithm (GPSA) was used. The GA/GPSA hybrid algorithm was created using the MATLAB Optimization Toolbox [19].

Hybrid algorithms generally aim to create a new powerful algorithm by combining the superior features of two different algorithms and, thus, achieving the most accurate result in the optimization. Hybrid algorithms are used in many fields, such as engineering, for the solution of complex problems in the literature.

Genetic algorithm (GA) was discovered in 1975 by John Holland et al. It is a stochastic search method that carries Charles Darwin's theory of natural selection to the computer environment by modeling Darwin's theory of biological evolution, which is based on the survival of the best and aims to constantly reach the best [20]. GA aims to reach the optimum solution by determining the global optimum solution among more than one possible solution to a problem by determining the appropriate algorithm parameters [21]. GA randomly selects a population of individuals to begin its research. Each member of the population has a chromosome that encodes certain traits and assigns a degree of fitness according to specifications. This fitness rating is used to find designs that outperform their competitors. In the preceding step, the desired genetic material is used to protect a new part. This part pays off by applying more operators like genetic processing called gene crossover, gene mutation, and substitution. This process is repeated over many generations until the optimum value is achieved [22].

The second algorithm, the generalized pattern search algorithm (GPSA), was defined by Torczon [23] for the undifferentiated, unconstrained optimization of functions and then expanded to consider nonlinearly constrained optimization problems. GPSA approaches the most suitable point or points that will lead the problem to a global solution. Direct search does not require any gradient knowledge of the objective function and can be used to solve problems where the objective function is not differentiable, stochastic, or continuous.

The optimization method, which states how the hybrid algorithm GA used in the design works and interacts with GPSA, is given in Figure 2 and explained step by step.

Step 1. Starting with GA, all possible solutions in the search space are encoded as sequences.

Step 2. Usually, a random solution set is chosen and considered as the initial population.

Step 3. A fitness value is calculated for each array; the found fitness values show the solution quality of the arrays.

Step 4. A group of sequences is randomly selected according to a certain probability value, multiplication is performed, and the fitness values of the new individuals are calculated.

Step 5. The crossover operator is used to create new chromosomes with better qualities than the previous generation.

Step 6. The mutation operation generates new chromosomes from existing chromosomes.

Step 7. At the end of the GA, the optimal solution obtained is used as a starting point for the GPSA.

Step 8. GPSA starts the search with the first solution x_0 and obtains the initial mesh size Δ_0^m.

Step 9. In the search phase, if it finds a solution with an objective function value lower than the best solution, the algorithm stops.

Step 10. If the termination criteria are not met, the algorithm goes into the polling phase and creates a series of neighboring network points x_i^m by multiplying the current mesh size by each pattern vector $\{d_i\}$.

Step 11. Fixed directional pattern vectors, points to look for at each iteration used to clarify and define arguments in the objective function; the highest base with 2N vectors and the lowest base with N+1 vectors, usually consisting of N positive and B negative vectors.

Step 12. In the *k*th iteration step, GPSA probes all network points by calculating objective function values to find a satisfying point.

Step 13. If the polling was successful, that is, an improved point is found, it is multiplied by the existing mesh size, and this point is updated with the new mesh size for the next iteration *k*+1. an optimized point, the mesh size is reduced, and this current point is reused for the next iteration.

Step 14. This process continues with many iterations until the global optimum is reached. It is previously reported that the GA/GPSA hybrid algorithm finds better results compared to the previous results in the literature in test problems and shows very good performance in terms of speed and capability in searching design space for laminated composite problems [24].
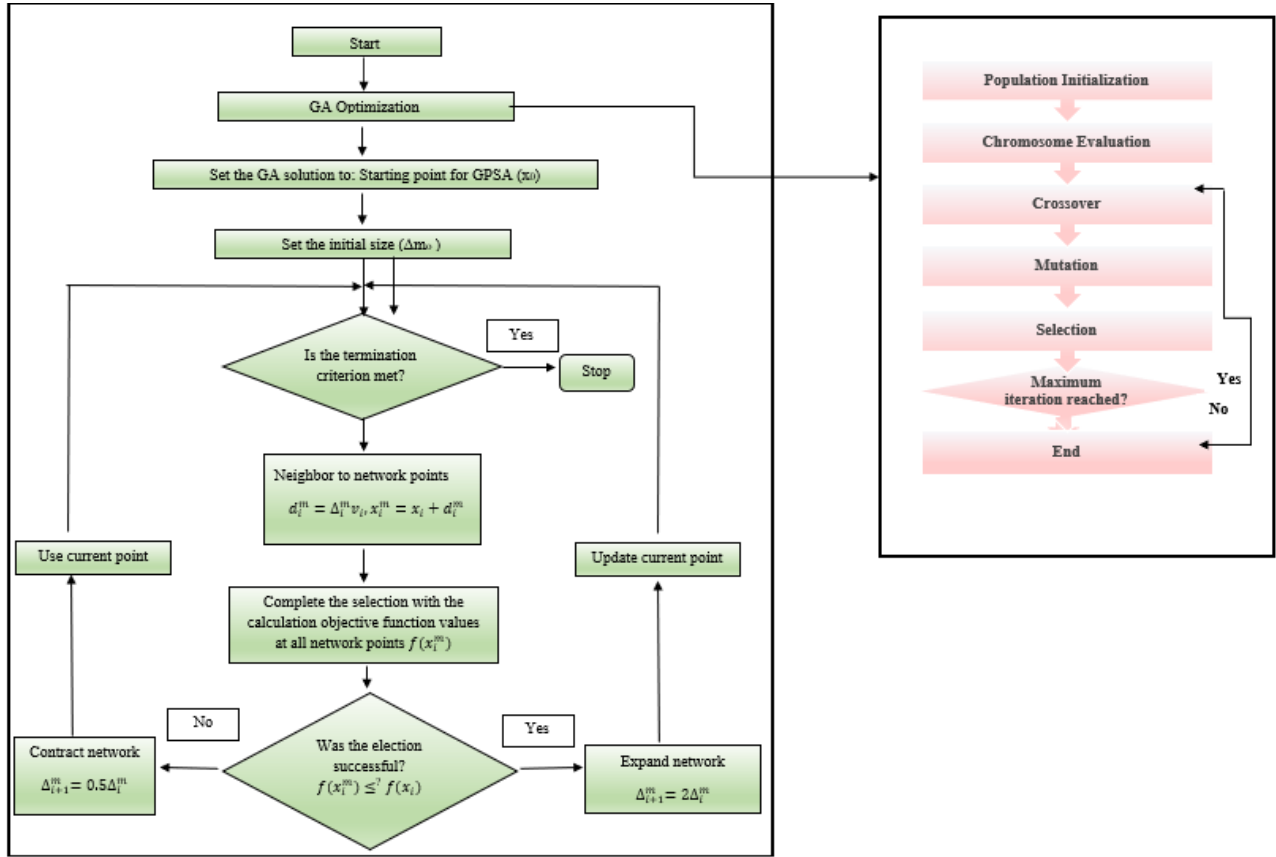
Figure 2. Flowchart of GA/GPSA hybrid algorithm

5. Problem Definition

The highest dimensional stability was investigated in hybrid composite laminates by minimizing the thermal expansion coefficients with the optimum stacking sequences. For this purpose, eight different composite materials, Aramid/Epoxy, AS4/Epoxy, Boron/Epoxy, E-glass/Epoxy, IM6/Epoxy, GY70/Epoxy, Kevlar49/Epoxy, and Spectra/Epoxy were selected to hybridize the laminates [25], [26]. The mechanical properties of these materials are presented in Table 1.

Table 1. Material properties used in layered composite design

Material property	Spectra/ Epoxy	E-Glass/ Epoxy	Kevlar 49/ Epoxy	AS4/ Epoxy	IM6/ Epoxy	Boron/ Epoxy	GY70/ Epoxy	Aramid/ Epoxy
E_1 (GPa)	31	43	76	138	172	240	325	95
E_2 (GPa)	3.4	9.7	5.5	10.3	10.0	18.6	6.2	5.1
G_{12} (GPa)	1.4	6.2	2.1	6.9	6.2	6.6	5.2	1.8
ν_{12}	0.32	0.26	0.34	0.30	0.29	0.23	0.26	0.34
X_1^T (MPa)	1100	1070	1380	2275	2760	1590	760	2100
X_2^T (MPa)	8	38	30	52	50	60	26	1200
X_1^C (MPa)	83	870	275	1590	1540	2930	705	30
X_2^C (MPa)	48	185	138	207	152	200	70	130
S_6 (MPa)	24	72	43	131	124	108	27	30
$\alpha_1 (10^{-6})/°C$	-11	6.4	-2	-0.1	-0.4	4.5	-0.5	-3.6
$\alpha_2 (10^{-6})/°C$	120	16	57	18	18	20	1895	60

The optimization problems for this study can be stated in general as follows:

Find: $\{\theta_k, n\}, \{-90:90\} \wedge \{0,45,90\}, k = 1, \cdots, n$
Minimize: α_x, α_y (single-objective functions)
Constraints: $[A/B]_{4S}$, $[A_4/B_4]_S$ material sequences
Algorithm: GA/GPSA hybrid algorithm (MATLAB Optimization Toolbox).

In the optimization problems, fiber angles as design variables in stacking sequences were considered as both continuous fiber angles $(-90°:90°)$ and traditional fiber angles $(0°, 45°, 90°)$. Thus, the number of design variables, n becomes 8. A hybrid composite lay-up was applied as geometrical constraints in two different material sequences, with two selected materials represented as A and B. These material sequences are shown schematically in detail in Figures 3(a) and 3(b). The thickness of each layer was taken as 0.125 mm. For optimization problems, objective functions, which are coefficients of thermal expansion, are minimized, considering them as single-objective functions. As the problems are single objectives, when a minimum thermal expansion coefficient in one direction was found, the other thermal expansion coefficient in the other direction was calculated considering the optimum stacking sequence of the related laminate. Five different optimization scenarios for hybrid and non-hybrid composite designs were considered.

5.1. Non-hybrid Optimization

Before the hybrid composite material optimization, non-hybrid stacking sequence optimization of the composite materials was performed by using both the continuous fiber angles (-90° - 90°) and traditional fiber angles (0°, 45°, 90°) to find the minimum thermal expansion coefficients (α_x and α_y) and compare them to the hybrid optimization results. The composite laminates were taken as 16-layer and symmetric in compliance with the hybrid problems.

5.2. Hybrid Optimization

In the optimization of hybrid composite plates, four optimization scenarios were considered, including both continuous and conventional fiber angles. These scenarios are briefly explained below:

Optimization scenario 1

In the first scenario, the $[A/B]_{4S}$ material sequence was considered for optimization, and the continuous fiber angles (-90° - 90°) were used in the search for design variables of the problems. GY70/Epoxy and AS4/Epoxy composites were selected as the A materials in the sequence. The A materials were hybridized with the composite materials, the B materials, which are selected from Table 1.

Optimization scenario 2

In the second scenario, the $[A/B]_{4S}$ material sequence was taken into consideration with 0°, 45°, and 90° traditional fiber angles to investigate the minimums of thermal expansion coefficients of the hybrid composite laminates. GY70/Epoxy and AS4/Epoxy composites are the A materials in the sequence. These composite materials were hybridized with the B materials selected from Table 1.

Optimization scenario 3

In the third scenario, the $[A_4/B_4]_S$ material sequence was considered with the continuous fiber angles (-90°- 90°) to obtain the optimum stacking sequences of the dimensionally stable hybrid composite laminates. Similarly, GY70/Epoxy and AS4/Epoxy composites are specified as the A materials in the sequence, and these materials were hybridized with the other materials given in Table 1 as the B materials.

Optimization scenario 4

As a final optimization scenario, the $[A_4/B_4]_S$ material sequence was used by considering 0°, 45°, and 90° traditional fiber angles in the stacking sequence optimization to reach the dimensionally stable hybrid composite laminates. Similarly, GY70/Epoxy and AS4/Epoxy composites are the A materials in the sequence, and these composite materials were hybridized with the materials in Table 1 as the B materials.

Considering these optimization scenarios, 198 optimization problems, of which 16 were for non-hybrid laminated composites and 182 were for hybrid laminated composites, were solved in total.
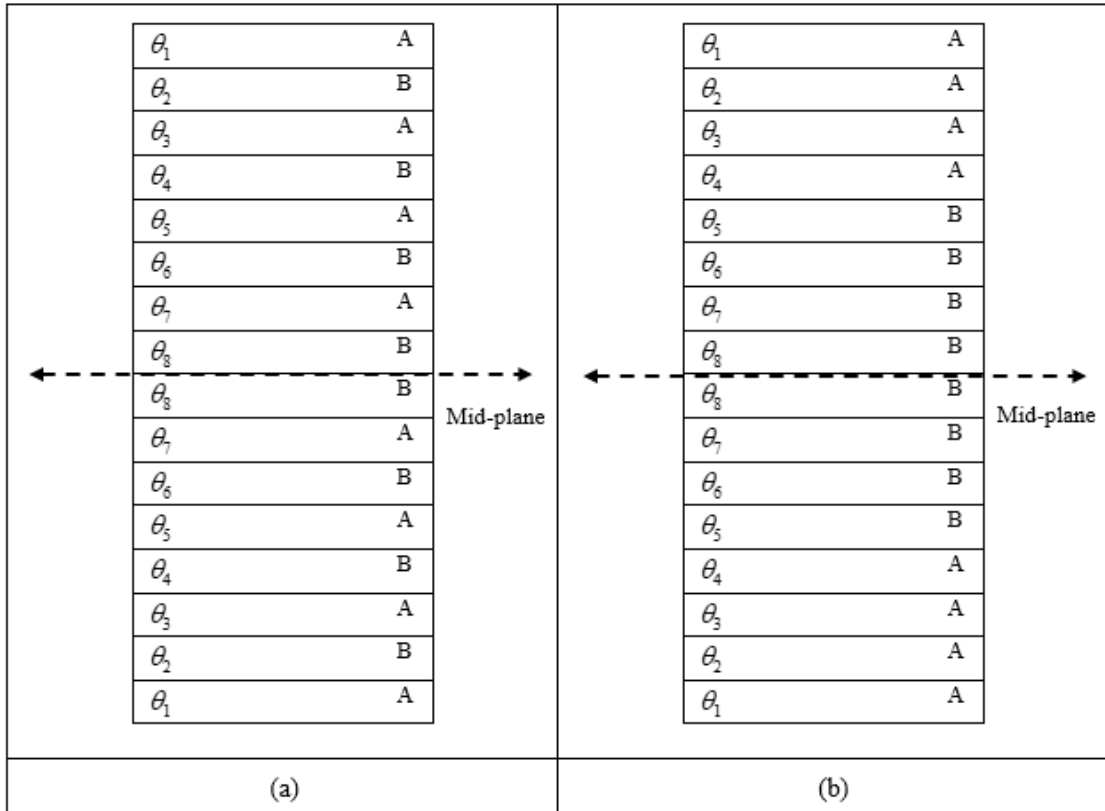
Figure 3. (a) Arrangement of 16-layered [A/B]$_{4S}$
hybrid composite plates (b) Arrangement of 16-layered [A$_4$/B$_4$]$_S$ hybrid composite plates

6. Results and Discussion

6.1. Optimization results

In the optimization, each problem was solved at least 100 times using the GA/GPSA hybrid algorithm created by the MATLAB program, and the results were presented in the tables. The result tables include material type, stacking sequence, minimized thermal expansion coefficients, and calculated thermal expansion coefficients. First, the non-hybrid composite laminate optimization results obtained using the continuous and traditional angles are given in Table 2 and Table 3, respectively. It should be noted that any result of a thermal expansion coefficient value below an order of 10^{-6} can be accepted as an optimum design in terms of dimensional stability [27].

It is seen in Table 2 that thermal expansion coefficients α_x and α_y were minimized to values in the order of $10^{-9} - 10^{-6}$ for AS4/Epoxy, IM6/Epoxy, Spectra/Epoxy, and Boron/Epoxy non-hybrid composites with the optimum continuous angled designs. In the other materials, the minimum values were mostly obtained in the order of 10^{-6}.

In Table 3, it can be noted that α_x and/or α_y could be minimized to the order of 10^{-8} at most for the model problems AS4/Epoxy, IM6/Epoxy, Gy70/Epoxy, and Boron/Epoxy with the optimum traditional angled designs. It can be said that these thermal expansion coefficient values are smaller as compared to those obtained by the continuous-angled designs. The results of optimization scenarios 1 – 4, including hybrid composite plates, are presented in Tables 4 – 11. The results of optimization scenario 1 are given in Tables 4 and 5.

Table 2. Optimization results of the continuous angled non-hybrid composite plates

Opt.	Composite	Stacking sequence	α_x (1/°C)	α_y (1/°C)
Min α_x	E-Glass/ Epoxy	$[19_4/86/16/1/75]_s$	$8.0417 \cdot 10^{-6}$	$1.0595 \cdot 10^{-5}$
Min α_y		$[73/90_7]_s$	$1.5816 \cdot 10^{-5}$	$6.3947 \cdot 10^{-6}$
Min α_x	Kevlar49/Epoxy	$[84/81/88/59/83/89/82/62]_s$	$4.1884 \cdot 10^{-6}$	$-7.5086 \cdot 10^{-7}$
Min α_y		$[89/70/67/75/86/67/71/82]_s$	$6.3444 \cdot 10^{-6}$	$-2.9069 \cdot 10^{-6}$
Min α_x	AS4/ Epoxy	$[10/14/0/30/0/2/82/84]_s$	$5.3587 \cdot 10^{-6}$	$1.1134 \cdot 10^{-6}$
Min α_y		$[58/44/28/90/34/90/21/26]_s$	$1.3947 \cdot 10^{-6}$	$-2.7594 \cdot 10^{-7}$
Min α_x	IM6/ Epoxy	$[79/61/8/88/79/75/88_2]_s$	$3.2160 \cdot 10^{-8}$	$3.2160 \cdot 10^{-7}$
Min α_y		$[63/89_2/76/87/63/74/87]_s$	$1.2026 \cdot 10^{-8}$	$1.2026 \cdot 10^{-8}$
Min α_x	GY70/Epoxy	$[88/49/66/58/85/89/90_2]_s$	$1.4244 \cdot 10^{-6}$	$-3.2458 \cdot 10^{-7}$
Min α_y		$[88/49/66/59/85/90_3]_s$	$1.4183 \cdot 10^{-6}$	$-3.2458 \cdot 10^{-7}$
Min α_x	Aramid/ Epoxy	$[65/81/73/7/16/65/14/31]_s$	$3.5661 \cdot 10^{-6}$	$-4.1119 \cdot 10^{-8}$
Min α_y		$[41/9/73/50/59/42/81]_s$	$7.1708 \cdot 10^{-8}$	$3.4533 \cdot 10^{-6}$
Min α_x	Spectra/ Epoxy	$[21/82/5/60/19/12/42/11]_s$	$6.8621 \cdot 10^{-6}$	$-4.9593 \cdot 10^{-8}$
Min α_y		$[56/28/20/30/42/66/83/86]_s$	$6.8260 \cdot 10^{-6}$	$-1.3531 \cdot 10^{-8}$
Min α_x	Boron/ Epoxy	$[26/51/39/68/20/55/62]_s$	$1.4421 \cdot 10^{-8}$	$1.5168 \cdot 10^{-6}$
Min α_y		$[74/50/30/14/69/5/36/5]_s$	$1.5299 \cdot 10^{-6}$	$1.3757 \cdot 10^{-9}$

Table 3. Optimization results of the traditional angled non-hybrid composite plates

Opt.	Composite	Stacking sequence	α_x (1/°C)	α_y (1/°C)
Min α_x	E-Glass/ Epoxy	$[0_3/45_5]_s$	$7.6030 \cdot 10^{-6}$	$1.2081 \cdot 10^{-5}$
Min α_y		$[90_4/45/90_2]_s$	$1.4571 \cdot 10^{-5}$	$6.4999 \cdot 10^{-6}$
Min α_x	Kevlar49 / Epoxy	$[0/90_7]_s$	$-1.2500 \cdot 10^{-7}$	$3.5625 \cdot 10^{-6}$
Min α_y		$[90_6/45/90]_s$	$3.5625 \cdot 10^{-6}$	$-2.500 \cdot 10^{-7}$
Min α_x	AS4/ Epoxy	$[45_8]_s$	$5.5937 \cdot 10^{-7}$	$5.5938 \cdot 10^{-7}$
Min α_y		$[90_5/45/90/45]_s$	$1.1965 \cdot 10^{-6}$	$-7.7743 \cdot 10^{-6}$
Min α_x	IM6/ Epoxy	$[0/90_7]_s$	$-2.5000 \cdot 10^{-6}$	$1.1250 \cdot 10^{-6}$
Min α_y		$[90_8]_s$	$1.1250 \cdot 10^{-6}$	$-2.5000 \cdot 10^{-6}$
Min α_x	GY70/ Epoxy	$[45_8]_s$	$5.4687 \cdot 10^{-7}$	$5.4687 \cdot 10^{-7}$
Min α_y		$[90_8]_s$	$1.1250 \cdot 10^{-6}$	$-3.1250 \cdot 10^{-8}$
Min α_x	Aramid/ Epoxy	$[45_8]_s$	$1.7625 \cdot 10^{-6}$	$1.7625 \cdot 10^{-6}$
Min α_y		$[90_8]_s$	$3.7500 \cdot 10^{-6}$	$-2.2500 \cdot 10^{-7}$
Min α_x	Spectra/ Epoxy	$[0/90_7]_s$	$-6.8750 \cdot 10^{-7}$	$7.5000 \cdot 10^{-6}$
Min α_y		$[90_8]_s$	$7.5000 \cdot 10^{-6}$	$-6.8750 \cdot 10^{-6}$
Min α_x	Boron/ Epoxy	$[0/45_2/90_3/90/45/90]_s$	$1.5818 \cdot 10^{-8}$	$1.5154 \cdot 10^{-6}$
Min α_y		$[90/45_2/90/45/90_3]_s$	$1.5154 \cdot 10^{-6}$	$1.5818 \cdot 10^{-8}$

Table 4 shows the results of the stacking sequence with continuous fiber angles for the $[A/B]_{4S}$ hybrid laminates of GY70/Epoxy material. Most of the designs with thermal expansion coefficients in the order of $10^{-7} – 10^{-9}$ were achieved. The lowest α_x value giving minimum dimensional change is obtained as $1.1924 \cdot 10^{-8}$ 1/°C for the GY70-IM6/Epoxy hybrid composite, and the lowest α_x value giving minimum dimensional change is obtained as $1.1932 \cdot 10^{-9}$ 1/°C for the GY70-Spectra/Epoxy hybrid composite.

Table 5 presents the results of the stacking sequence with continuous fiber angles for the $[A/B]_{4s}$ hybrid laminates of AS4/Epoxy material. As seen in Table 5, it is observed that the α_x value was minimized to the order of 10^{-10}, and the α_y value is minimized to the order of 10^{-8} at most. Hence, more dimensionally stable hybrid laminates were obtained when the x direction value was minimized to the order of 10^{-10}, and the α_y value was minimized to the order of 10^{-8} at most. Hence, more dimensionally stable hybrid laminates were obtained in the x direction compared to the y direction.

Table 4. $[A/B]_{4S}$ optimization results of hybrid composite plates with the continuous angles (A - GY70/Epoxy)

Opt.	Hybrid Composite	Stacking Sequence	α_x (1/°C)	α_y (1/°C)
Min α_x	GY70-Spectra/Epoxy	$[5/75/69_2/0_2/1/72]_S$	$2.6534.10^{-8}$	$3.8923.10^{-5}$
Min α_y		$[67/41/37/78/89/46/76/40]_S$	$3.8949.10^{-5}$	$1.1932.10^{-9}$
Min α_x	GY70-Kevlar 49/Epoxy	$[25/65/90/68/33/63/12/5]_S$	$-2.2366.10^{-8}$	$1.4153.10^{-5}$
Min α_y		$[3/25/54/76/16/43/29/84]_S$	$1.4104.10^{-5}$	$2.7420.10^{-8}$
Min α_x	GY70-IM6/Epoxy	$[41/8/52/23/51/8/27/26]_S$	$1.1924.10^{-6}$	$1.1385.10^{-6}$
Min α_y		$[90/35_2/7/64/39/42/44]_S$	$1.1401.10^{-5}$	$3.8628.10^{-9}$
Min α_x	GY70- E-Glass/Epoxy	$[3/43/18/74/22/64/23/38]_S$	$-1.8190.10^{-8}$	$1.3181.10^{-6}$
Min α_y		$[28/5/20/7/29/14/20/22]_S$	$1.3108.10^{-6}$	$1.8696.10^{-8}$
Min α_x	GY70-AS4/Epoxy	$[82/10/37/9/84/54/83/48]_S$	$8.0163.10^{-7}$	$-1.2367.10^{-8}$
Min α_y		$[1/0/1/2/0_3/-1]_S$	$3.1808.10^{-8}$	$5.3994.10^{-6}$
Min α_x	GY70-Aramid/Epoxy	$[49/36/49/67/73/35/46/31]_S$	$-2.5290.10^{-7}$	$1.4687.10^{-5}$
Min α_y		$[89/80/22/80/0/88/60/67]_S$	$1.4385.10^{-5}$	$4.9351.10^{-8}$
Min α_x	GY70- Boron/Epoxy	$[41/80/46/79/49/64/4/85]_S$	$4.6718.10^{-7}$	$2.4544.10^{-6}$
Min α_y		$[72/14/63/33/72/6/65/2]_S$	$2.6204.10^{-6}$	$-4.2191.10^{-9}$

Table 5. $[A/B]_{4S}$ optimization results of hybrid composite plates with the continuous angles (A - AS4/Epoxy)

Opt.	Hybrid Composite	Stacking Sequence	α_x (1/°C)	α_y (1/°C)
Min α_x	AS4-Spectra/Epoxy	$[19/1/0/1/0/1/-1/1]_S$	$-1.1329.10^{-8}$	$1.4595.10^{-5}$
Min α_y		$[49/10/85/31/71/28/87/54]_S$	$1.4540.10^{-5}$	$4.3517.10^{-8}$
Min α_x	AS4-E-Glass/Epoxy	$[39/89/42/3/42/84/39/83]_S$	$-5.4662.10^{-9}$	$2.6115.10^{-6}$
Min α_y		$[50/4/53/4/50/4/50/4]_S$	$1.2729.10^{-6}$	$1.4327.10^{-6}$
Min α_x	AS4-IM6/Epoxy	$[1/2/1/-1/2/0/2/1]_S$	$8.4299.10^{-9}$	$7.9839.10^{-6}$
Min α_y		$[77/38/80/70/54/18/67/5]_S$	$8.0075.10^{-6}$	$-1.5086.10^{-8}$
Min α_x	AS4-GY70/Epoxy	$[1/86/1/2/1/-1_2/0]_S$	$6.4736.10^{-9}$	$5.3934.10^{-6}$
Min α_y		$[74/50/73/77/69/1438/34]_S$	$5.4123.10^{-6}$	$-1.2453.10^{-8}$
Min α_x	As4-Kevlar49/Epoxy	$[89/-1/1/0_3/7/2]_S$	$-3.4388.10^{-10}$	$1.1534.10^{-5}$
Min α_y		$[55/30/62/50/80/51/64/90]_S$	$1.1512.10^{-5}$	$2.1798.10^{-8}$
Min α_x	AS4-Aramid/Epoxy	$[47/54/19/0/66/3/20/10]_S$	$4.7703.10^{-8}$	$2.4953.10^{-5}$
Min α_y		$[90/77/53/69/51/77/43/38]_S$	$2.4941.10^{-5}$	$6.0218.10^{-8}$
Min α_x	AS4-Boron/Epoxy	$[45/90/45/82/45/90/45/82]_S$	$1.7397.10^{-6}$	$3.3066.10^{-6}$
Min α_y		$[45/-17/45/-17/45/17/45/17]_S$	$3.3878.10^{-6}$	$1.7243.10^{-6}$

The results of optimization scenario 2 ware given in Tables 6 and 7. Table 6 shows the results of the optimum stacking sequences with traditional 0°, 45°, and 90° fiber angles for the $[A/B]_{4S}$ hybrid laminates of GY70/Epoxy. As seen in Table 6, most of the designs with thermal expansion coefficients in the order of $10^{-7} - 10^{-8}$ were obtained. The best thermal expansion coefficient value of α_x for dimensional stability was achieved in GY70-E-Glass/ Epoxy hybrid composite with $7.9853 \cdot 10^{-8}$ 1/°C. For the thermal expansion coefficient of (α_y), the best dimensional stability was reached in GY70-AS4/Epoxy with a value of $3.5850 \cdot 10^{-8}$ 1/°C. Furthermore, it is seen that more optimum stacking sequences with lower thermal expansion coefficients were obtained in the y direction of the laminates than in the x direction in terms of dimensional stability. Table 7 indicates the results of the stacking sequences with the traditional fiber angles for the $[A/B]_{4S}$ hybrid laminates of AS4/Epoxy.

It is noticed that the coefficients of thermal expansion (CTEs) were mainly obtained in the order of 10^{-8} in the optimization problems. Moreover, lower CTE values were found for the α_y compared to the α_x. However, it is seen that the desired dimensional stability could not be reached for the AS4-Boron/Epoxy hybrid laminate design cases.

Considering the dimensionally stable hybrid designs of the traditional fiber and continuous fiber angles (optimization scenario 1 and 2) comparatively, it can be said that the trend of finding lower CTE is higher in the hybrid designs with the continuous fiber angles, as can be expected. However, it is seen that the hybrid laminate optimization with the traditional angles yielded competitive results in several cases as well.

On the other hand, when all continuous angled-hybrid designs are compared with continuous-angled non-hybrid designs, it can be interpreted that the dimensional stability performances of the hybrid designs are mainly at a better level than the non-hybrid designs. However, considering the comparison of the traditional angled hybrid and non-hybrid designs, it is seen that IM6/Epoxy and Boron/Epoxy non-hybrid composites provided better results alone than most of the hybrid designs. Furthermore, unexpectedly, the α_x values were obtained lower in the non-hybrid designs of GY70/Epoxy compared to its hybrid designs, and the α_y values were obtained lower in the non-hybrid designs of AS4/Epoxy compared to its hybrid designs.

Table 6. $[A/B]_{4S}$ optimization results of hybrid composite plates with the traditional angles (A - GY70/Epoxy)

Opt.	Hybrid Composite	Stacking Sequence	α_x (1/°C)	α_y (1/°C)
Min α_x	Gy70-Spectra/Epoxy	$[0/45_7]_S$	$-2.1054.10^{-7}$	$1.6145.10^{-5}$
Min α_y		$[90/45/90/0/45/0/45/0]_S$	$1.5838.10^{-5}$	$9.6472.10^{-8}$
Min α_x	GY70-Kevlar 49/Epoxy	$[45_4/90/45_2/0]_S$	$-3.6668.10^{-7}$	$1.4168.10^{-5}$
Min α_y		$[90_4/45/90_3]_S$	$1.4168.10^{-5}$	$-3.6818.10^{-8}$
Min α_x	Gy70-E-Glass/Epoxy	$[45_3/90/45_3/90]_S$	$7.9853.10^{-8}$	$1.2666.10^{-6}$
Min α_y		$[45/0/45/0/45/0/90/0]_S$	$1.2028.10^{-6}$	$1.1590.10^{-7}$
Min α_x	Gy70-IM6/Epoxy	$[0/90/0/90/0/90/45/90]_S$	$2.8254.10^{-7}$	$1.1114.10^{-5}$
Min α_y		$[45_4/90_4]_S$	$1.1504.10^{-5}$	$-1.0670.10^{-7}$
Min α_x	Gy70-AS4/Epoxy	$[45_8]_S$	$2.6999.10^{-6}$	$2.6999.10^{-6}$
Min α_y		$[90_8]_S$	$5.3640.10^{-6}$	$3.5850.10^{-8}$
Min α_x	Gy70-Aramid/Epoxy	$[0/45_2/0/45_3/0]_S$	$-4.0097.10^{-7}$	$2.8601.10^{-5}$
Min α_y		$[45/90/45_2/90/45_3]_S$	$2.8601.10^{-5}$	$-4.0097.10^{-7}$
Min α_x	Gy70-Boron/Epoxy	$[45/90/45_3/90]_S$	$2.8872.10^{-6}$	$2.5032.10^{-6}$
Min α_y		$[45/0/45/0/45/0/90/0]_S$	$9.1449.10^{-8}$	$3.6559.10^{-7}$

Table 7. [A/B]$_{4S}$ optimization results of hybrid composite plates with the traditional angles (A - AS4/Epoxy)

Opt.	Hybrid Composite	Stacking Sequence	α_x (1/°C)	α_y (1/°C)
Min α_x	AS4- Spectra/Epoxy	[0/90/0/45$_5$]$_S$	1.8388.10^{-8}	1.4565.10^{-5}
Min α_y		[45/0/90/45/90/45$_3$]$_S$	14565.10^{-5}	1.8388.10^{-8}
Min α_x	AS4-E-Glass/Epoxy	[45/90]$_{4S}$	-3.9553.10^{-8}	2.6416.10^{-6}
Min α_y		[45/0]$_{4S}$	2.6416.10^{-6}	-3.9553.10^{-8}
Min α_x	AS4-Kevlar 49/Epoxy	[90/45$_3$/90/45$_2$/0]$_S$	-2.9896.10^{-7}	1.1833.10^{-5}
Min α_y		[90$_8$]$_S$	-7.3619.10^{-5}	1.1608.10^{-8}
Min α_x	AS4- IM6/Epoxy	[45/90/45$_6$]$_S$	8.0512.10^{-7}	7.1873.10^{-6}
Min α_y		[90$_8$]$_S$	8.0123.10^{-6}	-1.9915.10^{-8}
Min α_x	AS4- GY70/Epoxy	[45$_8$]$_S$	2.6999.10^{-6}	2.6999.10^{-6}
Min α_y		[90$_8$]$_S$	5.3640.10^{-6}	3.5850.10^{-8}
Min α_x	AS4-Aramid/Epoxy	[90/45$_6$/0]$_S$	3.2255.10^{-7}	3.9063.10^{-5}
Min α_y		[0/45$_2$/90$_4$]$_S$	3.9063.10^{-5}	3.2255.10^{-7}
Min α_x	AS4-Boron/Epoxy	[45/90]$_{4S}$	1.7403.10^{-6}	3.2993.10^{-6}
Min α_y		[45/0]$_{4S}$	3.2993.10^{-6}	1.7403.10^{-6}

The results of optimization scenario 3 are given in Tables 8 and 9. Table 8 shows the results of the optimum stacking sequences with the continuous fiber angles for the [A/B]$_{4S}$ hybrid laminates of GY70/Epoxy, and Table 9 presents the results of the continuous fiber-angled hybrid designs for the [A/B]$_{4S}$ hybrid laminates of AS4/Epoxy. As seen in Table 8, in most of the designs, thermal expansion coefficients have been obtained in the order of 10^{-7} –

10^{-9}. The lowest α_x value was obtained with GY70-Kevlar49/Epoxy hybrid design as $4.3532 \cdot 10^{-9}$ 1/°C, and the lowest α_y value was obtained as $3.3355 \cdot 10^{-9}$ 1/°C in the GY70-E-Glass/Epoxy hybrid design. However, any optimum design that provides better dimensional stability in both directions could not be reached with the GY70-Boron/Epoxy design.

Table 8. [A/B]$_{4S}$ optimization results of hybrid composite plates with the continuous angles (A - GY70/Epoxy)

Opt.	Hybrid Composite	Stacking Sequence	α_x (1/°C)	α_y (1/°C)
Min α_x	GY70-Spekctra /Epoxy	[4/23/11/36/38/32/43/67]$_S$	-3.9410.10^{-8}	-1.5974.10^{-5}
Min α_y		[55/72/83/88/19/45/70/62]$_S$	1.5961.10^{-5}	-2.6662.10^{-8}
Min α_x	GY70-Kevlar49/Epoxy	[1$_2$/0/29/1/2$_2$/1]$_S$	4.3532.10^{-9}	1.4127.10^{-6}
Min α_y		[84$_2$/56/52/42/63/5/57]$_S$	1.4114.10^{-5}	1.6471.10^{-8}
Min α_x	GY70-E-Glass/Epoxy	[25/80/57/45/36/16/57/71]$_S$	-7.4635.10^{-8}	1.6722.10^{-6}
Min α_y		[0/84/89/36/49/46/48/5]$_S$	1.6799.10^{-6}	3.3555.10^{-9}
Min α_x	GY70- IM6/Epoxy	[5/58/6/0$_2$/83/56/38]$_S$	4.1138.10^{-8}	1.1356.10^{-5}
Min α_y		[73/80/77/53/36/72/89/28]$_S$	1.1334.10^{-5}	6.3394.10^{-8}
Min α_x	GY70- AS4/Epoxy	[82/10/37/9/84/54/83/48]$_S$	8.0163.10^{-7}	-1.2367.10^{-8}
Min α_y		[1/0/1/2/0$_3$/-1]$_S$	3.1808.10^{-8}	5.3994.10^{-6}
Min α_x	GY70-Aramid/Epoxy	[37/21/48/61/82/6/50/37]$_S$	1.1212.10^{-7}	2.8088.10^{-5}
Min α_y		[56/65/15/78/35/85/75/36]$_S$	2.8290.10^{-5}	-8.9561.10^{-8}
Min α_x	GY70- Boron/Epoxy	[45/32/60/48/0/21/16/12]$_S$	1.9348.10^{-6}	1.1787.10^{-8}
Min α_y		[20/25/19/22/48/78/76/63]$_S$	1.4528.10^{-6}	25505.10^{-6}

In Table 9, it can be noted that high dimensional stability at adequate levels was met in almost all design cases, and the CTE values were obtained generally in the order of $10^{-8} – 10^{-10}$. The hybrid designs of Spectra/Epoxy, Kevlar 49/Epoxy, and E-Glass/Epoxy composites are better in terms of dimensional stability than the other designs. However, similarly as in the hybrid of GY70/Epoxy, an optimum design solution for high dimensional stability also could not be found in the AS4-Boron/Epoxy hybrid composite.

Table 9. $[A_4/B_4]_S$ optimization results of hybrid composite plates with the continuous angles (A - AS4/Epoxy)

Opt.	Hybrid Composite	Stacking Sequence	α_x (1/ °C)	α_y (1/ °C)
Min α_x	AS4-Spectra/Epoxy	$[61/56/88_2/7/36/88/34]_S$	$8.4239.10^{-10}$	$1.4587.10^{-5}$
Min α_y		$[1/28/0_2/1/21/1/0]_S$	$1.4582.10^{-5}$	$-3.7348.10^{-9}$
Min α_x	AS4-Kevlar 49/Epoxy	$[7/0/1_2/0/-1/0_2]_S$	$1.4736.10^{-8}$	$1.1519.10^{-5}$
Min α_y		$[66/88/48/68/41/1/22/19]_S$	$1.1558.10^{-5}$	$-2.3927.10^{-8}$
Min α_x	As4-IM6/Epoxy	$[2/0/2_2/1/0/2/-1]_S$	$8.5961.10^{-9}$	$7.9838.10^{-6}$
Min α_y		$[42/78/90/87/70/31/37]_S$	$8.2459.10^{-6}$	$-2.5348.10^{-7}$
Min α_x	AS4-GY70/Epoxy	$[31/22/14/6/39/72/1/18]_S$	$2.0431.10^{-9}$	$5.3978.10^{-6}$
Min α_y		$[1/0_3/84/3/0_2]_S$	$-3.8115.10^{-9}$	$5.4036.10^{-6}$
Min α_x	AS4-E-Glass/Epoxy	$[40/43/40_2/88/83/76/87]_S$	$1.7913.10^{-9}$	$2.6082.10^{-6}$
Min α_y		$[51/50/52_2/4_3/8]_S$	$2.6075.10^{-6}$	$-3.7028.10^{-9}$
Min α_x	AS4-Aramid/Epoxy	$[51/32/86/46/65/4/44/48]_S$	$1.1744.10^{-8}$	$3.9374.10^{-7}$
Min α_y		$[36/57/43/77/69/52/90/80]_S$	$3.9461.10^{-5}$	$-7.5021.10^{-8}$
Min α_x	AS4- Boron/Epoxy	$[45_4/90/82_2/90]_S$	$1.7397.10^{-6}$	$3.3066.10^{-6}$
Min α_y		$[45_4/-18_4]_S$	$1.7619.10^{-6}$	$3.3415.10^{-6}$

The results of optimization scenario 4 were presented in Tables 10 and 11. Tables 10 and 11 show the results of the optimum stacking sequence designs with the traditional fiber angles for the $[A/B]_{4S}$ hybrid laminates of GY70/Epoxy and AS4/Epoxy, respectively.

Table 10. $[A_4/B_4]_S$ optimization results of hybrid composite plates with the traditional angles (A -GY70/Epoxy)

Opt.	Hybrid Composite	Stacking Sequence	α_x (1/ °C)	α_y (1/ °C)
Min α_x	Gy70-Spectra/Epoxy	$[0/45_7]_S$	$-2.1054.10^{-7}$	$1.6145.10^{-5}$
Min α_y		$[45/90_2/45/9045/90_2]_S$	$1.5838.10^{-5}$	$9.6472.10^{-8}$
Min α_x	GY70-Kevlar 49/Epoxy	$[0/45_3/90/45_3]_S$	$2.8727.10^{-7}$	$1.3844.10^{-5}$
Min α_y		$[45/90_3/0_4]_S$	$1.4092.10^{-7}$	$3.8510.10^{-8}$
Min α_x	GY70-E-Glass/Epoxy	$[90_2/45_3/90]_S$	$6.5897.10^{-9}$	$1.7011.10^{-6}$
Min α_y		$[45_6/90/45]_S$	$1.4399.10^{-6}$	$3.9905.10^{-8}$
Min α_x	GY70- IM6/Epoxy	$[0_3/45/90_4]_S$	$2.8254.10^{-7}$	$1.1114.10^{-5}$
Min α_y		$[45_2/90_3/45_2/90]_S$	$1.1504.10^{-5}$	$-1.0670.10^{-7}$
Min α_x	GY70-AS4/Epoxy	$[45_8]_S$	$2.6999.10^{-6}$	$2.6999.10^{-6}$
Min α_y		$[90_8]_S$	53640.10^{-6}	$3.5850.10^{-8}$
Min α_x	GY70-Aramid/Epoxy	$[90_2/45/90/0_4]_S$	$-4.3333.10^{-7}$	$1.4868.10^{-5}$
Min α_y		$[90_2/45/90_5]_S$	$1.4868.10^{-5}$	$-4.3333.10^{-7}$
Min α_x	GY70- Boron/Epoxy	$[45_4/90/45/90/45]_S$	$1.5102.10^{-6}$	$2.8872.10^{-6}$
Min α_y		$[45_3/90/0_4]_S$	$1.8574.10^{-6}$	$3.6559.10^{-7}$

Tablo 11. [A$_4$/B$_4$]$_S$ optimization results of hybrid composite plates with the traditional angles (A - AS4/Epoxy)

Opt.	Hybrid Composite	Stacking Sequence	α_x (1/ °C)	α_y (1/ °C)
Min α_x	AS4-Spektra/Epoxy	[0$_2$45$_2$/90/45$_3$]$_S$	1.4565.10^{-8}	1.8388.10^{-5}
Min α_y		[45/90$_2$/45/90/45$_3$]$_S$	1.8388.10^{-5}	1.4565.10^{-8}
Min α_x	AS4Kevlar 49/Epoxy	[0/45$_7$]$_S$	-5.5543.10^{-7}	-1.2090.10^{-5}
Min α_y		[90$_8$]$_S$	1.1608.10^{-5}	-7.3619.10^{-8}
Min α_x	AS4- E-Glass/Epoxy	[45/90]$_{4S}$	-3.9553.10^{-8}	2.6416.10^{-6}
Min α_y		[45/0]$_{4S}$	2.6416.10^{-6}	-3.9553.10^{-8}
Min α_x	AS4-IM6/Epoxy	[0/45$_3$/90/45$_3$]$_S$	8.0512.10^{-7}	7.1873.10^{-6}
Min α_y		[90$_8$]$_S$	8.0123.10^{-6}	-1.9915.10^{-8}
Min α_x	AS4-GY70/Epoxy	[45$_8$]$_S$	2.6999.10^{-6}	2.6999.10^{-6}
Min α_y		[90$_8$]$_S$	5.3640.10^{-6}	3.5850.10^{-8}
Min α_x	AS4-Aramid/Epoxy	[90$_4$/0$_4$]$_S$	8.8268.10^{-7}	2.4118.10^{-5}
Min α_y		[90$_8$]$_S$	2.4118.10^{-5}	8.8268.10^{-7}
Min α_x	AS4-Boron/Epoxy	[45$_4$/90$_4$]$_S$	1.7403.10^{-6}	3.2993.10^{-6}
Min α_y		[45$_4$/0$_4$]$_S$	3.2993.10^{-6}	1.7403.10^{-6}

It is seen from Table 10 that the dimensional stability performance of the GY70/Epoxy hybrid composites has been improved in the order of 10^{-7} – 10^{-9} in most of the design problems except for the GY70-Boron/Epoxy hybrid design. Besides, the performance of the dimensional stability of the AS4/Epoxy hybrids (Table 11) has also been improved to the order of 10^{-8} in many problems except for the AS4-Boron/Epoxy hybrid composite.

If the hybrid designs of the continuous fiber angles are compared to the designs of the traditional fiber angles (optimization scenarios 3 and 4), it is seen that the trend of finding lower CTE is higher in the hybrid designs with the continuous fiber angles, which is similar to the design cases in the optimization scenarios 1 and 2. In particular, the CTE values of the hybrid designs of AS4/Epoxy with the continuous angles were obtained lower (in the order of 10^{-9} and 10^{-10}) than the hybrid designs of GY70/Epoxy (in the order of 10^{-8} and 10^{-9}).

On the other hand, considering hybrid and non-hybrid designs of the continuous angled laminates, all the optimum designs of the GY70/Epoxy hybrids provide lower CTE values compared to the non-hybrid GY70/Epoxy design. However, the hybrid designs of GY70/Epoxy could not reach the minimum CTE values, in which min α_x was obtained by the non-hybrid AS4/Epoxy design and min α_y was obtained by the non-hybrid Boron/Epoxy design. When the hybrid designs of AS4/Epoxy are compared with the non-hybrid

designs of AS4/Epoxy, it is seen that α_y values are lower in all the hybrid designs; however, α_x values are lower in hybrid designs of AS4-Spectra/Epoxy, AS4-GY70/Epoxy, and AS4-E-Glass/Epoxy. Regarding the comparison of the AS4/Epoxy hybrid designs and the other non-hybrid designs, α_x values were obtained lower in of AS4-Spectra/Epoxy, AS4-GY70/Epoxy, and AS4-E-Glass/Epoxy composites as compared to the best min α_x value of the non-hybrid designs other than AS4/Epoxy. However, any optimum designs of min α_y were not found by any of the hybrids of AS4/Epoxy, considering the min α_y non-hybrid designs of materials other than AS4/Epoxy.

Considering the comparison of hybrid and non-hybrid designs of the traditional angled laminates, it can be said that all the designs of the GY70/Epoxy hybrids provided higher dimensional stability compared to the non-hybrid GY70/Epoxy design, which is similar to the continuous case. If the AS4/Epoxy hybrid designs are compared to the AS4/Epoxy non-hybrid designs, it can be noted that AS4-Spectra/Epoxy, AS4-Kevlar 49/Epoxy, and AS4-E-Glass/Epoxy hybrid designs ensured lower CTE values than the non-hybrid design for min α_x optimization. However, only AS4-Kevlar 49/Epoxy yielded a lower CTE value in min α_y optimization. Considering the comparison of AS4/Epoxy hybrids and the non-hybrid designs other than AS4/Epoxy, better CTE values were obtained for only the AS4-Spectra/Epoxy hybrid design for both minimum α_x

and α_y.

It is also important to compare the results of optimum continuous and traditional angled hybrid laminate designs of the $[A/B]_{4s}$ sequence with the results of the $[A_4/B_4]_S$ sequence. In continuous angled designs, for the min α_x optimization of GY70/Epoxy hybrids, all the designs of $[A/B]_{4s}$ sequence provide better dimensional stability than the designs of $[A_4/B_4]_S$ sequence, except GY70-Kevlar 49/Epoxy laminate. For the min α_y optimization of GY70/Epoxy, all the hybrid designs of the $[A/B]_{4s}$ sequence yield higher dimensional stability than the designs of the $[A_4/B_4]_S$ sequence, apart from the GY70-Kevlar 49/Epoxy and GY70-E-Glass/Epoxy designs.

In the AS4/Epoxy hybrid designs, AS4-Spectra/Epoxy, AS4-E-Glass/Epoxy, AS4-GY70/Epoxy, and AS4-Aramid/Epoxy laminates give lower CTE values of α_x in the $[A_4/B_4]_S$ sequence than the $[A/B]_{4s}$ sequence. Besides, AS4-Kevlar 49/Epoxy, AS4-IM6/Epoxy, and AS4-Boron/Epoxy laminate designs of the $[A_4/B_4]_S$ sequence yield smaller CTE values of α_x compared to the $[A_4/B_4]_S$ sequence. On the other hand, it is seen for the min α_y optimization that the hybrid designs of the $[A/B]_{4s}$ sequence provide better dimensional stability except for AS4-Spectra/Epoxy and AS4-E-Glass/Epoxy laminates than the designs of the $[A_4/B_4]_S$ sequence.

Considering the traditional angled case, for the min α_x optimization cases, the GY70/Epoxy hybrid laminate designs of Spectra/Epoxy and IM6/Epoxy give the same results for both $[A/B]_{4s}$ and $[A_4/B_4]_S$ sequences. The hybrid designs of GY70-Kevlar 49/Epoxy and GY70-E-Glass/Epoxy show higher dimensional stability in the $[A_4/B_4]_S$ sequence than the $[A/B]_{4s}$ sequence. However, the optimum GY70-Aramid/Epoxy design has lower CTE and thus higher dimensional stability in the $[A/B]_{4s}$ sequence compared to the $[A_4/B_4]_S$ sequence. For the min α_y optimization cases, GY70-Spectra/Epoxy, GY70-IM6/Epoxy, and GY70-AS4/Epoxy laminate designs yield the same results for both sequences. Moreover, the $[A/B]_{4s}$ sequence shows better dimensional stability performance in GY70-Kevlar 49/Epoxy and GY70-Aramid/Epoxy laminate designs, and the $[A_4/B_4]_S$ sequence provides a lower CTE-valued hybrid design with E-Glass/Epoxy.

In the results of AS4/Epoxy hybridized designs, it is noted for the min α_x optimization that the dimensional stability performance was obtained at the same level for AS4-E-Glass/Epoxy and AS4-IM6/Epoxy hybrid laminates in both material sequences. Besides, lower CTE values for the $[A/B]_{4s}$ sequence were obtained in the hybrid designs of AS4-Kevlar 49/Epoxy and AS4-Aramid/Epoxy compared to the $[A_4/B_4]_S$ sequence results. However, it is seen that the AS4-Spectra/Epoxy hybrid gives a better min α_x result for the $[A_4/B_4]_S$ sequence than the $[A/B]_{4s}$ sequence. Regarding the min α_y optimization, lower CTE values were obtained at the same level for AS4-E-Glass/Epoxy, AS4-IM6/Epoxy, and AS4-GY70/Epoxy hybrid laminates in both material sequences. Similar to the min α_x case, lower CTE values for the $[A/B]_{4s}$ sequence were obtained in the hybrid designs of AS4-Kevlar 49/Epoxy and AS4-Aramid/Epoxy compared to the $[A_4/B_4]_S$ sequence results, whereas the AS4-Spectra/Epoxy hybrid gives better results for the $[A_4/B_4]_S$ sequence than the $[A/B]_{4s}$ sequence.

Considering the studies in the literature [9], [10], it can be seen that CTE values range between the orders of 10^{-6} and 10^{-7} in general. However, when compared to the results in the literature, minimum CTE values of up to the 10^{-10} order could be obtained by optimization, using continuous fiber angles in particular.

6.2. Dimensional Stability Performance of the Optimum Designs

In this section, the optimum hybrid min α_x and α_y designs that are better in terms of dimensional stability were selected to test their durability under specific thermal changes. Tsai-Wu and Hashin-Rotem failure criteria were considered to evaluate whether the hybrid composites in question would fail or not. Thermal loads were determined as a maximum negative and a maximum positive temperature change according to the reference values, $\Delta T = -157\,°C$ and $\Delta T = 121\,°C$, which were reported by NASA as the maximum temperature changes that materials in space are subjected to [28].

It is worth mentioning that the selection of the hybrid designs to be tested in terms of thermal durability was made according to the optimum designs with lower thermal expansion coefficient values among all designs. In this regard, for the $[A/B]_{4s}$ sequence, the selected optimum hybrid composites are GY70-IM6/Epoxy and AS4-E-Glass/Epoxy laminates of both traditional and continuous fiber-angled designs. Figures 4–7 show the thermal durability of these hybrid composites, respectively.
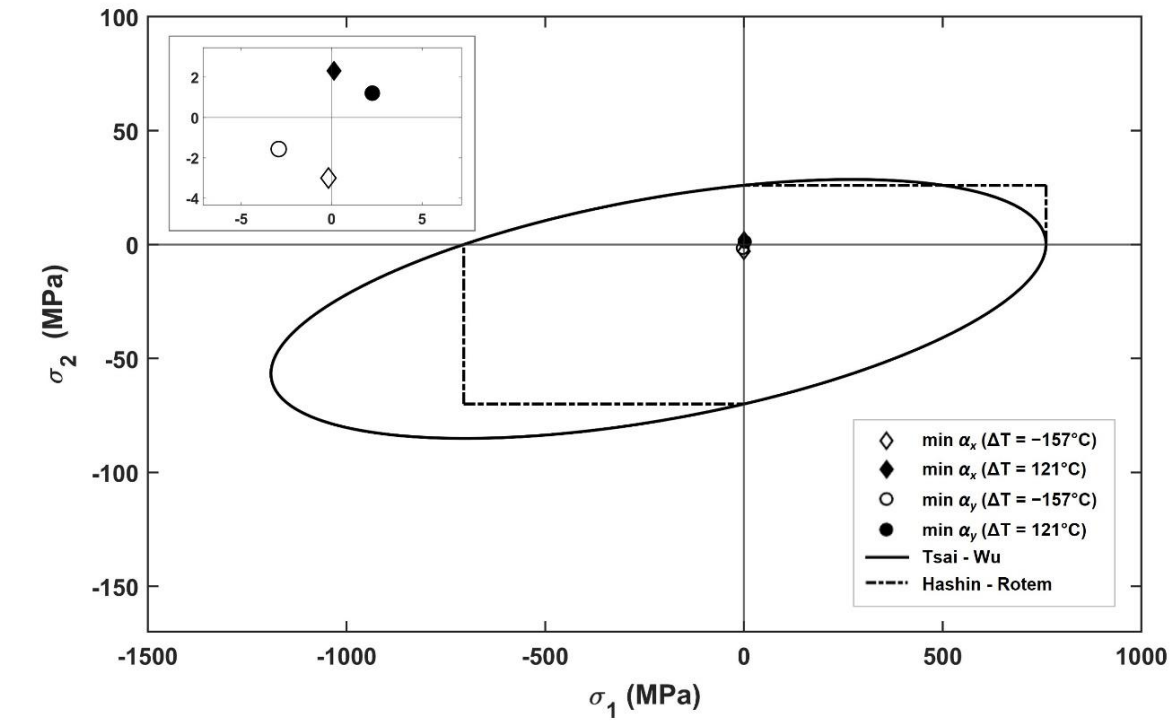
(a)
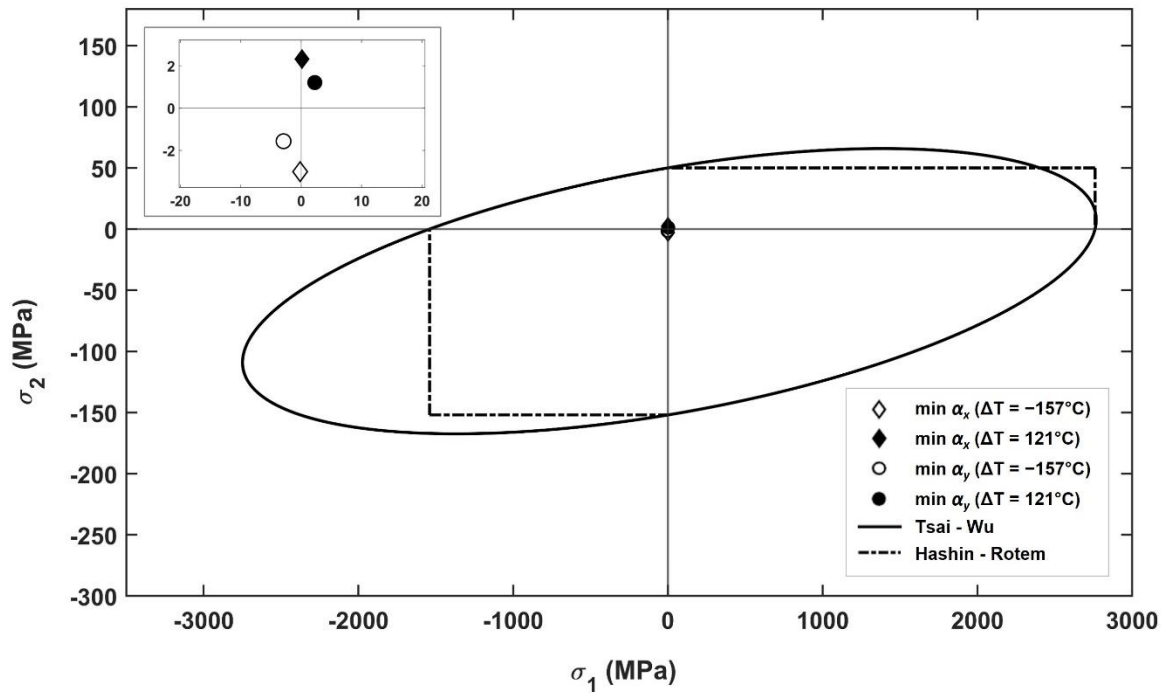
(b)

Figure 4. Thermal loading performances of min (α_x) $[(0_{GY70}/90_{IM6})_3/45_{GY70}/90_{IM6}]s$, and min (α_y) $[(45_{GY70}/45_{IM6})_2/(90_{GY70}/90_{IM6})_2]$ hybrid designs: (a) GY70 laminate, (b) IM6 laminate
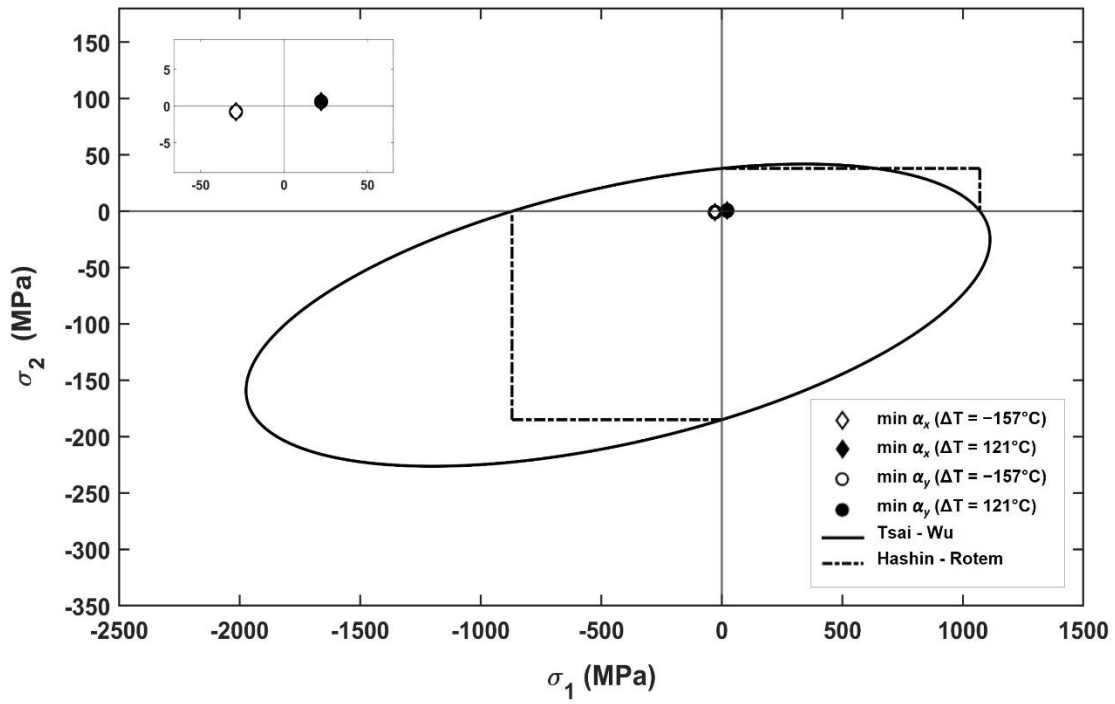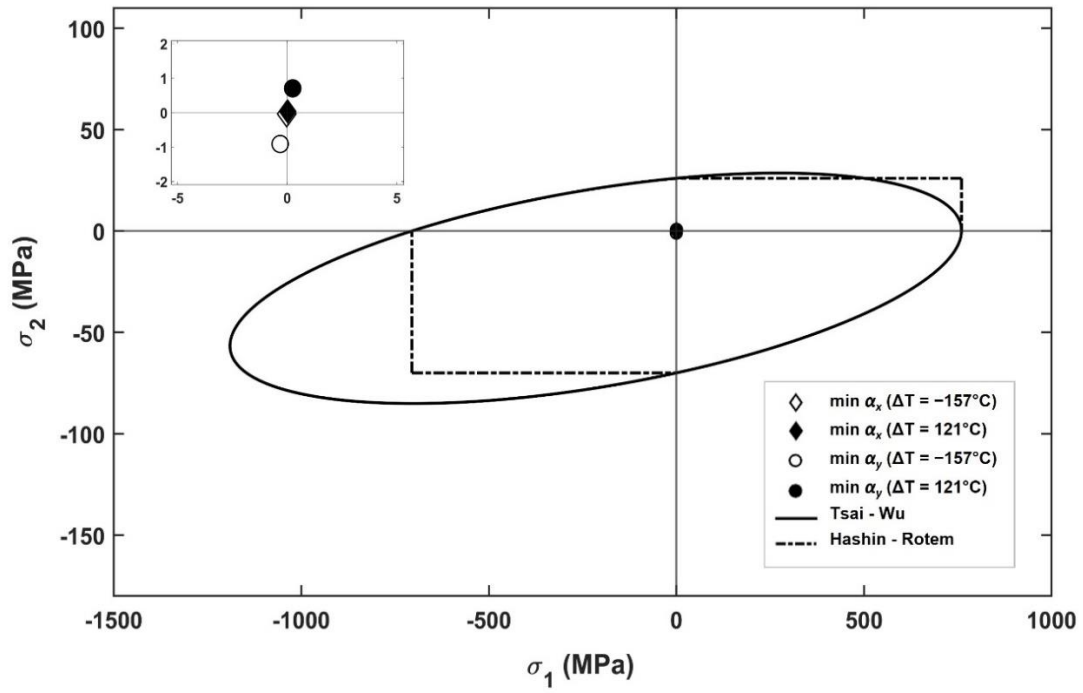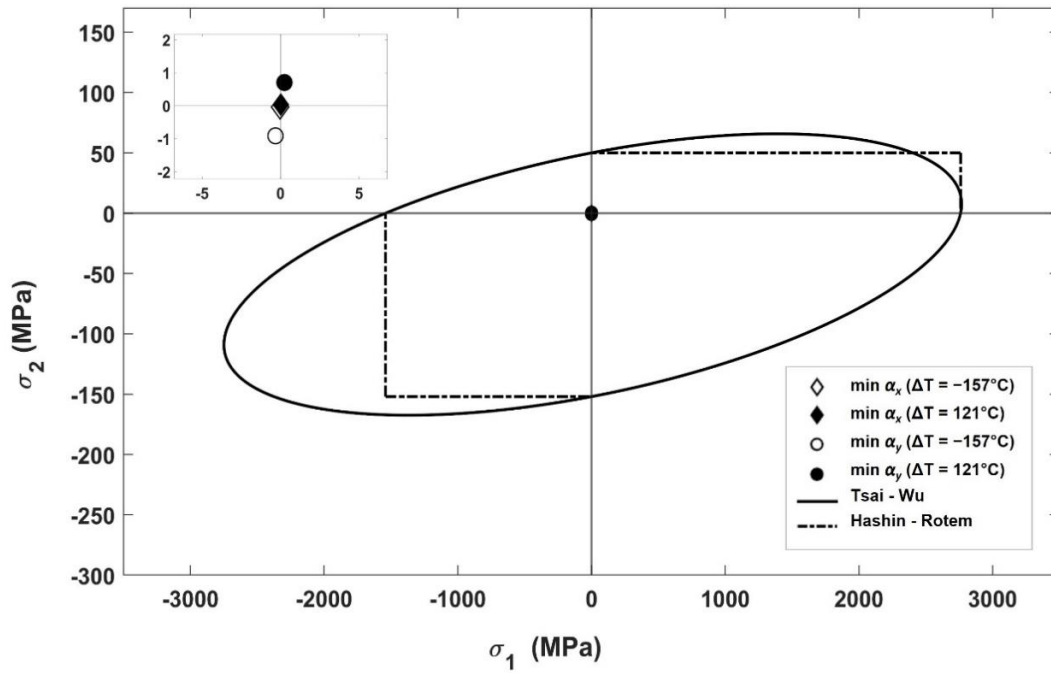
(a)
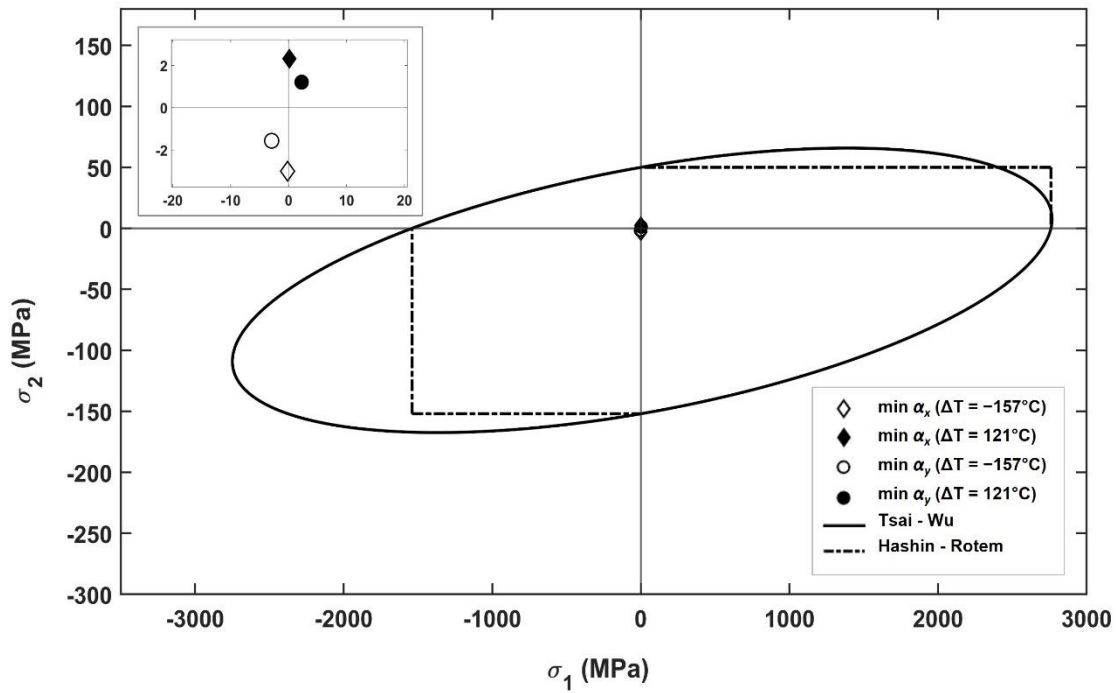
(b)

Figure 5. Thermal loading performances of min (α_x) [45$_{AS4}$/90$_{Gl}$]$_{4S}$, and min (α_y) [45$_{AS4}$/0$_{Gl}$]$_{4S}$ hybrid designs: (a) AS4 laminate, (b) E-Glass (Gl) laminate

(a)

(b)

Figure 6. Thermal loading performances of min (α_x) $[41_{GY70}/8_{IM6}/52_{GY70}/23_{IM6}/51_{GY70}/8_{IM6}/27_{GY70}/26_{IM6}]_S$, and min (α_y) $[90_{GY70}/35_{IM6}/35_{GY70}/7_{IM6}/64_{GY70}/39_{IM6}/42_{GY70}/44_{IM6}]_S$

hybrid designs: (a) GY70 laminate, (b) IM6 laminate

(a)

(b)
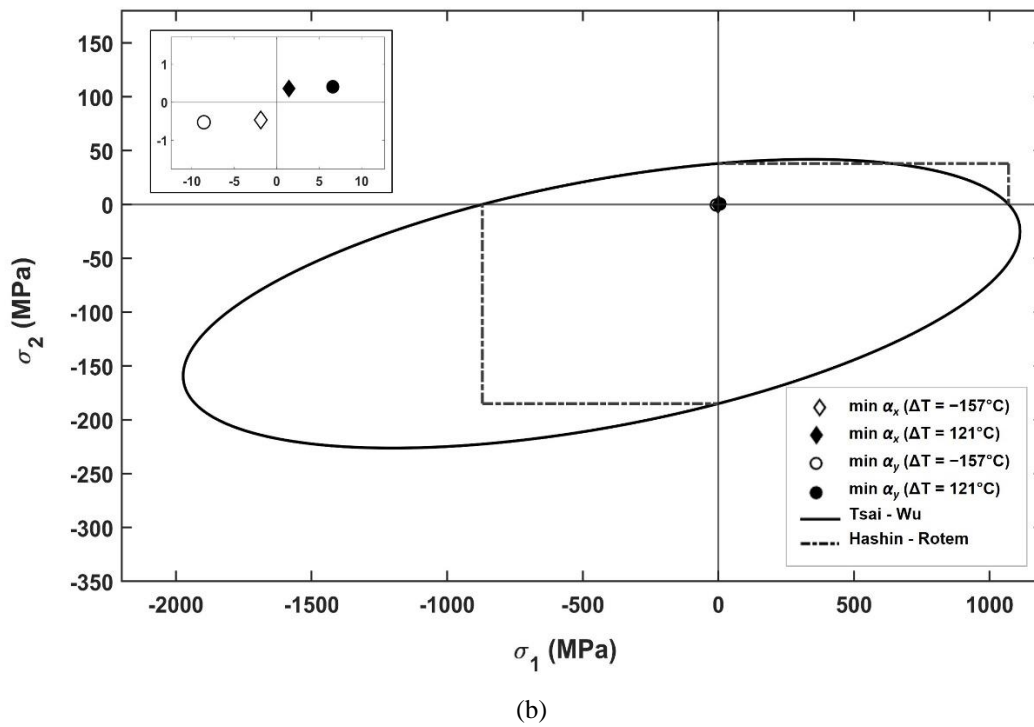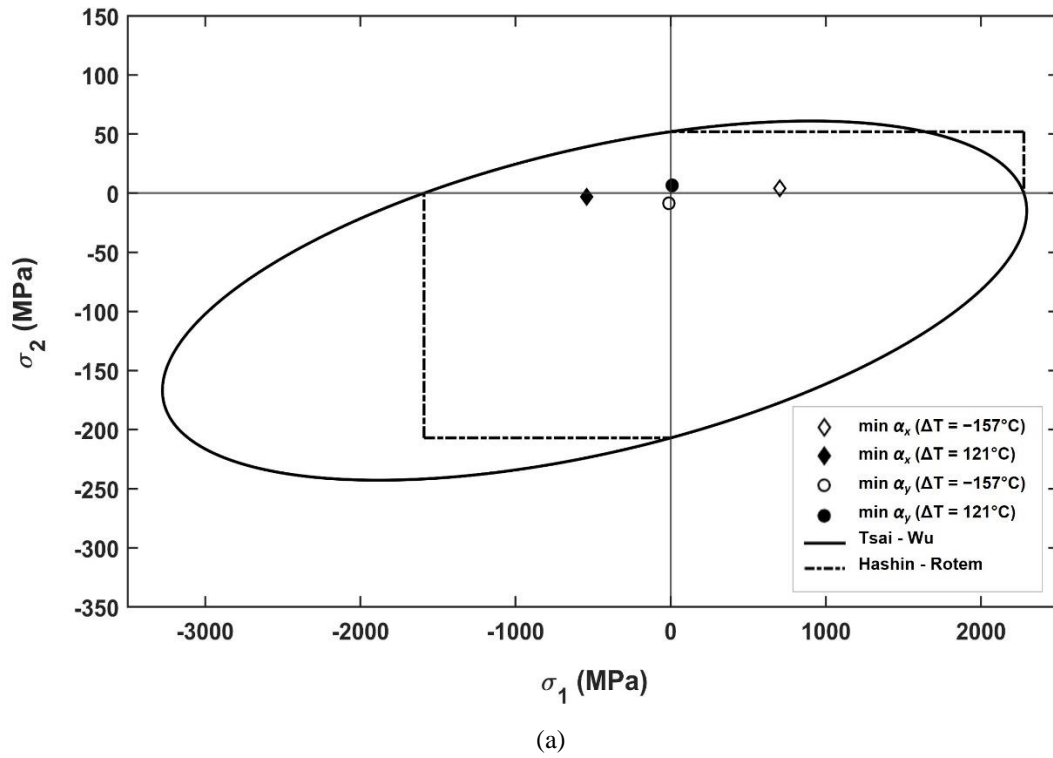
Figure 7. Thermal loading performances of min (α_x) [$39_{AS4}/89_{Gl}/42_{AS4}/83_{Gl}/42_{AS4}/84_{Gl}/39_{AS4}/83_{Gl}$]$_s$, and min (α_y) [$50_{AS4}/4_{Gl}/53_{AS4}/4_{Gl}/(50_{AS4}/4_{Gl})_2$]$_s$ hybrid designs: (a) AS4 laminate, (b) E-Glass (Gl) laminate

It is seen from the figures that min α_x and min α_y designs do not fail according to the Tsai-Wu (TW) and Hashin-Rotem (HR) failure criteria for all the layers, which is shown in detail in the small figure on the upper left of the figure. However, it can be noted that GY70/Epoxy and IM6/Epoxy laminates of min α_x $[(0_{GY70}/90_{IM6})_3/45_{GY70}/90_{IM6}]_S$ hybrid design (Figure 4) are very close to the failure limit under both thermal loads of $\Delta T = -157$ °C and $\Delta T = 121$ °C according to the Hashin-Rotem failure criterion. Considering Figure 5, it was observed that the AS4 laminates of min α_x and min α_y hybrid designs have the same failure index values, close to the failure limit of HR for each thermal load. Also, it can be said that E-Glass laminates of min α_x design are on the critical edge of failure for both thermal loads. As for Figure 6, it is seen that thermal loads cause relatively small values of stresses in the GY70 and IM6 laminates of the hybrid designs due to the utilization of continuous fiber angles in stacking sequences. A similar situation is also valid for the min α_x and min α_y designs of the AS4-E-Glass/Epoxy hybrid composite depicted in Figure 7.

As for the $[A_4/B_4]_S$ sequence, the selected optimum hybrid designs are GY70-E-Glass/Epoxy laminates in both traditional and continuous designs. On the other hand, the selected optimum hybrid continuous designs of AS4/Epoxy include combinations with IM6/Epoxy and Spectra/Epoxy laminates. The thermal durability of these hybrid composites is shown in Figures 8–1, respectively.
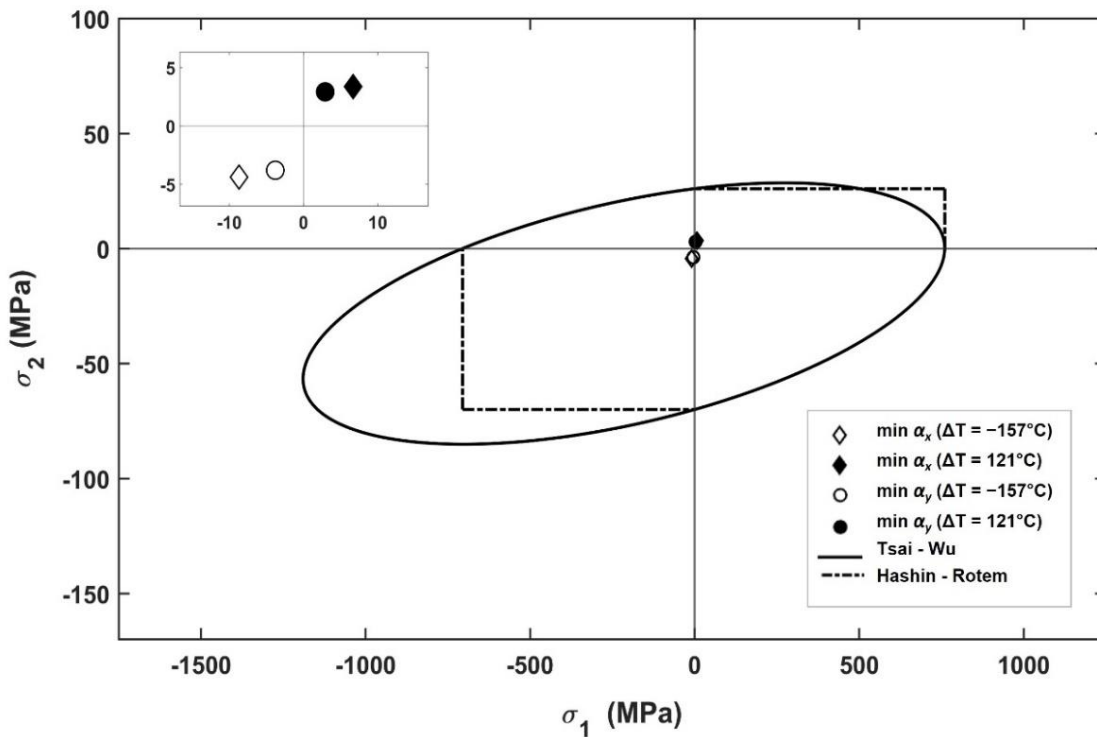
(a)
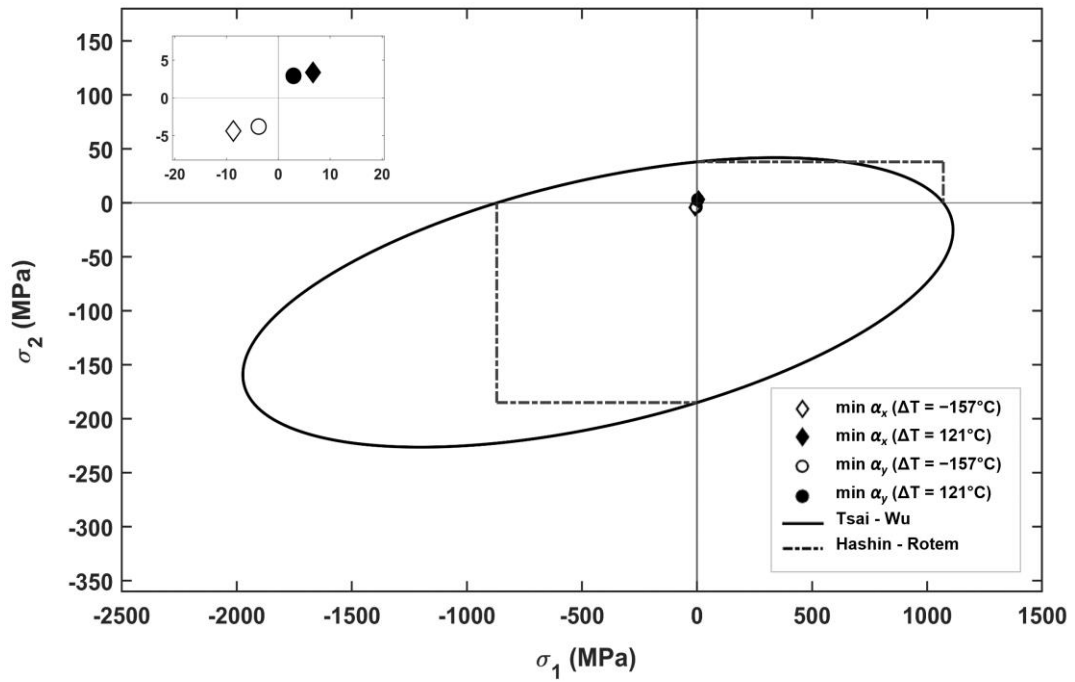
(b)

Figure 8. Thermal loading performances of min (α_x) [$(90_{GY70})_2/(45_{GY70})_2/(45_{Gl})_3/90_{Gl}$]s, and min (α_y) [$(45_{GY70})_4/(45_{Gl})_2/90_{Gl}/45_{Gl}$]s hybrid designs: (a) GY70 laminate, (b) E-Glass (Gl) laminate
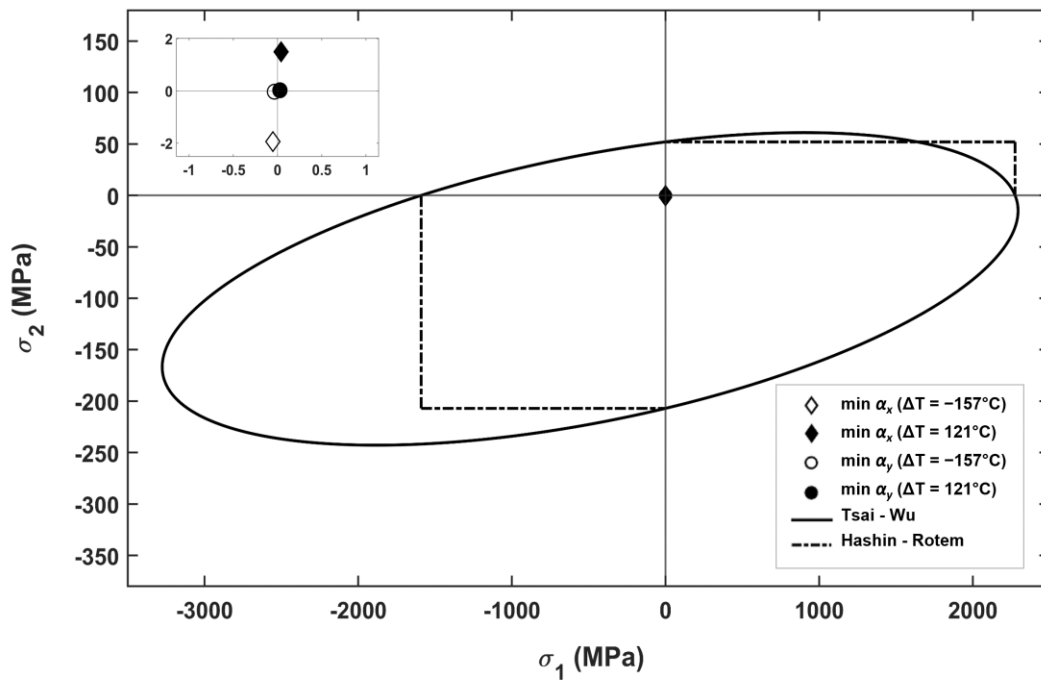
(a)
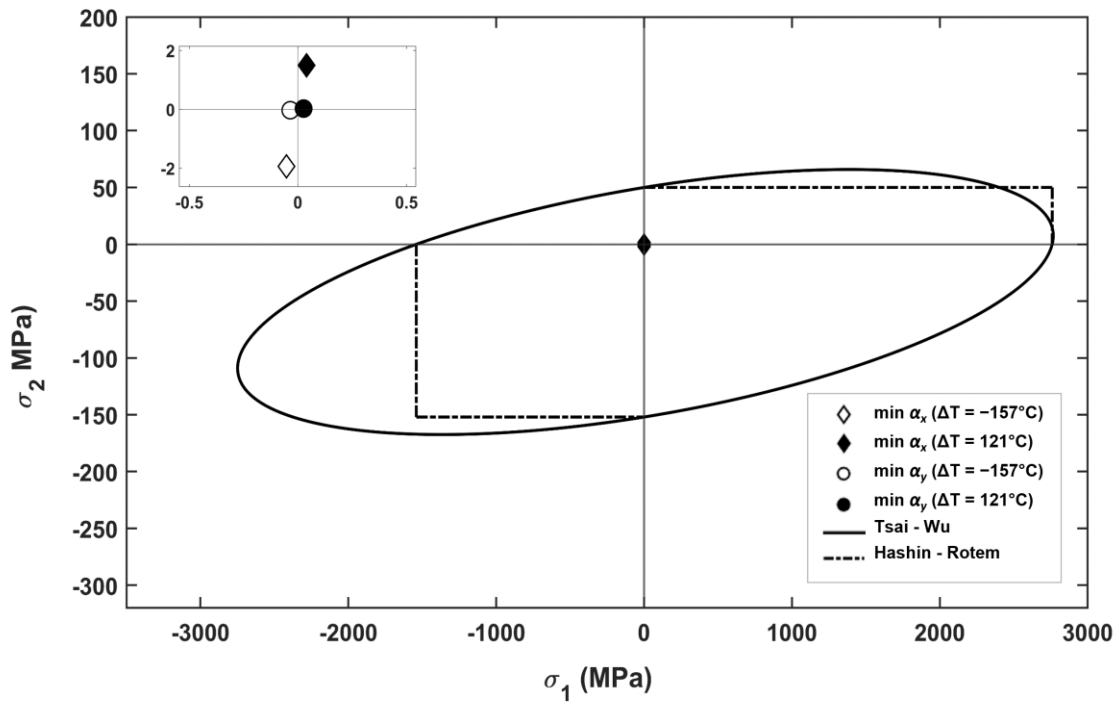
(b)

Figure 9. Thermal loading performances of min (α_x) $[0_{AS4}/(45_{AS4})_3/90_{IM6}/(45_{IM6})_3]_S$, and min (α_y) $[(90_{AS4})_4/(90_{IM6})_4]_S$ hybrid designs: (a)AS4 laminate, (b) IM6 laminate
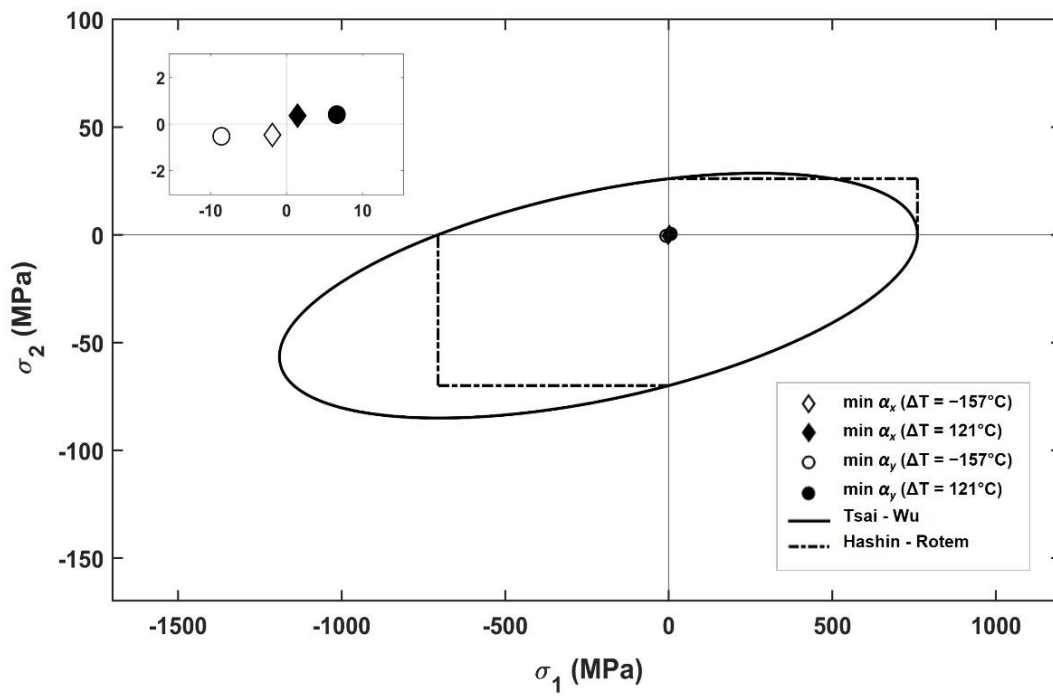
(a)
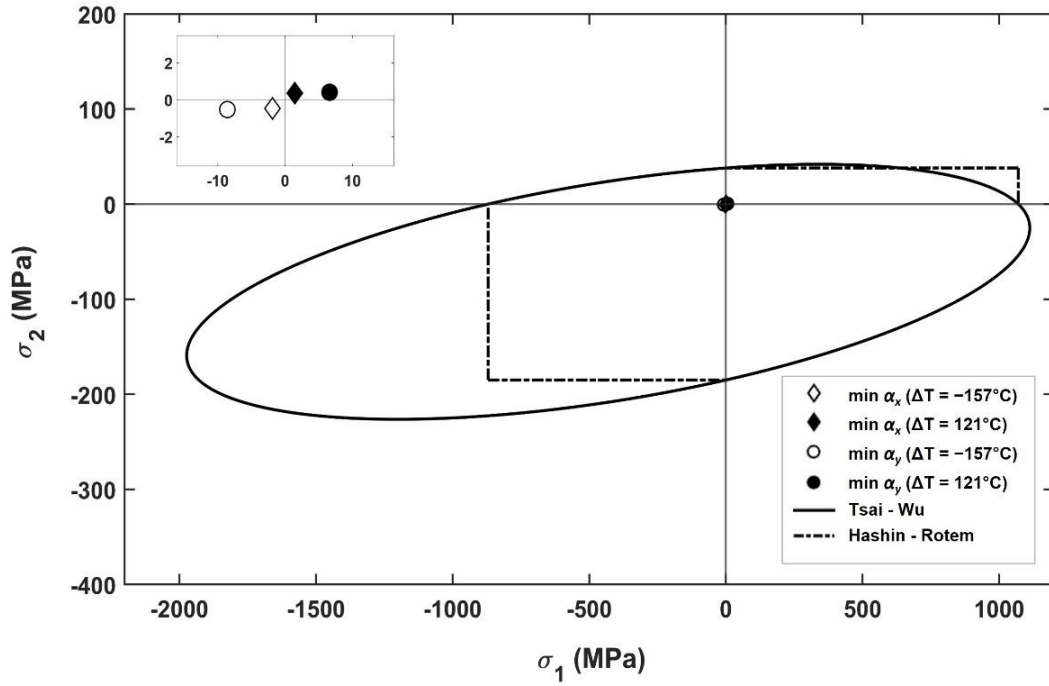
(b)

Figure 10. Thermal loading performances of min (α_x) $[25_{AS4}/80_{AS4}/57_{AS4}/45_{AS4}/36_{IM6}/16_{IM6}/57_{IM6}/71_{IM6}]_S$, and min (α_y) $[0_{AS4}/84_{AS4}/89_{AS4}/36_{AS4}/49_{IM6}/46_{IM6}/48_{IM6}/5_{IM6}]_S$ hybrid designs: (a)AS4 laminate, (b) IM6 laminate

(a)

(b)
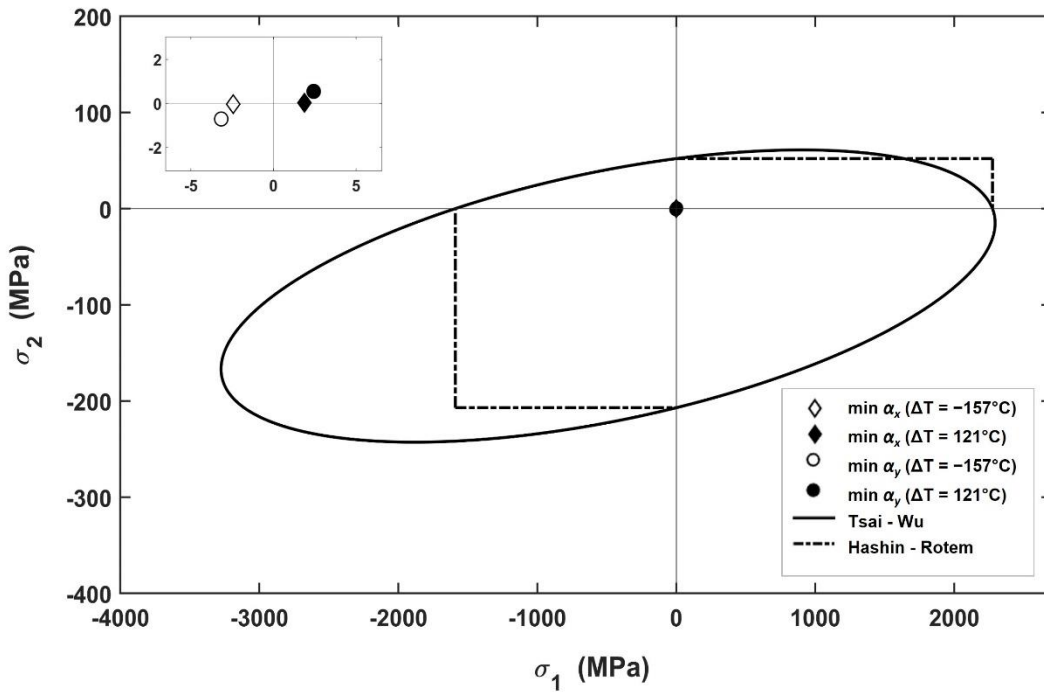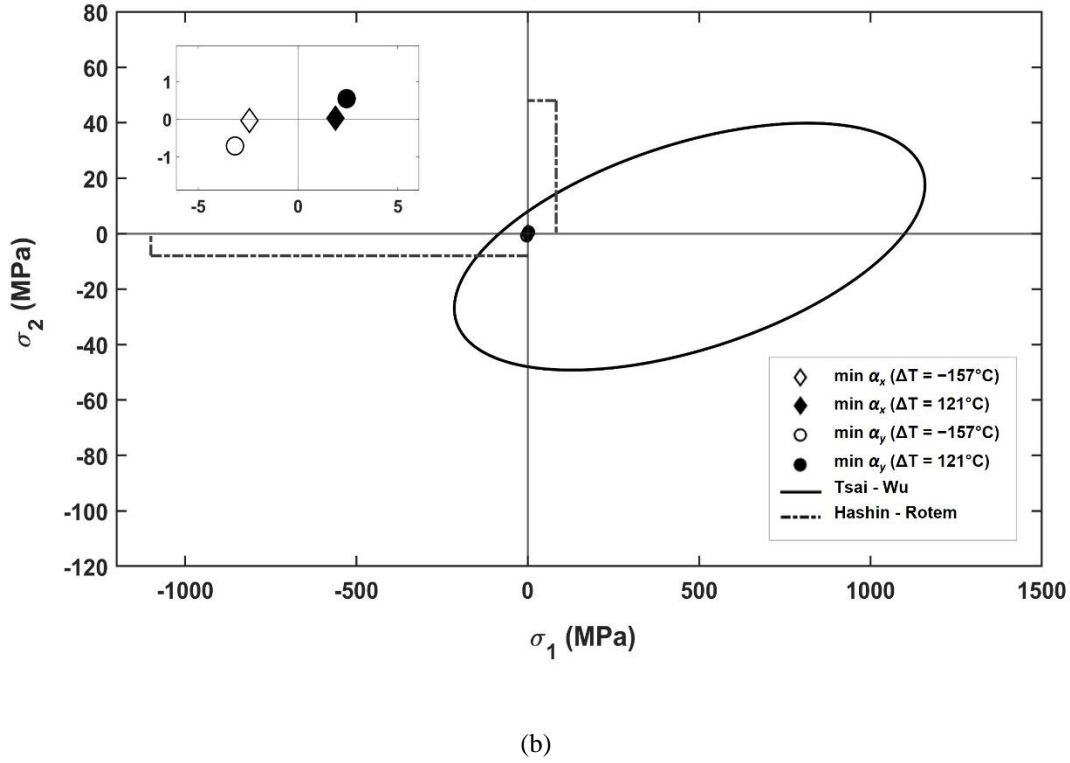
Figure 11. Thermal loading performances of min (α_x) [61$_{AS4}$/56$_{AS4}$/(88$_{AS4}$)$_2$/7$_{Sp}$/36$_{Sp}$/88$_{Sp}$/34$_{Sp}$]$_S$, and min (α_y) [1$_{AS4}$/28$_{AS4}$/(0$_{AS4}$)$_2$/1$_{Sp}$/21$_{Sp}$/1$_{Sp}$/0$_{Sp}$]$_S$ hybrid designs: (a)AS4 laminate, (b) IM6 laminate

Figures 8–11 show that min α_x and min α_y designs do not fail according to both Tsai-Wu (TW) and Hashin-Rotem (HR) failure criteria for all layers of the hybrid composites. That can be observed in more detail at the top left of all the figures. As in the case of the [A/B]$_{4S}$ sequence (Figures 4–7), it can be said that all the [A$_4$/B$_4$]$_S$ hybrid designs are readily within the safe zone according to the TW failure criterion. However, it seems that the stress values of many min α_x and min α_y designs are very close to the failure envelope of the HR failure criterion, even if these hybrid laminates can still be accepted in a safe zone. This situation can be noted mainly for the hybrid laminates presented in Figures 9 and 10.

7. Conclusion

In this study, the focus was on achieving dimensional stability optimization using hybrid composite materials. The selected hybrid composite materials to be used were Aramid/Epoxy, AS4/Epoxy, Boron/Epoxy, E-Glass/Epoxy, IM6/Epoxy, GY70/Epoxy, Kevlar49/Epoxy, and Spectra/Epoxy. The optimum fiber orientations in the [A/B]$_{4s}$ and

[A$_4$/B$_4$]$_S$ laminate sequences of the 16-layer hybrid composite laminates having minimum thermal expansion coefficients in the x and y directions were investigated by the GA/GPSA hybrid algorithm constituted via the MATLAB program.

All the non-hybrid and hybrid composite laminate results indicate that both optimum stacking sequences of the [A/B]$_{4S}$ and [A$_4$/B$_4$]$_S$ material sequences can minimize the thermal expansion coefficients, min α_x and min α_y up to the order of 10^{-10}. It was noted that [A/B]$_{4S}$ hybrid designs are slightly better than [A$_4$/B$_4$]$_S$ hybrid designs. When comparing the non-hybrid designs with all the hybrid designs, it was observed that the dimensional stability levels of the non-hybrid designs can be reduced to the order of 10^{-9}, whereas the hybrid designs can achieve even lower dimensional stability levels. Considering the continuous and traditional fiber-angled designs obtained through dimensional stability optimization, it was found that the optimum stacking sequences using continuous fiber angles provide better dimensional stability compared to the results of using traditional fiber angles in both material sequences. Furthermore, it can be stated that

131

all hybrid designs obtained for both material configurations exhibited dimensional stability levels according to the coefficients of thermal expansion ranging from 10^{-7} to 10^{-10} in general.

Additionally, the selected dimensionally stable hybrid designs were tested for their durability to temperature changes using the Tsai-Wu and Hashin-Rotem failure criteria. The results indicated that the majority of the selected optimum hybrid composite laminate designs were safe according to the failure criteria under positive and negative temperature changes. Overall, this study highlights the significant role of optimizing hybrid laminated composite laminate designs using various composite materials in achieving the maximum possible dimensional stability. Furthermore, these findings may provide valuable insights for future optimization studies in the design of laminated composite materials, particularly for aerospace applications.

Contributions of the authors

The first author, Hacer Geçmez has run all the optimization problems defined earlier and wrote the paper. The second author, Hamza Arda Deveci has constituted the structure of the study, and supported the writing part.

Conflict of Interest Statement

There is no conflict of interest between the authors.

References

[1] S. G. Lim and C. S. Hong, "Effect of transverse cracks on the thermomechanical properties of cross-ply laminated composites," *Compos. Sci. Technol.*, vol. 34, no. 2, pp. 145–162, 1989.

[2] K. J. Yoon and J. Kim, "Prediction of Thermal Expansion Properties of Carbon/Epoxy Laminates for Temperature Variation," *J. Compos. Mater.*, vol. 34, no. 2, pp. 90–100, Jan. 2000.

[3] R. Y. Kim and A. S. Crasto, "Dimensional stability of composites in space: CTE variations and their prediction," in *ICCM-10*, 1995, pp. 513–520.

[4] R. L. Riche and R. Gaudin, "Design of dimensionally stable composites by evolutionary optimization," *Compos. Struct.*, vol. 41, no. 2, pp. 97–111, Feb. 1998.

[5] M. Khalil, E. Bakhiet, and A. El-Zoghby, "Optimum design of laminated composites subjected to hygrothermal residual stresses," *Proc. Inst. Mech. Eng. L J. Mater. Des. Appl.*, vol. 215, no. 3, pp. 175–186, July 2001.

[6] R. P. Zhu and C. T. Sun, "Effects of fiber orientation and elastic constants on coefficients of thermal expansion in laminates," *Mech. Adv. Mater. Struct.*, vol. 10, no. 2, pp. 99–107, 2003.

[7] C. G. Diaconu and H. Sekine, "Flexural characteristics and layup optimization of laminated composite plates under hygrothermal conditions using lamination parameters," *J. Therm. Stresses*, vol. 26, no. 9, pp. 905–922, 2003.

[8] L. Aydin and H. S. Artem, "Single and multi-objective genetic algorithm optimizations of the laminated composites used in satellite structures," in *Proceedings of the International Symposium of Mechanism and Machine Science*, Izmir, Turkey, 2010, pp. 219–226.

[9] Z. Zhang, W. Zhong, and H. Song, "Design of hybrid composites with zero coefficient of thermal expansion," *J. Mater. Sci. Technol.*, vol. 12, no. 4, pp. 241–248, July 1996.

[10] F. Bressan, F. De Bona, and A. Somà, "Design of composite laminates with low thermal expansion," *Proc. Inst. Mech. Eng. L J. Mater. Des. Appl.*, vol. 218, no. 3, pp. 201–209, July 2004.

[11] S. Adali and K. Duffy, "Minimum cost design of vibrating laminates by hybridization," *Eng. Optim.*, vol. 19, no. 4, pp. 255–267, 1992.

[12] S. Adali and V. E. Verijenko, "Optimum stacking sequence design of symmetric hybrid laminates undergoing free vibrations," *Compos. Struct.*, vol. 54, no. 2–3, pp. 131–138, Nov.-Dec. 2001.

[13] M. Abachizadeh and M. Tahani, "An ant colony optimization approach to multi-objective optimal design of symmetric hybrid laminates for maximum fundamental frequency and minimum cost," *Struct. Multidiscipl. Optim.*, vol. 37, no. 4, pp. 367–376, Jan. 2009.

[14] M. Savran and L. Aydin, "Stochastic optimization of graphite-flax/epoxy hybrid laminated composite for maximum fundamental frequency and minimum cost," *Eng. Struct.*, vol. 174, pp. 675–687, Nov. 2018.

[15] A. K. Kaw, *Mechanics of composite materials*. Taylor and Francis, London, 2006.

[16] H. A. Deveci, L. Aydin, and H. Seçil Artem, "Buckling optimization of composite laminates using a hybrid algorithm under Puck failure criterion constraint," *J. Reinf. Plast. Compos.*, vol. 35, no. 16, pp. 1233–1247, Aug. 2016.

[17] S. W. Tsai and E. M. Wu, "A general theory of strength for anisotropic materials," *J. Compos. Mater.*, vol. 5, no. 1, pp. 58–80, Jan. 1971.

[18] Z. Hashin and A. Rotem, "A fatigue failure criterion for fiber reinforced materials," *J. Compos. Mater.*, vol. 7, no. 4, pp. 448–464, Oct. 1973.

[19] *MATLAB Optimization Toolbox. Computer software. Version R2019b.* The Mathworks, Inc. 2019.

[20] T. Weise, "Global Optimization Algorithms Theory and Application," *Journal of Computer and Communications*, 2008.

[21] X. S. Yang, *Engineering optimization: an introduction with metaheuristic applications*. NJ: John Wiley, 2010.

[22] S. S. Rao, *Engineering optimization theory and practice. NJ: John Wiley*, 2009.

[23] V. Torczon, "On the convergence of pattern search algorithms," *SIAM J. Optim.*, vol. 7, no. 1, pp. 1–25, 1997.

[24] H. A. Deveci and H. S. Artem, "Optimum design of fatigue-resistant composite laminates using hybrid algorithm," *Compos. Struct.*, vol. 168, pp. 178–188, May 2017.

[25] J. R. Vinson, R. L. Sierakowski, and C. W. Bert, "The behavior of structures composed of composite materials," *J. Appl. Mech.*, vol. 54, no. 1, pp. 249–249, 1987.

[26] F. Donald, A. Leif, A. Carlsson, and R. Byron, *Experimental Characterization of Advanced Composite Materials*. New York, 2002.

[27] R. R. Johnson, M. H. Kural, and G. B. Mackey, *Thermal Expansion Properties of Composite Materials*, California, 1981.

[28] NASA, "Thermal loadings that materials in space can withstand," 2022. [Online]. Available: https://www.nasa.gov/. [Accessed: Dec.28, 2021].

Using Quality Control Charts for Monitoring COVID-19 Daily Cases and Deaths in Türkiye

Esra POLAT[1*]

[1]*Department of Statistics, Faculty of Science, Hacettepe University, 06800, Ankara, Türkiye*

(ORCID: 0000-0001-9271-485X)

Abstract

In this study, since the nationwide partial curfews during the COVID-19 process in Türkiye began on November 18, 2020; especially for the periods between 25.11.2020-31.05.2022, the daily new cases and for the periods between 27.03.2020-31.05.2022, deaths and for the periods between 27.03.2020 to 04.07.2021, fatality rates are monitored by quality control charts. In this research, Run charts, EWMA control charts, and p-control charts are used for monitoring the COVID-19 process in Türkiye. In the periods of nationwide extended curfews (December 1, 2020–February 28, 2021), full lockdown (April 29–May 16, 2021), and gradual normalization (May 17– May 31, 2021), the number of daily cases and deaths show downward trend as it is expected. However, in periods of the local decision-making phase (March 1–29, 2021) and revised local decision-making phase (March 30–April 13, 2021), the number of new daily cases and deaths show an upward trend. In partial lockdown period (April 14-28, 2021), while the number of daily cases shows a downward trend, the number of deaths shows an upward trend. For January 1-May 31, 2022, both the number of daily cases and deaths show an upward trend until February 2022, when they reach a peak for this month then they start to decrease gradually. Fatality rate results show that in the periods of 27.03.2020–17.11.2020, 01.12.2020–28.02.2021, 01.03.2021–29.03.2021, 29.04.2021–16.05.2021 and 01.06.2021-04.07.2021, there are uptrends or downtrends. The daily new cases/deaths and fatality rates due to COVID-19 are monitored rapidly and effectively by control charts. In the future, the risks of this pandemic could be raised again and in that case, the effects of various precautions on the number of cases or deaths could be monitored by using various quality control charts and the process could be managed logically and scientifically for Türkiye.

1. Introduction

The outbreak of COVID-19 rapidly disseminated from China in December 2019, and in March 2020, stated as a pandemic by the World Health Organization. Türkiye reported its first COVID-19 case on 11.03.2020, and since that time, more than 17 million cases and 100000 deaths reported in the country. The surge in the number of new patients, cases, and deaths has posed a significant risk to public health in Türkiye, as in other countries. To mitigate

this risk, Türkiye and other nations have implemented measures to contain the spread of the virus, and mitigate the pandemic's negative impact on public health and economies [1].

Statistical Process Control (SPC) methods have significant roles in monitoring hospital performance, for example, fatality rate, pre and post-operative complexities, and number of infections in a hospital, etc. [2, 3]. SPC and the control chart, which is its prime instrument, allow researchers better with communicating and understanding data from

healthcare advance attempts [4]. Hence, the usage of SPC appears well-fitted for directing the pandemic by carefully observing indicators for the active development of the control plans applied by healthcare practitioners and political authorities.

There are studies on using quality control charts for monitoring COVID-19 data sets for different countries. Some of them listed below [5].

Arafah [6] inspected the usage of Laney p' control chart and the practice of test rules for evaluating governmental intercessions during the COVID-19 pandemic and understanding how specific actions and circumstances that happened affected the infection proportion. Laney (2002) has warned about the potential for overdispersion when employing the p-control chart, particularly for scenarios with large sample sizes, which could result in control limits too closely spaced. This closeness may lead to identify an excessive number of data points signal particular cause variation inappropriately. Laney introduced the concept of the Laney p' control chart to mitigate this risk. The infection rate (IR) data for the period of 31.10.2020-19.03.2022 used. IR computed by dividing the number of confirmed cases by the number of PCR (polymerase chain reaction) tests conducted. He used the Laney p' control chart for monitoring the COVID-19 IR and compared its performance with the exponentially weighted moving average (EWMA) control chart. Moreover, the performance of different test rules in observing IR changes analyzed. Making a comparison of the EWMA control chart with the Laney p' control chart, the data revealed that in most situations, the Laney p' control chart could specify the variation of IR faster. Odunayo et al. [7] monitored the analysis of COVID-19 in Africa. The data set was obtained from the Africa Centre for Disease Control (Africa CDC) at 10:00 PM on 24.04.2020, which contains several African countries with a number of deaths, number of discharged/recovered cases, and confirmed cases. Control charts, Pareto analysis, fishbone diagram, pie chart, and bar chart were the quality control methods used in this study. For Pareto analysis to identify the Areas (Countries) where more intervention would be needed, they draw a horizontal line from the 80% mark on the vertical cumulative percentage axis and, where it crosses the line graph, a line down to the horizontal axis also was drawn. The Pareto analysis indicated that 14 countries to the left of this line comprised 80% of the whole of the infected countries and the fishbone diagram described the symptoms for checking out for a patient infected by COVID-19. The trend analysis showed that the spread of the pandemic keeping going on to increase. The pie chart showed that pandemic has been still under control while the

death proportion has not been under control. Odunayo et al. [8] used the data retrieved from the Africa CDC at 10:00 PM on 27.05.2020, which consisted of several African countries' COVID-19 data. The number of deaths, a number of recovered cases, and confirmed cases of African countries' were used. In this study monitoring and tracking tools were trend plot, pie chart, Pareto analysis, bar chart, and control chart. The trend plot depicted the trend of the outbreak of the disease. The Pareto analysis indicated that 13 countries (South Africa, Egypt, Algeria, Nigeria, Morocco, Ghana, Cameroon, Sudan, Guinea, Djibouti, Republic of Congo, Gabon, and Somalia) were the most infected African countries. The trend analysis indicated a geometric increase in the spread of the pandemic despite the lockdown, and other measures put in place to curb the pandemic. Finally, from the performance evaluation, it was clear that the spread was likely to be under control from the pie chart. However, the death proportion has already been not under control. Fawzy and Ghalib [9] used the K-Nearest Neighbor Control Chart (K2-chart) and Kernel Principal Component Analysis Control Chart for the analysis. Relying on the daily epidemiological position of the Public Health Department of the Iraqi Ministry of Health, 18 variables representing the governorates of Iraq were used. An average run length metric was employed to assess the effectiveness of the charts. The findings indicated that the spread of infections related to the new coronavirus increased without control. Notably, the K2 chart exhibited superior performance in the short term, while both charts demonstrated relatively equal performance in the medium and long term. Hidayat et al. [10] assessed the data quality for determining the possible errors, which was sourced from the 'COVID-19 Data Repository by the Center for Systems Science and Engineering (CSSE) at Johns Hopkins University. They wanted to provide researchers with insights into the data's reliability before usage and then used control charts and acceptance sampling. 30% of the data was detected using a control chart and examined for potential errors. COVID-19 time-series data, 22.07.2020-01.08.2020 was used. The methods used were acceptance sampling and control charts. The Shewhart individual control chart was used. They detected data input errors, confirmed data is lower than recover, decreasing value, confirmed data is lower than death, zero confirm on the first date, not zero recovers on the first date, and not zero death on the first date. Their suggestion to researchers was to check and correct the dataset obtained from this data source before usage. Hidayat et al. [11] used a Tangent Control Chart (t-control chart) to determine countries that have identical positive case data trends

with Indonesia. t-control chart and Individual Moving Range Chart (I-MR Chart) showed that 71 countries out of 183 countries affected by the COVID-19 epidemic, have a positive case data trend similar to Indonesia. Irhaif et al. [12] used EWMA and moving average control charts to monitor the number of people infected with COVID-19 for April 2020 and they compared it with the dataset from April 2021. The results showed that there were out-of-control points for both of these two years. However, in 2021 the number of infections became double what it was in 2020 which indicated an increment in the number of patients infected with the virus. Mbaye et al. [5] used p-control chart to monitor the positivity rate, cure rate, and fatality rate for Senegal. The positivity fraction was moving away from the UCL as of 07.06.2020, which indicated that the condition has been yet under control. The progress of the cure fraction exhibited irregularities, followed by an increase, and gradually reached its maximum between 12.04.2020 and 20.04.2020. This period marked the widespread use of chloroquine for the treatment of COVID-19 in Senegal. The fatality fraction was rather low and was closer to the lower limit. But a slight increment had been seen in the latter. The observed phenomenon might be attributed to the rise in the incidence of COVID-19 cases, which in turn increased the number of severe cases and ultimately led to an increment in mortality. Mahmood et al. [13] conducted a comprehensive study to track variations in the number of deaths and classify growth phases, namely pre-growth, growth, and post-growth for Pakistan during the COVID-19 pandemic. To observe these changes, the authors employed c and EWMA control charts, based on secondary data of daily reported deaths in Pakistan owing to the pandemic. As per the c-control chart, Pakistan shifted from the pre-growth phase to the growth phase on 31.03.2020. Meanwhile, the EWMA control chart indicated that Pakistan remained in the growth phase from 31.03.2020 to 17.08.2020, with certain markers suggesting a decline in the number of deaths. The study inferred that Pakistan briefly entered the post-growth phase from 27.07.2020 to 28.07.2020, following which it re-entered the growth phase with an alarm on 31.07.2020. Subsequently, the number of deaths began to decrease in August, implying a probable approximation of the post-growth phase in Pakistan. In their study, Mukhaiyar et al. [14] utilized a p-control chart for monitoring the fraction of positive COVID-19 cases in DKI Jakarta Province. The data used were derived from a sample of COVID-19 tests conducted between April 2020 and January 2021. Notably, the researchers did not statistically control the process of daily new COVID-19 cases,

and several mean shifts in the fraction of positive cases were observed at different time intervals. The results of the study revealed a sustained upward trend in the fraction of positive cases, indicating a gradual rise in COVID-19 cases within the region. The study suggested that public behavior in Jakarta could serve as a model for the government in developing policies to contain the spread of COVID-19. The authors inferred that the COVID-19 situation persisted to be unmanageable due to the increased mobility of Jakarta's inhabitants, and the irregularities in the region. Parry et al. [15] devised a hybrid Shewhart control chart that integrates an I-control chart and c-control chart with a log-regression slope to identify four distinct 'epochs' of the COVID-19 epidemic, namely, (i) pre-exponential growth, (ii) exponential growth, (iii) plateau or descent, and (iv) stability after descent. The chart's efficacy was validated using global data from various levels, including national, regional, and local. Local experts in the field were involved in the validation process, which entailed analyzing COVID-19 cases, hospitalizations, and deaths. They observed that the hybrid chart promptly and effectively indicated the onset of each of the four epochs. For instance, in the UK, a signal of the exponential growth of COVID-19 deaths was identified on 17 September, 44 days before the announcement of a comprehensive lockdown. Similarly, in California, USA signals highlighting increases in COVID-19 cases at the county level were noticed in December 2020 before the implementation of statewide stay-at-home orders, with subsequent declines in the weeks that followed. In Ireland, during December 2020, the hybrid chart identified rises in COVID-19 cases, succeeded by increases in hospitalizations, the number of deaths, and intensive care unit admissions. After national restrictions in late December, a parallel sequence of reductions in these measures was identified in January and February 2021. Rashed and Eissa [16] sorted countries in descending order based on their respective residential census. The authors analyzed the top contributing countries, which accounted for approximately 60% of the total COVID-19 cases and deaths. The countries were ranked in decreasing order of cases as follows: USA, Italy, Spain, China and Germany. Similarly, for deaths, the order was Spain, the USA, and France. The authors identified a cubic relationship between the increasing number of cases and daily deaths. CUSUM control charts were utilized to monitor the daily changes in the epidemic disease registers, revealing that the disease's daily fluctuations had been on the rise and statistically out of control by 17.03.2020 and 19.03.2020. Singh et al. [17] employed an X-bar control chart and EWMA control

chart to assess the transmission of COVID-19 in several major provinces of India, as well as all of India. Warning and control limits were calculated and analyzed for the average weekly growth. The study indicated that the pandemic cannot be expected to be brought under control shortly, as the average weekly growth index of COVID-19 continues to exceed 0. Yupaporn and Rapin [18] employed the cumulative distribution function of the total number of COVID-19 cases over time to develop a quantile function to determine the levels of COVID-19 alarm. The authors monitored COVID-19 outbreaks using the EWMA control chart, and the control limits were established using both the delta technique, and the sample mean and variance technique. The study focused on selected countries and regions, namely Singapore, Thailand, Hong Kong, and Vietnam, for which the total number of COVID-19 cases from 15.02.2020 to 16.12.2020 exhibited symmetric patterns. To compare the effectiveness of the two techniques, the authors applied them to an EWMA control chart based on the first hitting time to detect COVID-19 outbreaks in the selected regions and countries. The results indicate that the sample mean and variance method outperforms the delta method in detecting the first hitting time. Additionally, the COVID-19 alert levels can be categorized into four stages to effectively monitor the COVID-19 situation. These stages assist authorities in formulating policies for monitoring, controlling, and safeguarding the population against a COVID-19 outbreak. Waqas et al. [19] explored Shewhart (X, R, C) control charts and EWMA control chart for their study. They used the EWMA control chart due to its exceptional capability in detecting shifts and its compatibility with the dataset they employed. Daily deaths have been monitored for the period between March 2020 to February 2023. During the application on COVID-19 deaths, the EWMA control chart accurately depicted mortality dynamics from March 2020 to February 2022, indicating six distinct stages of death. The 3rd and 5th waves had been extremely catastrophic, resulting in a considerable loss of life. Notably, a persistent sixth wave appeared from March 2022 to February 2023. The EWMA map effectively pinpointed the peaks associated with each wave by thoroughly examining the time and amount of deaths, providing vital insights into the pandemic's progression. The USA entered a seventh phase (6th wave) from March 2022 to February 2023, marked by fewer deaths. They pointed out the ongoing importance of maintaining vaccination campaigns and pandemic control measures. The authors recommended the incorporation of the EWMA

control chart for monitoring immunization progress, deaths, and cases.

Control charts contribute to the ability to manage disease outbreaks efficiently, minimize their impact, and inform evidence-based decision-making. They are valuable tools for public health officials, epidemiologists, and policymakers, helping them respond effectively to such crises. After examining the studies on using quality control charts for monitoring COVID-19 data sets for different countries, it is realized that there is no study yet for Türkiye. In this study, COVID-19 data sets for Türkiye considered. The aim of the study is a comprehensive monitoring of daily cases, deaths, and fatality rates in Türkiye, especially considering the periods of restrictions. Hence, the effects of various precautions on the number of cases or deaths could monitored using quality control charts, and the process could be managed logically and scientifically for Türkiye in the future for risks of a pandemic.

The rest part of the study is organized as follows. In Section 2, the COVID-19 process in Türkiye is presented. In section 3, a brief theory for the Run chart, EWMA control chart, and p-control chart are presented. In Section 4, Run charts, EWMA control charts, and p-control charts for the COVID-19 data set of Türkiye are presented, and the comments are presented. Lastly, general comments and a summary of the results are presented in the last section.

2. The Covid-19 Period in Türkiye

On 11.03.2020, the initial COVID-19 cases were reported in Türkiye, leading to a set of limitations imposed from the start of the outbreak until autumn 2020, containing the summer for the year 2020. The measures taken during this period in Türkiye included the suspension of education on March 16, 2020, and the imposition of a curfew on March 20, 2020, for people over the age of 65. Travel between cities was restricted in 31 regions on April 3, 2020, followed by a curfew for those under the age of 20 on April 4, 2020. A weekend curfew was imposed in 31 cities on April 10, 2020. On May 11, 2020, the first phase of the normalization plan was initiated, enabling the reopening of barbershops, marketplaces, shopping malls, cafes, and restaurants. Under certain conditions, hotels and hostels began accepting guests on May 27, 2020. On June 1, 2020, a policy of "new normalization" was instituted, which enabled the resumption of operations at resting areas, public entertainment venues, association clubs, tea gardens, sports halls, and swimming pools. Wedding halls

were allowed to reopen with the condition of operating at a maximum capacity of 25%. Restrictions in performance centers, wedding venues, and theaters were lifted on July 1, 2020 [20]. The upsurge in the number of COVID-19 infected patients has been attributed to non-compliance with health guidelines such as wearing masks and avoiding contact with infected individuals in workplaces, markets, or enclosed areas. The continued violation of health protocols in 2021 by some residents is indicative of their disregard for the harm inflicted in 2020. After the end of the normal period in the summer of 2020, nationwide partial curfews were imposed on November 18th in Türkiye. On November 25th, the Republic of Türkiye Ministry of Health reported the first daily number of COVID-19 cases. Several nonpharmaceutical interferences were implemented during the pandemic in Türkiye, which were categorized by İlhan et al [20] based on their characteristics. The authors used circulars from the Ministry of İnternal Affairs to label each period of restrictions. Table 1 provides an overview of the different periods of limitations in Türkiye since 18.11.2020 [20].

Table 1. Periods of limitations in Türkiye since 18.11.2020.

Periods of Restrictions	Implementation Date	Number of Days
Nationwide partial curfews	November 18-30, 2020	13
Nationwide extended curfews	December 1, 2020-February 28, 2021	90
Local decision-making phase	March 1-29, 2021	29
Revised local decision-making phase	March 30–April 13, 2021	15
Partial lockdown	April 14-28, 2021	15
Full lockdown	April 29–May 16, 2021	18
Gradual normalization	May 17–31, 2021	15
2th phase of gradual normalization	June 1, 2021-May 31, 2022	365

Nationwide partial curfews (Starting from November 18th, 2020): Türkiye imposed nationwide partial curfews with weekend curfews, excluding the hours between 10:00 and 20:00. This regulation came into effect from November 21st onwards. During this period, cafes, restaurants, and patisseries were allowed to operate between 10:00 and 20:00 but only provided take-out or pick-up services. Age-specific limitations were imposed, allowing persons aged 65 and over to leave their homes between 10:00 and 13:00, whereas those under the age of 20 were authorized to leave between 13:00 and 16:00. İlhan et al. [20] referred to this period as "nationwide partial curfews," which was the least restrictive measure at the national level, except the final phase (the second phase of gradual normalization). The Republic of Türkiye Ministry of Health used the terms "patient" and "case" with varying definitions for epidemic data reporting. An individual was classified as a patient if they tested positive for the virus through PCR tests, but only if they displayed symptoms. On one hand, a patient was considered as an individual who exhibited symptoms and tested positive with PCR tests. On the other hand, a case was defined as an individual who tested positive with PCR tests, regardless of whether they showed symptoms or not. From November 25th, daily cases began to be reported [20].

Nationwide extended curfews (Starting from December 1st, 2020): The implementation of the curfew was extended throughout the weekend, beginning at 10:00 p.m. on Friday, and a separate curfew was enforced during weekdays beginning at 9:00 p.m. İlhan et al. [20] identified this period as the "nationwide extended curfews" [20].

Local decision-making phase (Starting from March 1st, 2021): "Local decision-making phase" was implemented in Türkiye to manage the COVID-19 pandemic. The provinces were assessed and classified as "low, medium, high, and very high" according to their level of risk. The categorization was updated every two weeks based on the current status of each province. This phase was called the blue-yellow-orange-red provinces approach. Weekend curfews were lifted in low and medium-risk provinces, while they continued only on Sundays in high and very high-risk provinces. In low and medium-risk provinces, restrictions for those over 65 and under 20 had been lifted, and education at all levels resumed. In high and very high-risk provinces, primary schools, 8th, and 12th grades, and preschool education institutions had been allowed to open. The curfew was still in place for those over 65 and under 20, and it was also extended. Going out on Sunday was allowed only in low and medium-risk provinces. Except in very high-risk provinces, cafes and restaurants began

to operate again with a maximum capacity of 50%. The nationwide curfew was from 21:00 to 05:00.

Revised local decision-making phase (Starting from March 30th, 2021): The curfews implemented during weekdays and weekends based on the risk categories have been revised. In high-risk provinces, the weekend curfew had been implemented only on Sundays, while in very high-risk provinces, it was implemented on both Saturdays and Sundays. Public places like restaurants and cafes were allowed to accept customers with a 50% capacity restriction between 07:00 and 19:00. In provinces categorized as low and medium-risk, a maximum of four individuals were permitted to sit together at the same table, whereas in provinces classified as very high-risk and high, only two individuals had been allowed for sitting together. This period has been referred to as the "revised local decision-making phase" by İlhan et al. [20].

Partial lockdown (Starting from April 14th, 2021): On April 14th, 2021, a "partial lockdown" was instituted, which involved updating the hours of the weekday curfew to 7:00 p.m. and 05:00 in the morning. Extra precautions were implemented for Ramadan. A weekend curfew had been imposed in all provinces, and public spaces, for instance, cafes and restaurants, were closed.

Full lockdown (Starting from 29th April 2021): On April 29th, 2021, a comprehensive lockdown was declared in Türkiye. All levels of education were postponed, including exams. In addition, inter-provincial public transport was allowed to operate at only 50% of its normal capacity.

Gradual normalization (Starting from May 17th, 2021): On May 17th, 2021, a phase "gradual normalization" was declared. During weekdays, the curfew enforced from 21:00 to 5:00, curfew covered the entire Saturdays and Sundays in weekends, ending at 05:00 on Mondays. Public establishments, for instance cafes, restaurants, and patisseries, allowed offering only takeaway service.

Second phase of gradual normalization (Starting from June 1st, 2021): The period of "gradual normalization" in Türkiye ended and the period followed by the second phase of gradual normalization from June 1st, 2021. The updated curfew rule mandated individuals to stay indoors between 22:00 and 05:00 on Saturdays and Mondays, while a full-day curfew implemented on Sundays. The Republic of Türkiye Ministry of Healths' Epidemic Management and Working Guide required restaurants, patisseries, cafeterias, and other food and drink establishments following a set of guidelines to ensure public health. Specifically, tables placed 2 meters apart from each other, and chairs placed 60 centimeters apart from each other. These establishments were permitted to serve customers between 7:00 and 24:00 on Sundays and between 21:00 and 24:00 on the other days, exclusively as takeaway services.

3. Material and Methods

Control charts can help in the early detection of outbreaks by monitoring relevant variables such as the number of cases, hospitalizations, or deaths. Sudden shifts or unusual patterns in the data can indicate a potential problem, allowing for a prompt response. Control charts contribute to the ability to manage disease outbreaks efficiently, minimize their impact, and inform evidence-based decision-making. They are valuable tools for public health officials, epidemiologists, and policymakers, helping them respond effectively to such crises. In this study, Run charts, EWMA control charts, and p-control charts used for monitoring the COVID-19 data set of Türkiye.

3.1. Run Chart

A run chart is a basic line graph that displays a measurement over time, featuring a horizontal line representing the median. This line divides the data points, with half of data points located above the median and the other half below it (Figure 1). The primary aim of a run chart is to detect the process improvement or deterioration, which manifests as non-random patterns in the arrangement of data points relative to the median. When the process of interest exhibits purely random variation, the data points will randomly dispersed around the median.

"Random" signifies that we cannot predict whether the next data point will be higher or lower than the median, with each event having a probability of 50% and the data points being unrelated. Independence implies that the location of one data

point does not affect on the location of the following data point, indicating an autocorrelation does not exist in the data. When the process undergoes a shift, these conditions cease to hold, and statistical tests may reveal patterns of non-random variation. Hence, run charts are serving as valuable tools for enhancing healthcare processes and identifying process deterioration [21, 22].
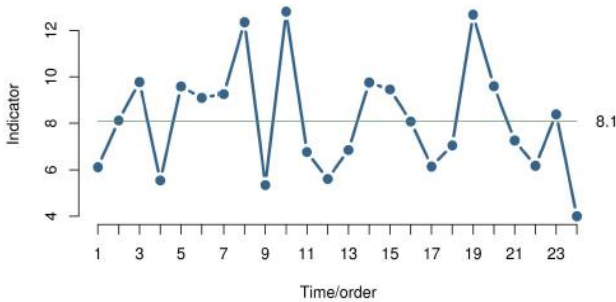

Figure 1. Run Chart.

Variations that are not random can manifest in various ways. When the processing center shifts due to improvement or degradation, we may witness unusually extended sequences of consecutive data points on one side of the median or notice an unusually infrequent crosses the median on the graph [21, 22, 23].

3.2. EWMA Control Chart

An EWMA control chart is a statistical process control chart presented by Roberts [24], a well-established method, namely, employed to identify shifts in process parameters over time. Let a random variable x_i represents the observations, and λ is a smoothing constant and satisfies the expression $0 < \lambda \leq 1$. Then EWMA statistic is defined as follows [13, 19]:

$$Z_i = \lambda x_i + (1-\lambda) Z_{i-1}, \text{ where } i = 1, 2, 3, ..., \quad (1)$$

Here, Z_{i-1} is the previous EWMA statistic. Hence, the Z_i is a weighted mean of both historical and recent observations, assigning greater importance to more recent observations. To establish the control limits for the control chart, you must first define the initial value μ_0, which represents the in-control process mean. The standard deviation (σ) of the independent random observations (x_i) needs to be calculated. Finally, the control limits' width, denoted as *L* and typically set at 3, needs to be defined. The effectiveness of the EWMA control chart relies on the chosen value of λ, with a smaller λ resulting in faster detection of minor

shifts in the mean. When the EWMA statistic Zi exceeds these control limits, it signifies a mean shift. The EWMA control chart is particularly useful for detecting slight mean variations, particularly when λ is small. In our study, the EWMA control chart with smoothing parameter $\lambda = 0.25$ is used from the values of $\lambda = 0.25, 0.50, 0.75,$ and 1. Because it was determined to be the most effective for observing patterns and out-of-control situations. The EWMA statistic can be seen as a weighted mean of both historical and recent observations, making it insensitive to the normality assumption. Hence, the EWMA control chart is well-suited for individual observations. The control limits for the EWMA control chart are presented as follows [13, 19]:

$$UCL = \mu_0 + L\sigma\sqrt{\lambda(2-\lambda)^{-1}\left[1-(1-\lambda)^{2i}\right]}$$
$$CL = \mu_0 \quad (2)$$
$$LCL = \mu_0 - L\sigma\sqrt{\lambda(2-\lambda)^{-1}\left[1-(1-\lambda)^{2i}\right]}$$

If the i increases to infinity, then the term $\left[1-(1-\lambda)^{2i}\right]$ approaches 1, at which point the time-varying limits transition into asymptotic limits and are defined as follows:

$$UCL = \mu_0 + L\sigma\sqrt{\lambda(2-\lambda)^{-1}}$$
$$CL = \mu_0 \quad (3)$$
$$LCL = \mu_0 - L\sigma\sqrt{\lambda(2-\lambda)^{-1}}$$

3.3. p-Control Chart

p-control chart used for monitoring the fraction of nonconforming units, for instance, the proportion nonconforming or proportion of defective, showing the fatality proportion for this study. In this case, it is a proportion of the daily number of patients who died to the daily number of ill people. The centerline (CL) and upper and lower limits (UCL, LCL) of the p-control chart are computed as follows. Here, D_i shows the nonconforming items in sample i, n_i (sample size) is the number of units per sample i, and m shows the number of samples [6].

$$CL = \bar{p} = \frac{\sum_{i=1}^{m} D_i}{\sum_{i=1}^{m} n_i}, \qquad LCL = \bar{p} - 3\sqrt{\frac{\bar{p}(1-\bar{p})}{n_i}}, \qquad UCL = \bar{p} + 3\sqrt{\frac{\bar{p}(1-\bar{p})}{n_i}} \quad (4)$$

3-sigma limits are used as it is a popular choice in literature. The reason is found partially in statistical theory and partially in practicality. Lloyd [25] summarizes the reasons and lists the studies mentioning the reasons for the usage of 3-sigma limits. Shewhart's use of 3 sigma limits (i.e., three above the mean and three below the mean for a total of 6 sigma units) as opposed to any other multiple of sigma did not stem from any specific mathematical computation. Shewhart mentioned that 3 "seems to be an acceptable economic value," and that the choice of 3 was justified by "empirical evidence that it works". A summary of the rationale for using Shewhart's 3-sigma limits mentioned by Provost and Murray (2011) [26] listed below [25]:

- The limits have a basis in statistical theory.
- The limits have proven in practice to distinguish between special and common causes of variation.
- In most cases, the use of the limits will approximately minimize the total cost due to overreaction and underreaction to variation in the process.
- The limits protect the morale of the workers in the process by defining the magnitude of the variations that has been built into the process.
- The combined total risk of type I and type II errors is minimized when 3-sigma limits are used.

Interested readers could access detailed information on why 3-sigma limits are used popularly and the article titles on this issue from Lloyd [25].

4. Results and Discussion

Control charts are statistical tools for monitoring and maintaining the stability of processes or situations. Control charts play crucial role in tracking and managing the outbreak for COVID-19. They help public health officials monitor important indicators, identify unusual patterns or trends, and assess the effectiveness of interventions. Control charts also enable data-driven decision-making. For COVID-19, a situation is considered "under control" when the disease spreads within acceptable limits, and the number of cases and deaths, fatality rate, and other relevant indicators remain relatively stable. It means that outbreak is not experiencing sudden, unexplained surges or declines. Achieving control may involve maintaining certain thresholds for significant parameters, such as the number of new cases per day. After examining the literature review over quality control charts implementations on COVID-19 datasets for different countries, in this study, Türkiye considered, and the dataset of the number of daily

COVID-19 cases and deaths, fatality rates of Türkiye are used. The data was obtained from the website of the Republic of Türkiye Ministry of Health. The Ministry of Health employed distinct definitions for the terms "patient" and "case" when presenting information about the epidemic. As of 25.11.2020, the number of daily cases started to be declared [27]. The analyses were performed using R software.

4.1. Monitoring the Daily Cases

The General Coronavirus Chart dataset of the Republic of Türkiye Ministry of Health is used as the data source. When we monitor the daily cases with Run charts as given in Figure 2, it is clear that for the period of **25.11.2020–30.11.2020**, there is an upward trend, and then it stabilizes, and again the upward trend starts. For the period of **01.12.2020–28.02.2021**, there is a downward trend. For the period **01.03.2021–29.03.2021**, an upward trend starts, and for the period **30.03.2021–13.04.2021**, this trend continues. For the period **14.04.2021–28.04.2021**, a downward trend starts and continues until **01.06.2021**. For the period of **01.06.2021-31.12.2021** (last 7 months of 2021), the number of daily cases begins increasing at the end of July and then shows small waves until the last days of December as it starts upward trend again. For the period of **01.01.2022-31.05.2022** (first 5 months of 2022), the number of daily cases shows an upward trend until February 2022 when it reaches a peak on this month then it starts to decrease gradually.
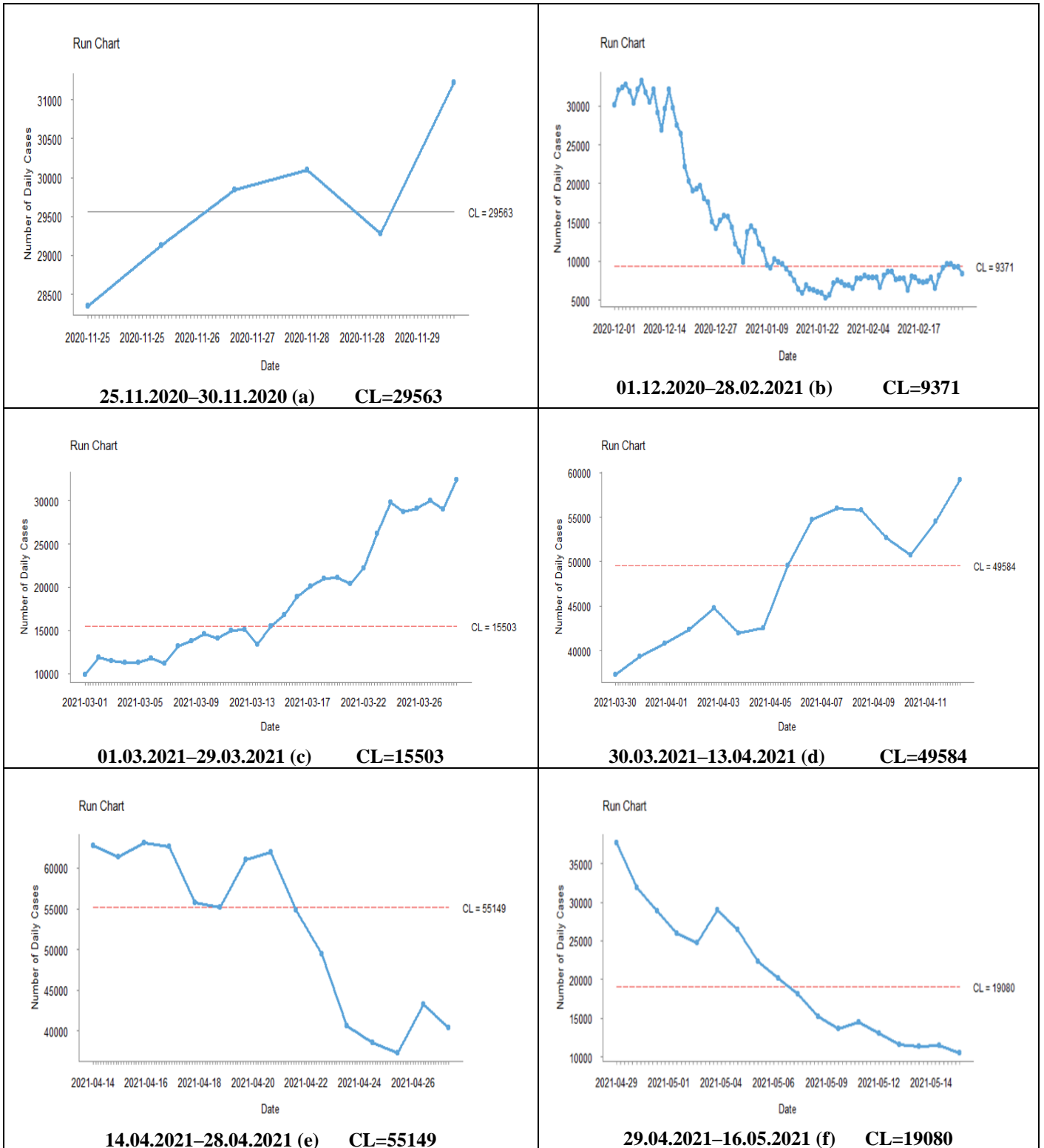
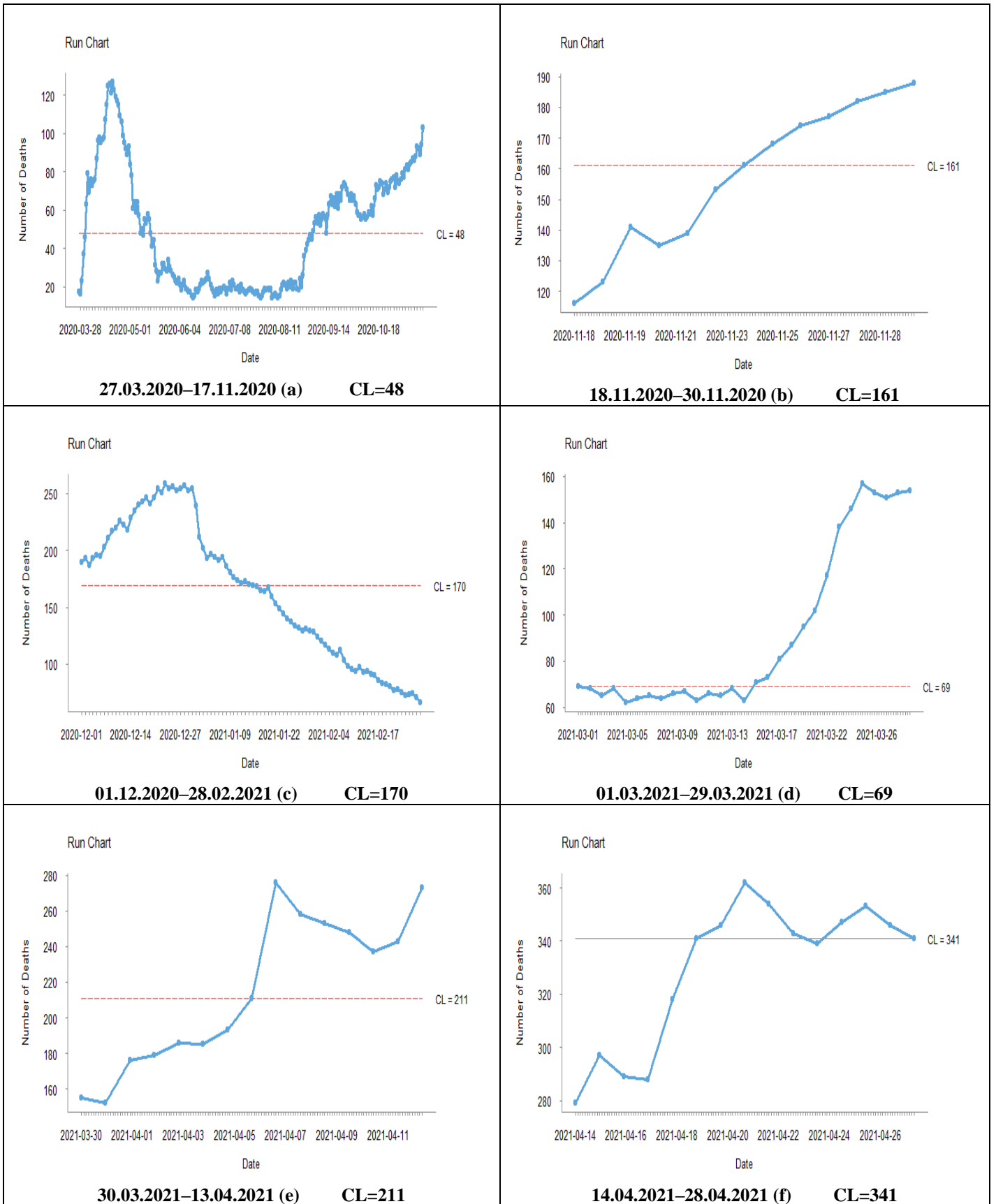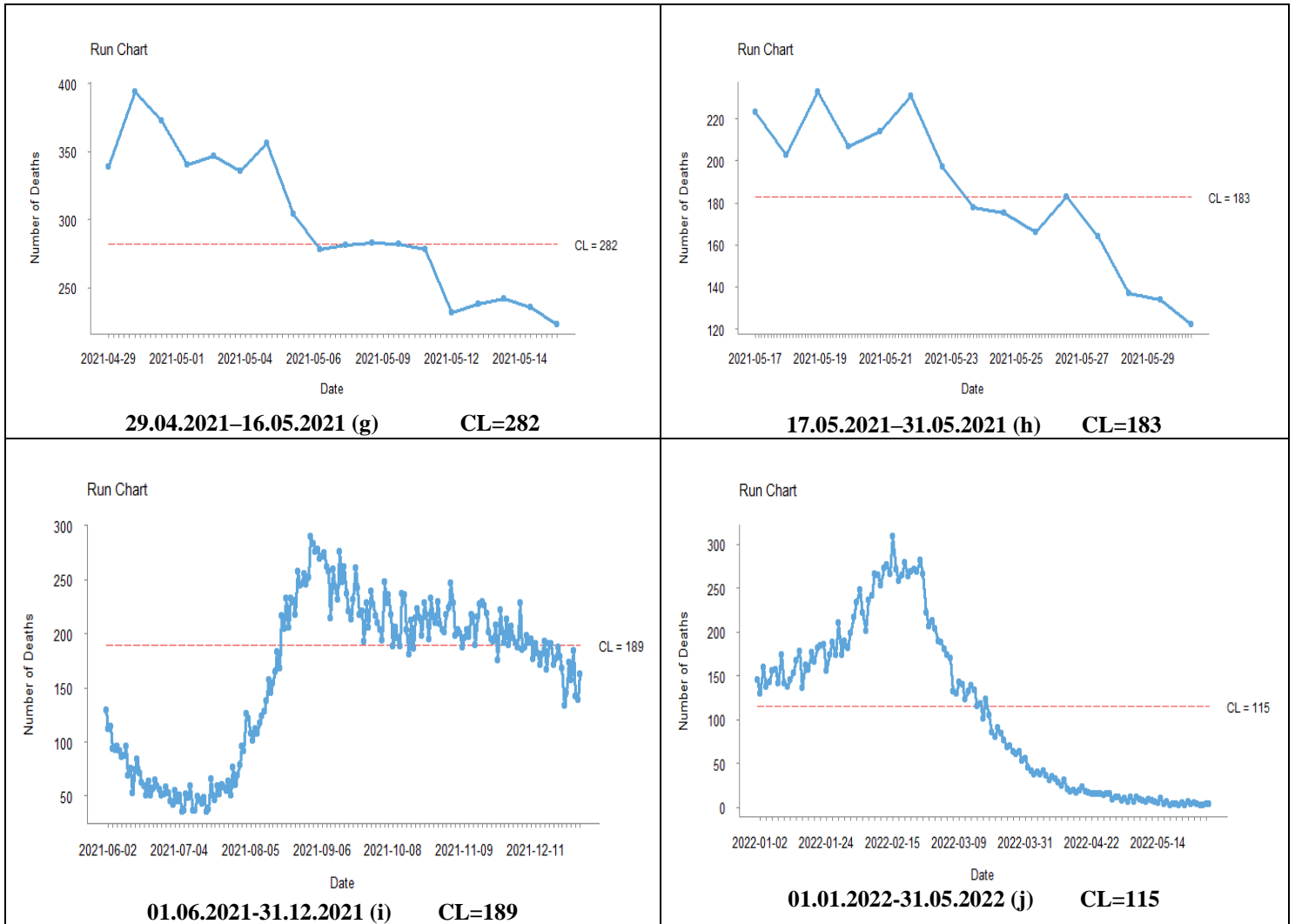**Figure 2.** Run charts for number of daily cases.
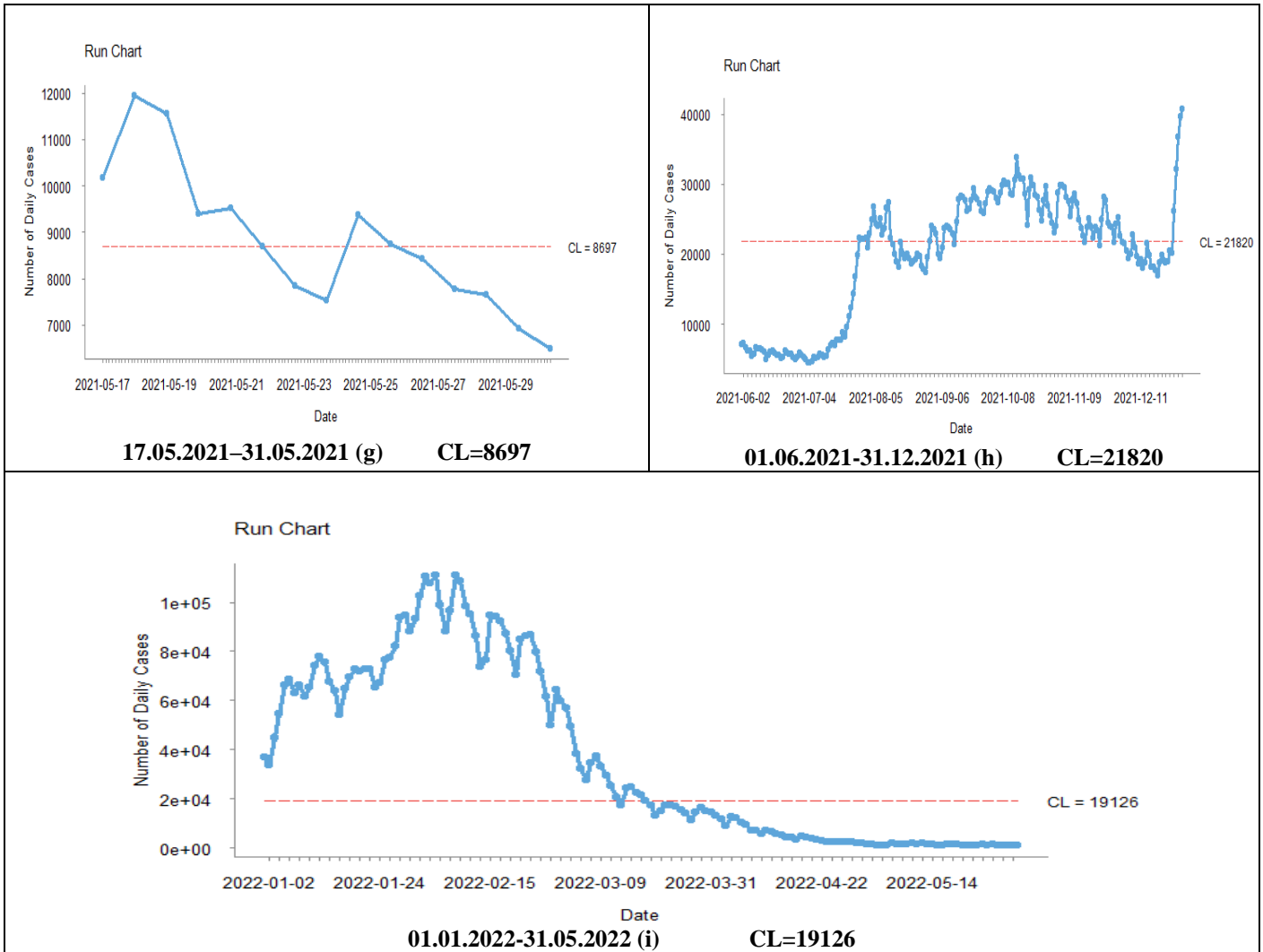
Figure 2. Run charts for number of daily cases (continued).

The EWMA control chart offers a versatile method for modeling the number of cases, as it can customize by altering the smoothing parameter. This adjustment enables you to have greater or lesser responsiveness to changes in the dataset, providing flexibility in the modeling approach.

This study aims to monitor the changes in daily cases; hence, after conducting a thorough literature review, an ideal chart is the EWMA control chart. Because it provides rapid detection of minor shifts. Figure 3 shows that during these periods, the daily cases are out of control for all periods except **25.11.2020–30.11.2020**, as only 5 days were monitored. However, for all of the periods, there are upward or downward trends or wavy trends. Figure 3 (a) depicts that no point falls beyond the control limits, meaning that Türkiye's COVID-19 pandemic is at the start of the growth phase. It is evident from Figure 3 (b) that Türkiye has sustained the growth phase until the middle of

December 2020. Starting from January 14, 2021, the number of daily cases stays below 14110 daily cases on average per day, and it shows a downward trend. From Figure 3 (c), it is clear that for the period of **1.03.2021–29.03.2021**, the EWMA control chart monitored 18585 daily cases on average per day, until March 18, 2021, the downward trend continued, after this date upward trends started. A sudden rise (exponential growth) was identified when 26182 daily cases were reported in a day in March 2021, and March 2021 remained higher in daily cases. As seen from Figures 3 (d) and 3 (e) the number of daily cases is increasing even further starting from April 9, 2021. The number of daily cases started to decrease on April 23, 2021, the last days of April 2021, the number of daily cases remains in lower values. As the spring period starts Figure 3 (f) shows that the number of daily cases is decreasing, even further starting from May 10, 2021, the daily cases less

than average. Figure (g) shows that for the second half of May, 7 days of 14 days are out of control and there is a sudden downward trend. Figure 3 (h) shows that in June and until the last days of July 2021, the number of daily cases remained lower than the central limit, however, after July 2021 it started to get higher. For the latest period of **01.01.2022-31.05.2022**, for the year 2022, during the winter season of January and February, the number of daily cases touched a peak, such as the number of daily cases reached 111157 on February 4, 2022. From March 2022, a downward trend starts gradually.
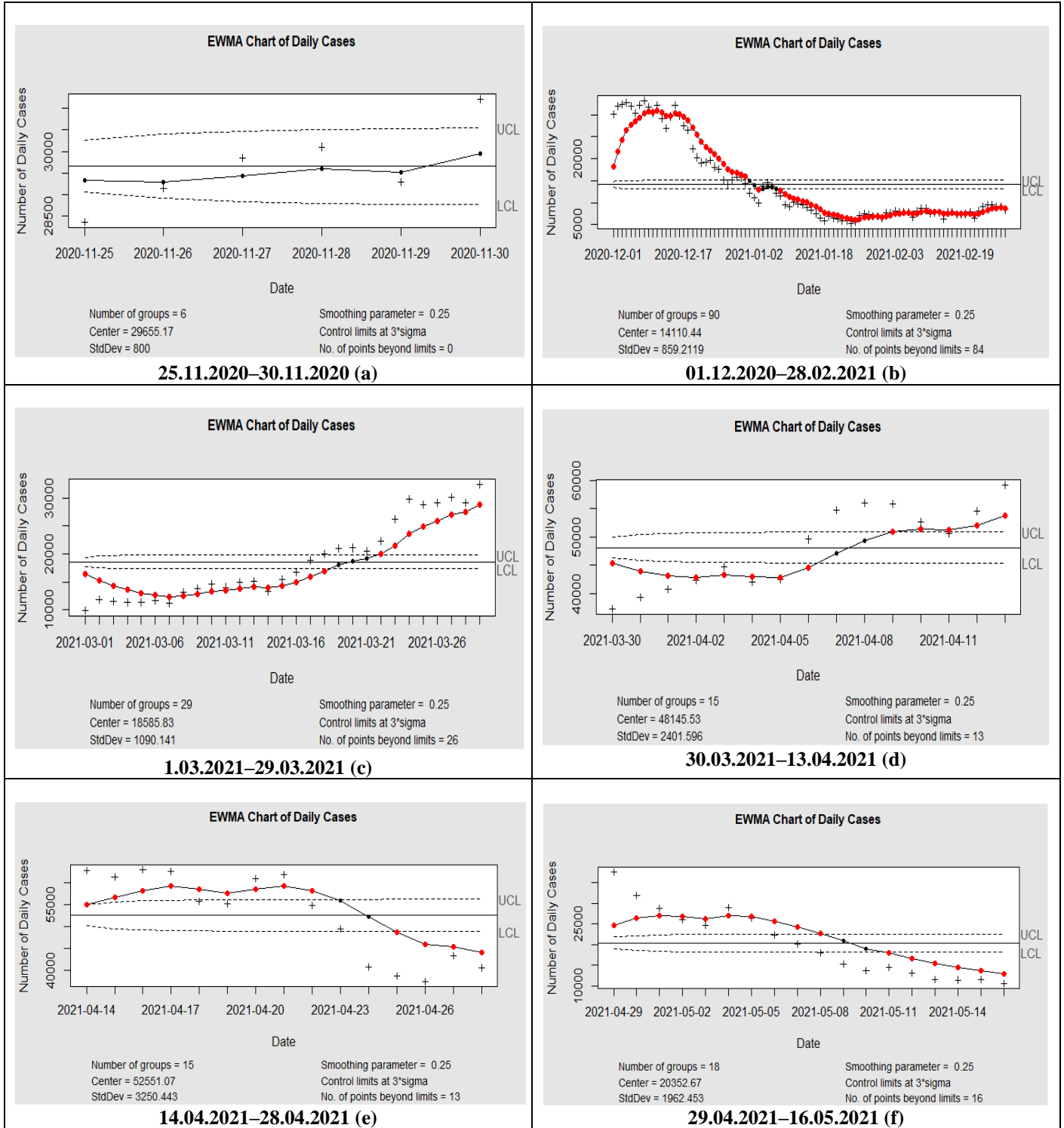
Figure 3. EWMA control charts for number of daily cases.
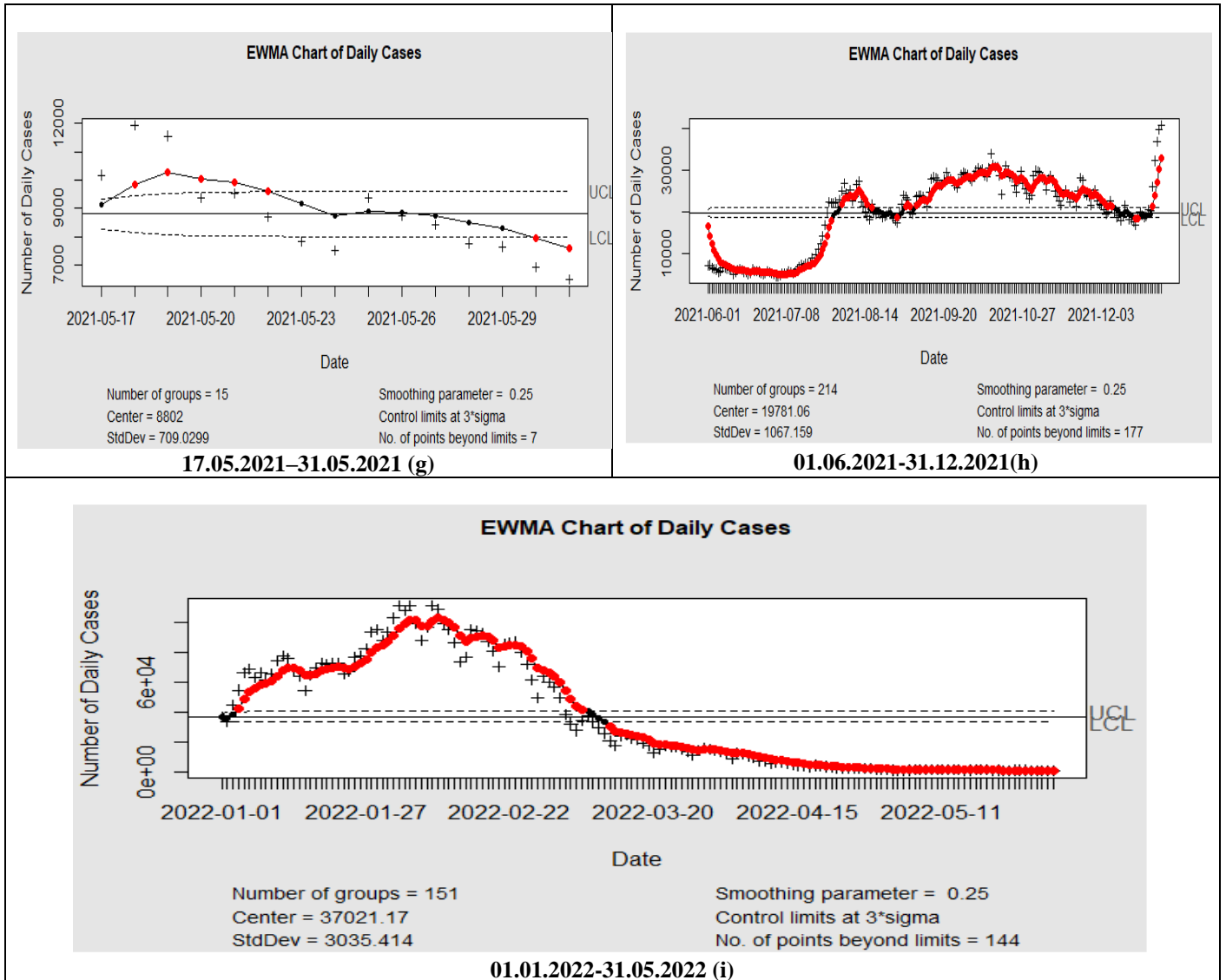
Figure 3. EWMA control charts for number of daily cases (continued).

4.2. Monitoring the Deaths

When we monitor Run charts for the deaths as given in Figure 4, it is clear that for the period of **27.03.2020–17.11.2020**, there is an upward trend, and then a sudden decrease and stabilizes between May and August, and again upward trend starts in September. For the period of **18.11.2020–30.11.2020**, there is an upward trend. For the period of **01.12.2020–28.02.2021**, there is a downward trend. For the period **01.03.2021–29.03.2021** an upward trend starts again and for the **30.03.2021–13.04.2021** and **14.04.2021–28.04.2021** periods this upward trend continues. For the period **29.04.2021–16.05.2021**, a downward trend starts, and this trend continues until the **01.06.2021** period. In the period of **01.06.2021-31.12.2021** (the last 7 months of 2021) the number of deaths starts to increase in August 2021 and peaks in September 2021 then starts to decrease gradually. For the period of **01.01.2022-31.05.2022** (first 5 months of 2022), the number of deaths shows an upward trend until February 2022 when it reaches a peak in this month then it starts to decrease gradually.

Figure 4. Run charts for number of deaths.

29.04.2021–16.05.2021 (g)   **CL=282**

17.05.2021–31.05.2021 (h)   **CL=183**

01.06.2021-31.12.2021 (i)   **CL=189**

01.01.2022-31.05.2022 (j)   **CL=115**

Figure 4. Run charts for number of deaths (continued).

4.3. Monitoring the Fatality Rate

The fatality rate, defined as the daily number of deaths per daily number of patients, was calculated over a period from **27.03.2020** to **04.07.2021**. Since the sample size of daily number of patients varies, a p-control chart with a variable sample is the most suitable control chart for analyzing the data.

Figure 5 shows the trend of the fatality rate over time. The grey region on the charts shows the control area that the points out of this area are out of control and that they fall outside the LCL or UCL values. Fatality rate was under control during specific periods, namely from **18.11.2020–30.11.2020**, **30.03.2021–13.04.2021,** and **17.05.2021–31.05.2021**. A sequence of 6 consecutive points, whether all increasing or all decreasing, is commonly referred to as the "trend rule." This test encompasses two scenarios. A gradual shift of data points towards a control limit

defined as a "trend." Conversely, when there are 6 consecutive points either all increasing or all decreasing, it's known as a "run-up" or "run-down." 6 consecutive decreasing points show an improvement, demonstrating that the fatality rate is under control and affirming that the measures are taken yielding results. However, if there are 6 consecutive increasing points, it serves as an alert, indicating that the virus is spreading and the death toll is rising, signifying the need for immediate action. Upward or downward trends suggest changes in the process. Hence, from Figure 5 (a) it is clear that trends moving up and down that summer season there is a downward trend. Figure 5 (c) shows that in the winter season fatality rate causes an alarm that an upward trend is observed, moreover, it is out of control. Figure 5 (d) shows that during March 2021 trends moved from down to up. Figure 5 (g) shows that after May 11, 2021, there is an alarming upward trend in the fatality

rate. Figure 5 (i) indicates an improvement and shows that the fatality rate is out of control, that in this period the fatality rate decreased.

27.03.2020–17.11.2020 (a)
CL=278.3%, LCL=202.3%, UCL= 354.3%

18.11.2020–30.11.2020 (b)
CL=260.1%, LCL=199%, UCL= 321.3%

01.12.2020–28.02.2021 (c)
CL=789.7 %, LCL=471.2 %, UCL=1108.3%

01.03.2021–29.03.2021 (d)
CL=1011.9%, LCL=768 %, UCL=1255.8%

30.03.2021–13.04.2021 (e)
CL=1074.6%, LCL=899.1%, UCL=1250.2%

14.04.2021–28.04.2021 (f)
CL=1155.2%, LCL=971.2 %, UCL=1339.3%

Figure 5. p-control charts for fatality rate.

29.04.2021–16.05.2021 (g)
CL=1532.9 %, LCL=1177.2 %, UCL=1888.7 %

17.05.2021–31.05.2021 (h)
CL=2462.5 %, LCL=1935.7 %, UCL=2989.2 %

1.06.2021-04.07.2021 (i)
CL=1376.2 %, LCL= 862 %, UCL=1890.4 %
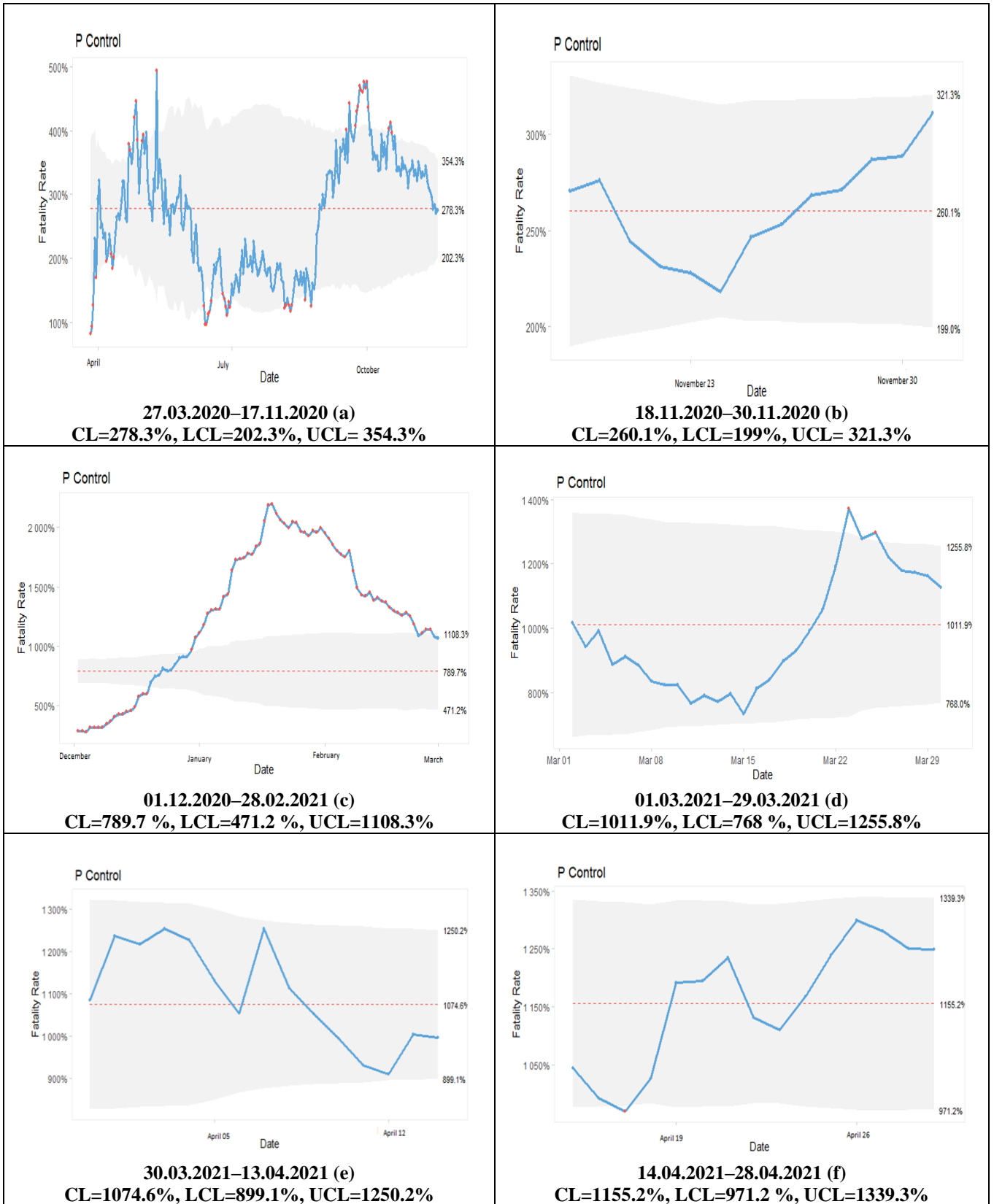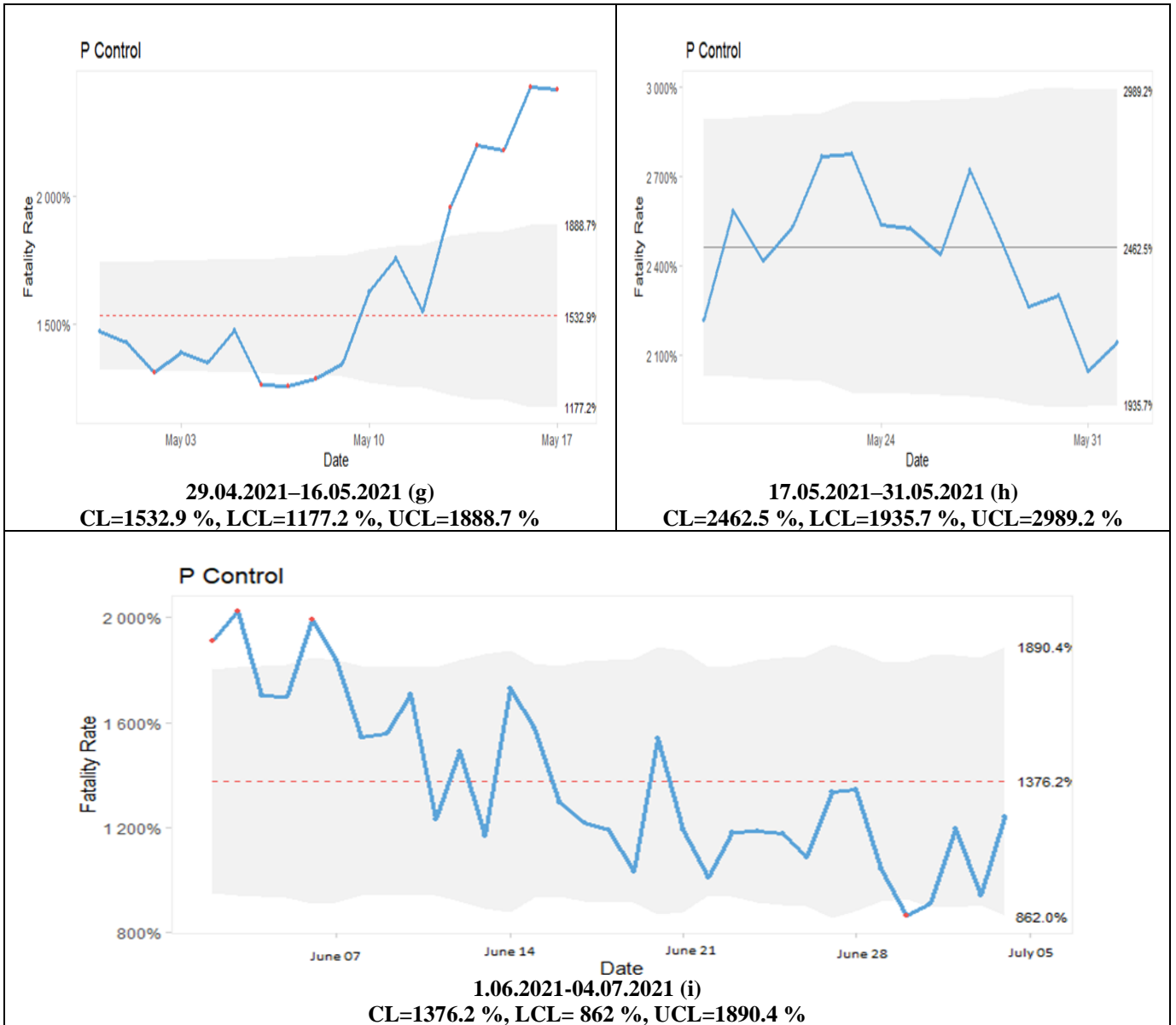
Figure 5. p-control charts for fatality rate (continued).

5.Conclusion and Discussion

As a result of Run charts, in the periods of nationwide extended curfews (December 1, 2020–February 28, 2021), full lockdown (April 29–May 16, 2021), and gradual normalization (May 17–31, 2021) the number of deaths and daily cases show downward trend as expected. However, in the periods of nationwide partial curfews (November 18-30, 2020), local decision-making phase (March 1–29, 2021), and revised local decision-making phase (March 30–April 13, 2021), the number of deaths and daily cases show an upward trend. In these periods, since provinces in low-risk status lost the restrictions, the cases, therefore, deaths may have started to increase again.

In the partial lockdown period (April 14-28, 2021), while the number of daily cases shows a downward trend, the number of deaths shows an upward trend. For January 1- May 31, 2022, both the daily cases and deaths show an upward trend until February 2022, in this month, when they reach a peak then they start to decrease gradually.

Detailed monitoring for the COVID-19 period was performed by EWMA control charts and p-control charts. The growth, peak, wavy, and decline periods for the number of daily cases detected by EWMA control charts. In nationwide partial curfews (November 25-30, 2020), the COVID-19 pandemic is at the start of the growth phase. Nationwide extended curfews period (December 1, 2020- February 28, 2021), the growth phase of a number of daily cases

continues until the middle of December 2020. The downward trend starts from January 14, 2021. For the period of the local decision-making phase (March 1, 2021- March 29, 2021), it is clear that the downward trend continues until March 18, 2021, after this date upward trend starts. Overall, in March 2021 the number of daily cases continues to rise. The revised local decision-making phase (March 30, 2021- April 13, 2021) and partial lockdown (April 14-28, 2021) are the periods in which the number of daily cases is increasing even further starting from April 9, 2021. The number of daily cases started to decrease on April 23, 2021, the last days of April 2021, the number of daily cases remains in lower values. When the spring period starts, in the full lockdown period (April 29, 2021- May 16, 2021), the number of daily cases is decreasing even further than beginning from May 10, 2021. It could be declared that a full lockdown could be also effective in this decrease. In the gradual normalization period (May 17–31, 2021), there is a sudden downward trend. After the 2nd phase of gradual normalization in June 2021 and until the last days of July 2021, the number of daily cases remained lower, though after July 2021 started to increase even further. For 2022 during the winter season in January and February, the number of daily cases touched the peak. From March 2022, a downward trend starts gradually for a number of cases. Overall, EWMA quality control charts reveal that the COVID-19 pandemic is experiencing sudden or non-sudden surges, increases, or declines due to seasonal changes and restrictions or other factors that must be examined.

After drawing the p-control charts for the fatality rate for the periods between March 27, 2020-July 4, 2021 it is seen that this ratio is out of control, especially for the periods March 27–November 17, 2020 (nearly after the start of the pandemic March 11, 2020) and December 1, 2020-February 28, 2021 (nationwide extended curfews). For these periods, fatality rate did not remain relatively stable. It means that the outbreak was experiencing sudden, unexplained surges, rises, or declines. For the period of 27.03.2020-17.11.2020, it is clear that trends moving up and down that summer season there is a downward trend. For the nationwide extended curfews period (December 1, 2020–February 28, 2021), the fatality rate caused an alarm that upward trend was observed. After the 2nd phase of gradual normalization for June 1, 2021-July 4, 2021 the impact of the pandemic is diminishing the fatality rate in low proportions.

The escalation in the number of individuals contracting the virus could be reflection of non-adherence to health protocols, which include mask-wearing and avoidance of contact with infected individuals in work, market, or enclosed environments or because of seasonal changes. The rapid spread of infection is attributed to non-compliance with the urbanization directives imposed by the health crisis cell. A considerable number of infections identified in the early stages of the epidemic had been recent, and consequently, some eventually led to fatalities. Therefore, in the early stages of the pandemic, an increase in the fatality rate was inevitable. Moreover, due to sporadic testing for the virus, many infections have gone undetected in the early stage and numerous mild cases of the disease have not been observed. Many studies indicate that the respiratory system is adversely affected by exposure to air pollutants, leading to the production of free radicals in the body and a reduction in resistance to viral and bacterial infections. Moreover, it was found in the literature that there is a direct correlation between COVID-19-related fatalities and socioeconomic status. It has been observed that individuals with lower incomes are more susceptible to diseases and have a higher mortality rate. Therefore, the factors of changes in the number of cases/deaths or mortality rates can be examined in more detail in future studies.

Quality control charts are widely used in healthcare quality monitoring. After the COVID-19 pandemic, control charts were also utilized for monitoring COVID-19 datasets from various countries all around the world. Using the control charts is valuable for monitoring COVID-19 data, especially in assessing the impact of different measures such as curfews, lockdowns, and risk categorizations on the number of cases/deaths, fatality rates, etc. Each study that uses quality control charts for monitoring the COVID-19 process provides unique insights into the specific dataset (deaths, discharged/recovered cases, confirmed cases, positivity rate, cure rate, fatality rate, infection rate), period, and country it examines. Literature on monitoring COVID-19 data with quality control charts highlights the diversity of methods used globally to monitor and analyze the COVID-19 pandemic. EWMA control charts seem efficient in capturing sudden variations and are one of the most popular ones in the literature. The contribution of our study to the literature is comprehensive monitoring of daily cases, deaths, and fatality rates in Türkiye, especially for considering the periods of restrictions. Since Türkiye is known to be one of the countries that efficiently fought against the pandemic, this study contributes to evaluating this process. In future

studies, quality control charts, regression models, and other statistical techniques could be used with various variables and factors together for a detailed review of the pandemic process for Türkiye or other countries. More detailed data can be obtained and examined, especially for cities such as İstanbul, Ankara, and İzmir, where the population is densest. Thus, more detailed comments can be made about Türkiye in general. In the future, the risks of this pandemic could be raised again. In this situation, the effects of various precautions on the number of cases, deaths, etc., could monitored by using quality control charts so that the process could managed logically and scientifically for Türkiye. Hence, this study and future studies could help political authorities and healthcare practitioners develop active control plans for a pandemic in the future.

Statement of Research and Publication Ethics
The study is complied with research and publication ethics

References

[1] M. T. Kartal, Ö. Depren, S. K. Depren, "The relationship between mobility and COVID-19 pandemic: Daily evidence from an emerging country by causality analysis", *Transportation Research Interdisciplinary Perspectives*, vol. 10, pp. 1-10, 2021.

[2] J. C. Benneyan, "Statistical Quality Control Methods in Infection Control and Hospital Epidemiology, Part II: Chart Use, Statistical Properties, and Research Issues", *Infection Control & Hospital Epidemiology*, vol. 19, no. 4, pp. 265-283, 1998.

[3] G. Suman and D. Prajapati, "Control Chart Applications in Healthcare: A Literature Review", *Int. J. Metrol. Qual. Eng.,* vol. 9, no. 5, pp. 1-21, 2018.

[4] J. C. Benneyan, R. C. Lloyd, P. E. Plsek, "Statistical Process Control as a Tool for Research and Healthcare Improvement", *Qual Saf Health Care*, vol. 12, pp. 458-464, 2003.

[5] M. F. Mbaye, N. Sarr, B. Ngom, "Construction of Control Charts for Monitoring Various Parameters Related to the Management of the COVID-19 Pandemic*", Journal of Biosciences and Medicines*, vol. 9, pp. 9-19, 2021.

[6] M. Arafah, "Using the Laney p' Control Chart for Monitoring COVID-19 Cases in Jordan", *Journal of Healthcare Engineering* Volume, Article ID 6711592, pp. 1-18, 2022.

[7] B. J. Odunayo, E. Nnamdi, E. S. Oluwatosin, "Monitoring corona virus disease 2019 (COVID-19) pandemic outbreak in Africa", *MOJ App Bio Biomech.,* vol. 4, no. 3, pp. 67–71, 2020.

[8] B. J. Odunayo, E. S. Oluwatosin, E. Nnamdi, "On the Monitoring of Coronavirus (COVID-19) Disease in Africa", *The Parisian Academic Journal Applied and Natural Sciences*, vol. 3, pp. 12-20, 2020.

[9] H. M. Fawzy, A. Ghalib, "Predicting of infected People with Corona virus (covid-19) by using Non-Parametric Quality Control Charts", *Int. J. Nonlinear Anal. Appl.*, vol. 13, no. 1, pp. 2115–2126, 2022.

[10] Y. Hidayat, D. S. Pangestu, T. Purwandari, "Covid-19 Time Series Data Quality Analysis (Case study at COVID-19 Data Repository by the Center for Systems Science and Engineering (CSSE) at Johns Hopkins University)", in *Proceedings of the 2nd African International Conference on Industrial Engineering and Operations Management*, Harare, Zimbabwe, December 7-10, 2020, pp. 1904-1910.

[11] Y. Hidayat, F. Utama, T. Purwandari, "The Implementation of Tangent Control Chart for Identification of Countries that have Positive Covid-19 Cases Data Trend Similar to Indonesia", in Proceedings of the 2nd African International Conference on Industrial Engineering and Operations Management, Harare, Zimbabwe, December 7-10, 2020, pp. 1917-1926.

[12] N. H. Irhaif, Z. I. Kareem, A. D. A. Kareem, S. M. Al-joboori, "Using the moving average and exponentially weighted moving average with COVID 19", *Periodicals of Engineering and Natural Sciences Methodology/Method*, vol. 9, no. 3, pp. 625-631, 2021.

[13] Y. Mahmood, S. Ishtiaq, M. B. C. Khoo, S. Y. Teh, H. Khan, "Monitoring of three-phase variations in the mortality of COVID-19 pandemic using control charts: where does Pakistan stand?", *International Journal for Quality in Health Care*, vol. 33, no. 2, pp. 1–8, 2021.

[14] U. Mukhaiyar, K. N. Sari, Y. S. Afrianti, A. M. R. Saputra, "The P-chart Implementation in Evaluating the Number of New COVID-19 Cases", in *the 8th Symposium on Biomathematics (Symomath) 2021 AIP Conf. Proc. 2498*, Published by AIP Publishing, 2021, pp. 020022-1–020022-10.

[15] G. Parry, L. P. Provost, S. M. Provost, K. Little, R. J. Perla, "A hybrid Shewhart chart for visualizing and learning from epidemic data", *International Journal for Quality in Health Care*, vol. 33, no. 4, pp. 1–10, 2021.

[16] E. R. Rashed, M. E. Eissa, "Global assessment of morbidity and mortality pattern of CoVID-19: Descriptive statistics overview", *Iberoamerican Journal of Medicine*, vol. 2, pp. 68-72, 2020.

[17] B. P. Singh, J. V. Madhusudan, A. K. Tiwari, S. Singh, U. D. Das, "Evaluation of EWMA control charts for monitoring spread of transformed observations of COVID-19 in India", *Asian Journal of Research in Infectious Diseases.*, vol. 5, no. 2, pp. 25-36, 2020.

[18] A. Yupaporn, S. Rapin, "EWMA control chart based on its first hitting time and coronavirus alert levels for monitoring symmetric COVID-19 cases", *Asian Pacific Journal of Tropical Medicine*, vol. 14, no. 8, pp. 364-374, 2021.

[19] M. Waqas, S. H. Xu, S. M. Anwar, Z. Rasheed, J. Shabbir, "The optimal control chart selection for monitoring COVID-19 phases: a case study of daily deaths in the USA", *Quality in Health Care*, 35(3), 1-9, 2023.

[20] M. N. İlhan, H. Tüzün, R. Kılıç, N. Yıldırım, "Nonpharmaceutical interventions in Turkey and worldwide during COVID-19 pandemic", *Turkish Journal of Medical Sciences*, vol. 51, pp. 3207-3214, 2021.

[21] J. Anhøj, A. V. Olesen, "Run Charts Revisited: A Simulation Study of Run Chart Rules for Detection of Non-Random Variation in Health Care Processes", *PLoS ONE*, 9(11): e113825, pp. 1-13, 2014.

[22] Run charts with R (Jacob Anhøj). [Online]. Available: https://cran.r-project.org/web/packages/qicharts/vignettes/runcharts.html [Accessed: 31 October, 2023].

[23] J. Anhøj, "Diagnostic Value of Run Chart Analysis: Using Likelihood Ratios to Compare Run Chart Rules on Simulated Data Series", *PLoS ONE*, vol.10, no. 3: e0121349, pp. 1-9, 2015.

[24] S. W. Roberts. "Control Chart Tests Based on Geometric Moving Averages." *Technometrics*, vol. 1, no. 3, pp. 239–250, 1959.

[25] R. C. Lloyd, *Quality Health Care: A Guide to Developing and Using Indicators*, CHAPTER 9: Understanding Variation with Shewhart Charts, 2nd Edition, Jones & Bartlett Learning, 2019, pp. 211-258. [Online]. Available: https://www.cec.health.nsw.gov.au/__data/assets/pdf_file/0011/605657/Understanding-Variation-with-Shewart-Charts.pdf [Accessed: 2 December, 2023].

[26] L P. Provost, S. Murray, *The Health Care Data Guide: Learning from Data for Improvement*. San Francisco: Jossey-Bass, 2011.

[27] General Coronavirus Chart data from website of the Republic of Türkiye Ministry of Health. [Online]. Available: https://covid19.saglik.gov.tr/TR-66935/genel-koronavirus-tablosu.html [Accessed: 9 January, 2023].

Classification of Liver Disorders Diagnosis using Naïve Bayes Method

Özlem BEZEK GÜRE[*]

Batman University, Department of Medical Documentation, Secretariat Program Health Services Vocational School, Batman, Turkey
(ORCID: 0000-0002-5272-4639)

Abstract

Liver diseases pose a significant health challenge, necessitating robust predictive tools for early diagnosis. This study aims to determine the predictive performance of Naive Bayes classifier, one of the data mining algorithms, in the classification of liver patients. The study applied 2, 5, 10 and 20-fold cross-validation method. Trying to determine the effect of the cross-validation (CV) method used on the classification performance, this study used the "BUPA" dataset in the UCI Machine Learning Repository database for this purpose. The dataset consists of 6 variables and 345 examples. Orange program was used for data analysis. As a result of the analysis, the accuracy for the Naive Bayes method was determined to be 62.9%, 63.5%, 63.8%, and 64.3%, respectively. The AUC values were 0.68, 0.66, 0.66, and 0.67, respectively; the F1 scores were 0.56, 0.57, 0.58, and 0.58, respectively. On the other hand, the precision values were 0.60, 0.60, 0.60, and 0.62, respectively, while the recall values were determined to be 0.52, 0.53, 0.55, and 0.54. Additionally, the MCC values were determined to be 0.24, 0.26, 0.26, and 0.27, respectively. The analysis results indicate that the 20-fold CV method demonstrates marginally superior performance. The use of the free and easy-to-use program is recommended.

1. Introduction

Data mining can be characterized as a suite of techniques aimed at unveiling hidden patterns and trends within datasets. It encompasses the processes of model construction, data selection, and data discovery based on hitherto unknown patterns [1,2]. Briefly, this method serves to extract understandable and actionable information from datasets [3-5]. Data mining amalgamates methods from statistics, machine learning, and pattern recognition [6]. The accelerated advancements in computer technologies and the consequent proliferation of large datasets have fueled increased interest in data mining methodologies. These techniques have found extensive application across diverse fields such as engineering, economics, education, and healthcare. Due to their inherently complex and voluminous nature, traditional statistical methods often fall short in analyzing the extensive data generated within the healthcare sector. Data mining techniques are leveraged to transform these extensive data repositories into actionable insights for decision-makers. This, in turn, enhances healthcare operations and facilitates medical research [7]. Utilizing these methodologies enables capabilities such as predicting patient responses to medication dosages, identifying healthcare insurance fraud, and diagnosing or projecting specific diseases [2,7-8].

Being the body's second-largest organ, the liver plays a crucial role in maintaining human well-being.In addition to its role in nutrient storage, it performs a wide range of functions related to digestion, metabolism, and immunity, such as the breakdown of red blood cells, protein production, and the elimination of toxins from the body [9-11]. In recent years, an increase in liver-related diseases has been observed. Stress, inhalation of harmful gases, poor nutrition, excessive alcohol consumption, unnecessary medication intake, and viruses are

---

[*]Corresponding author: *ozlem.bezekgure@batman.edu.tr*

among the factors contributing to liver diseases [11-13]. Liver diseases are considered one of the most significant health issues globally [14]. If left untreated, liver diseases can lead to serious health problems. Therefore, early and accurate diagnosis of diseases related to this vitally important organ is crucial [15]. In recent years, an excessive increase in liver disorders has been observed in many countries. Consequently, liver diseases have begun to rank among the leading causes of death in these countries [8]. This study employed the BUPA Liver Disorder dataset to develop classification models using the Naïve Bayes method, aiming to predict liver diagnosis.

Given the vital functions of the liver and the rising prevalence of liver diseases globally, there is a clear need for accurate diagnosis of these conditions. Data mining methods can be leveraged to analyze healthcare data and gain insights into liver disease prediction and diagnosis.

Data mining methods are frequently observed to be used for predicting diseases. The present study employs the Naive Bayes method from data mining techniques for the prediction of liver diseases. A review of the literature reveals numerous studies that have utilized this method for the same purpose [12,16-20]. Unlike other studies, this research also evaluates the classification performance of the Naive Bayes method when applied with different Cross-Validation techniques.

Other studies have also applied data mining techniques, including Naive Bayes, to liver disease prediction. However, this study takes the additional step of assessing the classification performance with different cross-validation methods. By evaluating multiple techniques, this allows for a more robust analysis of the predictive capabilities of data mining for liver diseases.

Numerous studies have applied various data mining methods to data related to liver diseases. Ram et al. [19] used Naive Bayes (NB), SMO, and Bayes Net methods in their study to predict liver diseases, noting that the SMO method displayed superior performance. Vijayarani and Dhayanand [21] implemented NB and Support Vector Machine (SVM) methods in their research, indicating that the SVM method performed better. Similarly, Kamruzzaman, Mahbub, and Hakim [22] used, in addition to these two methods, K-Nearest Neighbors (KNN) and Decision Tree (DT) methods, concluding that SVM showed better performance. Additionally, Abdar [16] used Linear Regression, KNN, C4.5, C5.0, CHAID, Neural Net, and Random Forest (RF) methods and found that the C4.5 algorithm

demonstrated better classification performance. Sug [17] also utilized DT, C4.5, and CART algorithms.

The literature contains many examples of data mining methods being applied to predict liver diseases, with studies comparing the performance of different techniques. This highlights the utility of data mining for gaining insight into liver conditions, though it also suggests Naive Bayes may not always be the optimal method.

On the other hand, Nahar et al. [23] used decision tree methods like J48, LMT, Random Tree, RF, REPTree, Decision Stump, and Hoeffding Tree for predicting liver diseases. A study by Kuppan and Manoharan [11] employed J48 and NB methods. Baitharu and Pani [10] used J48 and NB methods along with DT, Multilayer Perceptron Neural Network (MLP), ZeroR, KNN, and VFI, determining that the MLP method outperformed others. Similarly, Al-Aidaroos, Bakar, and Othman [24] used NB, Logistic Regression, Kstar, DT, Neural Network, and Zero R methods and found that the NB method performed better compared to others. Bhardwaj, Mehta, and Ramani [25] used DT, RF, NB, KNN, SVM, Artificial Neural Networks (ANN), and Extreme Gradient Boost (XGBoost) methods for the same purpose. A study by Ramana, Babu, and Venkateswarlu [12] employed NB, C4.5, Back Propagation Neural Network, and SVM methods.

While some studies have found Naive Bayes to perform well for liver disease prediction, the literature also contains examples of other methods like decision trees, neural networks, and support vector machines outperforming Naive Bayes. More research is still needed to determine the optimal data mining techniques for this application.

2. Material and Method

The current study employs the "BUPA" data set. obtained from the UCI Machine Learning Repository. The data file was obtained from https://archive.ics.uci.edu/dataset/60/liver+disorders [26]. The dataset consists of 345 rows and 7 columns, with each row containing information about male individuals. The first 5 columns contain blood test results that can be used in the diagnosis of liver diseases related to alcohol. The 6th column includes the number of alcoholic drinks consumed daily as reported by the individuals. The last column contains a variable intended for use in dividing the data into training and testing sets [27]. In the study, the drinks (number of half-liter equivalents of alcoholic beverages consumed per day) variable was treated as the dependent variable; selector, mcv (mean corpuscular volume), alkphos (alkaline phosphatase),

sgpt (alanine aminotransferase), sgot (aspartate aminotransferase), and gammagt (gamma-glutamyl transpeptidase) were analyzed as independent variables. Subsequently, the dependent variable, drinks, was categorized into two groups: those with a value of 3 and below, and those above 3. Following this, the analyses using the Naïve Bayes method were conducted through Orange, a free Python-based software, to conduct the data analyses. [28]. Descriptive statistics of the independent variables are given in Table 1.

Table 1. Descriptive statistics of predictive variables

Variables	Mean	Standard deviation	Min	Max
Mcv	90,16	4,45	65	103
Alkphos	69,87	18,35	23	138
Sgpt	30,41	19,51	4	155
Sgot	24,64	10,06	5	82
Gammagt	38,28	39,25	5	297
Drinks	3,45	3,34	0	20

Naïve Bayes Method

The Naive Bayes method is a highly effective and robust probability-based classifier that employs Bayes' theorem in classification, under strong independence assumptions [29-30]. The method is an algorithm that is easy and quick to structure and interpret, without the need for complex iterative parameter estimations [31]. Because of these characteristics, the NB algorithm is commonly employed in extensive data analysis and various other domains [32]. This method analyzes the relationship between the independent and dependent variables by obtaining a conditional probability for each relationship [33]. NB computes probabilities by analyzing the frequency and combinations of values in a given dataset [34], and it is successful in high-dimensional datasets [35]. Compared to other data mining algorithms, NB is more resilient to overfitting and noisy data because it estimates fewer parameters [36].

The Naive Bayes classifier, one of the supervised learning algorithms, assumes that each attribute value is independent of the values of other attributes within the class. This assumption is termed class-conditional independence [37-38]. This assumption is referred to as "naive" because it is rarely valid in real-world applications. The algorithm tends to learn rapidly in various controlled classification problems [34]. Due to the independence assumption of the variables in this method, it is necessary to estimate each variable rather than the covariance matrix [39]. When this assumption holds, the learning process of Bayes classifiers becomes simpler, thereby achieving optimal assignment using the vector of observable factors. In addition to the independence assumption, it is assumed that the factors affecting the outcome of interest are not hidden [40]. Moreover, the method necessitates minimal training data to determine the parameters essential for classification [39,41].
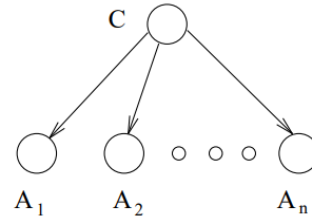
Figure 1. Structure of the Naive Bayes Classifier [29].

Different Naive Bayes (NB) classifiers vary chiefly due to the assumptions they hold about feature distribution. For discrete features, typically Multinomial or Bernoulli distributions are applied, whereas the Gaussian distribution is chosen for continuous features [42].

Bayes' Theorem

Developed by Thomas Bayes in the 1800s, this theorem pertains to probability and decision theory. Let Ω be a complete set and, $C_1, C_2, C_3, \ldots \ldots C_n \in \Omega$, C_i, represent i[st] category, where $P(C_i) > 0, i = 1,2, \ldots \ldots n$. Each category is distinct from the other, and $\bigcup_{i=1}^{n} C_i = \Omega$. For any X if $P(X) > 0$, then the Bayes equation is given in Equation 1.

$$P(C_i \backslash X) = \frac{P(X \backslash C_i) P(C_i)}{\sum_{i=1}^{n} P(X \backslash C_i) P(C_i)} \tag{1}$$

[39].

Naive Bayes Classifier

The Naive Bayes classifier uses the concept of maximum likelihood estimation to classify a sample according to the highest probable category.

$$P(C_i \backslash X) = Max\{P(C_1 \backslash X), P(C_2 \backslash X), P(C_3 \backslash X), \ldots \ldots \ldots P(C_n \backslash X)\} \tag{2}$$

Let $X = (A_1, A_2, A_3, \ldots \ldots A_k)$ be a feature vector, where A_j represents the jth feature of x_j.

The Naive Bayes classifier assumes that attributes function independently from one another. Therefore, the conditional probability, $P(X\backslash Ci)$ can be expressed as:

$$P(X\backslash C_i) = \prod_{j=1}^{k} P(A_j = x_j \backslash C_i) \qquad (3)$$

When the third equation is substituted into the Bayes formula given in the first equation, we obtain:

$$P(C_i\backslash X) = \frac{\prod_{j=1}^{k} P(A_j = x_j \backslash C_i) P(C_i)}{P(X)} \qquad (4)$$

When $\frac{1}{P(X) = \alpha (>0)}$, we have:

$$P(C_i\backslash X) = \alpha \prod_{j=1}^{k} P(A_j = x_j) C_i) P(C_i) \qquad (5)$$

Let N(D) represent the total number of samples in the sample set $N(C_i)$, represent the number of samples in C_i, and $N(C = C_i, A_j = x_j)$, A_j C_i'deki x_j A_j represent the number of samples in C_i where the feature $A_j = x_j$

We can express $P(Ci)$ and $P(Aj=xj|Ci)$ as:

$$P(C_i) = \frac{N(C_i)}{N(D)} \qquad (6)$$

$$P\left(A_j = x_j \backslash C = C_i\right) = \frac{N(C = C_i, A_j = x_j)}{N(C_i)} \qquad (7)$$

Inserting equations 6 and 7 into equation 5 yields the subsequent result:

$$P(C_i\backslash X) = \alpha \prod_{j=1}^{k} \frac{N(C = C_i, A_j = x_j)}{N(C_i)} \cdot \frac{N(C_i)}{N(D)} \qquad (8)$$

[39].

Performance Criteria

The confusion matrix indicates the degree to which the classifier used recognizes patterns in different classes.

Table 2. Confusion matrix

		Estimated		
		No	Yes	Total
Real	No	TN	FP	TN+FP
	Yes	FN	TP	FN+TP
	Total	TN+FN	FP+TP	TN+FN+FP+TP

This research intends to assess the effectiveness of the Naive Bayes classification algorithm concerning different Cross-Validation CV methodologies. CV serves as an instrumental technique for assessing the validity of the predictive model under consideration. In the instance of k-fold CV, the dataset is partitioned into k subsets. One of these subsets is employed as the test data, while the remaining subsets function as the training data. The mean error rate from these k subsets is calculated to estimate the overall error rate of the classification model [43]. In this research, performance metrics such as Area Under the Curve (AUC), accuracy, precision, recall, F1 score, and Matthews's correlation coefficient (MCC) have been utilized.

AUC: AUC, also known as the Area Under the Receiver Operating Characteristic (ROC) Curve, serves as a quantitative indicator of the model's accuracy. The magnitude of this area is a demonstrative measure of the classification model's performance efficacy [44].

MCC: Matthews correlation coefficient is a measure that shows the relationship between the predicted class and the actual class, ranging between [-1,1]. If the coefficient is +1, it indicates that the predictions made by the classifier are correct, whereas if it is -1, it indicates that the predictions are incorrect [45].

$$MCC = \frac{(TP*TN)-(FP*FN)}{\sqrt{(TP+FP)*(TP+FN)*(TN+FP)*(TN+FN)}} \qquad (9)$$

$$Accuracy = \frac{TP+TN}{TP+TN+FP+FN} \qquad (10)$$

$$Precision = \frac{TP}{TP+FP} \qquad (11)$$

$$Recall = \frac{TP}{TP+FN} \qquad (12)$$

$$F1\ score = 2x \frac{(Precision\ x\ Recall)}{(Precision + Recall)} \qquad (13)$$

3. Results and Discussion

Table 3. Confusion Matrix Obtained Using the Naive Bayes Method

CV method		No	Yes
2	No	136	54
	Yes	74	81
5	No	137	53
	Yes	73	82
10	No	135	55
	Yes	70	85
20	No	138	52
	Yes	71	84

Table 4. Performance Criteria

CV method	AUC	CA	F1	Precision	Recall	MCC
2	0.678	0.629	0.559	0.600	0.523	0.242
5	0.660	0.635	0.565	0.607	0.529	0.255
10	0.657	0.638	0.576	0.607	0.548	0.262
20	0.669	0.643	0.577	0.618	0.542	0.273

Table 4 indicates that the 20-fold cross-validation method exhibits a marginally better performance compared to other methods.
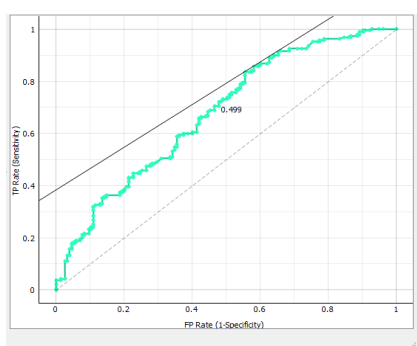
Figure 2. Area Under the ROC Curve (2-fold CV)
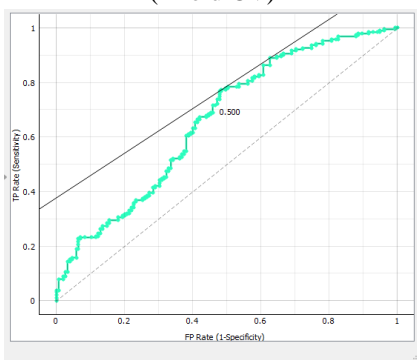
Figure 3. Area Under the ROC Curve (5-fold CV)
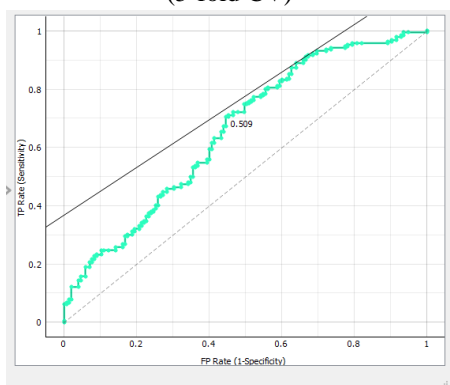
Figure 4. Area Under the ROC Curve
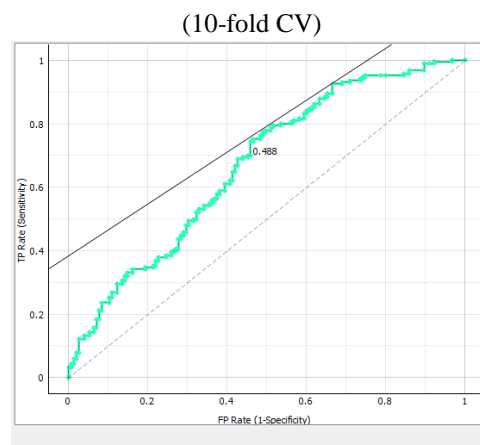
Figure 5. Area Under the ROC Curve (20-fold CV)

In the academic literature, there are numerous studies that utilize the BUPA dataset for the classification of liver diseases. It has been observed that the Naive Bayes method is frequently employed in these studies. Similar to our research, a study conducted by Sujana, Rao, and Reddy [46] used the Weka software and applied 2, 5, and 10-fold CV methods; according to their analysis, the accuracy rates were determined to be 60.58%, 60.89%, and 62.32%, respectively. Another study by Ramana, Babu, and Venkateswarlu [12] also used the Weka software and implemented the 10-fold CV method, determining the accuracy, precision, sensitivity, and specificity of the Naive Bayes method to be 51.59%, 45.17%, 71.03%, and 37.5%, respectively. Ruengdetkharn and Lohpetch [47] applied a 5-fold cross-validation method in their study and determined the accuracy to be 62.90%. Pradhan et al. [48] employed a two-fold CV method in their study and used performance indicators such as Type I error, Type II error, true negative rate, true positive rate, accuracy, and F1 score; these metrics were determined to be 0.51, 0.4, 0.49, 0.6, 0.53, and 0.52, respectively. Compared to similar studies, the analysis results obtained using the Orange software appear to yield slightly better outcomes than those from other programs.

In the existing literature, datasets focusing on liver diseases have been employed in various studies. Abdar [16]) utilized the Indian Liver Patient Dataset (ILPD) from the UCI database for this purpose. The study employed both RapidMiner and SPSS Modeler for analysis. According to the results, the accuracy and precision rates obtained through the RapidMiner program using the Naive Bayes method were 66.92% and 45.13%, respectively. In contrast, the SPSS Modeler yielded an accuracy of 74.26% and a precision of 40.24%. Similarly, Ram et al. [19]

conducted analyses using Python to predict liver diseases, employing methods such as Naive Bayes (NB), SMO, and Bayes Net. On the other hand, Alam, Rahman, and Rahman [49] used the Weka software in their study, applying the Bayes Net method. They reported an accuracy rate of 0.68 using ten-fold CV.

4. Conclusion and Suggestions

This research seeks to ascertain the predictive performance of the Naive Bayes classifier of the Naive Bayes classifier when categorizing liver disorder diagnosis through data mining methods. The study has implemented 2, 5, 10, and 20-fold CV methods. An attempt has been made to ascertain the impact of the employed CV method on classification performance. Analyses were conducted in the Orange program, which is a Python-based free software. Performance measures such as AUC, accuracy, precision, recall, F1 score and MCC were used. As a result of the analysis, the accuracy for the Naive Bayes method was determined to be 62.9%, 63.5%, 63.8%, and 64.3%, respectively. The AUC values were 0.68, 0.66, 0.66, and 0.67, respectively; the F1 scores were 0.56, 0.57, 0.58, and 0.58, respectively. On the other hand, the precision values were 0.60, 0.60, 0.60, and 0.62, respectively, while the recall values were determined to be 0.52, 0.53, 0.55, and 0.54. Furthermore, the MCC values were identified as 0.24, 0.26, 0.26, and 0.27, respectively. Based on the analysis results, it can be claimed that the 20-fold CV method exhibited better performance Based on these results, it is observed that the 20-fold CV method showed slightly better performance.

In the current study, the Orange program was utilized to examine the performance of cross-validation methods. A review of the literature indicates that programs such as Weka and SPSS Modeler are preferred for implementing machine learning methods, while the use of the Orange program is limited. It is recommended to use this free and user-friendly program since it appears based on the findings that the Orange software may offer advantageous outcomes. The dataset used in this study is small; therefore, larger datasets can be utilized to examine cross-validation methods. On the other hand, investigations can be conducted using different data mining methods.

Acknowledgment

Statement of Research and Publication Ethics

The dataset used in the present study was sourced from the publicly accessible UCI database; therefore, the research did not necessitate ethical committee approval."

References

[1] M.Kayri, İ.Kayri and M.T. Gencoglu, "The performance comparison of Multiple Linear Regression, Random Forest and Artificial Neural Network by using photovoltaic and atmospheric data", *IEEE 14th International Conference on Engineering of Modern Electric Systems (EMES),* pp.1-4, June 2017.

[2] H. C. Koh and G. Tan, "Data mining applications in healthcare", *Journal of Healthcare Information Management*, vol.19, no.2, pp.65-72, 2011.

[3] A. Peña-Ayala, "Educational data mining: A survey and a data mining-based analysis of recent works", *Expert systems with applications*, vol.41, no.4, pp.1432-1462, 2014.

[4] M., Kayri and, İ. Kayri, "The comparison of Gini and Twoing algorithms in terms of predictive ability and misclassification cost in data mining: an empirical study", *International Journal of Computer Trends and Technology (IJCTT),* vol. 27, no. 1, pp.21-30, 2015.

[5] Ö. B. Güre, M. Kayri and F.Erdoğan, "Analysis of Factors Effecting PISA 2015 Mathematics Literacy via Educational Data Mining", *Education & Science/Egitim ve Bilim*, vol.45, no.202, pp.393-415, 2020.

[6] M. Sharma, "Data mining: A literature survey", *International Journal of Emerging Research in Management & Technology*, vol.3, no.2, pp.1-4, 2014.

[7] R. H. Khokhar, R. Chen, B.C. Fung and S.M. Lui, "Quantifying the costs and benefits of privacy-preserving health data publishing", *Journal of biomedical informatics*, vol.50, pp.107-121, 2014.

[8] S. Bahramirad, A. Mustapha and M. Eshraghi," Classification of liver disease diagnosis: A comparative study", *IEEE 2013 Second International Conference on Informatics & Applications (ICIA),* pp.42-46, September 2013.

[9]   P. Kumar and R.S. Thakur, "Liver disorder detection using variable-neighbor weighted fuzzy K nearest neighbor approach", *Multimedia Tools and Applications*, vol.80, pp.16515-16535, 2021.

[10] T. R. Baitharu and S.K. Pani, "Analysis of data mining techniques for healthcare decision support system using liver disorder dataset", *Procedia Computer Science*, vol.85, pp.862-870, 2016.

[11] P. Kuppan and N. Manoharan, "A Tentative analysis of Liver Disorder using Data Mining Algorithms J48, Decision Table and Naive Bayes", *International Journal of Computing Algorithm*, vol.6, no.1, pp.2278-239, 2017.

[12] B. V. Ramana, M. S. P. Babu and N.B. Venkateswarlu, "A critical study of selected classification algorithms for liver disease diagnosis*", International Journal of Database Management Systems*, vol.3, no.2, pp.101-114, 2011.

[13] R. Kalaviselvi and G. Santhoshni, "A Comparative Study on Predicting the Probability of Liver Disease", *International Journal of Engineering Research & Technology (IJERT)*, vol.8, no. 10, pp.560-564, 2019.

[14] R. H. Lin, "An intelligent model for liver disease diagnosis", *Artificial Intelligence in Medicine*, vol.47 no.1, pp.53-62, 2009.

[15] S. N. N. Alfisahrin and T. Mantoro, "Data mining techniques for optimization of liver disease classification" *IEEE 2013 International Conference on Advanced Computer Science Applications and Technologies*, pp.379-384, *December 2013*.

[16] M. Abdar, "A survey and compare the performance of IBM SPSS modeler and rapid miner software for predicting liver disease by using various data mining algorithms", *Cumhuriyet University Faculty of Science Science Journal (CSJ)*, vol.36, no.3, pp.3230-3241, 2015.

[17] H. Sug, "Improving the prediction accuracy of liver disorder disease with oversampling", *Proc. of the 6th WSEAS international conference on Computer Engineering and Applications, and Proceedings of the 2012 American conference on Applied Mathematics, Wisconsin United States, January, 25-27, 2012*.

[18] H. Subhani and S. Badugu, "A study of liver disease classification using data mining and machine learning algorithms", in Learning and Analytics in Intelligent Systems : Proc. of the the Advances in Decision Sciences, Image Processing, Security and Computer Vision: International Conference on Emerging Trends in Engineering (ICETE), Hyderabad, India, March 22–23, 2019, George A. Tsihrintzis, Maria Virvou, Lakhmi C. Jain, Eds. Berlin: Springer,2019. Vol. 2, pp. 630-640.

[19] M. K. Ram, C. Sujana, R. Srinivas and G. S. N. Murthy, "A fact-based liver disease prediction by enforcing machine learning algorithms". in *Advances in Intelligent Systems and Computing Proc. Of the Computational Vision and Bio-Inspired Computing: ICCVBIC*, Coimbatore, India, November 19-20, 2020. Janusz Kacprzyk Eds. Berlin: Springer, 2020. pp.567-586

[20] S.Wang, J. Ren and R. Bai, "A semi-supervised adaptive discriminative discretization method improving discrimination power of regularized Naive Bayes", *Expert Systems with Applications*, vol. 225, no. 120094, pp. 1-7, 2023.

[21] S. Vijayarani and S. Dhayanand, "Liver disease prediction using SVM and Naïve Bayes algorithms", *International Journal of Science, Engineering and Technology Research (IJSETR)*, vol.4, no.4, pp.816-820, 2012.

[22] T. M., Kamruzzaman, M. S., Mahbub and M. A. Hakim, "A Structured Method For Predicting Liver Disease Using Machine Learning Techniques & Improvements In Correctness", *IEEE 12th International Conference on Computing Communication and Networking Technologies (ICCCNT*), pp.01-07, July 2021.

[23] N., Nahar and F. Ara, "Liver disease prediction by using different decision tree techniques", *International Journal of Data Mining & Knowledge Management Process*, vol.8 no.2, pp.01-09, 2018 .

[24] K. Al-Aidaroos, A. A., Bakar and Z. Othman, "Medical data classification with Naive Bayes approach", *Information Technology Journal*, vol.11, no.9, pp.1166-1174, 2012.

[25] R. Bhardwaj, R. Mehta and P. Ramani, "A comparative study of classification algorithms for predicting liver disorders", *Intelligent Computing Techniques for Smart Energy Systems. Lecture Notes in Electrical Engineering*, vol 607. Springer, Singapore.

[26] UCI   Machine   Learning   Repository: BUPA   data   Set.   Available: https://archive.ics.uci.edu/ml/datasets/Higher+Education+Students+Performance+Evaluation+Dataset#

[27] J. McDermott and R.S. Forsyth, "Diagnosing a disorder in a classification benchmark", *Pattern Recognition Letters*, vol.73, pp. 41-43, 2016.

[28] Orange programming. Available: https://orangedatamining.com/

[29] N. Friedman, D. Geiger and M. Goldszmidt, M.,"Bayesian network classifiers", *Machine learning*, vol.29, pp.131-163, 1997.

[30] I. Wickramasinghe and H. Kalutarage, "Naive Bayes: applications, variations and vulnerabilities: a review of literature with code snippets for implementation", *Soft Computing*, vol.25, no.3, pp.2277-2293, 2021.

[31] X. Wu and V. Kumar, *The top ten algorithms in data mining*, CRC press, 2009.

[32] A. Choi, N. Tavabi, and A. Darwiche, "Structured features in Naive Bayes classification" in the *AAAI Conference on Artificial Intelligence,* vol.3 no.1, pp.3233-3240, *February, 2016*.

[33] Z. Muda, W. Yassin, M.N. Sulaiman and N.I. Udzir, "A K-Means and Naive Bayes learning approach for better intrusion detection", *Information technology journal*, vol.10 no.3, pp.648-655, 2011.

[34] M. M. Saritas and A. Yasar, "Performance analysis of ANN and Naive Bayes classification algorithm for data classification", *International journal of intelligent systems and applications in engineering*, vol.7 no.2, pp.88-91, 2019.

[35] S. S. Nikam, "A comparative study of classification techniques in data mining algorithms", *Oriental Journal of Computer Science and Technology*, vol.8 no.1, pp.13-19, 2015.

[36] R. Blanquero, E. Carrizosa, E., P.Ramírez-Cobo and M.R. Sillero-Denamiel, "Variable selection for Naïve Bayes classification", *Computers & Operations Research*, vol.135, no.105456, pp.1-11, 2021.

[37] J. Han and M. Kamber, M. *Data mining: concepts and techniques*, Second Edi. TM KSIDMA Systems, ed., Morgan Kaufmann Publisher, 2006

[38] S. Mukherjee and N. Sharma, "Intrusion detection using naive Bayes classifier with feature reduction", *Procedia Technology*, vol.4, pp.119-128, 2012.

[39] H. Chen, S. Hu, R. Hua and X. Zhao, "Improved naive Bayes classification algorithm for traffic risk management", *EURASIP Journal on Advances in Signal Processing*, vol. 2021 no.1, pp.1-12, 2021.

[40] S. K. Depren, Ö. E. Aşkın and E. Öz, "Identifying the classification performances of educational data mining methods: A case study for TIMSS", *Educational Sciences: Theory & Practice*, vol.17, no.5, pp.1605-1623, 2017.

[41] G. Kaur and E.N. Oberai, "A review article on Naive Bayes classifier with various smoothing techniques", *International Journal of Computer Science and Mobile Computing*, vol.3, no.10, pp.864-868, 2014.

[42] S. Xu, "Bayesian Naïve Bayes classifiers to text classification", Journal of Information Science, vol.44, no.1, pp.48-59, 2018.

[43] D. Berrar, Cross-validation, Encyclopedia of Bioinformatics and Computational Biology, Vol. 1, Elsevier, pp. 542–545, 2018.

[44] H. Şevgin and E. Önen, "Comparison of Classification Performances of MARS and BRT Data Mining Methods: ABİDE- 2016 Case", Education & Science/Egitim ve Bilim, vol.47, no.211, pp.195-222, 2022.

[45] G. Akgül, A.A. Çelik, Z.E. Aydın and Z.K. Öztürk, "Hipotiroidi Hastalığı Teşhisinde Sınıflandırma Algoritmalarının Kullanımı", *Bilişim Teknolojileri Dergisi*, vol.13, no.3, pp.255-268, 2020.

[46] T. S. Sujana, N. M. S. Rao and R. S. Reddy, "An efficient feature selection using parallel cuckoo search and naïve Bayes classifier", *IEEE 2017 International Conference on Networks & Advances in Computational Technologies (NetACT),* pp.167-172, July 2017.

[47] C. Ruengdetkhachorn and D. Lohpetch, "Feature Selection using Parallel Cuckoo Algorithm with Naïve Bayes Classifier based on Two Different Strategies", *IEEE 22nd International Computer Science and Engineering Conference (ICSEC),* pp.1-4, November 2018,

[48] D. Pradhan, B.B. Misra, B. Sahoo and D.K. Jena, "Evolutionary Teaching-Learning Based Modified Polynomial Classifier", *IEEE 19th OITS International Conference on Information Technology (OCIT),* pp.313-318, December 2021.

[49] M. Z. Alam, M. S. Rahman and M. S. Rahman, "A Random Forest based predictor for medical data classification using feature ranking", *Informatics in Medicine Unlocked*, vol.15, no.100180, pp.1-11, 2019.

On Conic Equations Under Bernstein Operators

Tuncay TUNC[1*], Ghofran ALHAZZORI[2]

[1] Department of Mathematics, Faculty of Science, Mersin University, Mersin, Türkiye
[2] Department of Mathematics, Institute of Science, Mersin University, Mersin, Türkiye
(ORCID: 0000-0002-3061-7197) (ORCID: 0000-0003-0342-1575)

Keywords: Bivariate Bernstein polynomials, Conic equations, Shape-preserving approximation, Korovkin type theorem.

Abstract

One of the most important problems in approximation theory in mathematical analysis is the determination of sequences of polynomials that converge to functions and have the same geometric properties. This type of approximation is called the shape-preserving approximation. These types of problems are usually handled depending on the convexity of the functions, the degree of smoothness depending on the order of differentiability, or whether it satisfies a functional equation. The problem addressed in this paper belongs to the third class. A quadratic bivariate algebraic equation denotes geometrically some well-known shapes such as circle, ellipse, hyperbola and parabola. Such equations are known as conic equations. In this study, it is investigated whether conic equations transform into a conic equation under bivariate Bernstein polynomials, and if so, which conic equation it transforms into.

1. Introduction

One of the important problems in approximation theory is to identify sequences of polynomials that converge to functions and have the same geometric properties. This type of approximation is called the shape-preserving approximation. The issue of shape-preserving approximation with algebraic polynomials has a long history and probably begins in 1925 with a result of Pal [1] stating that any convex function defined in the interval $[a, b]$ can be properly approximated by convex polynomials in that interval. The first structural answer to Pal's conclusion seems to have been given by Popoviciu [2] in 1937 with the help of Bernstein polynomials: For $f: [0,1] \to \mathbb{R}$ and $n \in \mathbb{N}$, the nth Bernstein polynomial is defined by

$$B_n(f; x) = \sum_{k=0}^{n} f\left(\frac{k}{n}\right) \binom{n}{k} x^k (1-x)^{n-k}$$

The sequence of Bernstein polynomials is the best-known that has the property of shape-preserving approximation. There have been many studies on whether the sequence of Bernstein polynomials

preserves which geometric properties, especially convexity types. For $k \in \mathbb{N}$, Popoviciu showed that the Bernstein polynomials $B_n(f)$ are also k-convex for each $n \in \mathbb{N}$, if f is a k-convex function [2]. Over time, many mathematicians have made great efforts to contribute to this topic. The studies of Lupaş [3], Leviatan [4,5], Kocic and Milovanovic [6] and Hu-Yu [7] can be mentioned as good examples of studies on the shape-preserving approximation of univariate real functions with polynomials.

Despite the large number of articles in the literature, there are not many books dealing with the shape-preserving approximation in the bivariate or multivariate case. First, Gal [8] dealt with it. Using the method of forming Bernstein polynomials dependent on univariate functions, Hildebrant and Schoenberg [9] defined bivariate Bernstein polynomials with double indices

$$B_{n,m}(f; x, y) = \sum_{k=0}^{n} \sum_{j=0}^{m} f\left(\frac{k}{n}, \frac{j}{m}\right) \binom{n}{k} \binom{m}{j} x^k$$
$$\times (1-x)^{n-k} y^j (1-y)^{m-j}$$

*Corresponding author: *ttunc@mersin.edu.tr*

dependent on bivariate functions defined on the $[0,1] \times [01]$ and examined their approximation properties. Kingsley [10] showed that this set of operators converges uniformly to the partial derivatives of the function f. $(r, s) -$convex functions defined by Popoviciu [11] are protected under $B_{n,m}$ operators [8]. Tunç and Uzun [12] obtained results that B-convex functions are not conserved under these operators, but B-concave functions are preserved in some special cases.

In this study, we have examined whether the geometric shapes specified by the conic equations were preserved under Bernstein operators mentioned above.

2. Material and Method

The moment formulas given below are correct for the bivariate Bernstein operators with double indices that are defined by

$$B_{n,m}(f; x, y) = \sum_{k=0}^{n} \sum_{j=0}^{m} f\left(\frac{k}{n}, \frac{j}{m}\right) \binom{n}{k} \binom{m}{j} x^k$$
$$\times (1 - x)^{n-k} y^j (1 - y)^{m-j}.$$

Let us define the functions $e_{i,j}$, $i, j \in \mathbb{N}_0$, by $e_{i,j}(x, y) = x^i y^j$ on $\mathbb{R}^2$.

Lemma 2.1. ([9])
i. $B_{n,m}(e_{i,j}; x, y) = e_{i,j}(x, y)$, for all $i, j \in \{0,1\}$
ii. $B_{n,m}(e_{0,2}; x, y) = e_{0,2}(x, y) + \frac{y(1-y)}{m}$,
iii. $B_{n,m}(e_{2,0}; x, y) = e_{2,0}(x, y) + \frac{x(1-x)}{n}$

Teorem 2.2. ([9]) If f is a continuous function on $[0,1] \times [0,1]$ then the sequence $(B_{n,m}(f))$ converges uniformly to f function on $[0,1] \times [0,1]$.

In the article referenced for the proof of this theorem, it is said that it can be done in a similar way by referring to the work of Bernstein [13]. However, a simpler method can be proved. [14] and Lemma 2.1 can be used for this.

3. Results and Discussion

3.1. Circles Under Bivariate Bernstein Operators

In this section, firstly, conic equations will be discussed under the bivariate Bernstein Operators with double index. For $A, B, C, D, E, F \in \mathbb{R}$, the equation

$$f(x, y) = Ax^2 + Bxy + Cy^2 + Dx + Ey + F = 0 \quad (1)$$

looks like following under the $B_{n,m}$ operator:

$$B_{n,m}(f; x, y) = A'x^2 + B'xy + C'y^2 + D'x + E'y$$
$$+ F' = 0$$

where

$$A' = \frac{n-1}{n}A; \ B' = B; \ C' = \frac{m-1}{m}C; \ D' = D +$$
$$\frac{A}{n}; \ E' = E + \frac{C}{m}; \ F' = F \quad (2)$$

In Theorem 2.2, the double-index bivariate Bernstein operators are defined according to their values in the domain of the function, and it is said that the sequence formed by these operators converges properly in the domain of the function. However, the equations in Lemma 2.1 are valid at every point of the plane. So the following theorem is true.

Theorem 3.1. For the function f defined by (1), the sequence $(B_{n,m}(f))$ is uniformly convergent to the function f on every compact subset of the plane.

Proof. It is easily obtained from Lemma 2.1.

Let

$$\Delta_0 = D^2 + E^2 - 4F;$$
$$\Delta_1 = D + E + 2F.$$

It is well known that, if $A = C = 1$, $B = 0$ and $\Delta_0 > 0$ then the equation (1) indicates a circle in the cartesian plane.

Theorem 3.2. Let the equation $f(x, y) = 0$ given by (1), where $A = C = 1$, specify a circle and let $n \in \mathbb{N}_2 := \{2,3,4, \dots\}$. In this case, the necessary and sufficient condition for the equation $B_{n,n}(f; x, y) = 0$ to specify a circle is

$$n^2 \Delta_0 + 2n\Delta_1 + 2 > 0.$$

Proof. Since $A = C = 1$ and $B = 0$, if $m = n$ is taken in equations (2), the appearance of equation (1) under the $B_{n,n}$ operator will be as follows

$$B_{n,n}(f; x, y) = \left(\frac{n-1}{n}\right)x^2 + \left(\frac{n-1}{n}\right)y^2$$
$$+ \frac{Dn+1}{n}x + \frac{En+1}{n}y + F = 0.$$

For $n > 1$, we get

$$\frac{n-1}{n}\left[x^2 + y^2 + \frac{Dn+1}{n-1}x + \frac{En+1}{n-1}y + \frac{n}{n-1}F\right] = 0.$$

If we write

$$D'' = \frac{Dn+1}{n-1}, \qquad E'' = \frac{En+1}{n-1}, \qquad F'' = \frac{nF}{n-1},$$

by simple calculations

$$D''^2 + E''^2 - 4F''$$
$$= \left(\frac{Dn+1}{n-1}\right)^2 + \left(\frac{En+1}{n-1}\right)^2$$
$$- 4\left(\frac{nF}{n-1}\right)$$
$$= \frac{(Dn+1)^2}{(n-1)^2} + \frac{(En+1)^2}{(n-1)^2}$$
$$- \frac{4nF(n-1)}{(n-1)^2}$$
$$= \frac{1}{(n-1)^2}[(Dn+1)^2$$
$$+ (En+1)^2 - 4nF(n-1)]$$
$$= \frac{1}{(n-1)^2}[D^2n^2 + E^2n^2 - 4Fn^2$$
$$+ 2Dn + 2En + 4Fn + 2]$$
$$= \frac{1}{(n-1)^2}[n^2\Delta_0 + 2n\Delta_1 + 2]$$

are obtained. So that we get desired result.

Remarks 3.3.

1. In Theorem 3.2, if $n = 1$, the equation $B_{n,n}(f;x,y) = 0$ indicates a line. The equation of this line is $(D+1)x + (E+1)y + F = 0$.
2. In Theorem 3.2, if $n > 1$, the equation $B_{n,n}(f;x,y) = 0$ refers to the circle with radius $\frac{\sqrt{n^2\Delta_0+2n\Delta_1+2}}{2n-2}$ centered at $\left(\frac{Dn+1}{2n-2}, \frac{En+1}{2n-2}\right)$.
3. Since $\Delta_0 > 0$, the condition $n^2\Delta_0 + 2n\Delta_1 + 2 > 0$ in Theorem 3.2 will be satisfied for every sufficiently large natural number n. Therefore, if the equation $f(x,y) = 0$ indicates a circle, the equation $B_{n,n}(f;x,y) = 0$ indicates a circle except for a finite number of n.

Since $\Delta_0 > 0$, the following result can be easily obtained from Theorem 3.2.

Corollary 3.4. Under the conditions of Theorem 3.2, if $\Delta_1 > -1/n$, then $B_{n,n}(f;x,y) = 0$ indicates a circle.

Example 3.5. If the circle specified by the equation $f(x,y) = x^2 + y^2 + 4x - 6y - 12 = 0$ is taken into account, since $\Delta_0 = 100$ and $\Delta_1 = -26$, from Corollary 3.4, it is not clear that the equations $B_{n,n}(f;x,y) = 0$ specify a circle. However, since

$$n^2\Delta_0 + 2n\Delta_1 + 2 = 100n^2\Delta_0 - 52n\Delta_1 + 2 > 0,$$

the equation $B_{n,n}(f;x,y) = 0$ specify a circle by Theorem 3.2. (see Figure 1)
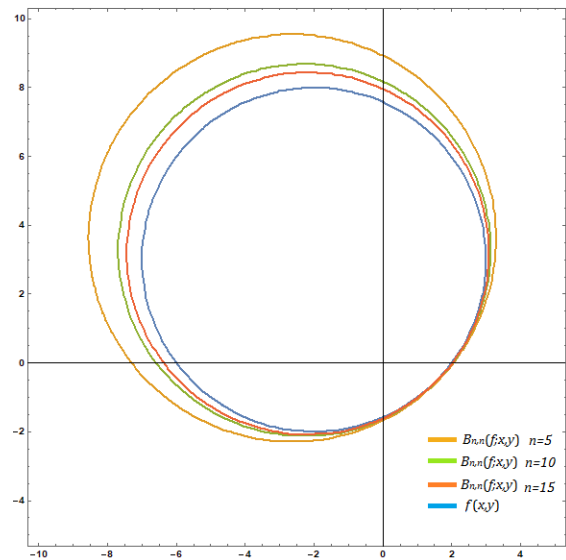
Figure 1. Images of the circle given in Example 3.5 under the operator $B_{n,n}$ for $n = 5, 10, 15$.

Theorem 3.6. Let the equation $f(x,y) = 0$ given by (1), where $A = C = 1$, specify a circle and let $n, m \in \mathbb{N}_2$. If $n \neq m$, then the equation $B_{n,m}(f;x,y) = 0$ specifies an ellipse.

Proof. Since $A = C = 1$ and $B = 0$, from the equations (2), the appearance of equation (1) under the $B_{n,m}$ operators will be as follows

$$B_{n,m}(f;x,y) = \left(\frac{n-1}{n}\right)x^2 + \left(\frac{m-1}{m}\right)y^2$$
$$+ \frac{Dn+1}{n}x + \frac{Em+1}{m}y + F = 0.$$

For $n, m > 1$, we get

$$B'^2 - 4A'C' = -4A'C' = -4\left(\frac{n-1}{n}\right)\left(\frac{m-1}{m}\right) < 0.$$

Since $n \neq m$, the equation $B_{n,m}(f; x, y) = 0$ specifies an ellipse.

Example 3.7. If the circle specified by the equation $f(x, y) = x^2 + y^2 + 4x - 6y - 12 = 0$ is taken into account, the equations

$$B_{n,m}(f; x, y) = \left(\frac{n-1}{n}\right) x^2 + \left(\frac{m-1}{m}\right) y^2$$
$$+ \frac{4n+1}{n} x + \frac{1-6m}{m} y - 12 = 0$$

specify ellipses under the condition $n \neq m$ (see Figure 2).

Theorem 3.8. Let the equation $f(x, y) = 0$ given by (1), where $A = C = 1$, specify a circle and let $n, m \in \mathbb{N}$. If $n \neq m$ and $min\{n, m\} = 1$ then the equation $B_{n,m}(f; x, y) = 0$ specifies a parabola.

Proof. Since it does not violate generality, let $n = 1$ and $m > 1$. Since $A = C = 1$ and $B = 0$, from the equations (2), the appearance of equation (1) under the $B_{n,m}$ operators will be as follows
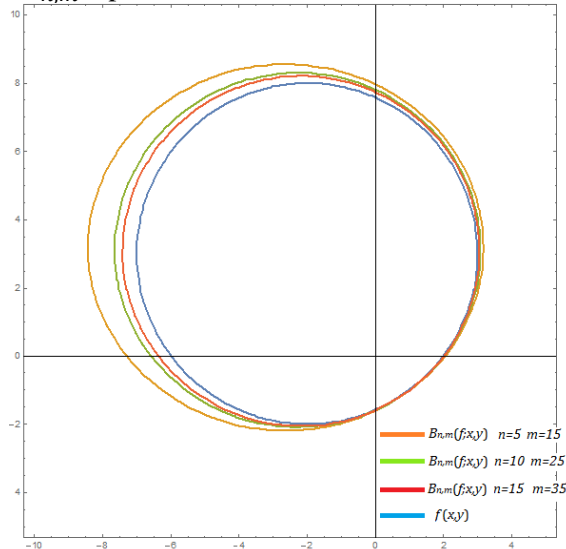
Figure 2. Images of the circle given in Example 3.7 under the operators $B_{n,m}$ for $(n, m) = (5,15)$, $(10,25), (15,35)$.

$$B_{n,m}(f; x, y) = \left(\frac{m-1}{m}\right) y^2 + (D+1)x$$
$$+ \frac{Em+1}{m} y + F = 0.$$

Since $B'^2 - 4A'C' = 0$, the equation $B_{n,m}(f; x, y) = 0$ specifies a parabola.

Example 3.9. If the circle specified by the equation $f(x, y) = x^2 + y^2 + 4x - 6y - 12 = 0$ is taken into account, the equations

$$B_{1,m}(f; x, y) = \left(\frac{m-1}{m}\right) y^2 + 5x + \frac{1-6m}{m} y - 12 = 0$$

specify parabolas under the condition $m > 1$ (see Figure 3).
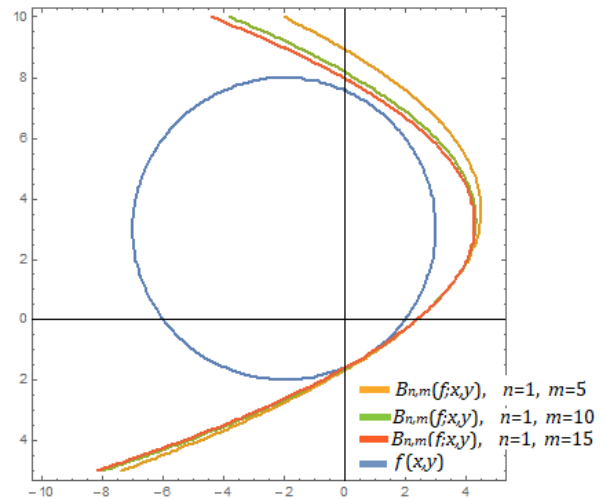
Figure 3. Images of the circle given in Example 3.9 under the operators $B_{n,m}$ for $(n, m) = (1,5), (1,10), (1,15)$.

3.2. Ellipses Under Bivariate Bernstein Operators

Theorem 3.10. Let the equation $f(x, y) = 0$ given by (1) specify an ellipse. Then the equation $B_{n,m}(f; x, y) = 0$ specifies

i. an ellipse for all $n, m \in \mathbb{N}_2$ with the condition $\frac{B^2}{4AC} < \left(\frac{n-1}{n}\right)\left(\frac{m-1}{m}\right)$,

ii. a hyperbola for all $n, m \in \mathbb{N}_2$ with the condition $\frac{B^2}{4AC} > \left(\frac{n-1}{n}\right)\left(\frac{m-1}{m}\right)$,

iii. a parabola for all $n, m \in \mathbb{N}_2$ with the condition $\frac{B^2}{4AC} = \left(\frac{n-1}{n}\right)\left(\frac{m-1}{m}\right)$.

Proof. Since the equation $f(x, y) = 0$ given by (1) indicates an ellipse, the inequality $B^2 - 4AC < 0$ and thus $AC > 0$ is satisfied. From the equations (2), the appearance of equation (1) under the $B_{n,m}$ operators will be as follows

$$B_{n,m}(f; x, y) = \left(\frac{n-1}{n}\right) Ax^2 + Bxy$$
$$+ \left(\frac{m-1}{m}\right) Cy^2 + \frac{Dn+A}{n} x$$
$$+ \frac{Em+C}{m} y + F = 0.$$

Since

$$B'^2 - 4A'C' = B^2 - 4AC\left(\frac{n-1}{n}\right)\left(\frac{m-1}{m}\right)$$

for all $n, m \in \mathbb{N}_2$, we have desired results.

Example 3.11. If the ellipse specified by the equation $f(x,y) = 15x^2 + 15xy + 6y^2 + 4x - 6y - 12 = 0$ is taken into account, we get $B^2/4AC = 5/8$. Hence, according to Theorem 3.10, the equation

$$B_{n,m}(f;x,y) = 15\left(\frac{n-1}{n}\right)x^2 + 15xy$$
$$+ 6\left(\frac{m-1}{m}\right)y^2 + \left(\frac{15}{n} + 4\right)x$$
$$+ \left(\frac{6}{m} - 6\right)y - 12 = 0$$

specifies an ellipse for $n = 6$, $m = 8$, a parabola for $n = 4$, $m = 6$ and a hyperbola for $n = 2$, $m = 4$ (see Figure 4)
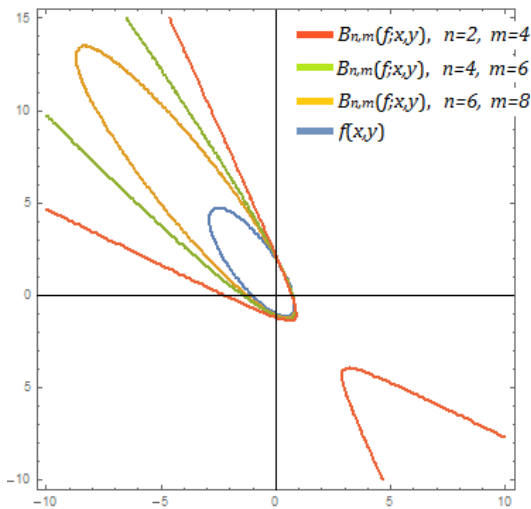
Figure 4. Images of the ellipse given in Example 3.11 under the operators $B_{n,m}$ for $(n,m) = (2,4)$, $(4,6)$, $(6,8)$.

Theorem 3.12. Let the equation $f(x,y) = 0$ given by (1) specify an ellipse. Then, if $n \neq m$ and $\min\{n,m\} = 1$, the equation $B_{n,m}(f;x,y) = 0$ specifies
i. a hyperbola for $B \neq 0$,
ii. a parabola for $B = 0$.

Proof. Since it does not violate generality, let $n = 1$ and $m > 1$. From the equations (2), the appearance of equation (1) under the $B_{n,m}$ operators will be as follows

$$B_{n,m}(f;x,y) = Bxy + \left(\frac{m-1}{m}\right)Cy^2 + (D+A)x$$
$$+ \frac{Em+C}{m}y + F = 0.$$

Since $B'^2 - 4A'C' = B^2$, the equation $B_{n,m}(f;x,y) = 0$ specifies a parabola for $B = 0$ while a hyperbola for $B \neq 0$.

Example 3.13.
(a) If the ellipse specified by the equation

$$f(x,y) = 15x^2 + 15xy + 6y^2 + 4x - 6y - 12 = 0$$

is taken into account, the equation

$$B_{1,m}(f;x,y) = 15xy + 6\left(\frac{m-1}{m}\right)y^2 + 19x$$
$$+ \left(\frac{6}{m} - 6\right)y - 12 = 0$$

specifies a hyperbola for each $m > 1$ (see Figure 5).
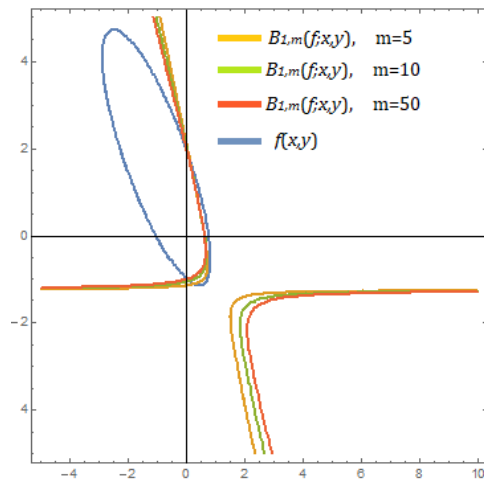
Figure 5. Images of the ellipse given in Example 3.13(a) under the operators $B_{1,m}$ for $m = 5, 10, 50$

(b) If the ellipse specified by the equation

$$f(x,y) = 15x^2 + 6y^2 + 4x - 6y - 12 = 0$$

is taken into account, the equation

$$B_{1,m}(f;x,y) = 6\left(\frac{m-1}{m}\right)y^2 + 19x + \left(\frac{6}{m} - 6\right)y$$
$$- 12 = 0$$

specifies a parabol for each $m > 1$ (see Figure 6).
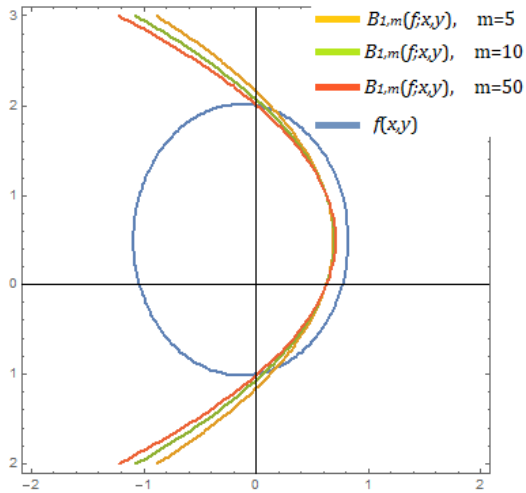
Figure 6. Images of the ellipse given in Example 3.13(b) under the operators $B_{1,m}$ for $m = 5, 10, 50$

3.3. Hyperbolas Under Bivariate Bernstein Operators

Theorem 3.14. If the equation $f(x, y) = 0$ given by (1) specifies a hyperbola, then the equations $B_{n,m}(f; x, y) = 0$ specify hyperbola for all $n, m \in \mathbb{N}_2$.

Proof. Since the equation $f(x, y) = 0$ given by (1) indicates a hyperbola, the inequality $B^2 - 4AC > 0$ is satisfied. From the equations (2), the appearance of equation (1) under the $B_{n,m}$ operators will be as follows

$$B_{n,m}(f; x, y) = \left(\frac{n-1}{n}\right) Ax^2 + Bxy$$
$$+ \left(\frac{m-1}{m}\right) Cy^2 + \frac{Dn + A}{n} x$$
$$+ \frac{Em + C}{m} y + F = 0.$$

Since $0 < \left(\frac{n-1}{n}\right)\left(\frac{m-1}{m}\right) < 1$, then we have

$$B'^2 - 4A'C' = B^2 - 4AC \left(\frac{n-1}{n}\right)\left(\frac{m-1}{m}\right) > 0$$

for all $n, m \in \mathbb{N}_2$.

Remarks 3.15.
1. Let the equation $f(x, y) = 0$ given by (1) specify a hyperbola and let $AC < 0$. In this case, the possibility of $B = 0$ arises. If this situation occurs, the equation $B_{n,m}(f; x, y) = 0$ for every $n, m \in \mathbb{N}$ with $min\{n, m\} = 1$ and $n \neq m$ also indicates a

parabola. Because under these conditions will be $B'^2 - 4A'C' = 0$.
2. If $B \neq 0$, Theorem 3.14 is valid for every $n, m \in \mathbb{N}$ with $max\{n, m\} \neq 1$.

Example 3.15.
(a) If the hyperbola specified by the equation $f(x, y) = 15x^2 + 15xy + 2y^2 + 4x - 6y - 12 = 0$ is taken into account, the equations

$$B_{n,m}(f; x, y) = 15\left(\frac{n-1}{n}\right) x^2 + 15xy$$
$$+ 2\left(\frac{m-1}{m}\right) y^2 + \left(\frac{15}{n} + 4\right) x$$
$$+ \left(\frac{2}{m} - 6\right) y - 12 = 0$$

specify hyperbola for all $n, m \in \mathbb{N}_2$. Note that $AC = 15.2 = 30 > 0$ (see Figure 7).
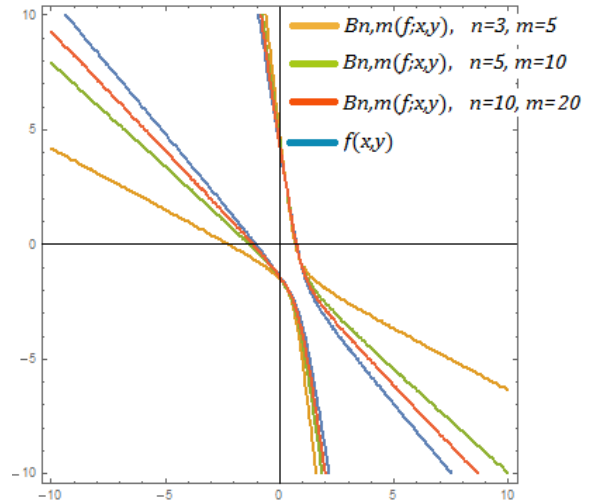
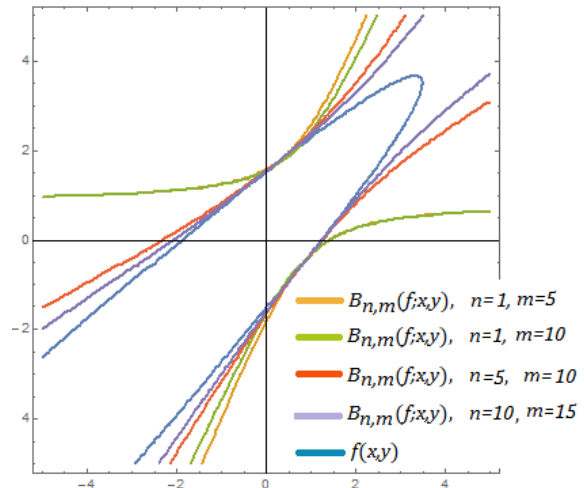**Figure 7.** Images of the hyperbola given in Example 3.15(a) under the operators $B_{n,m}$ for $(n, m) = (3,5), (5, 10), (10,20)$.

(b) If the hyperbola specified by the equation

$$f(x, y) = 15x^2 + 15xy + 4x - 6y - 12 = 0$$

is taken into account, the equations

$$B_{n,m}(f; x, y) = 15\left(\frac{n-1}{n}\right) x^2 + 15xy$$
$$+ \left(\frac{15}{n} + 4\right) x - 6y - 12 = 0$$

specify hyperbola for all $n, m \in \mathbb{N}_2$. Note that $AC = 0$ (see Figure 8).
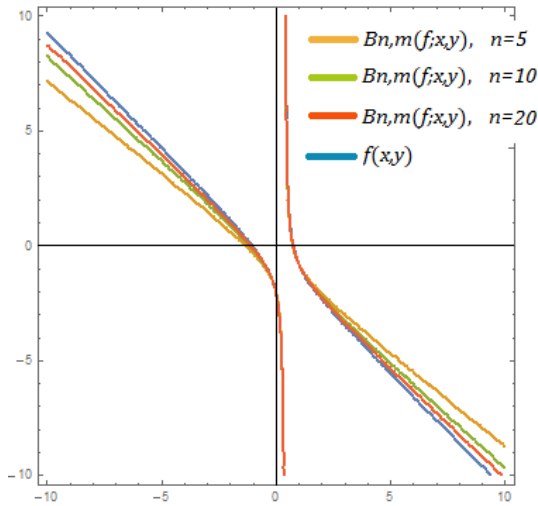
Figure 8. Images of the hyperbola given in Example 3.15(b) under the operators $B_{n,m}$ for $(n, m) = (5, m), (10, m), (20, m)$.

(c) If the hyperbola specified by the equation

$$f(x, y) = 15x^2 + 15xy + 4x - 6y - 12 = 0$$

is taken into account, the equations

$$B_{n,m}(f; x, y) = 15\left(\frac{n-1}{n}\right)x^2 - 2\left(\frac{m-1}{m}\right)y^2$$
$$+ \left(\frac{15}{n} + 4\right)x + \left(-\frac{2}{m} - 6\right)y - 12$$
$$= 0$$

specify hyperbola for all $n, m \in \mathbb{N}_2$. Note that $AC = -30 < 0$ (see Figure 9). On the other hand, the equations

$$B_{1,m}(f; x, y) = -2\left(\frac{m-1}{m}\right)y^2 + 19x + \left(-\frac{2}{m} - 6\right)y - 12 = 0,$$

$$B_{n,1}(f; x, y) = 15\left(\frac{n-1}{n}\right)x^2 + \left(\frac{15}{n} + 4\right)x - 8y - 12 = 0$$

specify parabolas for all $n, m \in \mathbb{N}_2$ (see Figure 10).
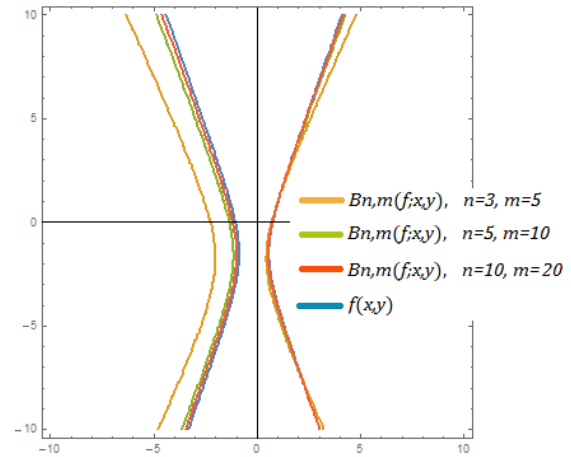
Figure 9. Images of the hyperbola given in Example 3.15(c) under the operators $B_{n,m}$ for $(n, m) = (3,5), (5, 10), (10,20)$.
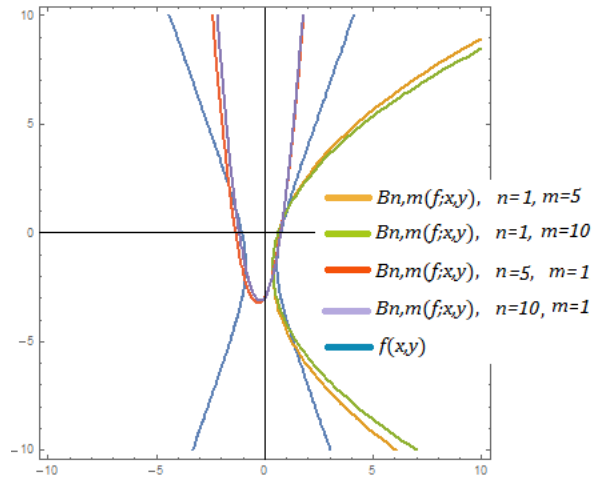
Figure 10. Images of the hyperbola given in Example 3.15(c) under the operators $B_{n,m}$ for $(n, m) = (1,5), (1, 10), (5,1), (10,1)$.

3.4. Parabolas Under Bivariate Bernstein Operators

Theorem 3.16. Let the equation $f(x, y) = 0$ given by (1) specify a parabola. Then, for all $n, m \in \mathbb{N}_2$, the equation $B_{n,m}(f; x, y) = 0$ specifies
i. a hyperbola if $AC \neq 0$,
ii. a parabola if $AC = 0$.

Proof. Since the equation $f(x, y) = 0$ given by (1) indicates a parabola, the equality $B^2 - 4AC = 0$ is satisfied. Therefore, it must be $AC \geq 0$ and A and C cannot be zero at the same time. From the equations (2), the appearance of equation (1) under the $B_{n,m}$ operators will be as follows

$$B_{n,m}(f;x,y) = \left(\frac{n-1}{n}\right)Ax^2 + Bxy$$
$$+ \left(\frac{m-1}{m}\right)Cy^2 + \frac{Dn+A}{n}x$$
$$+ \frac{Em+C}{m}y + F = 0.$$

Hence

$$B'^2 - 4A'C' = B^2 - 4AC\left(\frac{n-1}{n}\right)\left(\frac{m-1}{m}\right)$$

for all $n, m \in \mathbb{N}_2$. If $AC > 0$, then since $0 < \left(\frac{n-1}{n}\right)\left(\frac{m-1}{m}\right) < 1$, we have

$$B'^2 - 4A'C' = B^2 - 4AC\left(\frac{n-1}{n}\right)\left(\frac{m-1}{m}\right)$$
$$> B^2 - 4AC = 0$$

hence the equation $B_{n,m}(f;x,y) = 0$ specifies a hyperbola. If $AC = 0$, since $B = 0$, the equality $B'^2 - 4A'C' = 0$ is obtained, therefore the equation $B_{n,m}(f;x,y) = 0$ specifies a parabola.

Remark 3.17. Let the equation $f(x,y) = 0$ given by (1) specify a parabola and let $AC > 0$. In this case, the equation $B_{n,m}(f;x,y) = 0$ for every $n, m \in \mathbb{N}$ with $min\{n,m\} = 1$ and $n \neq m$ also indicates a hyperbola. Because under these conditions $B'^2 - 4A'C'$ will be $B^2 > 0$.

Example 3.18.
(a) If the parabola specified by the equation $f(x,y) = 3x^2 - 6xy + 3y^2 + 2x - 7 = 0$ is taken into account, it is clear that $AC = 3.3 = 9 > 0$ and the equations

$$B_{n,m}(f;x,y) = 3\left(\frac{n-1}{n}\right)x^2 - 6xy$$
$$+ 3\left(\frac{m-1}{m}\right)y^2 + \left(\frac{3}{n}+2\right)x + \frac{3}{m}y$$
$$- 7 = 0$$

specify hyperbola for all $n, m \in \mathbb{N}_2$ (see Figure 11).

(b) If the parabola specified by the equation $f(x,y) = 3y^2 + 2x - 7 = 0$ is taken into account, it is clear that $AC = 0$ and the equations

$$B_{n,m}(f;x,y) = 3\left(\frac{m-1}{m}\right)y^2 + 2x + \frac{3}{m}y - 7 = 0$$

specify hyperbola for all $n, m \in \mathbb{N}_2$ (see Figure 12).

Figure 11. Images of the parabola given in Example 3.17(a) under the operators $B_{n,m}$ for $(n,m) = (1,5), (1,10), (5,10), (10,15)$.
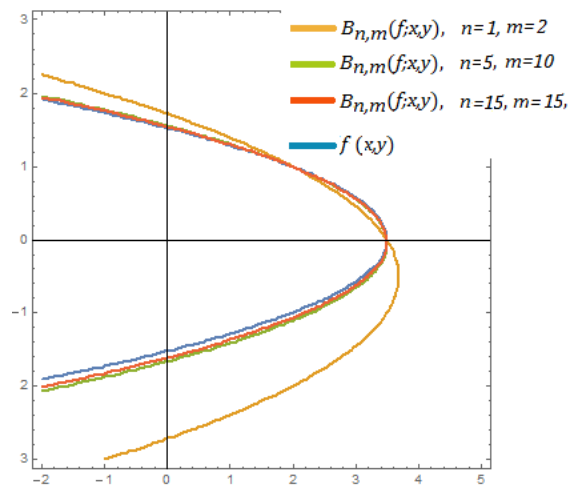
Figure 12. Images of the parabola given in Example 3.17(b) under the operators $B_{n,m}$ for $(n,m) = (1,2), (5,10), (15,15)$.

4. Conclusion and Suggestions

The equation $B_{n,m}(f;x,y) = 0$ is a quadratic two-variable equation, where $f(x,y) = 0$ is a conic equation and $B_{n,m}$ is a double-indexed two-variable Bernstein operator. If the equation $f(x,y) = 0$ indicates a circle, then the equations $B_{n,n}(f;x,y) = 0$ specify a circle for sufficiently large numbers n. However, in cases where the indices are different, that is, for $n \neq m$, $B_{n,m}(f;x,y) = 0$ equations indicate an ellipse or parabola. If the equation $f(x,y) = 0$ specifies an ellipse, the equations $B_{n,m}(f;x,y) = 0$ specifies an ellipse, hyperbola or parabola in certain cases. If the equation $f(x,y) = 0$ specifies a

hyperbola, the equations $B_{n,m}(f; x, y) = 0$ specifies hyperbola. Finally, if the equation $f(x, y) = 0$ specifies a parabola, the equations $B_{n,m}(f; x, y) = 0$ specifies a hyperbola or parabola, depending on whether the AC product is zero or not.

Conflict of Interest Statement

There is no conflict of interest between the authors.

Statement of Research and Publication Ethics

The study is complied with research and publication ethics

References

[1] J. Pal, "Approksimation of konvekse Funktioner ved konvekse Polynomier," *Mat. Tidsskrift, B,* pp. 60–65, 1925.

[2] T. Popoviciu, "About the Best Polynomial Aprroximation of Continious Functions," *Mathematical Monography*, Sect. Mat. Univ. Cluj, III, 1937.

[3] L. Lupaş, "A property of the S. N. Bernstein Operator." *Mathematica (Cluj)*, vol. 9, no. 32, pp. 299-301, 1967.

[4] D. Leviatan, "Shape preserving approximation by polynomials and splines, in: Approximation Theory and Function Series," *Bolyai Soc. Math. Stud.* vol. 5, no. 1, pp. 63–84, 1996.

[5] D. Leviatan, "Shape preserving approximation by polynomials," *J. Comput. Appl. Math.* vol. 121, no. 1–2, pp. 73–94, 2000.

[6] L. M. Kocic and G. M. Milovanovic, "Shape preserving approximation by polynomials and splines," *Comput. Math. Appl.,* vol. 33, vo. 11, pp. 59–97, 1997.

[7] Y. K. Hu and X. M. Yu, "Copositive polynomial approximation revisited," *Applied Mathematics Reviews* (G.A. Anastassiou ed.), vol. I, pp. 157–174, 2000.

[8] S. G. Gal, *Shape Preserving Approximation By Real and Complex Polynomials*. 1th ed.; Springer Science and Business Media. 2008.

[9] T. H. Hildebrandt and I. J. Schoenberg, "On Linear Functional Operations and the Moment Problem for a Finite Interval in One or Several Dimensions." *Annals of Mathematics*, vol. 34, no. 2, pp. 317-328, 1933.

[10] E. H. Kingsley, "Bernstein polynomials for functions of two variables of class C(k)." *Proceedings of the American Mathematical Society*, vol. 12, no. 1, pp. 64-71, 1951.

[11] T. Popoviciu, "Sur Quelques Proprietes Des Fonctions D'une Ou De Deux Variables Reelles". *Mathematica (Cluj).* vol. 8, no. 1, pp. 1-85, 1934.

[12] M. Uzun, and T. Tunc, "B-Convexity and B-Concavity Preserving Property Of Two-Dimensional Bernstein Operators." 7th Int. IFS and Contemporary Mathematics Conf., May, 25-29, 2021, Türkiye, 1-7.

[13] S.N. Bernstein, "Demonstration Du Theoreme De Weierstrass Fondee Sur Le Calcul De Probabilities," *Comm. Soc. Math. Kharkov*, vol. 13, no.2, pp. 1-2, 1912.

[14] D. D. Stancu, "A method for obtaining polynomials of Bernstein type of two variables." *The American Mathematical Monthly*, vol. 70, no. 3, pp. 260-264, 1963.

Determination of Some Atomic Parameters for Aktaş, Çıldır Lake, and Kura River Water with the Help of WinXCom

Burcu AKÇA[1*], Rumeysa Günay AĞAOĞLU[2]

[1]Department of Medical Services and Techniques, The Medical Imaging Techniques Programme, Ardahan Health Services Vocational School, Ardahan, TURKEY
[2]Ardahan University Graduate Education Institute, Environmental Health Graduate Education Institute, Ardahan, TURKEY

(ORCID: 0000-0003-2399-5971) (ORCID: 0000-0002-6386-9403)

Keywords: Aktaş Lake, Çıldır Lake, Kura River, WinXCom, Radiation

Abstract
In this study, elemental analyses of water samples taken from Aktaş, Çıldır Lake, and Kura River basins in Ardahan province were carried out using Inductively Coupled Plasma Mass Spectrometry. The mass attenuation coefficients, total photon interaction cross sections, effective atomic numbers, and electron densities were determined with the help of WinXCom for the main gamma-ray energies released when Ra-226, which is an important source of natural radiation, decays into Rn-222, Bi-214, and Po-214. As a result of the study, it was determined that Çıldır Lake would have more γ-ray interaction than Aktaş Lake and Kura River for the γ-ray energies taken into account. For γ-ray interaction degrees, the order can be made: Çıldır Lake > Kura River > Aktaş Lake.

1. Introduction

Information on the interaction of electromagnetic radiation with matter and energy loss is the basis for detecting radiation, determining protection principles, studying its biological effects, and using nuclear techniques in a wide variety of fields. The main agents in the interaction of electromagnetic radiation with matter are atomic electrons [1]. The interaction of electromagnetic radiation with matter reveals two main events, absorption and scattering. As a result of these events, atomic and molecular information about the matter can only be obtained by determining atomic parameters. Determination of atomic parameters: It is also very important in radiation applications such as space physics, astronomy, nuclear physics, nuclear weapon construction, solid state physics, cosmic ray studies, geology, plasma physics, satellite construction, determination of material thickness, dosimetry, radiology, and radiotherapy [2].

In many studies, atomic parameters at different energies for different substances are determined theoretically or experimentally. In our literature review, it has been seen that the subject has been popular in recent years, and sample studies are given. Akhdar et al. [3] investigated the mass attenuation coefficients, effective atomic numbers, and electron densities of the polyethylene glycol material for the energy range of 8.67-23.19 keV. The obtained results were compared with the XCom and Monte Carlo results. A good agreement was found between the measured experimental results and the theoretical values, and there was a 5% deviation in the XCom values. Tech et al. [4] calculated the mass attenuation coefficients, atomic and electronic cross sections, and effective atomic numbers of cambisol soils in Serra Dourada State Park in Brazil using XCom for 1-100 keV energy. In addition, oxide analysis in combisol soils was performed with EDXRF (Energy Dispersive X-ray Florescence) and WDXRF (Wavelength Dispersive X-ray Florescence). It was observed that the radiation

---

interaction parameters depend on the chemical composition of the material. Seenappa et al. [5] calculated effective atomic numbers, electron densities, and CT (Computerized Tomography) numbers of newborn and adult tissue of organs such as the lungs, hearts, kidneys, and brain. Moreover, for the energy range of 1 keV-100 keV, the effective atomic numbers were calculated with the WinXCom program by calculating molecular, atomic, and electronic cross-sections. It was determined that atomic number, CT number, and electron density were different in newborn tissue and adult tissue, and other calculated atomic parameters were similar. It has been stated that these results will be useful in radiotherapy and radiology [5].

Akça [6] measured the γ-ray linear attenuation coefficients and transmission factors for Erzurum Ispir dry bean and Ankara Kızılcahamam dry bean. It has been observed that Ankara Kızılcahamam dry beans absorb more γ-ray than Erzurum Ispir dry beans. Saim et al. [7] examined the total mass attenuation coefficient of trichloride gadolinium using Geant4 compared with WinXCom theoretical data for 1–10 MeV energies. The theoretical results have been used to calculate the total cross-section, atomic, and electronic cross-sections. Akça and Erzeneoğlu [8] measured important atomic parameters for compounds of biomedically important elements at 59.54 keV gamma-ray energy. Böke [9] calculated the photon interaction cross sections of human cortical bone tissue at smaller angles.

As a result of the literature search, no studies on radiation and interaction with radiation related to Aktaş, Çıldır Lakes, and Kura River were found. When determining the atomic parameters, the mixing rule is used if the substance is complex. According to the mixing rule, the mass percent of the elements in the substance must be known, and these must be taken into account in the atomic parameters. releases.

2. Material and Method

2.1. Theoretical Basis

The overall total mass attenuation coefficient for the multi-element compound is the sum of the mass attenuation coefficients of each element according to the mixing rule.

$$\frac{\mu}{\rho} = \sum_i \omega_i \left(\frac{\mu}{\rho}\right)_i \tag{1}$$

ω_i term in Equation (1) weight fraction of the element, $(\mu/\rho)_i$ (cm²/g) is the mass attenuation coefficient of the element. Also, here μ (cm⁻¹) is the linear attenuation coefficient and ρ (g/cm³) is the density of the sample. For the material obtained from the mass attenuation coefficient mixing rule, the total photon interaction cross section (barn/atom) is expressed by the following equation.

$$\sigma_a = \frac{\mu/\rho}{N_A \sum_i w_i/A_i} \tag{2}$$

The mass attenuation coefficient μ/ρ in the formula, A_i, atomic weight of the element, and N_A is Avogadro's constant [10]. The effective atomic number of any compound using the mixing rule;

$$Z_{eff} = \frac{Z_1(\log\sigma_2 - \log\sigma) + Z_2(\log\sigma - \log\sigma_1)}{\log\sigma_2 - \log\sigma_1} \tag{3}$$

It is calculated using the equation. Here, σ_1 and σ_2 are the basic sections in between, and Z_1 and Z_2 are the atomic numbers of the elements in which the atomic section of the material is found [11].

The electron density (electron/g);

$$N_e = N_A \frac{nZ_{eff}}{\sum_i n_i A_i} \tag{4}$$

is obtained by the equation. In the formula, n is the number of atoms in the mixture, and Z_{eff} is the effective atomic number [12].

2.2. Collection and Preparation of Water Samples

The theoretical calculations of the study started with taking water samples from Aktaş, Çıldır Lakes, and Kura River. To ensure the accuracy expected from water analysis, act within some principles while taking water samples, packaging them, and transporting them to the laboratory environment [13]. Water samples were collected considering these principles. Water samples were collected by immersing the sterilized bottle in water at least 25-30 cm downwards. The collected samples were filtered through a medical sterile cloth and cleaned of small residues in the water. All of these samples were collected in sterile and individually bagged conical bottom 15 ml falcon tubes. The lids of the falcon tubes were tightly closed and numbered with numbers according to the order of sampling.

The water samples taken from Aktaş Lake were taken from 10 different points, covering the entire water environment on the Turkish side of the lake, with a distance of 10 m in some places and 100-150 m in others. Çıldır Lake water samples were taken from 10 different points, starting from the opposite

shore of Gölebakan Village of Çıldır District, at a distance of 10 m or 50 m, and at a distance of 100-150 m in some coastal areas. Water samples from the Kura River were taken from 3 different regions. Kura River water samples were taken from 3 different points from the entrance of the Kura River to Ardahan, from 4 different points from the city center of Ardahan, and 3 different points from the exit part of the river from the center of Ardahan. Water samples were taken from 10 different points for each of Aktaş, Çıldır Lake, and Kura River water, a total of 30 samples were obtained and numbered. While collecting all water samples, attention was paid to ensuring that the weather was not rainy and the lakes and rivers were not frozen to carry out the operations properly and to obtain healthy results. All water samples were taken on the same day in early October 2022. An earthquake with a magnitude of approximately 5 occurred in Ardahan province in September of the same year. Çıldır Lake is 1959 meters above sea level, and Aktaş Lake is 1798 meters above sea level. While the bottom altitude of the Kura River above the sea is 1800 m when entering the Ardahan plain, it drops to 1300 m when leaving the Turkish territory. Metsamor nuclear power plant is 197 km away from Çıldır Lake, 219 km away from Kura River, and 241 km away from Aktaş Lake.

2.3. Elemental Analysis with Inductively Coupled Plasma Mass Spectrometry

In the study, elemental analyses of lake and river waters were made with the ICP-MS (Inductively Coupled Plasma-Mass Spectrometer) device, with the support of the scientific research project titled "Determination of Atomic Parameters of Aktaş, Çıldır Lake and Kura River Water with the Help of WinXCom" and with the support of the "2022-2 ÖNP-Sağl-005" service to DAYTAM. "Inductively Coupled Plasma-Mass Spectrometer (ICP-MS-Agilent 7800 series, Agilent Technologies, Japan)" was used to determine the concentrations of the elements in the solution. In the process of preparing the water samples for the device, the water samples were first filtered with a syringe filter. Ultrapure water was used as a blank solution. Samples and blank samples were analyzed by giving them to the device. Each reading is the average of 3 parallel readings in itself. 0, 250, 500, 750, and 1000 ppb for Si; for Hg, 0, 2.5, 5, 7.5, and 10 ppb, and other studied elements, the reference range is 0, 10, 25, 50, 100, 250, and 500 ppb. While preparing the standards, for the 10 ppb standard solutions; separately from the 10 ppm stock standard solutions 30 μl, and 7.5 μl of Hg solution were taken with a micropipette and transferred to a 50

ml falcon tube, and the volume of the solution was completed to 30 ml with 2% HNO_3 solution using a micropipette.

2.4. WinXCom

The WinXCom program is used to theoretically calculate the mass attenuation coefficients, which are atomic parameters. WinXCom is a mixture rule-based program that is calculated considering the element's mass attenuation coefficients. According to this rule, the elements in the material are examined one by one, and the calculation is made by accepting them as independent from each other. However, this rule neglects the changes in the atomic wave function resulting from changes in the molecular and chemical environment of the atom [14]. [15] developed the XCom program to calculate each element's total mass attenuation coefficients, or photon-interacting cross sections. With the help of this program, calculations of elements and mixtures with large photon energies ranging from 1 keV to 100 GeV can be made. WinXCom: It is the version of XCom transferred to Windows in 2001 by [16]. The program allows total cross-section, attenuation coefficients, and particle cross-section calculations for various interaction processes (atomic photoelectric effect, incoherent, coherent scattering) [16]. This program can theoretically calculate the mass attenuation coefficients of an element, compound, or mixture. The WinXCom program was very useful and was developed for radiological physics and dosimetry [17]. The energy values to be calculated first while using the program (0.053, 0.186, 0.242, 0.295, 0.352, 0.609, 0.665, 0.768, 0.786, 0.806, 0.934, 1.120, 1.155, 1.238, 1.281, 1.378, 1.401, 1.408, 1.509, 1.661, 1.730), 1.764, 1.847, 2.119, 2.204, and 2.448 MeV) were entered into the program manually. Since WinXCom calculates using the mixing rule (according to equation (1)), the elemental contents analyzed using ICP-MS and mass percentages of the water samples are entered into the system one by one, and the water samples are introduced to the program. Then, the sum (cm^2/g) values against the energy entered from the program, the mass attenuation coefficient, were obtained. This process was repeated for all samples and mass attenuation coefficients were obtained with the help of the WinXCom program. Other atomic parameters (Total Photon Interaction Cross Section, Effective Atomic Number, and Electron Density) were calculated with the help of formulas ((2), (3), and (4) equations) using the mass attenuation coefficient values calculated with WinXCom.

3. Results and Discussion

In this study, the extent to which Ra-226, which is known to be an important source of ionizing radiation, interacts with γ-rays in the radioactive decay chain was determined with the help of atomic parameters. In the study, the energies considered are the γ-energies in the products formed in the decay chain of Ra-226, which is seen as the most important cause of natural radiation. These γ-energies are the main γ-ray energy lines released as Ra-226 decays to Rn-222, Bi-214, and Po-214 (186.211 for Rn-222, 53.2275, 241.997, 295.224, 351.932, 785.96 for Bi-214, 609.312, 665.453, 768.356, 806.174, 934.061, 1120.287, 1155.19, 1238.111, 1280.96, 1377.669, 1401.50, 1407.98, 1509.228, 1661.28, 1729.595, 1764.494, 1847.420, 2118.55, 2204.21 and 2447.86 keV for Po-214) [18]. The reason for choosing Ra-226 in our study is the emergence of radon gas, which is known to be an important source of natural radiation and is the second most important cause of lung cancer after smoking, as a result of these radioactive decays. It is known that as a result of these radioactive decays, not only gamma rays ($_0^0\gamma$) but also alpha ($_2^4\alpha$) and beta particles ($_{-1}^0\beta$) which is in the ionizing radiation group. However, in our study, γ-rays were preferred because they are the most energetic and penetrating [19].

Today, the existence of Metsamor, which has all kinds of features that should not be in the standards related to nuclear power plants, poses a serious threat to Azerbaijan, Iran, and the whole region, especially Turkey, which is 16 kilometers away from the power plant [20]. Therefore, it is very important to study the radiation effect in Ardahan and its surroundings, which are close to Iğdır. The interaction of ionizing radiation with river and lake waters poses a threat to aquatic creatures, those who consume these creatures, and those who benefit from these waters at high interactions. The large interaction with radiation suggests that the dose taken by living things may also be large. It is very important to know the radiation that can cause fatal diseases such as cancer and the ways to protect yourself. In this study, the degree of interaction was determined by making calculations of the radiation interaction, especially in natural radiation energies. Since it is known that the naturally occurring radiation effect is constantly present, contributions from the environment will increase this amount.

Elemental content of Aktaş and Çıldır Lakes, Kura River waters obtained by ICP-MS (Li, Be, B, Na, Mg, Al, Si, P, K, Ca, Ti, V, Cr, Mn, Fe, Co, Ni, Cu, Zn, As, Se, Sr, Zr, Mo, Ru, Rh, Pd, Ag, Cd, In, Sn, Sb, Te, Ba, La, Ce, Ta, W, Re, Os, Ir, Pt, Au, Hg, Tl, Pb, Bi) and their concentration (ppb) are given in Table 1. The mass attenuation coefficients, total photon interaction cross sections, effective atomic numbers, and electron densities of Aktaş, Çıldır Lake, and Kura River water determined with the help of WinXCom are given in Table 2-4. The change of the mean values of the mass attenuation coefficients, total photon interaction cross sections, effective atomic numbers, and electron densities of Aktaş, Çıldır Lake, and Kura River waters determined with the help of WinXCom with energy is given in Figure 1-12. Graphics are drawn using Origin Pro 8.

When Tables 2, 3, 4, and Figures 1, 5, and 9 are examined, it is seen that the mass attenuation coefficients of Aktaş and Çıldır Lakes, and Kura River water decrease as the energy increases. That is, as the energy increased, the mass attenuation coefficient decreased; in other words, the γ-ray interaction decreased. Increasing the γ-ray or γ-radiation energy caused the already highly penetrating beam to become more penetrating. If the beam is very fast when it hits the material, it will be more penetrating, pass faster, spend less time on the material, and create less interaction. Since this causes the duration of the interaction to be shorter, the mass attenuation coefficient value will be smaller. While the mass attenuation coefficient values of Çıldır Lake and Kura River are very close to each other, these values are larger than the Aktaş Lake mass attenuation coefficient values. Accordingly, the γ-ray interaction in Lake Çıldır and Kura River will be higher than in Lake Aktaş. When Tables 2, 3, 4, and Figures 2, 6, and 10 are examined, it is seen that the total photon interaction cross-section values of Aktaş, Çıldır Lake, and Kura River waters decrease with the increase in energy. When sorting is done for the total photon interaction cross-section values, it becomes Çıldır Lake> Kura River> Aktaş Lake. According to this result, Çıldır Lake will interact with γ-rays more than Aktaş Lake and Kura River. It can be said that Çıldır Lake is more dangerous, especially for the creatures living in it, due to its high γ-ray absorption potential. However, if its usability as a shielding material is evaluated, Çıldır Lake water is better. When Table 2 and Figure 3 are examined, the effective atomic number value for Aktaş Lake increased with energy but decreased at 1.847 MeV energy. The effective atomic number of Aktaş Lake is in the range of $50.299 \leq Z_{eff} \leq 52.438$. When we look at the periodic table, it is thought that the effective atomic number values of Aktaş Lake water are close to the atomic numbers of Sn-50, Sb-51, and Te-52 elements, so it may show similar properties with the aforementioned elements. Aktaş Lake may exhibit weak and semi-metallic behavior accordingly. While $Z_{eff} \leq 10$

indicates organic substances, a large Z_{eff} is generally an indicator of inorganic compounds and metals [21]. When this situation is evaluated, the effective atomic number values of Aktaş Lake show inorganic or metal properties because $Z_{eff} \geq 10$.

When Table 3 and Figure 7 are examined, the effective atomic number for Çıldır Lake increases at an energy of 0.186 MeV and reaches its maximum. It then decreases at 0.352 MeV and becomes almost constant up to 2.448 MeV. The effective atomic number of Çıldır Lake is generally in the range of $68.930 \leq Z_{eff} \leq 69.971$. When we look at the periodic table, since these values are close to the atomic numbers of the elements Er-68 and Tm-69, it can be thought that they may show similar properties to the aforementioned elements. In this case, it can act as Lanthanide or Rare earth elements. When the effective atomic number values of Çıldır Lake are taken into account, $Z_{eff} \geq 10$ shows inorganic or metal properties.

When Table 4 and Figure 11 are examined, while the effective atomic number for the Kura River is at a minimum value of 0.053 MeV, it has a maximum value of 2.448 MeV. The effective atomic number first increased with energy increase, decreased after 0.609 MeV, remained almost constant up to 2.204 MeV, then increased again at 2.448 MeV. The effective atomic number of the Kura River is generally in the range of $63.228 \leq Z_{eff} \leq 64,439$. When we look at the periodic table, since these values are close to the atomic numbers of Eu-63 and Gd-64 elements, it is thought that they may show similar properties to the mentioned elements. In this case, it can act as Lanthanide or Rare earth elements. When the effective atomic number values of the Kura River are taken into account, $Z_{eff} \geq 10$ shows inorganic or metal properties.

When Figures 3, 7, and 11 are examined, it is seen that the effective atomic number changes depending on the energy. The partial effects of the Photoelectric Effect, Coherent Scattering, and Pair Production cause this change. Apart from this, the Photoelectric Effect is more dominant at energies below 100 KeV. In addition, it is seen that the effective atomic number and energy change graphs of river and lake waters are characteristic. It is thought that this situation is caused by the different interaction cross-sections and elemental contents. Aktaş and Çıldır Lakes, the effective atomic number order for the Kura River is Lake Çıldır>Kura River>Aktaş Lake. According to this order, Aktaş Lake has the smallest effective atomic number value. Çıldır Lake interacts more with γ-rays and exhibits more absorbing properties for γ-rays. When Tables 2, 3, 4 and Figures 4, 8, and 12 are examined, the changes in electron densities with energy are similar to the change in effective atomic number for Aktaş, Çıldır Lake, and Kura River. When we sort by considering the electron densities, it becomes Çıldır Lake>Kura River>Aktaş Lake. According to this order, as the electron density of Çıldır Lake is higher, its interaction with γ-rays will be greater. The high electron density indicates that the γ-ray will encounter more electrons in the medium it enters and will create a greater interaction. The most basic atomic parameters for calculating the average radiation absorption in a medium or material are the effective atomic number and electron density. It is seen that the electron density and energy exchange graphs of river and lake waters are characteristic, as are the effective atomic number and energy exchange graphs. In this case, the interaction cross-sections and elemental contents are thought to be different. Aktaş and Çıldır Lakes, the distance of Kura River to Metsamor Nuclear Power Plant is Çıldır Lake<Kura River<Aktaş Lake. This means that the degree of interaction of Çıldır Lake with radiation is quite large.

Table 1. Elemental analysis of Aktaş, Çıldır Lake, and Kura River water .

	Li	Be	B	Na	Mg	Al	Si	P	K	Ca
Sample	Concentration (ppb)									
Aktaş Lake$_{Avg}$	24.45660	0.03460	857.19920	333258.39360	39826.01510	1157.78740	7291.50480	257.12700	26072.42110	3625.21540
Çıldır Lake$_{Avg}$	1.79200	0.00125	46.42370	6384.07420	4726.32320	27.12820	2968.46640	123.71470	3165.95220	1889.32080
Kura River$_{Avg}$	8.05170	<0.001	133.37030	13333.26130	11414.49890	17.43400	17536.90130	297.93380	5807.28310	5067.64390

	Ti	V	Cr	Mn	Fe	Co	Ni	Cu	Zn	As
Sample	Concentration (ppb)									
Aktaş Lake$_{Avg}$	53.62790	16.25290	1.92590	32.40900	606.61530	3.95160	9.50310	13.80410	87.63870	56.22140
Çıldır Lake$_{Avg}$	0.97430	2.63930	0.03940	0.62990	15.54210	0.03280	1.65920	0.93830	0.52870	2.12980
Kura River$_{Avg}$	0.72310	4.77380	0.17960	2.61110	25.01170	0.15130	1.93500	1.42840	1.06310	6.75640

	Se	Sr	Zr	Mo	Ru	Rh	Pd	Ag	Cd	In
Sample	Concentration (ppb)									
Aktaş Lake$_{Avg}$	0.32980	307.26640	3.17820	19.58660	0.00500	0.01400	0.02840	0.90460	0.05090	<0.001
Çıldır Lake$_{Avg}$	0.05870	66.32910	0.06590	0.72990	<0.000	0.03667	0.00744	0.00550	0.00170	<0.001
Kura River$_{Avg}$	0.09350	138.86900	0.08350	1.06720	<0.001	<0.001	0.00590	0.00100	0.00260	<0.001

	Sn	Sb	Te	Ba	La	Ce	Ta	W	Re	Os
Sample	Concentration (ppb)									
Aktaş Lake$_{Avg}$	0.68430	0.49590	0.02970	94.13060	0.66020	1.30100	0.04210	0.46470	0.01700	<0.001
Çıldır Lake$_{Avg}$	0.04860	0.07570	0.00356	21.92220	0.03240	0.04650	0.02100	0.54200	0.00500	<0.001
Kura River$_{Avg}$	0.10090	0.04830	0.00414	12.53580	0.01850	0.02630	0.00810	<0.001	0.00120	<0.001

	Ir	Pt	Au	Hg	Tl	Pb	Bi	-	-	-
Sample	Concentration (ppb)									
Aktaş Lake$_{Avg}$	0.08000	<0.001	0.04060	0.00540	0.01380	0.98150	<0.001	-	-	-
Çıldır Lake$_{Avg}$	0.18933	<0.001	0.10450	0.00267	0.01010	0.01920	0.04100	-	-	-
Kura River$_{Avg}$	<0.001	<0.001	<0.001	<0.001	0.00178	0.02760	<0.001	-	-	-

Table 2. Mass attenuation coefficients, total photon interaction cross sections, effective atomic numbers, and electron densities for Aktaş Lake average value.

Sample	Daughter	Energy (MeV)	μ/ρ (cm²/g)	σ_a (x10⁻²¹) (cm²/atom)	Z_{eff}	N_e (x10²⁴) (elektrons/kg)
	Rn-222	0.186	0.12506	12.22546	52.04028	3.15400
		0.053	0.31055	30.33736	50.29882	3.04800
		0.242	0.11291	11.03794	52.05297	3.15500
	Bi-214	0.295	0.10448	10.21385	52.11167	3.15800
		0.352	0.09742	9.52450	52.22950	3.16900
		0.786	0.06881	6.72747	52.28910	3.16900
		0.609	0.07728	7.55481	52.36640	3.17400
		0.665	0.07428	7.26207	52.33417	3.17200
		0.768	0.06954	6.79863	52.28281	3.16900
		0.806	0.06800	6.64831	52.30423	3.17000
		0.934	0.06341	6.19903	52.43804	3.17800
		1.120	0.05794	5.66461	52.28843	3.16900
		1.155	0.05705	5.57778	52.29544	3.16900
Aktaş Lake$_{Avg}$		1.238	0.05509	5.38597	52.31114	3.17000
		1.281	0.05415	5.29347	52.30148	3.17000
		1.378	0.05217	5.09995	52.24508	3.16600
	Po-214	1.401	0.05173	5.05691	52.23050	3.16500
		1.408	0.05159	5.04401	52.22626	3.16500
		1.509	0.04979	4.86793	52.18691	3.16300
		1.661	0.04740	4.63394	52.20970	3.16400
		1.730	0.04642	4.53809	52.22327	3.16500
		1.764	0.04596	4.49294	52.22585	3.16500
		1.847	0.04488	4.38801	52.21364	3.16400
		2.119	0.04182	4.08878	51.94764	3.14800
		2.204	0.04099	4.00762	51.86659	3.14300
		2.448	0.03888	3.80097	51.70584	3.13400
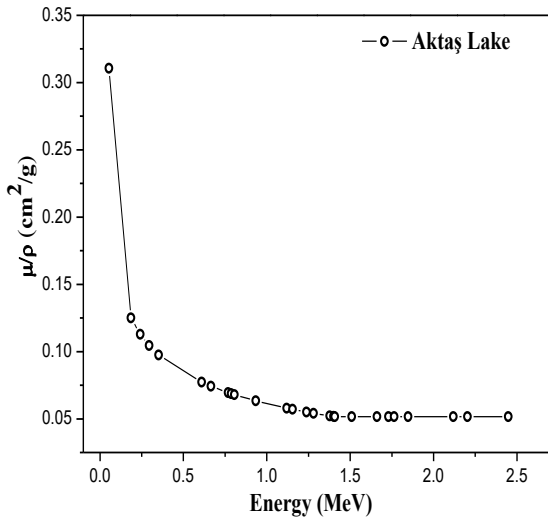
Figure 1. Variation of mass attenuation coefficients with energy for Aktaş Lake average value.
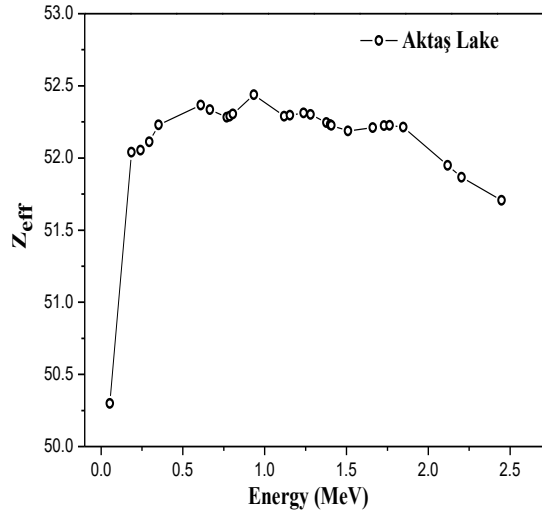
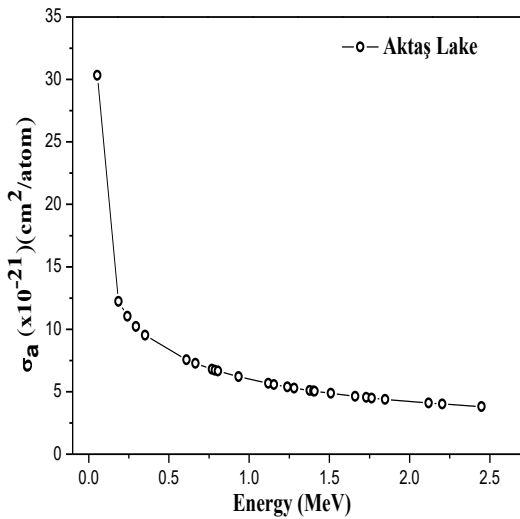**Figure 3**. Variation of effective atomic numbers with energy for Aktaş Lake average value.

Figure 2. Variation of total photon interaction cross sections with energy for Aktaş Lake average value.
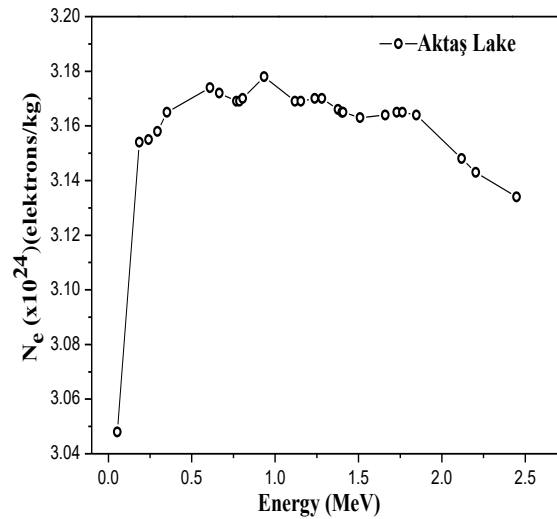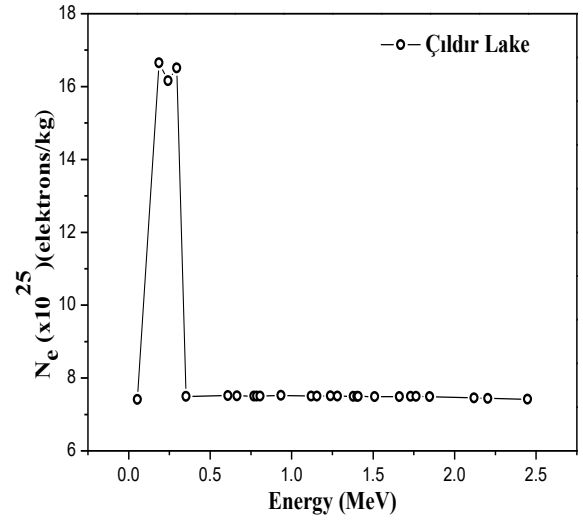

Figure 4. Variation of electron densities with energy for Aktaş Lake average value.

Table 3. Mass attenuation coefficients, total photon interaction cross sections, effective atomic numbers, and electron densities for Çıldır Lake average value.

Sample	Daughter	Energy (MeV)	μ/ρ (cm²/g)	σ_a(x10⁻¹⁹) (cm²/atom)	Z_{eff}	N_e (x10²⁵) (elektrons/kg)
	Rn-222	0.186	0.13073	3.03054	154.78946	16.65000
		0.053	0.45865	10.63216	68.92968	7.41300
		0.242	0.11648	2.70014	150.29052	16.16000
	Bi-214	0.295	0.10717	2.48438	153.50814	16.51000
		0.352	0.09961	2.30924	69.70509	7.49700
		0.786	0.06998	1.62231	69.77047	7.50400
		0.609	0.07865	1.82335	69.87957	7.51600
		0.665	0.07558	1.75219	69.83466	7.51100
		0.768	0.07073	1.63961	69.76232	7.50300
		0.806	0.06915	1.60306	69.79060	7.50600
		0.934	0.06444	1.49394	69.97148	7.52500
		1.120	0.05890	1.36535	69.77079	7.50400
Çıldır Lake$_{Avg}$		1.155	0.05799	1.34435	69.77978	7.50500
		1.238	0.05599	1.29797	69.79949	7.50700
		1.281	0.05503	1.27565	69.78563	7.50500
		1.378	0.05302	1.22912	69.70785	7.49700
	Po-214	1.401	0.05258	1.21879	69.68786	7.49500
		1.408	0.05244	1.21570	69.68204	7.49400
		1.509	0.05062	1.17351	69.62812	7.48800
		1.661	0.04821	1.11758	69.65893	7.49200
		1.730	0.04722	1.09473	69.67729	7.49400
		1.764	0.04676	1.08399	69.68071	7.49400
		1.847	0.04569	1.05907	69.66380	7.49200
		2.119	0.04264	0.98846	69.29943	7.45300
		2.204	0.04181	0.96934	69.18806	7.44100
		2.448	0.03972	0.92069	68.96592	7.41700
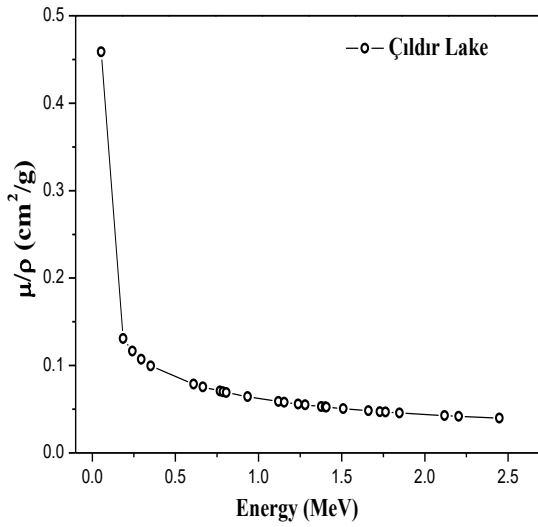
Figure 5. Variation of mass attenuation coefficients with energy for Çıldır Lake average value
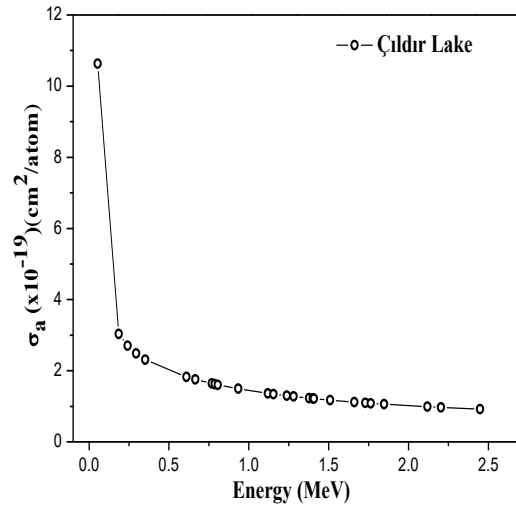
Figure 6. Energy variation of total photon interaction cross sections for Çıldır Lake average value
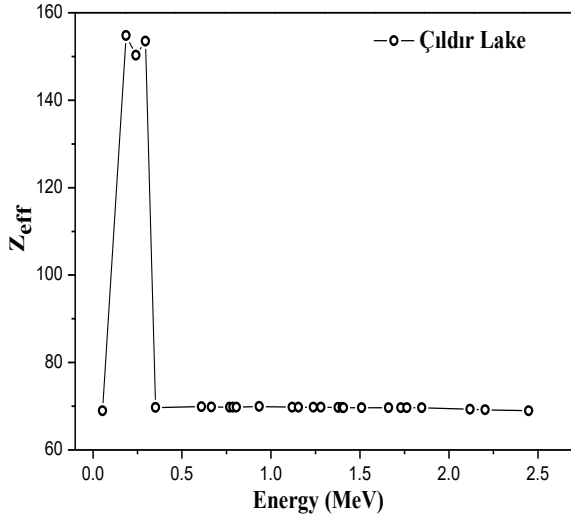
Figure 7. Variation of effective atomic numbers with energy for Çıldır Lake average value

Figure 8. Variation of electron densities with energy for Çıldır Lake average value

Table 4. Mass attenuation coefficients, total photon interaction cross sections, effective atomic numbers, and electron densities for Kura River average value

Sample	Daughter	Energy (MeV)	μ/ρ (cm²/g)	σ_a(x10⁻²⁰) (cm²/atom)	Z_{eff}	N_e (x10²⁵) (elektrons/kg)
	Rn-222	0.186	0.13074	11.03131	141.60246	5.57200
		0.053	0.43698	36.88448	63.22771	2.48800
		0.242	0.11677	9.85250	137.58028	5.41400
	Bi-214	0.295	0.10755	9.07470	140.50841	5.52900
		0.352	0.10003	8.43970	142.30428	5.60000
		0.786	0.07034	5.93493	64.25522	2.52800
		0.609	0.07905	6.66935	64.35485	2.53200
		0.665	0.07597	6.40954	64.31386	2.53100
		0.768	0.07109	5.99820	64.24779	2.52800
		0.806	0.06951	5.86451	64.27360	2.52900
		0.934	0.06478	5.46533	64.43871	2.53600
		1.120	0.05921	4.99567	64.25526	2.52800
		1.155	0.05830	4.91883	64.26353	2.52900
Kura River$_{Avg}$		1.238	0.05629	4.74904	64.28168	2.52900
		1.281	0.05532	4.66737	64.26908	2.52900
	Po-214	1.378	0.05330	4.49707	64.19814	2.52600
		1.401	0.05285	4.45928	64.17990	2.52500
		1.408	0.05272	4.44796	64.17460	2.52500
		1.509	0.05089	4.29355	64.12557	2.52300
		1.661	0.04846	4.08875	64.15437	2.52400
		1.730	0.04747	4.00510	64.17157	2.52500
		1.764	0.04700	3.96579	64.17495	2.52500
		1.847	0.04592	3.87464	64.16018	2.52500
		2.119	0.04286	3.61667	63.83018	2.51200
		2.204	0.04204	3.54675	63.72929	2.50800
		2.448	0.03992	3.36850	142.33755	5.60100
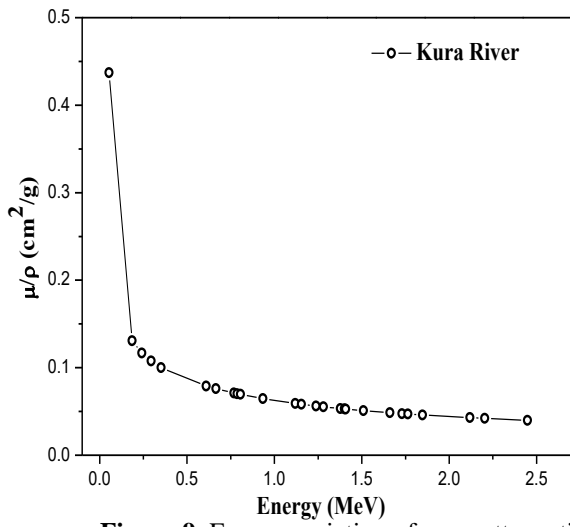
Figure 9. Energy variation of mass attenuation coefficients for Kura River average value
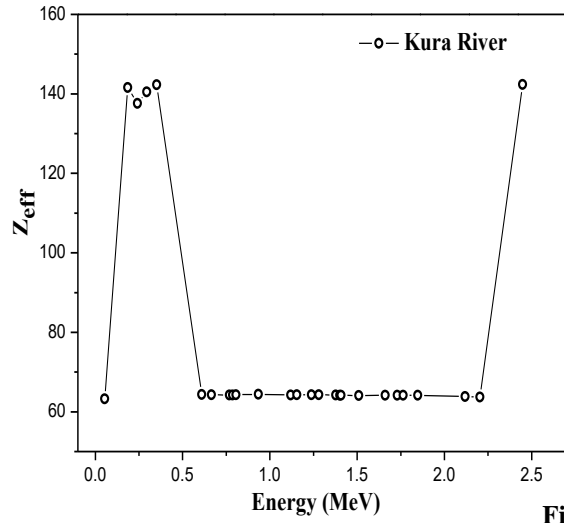
Figure 11. Energy variation of effective atomic numbers for Kura River average value
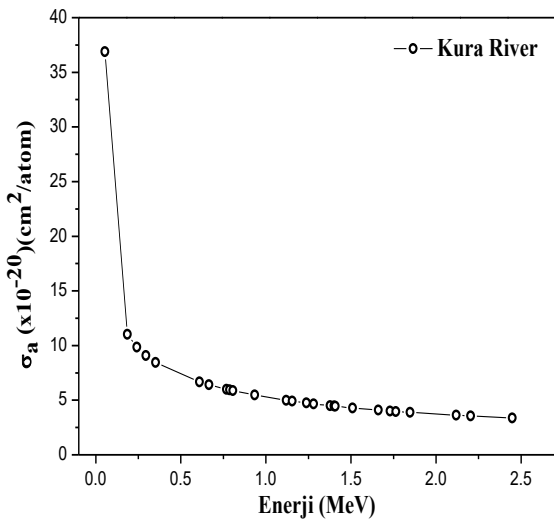
Figure 10. Energy variation of total photon interaction cross sections for Kura River average value
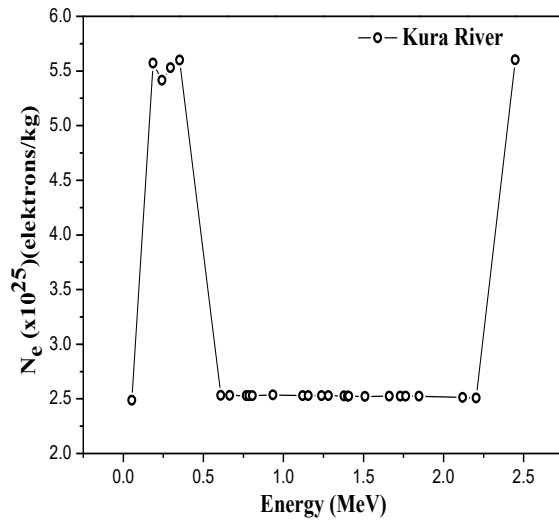
Figure 12. Variation of electron densities with energy for Kura River average value

4. Conclusion and Suggestions

As a result, when the atomic parameters for Aktaş, Çıldır Lake, and Kura River waters are examined, the interaction of γ-ray and the degree of interaction are Çıldır Lake>Kura River>Aktaş Lake. In other words, since Çıldır Lake interacts more with γ-rays than others, it tends to absorb the rays more. Aktaş Lake, on the other hand, has the smallest degree of interaction, meaning it interacts less with the γ-ray.
In the future, this work should be done experimentally or with different theoretical programs for different energies.

Contributions of the authors

B. Akça: Writing, review, editing, investigation, supervision, project, original draft administration, conceptualization, methodology, **R. G. Ağaoğlu:** Review, editing, investigation, data curation, original draft, conceptualization, methodology.**Conflict of Interest Statement**

There is no conflict of interest between the authors.

Statement of Research and Publication Ethics

The study has complied with research and publication ethics.

References

[1]. B. Akca, "Measurement of mass attenuation coefficients of compounds of biomedically important elements and change according to the annealing temperature and time of transmission factors at doped, undoped semiconductors", *Physics Department*, 2014.

[2]. I. Han and L. Demir, "Determination of mass attenuation coefficients, and effective atomic and electron numbers for Cr, Fe, and Ni alloys at different energies". Nuclear Instruments and Methods in," *Physics Research Section B*, vol. 267, pp. 3–8, 2009.

[3]. H. Akhdar, M. W. Marashder, and M. Alagell, "Investigation of Gamma Radiation Shielding Properties of Polyethylene Glycol in the Energy from 8.67 to 23.19 keV", *Nuclear Engineering and Technology*, vol. 54, pp. 701–708, 2022.

[4]. L. Tech, L. F. Pires, A. M. Brinatti, S. C. Sabb, V. Correctel, R. S. Momoli, "Elemental and Radiation Attenuation Parameter Analyses to Characterise a Cambisol from the Serra Dourade State Park", *Brazil, Environmental Earth Sciences*, vol. 81, no. 63, 2022.

[5]. L. Seenappa, H. C. Manjunatha, K. N. Sridhar, N. Nagaraja, H. D. Vijaykumar, "A Study of Dosimetric Parameters of New Born Tissue and Adult Tissue of Some Organs", *Materials Today: Proceedings*, vol. 49, pp. 878–881, 2022.

[6]. B. Akça, "An experimental study on the measurement of gamma-ray linear attenuation coefficients with transmission factors for İspir and Kızılcahamam dry bean", *Osmaniye Korkut Ata University Journal of the Institute of Science and Technology*, vol. 6, no. 1, pp. 585–593, 2023.

[7]. A. Saim *et al.*, "Photon attenuations of trichloride of gadolinium by Geant4 and XCom: a comparative study", *Journal of Taibah University for Science*, vol. 17, 2023.

[8]. B. Akça and S. Z. Erzeneoğlu, "The Mass Attenuation Coefficients, Electronic, Atomic, and Molecular Cross Sections, Effective Atomic Numbers, and Electron Densities for Compounds of Some Biomedically Important Elements at 59.5 keV", *Science and Technology of Nuclear Installations*, vol. 2014, 2014.

[9]. A. Böke, "The photon interaction cross sections of human cortical bone tissue", *Chin. J. Phys.*, vol. 55, no. 6, pp. 2165–2172, 2017.

[10]. H. Alaviana, A. Samieb, and H. T. Anbaran, "Experimental and Monte Carlo investigations of gamma-ray transmission and buildup factors for inorganic nanoparticle/epoxy composites", *Radiat. Phys. Chem*, vol. 174, pp. 108–960, 2020.

[11]. T. Singh, P. Kaur, and P. S. Singh, "A study of photon interaction parameters in some commonly used solvents", *Journal Radiol. Protection*, vol. 27, pp. 79–85, 2007.

[12]. S. R. Manohara, S. M. Hanagodimath, and K. S. Thind, "On the effective atomic number and electron density: a comprehensive set of formulas for all types of materials and energies above 1 keV", *Nuclear Instr. Meth. B*, vol. 266, 2008.

[13]. R. Karataş, *Bitki ve Su Örneklerinin Alımı ve Laboratuvara Taşınma Teknikleri", Süleyman Demirel Üniversitesi Fen Bilimleri Enstitüsü, Yüksek Lisans Seminer Orman Mühendisliği Anabilim Dalı*. Isparta, Türkiye, 2013.

[14]. B. R. Kerur, S. R. Thontadarya, and B. Hanumaıah, "Anomalous X-Ray Attenuation Coefficients Around the Absorption Edges Using Mn Kα, and Cu Kα X-Rays", *Appl. Radiat*, vol. 45, no. 2, pp. 159–163, 1994.

[15]. M. J. Berger and J. H. Hubbell, *Photon Cross Sections Database, Web Version 1.2. National Institute of Standards and Technology", Gaithersburg. (Originally Published as NBSIR 87-3597 "XCOM: Photon Cross Sections on a Personal Computer)*. 1987.

[16]. L. Gerward, N. Guilbert, K. B. Jensen, and H. Levring, "X-ray absorption in matter Reengineering XCOM", *Radiation Physics and Chemistry*, vol. 60, pp. 23–24, 2001.

[17]. A. R. El-Sersy, A. Hussein, H. M. El-samman, N. E. Khaled, A. El-Adawy, and H. Donya, "Mass attenuation coefficients of B2O3–Al2O3–SiO2–CaF2 glass system at 0.662 and 1.25 MeV gamma energies," *J. Radioanal. Nucl. Chem.*, vol. 288, no. 1, pp. 65–69, 2011.

[18]. V. Chiste, M. M. Be, and C. Dulieu, "Evaluation of Decay Data of Radyum-226 and its Daughters", *International Conference on Nuclear Data for Science and Technology*, 2007.

[19]. R. G. Ağaoğlu, *Determination of The Mass Attenuation Coefficients, Total Photon Interaction Cross Sections, Effective Atomic Numbers, and Electron Densities of Aktaş, Çıldır Lake, and Kura River Water with the Help of WinXCom"*. Ardahan, Turkey, 2023.

[20]. E. Özdaşlı, "Kafkasya'nın Çernobil'i Metsamor Nükleer Santrali", *Çernobil'i Metsamor Nükleer Santrali", Karadeniz Araştırmaları*, vol. 13, no. 50, pp. 45–64, 2016.

[21]. H. Baltaş and U. Çevik, "Determination of the effective atomic numbers and electron densities for YBaCuO superconductor in the range 59.5-136 keV," *Nuclear Instruments and Methods in Physics Research B: Beam Interactions with Materials and Atoms*, vol. 266, pp. 1127–1131, 2008

Analysis of Mechanical Properties of EVOH/LDPE Films Produced with Waste EVOH and LDPE

Yunus Emre DUYĞUN[1], Münir TAŞDEMİR[2*]

[1]Marmara University, Institute of Pure and Applied Science, Department of Metallurgical and Materials Engineering, Istanbul, Türkiye
[2]Marmara University, Technology Faculty, Department of Metallurgical and Materials Engineering, Istanbul, Türkiye

(ORCID: 0000-0002-5636-0254) (ORCID: 0000-0001-8635-7251)

Abstract

The importance of plastic materials continues to develop more and more every year from past to present. As important as the plastics used in almost every area of life are, it is equally important to keep these materials in the environmental cycle. Since 1970, the use and consumption of plastic has increased almost 10 times. A large share of the use of these plastics occurs in the flexible packaging sector. In the multi-layer films used on flexible packaging in the packaging industry, one of the most important issues of the future is the crisis of raw materials, and the other is recycling and sustainability. In this study, it is aimed to evaluate the low density polyethylene/ poly(ethylene-co-vinyl alcohol)/low polyethylene (LDPE/EVOH/LDPE) structured flexible packaging film waste produced by multilayer blown extrusion method within the same LDPE/EVOH/LDPE flexible packaging film and to examine the mechanical property changes of the material. Sustainable environment and economy, reducing the cost of raw materials, obtaining approximately similar mechanical properties are among the objectives of the study. The wastes released from the LDPE/EVOH/LDPE film were granulated in a single screw extruder. Then, the amount of these waste EVOH granules was 5%, 10%, 20% and 25% by weight in the total film, and their production was carried out with reference to the pure EVOH film in a 7-layer blown film extruder. Samples were taken from the films produced in 50μm thickness in accordance with the standards. Tensile test, tear test, puncture resistance test, sealing force test, shrinkage tests were performed. According to the results of the tests, analyzes on the use of scrap EVOH were concluded.

1. Introduction

The demand for the packaging industry, which is one of the most important branches of the plastics industry, is increasing day by day. In the packaging industry, various product groups are produced with superior features that can meet the sectoral needs in both rigid and flexible packaging categories. Various packaging demands of many fields such as food, non-food, medicine, hygiene are provided with flexible packaging. Film structures suitable for the desired properties can be provided with multi-layer film production. Multi-layer films can be produced in layers according to the desired mechanical, physical, light transmittance and barrier properties, similar to composite materials. This situation plays a very important role in increasing the demand of the flexible packaging industry [1]. With the rapid growth of the sector, the acceleration of production processes, and the development of technology, environmental economy and sustainability have increased their importance. Many sustainable solutions such as reusing packaging waste, reducing raw material consumption, reintroducing them into production methods, creating films with a uniform material have begun to be produced and legally implemented [2]. At

this point, starting from the general structures of polymers, studies on the structures of materials and their reuse are increasing. Mechanical and chemical recycling methods are the most preferred recycling methods [3].

In this study, four different weight ratios of LEL (LDPE/EVOH/LDPE) scrap were added (5%, 10%, 20% and 25%) to the LEL film produced with a 7-layer blown extruder, with a total thickness of 50 microns, in order to contribute to the raw material problems experienced in the packaging industry and to reduce environmental pollution. After feeding PE-g-MA as compatibilizer at certain rates and reuse in LEL film, the mechanical properties of the material were examined in detail.

2. Material and Method

2.1 Material
Low density polyethylene (LDPE 310 E), polyethylene grafted maleic anhydride (Bynel 4157) from Dow Chemical Company and polyethylene grafted maleic anhydride (PE-g-MA) (Retain 3000) specially produced for waste use, low density polyethylene (Enable 2010 Series Blown 2010MA) from Exxon Mobil, ethylene vinyl alcohol (Evasin EV3251F) from Chang Chun Petrochemicals and, finally, granulated waste PE/EVOH granule from production.

2.2 Preparation of waste LEL granules with a single screw extruder
During the production of 50 micron thick multi-layer LEL films, the waste, waste and parts that are shaved off the reel are set aside. It was stored in baskets and decomposed to be re-extruded into the Erema single screw extruder. Clipped flexible packaging waste is placed on the belt system. After feeding, firstly, before entering the extruder, the clipped films were pre-grinded at 104°C in the pre-grinder part of the Erema machine in order to make them smaller and easier to process, and the waste films were mixed within themselves and divided into smaller pieces. After this process, the clipped waste films were fed into the Erema single screw extruder, which has a total of 7 heating zones. It was ensured that the material became molten in the temperature range of 120°C-200°C at a speed of 240 rpm. Extruder operating temperatures are shown in Table 1 below.

Table 1. Working range of single screw extruder

Process	Heating zones							
	1	2	3	4	5	6	7	Die
Temperature (°C)	130	190	190	200	190	200	200	230

Pressure average 160 bar and screw rotation speed 240 rpm

Afterwards, the melt that came out in the form of spaghetti from the perforated area in the head area was divided into small pieces with the help of a knife and cooled in cooling water at approximately room temperature. In the cooling process, the cooled granules were sieved with vibration. As a final process, the granule, which was transported to the dryers, was dried and filled into 25 kg sacks. The waste films passed through the single screw extruder and the last granules are shown in Figure 1.

(a)   (b)

Figure 1. Granules produced from single screw extruder
a) waste LEL flexible packaging films
b) waste LEL granules

2.3 Use of waste LEL granules with multi screw extruder
The obtained waste LEL granules are now in a form suitable for use in the multilayer extruder. With the 7-layer Kiefel Kirion model blown extruder, 50μ thick films with different waste LEL ratios were produced. In the 7-layer extruder, the recipe of the film was created for the layer distributions shown in Table 2. The indicated plies A-B-C-D-E-F-G refer to each screw-sleeve in the multilayer extruder film. Layers A-B and F-G represent the layer on which the LDPE and LLDPE polymer is fed. C and E layers represent the adhesive (tie) layer. The D layer is the barrier layer where the EVOH material is fed. As seen in Table 3 in the contents of the films produced, a total of 5 different barrier extruder films were produced, of which 5%, 10, 20 and 25 by weight of the film contains waste and in pure form. During production, waste-free pure LEL film was produced primarily for

reference. In Table 2, the ratio of waste LEL in the total film was calculated as a weight ratio of 50μ film.

Table 2. Seven layer extruder floor distributions total 50μ

A Screw 1 13μ	B Screw2 7μ	C Screw 3 4μ	D Screw4 2μ	E Screw 5 4μ	F Screw6 7μ	G Screw7 13μ
LDPE LLDPE	LDPE LLDPE	g-maleic anhydrite LDPE	EVOH	g-maleic anhydrite LDPE	LDPE LLDPE	LDPE LLDPE

Adhesive solid waste LEL ratio was calculated with the ratio of the weight of the C and E screws to the 50μ film. Likewise, the ratio of LDPE solid waste LEL was calculated with the ratio of the total weight of A-B-F-G screws to 50μ film. The ratio of adhesive

layer Retain 3000 was calculated by the ratio of C and E screws, and the ratio of LDPE layer Retain 3000 by weight of A-B-F-G screws to 50μ film. Table 3 shows the ratios of waste LEL used in the extruder layers. The images of the films coming out of the extruders are shown in Figure 2.

Pure LEL	%5 Waste LEL	%10 Waste LEL	%20 Waste LEL	%25 Waste LEL
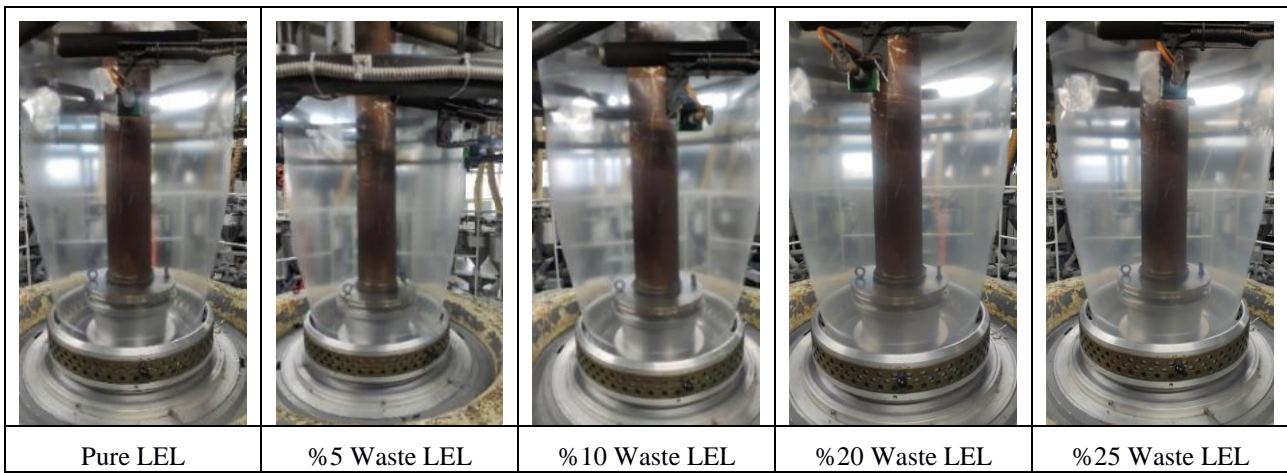
Figure 2. Output of films with different waste LEL ratio from the extruder heat

Table 3. Waste LEL mixing ratios by weight

50 Micron	Tie (C-E) layers waste LEL rate[1] (%)	Tie (C-E) layers Retain 3000 rate (%)	LDPE (A-B-F-G) layers waste LEL rate[1] (%)	LDPE (A-B-F-G) layers Retain 3000 rate (%)
Pure LEL	-	-	-	-
%5 waste LEL	0	0	17,25	0,5
%10 waste LEL	25	0,5	27,5	1
%20 waste LEL	50	1	41,5	1,5
%25 waste LEL	50	1,5	55	2

[1] waste LEL contains 5% EVOH granules

3. Results and Discussion

3.1 Tensile strength

The maximum tension value that flexible packaging films can withstand is defined as tensile strength. The tensile behavior of flexible packaging films is tested in the machine direction and transversely. This situation is also called machine longitudinal and

machine transverse samples. The tensile strength value is expressed in MPa. Tensile strength, σÇ: Tensile strength, Pmax.: It is measured as the ratio of maximum force to A0: initial surface area [4].

$$\sigma Ç = Pmax / A0 \qquad (1)$$

The graphical expression of the values is shown machine direction (MD) in Figure 3 and cross

direction (CD) in Figure 4. According to the test results, it was observed that the tensile strength values decreased as the amount of waste LEL granule increased in the MD and CD tensile strength results. The tensile strength values of 26,60 MPa MD and 23,40 MPa CD tensile strength were measured in pure LEL material. When 5% waste LEL granules were added, the MD tensile strength decreased by 4%, while the CD tensile strength decreased by 4,3%. When the waste LEL granule ratio was increased to 10%, the MD tensile strength decreased by 10,3% compared to the pure LEL film, while the CD tensile strength decreased by 6,2%.

When the amount of waste LEL granule was increased to 25%, the MD tensile strength value decreased by 17,1% compared to the pure LEL film, while the CD tensile strength decreased by 12,2%. In general, it was observed that as the amount of waste LEL granules increased, the CD and MD tensile strength values decreased. When Feng et al. followed the mechanical behavior of the material with LDPE and EVOH films and foams with different ratios of mixtures, they observed that the tensile strength decreased with the increase in the amount of LDPE foam [5]. Chi-Hsien Huang et al. observed that the tensile strength of the material decreased with the increase of the amount of PE-g-MAH in the PE/EVOH mixture [6]. In a study by Kalfoglou et al., when the compatibility of Poly(ethylene-co-vinyl alcohol) and EVOH-HDPE mixtures was examined, it was observed that the tensile strength value decreased as the amount of SEBS-g-MA was added to the film prepared with the melt mixture [7].

In this study, we can say that there is a decrease in mechanical tensile strength since the amount of LDPE by weight increases in the waste LDPE and EVOH granules added and incompatible regions are formed.
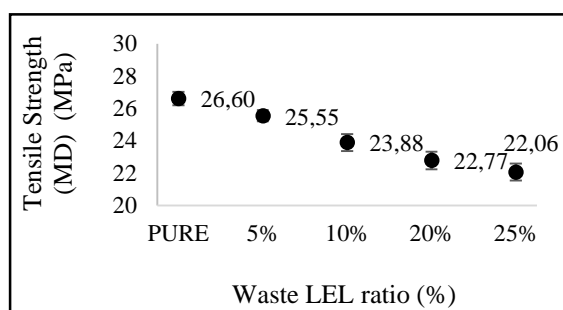
Figure 3. Graphical representation of MD tensile strength values of LEL films
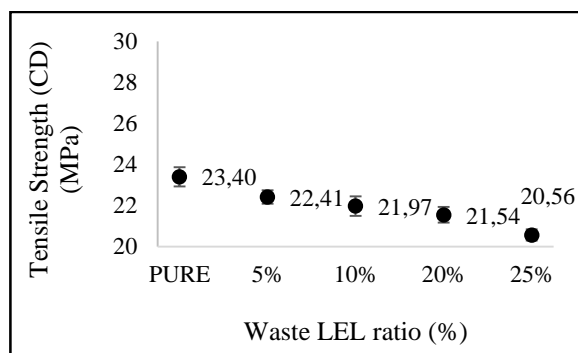
Figure 4. Graphical representation of CD tensile strength values of LEL films

3.2 Breaking strength

The part where the flexible packaging films break after a certain tension value is defined as the breaking strength. Tensile strength is measured in the same way as tensile strength in 2 regions, machine direction (MD) and cross direction (CD). The breaking strength values are expressed in MPa. The graphical expression of the values is shown MD in Figure 5 and CD in Figure 6. According to the test results, it was observed that as the amount of waste LEL granule increased in the MD and CD tensile strength results, there was a decrease in the breaking strength values similar to the tensile strength. In pure LEL material, 26,18 MPa MD and 23,41 MPa CD breaking strength values were measured. When 5% waste LEL granules were added, the MD breaking strength decreased by 4,4%, while the CD breaking strength decreased by 4,9%. When the ratio of waste LEL granule was increased to 10%, the MD breaking strength decreased by 13,3% compared to the pure LEL film, while the CD breaking strength decreased by 7,9%. Compared to the pure LEL film, the MD breaking strength of the film containing 20% waste LEL granules decreased by 16,7%, while the CD breaking strength decreased by 11,4%. When the amount of waste LEL granule was increased to 25%, the MD breaking strength value decreased by 21% compared to the pure LEL film, while the CD breaking strength decreased by 14,4%. In general, it was observed that as the amount of waste LEL granules increased, the CD and MD breaking strength values decreased. This situation can be interpreted as the decrease in breaking strength with the increase of the void structure between the polymers.
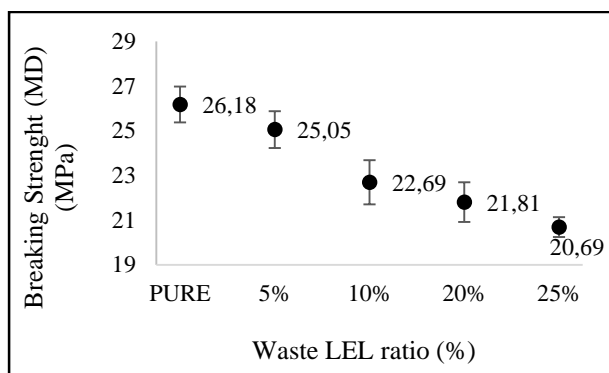
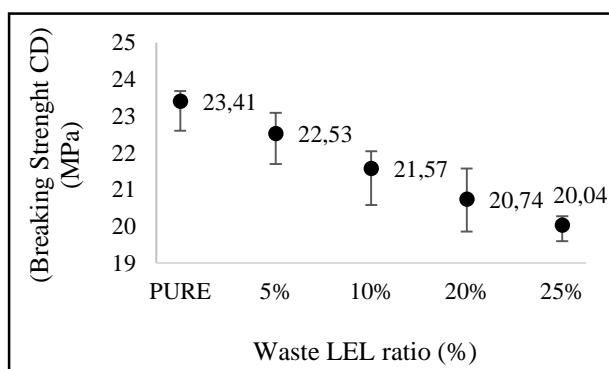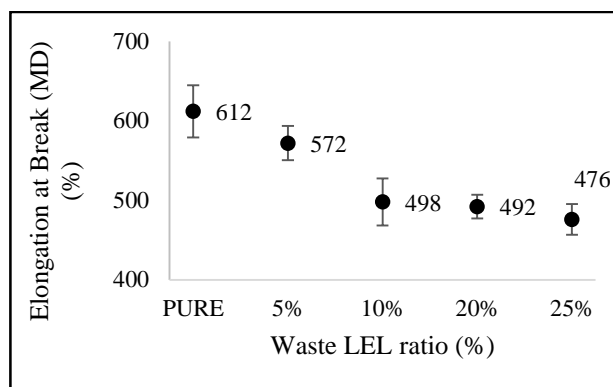**Figure 5**. Graphical representation of the MD breaking strength values of LEL films

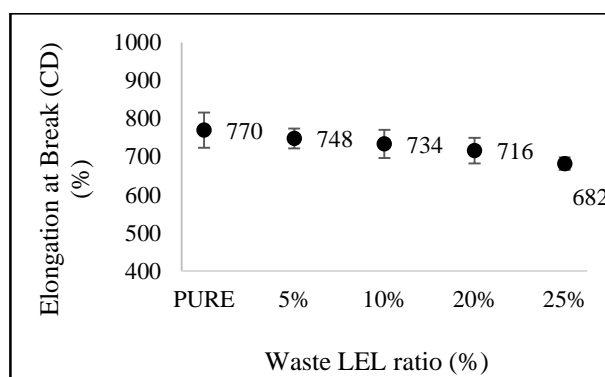**Figure 7.** Graphical representation of MD elongation at break values of LEL films

Figure 6. Graphical representation of the CD breaking strength values of LEL films

Figure 8. Graphical representation of CD elongation at break values of LEL films

3.3 Elongation at break

In the tensile test of flexible packaging films, the maximum elongation rate that occurs in the material is defined as the elongation at break. In the elongation at break, comments are made about the ductile structure and brittleness of the material. The elongation at break is expressed in %. The decrease in the ductility of the material in flexible packaging films reduces the elongation of the film. The elongation at break is also measured in the tensile test, both MD and CD. The graphical expression of the values is shown MD in Figure 7 and CD in Figure 8. In a study conducted by Saini et al., they found that the elongation at break value decreased when the composite material was made with a mixture of PE-g-MAH material and paper powder in different weight ratios [8].

According to the test results, a similar decrease in elongation at break values was observed as the amount of waste LEL granule increased in the MD and CD elongation results. In pure LEL material 612% MD and 770% CD elongation at break were measured. When 5% waste LEL granules were added the MD elongation at break decreased by 6,6%, while the CD elongation at break decreased by 2,9%. When the ratio of waste LEL granule was increased to 10%, the MD elongation at break decreased by 18,7% compared to the pure LEL film, while the CD elongation at break decreased by 4,7%. While the MD elongation at break of the film containing 20% waste LEL granules decreased by 19,7% compared to the pure LEL film, the CD elongation at break decreased by around 7,1%. When the amount of waste LEL granule was increased to 25%, the MD elongation at break decreased by 22,3%, while the CD elongation at break decreased by 11,5% compared to pure LEL film. In general, as the amount of waste LEL granules increased, it was observed that the elongation at break decreased in both CD and MD. This can be interpreted as the ductility of the flexible film decreases as the amount

of waste increases. The reason for this can be interpreted as the fact that the materials mixed in the molten state could not bond with each other to form long chains.

3.4 Tear force

The tear strength of flexible packaging films is measured by the resistance of the sample against tearing. During the tear test, the tear value of the material at a given load is measured in mN using the elmandorf tear method. The higher the tearing force of the film, the higher the tear resistance of the material. The test is measured by determining the average force to propagate the tear across a specified length of plastic film or non-rigid sheet after tearing has begun, using an Elmendorf type tear tester [9]. In the application of the test, samples were prepared in the form of a rectangular plate with a width of 76 mm and a length of 63 mm. Afterwards, the test was carried out with a load of 800 g, both transversely and longitudinally. Tear resistance is also measured both in MD and CD. The graphical expression of the values is shown in Figure 9 for the MD tearing force, and in Figure 10 the CD tearing force is shown. According to the test results, it was observed that there was a similar decrease in the tearing force values as the amount of waste LEL granule increased in the MD and CD shear force results. In pure LEL material, 4434 mN MD and 5378 mN CD shear forces were measured. When 5% waste LEL granules were added, the MD tear force value decreased by 11,5%, while the CD tear force value decreased by 7,4%. When the ratio of waste LEL granule was increased to 10%, the MD tearing force value decreased by 15,8% compared to the pure LEL film, while the CD tearing force value decreased by 12%. The MD tearing force value of the film containing 20% waste LEL granules decreased by 31,3%, while the CD tearing force value decreased by around 33,2% compared to the pure LEL film. When the amount of waste LEL granule was increased to 25%, the MD tearing force value decreased by 39,4%, while the CD tearing force value decreased by 48% compared to the pure LEL film. In general, as the amount of waste LEL granule increased, there was a clear decrease in the CD and MD tearing force value. The decrease in this tearing force can be interpreted as the fact that the material is more brittle, its ductility decreases and its resistance to tearing decreases. In a different study by Huang, C. H et al., they observed that the tear strength of the film decreased with the increase in the amount of PE-g-MAH used in the EVOH and LDPE mixture [10].
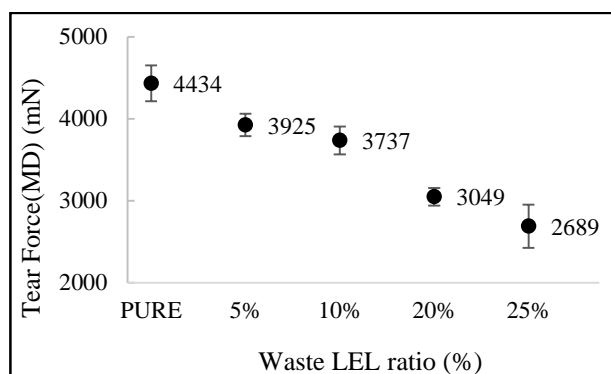
Figure 9. Graphical representation of MD tearing force values of LEL films
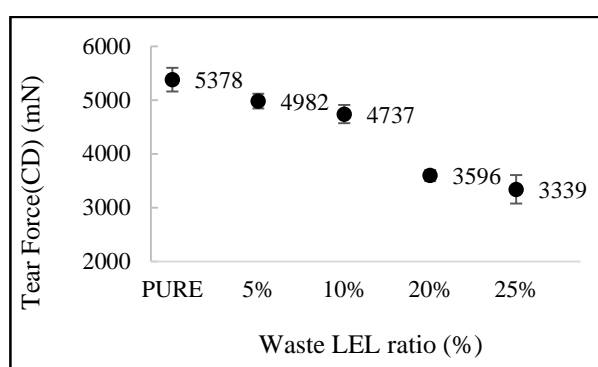
Figure 10. Graphical representation of MD tearing force values of LEL films

3.5 Puncture resistance

In flexible packaging films, the puncture resistance of the material expresses the maximum point at which it resists a probe as the puncture force. Materials with high puncture strength are generally referred to as ductile materials [11]. Test results are expressed in N. The graphical expression of the values is shown in Figure 11.
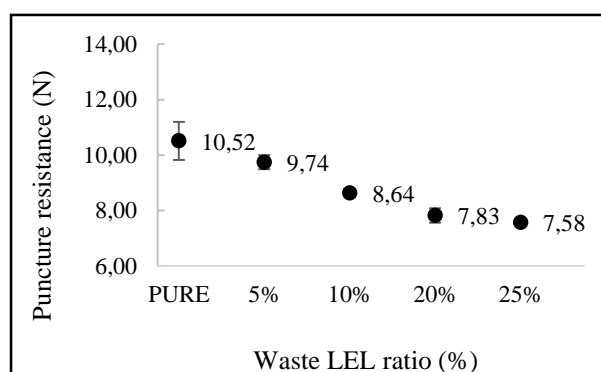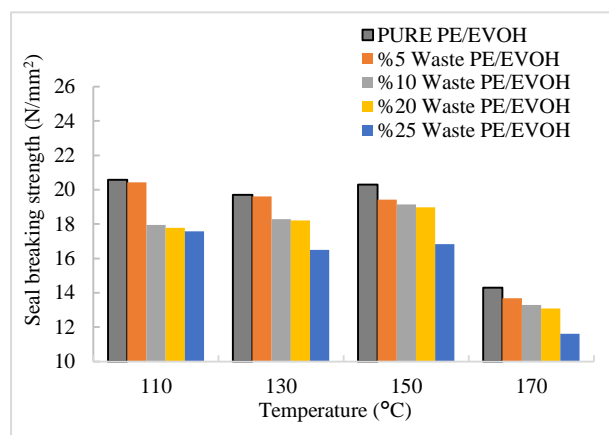

Figure 11. Graphical representation of puncture force values of LEL films

According to the test results, it was observed that the puncture resistance values decreased as the amount of waste LEL granules increased in the puncture resistance results. The puncture resistance value of 10,52 N was measured in pure LEL material. The puncture resistance value of 5% waste LEL granules decreased by 7,5%. When the ratio of waste LEL granules was increased to 10%, the puncture resistance value decreased by 17,9% compared to pure LEL film. The puncture resistance value of the film containing 20% waste LEL granules decreased by 25,6% compared to the pure LEL film. When the amount of waste LEL granule was increased to 25%, the puncture resistance value decreased by 28% compared to the pure LEL film. In general, the puncture resistance of the material decreased as the amount of added waste increased.

3.6 Seal breaking strength

Determination of seal strength on flexible packaging films is a test method for the determination of the adhesion force of a material to itself or to another surface. Here, the breaking strength value is found by the ratio of the force per unit area in the region where the film is sealed [12]. LEL films were sealed between 110°C-130°C-150°C and 170°C and the breaking strength was expressed in N/mm2. The high seal break strength of a flexible packaging film means that the material itself or the adhesion force on the different surface to which it is attached is high and it is a strong seal. According to the test results graphical expression of the values is shown in Figure 12.

Figure 12. Graphical representation of seal breaking strength values of LEL films

According to the test results, it was observed that as the amount of waste LEL granule increased in the seal breaking strength results, there was a decrease in

the seal breaking strength values at 110°C-130°C-150°C and 170°C temperatures. In pure LEL material, seal breaking of 20,5 N/mm2 at 110°C, 19,7 N/mm2 at 130°C, 20,3 N/mm2 at 150°C and 14,3 N/mm2 at 170°C strength was measured. When 5% waste LEL granules were added, the seal breaking strength decreased by 0,7%, 0,6%, 4,4% and 4,4% at temperatures of 110°C-130°C-150°C and 170°C, respectively. When the waste LEL granule ratio is increased to 10%, the seal breaking strength value is 12,8%, 7,3%, 5,7% and 7,1% at 110°C-130°C-150°C and 170°C temperatures, respectively, compared to pure LEL film rate decreased. The seal breaking strength value of the film containing 20% waste LEL granules compared to the pure LEL film was 13,7%, 7,7%, 6,5% and 8,5% decreased respectively at 110°C-130°C-150°C and 170°C temperatures. When the amount of waste LEL granule is increased to 25%, the seal breaking strength values compared to pure LEL film are 14,6%, 16,3%, 17,1% and 18% decreased respectively at 110°C-130°C-150°C and 170°C temperatures. According to the results here, it can be interpreted that the increase in the amount of waste in the material decreases the adhesion of the chains to each other with the increase of the adhesion force on the source surface of the film. At the same time, the material was deformed when sealed at 170°C. In a study by Giovanni De Martino et al., they compared the production of barrier films in 5, 7 and 9 layer extruders. Here, in the seal data, it was observed that as the number of extruder layers increased, the seal strength increased [13].

3.7 Seal elongation at break

In the determination of the sealing elongation at break of flexible packaging films, it is measured as the amount of elongation of the film made under a certain tension when it reaches the breaking point. LEL films were sealed between 110°C-130°C-150°C and 170°C and elongation at break expressed in %. The elongation at break of a flexible packaging film means that the adhesion force on the material itself or on the different surface to which it is attached is high, and the material elongates in the sealed area. According to the test results graphical expression of the values is shown in Figure 13.
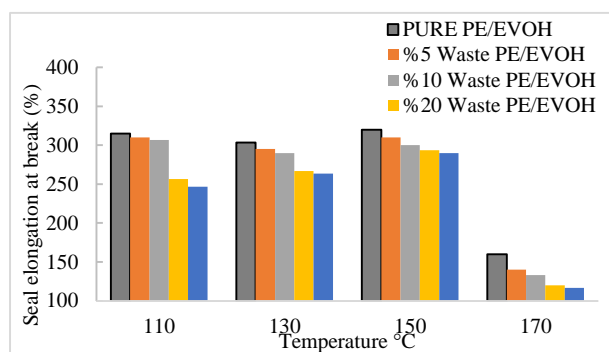
Figure 13. Graphical representation of seal elongation at break values of LEL films

According to the test results, it was observed that as the amount of waste LEL granule increased in the seal elongation results, there was a decrease in the seal elongation values at 110°C-130°C-150°C and 170°C temperatures. In pure LEL material, 315% at 110°C, 303% at 130°C, 320% at 150°C and 160% at 170°C were measured. When 5% waste LEL granules were added, seal break elongation decreased by 1,6%, 2,7%, 3,2% and 12,5% respectively at 110°C-130°C-150°C and 170°C temperatures. When the ratio of waste LEL granule is increased to 10%, the weld elongation value is 2,6%, 4,2%, 6,2% and 16% decreased respectively at 110°C-130°C-150°C and 170°C degrees compared to pure LEL film. The seal elongation value of the film containing 20% waste LEL granules decreased by 18,5%, 11,9%, 8,5% and 25% respectively at 110°C-130°C-150°C and 170°C degrees compared to the pure LEL film. When the amount of waste LEL granule is increased to 25%, the seal elongation value compared to pure LEL film is 21,6%, 23,2%, 9,4% and 26% decreased respectively at 110°C-130°C-150°C and 170°C temperatures. According to the results here, the increase in the amount of waste in the material adversely affected the elongation values of the film. A significant decrease in elongation values at 170°C led to the conclusion that the material combustion at this temperature and the film became embrittled.

3.8 Shrinkage rate
The shrinkage rate gives the shrinkage value of the flexible packaging film when it is cooled under a certain temperature, after a certain period of time. At this point, the shrinkage rate of the flexible packaging film is determined as % according to the rate of the first and last measurements. The fact that this value is low is interpreted as the decrease in the

central melting point of the film under a certain temperature and time, and the decrease in the threshold energies of the polymer chains and the weakening of the bonds by breaking [14]. The high shrinkage rate of a film indicates the stable position of the film in its form. The graphical expression of the values is shown in Figure 14. As seen in the graph, as the waste LEL ratio increased, the shrinkage ratio decreased.
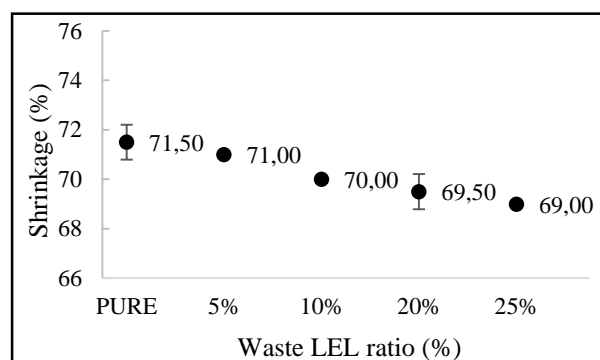
Figure 14. Graphical representation of shrinkage values of LEL films

3.9 Polarized optical microscope
In Figure 15, the black parts are the parts where the test sample is held. The region of scaling is the part where the sample is located. The first region is the LDPE and g-maleic anhydride layers, the middle part is the EVOH layer and again symmetrically the LDPE and g-maleic anhydride layers. Based on the microscope images, it has been observed that the clean appearance of the layers in the cross-sectional area gradually deteriorates with the increase in the amount of waste. Total film thickness was measured as 50,22 μm in the a, pure LEL sample. LDPE and adhesive layer were measured as 22,35 μm on the left side of the sample and 22,90 μm on the right side of the sample, similar to a single layer by interfering with each other. In the EVOH layer, the measurement was taken as 1,93 μm. The total film thickness was measured as 51,60 μm in b, which is a 5% waste LEL sample. Here too, the LDPE and adhesive layers interfere with each other and are measured as 22,35 μm on the left side of the sample sample and 24,01 μm on the right side, similar to a single layer. A similar measurement was observed as 1,93 μm on the EVOH layer. Total film thickness was measured as 51,05 μm in c, which is 10% waste LEL sample. Here, again, the LDPE and adhesive layers interfere with each other, and the left part of the sample sample is measured as 21,80 μm and the

right part as 22,63 µm. The EVOH layer is seen as 1,94 µm. At this point, it is seen that the homogeneous appearance of the material among each other begins to decrease compared to the pure state in the LDPE adhesive layers. A total film thickness of 5,.36 µm was measured in d, a 20% waste LEL sample. Likewise, the LDPE and adhesive layers interfered with each other, and the left part of the sample sample was measured as 22,49 µm and the right part as 22,35 µm. Although the EVOH solid was measured as 1,93 µm, thinning and thickening started to increase. In the image here, it is seen that the homogeneity of the film has decreased and the indentation has increased. A total film thickness of 50,64 µm was measured in e, a 25% waste LEL sample. Similar to 20% waste LEL film, the interference of LDPE and adhesive layer measured 21,80 µm on the left and 22,63 µm on the right. The EVOH solid was measured as 1,93 µm and showed more indentations than 20% waste LEL film. When Lılı Wang's study on the effect of regrind content on PP-EVOH sheet properties and the effect of orientation on the permeability of EVOH multilayer films was examined, they observed that the adhesive layer and PE material interfered more with each other at different BUR rates and tension [15]. In the study conducted by Yiwu Liu and his colleagues, it was determined under the microscope that when the EVOH/nano SiO2 film was produced in the twin screw extruder by melt blending and inflation and production in the extruder, the brightness value increased inversely proportional to the decrease in haze [16].
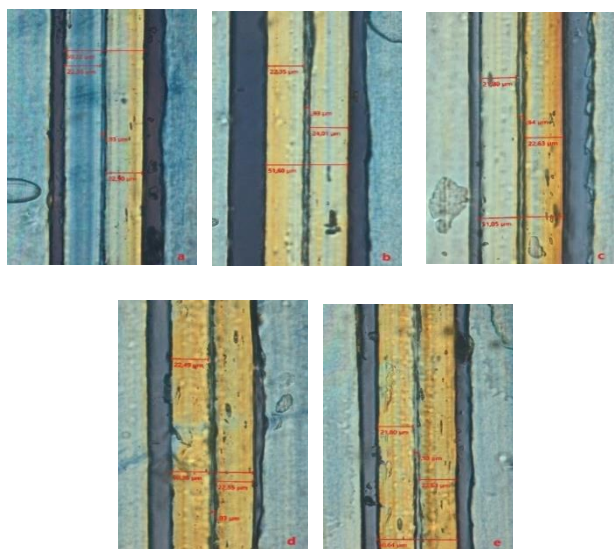
Figure 15. Microscopic views of LEL films formed with waste EVOH and LDPE a) Pure LEL, b) 5% waste LEL, c) 10% waste LEL, d) 20% waste LEL, e) 25% waste LEL

4. Conclusion and Suggestions

In this study, after the waste LEL films were granulated, they were successfully used again in LEL multilayer films. In general, a decrease in the mechanical values of the flexible packaging film was observed with the increasing amount of waste LEL granules. When the tests performed on the barrier flexible packaging films containing waste LEL granules are examined; It was observed that the tensile strength and breaking strength values in mechanical values decreased both in machine length and width. The tensile elongation and elongation at break were also found to decrease gradually. Looking at the elastic modulus, it was seen that the modulus of elasticity decreased as the amount of waste of the material increased, along with the decrease in tensile and elongation data. In the control of tearing forces, it was observed that as the amount of waste increased, there was a decrease in the longitudinal and transverse tearing forces. In parallel with the puncture resistance results, the increase in the amount of waste weakened the puncture resistance of the material. When the films with different temperatures and waste LEL granule ratios were examined during the control of seal breaking force and elongation at break, a decrease was observed in the values in this part as well. During the shrinkage control, it was determined that the amount of shrinkage of the material increased. During the control under the polarized optical microscope, it was determined that the amount of waste increased and the cross-sectional area of the film was defected. Considering these points, it can be said that the Retain 3000 (MAH g-PE) material used is fed in multilayer extruders at different rates, giving a successful appearance to the film containing up to 20% waste LEL granules and promising for its development.

Contributions of the authors
The authors performed the experiments together, analyzed the results and performed the writing process together.

Conflict of Interest Statement

There is no conflict of interest between the authors.

Statement of Research and Publication Ethics

The study is complied with research and publication ethics

References

[1] https://www.globenewswire.com/en/news-release/2022/07/05/2474204/0/en/Europe-Flexible-Packaging-Market-to-Projected-to-Cross-USD-71-3-Billion-by-2028-BlueWeave-Consulting.html, Access:2022.

[2] TMMOB Kimya Mühendisleri Odası İstanbul Şubesi Plastik ve Kauçuk Komisyonu, 2021, Türkiye`de Plastik Geri Dönüşümü ve Atık İthalatı Raporu, 5.

[3] O., Horodytska, F. J., Valdés, A. Fullana, "Plastic flexible films waste management–A state of art review", *Waste management*, vol.77, pp.413-425, 2018.

[4] ISO 527-1 Plastics—Determination of tensile properties—Part 1: General principles. International Organization of Standardization: Geneva, Switzerland, 2024.

[5] J., Feng, Z., Li, A., Olah, E. Baer, "High oxygen barrier multilayer EVOH/LDPE film/foam,", *Journal of Applied Polymer Science*, vol.135, no. 26, pp.46425, 2018.

[6] C. H., Huang, J. S., Wu, C. C., Huang, L. S. Lin, "Morphological, thermal, barrier and mechanical properties of LDPE/EVOH blends in extruded blown films", *Journal of Polymer Research*, vol.11, no. 1, pp.75-83, 2004.

[7] N.K., Kalfoglou, C.K., Samios, C.P. Papadopoulou, 'Compatibilization of poly (ethylene-co-vinyl alcohol) (EVOH) and EVOH–HDPE blends: Structure and properties', *Journal of applied polymer science*, vol.68, no. 4, pp.589-596, 1998.

[8] A. Saini, C. Yadav, M. Bera, P. Gupta, and P. K. Maji, "Maleic anhydride grafted linear low-density polyethylene/waste paper powder composites with superior mechanical behavior," *J. Appl. Polym. Sci.*, vol. 134, no. 31, 2017.

[9] A. C. Chang, T. Inge, L. Tau, A. Hiltner, and E. Baer, "Tear strength of ductile polyolefin films," *Polym. Eng. Sci.*, vol. 42, no. 11, pp. 2202–2212, 2002

[10] C.-H. Huang, J.-S. Wu, C.-C. Huang, and L.-S. Lin, "Adhesion, permeability, and mechanical properties of multilayered blown films using maleated low-density polyethylene blends as adhesion-promoting layers," *Polym. J.*, vol. 35, no. 12, pp. 978–984, 2003

[11] F. Hosseinabadi, S. M. Zebarjad, and M. Mazinani, "Investigation on perforation mechanism of medium density polyethylene," *Mater. Sci. For.*, vol. 675–677, pp. 387–390, 2011.

[12] ASTM F88/F88M-15, 2015, Standard test method for seal strength of flexible barrier materials.

[13] G. De Martino, L. Barnini, R. Pariante, & O. R. de Ballseteros, "Films with nine layers coextrusion technology, new challenge for food packaging" *Journal of Applied Packaging Research,* vol. 10, no. .2, p. 6, 2018.

[14] ASTM D2732-03. Unrestrained linear thermal shrinkage of plastic film and sheeting, 2024.

[15] L. Wang, "Effect of regrind content on PP-EVOH sheets properties and effect of orientation on permeability of EVOH multilayer films" Doctoral dissertation, Ecole Polytechnique, Montreal- Canada, 2019.

[16] Y. Liu, S. Wei, "Processing technologies of EVOH/nano-SiO$_2$ high-barrier packaging composites." *In Proc. 17th IAPRI World Conf. Packaging*, pp. 269-74. Tianjin: Scientific Research Publishing, 2010.

Design and Implementation of an Optimized PID Controller for Two-Limb Robot Arm Control

Said MÜFTÜ[1*], Barış GÖKÇE[2]

[1] *Pamukkale University, Department of Mechatronics Engineering, Denizli,20160, Türkiye*
[2]*Necmettin Erbakan University, Department of* Mechatronics *Engineering, Konya, 42090, Türkiye*
(ORCID: 0000-0001-5621-7805) (ORCID: 0000-0001-6141-7625)

Abstract

Advances in technology have increased the use of robot arms and led to more research and development on robot arms. Controllability, which is the main focus of the studies on robot arms, generally provides speed and precision to robot arms. In this study, a two-limbed robot arm is controlled using the MATLAB support package for Arduino Hardware, and a microcontroller is used to optimize the control of this robot arm with a PID controller. In addition, in the direct current (DC) brushed motor system, the transfer function was obtained using values from the motor data sheet. Feedback is provided to this control system with a Hall-effect encoder. For the square reference tracking of the gripper end of the two-armed robot arm, the controller parameters were obtained by particle swarm (PSO), artificial bee colony (ABC), and chaos game optimization (CGO) algorithms, and these parameters were applied to the robot arm. The CGO algorithm, which is one of the methods in the literature and has become popular in recent years, was used for the first time to determine the PID parameters. It has been shown that the CGO algorithm can be used to determine the coefficients of the PID controller.

1. Introduction

Two-limbed robotic arms are a widely used manipulator in industry for many different purposes. It can perform complex work with rotational movement at two separate connection points. With this robotic system, which can work quickly, precisely, and without fatigue, many applications in the industry, such as material handling, mass production in automotive, and welding processes, can be realized. The importance of these robot arms, which save manpower, is increasing day by day, with the ability to do sensitive work at the same time.

The use of robot arms in industry started with a crane-like robot made by P. Taylor in 1937 [1]. Since 1937, there have been many developments in robotic systems. Studies on the controllability of robot arms, which is one of these developments, have increased. Many different controllers have been developed for the control of robot arms, and

determining the coefficients that make up this controller has created a new problem.

PID control is used to minimize the error between the reference and the measured value determined in robotic systems [2]. In a study conducted in 2001, it was concluded that the rate of using a PID controller for a system that requires control is more than 90%. It was observed that this rate decreased by 50% in 2017, but it is still the most preferred controller [3]. PID controllers, which date back to the 1890s, are generally used to control robot arms [4].

There are proportional (k_p), derivative (k_d), and integral (k_i) constants in the PID controller. With the proportional gain coefficient (k_p), the error in the process output can be directly controlled; with the derivative coefficient (k_d), it can control the rate of change of the error, and the integral (k_i) controls the sum of the error over time. It is aimed at obtaining the closest result to the reference determined by these

three coefficients that make up the controller. If these coefficients are chosen smaller or larger than the required value, the targeted result cannot be achieved, and the control performance can be increased if the correct parameter is selected. Therefore, determining the coefficients of the PID controller is of great importance for the robot to perform the desired task.

There are many methods used to determine PID control parameters. In their most general form, classical techniques can be classified as analytical, parametric, frequency response, adaptive tuning, and metaheuristic algorithms such as the Ziegler-Nichols and Cohen Coon methods. Metaheuristic optimization algorithms can be divided into swarm intelligence, Evolutionary Immunity, neural, probability, and physics-related algorithms [4]. In this study, swarm intelligence algorithms are used to solve the problem of determining the parameters of the PID controller.

In this study, a PID controller was designed for the control of the two-limb robot arm, and it was aimed at obtaining the most appropriate controller parameters with the PSO, ABC, and CGO algorithms, which are metaheuristic optimization algorithms. PSO and ABC have been used in studies on existing robotic system control, but it is thought that CGO will contribute to existing studies with this study. It is seen as a great advantage that the CGO algorithm has certain parameters, such as other optimization algorithms based on swarm intelligence, and it does not contain any parameters other than these. The parameters found were tested on the realized robot arm, and the results were compared both as a simulation and on the real robot arm.

2. Material and Method

The two-legged robot arm is the simplest robotic arm in robotic systems. Two separate drive elements are required to perform. In this study, a 1524006SR DC motor from Faulhaber company, an L298 motor driver relay to drive motors, and an Arduino Mega as a microcontroller were used. The parts of the designed robot arm were obtained from the 3D printer. The designed two-limbed robot arm can be seen in Figure 1 a-), and the produced two-limbed robot arm can be seen in Figure 1 b-).

The 1524006R model of Faulhaber has a DC motor with a 76:1 rotation ratio and a 2-channel field effect encoder. This brand has clearly presented all the necessary parameters to its users to obtain the transfer function of the DC motor required for control.
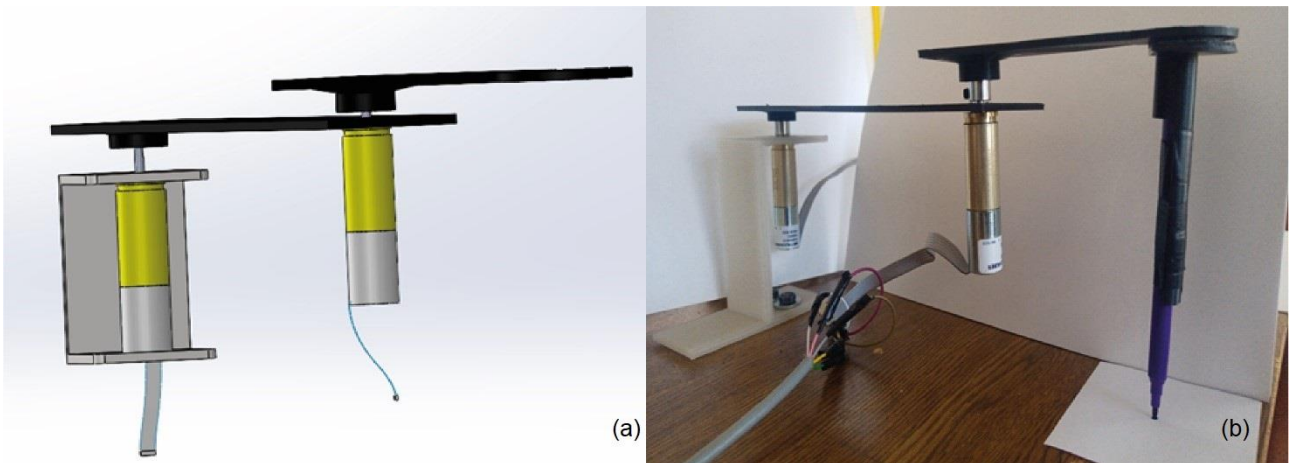

Figure 1. Two-limbed robotic arm (a) Designed two-limbed robot arm (b) two-limbed robot arm produced.

The distance between the shaft of the motor fixed to the floor of the robot arm and the motor connected to the gripper end is L1, 17.75 cm, and the other has a length of 8.25 cm. With an arm connected to the end of a single motor, only a circle with a radius of arm length can be drawn, while the gripper end of the robot arm can be guided in any way between the two-limb system and an outer circle with a radius of L1+L2 and an inner circle with a radius of L1-L2. The working area of the robot arm is shown in Figure 2.
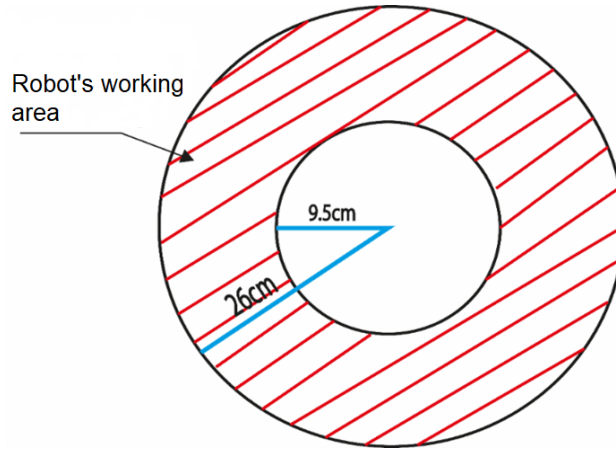
Figure 2. The working area of a two-limbed robotic arm.

2.1. Controller Design of a Two-Limb Robot Arm

In robotic systems, there are two mathematical approaches to moving the end point of the robot arm from the starting point to a determined point. These are expressed as forward and reverse kinematics. The forward kinematics approach allows us to calculate the position and direction change with the values given to the variables, while the inverse kinematics approach allows the values of the variables to be obtained for the robot arm to reach a certain position. Inverse kinematic analysis is of great importance for the control of the robot. The schematic representation of the robot arm realized in the study is given in Figure 3.
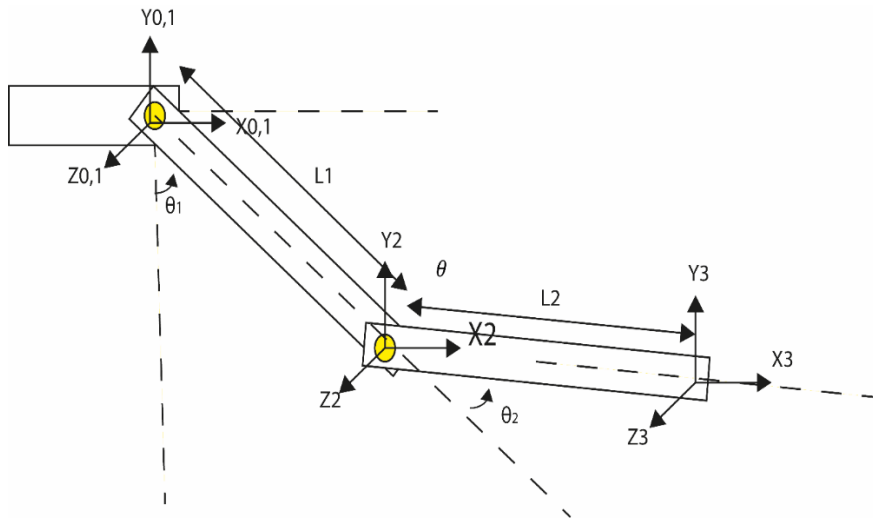
Figure 3. Schematic representation of the two-limb robot arm.

The geometric kinematic analysis of the two-legged robot arm can be easily calculated. The projection along the x-axis in equation (1) is indicated along the y-axis in equation (2). This kinematic analysis gives the position of the robot's endpoint in the x and y axes versus the two-limb robot's variables θ_1 and θ_2.

$$x = l_1 cos\theta_1 + l_2 cos(\theta_1 + \theta_2) \tag{1}$$

$$y = l_1 sin\theta_1 + l_2 sin(\theta_1 + \theta_2) \tag{2}$$

Kinematically, equations (1) and (2) are used in the gripper end position problem of the robot at any moment, while inverse kinematics is the most used mathematical expression in robotic systems, as it creates the result of variable values against the entered position value. Inverse kinematic values can be found as a result of many operations

194

performed in the robotic system. In equations (3) and (4), the inverse kinematics expression of the variables θ_1 and θ_2., which are the variables of the two-limbed robot, are stated, respectively [5].

$$\theta_1 = atan\left(\frac{y}{x}\right) + tan^{-1}\left(\frac{l_2 sin\theta_2}{l_1 + l_2 cos\theta_2}\right) \tag{3}$$

$$\theta_2 = + cos^{-1}\left(\frac{x^2 + y^2 - l_1{}^2 - l_2{}^2}{2l_1 l_2}\right) \tag{4}$$

There are many systems used as drive elements in robot arms. One of them, DC motors, are electromechanical devices that convert electrical energy into mechanical energy. In control science, the transfer function is used to model the behavior of a DC motor. It connects the electrical voltage information entering the system with the output mechanical position information. The Laplace transform is used to model the nonlinear behavior around the equilibrium point of the DC motor. The transfer function for the 1512406sr type DC motor of the Faulhaber company used in this study was found with the values specified in the catalog section. In Table 1, the required features of the Faulhaber 1524006sr DC motor for TF are given.

Table 1. Faulhaber 1524006sr DC motor specifications.

Feature Name	Value
Rotor Inertia	$0.66\ gcm^2$
Viscous Damping	0
Electrical Constant	$0.172\ \frac{A}{mNm}$
Torque Constant	$5.8\ \frac{mNm}{A}$
Robor Inductance	$70\ \mu H$
Terminal Resistance	$1.1\ \Omega$

We can consider the equivalent circuit of the DC motor as in equation 5 [6].

$$\frac{\theta(s)}{V(s)} = \frac{K_t}{(R_a + s + La)(J*S*B)s + K_t*K_b*s} \tag{5}$$

The values in Table 1 are replaced by the Rotor inertia J, viscous damping B, electrical constant K_b, torque constant K_t, Rotor inductance L rotor resistance R in the transfer function found in Equation (16), and the transfer function for the Faulhaber DC motor is found. The transfer function for the DC motor is given in Equation (6). If the unknowns in equation 5 are filled by means of table (1), equation (6) is obtained.

$$\frac{\theta(s)}{V(s)} = \frac{5,8 \times 10^{-3}}{(5.1 + 70 \times 10^{-6}s)(0.66 \times 10^{-7}s + 1)s + 5,8 \times 10^{-3}s} \tag{6}$$

If PID control is used correctly in robot arms, it enables robots to save energy with precision, stability, and less movement. Since the study has two degrees of freedom, two PID control blocks were used. The reference value for the PID control block is obtained from inverse kinematic analysis. Since each PID control has three variables, there are six parameter values in total. Angle obtained after the PID control block value is sent to the motors, respectively. The operation block of the angle values sent to the motors against the entered reference x and y axes is given in Figure 4.
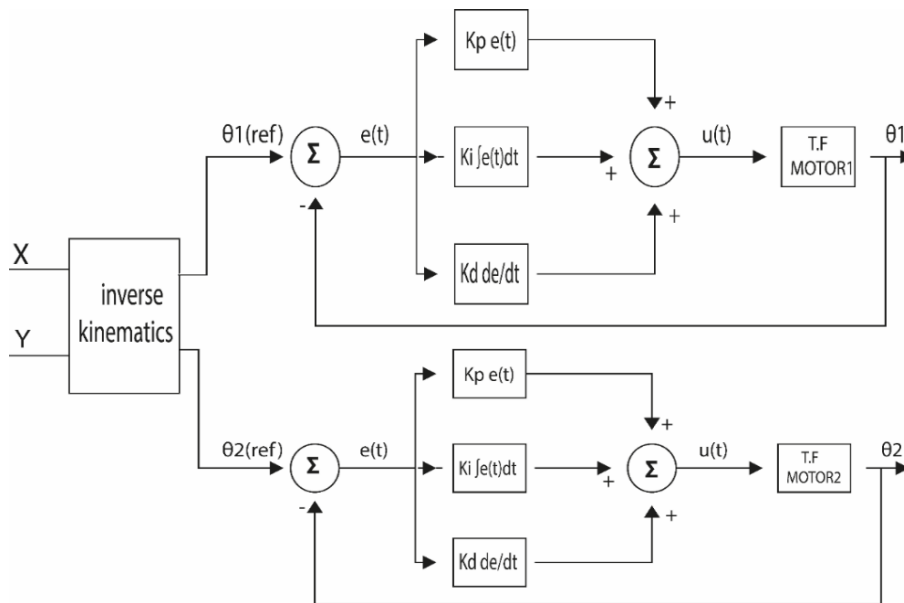

Figure 4. Blok diagram of the robot arm.

For square movement, the robot arm started from the point where theta1 and theta2 limb angles were 0 degrees and followed the points determined on a coordinate axis. The determined points form a square shape. The gripper end of the two-limbed robot arm first starts from point (3.19) and goes to point (8.19). Afterwards, it goes to (8.14), (3.14), and (3.19) points, respectively, and finishes the movement. The end point of the robot arm follows a square shape with a corner length of 5cm. The reference dimension placed on the coordinate axis of the square shape is indicated in Figure 5.
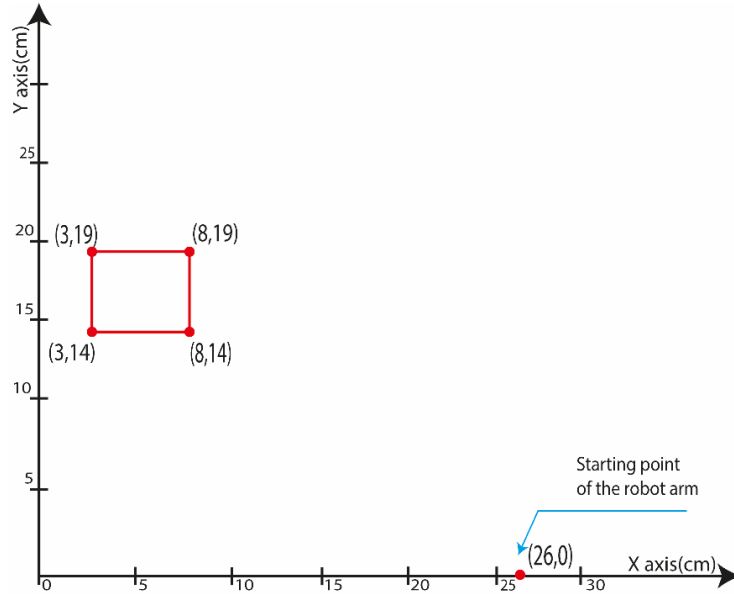
Figure 5. Square motion plan of a two-pronged robotic arm.

In order to achieve the desired movement in robot arms, it is necessary to utilize inverse kinematics and any controller. The trajectory created with the Simulink Support Package for Arduino Hardware was converted into an angle value with inverse kinematics and sent to the PID expression for control. The PID parameters obtained as a result of the optimization process were set as controller parameters in the real system. The block diagram of the realized system is shown in Figure 6.
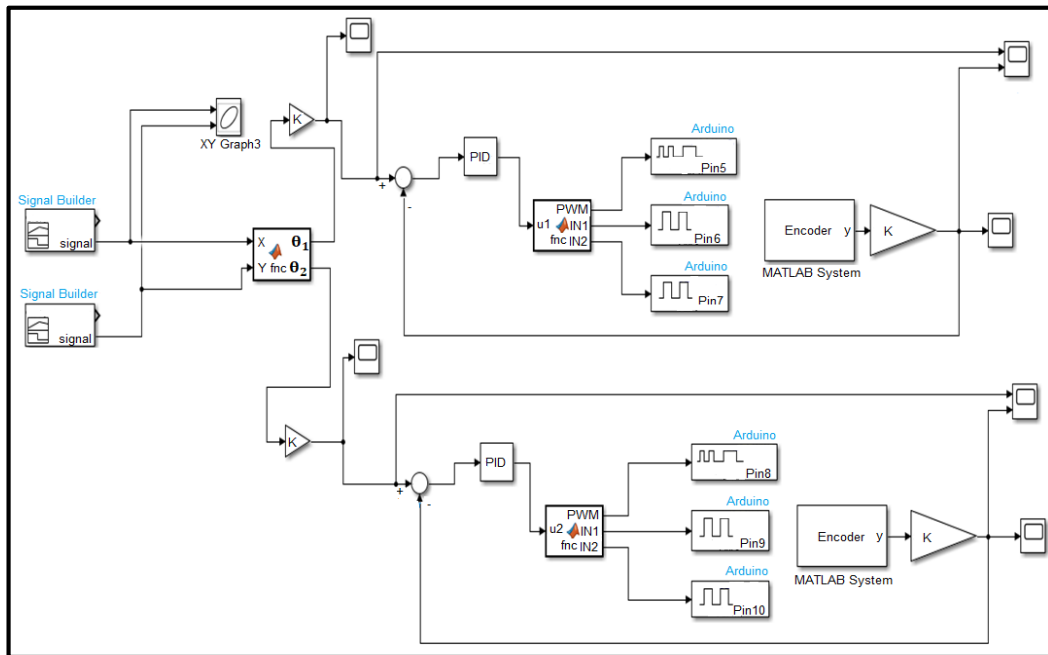
Figure 6. Block diagram of the two-limbed robot arm in the Simulink Support Package for Arduino Hardware.

In the system implemented with Arduino support from Simulink, 8 seconds are determined for square movement. During the sampling period, angular position data from the encoders provided feedback to the PID control block. The 8-second temporal change reference for θ_1 and θ_2 separately is given in Figure 7.
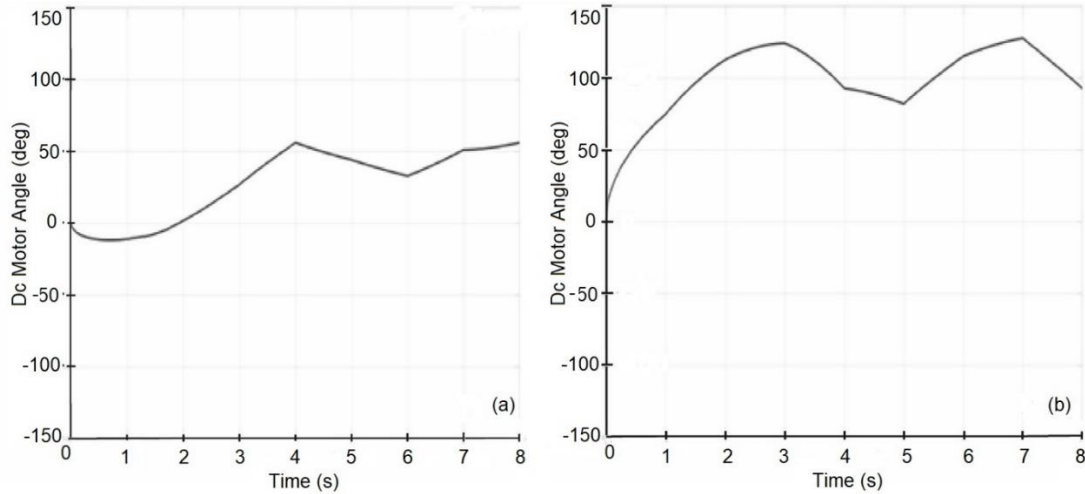

Figure 7. Angular positions that a two-limbed robot arm must make for square motion tracking.

2.2. Controller Parameter Optimization of a Two-Limbed Robot Arm

Optimization is the process of finding the best value of a given objective function with constraints. This process is encountered in many fields, from engineering systems to economics, from health to business. Optimization problems can be categorized as continuous or discrete, dynamic or static, constrained or unconstrained. These algorithms are a sub-branch of artificial intelligence, and as the popularity of artificial intelligence increases, so does its use for different problems [8].

Meta-heuristic algorithms can often be classified according to their inspiration. Another classification is the type of initial solution, i.e., multiple or single solution-based. Multiple solution-based algorithms are usually called population-based, while single solution-based algorithms are called trajectory-based [9]. Classifying metaheuristic optimization algorithms according to the source of inspiration is usually classified as human, evolutionary, swarm logic, or science-based. PSO, ABC, CGO meta-heuristic algorithms were used in this study.

2.2.1. Particle Swarm Optimization Algorithm

PSO is a meta-heuristic optimization algorithm that mimics particle swarm behavior to solve optimization problems. It was developed in 1995 by Dr. Kennedy and Dr. Eberhart. PSO is applied in many different fields thanks to its easy implementation, fast solution, and high success rate. PSO is based on the principle of particles searching for the optimal solution to a given problem [10].

The velocity and position of each particle are expressed as a vector. There is also a fitness function that measures the fitness of each particle, which varies according to the problem. Each particle also keeps track of its past best position (pbest) and the best position in the swarm (gbest). The particles move towards the optimal solution by continuously updating pbest and gbest. Finally, when the optimal solution is obtained, the solution is achieved [11]. The steps that the particle swarm optimization algorithm takes to solve a problem are shown in Figure 8 as a flowchart.
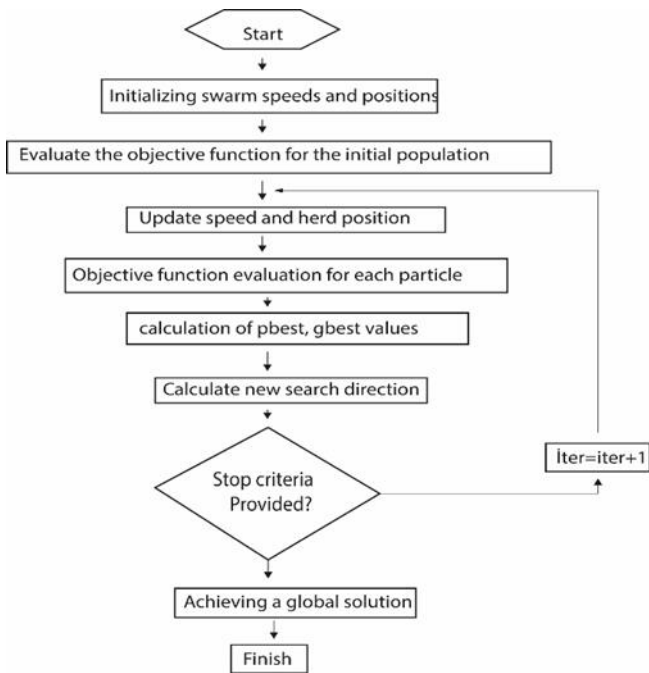
Figure 8. Flowchart of the particle swarm optimization algorithm [12].

The ability of each particle to solve the problem and find the best solution means individual performance for the PSO algorithm. The PSO algorithm tries to find the best solution by updating the position and velocity of each particle. In this way, the individual performance of each particle plays an important role in the process of solving the problem. The PSO algorithm encourages cooperation and information sharing between particles to optimize individual performance and improve each particle's ability to solve the problem. In this way, the algorithm is often used effectively in complex optimization problems.

2.2.2. Artificial Bee Colony Optimization Algorithm

ABC is a metaheuristic optimization algorithm developed by Karaboga in 2005. It is inspired by the behavior of bees as they forage for food sources and bring it back to their nests. The behavior of bees is modeled mathematically. The parts of ABC can be listed as relocation of bees, discovery of food sources, evaluation of food sources, and information sharing among bees [13].

The ABC algorithm is simulated in a search space where bees form a colony to represent potential solutions. The bees evaluate randomly selected solution candidates and use this information to generate new solution candidates by sharing the best

solutions with other bees. This process is iteratively repeated to optimize a given objective function [14]. More details about the ABC algorithm are given in Figure 9 as a flowchart.
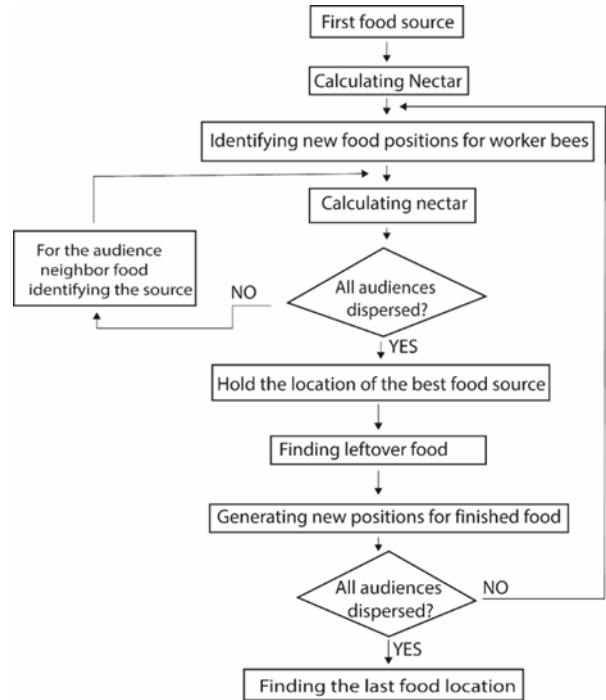

Figure 9. Flowchart of an artificial bee colony optimization algorithm flowchart [14].

Finding the optimal solution by mimicking the behavior of the bees to search for and gather the food source constitutes the individual performance of the ABC algorithm. As the bees communicate with each other, they work together to find the best solution. With the improvement in the performance of each bee, the problem-solving ability improves. As a result, thanks to the organization and cooperation exhibited by the bees, the ABC algorithm gives successful results in real-world optimization problems.

2.2.3. Chaos Game Optimization

The chaos game optimization algorithm is a population-based optimization algorithm developed by Talatahari and Azizi. This algorithm incorporates certain chaos theory principles where fractals are generated using chaos game methodology. This game, which aims to generate fractal patterns based on randomly generated starting points, is designed based on the hypothesis of generating the Sierpinski triangle geometric structure [15].

CGO is known for positive aspects such as high computation time efficiency and easy implementation to effectively solve constrained

optimization problems. The biggest difference from other optimization algorithms is that it is parameter-free. In other words, it does not need any additional parameters other than parameters such as population size, and maximum iteration. Thanks to this feature, it overcomes challenging problems. The algorithm starts optimization by initially generating random search candidates, and this initialization process is performed depending on the population size, the number of decision variables, and the bounds of the solution space [15]. More details about the CGO algorithm are given in Figure 10 as a flowchart.
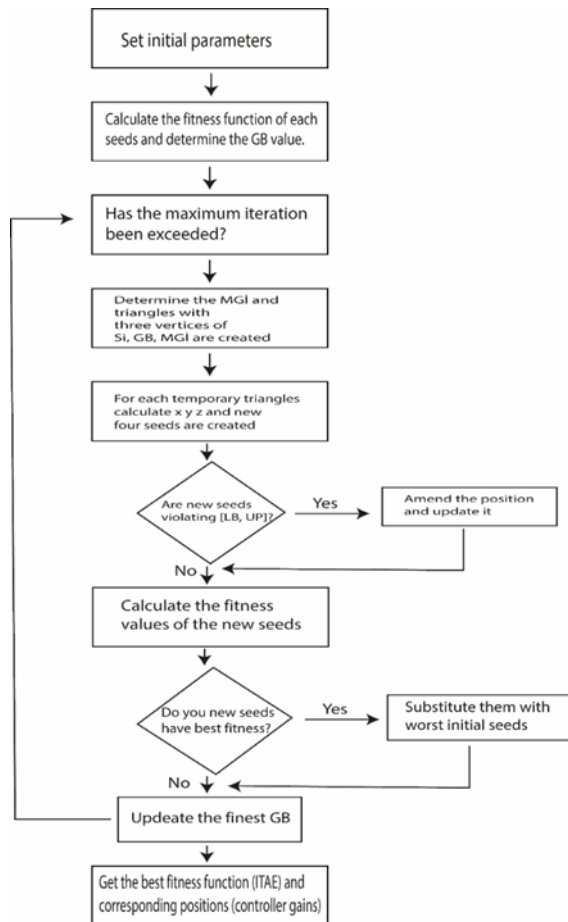
Figure 10. Flowchart of Chaos game optimization algorithm flowchart [16].

In the CGO algorithm, the success of each solution constitutes the individual performance of the algorithm. The CGO algorithm tries to find the best solution by randomly moving each solution candidate on a fractal structure. While solving the optimization problem, the CGO algorithm compares the similarities of the solution candidates and keeps the best solution.

3. Results and Discussion

There are six controller parameters in total for the realized two-legged robot arm. Particle swarm, artificial bee colony, and chaos game optimization algorithms were used to find the most suitable values of these parameters. The simulation results obtained from each metaheuristic optimization algorithm are compared. As a result of the simulation process, the controller parameters found for trajectory tracking in the real robot arm are specified.

In all three simulations, the maximum number of function evaluations was carried out at 40 and the number of populations at 50 in order to perform the most appropriate tracking of the square trajectory for the robot arm. The social and cognitive constants of the PSO algorithm were determined to be 2, and the inertia weight was determined to be [0.9, 0.4] [7]. The limit value for the ABC is determined to be 100. These coefficients were used at the same values for each step throughout the study. If we put the PID parameters in order $k_{p_1}, k_{i_1}, k_{d_1}, k_{p_2}, k_{i_2}, k_{d_2}$ limit [0 0 0 0 0 0], and upper limit [20,000 15,000 18,000 20,000 15,000 18,000]. The simulation results obtained as a result of the optimization process for frame motion tracking are shown in Figures 11 for the chaos game, 12 for the particle swarm, and 13 for the artificial bee colony.

It is clearly seen in Figure 8, Figure 9, and Figure 10 that CGO and ABC algorithms give better results than PSO algorithms. The ABC and CGO algorithms gave similar results. Figure 14 shows that the CGO algorithm gives better results than the ABC algorithm. In Figure 14, (A) is a close view of CGO, and (B) is a close view of the ABC algorithm at the point (8,14) forming the square. It is noted that CGO is closer to the reference value of red dots than ABC. In the simulation environment, all three algorithms gave successful results, but CGO gave better results with differences. For this problem, each algorithm is successful but the best ranking is CGO, ABC, and PSO. The reason for this is the parameters in the PSO and ABC algorithms, and it is thought that the CGO algorithm is more successful in generating new values.
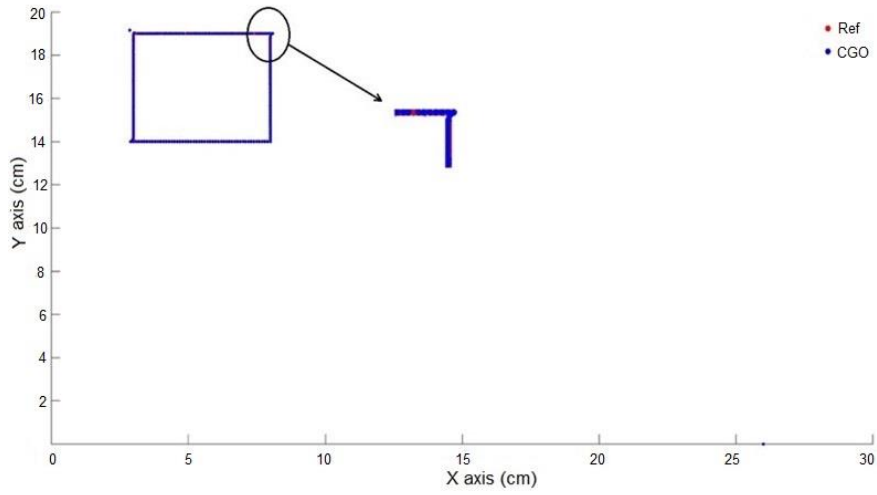
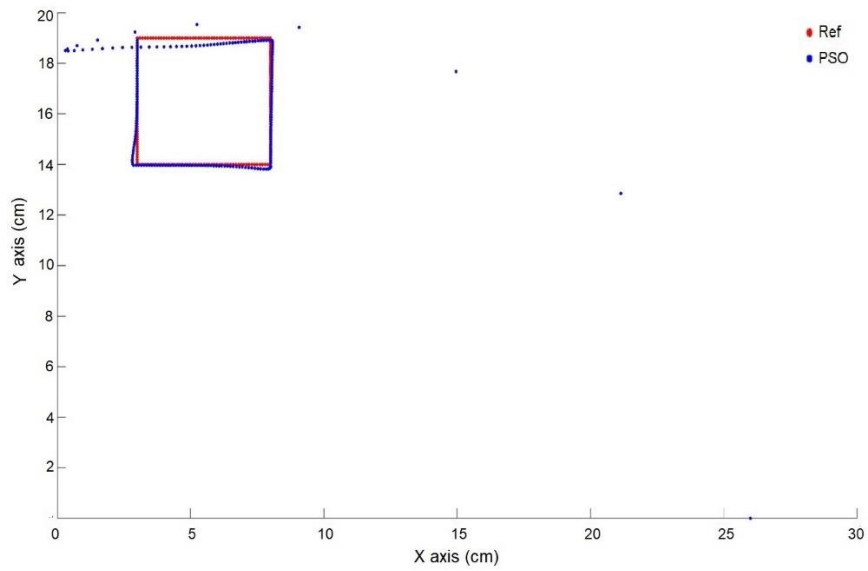**Figure 11.** CGO reference tracking for square motion.

Figure 12. PSO reference tracking for square motion
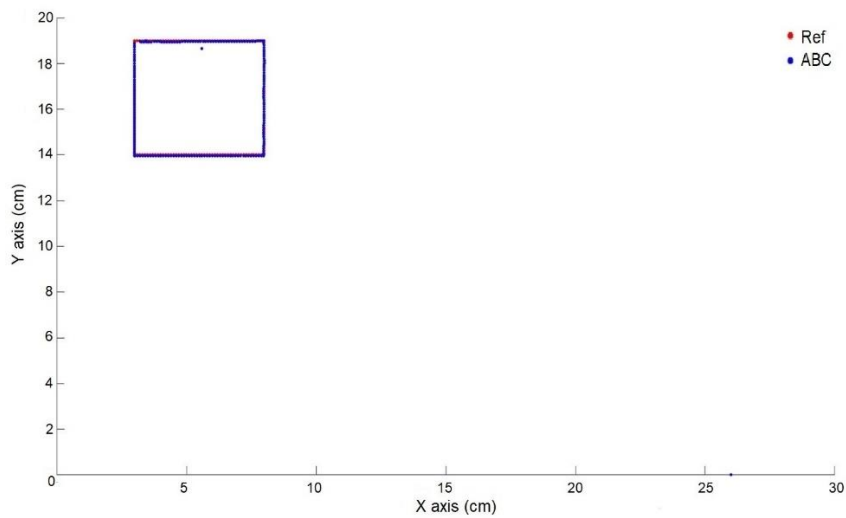

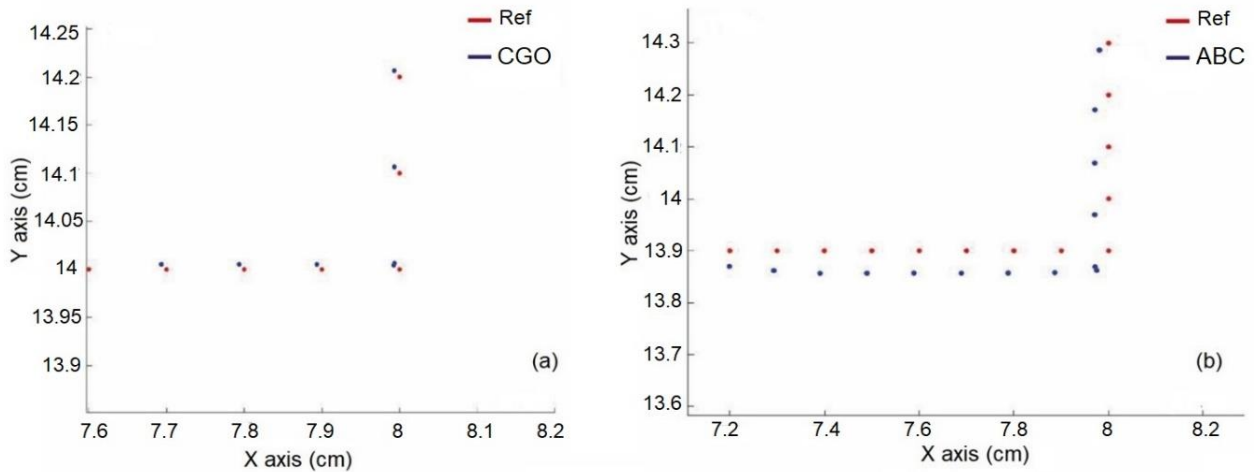**Figure 13.** ABC reference tracking for square motion

.

Figure 14. Comparison of ABC and CGO reference

Mean Square Error (MSE) and Root Mean Squared Error (RMSE) were used to compare the error parts of the optimization process of the angles θ_1 and θ_2 that make up the two-limbed robot arm. The MSE and RMSE values obtained by CGO, PSO, and ABC are given in Table 2.

Table 2. MSE and RMSE error metrics of CGO, PSO, and ABC algorithms for reference tracking.

	θ_1 angle		θ_2 angle	
	MSE	RMSE	MSE	RMSE
CGO	32.33	5.68	154.38	12.42
PSO	58.98	7.67	238.79	15.45
YAKA	32.74	5.72	155.36	12.46

As a result of the optimization process, six optimization parameters k_{p_1}, k_{i_1}, k_{d_1}, k_{p_2}, k_{i_2}, k_{d_2} were obtained for each optimization algorithm. The PID parameters found are given in Table 3.

Table 3. The PID parameters found for square motion.

	Controller Parameter	CGO	PSO	ABC
PID θ_1	k_{p_1}	19853	15.016	17667
	k_{i_1}	799	17675	0
	k_{d_1}	1082	3446	0
PID θ_2	k_{p_2}	19775	19374	20000
	k_{i_2}	0	9252	1835
	k_{d_2}	1118	3776	1157

Each metaheuristic optimization algorithm, CGO, PSO, and ABC, which determines the PID parameters obtained as a result of the simulation performed on the robot arm controlled in real time thanks to the Simulink support package for Arduino, has been tested separately on the real system. Table 2 shows the differences in the controller parameters obtained by the CGO, PSO, and ABC algorithms. These differences come from the structure of the optimization algorithms.

The angle value that each motor should make for 8 seconds in order for the two-limbed robot arm to perform the reference motion is given in Figure 7. The results obtained by realizing the PID controller parameters specified in Table 2 on the real system are given in Figure 15 (a) for θ_1 and Figure 15 (b) for θ_2 for the CGO algorithm, Figure 16 (a) for θ_1 and Figure 16 (b) for θ_2 for the PSO algorithm, Figure 17 (a) for θ_1, and Figure 17 (b) for θ_2 for the ABC algorithm.
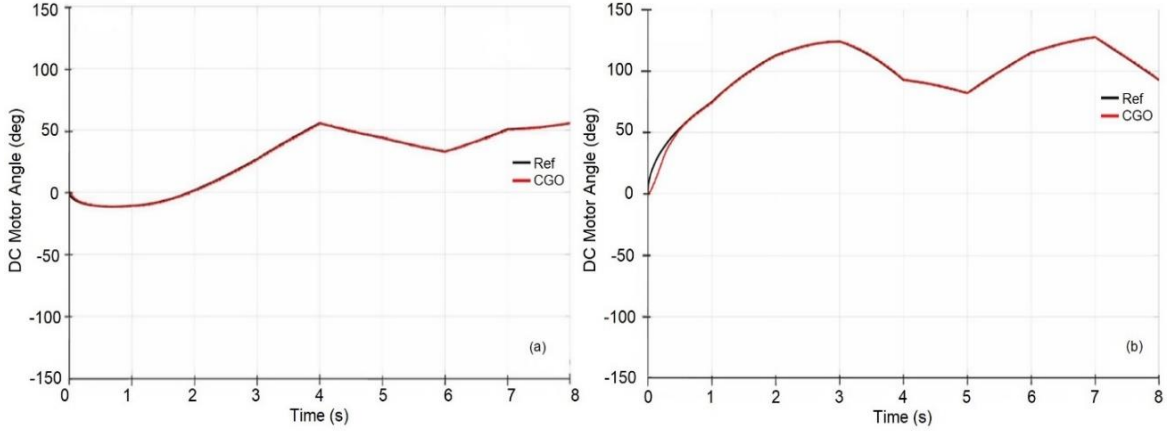
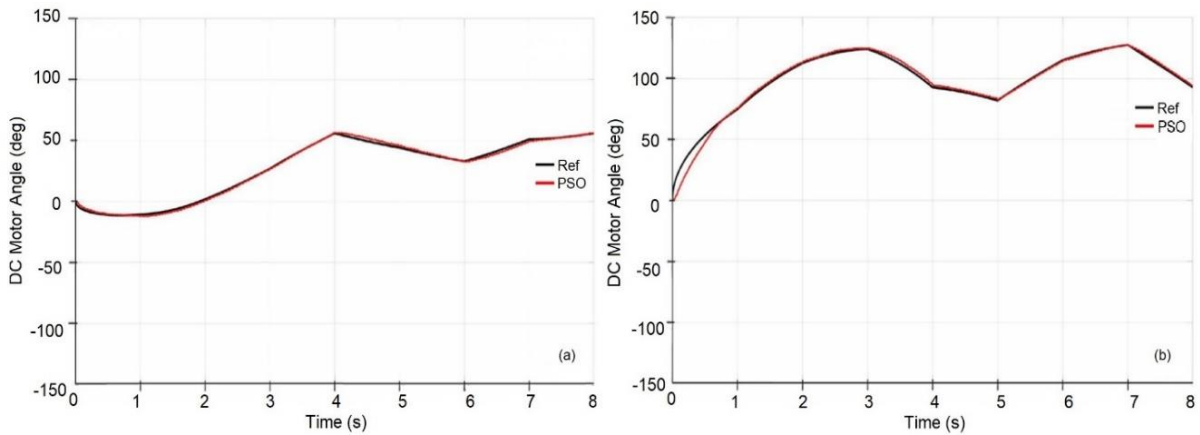**Figure 15.** Reference tracking of PID parameters obtained by CGO for square orbit at angle.

(a) θ_1 (b) θ_2.

Figure 16. Reference tracking of PID parameters obtained by PSO for square orbit at angle (a) θ_1 (b) θ_2.
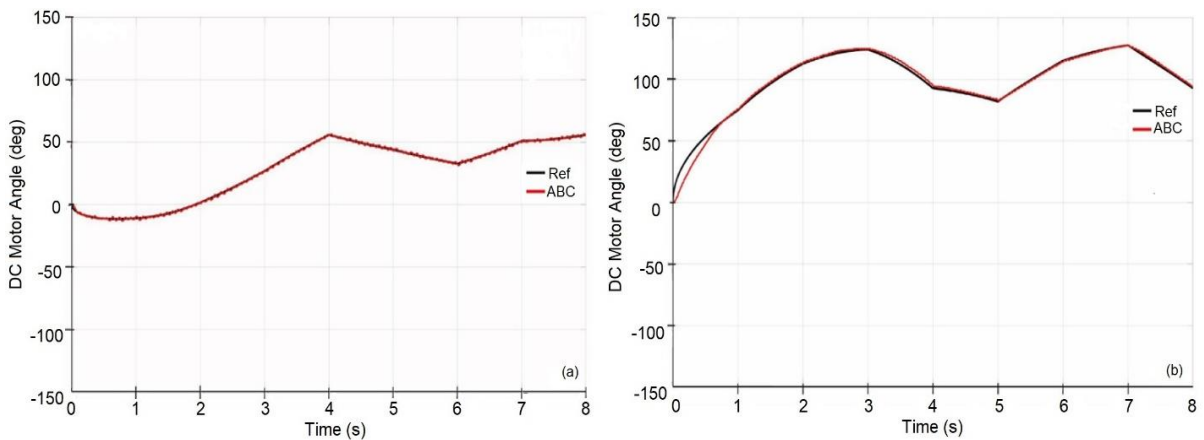

Figure 17. Reference tracking of PID parameters obtained by ABC for square orbit at angle (a) θ_1 (b) θ_2.

When the experimental data obtained from real-time measurements of the DC motors, which are the actuators of the two-limbed robot arm, are analyzed in Figures 15, 16, 17; PSO and ABC algorithms gave very close results to the reference as mentioned in the literature. For the square motion, which is one of the most difficult motions for a two-limbed robot arm, all three algorithms gave very successful results in real-time control. However, the recently popular and promising CGO algorithm gave slightly better results than the PSO and ABC algorithms. This is the same as the simulation result. This is due to the fact that the CGO algorithm finds the parameters of the PID controller closer to the correct values.

4. Conclusion and Suggestions

Many studies in the literature on robot control have been done with servo motors or stepper motors. The DC motor used in this study gave a very successful result and demonstrated that a DC motor with certain parameters can be used for robot control. The transfer function of the DC motor was obtained from the catalog values, and the controller feedback was provided by the encoder. There are many algorithms to determine the parameters of the PID controller used to control the two-limbed robot arm. In this study, the CGO algorithm is used for the first time to determine the PID parameters. The CGO, PSO, and ABC algorithms are compared as a result of the simulation of the transfer function of the DC motor. The parameters of the PID controller obtained as a result of the simulation were tested on the two-limbed robot arm.

As a result of the simulation process, the CGO algorithm gave a result closer to the reference than the PSO and ABC algorithms. In order for the two-limbed DC motors to perform square motion, the change in the angle value of the DC motors for 8 s was calculated, and the control was performed for each motor. When the motors run for 8 s, the end part of the robot draws a square motion. Thanks to the metaheuristic optimization algorithms used, the CGO

algorithm gave more successful results than the PSO and ABC algorithms in the PID controller parameters for the two-limbed robot arm. The success of metaheuristic optimization algorithms is not the same for every problem. The success of an optimization algorithm in one problem does not mean that it will be successful in another. This study has shown in the literature that the CGO metaheuristic optimization algorithm can be used to determine the coefficients of a PID controller.

The controller part is of great importance in the studies to be carried out on robotic systems. Among the methods to be used for the problem of determining controller parameters, methods with a small number of parameters should be chosen. Since the angular loss of any axis affects the holder end, the material to be used with the smallest error rate should be selected. Motor selection should be made according to the torque value required for the system. If the motor to be used as a drive element is a DC motor, the step range of the encoder should be high, the value of the motor speed should be low, and the cycle ratio of the reducer should be high.

Contributions of the authors

All authors contributed equally to the study.

Conflict of Interest Statement

There is no conflict of interest between the authors.

Statement of Research and Publication Ethics

The study is complied with research and publication ethics.

References

[1] W. S. Barbosa, M. M. Gioia, V. G. Natividade, R. F. Wanderley, M. R. Chaves, F. C. Gouvea and F. M. Gonçalves, "Industry 4.0: examples of the use of the robotic arm for digital manufacturing processes," *International Journal on Interactive Design and Manufacturing (IJIDeM)*, vol. 14, pp.1569-1575, 2020.

[2] S. K. Valluru and M. Singh, "Optimization strategy of bio-inspired metaheuristic algorithms tuned PID controller for PMBDC actuated robotic manipulator," *Procedia Computer Science*, vol.171, pp. 2040-2049, 2020.

[3] K. J. Åström and T. Hägglund. "The future of PID control," *Control engineering practice*, vol. 9, no. 11, pp.1163-1175, 2001.

[4] S. B. Joseph, E. G. Dada, A. Abidemi, D. O. Oyewola, and B. M. Khammas, "Metaheuristic algorithms for PID controller parameters tuning: Review, approaches and open problems," *Heliyon*, vol. 8, no. 5, p.e09399, 2022.

[5] S. Kucuk and Z. Bıngul, *Robot kinematics: Forward and inverse kinematics, London, UK*: INTECH Open Access Publisher, 2006, pp. 117-148.

[6] S. Maheriya and P. Parikh, "A review: Modelling of Brushed DC motor and Various type of control methods," *Journal for Research*, vol. 1, 2016.

[7] X. Hu, "Particle swarm optimization tutorial, titan.csit.rmit.edu, 2006. [Online]". Available: https://titan.csit.rmit.edu.au/ e46507/publications/pso-tutorial-seal06.pdf. [Accessed: March 22, 2021].

[8] J. Tang, G. Liu and Q. Pan, "A review on representative swarm intelligence algorithms for solving optimization problems," *Applications and trends. IEEE/CAA Journal of Automatica Sinica*, vol. 8, no. 10, pp.1627-1643, 2021.

[9] E. Boğar, "Optimizasyon kuramında yeni bir metasezgisel yaklaşım: Ergen kimlik arama algoritması (AISA) ve mühendislik uygulamaları," Doktora tezi, Pamukkale Üniversitesi Fen bilimleri Enstitüsü, Denizli, 2021.

[10] R. Eberhart and J. Kennedy, "Particle swarm optimization," *in Proceedings of the IEEE international conference on neural networks* vol. 4, pp. 1942-1948, November 1995.

[11] D. Bratton and J. Kennedy, "Defining a standard for particle swarm optimization," *In 2007 IEEE swarm intelligence symposium*, pp. 120-127, April 2007.

[12] M. Azab, "Global maximum power point tracking for partially shaded PV arrays using particle swarm optimization," *International Journal of Renewable Energy Technology*, vol. 1, no.2, pp. 211-235, 2009.

[13] D. Karaboga and B. Basturk, "A powerful and efficient algorithm for numerical function optimization: artificial bee colony (ABC) algorithm," *Journal of global optimization*, vol. 39, pp. 459-471, 2007.

[14] H. O. Erkol, "Ters sarkaç sisteminin yapay arı kolonisi algoritması ile optimizasyonu," *Politeknik Dergisi*, vol. 20, no. 4, pp.863-868, 2017.

[15] S. Hassan, B. Abdelmajid, Z. Mourad, S. Aicha and B. Abdenaceur, "An advanced MPPT based on artificial bee colony algorithm for MPPT photovoltaic system under partial shading condition. International," *Journal of Power Electronics and Drive Systems*, vol. 8, no. 2, p. 647, 2017.

[16] S. Talatahari and M . Azizi, "Chaos game optimization: a novel metaheuristic algorithm," *Artificial Intelligence Review*, vol. 54, no. 2 pp. 917-1004, 2021.

[17] M. Barakat, "Novel chaos game optimization tuned-fractional-order PID fractional-order PI controller for load–frequency control of interconnected power systems," *Protection and Control of Modern Power Systems*, vol. 7, no. 1, 2022.

Properties of Basalt Fiber-reinforced Lightweight Geopolymer Mortars Produced with Expanded Glass Aggregate

Adil GULTEKİN[1*]

[1]Duzce University, Faculty of Engineering, Department of Civil Engineering, Duzce, Turkiye
(ORCID: 0000-0002-5267-5312)

Abstract

Geopolymers are environmentally friendly binders with high mechanical properties and good durability characteristics. The advantages provided by geopolymers can be combined with the benefits of lightweight concrete. However, the number of studies on geopolymers produced with lightweight aggregates is limited. This study investigated the properties of fly-ash based geopolymer mortars prepared with expanded glass aggregate, as well as the influence of fiber addition on these mortar properties. For this purpose, fresh unit weight, water absorption, compressive strength and high-temperature resistance (upon exposure to 900°C) of the mortars were determined. The inclusion ratios of fibers were 0.1%, 0.2% and 0.4% by volume. Sodium silicate and sodium hydroxide were used as activators, and curing was carried out at 90°C for 24 hours in a laboratory-type oven. In addition to lightweight mortars, conventional geopolymer mortars were produced with limestone aggregate with similar gradation, and the obtained results were compared. The results have shown that the compressive strength of the reference mortar was 31.9 MPa, the use of expanded glass aggregate reduced the strength to 8.2 MPa, meanwhile, the fresh unit weight decreased by approximately 50%. After the high-temperature experiment, the compressive strength of the reference mortar decreased by 40%, while the strengths of lightweight mortars increased in the range of 61.3% to 76.4%. It was also determined that the use of fiber did not have a significant effect on compressive strength and unit weight. The results proved that it is possible to produce expanded glass aggregate-bearing lightweight geopolymer mortars with acceptable mechanical properties.

1. Introduction

Concrete is the most widely used construction material in the world [1]. A large amount of energy is consumed, and extensive quantities of CO_2 are emitted during cement production [2]. It is thought that the cement industry is responsible for 5-8% of the global CO_2 emissions [3]. It is crucial to develop sustainable materials that can reduce the economic and environmental drawbacks involved in producing cement [4].

Geopolymers are economic and environmentally friendly materials and have the potential to be an alternative to conventional concrete

[5]. According to Davidovits [6], incorporating by-product slag into geopolymer as binder can result in an 80% reduction in CO_2 emissions and a 59% decrease in energy consumption compared to those of the portland cement. Geopolymers possess outstanding mechanical and durability properties [7], as well as high early strength [8], which makes them suitable for use in various application fields. Binder and concrete production, 3D printing technology, refractory materials, fiber-reinforced composites and decoration are some of these areas [9].

Various types of materials like fly ash, ground granulated blast furnace slag, kaolin and metakaolin can be utilized as aluminosilicate source

in geopolymer production. Commonly employed alkali solutions for geopolymerization include sodium silicate, potassium silicate, sodium hydroxide, and potassium hydroxide [10]. For the sake of curing, temperatures below 100°C are generally preferred [11].

Lightweight concrete serves the purpose of reducing the dead load and provides heat insulation in various construction materials, including masonry blocks, wall panels and other precast elements [12]. The advantages of lightweight concrete and geopolymers can be combined in lightweight geopolymer mixtures [13]. Lightweight geopolymer composites offer multiple benefits, such as good fire resistance, heat insulation and sound absorption [14]. It is possible to use natural lightweight materials such as volcanic tuff, perlite and vermiculite or artificial lightweight aggregates in the production of lightweight concrete [15].

Recycling and utilizing waste glass in various fields are essential for sustainability. The construction industry, in particular, holds a potential for the recycling of glass wastes. Ongoing studies explore the incorporation of glass powder and glass bead in the production of building materials. Recently, expanded glass aggregates have attracted attention and emerged as a potential area of use [16].

Expanded glass aggregate is manufactured by subjecting recycled waste glass to high-temperatures with the inclusion of various additives. The production process involves several stages, including expansion under high-temperature, cooling and screening. Due to its cellular structure, expanded glass aggregate has low thermal conductivity, density, and mechanical properties [17].

Numerous studies investigated the properties of cement-based concrete, mortar, and other composite materials, incorporating expanded glass aggregate. Seputyte-Jucike et al. [18] investigated the properties of expanded glass aggregate-bearing lightweight concretes and reported the possibility of achieving densities in the range of 247-335 kg/m^3. Bumanis et al. [19] conducted a study on some properties of lightweight concretes prepared with limestone powder and varying proportions of expanded glass as aggregate. The researchers observed that the fresh density of lightweight concretes containing expanded glass aggregate ranged between 647-809 kg/m^3, and the compressive strength of the concretes varied from 4.0 to 5.8 MPa. In a similar study, Bumanis et al. [20] examined the strength, density and alkali-silica reaction expansions of lightweight concrete prepared with expanded glass aggregate and eight different types of cements. Findings of this study indicated that the concrete mixtures exhibited a density within the range of 734-

781 kg/m^3 and compressive strength ranging from 2.8 to 4.0 MPa.

While geopolymers offer numerous advantages, the production and properties of lightweight geopolymers using lightweight aggregates are the areas requiring further research [21]. Huiskes et al. [22] studied the impact of liquid/binder ratio, binder/aggregate ratio, aggregate gradation and alkali activator concentration on the strength, density and thermal properties of fly ash/blast furnace slag-based geopolymer mortars and concretes containing expanded glass aggregate. Humur and Cevik [23] investigated the influence of aluminosilicate type on the high-temperature resistance of PVA fiber-reinforced expanded glass aggregate-bearing geopolymer composites. Researchers reported that the compressive strengths of the geopolymer composites varied between 16.7 and 64.1 MPa, with a decrease of up to 79% upon exposure to 800°C. Priyanka et al. [24] explored the effect of inclusion of expanded clay aggregate instead of natural aggregate on the properties of fly ash-based geopolymer concretes and reported a gradual decrease in the compressive strength and density of concrete as the substitution ratio increased.

This study investigated the properties of fly-ash based geopolymer mortars prepared with expanded glass aggregate, as well as the influence of fiber addition on these mortars. For this purpose, the flow diameter, fresh unit weight, compressive strength, high-temperature resistance and water absorption tests were conducted. Basalt fiber was chosen as the fiber type due to its high-temperature resistant structure.

2. Material and Method

2.1. Materials

A Class F-fly ash was used as the aluminosilicate raw material. The chemical composition and some physical properties of the fly ash are given in Table 1. Lightweight mortars were produced using limestone aggregate (0-0.250 mm), expanded glass aggregate (various size fractions between 0.25 and 4 mm), activator and tap water. The images of expanded glass aggregates are given in Figure 1. Some physical properties and gradation of the limestone aggregate and combined aggregate are shown in Table 2 and Figure 2, respectively. Furthermore, a mixture labeled as "Ref" was produced using 0-4 mm limestone aggregate with a specific gravity of 2.60 and a gradation similar to that of the combined aggregate. Additionally, 6 mm-long basalt fibers were employed to assess the impact of fiber addition. Some

mechanical and physical properties of basalt fiber are given in Table 3.

A sodium silicate solution consisting of 9.25% Na_2O, 28.65% SiO_2, 62.10% water and a pellet-shaped sodium hydroxide with a purity of 98% were used to prepare the activator solution. The sodium hydroxide pellets were dissolved in the sodium silicate, and the solution was allowed to rest for 24 hours. The Ms ratio (the weight ratio of SiO_2 to Na_2O in the solution) and the amount of Na_2O (the weight ratio of Na_2O in the solution to the weight of fly ash) were 1.5 and 8%, respectively.

Table 1. Chemical composition and some physical properties of fly ash

Oxide	% (by weight)	Oxide/item	% (by weight)
SiO_2	55.9	TiO_2	1.0
Al_2O_3	23.3	P_2O_5	0.8
Fe_2O_3	6.3	Loss on ignition	2.0
CaO	5.3	Physical properties	
Na_2O	0.6	Specific gravity	2.21
K_2O	2.3	% retained on 32 µm	26.7
SO_3	0.2	% retained on 45 µm	20.0
MgO	2.1	% retained on 90 µm	6.4

Table 2. Some physical properties of aggregates

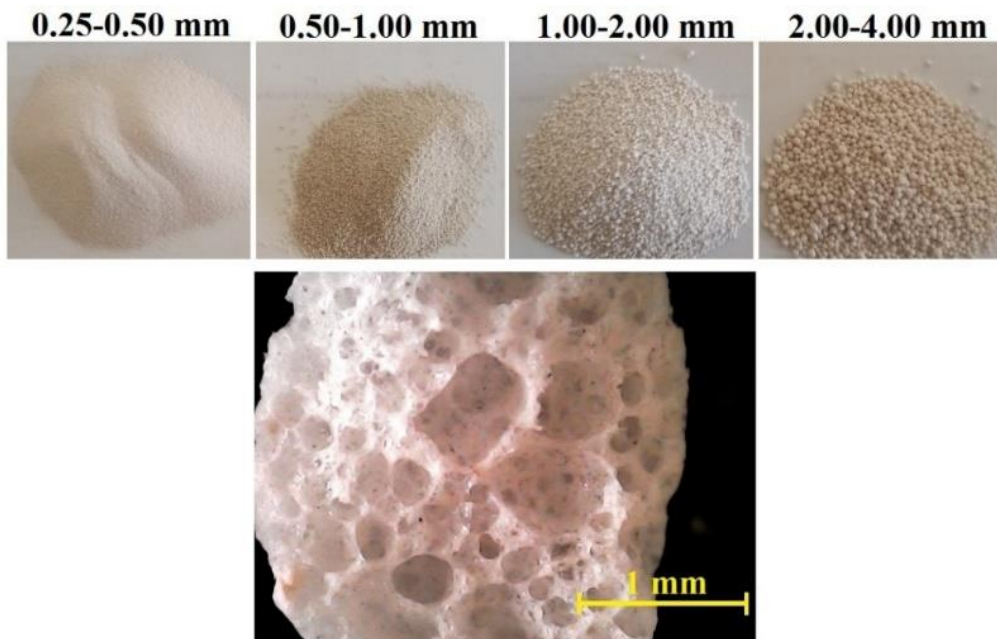| Property	Limestone aggregate	Expanded glass aggregate			
Particle size (mm)	0-4	0.25-0.50	0.50-1	1-2	2-4
Particle density (g/cm³)	2.60	0.52	0.42	0.37	0.34
Water absorption (%)	1.2	20	18	18	15

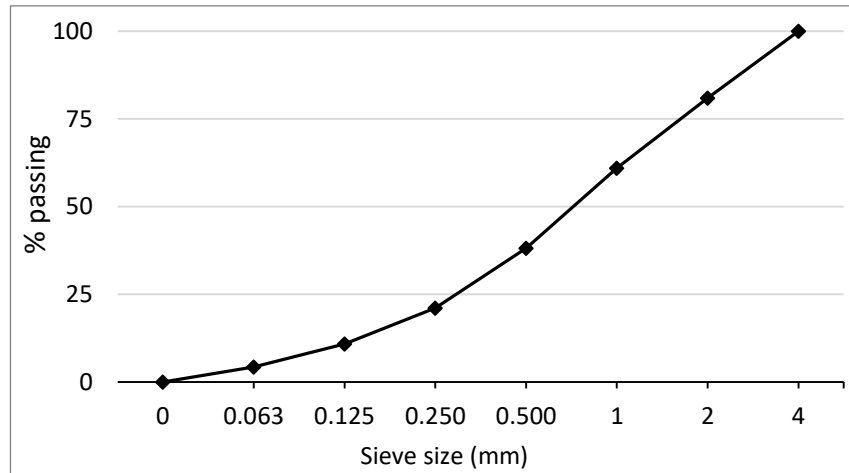**Figure 1.** Expanded glass aggregate size fractions and porous structure of the broken aggregate particle

Figure 2. Gradation of limestone aggregate and combined aggregate

Table 3. Properties of basalt fiber

Properties	Value
Diameter (µm)	13-20
Modulus of elasticity (GPa)	88
Tensile strength (MPa)	4000-4500
Density (g/cm^3)	2.80

2.2. Method

Limestone and glass aggregates were used in the saturated-surface-dry and oven-dry conditions, respectively. In the production of lightweight mortars, the aggregates, water and fiber (if any) were mixed for 90 seconds at a speed of 62.5 rpm. Subsequently, fly ash and activator solution were introduced into the bowl. The mixer was operated for 90 seconds at the same speed, and the material adhered to the bowl was scraped off in approximately 15 seconds. Finally, the mixer was run for an additional 90 seconds at 125 rpm. The flow diameters of mortar mixtures were determined in accordance with TS EN 459-2 standard [25]. The mixtures were cast into 50 mm steel cube molds and compacted in two layers each with 25 jolts using a jolting table. The molded specimens were placed in the oven immediately after preparation and were cured for 24 hours at 90°C. At the end of the curing period, specimens were taken out of the oven and demolded after cooling to room temperature. The samples removed from the mold were immediately used for hardened state tests.

High-temperature resistance test was performed using a muffle furnace. The temperature rise rate of the furnace and exposing temperature were 10°C/minute and 900°C, respectively. The specimens were kept in the furnace at 900°C for 3 hours, which was followed by gradual cooling to the room temperature in the furnace.

The compressive strength tests were conducted using a 500 kN mortar press at a constant loading rate of 0.9 kN/s. The reported strength values are the average of 3 specimens. Equation 1 was used to calculate the compressive strength (σ_c in MPa). In this formula P represents the maximum load (N) and A represents the cross-sectional area (mm^2) of the specimen.

While determining the unit weights, the weight of fresh mortar that completely filled the 50x50x50 mm mold was determined after compaction process and fresh unit weights in m^3 were calculated.

For water absorption determination, the samples cooled to room temperature after curing were used. The samples were kept in tap water for 48 hours, then the surfaces of the samples taken out of the water were dried with a towel and their saturated-surface-dry weights were measured. The samples were kept in the oven at 105°C until they reached a constant weight, and their oven-dry weights were determined. The water absorption of mortar samples was determined according to Equation 2. W_{ssd} and W_d represent saturated-surface-dry and oven-dry weights, respectively.

$$\sigma_c = \frac{P}{A} \qquad (1)$$

$$Water\ absorption\ (\%) = \frac{W_{ssd}-W_d}{W_d} x100 \quad (2)$$

Photographs of the performed tests are presented in the Figure 3.
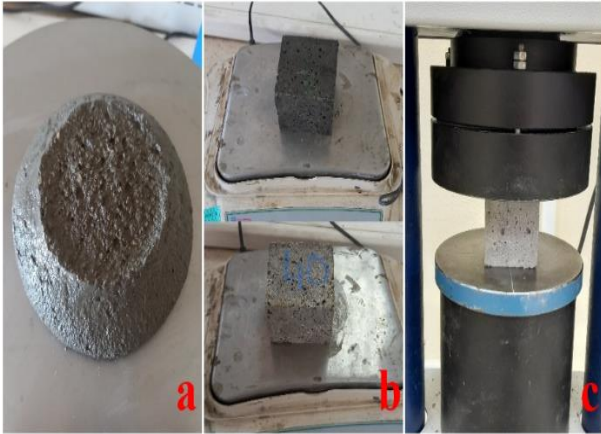

Figure 3. Photographs of tests (a: flow diameter test, b: weighing of specimens to determine water absorption, c: compressive strength test)

2.3. Mixtures

Within the scope of the study, five mixtures were prepared. The first was the reference mixture produced with limestone aggregate (0-4 mm) and denoted as "Ref." The other mixtures were plain and fiber-reinforced lightweight mortars prepared using limestone aggregate (0-0.25 mm) and various sizes of expanded glass aggregate (0.25-0.50, 0.50-1, 1-2, and 2-4 mm). The lightweight mortars were labeled according to the fiber dosage. For example, LW-0.1 designates the lightweight mortar mixtures containing 0.1 volume % fiber.

The proportions and flow diameters of the mixtures are given in Table 4. In order to obtain comparable flow to that of the reference mix, more water was added to the LW-0 mixture.

3. Results and Discussion

3.1 Unit Weight and Water Absorption

The fresh unit weight and water absorption values of the hardened mixtures are given in Figure 4. As expected, the fresh unit weights of mortar mixtures containing expanded glass were lower than that of the reference mixture due to the difference in the specific gravities of the aggregates. As a result of the lightweight nature of expanded glass, fresh unit weights of the lightweight mortars were approximately half of that of the reference mixture, ranging from 1021.4 to 1028.3 kg/m^3. The difference in density between limestone and expanded glass aggregate was the main cause of the decrease in unit weight. The extensive porous structure of the expanded glass aggregate, illustrated in Figure 1, contributes significantly to this phenomenon. Additionally, the uniformity in size among the expanded glass aggregates within a given size fraction adversely impacts compactness. Therefore, a decrease of up to 53% in unit weights was observed. In a similar investigation, Mermertas et al. [26] employed fly ash- and Portland cement-based artificial lightweight aggregate in preparation of fly ash-based lightweight mortar and reported that replacing of natural sand with lightweight aggregate resulted in a 17.5% reduction in the fresh density of the mortar Tayeh et al. [27] examined the effect of substituting pumice and expanded clay aggregate with coarse dolomite aggregate on the properties of fly ash-based geopolymer concrete. Researchers reported that the unit weight of hardened concrete decreased by approximately 20% and 22%, respectively, with the use of expanded clay and pumice aggregate.

Table 4. Proportions and some properties of mixtures

Ingredient/property	Ref	LW-0	LW-0.1	LW-0.2	LW-0.4
Fly ash (g)	420	420	420	420	420
Activator (g)	197	197	197	197	197
Water (g)	68	90	90	90	90
0-4.0 mm (Limestone) (g)	1202.6	-	-	-	-
0-0.25 mm (Limestone) (g)	-	24.2	24.2	24.2	24.2
0.25-0.50 mm (Expanded glass) (g)	-	19.6	19.6	19.6	19.6
0.50-1 mm (Expanded glass) (g)	-	26.2	26.2	26.2	26.2
1.0-2.0 mm (Expanded glass) (g)	-	22.9	22.9	22.9	22.9
2.0-4.0 mm (Expanded glass) (g)	-	21.8	21.8	21.8	21.8
Basalt fiber (g)	-	-	2.35	4.70	9.40
Flow diameter (cm)	15.0	14.9	14.5	13.7	13.1

The incorporation of basalt fiber demonstrated negligible impact on unit weight values. Due to reduced workability resulting in insufficient compacting, the mortar with the highest fiber dosage exhibited the lowest fresh unit weight among the samples. However, the differences between the unit weights of lightweight mixtures was insignificant. Water absorption test results revealed that samples containing expanded glass aggregate absorbed 97%-105% more water than the reference mixture. It is known that lightweight aggregates absorb higher amounts of water compared to the conventional natural aggregates used in concrete production due to their porous structure [17]. In lightweight mortars, some of the absorbed water was attributed to the water absorption capacity of expanded glass aggregates. Moreover, even though the aggregate gradations are the same, the similarity in grain sizes within specific size fractions of the expanded glass aggregate is another contributing factor to the formation of voids in the mixture.
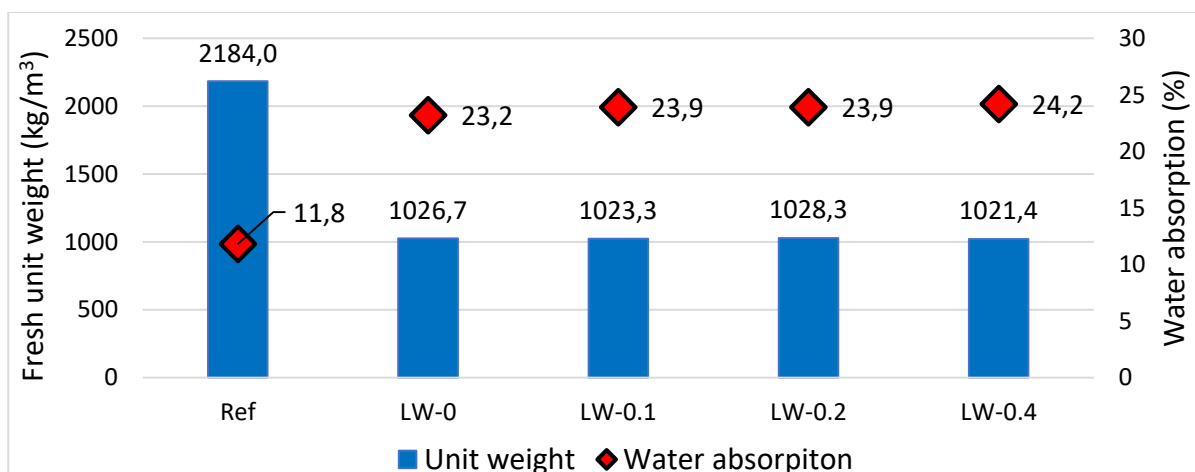

Figure 4. Fresh unit weight and water absorption of mortar mixtures

3.2. Compressive Strength

The compressive strengths of mortars are presented in Figure 5. The reference mixture containing entirely limestone aggregate demonstrated the highest strength as 31.9 MPa. With the addition of fiber to an optimum dosage (0.2%), the compressive strength of lightweight mortar mixtures increased slightly. Beyond the optimum level of fiber, the strength decreased slightly, probably due to the reduced workability. The compressive strengths of fiber-free lightweight mortar and mortars containing 0.1, 0.2 and 0.4% fiber were 8.2, 8.9, 9.0 and 8.0 MPa, respectively. Substituting limestone aggregate with expanded glass aggregate resulted in a decrease in compressive strength ranging from 71.8% to 74.9%. The main reason for this outcome is the low strength of glass aggregate attributable to its cellular structure. In a similar study, Priyanka et al. [24] stated that the substituting of natural coarse aggregate with expanded clay aggregate reduces the compressive strength, and with the increase in the substitution ratio, the strength losses escalated to higher levels. Elrahman et al. [28] reported that the compressive strengths of cement-based lightweight concretes produced with expanded glass and expanded clay varied between approximately 7-18 MPa, depending on the mixture design.
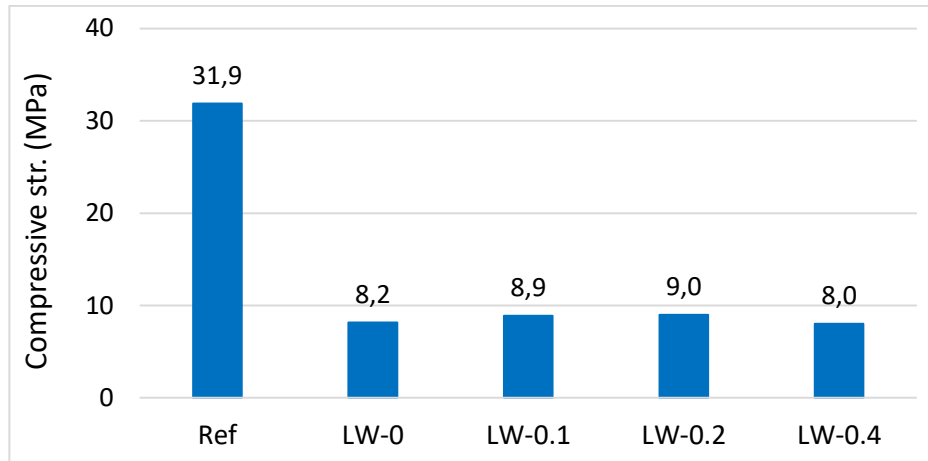
Figure 5. Compressive strength of mortar mixtures

3.3. High Temperature Resistance

Photographs of the samples before and after exposure to the high-temperature are shown in Figure 6. Despite the absence of any visible damage or cracks in any of the specimens, the color of the samples changed from gray to a slightly reddish hue due to the influence of elevated temperature. Similar color changes were observed in fly ash-based geopolymers by Hager et al. [29] and R. Zhao and Sanjayan [30], and researchers attributed this transformation to the oxidation of iron components. The broken cross section of a samples before and after being exposed to 900°C, followed by crushing in compression, is shown in Figure 7. It was observed that the expanded glass aggregate particles, melted under the influence of high temperature, resulted in pore formation in the areas originally occupied by the solid aggregate particles before the high-temperature tests. The expanded glass aggregates and pores formed by the aggregate melting are showed with black and red circles, respectively in Figure 7.

Figure 6. Pictures of specimens (a: before high-temperature test, b: after high temperature test)
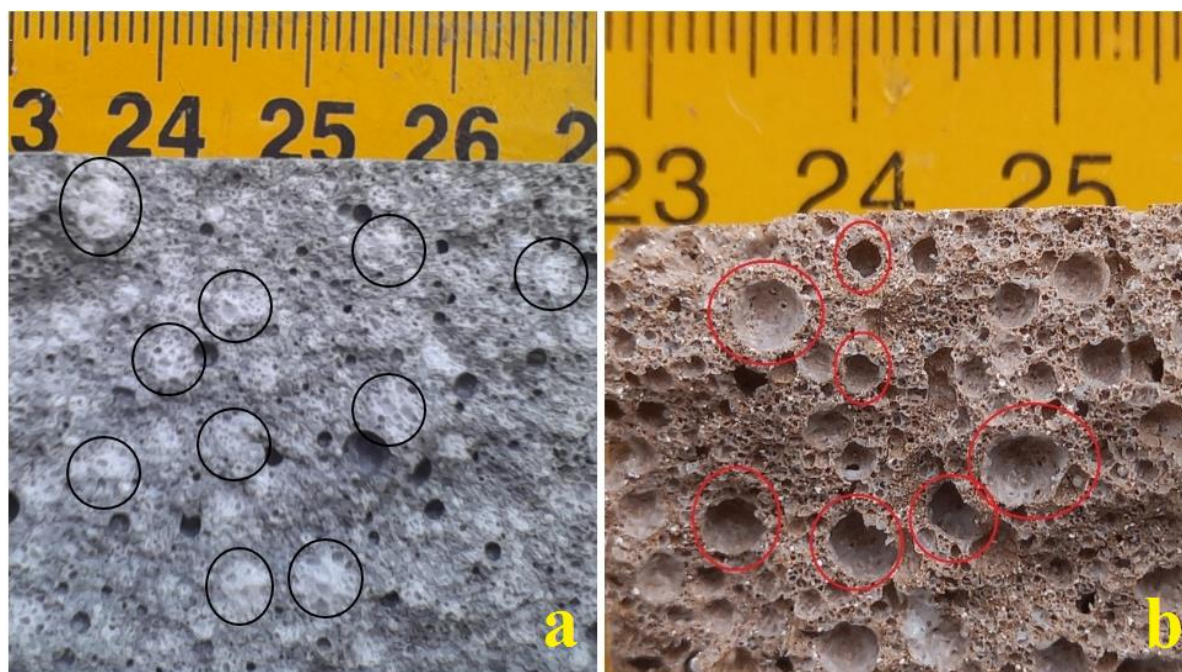
Figure 7. Broken cross-section of a compression test specimens (a: before and b: after exposure to high-temperature)

The compressive strength and relative strength values of mortars exposed to 900°C are given in Figure 8. Following the high-temperature test, two opposite outcomes were observed. The compressive strength of the reference mixture decreased by 39.8%, whereas the opposite trend was seen in lightweight specimens. The strengths of fiber-free lightweight mixture and fiber-reinforced mortars containing 0.1, 0.2 and 0.4% basalt fiber increased by 73.2%, 76.4%, 65.6% and 61.3%, respectively. Diverse factors play a role in the occurrence of these two conflicting situations.

The evaporation of both physically and chemically bound water in the geopolymer samples may result in thermal shrinkage and cracking at elevated temperatures. Additionally, the vapor pressure may cause internal stresses which adversely affect the structure, and the extent of damage is closely related to the pore structure [31]. The vapor pressure, which cannot be evacuated easily from dense structures, leads to severe damage [32]. Obviously, this was not the case in the porous (lightweight) mixtures used in this study.

In addition to the microstructure of the matrix, the high-temperature resistance is also influenced by the thermal expansion coefficient of the aggregate [33]. Rickard et al. [34] investigated the compressive strength and microstructure of two different geopolymer pastes exposed to elevated temperatures. The researchers reported a significant reduction in the compressive strength of the paste with high initial compressive strength and low permeability after exposure to the elevated temperatures. In contrast, compressive strength of the paste with low initial compressive strength and a more porous structure improved from approximately 30 MPa to about 90 MPa. Researchers also noted that upon increasing the temperature, the water vapor could be more easily evacuated from the low-strength samples, the newly formed crystalline compounds may cause less damage due to porous structure of the sample. Payakaniti et al. [35] investigated the effect of high temperatures on Class C fly ash-based geopolymers and stated that new crystalline products formed in the matrix at and beyond 800°C temperature may contribute to the strength of the mixture with filler effect. However, as their quantity increases, internal stresses occur in the matrix, which affect the strength adversely. In this study, glass aggregate particles in lightweight mortars were partially or completely melted at high temperature. It is thought that the voids formed by the fusion of glass particles provide sufficient space for the newly formed phases, preventing/reducing formation of the internal pressure and subsequent hazardous internal stresses.
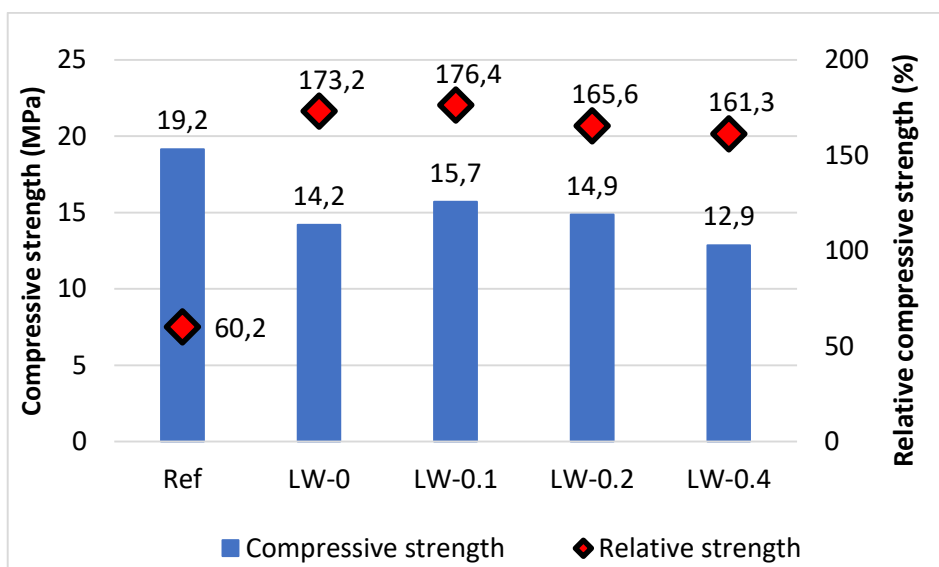
Figure 8. Compressive strengths and relative strengths of mortar mixtures after high-temperature effect

4. Conclusion

In this study, the properties of fly ash-based geopolymer mortars prepared with expanded glass aggregate and the effect of fiber addition on these mixtures were investigated. Based on the materials used and tests applied, the following conclusions can be drawn:

The fresh unit weight of the conventional geopolymer mortar produced with limestone aggregate was 2184 kg/m³. As expected, the unit weight of the mortar decreased by about 53% with the use of glass aggregate. Addition of basalt fibers had not a significant effect on the unit weight of the mixture.

The compressive strength of the conventional geopolymer mortar produced with limestone aggregate was 31.9 MPa, whereas the compressive strengths of mortars prepared with expanded glass aggregate varied between 8.0 and 9.0 MPa, depending on the fiber content. While there was a slight increase in compressive strengths with fiber addition up to a volume fraction of 0.2%, it can be said that inclusion of basalt fiber did not have a significant effect on the compressive strength.

As a consequence of the mortar's pore structure and the high water absorption of expanded glass aggregate, the water absorption of lightweight mortar mixtures was significantly higher than that of the reference sample. Additionally, due to the decrease in workability, water absorption values increased slightly with the addition of fiber.

Upon exposure to 900°C, compressive strength of the mortar prepared with limestone aggregate decreased by approximately 40%, while the strength of lightweight aggregate-bearing mortars increased considerably. These increases were 73.2%, 76.4%, 65.6%, and 61.3% for fiber-free lightweight mortar and mortars containing 0.1%, 0.2%, and 0.4% fiber, respectively. It is thought that the voids formed by the fusion of glass particles provide sufficient space for the newly formed phases, preventing/reducing formation of the internal pressure and subsequent internal stresses which may cause micro cracking in both matrix and interfacial transition zone.

The investigation of the strength and -especially- durability properties of geopolymer mortars and concretes produced using expanded glass aggregate is still a topic that needs further research. The effect of cooling regime after exposure to high temperature on the properties of lightweight geopolymer systems is also of interest.

Statement of Research and Publication Ethics

The study is complied with research and publication ethics.

This paper represents the extended full text of the study presented as an oral presentation at the "5th International Conference on Natural and Applied Science and Engineering" and published as an abstract in the abstract booklet.

References

[1]   C. Zhang, H. Khorshidi, E. Najafi and M. Ghasemi, "Fresh, mechanical and microstructural properties of alkali-activated composites incorporating nanomaterials: A comprehensive review," *J. Clean. Prod.*, vol. 384, 2023, Art. no.135390, doi: 10.1016/j.jclepro.2022.135390.

[2]   B. Kanagaraj, N. Anand, U. J. Alengaram, S. R. Raj and G Jayakumar, "Promulgation of engineering and sustainable performances of self-compacting geopolymer concrete," *J. Build. Eng.*, vol. 68, 2023, Art. no. 106093, doi: 10.1016/j.jobe.2023.106093.

[3]   A. M. Rashad, 2018. "A synopsis about the effect of basalt and natural fibers on geopolymer properties," *Nat. Resour. Conserve. Res.*, 1. doi: 10.24294/nrcr.v1i2.752.

[4]   J. Zhao, J. Xie, J. Wu, C. Zhao and B. Zhang, "Workability, compressive strength, and microstructures of one-part rubberized geopolymer mortar," *J. Build. Eng.*, vol. 68, 2023, Art. no. 106088, doi: 10.1016/j.jobe.2023.106088.

[5]   E. H. Alakara, "Investigation of the Use of Waste Bricks Obtained from Construction Demolition Wastes in Geopolymer Mortars," *Gaziosmanpasa J. Sci. Res.*, vol. 11, no. 3, pp. 251-259, 2022.

[6]   J. Davidovits, "Geopolymer cement a review," *Geopolymer Science and Technics*, Technical Paper 21, pp. 1-11, 2013.

[7]   Z. Zidi, M. Ltifi, Z. B. Ayadi, L. E. Mir and X. R. Novoa, "Effect of nano-ZnO on mechanical and thermal properties of geopolymer," *J. Asian Ceram. Soc.*, vol. 8, no. 1, pp. 1-9, 2020, doi: 10.1080/21870764.2019.1693682.

[8]   H. R. Pradeep, A. Shashishankar and B. R. Niranjan, "Development of geopolymer lightweight concrete using industrial by-products," *Int. J of Latest Tech. in Eng., Management & Applied Science*, vol. 6, no. 8, pp. 49-52, 2017.

[9]   K. Eryılmaz, R. Polat, F. Karagöl and D. Turhan, "Investigation of usability of aggregates obtained from geopolymer concrete wastes in geopolymer concrete," *Igdır University J. Ins. of Sci. Tech.*, vol. 13, no. 1, pp. 419-431, 2023.

[10]   M. R. Maaze, S. Shrivastava, "Design development of sustainable brick-waste geopolymer brick using full factorial design methodology," *Constr. Build. Mater.*, vol. 370, 2023, Art. no. 130655, doi: 10.1016/j.conbuildmat.2023.130655.

[11]   R. M. Novais, R. C. Pullar and J. A. Labrincha, "Geopolymer foams: An overview of recent advancements," *Prog. Mater. Sci.*, vol. 109, 2020, Art. no. 100621, doi: 10.1016/j.pmatsci.2019.100621.

[12]   W. I. Khalil, W. A. Abbas and I. F. Nasser, "Mechanical properties and thermal conductivity of lightweight geopolymer concrete," *1st International Scientific Conference of Engineering Sciences-3rd Scientific Conference of Engineering Science*, Diyala, Iraq, Jan. 10-11, 2018, p. 175-180.

[13]   O. Öztürk, "Engineering performance of reinforced lightweight geopolymer concrete beams produced by ambient curing," *Struct. Concr.*, vol. 23, pp. 2076-2087, 2022, doi: 10.1002/suco.202000664.

[14]   S. Saloma, A. P. Usman, H. Hanafiah and C. V. Ramadhanty, "The durability of lightweight geopolymer concrete (LGC) on chloride resistance," *Civ. Eng. Archit.*, vol. 10, no. 5, pp. 1881-1890, 2022, doi: 10.13189/cea.2022.100514.

[15]   R. Nemes and Z. Józsa, "Strength of lightweight glass aggregate concrete," *J. Mater. Civ. Eng.*, vol. 18, no. 5, pp. 710-714, 2006, doi: 10.1061/(ASCE)0899-1561(2006)18:5(710).

[16]   A. Yousefi, W. Tang, M. Khavarian, C. Fang and S. Wang, "Thermal and mechanical properties of cement mortar composite containing recycled expanded glass aggregate and nano titanium dioxide," *Appl. Sci.*, vol. 10, 2020, Art. no. 2246, doi: 10.3390/app10072246.

[17]   S. K. Adhikary, D. K. Ashish and Z. Rudzionis, "Expanded glass as light-weight aggregate in concrete – A review," *J. Clean. Prod.*, vol. 313, 2021, Art. no. 127848, doi: 10.1016/j.jclepro.2021.127848.

[18]   J. Seputyte-Jucike and M. Sinica, "The effect of expanded glass and polystyrene waste on the properties of lightweight aggregate concrete," *Eng. Struct. Tech.*, vol. 8, no. 1, pp. 31-40, 2016, doi: 10.3846/2029882X.2016.1162671.

[19]   G. Bumanis, D. Bajare and A. Korjakins, "Mechanical and thermal properties of lightweight concrete made from expanded glass," *J. Sustain. Archit. Civ. Eng.*, vol. 2, no. 3, pp. 26-32, 2013, doi: 10.5755/j01.sace.2.3.2790.

[20] G. Bumanis, D. Bajare, J. Locs and A. Korjakins, "Alkali–silica reactivity of expanded glass granules in structure of lightweight concrete," *IOP Conf. Ser.: Mater. Sci. Eng.*, vol. 47, pp. 1-6, 2013, doi: 10.1088/1757-899X/47/1/012022.

[21] W. Abbas, W. Khalil and I. Nasser, "Production of lightweight geopolymer concrete using artificial local lightweight aggregate,". *MATEC Web of Conferences*, vol. 162, 2018, Art. no. 02024, doi: 10.1051/matecconf/201816202024.

[22] D. M. A. Huiskes, A. Keulena, Q. L. Yua and H. J. H. Brouwers, "Design and performance evaluation of ultra-lightweight geopolymer concrete," *Mater. Des.*, vol. 89, pp. 516-526, 2016, doi: 10.1016/j.matdes.2015.09.167.

[23] G. Humur and A. Cevik, "Mechanical characterization of lightweight engineered geopolymer composites exposed to elevated temperatures," *Ceram. Int.*, vol. 48, pp. 13634-13650, 2022, doi: 10.1016/j.ceramint.2022.01.243.

[24] M. Priyanka, M. Karthikeyan and M. S. R. Chand, "Development of mix proportions of geopolymer lightweight aggregate concrete with LECA," *Mater. Today: Proc.*, vol. 27, pp. 958-962, 2020, doi: 10.1016/j.matpr.2020.01.271.

[25] TS EN 459-2, Building lime - Part 2: Test methods, Ankara, Turkiye, 2021.

[26] K. Mermerdas, S. Ipek, N. H. Sor, E. S. Mulapeer and S. Ekmen, "The Impact of Artificial Lightweight Aggregate on the Engineering Features of Geopolymer Mortar," *Turkish J. Nat. Sci.*, vol. 9, no. 1, pp. 79-90, 2020, doi: 10.46810/tdfd.718895.

[27] B. A. Tayeh, A. M. Zeyad, I. S. Agwa and M. Amin, "Effect of elevated temperatures on mechanical properties of lightweight geopolymer concrete," *Case Stud. Constr. Mater.*, vol. 15, 2021, Art. no. e00673, doi: 10.1016/j.cscm.2021.e00673.

[28] M. A. Elrahman, S. Y. Chung and D. Stephan, "Effect of different expanded aggregates on the lightweight concrete properties," *Mag. Concr. Res.*, vol. 71, no. 2, pp. 95-107, 2019, doi: 10.1680/jmacr.17.00465.

[29] I. Hager, M. Sitarz and K. Mroz, "Fly-ash based geopolymer mortar for high-temperature application – effect of slag addition," *J. Clean. Prod.*, vol. 316, 2021, Art. no. 128168, doi: 10.1016/j.jclepro.2021.128168.

[30] R. Zhao and J. G. Sanjayan, "Geopolymer and portland cement concretes in simulated fire," *Mag. Concr. Res.*, vol. 63, no. 3, pp. 163-173, 2011, doi: 10.1680/macr.9.00110.

[31] K. M. Klima, K.Schollbach, H. J. H. Brouwers and Q. Yu, "Enhancing the thermal performance of class F fly ash-based geopolymer by sodalite," *Constr. Build. Mater.*, vol. 314, 2022, Art. no. 125574, doi: 10.1016/j.conbuildmat.2021.125574.

[32] M. S. T. Masoule, N. Bahrami, M. Karimzadeh, B. Mohasanati, P. Shoaei, F. Ameri and T. Ozbakkaloglu, "Lightweight geopolymer concrete: A critical review on the feasibility, mixture design, durability properties, and microstructure," *Ceram. Int.*, vol. 48, pp. 10347-10371, 2022, doi: 10.1016/j.ceramint.2022.01.298.

[33] M. F. Ali and M. M. V. Natrajan, "A review of geopolymer composite thermal properties," *IOP Conf. Series: Earth and Environmental Science*, vol. 822, 2021, Art. no. 012051, doi: 10.1088/1755-1315/822/1/012051.

[34] W. D. A. Rickard, C.S. Kealley and A. van Riessen, "Thermally induced microstructural changes in fly ash geopolymers: experimental results and proposed model," *J. Am. Ceram. Soc.*, vol. 98, no. 3, pp. 929-939, 2015, doi: 10.1111/jace.13370

[35] P. Payakaniti, N. Chuewangkam, R. Yensano, S. Pinitsoontorn and P. Chindaprasirt, "Changes in compressive strength, microstructure and magnetic properties of a high-calcium fly ash geopolymer subjected to high temperatures," *Constr. Build. Mater.*, vol. 265, 2020, Art. no. 120650, doi: 10.1016/j.conbuildmat.2020.120650.

Bitlis Eren Üniversitesi Fen Bilimleri Dergisi

Comparison of New and Old Optimization Algorithms for Traveling Salesman Problem on Small, Medium, and Large-scale Benchmark Instances

Md Al Amin HOSSAIN[1*], Züleyha YILMAZ ACAR[2]

[1]Selçuk University, Graduate School of Natural and Applied Sciences, Department of Information Technology Engineering
[2]Selçuk University, Faculty of Technology, Department of Computer Engineering
(ORCID: 0000-0003-3382-5300) (ORCID: 0000-0002-4488-478X)

Keywords: Benchmark, Metaheuristic, Optimization, Travelling Salesman Problem.

Abstract

The Traveling Salesman Problem (TSP), a prominent combinatorial optimization issue, is the subject of this study's evaluation of the performance of new and old optimization techniques. This paper seeks to expand knowledge of optimization techniques and how they might be applied to solve TSP challenges. The goal of the research is to compare various algorithms' scalability, convergence, and computation times on benchmark instances of several sizes. To achieve this goal, this paper carried out extensive testing using the Artificial Bee Colony, Grey Wolf Optimization, and Salp Swarm Algorithm as new optimization algorithms and the Genetic Algorithm, Ant Colony Optimization, and Simulated Annealing as old optimization algorithms. In small, medium, and large-scale benchmark cases, these algorithms were examined. The findings of this investigation show that the new optimization techniques are more convergent and scalable than the old ones, especially for medium-scale scenarios. They perform better in terms of solution quality by applying objective function values. The new methods also exhibit improved scalability, successfully adjusting to medium-scale instances. However, there were no discernible changes between the smaller and larger instances. This study makes an impact by offering insightful information about how well optimization methods perform while solving the TSP. Each algorithm's strengths and downsides have been reported, and these details offer useful guidance for choosing an algorithm for a certain scenario. The results also show the practical ramifications of applying novel optimization techniques, especially in medium-scale instances.

1. Introduction

The study of optimization algorithms has grown significantly in relevance for their effective and economical solutions to challenging issues. The Traveling Salesman Problem (TSP) stands out among these issues because of its numerous real-world applications across multiple sectors [1]. The TSP is a prevalent issue in operations research and computational science that requires figuring out the quickest path a traveling salesperson can take to visit a certain list of cities, specifically once, and then head back to the beginning point [2]. Even though its formulation appears easy, the TSP becomes more difficult as the number of cities increases exponentially, creating a combinatorial eruption of alternative solutions [3]. Optimization algorithms provide promising avenues for tackling the inherent complexity of the TSP. These algorithms utilize advanced search and optimization techniques to explore the solution space efficiently and find high-quality solutions within a reasonable timeframe [3]. By intelligently navigating through the vast solution space, optimization algorithms can discover near-

optimal or even optimal solutions, resulting in minimized travel distances, optimized resource allocation, and improved overall efficiency in real-world scenarios [4].

The primary objective of this research is to comprehensively investigate and evaluate the performance of different optimization algorithms for solving the TSP. Specifically, we aim to compare the effectiveness of well-established algorithms such as Genetic Algorithms (GA), Ant Colony Optimization (ABC), and Simulated Annealing (SA) as old optimization algorithms and Artificial Bee Colony (ABC), Salp Swarm Algorithm (SSA), and Grey Wolf Optimization (GWO) as new optimization algorithms in finding optimal or near-optimal solutions to the TSP. By assessing their performance in terms of solution quality, convergence, and computational efficiency, we seek to provide valuable insights into the strengths and limitations of these algorithms in addressing the TSP's complexities.

This study's contribution lies in its rigorous evaluation and comparison of multiple optimization algorithms for the TSP. While previous studies have individually examined the performance of these algorithms, this research takes a comprehensive approach by directly comparing their effectiveness side by side. This comparative analysis enables us to identify the algorithm(s) that exhibit superior performance characteristics for solving the TSP, offering valuable guidance for researchers and practitioners in selecting the most suitable algorithm for their specific problem instances. Through a thorough evaluation of their performance in terms of solution quality, convergence, and computational efficiency, this analysis strives to provide comprehensive insights into the strengths and limitations of each algorithm, thus facilitating informed decision-making for future research and practical applications. By shedding light on the capabilities and performance trade-offs of different optimization algorithms for the TSP, this study endeavors to advance the understanding and utilization of these algorithms in solving real-world optimization problems.

The following is the format of the study's accomplishing sections: The literature on TSP is delved into in Section 2. Section 3 provides a summary of the approaches used to address the relevant TSP issues, with an emphasis on optimization algorithms and metaheuristic techniques. The experimental results and subsequent discussions are outlined in Section 4. Conclusions from the study's findings are in Section 5.

2. Literature Review

The TSP is a renowned stochastic optimization concern that seeks the fastest route to travel between a starting point and a number of cities. Numerous optimization techniques have been created over time to effectively solve the TSP. The usefulness and performance of several optimization algorithms for the TSP have been thoroughly evaluated through prior comparative studies. The available literature is reviewed in this section, and the conclusions of these comparative investigations are outlined. The study undertaken by Şahin [4] presents new relocation and city selection functions that are incorporated into the bees algorithm to improve its TSP solution efficiency. This work demonstrates the efficiency of the approach in optimizing TSP solutions by notably increasing solution reliability, especially in cases with higher city counts. Li et al. [5] proposed the TSP solution using a differential edge information-based ACO. Heterogeneous population automation, tour creation, and smooth search operators improve candidate solution quality in the algorithm. The algorithm outperformed state-of-the-art algorithms on TSPLIB benchmark examples for mid-scale and small-scale TSP instances. It surpassed the other methods, proving its efficacy. Middle-scale TSP situations need faster solving. Ajayi et al. [6] sought TSP optimization methods. ACO was compared to Dijkstra's method and particle swarm optimization. The ACO algorithm excelled in route quality and total length, while Dijkstra's method excelled in minimum cost calculations. The research's application to other optimization problems, the need for further parameter exploration, and the lack of comparison with other state-of-the-art TSP algorithms were shortcomings. The algorithm's large-scale TSP scalability needs further study. Mondal and Srivastava [7] used evolutionary algorithms to solve a time-limited TSP with time limits for each city. The technique used cyclic crossover and specific mutation operations. The approach worked with benchmark instances in computations. The authors advised future research on multiple TSPs, probabilistic TSPs with fuzzy parameters, cost-limited TSPs, and bi-objective TSPs in a fuzzy environment, as well as travel time and asymmetric cases.

Hasan [8] compared the Bat Algorithm (BA) and ABC for solving the TSP. ABC found the best tour faster than BA, but BA needed more parameters and a better control method. The conclusion suggests future research into combining both algorithms in a system. Khajehzadeh et al. [9] introduced an Adaptive Salp Swarm Algorithm (ASSA) for geotechnical structure optimization. A new leader and follower

position updating equations improved exploration and prevented premature convergence. ASSA outperformed other optimization methods in benchmark tests. ASSA optimized geotechnical constructions while satisfying geotechnical and structural limit states, yielding cost-effective designs with superior results than competing methods. Liu et al. [10] tackled complex optimization challenges involving multiple objectives and modes within the TSP. A test problem generator designed for problems involving multiple depots and multiple traveling salesmen simultaneously creates instances that exhibit known Pareto optimal solutions. This tool with three or more objectives, test problem generators for specific features, and crossover operators that investigate a wider solution space are future research possibilities. Khan et al. [11] provide Modified GWO to solve the multiple objectives and covering constraints for the salesman problem. K-bit exchange, K-opt, and non-dominated sorting-based GA are incorporated to improve search and solution quality. Their proposed algorithm outperforms other multi-objective optimization algorithms on standard benchmark examples, proving its multi-objective-based problem-solving efficiency. The suggested approach can only handle this covering problem with crisp data sets and needs adjustments to accommodate imprecise data sets.

Panwar and Deep [12] stated the Discrete Salp Swarm Algorithm (DSSA) as an improved version of the SSA for solving the TSP. Swap, shift, and symmetry operators are used for global exploration and local exploitation, while the 2-opt technique improves local search. DSSA outperformed the GA, ABC, Spider Monkey, Jaya, Black Hole, and Symbiotic Organism Search on 45 TSP instances. The paper advises using DSSA to solve other discrete optimization problems like scheduling and routing issues. Khan and Maiti [13] offer a modified ABC algorithm to solve the TSP in their research paper. Swap sequences and city sequence swap procedures create various solution-updating rules in the algorithm. The suggested method is tested on TSPLIB benchmark TSP problems, showing its accuracy, efficiency, and consistency compared to existing algorithms. With appropriate changes, ABC can handle discrete optimization problems, including TSP, according to the study. The existing literature includes computational evaluations on large-scale TSP scenarios, algorithm behavior analysis under varied issue forms or restrictions, and a defined benchmarking methodology for fair contrasts. These gaps suggest a full comparative study to solve these constraints and better understand TSP optimization algorithms' strengths and drawbacks. The literature

review section summarizes TSP optimization techniques, evaluates comparative research, and highlights gaps that require a complete comparative investigation. A brief summary of the explored literature is listed in Table 1.

3. Methodology

This section covers the theoretical basis of TSP as well as how the performance of various optimization algorithms, including GA, ACO, SA, ABC, SSA, and GWO, was compared in this study. Figure 1 displays the methodological approach's structural flowchart.
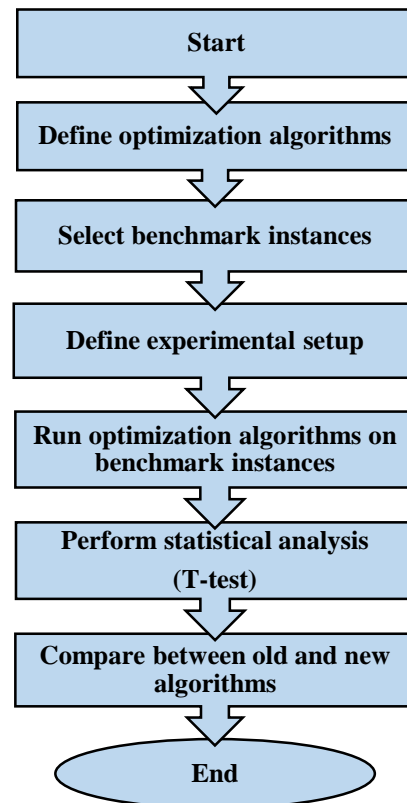

Figure 1. Structural flowchart of methodology.

3.1. Traveling Salesman Problem (TSP)

The TSP is a prominent optimization problem that includes finding the most efficient way for a salesperson to visit a series of cities and return to the beginning city [14]. The TSP reduces the salesman's route distance and cost [7]. This problem is formally described by creating choice variables to represent direct travel between cities and a distance or cost matrix to show distances between pairs of cities: a collection of n cities, $C = \{c_1, c_2, \ldots, c_n\}$, and a distance or cost matrix D, where D_{ij} is the distance between cities c_i and c_j. Some TSP variables and parameters represent :

Table 1. A brief overview of the reviewed literature

#	Author, Year	Used Algorithm	Problem – Average Value	Instance Size
1	Khan and Maiti, 2019 [13]	Swap sequece based ABC	berlin52 – 7543	small
2	Şahin, 2022 [4]	Improved bees algorithm	kroA100 – 21466	small
3	Ajayi et al., 2022 [6]	Particle swarm optimization and ant colony optimization with Dijkastra's algorithm	No specific problem	-
4	Hasan, 2022 [8]	Artificial bee colony and bat algorithm	No specific problem	-
5	Khajehzadeh et al., 2022 [9]	Adaptive salp swarm optimization	Real world problems	-
6	Panwar and Deep, 2022 [12]	Discrete salp swarm optimization	tsp225 – 3940.23	medium
7	Li et.al., 2023 [5]	Heuristic smoothing differential ACO	dsj1000 – 18897396.15	large
8	Mondal and Srivastava, 2023 [7]	cyclic crossover based GA	kro124p – 36612.94	small
9	Liu et al., 2023 [10]	Evolutionary mutltimodal multiobjective algorithm	TSPXEA problems	-
10	Khan et al., 2023 [11]	Decomposition based GWO	–	-

- Choice variables: If the salesman travels directly from city i to city j, $x_{ij} = 1$, *otherwise* $x_{ij} = 0$.
- Parameters: D_{ij} = Cost or distance between cities i and j.
  Mathematically optimize the TSP:
  $$minimize: Z = \Sigma\Sigma D_{ij} * x_{ij} \qquad (1)$$
- Subject to:
  1) For each city i, $\sum x_{ij} = 2$, ensuring that each city is visited precisely once.
  2) $\sum x_{ij} = 2$ for each city j to leave each city precisely once.
  3) The salesman travels to and from each city by setting $\sum x_{ij} - \sum x_{ij} = 0$

Solving the TSP involves finding choice variables x_{ij} that minimize the total distance or cost Z while fulfilling constraints. As the number of cities rises, solving the TSP optimally becomes an extremely difficult issue [3].

3.2. Optimization Algorithms and Benchmark Instances

In this study, a comprehensive comparison of optimization algorithms is conducted. A brief description is provided for each optimization algorithm, focusing on their underlying principles, search strategies, and important parameters that contribute to their performance. The algorithms considered in this research are GA, ACO, SA, ABC,

SSA, and GWO, all recognized for their efficacy in solving optimization problems.

I. Genetic Algorithm : Genetics-inspired GA optimizes. It addresses complicated problems like evolution [15]. GA analyzes potential solutions. Selection, crossover, and mutation generate new solutions. Repeat until a termination requirement is reached [7]. GA is utilized in many fields because it can handle complex search spaces and identify optimal or near-optimal answers. The stepwise GA algorithm to solve TSP is illustrated in Algorithm 1.

II. Ant Colony Optimization algorithm: ACO optimizes like ants. Pheromone trails help it find optimal solutions [16]. Ants use probabilistic pheromones and heuristics to solve problems. The quality of solutions determines pheromone trail updates. ACO promotes exploration and delays convergence [5]. It solved optimization difficulties. Algorithm 2 illustrates the stepwise ACO approach to solve TSP.

III. Simulated Annealing algorithm: Metallurgy's annealing process influenced SA's metaheuristic algorithm [17]. It starts with a solution and allows occasional "worse" steps based on a probability distribution to find better ones. Simulating cooling and adopting a worse answer reduces over time. SA helps avoid local optima and explore solution space [18]. Many optimization problems utilize it. Algorithm 3 depicts the stepwise SA algorithm to solve TSP.

Algorithm 1. GA algorithm to solve TSP

1: Initialize population *p* using the ***initialize_population*** method.
2: Calculate the fitness for each individual in *p* using the ***evaluate_fitness*** method.
3: Set the iteration counter *T = 0*.
4: Set *max_iterations = 1000.*
5: while *T < max_*iterations do
6: Select parents from the population *p* using the **selection** method.
7: Perform crossover on the selected parents with a probability of 0.8 using the ***crossover*** method to generate offspring.
8: Perform a mutation on the offspring with a probability of 0.2 using the ***mutation*** method.
9: Calculate fitness for each offspring using the ***evaluate_fitness*** method.
10: Replace the worst individuals in the population p with the best offspring.
11: Update the best solution found so far.
12: Increment iteration counter *T = T + 1*
13: End while
14:Return the best solution found (*best_individual*).

Algorithm 2. ACO algorithm to solve TSP

1: Initialize the pheromone matrix with *initial_pheromone*
2: Set *best_tour = none* and *best_distance = infinity.*
3: Start timer
4: Repeat *num_iterations* times:
5:　Generate tours using construct_tour method for num_ants.
6:　For each tour:
7:　　Calculate tour distance
8:　　If distance is less than *best_distance:*
9:　　　Update *best_tour* and *best_distance*
10: Update pheromone matrix using the *update_pheromone_matrix* method.
11: End repeat
12: Stop timer
13: Calculate *computation_time* as the difference between *start_time* and *end_time*.
13: Return *best_tour, best_distance,* and *computation_time*.

IV.　Artificial Bee Colony algorithm: Honeybee browsing inspired ABC, a population-based metaheuristic algorithm [19]. It simulates bee colony intelligence to find optimal solutions. The algorithm uses employed, bystanders, and scout bees. Onlooker bees choose solutions based on fitness, while employed bees move solutions across the search space. Scout bees randomly investigate new areas [20]. ABC solves complicated optimization issues quickly and easily. Algorithm 4 illustrates the stepwise ABC approach to solve TSP.

V. Salp Swarm Algorithm (SSA): The SSA optimizes marine invertebrates, salps, and swarming.

Buoyancy guides salps to better solutions when traversing the search space [21]. The SSA has found optimal solutions to several optimization issues [22]. The stepwise SSA algorithm to solve TSP is illustrated in Algorithm 5.

Algorithm 3. SA algorithm to solve TSP

1: Initialize Simulated Annealing with *cities, initial_temperature, cooling_rate, num_iterations*
2: Initialize the distances matrix by calculating the distances between cities.
3: Define the *calculate_tour_distance* function to calculate the total distance of a tour.
4: Define the *generate_neighbor* function to generate a neighbor tour by swapping two cities.
5: Define the *acceptance_probability* function to calculate the acceptance probability based on *current_distance, new_distance*, and temperature.
6: Initialize *current_tour* with a random tour.
7: Initialize *best_tour* and *current_distance* as *current_tour* and its distance.
8: Initialize *best_distance* as *current_distance* and temperature as *initial_temperature.*
9: Start the timer *T.*
10: Repeat *num_iterations* times:
11: Generate a new tour, *new_tour*, as a neighbor of *current_tour.*
12: Calculate the distance of *new_tour, new_distance*
13:　If *acceptance_probability* (*current_distance, new_distance, temperature*) is greater than a random number:
14:　　Update *current_tour* and *current_distance* as *new_tour* and *new_distance*
15:　If *current_distance* is less than *best_distance:*
16: Update *best_tour* and *best_distance* as *current_tour* and *current_distance.*
17: Decrease temperature by multiplying with *cooling_rate.*
18: End the timer.
19: Calculate *computation_time* as the difference between *start_time* and *end_time.*
20: Return *best_tour, best_distance*, and *computation_time.*

Algorithm 4. ABC algorithm to solve TSP

1: Initialize population *p*
2: Set iteration counter *T = 0.*
3: Set *max_iterations = 1000*
4: while *T < max_iterations* do
5:　Calculate fitness for each individual in *p* using f_i
6:　Perform an employed bees phase to generate a new population.
　　　list *new_population*
　　　select and swamp two positions (*i* and *j)* from the bee's solution.
7:　Perform the onlooker bee phase to select the population based on fitness
　　　list *selected_population*

Calculate the selection probabilities based on the fitness values.

8: Perform the scout bee phase to replace poor solutions.

Find the index of the bee with the best fitness (min distance)

Find the best fitness value

list *new_population*

9: Update the best solution found so far.

Find the index of the bee with the best fitness (min distance)

Update the best solution and best distance if the current best fitness is better

10: Increment iteration counter *T = T + 1*

11: End while

12: Return the best solution found.

VI. Grey Wolf Optimization algorithm: Grey wolves inspired GWO's metaheuristic algorithm. It simulates wolf leadership and cooperative hunting to find the best solutions. Alpha, beta, delta, and omega wolves signify hierarchy in the algorithm [23]. Wolves position themselves according to the alpha and hunting distance. Exploration and exploitation help GWO uncover optimal solutions [24]. It solved optimization difficulties. Algorithm 6 depicts the stepwise GWO algorithm to solve TSP.

Algorithm 5. SSA algorithm to solve TSP

1: Initialize salps population
2: Calculate the distance for each salp in the population using the given cities.
3: Set *best_salp* as None
4: Set the iteration counter to 0.
5: Set *max_iterations = 1000.*
6: while *iteration_counter < max_iterations* do
7: For each salp in the population, do
8: If *best_salp* is None or the distance of the current salp is smaller than the distance of *best_salp,* then
9: set *best_salp* as the current salp
10: Create a new salp by updating the position of the current salp based on the *best_salp.*
11: Update the population with the new salps.
12: Increment the iteration counter by 1.
13: End while
14: Return *best_salp(best_solution)*

Algorithm 6. GWO algorithm to solve TSP

1: Initialize wolves
2: Set the iteration counter.
3: Set the maximum number of iterations
4: while *iteration_counter < max_iterations* do
5: Evaluate fitness for each wolf
6: Update the best wolf found so far
7: Determine alpha, beta, and delta wolves as the best, second-best, and third-best solutions
8: For each wolf, do

9: Update the position of the wolf based on alpha, beta, and delta.
10: End for
11: Increment *iteration_counter*
12: End while
13: Return the best wolf found (*best_solution).*

4. Experimental Analysis

This section examines many aspects through a variety of experiments. This includes a close study of how to choose benchmark instances, the specifics of the experimental layout, how convergence works across optimization strategies, and how well statistical analysis works. Additionally, this segment provides a complete discussion of the insights gained from the results as well as a detailed explanation of the outcomes.

To assess the performance of the optimization algorithms, a selection of benchmark instances is made from the TSPLIB library [25]. The chosen instances encompass a range of problem sizes and complexities, ensuring a diverse set of challenges for the algorithms. The benchmark instances include burma14, berlin52, and kroA100 as small-sized instances, while ts225 and att532 represent medium-sized instances. Additionally, rat783 and dsj1000 are selected as large-sized instances. These carefully chosen instances enable a comprehensive analysis of the algorithms' performance across various problem sizes and complexities.

3.1. Experimental Setup

Table 2 presents common and specific parameters for several optimization algorithms, including GA, ACO, SA, ABC, SSA, and GWO. The population size is set to 100 for all algorithms with 1000 iterations. GA uses a crossover rate of 0.8 and a mutation rate of 0.2. ACO employs alpha and beta values of 1.0 and 5.0, respectively. SA starts with an initial temperature of 1000 and a cooling rate of 0.95. ABC has a limit of 5 for employed bee trials. Performance metrics for evaluation include the best optimal solution, average solution, standard deviation, standard deviation (%), and computation time. The algorithms are applied to different sets of city coordinates, including burma14, berlin52, kroA100, ts225, att532, rat783, and dsj1000.

3.2. The Statistical Tests for Comparing Performance

To evaluate the statistical significance of the obtained results, appropriate statistical tests will be employed.

Table 2. The common and specific parameters of optimization algorithms used

Parameter	Algorithm & Value					
	GA	ACO	SA	ABC	SSA	GWO
Population Size	100					
No. of Iterations	1000					
Crossover Rate	0.8					
Mutation Rate	0.2					
Alpha		1.0				
Beta		5.0				
Evaporation Rate		0.5				
Initial Temperature			1000			
Cooling Rate			0.95			
Limit	5					
City Coordinates	burma14, berlin52, kroA100, ts225 and att532, rat783 and dsj1000					
Performance Metrics	best optimal solution, average solution, standard deviation, standard deviation (%), and computation time					

Specifically, t-tests will be utilized to compare the convergence and efficiency of the optimization algorithms. The t-tests enable the determination of whether there exist statistically significant differences in the performance of the algorithms in terms of their convergence to the optimal solution. The t-test is a widely used statistical test that assesses the difference between the means of two groups [26]. In this case, the groups correspond to the different optimization algorithms under investigation. The t-test calculates a t-statistic, which measures the extent of the difference between the means of the two groups relative to the variability within each group (in this case, the algorithms). A larger absolute t-statistic indicates a greater difference between the means. The t-statistic is calculated using the following equation (2):

$$t = \frac{(mean_1 - mean_2)}{\sqrt{(std_1^2 / n_1)} + \sqrt{(std_2^2 / n_2)}} \qquad (2)$$

Where $mean_1$ and $mean_2$ are the sample means of the best optimal solution for the two algorithms, std_1 and std_2 are the sample standard deviations, and n_1 and n_2 are the sample sizes. The p-value, which the t-test also presents, denotes the likelihood of detecting the determined difference in means under the presumption that there is no real difference between the groups. A lower p-value indicates greater statistical significance and stronger evidence against the null hypothesis of no difference. The significance level in this study is 0.05, which denotes a 5% chance of detecting significant differences as a result of random oscillation. We deny the null assumption and endorse the alternative

hypothesis, determining that the algorithms differ effectively if the computed p-value is smaller than the significance level. This technique evaluates optimization algorithms across benchmark instances. The statistical tests reveal considerable differences in the convergence and effectiveness of the algorithms, revealing their relative performance and applicability for problem instances of varied sizes and complexities.

3.3. Results Assessments

In this paper, all of the suggested algorithms were coded in Python in the Anaconda environment using Matplotlib, Seaborn, SciPy, and the Pandas library, and several estimates were made. Table 3 presents a comprehensive comparison of three new metaheuristic algorithms— ABC, SSA, and GWO — on various instances of the TSP of different sizes. Table 3 includes seven TSP instances ranging from 14 to 1000 nodes, and for each instance, it provides the best optimal solution (best opt.), average solution (avg), standard deviation (std), standard deviation percentage (std%), and time taken by each algorithm to solve the TSP instance.

From Table 3, we can observe that for smaller TSP instances such as burma14 and berlin52, all three algorithms perform relatively well, with ABC and SSA providing the best solutions. The average solution metric reveals the algorithms' overall performance in finding solutions, with ABC consistently delivering low average solutions across all instances. The standard deviation metric highlights the stability of the algorithms' solutions, with ABC and GWO exhibiting low standard deviations.

Table 4 presents a detailed performance comparison of the GA, ACO, and SA algorithms on various instances of the TSP categorized into small,

medium, and large-scale instances. For small-scale instances, such as burma14, berlin52, and kroA100, the algorithms demonstrate similar trends. GA achieves the best optimal solutions of 42, 24,515, and 153,460, respectively. ACO and SA also perform well, with ACO achieving optimal solutions of 31, 7,677, and 22,946 and SA achieving optimal solutions of 30, 12,490, and 74,583 for the respective instances. The average solutions for these instances follow a similar pattern, with GA, ACO, and SA showing competitive performance. In the medium-scale instances, ts225 and att532, ACO outperforms the other algorithms. It achieves the best optimal

solutions of 133,285 and 99,268, respectively, whereas GA and SA achieve optimal solutions of 1,478,608 and 1,035,202 for ts225 and 1,538,293 and 1,034,340 for att532. The average solutions also show ACO as the top performer. For large-scale instances, rat783 and dsj1000, GA demonstrates its strength by achieving the best optimal solutions of 170,626 and 534,398,427, respectively. ACO and SA lag behind in these instances, with ACO achieving optimal solutions of 10,431 and 22,404,181, and SA achieving optimal solutions of 130,100 and 417,124,012.

In Table 4, we can see that the Std(%) values

Table 3. Performance comparison of new metaheuristic algorithms on tsp instances of diverse sizes

Algorithm	Performance metrics	Problem instance						
		burma14	berlin52	kroA100	ts225	att532	rat783	dsj1000
ABC	best opt.	66	31671	181460	1649553	1663663	184334	567420224
	avg	57	29331	170553	1585724	1612119	178992	555245806
	std	6	1447	8172	48380	30457	2845	7572149
	std (%)	11.83	4.93	4.79	3.05	1.88	1.58	1.35
	time (s)	4	14	29	63	163	239	317
SSA	best opt.	13	12879	95966	1116522	1087426	139897	475808151
	avg	57	29380	169162	1587326	1613307	179095	554705324
	std	7	1617	9358	43940	34175	2994	8011712
	std (%)	12.72	5.5	5.53	2.76	2.11	1.67	1.44
	time (s)	3	16	29	67	177	277	358
GWO	best opt.	21	16410	116098	1245252	1252724	152429	474605615
	avg	21	16485	116455	1247805	1255686	152592	475494467
	std	1	824	3402	25904	25024	1446	6689991
	std (%)	7.53	4.99	2.92	2.07	1.99	0.94	1.40
	time (s)	7	28	46	105	279	396	511

for all three algorithms are relatively low, ranging from 0.12% to 10.06%. This suggests that the algorithms are relatively robust and can provide consistent solutions across different TSP instances.

In Table 5, the t-test analysis revealed that there were no statistically significant differences between the performance of different optimization algorithms when considering all instances. However, in small

Table 4. Performance comparison of old metaheuristic algorithms on TSP instances of diverse sizes

Algorithm	Performance metrics	Problem instance						
		burma14	berlin52	kroA100	ts225	att532	rat783	dsj1000
GA	best opt.	42	24515	153460	1478608	1538293	170626	534398427
	average	57	29366	169691	1595693	1613034	179461	556043666
	std	5	1618	7476	44677	33547	2986	7717300
	std (%)	10.06	5.51	4.41	2.79	2.07	1.66	1.38
	time (s)	3	10	22	76	330	688	1200
ACO	best opt.	31	7677	22946	133285	99268	10431	22404181
	average	38	10838	32636	187488	139957	14227	30817615
	std	3	854	2219	11950	4937	395	947631
	std (%)	9.56	7.88	6.79	6.37	3.52	2.77	3.07
	time (s)	68	449	1476	4966	18075	27890	43420
SA	best opt.	30	12490	74583	904130	1035202	130100	417124012
	average	47	22784	190729	299669	983336	72635	557653234
	std	5	749	2183	12473	6616	526	701515
	std (%)	12.56	3.28	1.14	4.16	0.67	0.72	0.12
	time (s)	0.02	0.05	0.11	0.18	0.36	0.63	0.66

and large instances, no significant differences were observed either. On medium instances, the GA algorithm showed significantly better performance compared to the ACO, SA, ABC, SSA, and GWO algorithms, indicating its effectiveness in solving medium-sized TSP problems.

Table 5. T-test analysis between all old and new algorithms on different sizes ınstances for the best opt. solution

Instances	Algorithm 1	Algorithm 2	P-value	Significance	T-statistic
Small-scale instances (burma14, berlin52, kroA100)	GA	ACO	0.364547	-**	1.022030
	GA	SA	0.597260	-	0.573092
	ACO	SA	0.477207	-	-0.783348
	ABC	SSA	0.613100	-	0.547580
	ABC	GWO	0.707362	-	0.403291
	SSA	GWO	0.875125	-	-0.167471
	GA	ABC	0.880887	-	-0.159660
	GA	SSA	0.703137	-	0.409523
	GA	GWO	0.812443	-	0.253410
	ACO	ABC	0.340987	-	-1.079814
	ACO	SSA	0.445224	-	-0.845939
	ACO	GWO	0.409399	-	-0.920508
	SA	ABC	0.525536	-	-0.694607
	SA	SSA	0.857553	-	-0.191376
	SA	GWO	0.742382	-	-0.352314
Medium-scale instances (ts225&att532)	GA	ACO	**0.000608***	s**	40.530090
	GA	SA	**0.017399**	s	7.482005
	ACO	SA	**0.006236**	s	-12.604129
	ABC	SSA	**0.000849**	s	34.303569
	ABC	GWO	**0.000383**	s	51.060030
	SSA	GWO	**0.010278**	s	-9.787848
	GA	ABC	**0.040269**	s	-4.831471
	GA	SSA	**0.006605**	s	12.243384
	GA	GWO	**0.013171**	s	8.627054
	ACO	ABC	**0.000143**	s	-83.651662
	ACO	SSA	**0.000515**	s	-44.040645
	ACO	GWO	**0.000236**	s	-65.046094
	SA	ABC	**0.009082**	s	-10.421690
	SA	SSA	0.187524	-	-1.970884
	SA	GWO	0.051037	-	-4.255207
Large-scale instances (rat783 & dsj1000)	GA	ACO	0.439222	-	0.957841
	GA	SA	0.878502	-	0.173106
	ACO	SA	0.444202	-	-0.945509
	ABC	SSA	0.912785	-	0.123813
	ABC	GWO	0.911569	-	0.125553
	SSA	GWO	0.998748	-	0.001771
	GA	ABC	0.970035	-	-0.042397
	GA	SSA	0.942148	-	0.081953
	GA	GWO	0.940911	-	0.083711
	ACO	ABC	0.438202	-	-0.960386
	ACO	SSA	0.441407	-	-0.952411
	ACO	GWO	0.441436	-	-0.952339
	SA	ABC	0.850683	-	-0.213561
	SA	SSA	0.934531	-	-0.092787
	SA	GWO	0.935760	-	-0.091037

** The "Significance" column indicates the significance level (s for significant, - for not significant) of the difference between the algorithms.
* Significant p-values are bolded.

From Table 6, the t-test results of the average performance metric for medium-scale instances indicate statistically significant differences in the performance of certain optimization algorithms. On the contrary, the t-test findings for Table 7 show that there were no significant differences in the

computation time performance of the majority of algorithm pairs. Table 8 presents the results of a statistical analysis comparing the performance of two algorithm groups, "old" and "new," based on different metrics. The P-values indicate the statistical significance of the differences observed, while the T-statistic represents the magnitude of the differences.

Table 6. T-test results of all algorithms on medium-scale instances for average solution

Instances	Algorithm 1	Algorithm 2	P-value	Significance	T-statistic
	GA	ACO	**0.000308**	s	56.947378
	GA	SA	0.106373	-	2.815849
	ACO	SA	0.297916	-	-1.394332
	ABC	SSA	0.946	-	-0.075331
	ABC	GWO	**0.001570**	s	25.206599
	SSA	GWO	**0.001513**	s	25.677421
Medium-scale	GA	ABC	0.763239	-	0.344630
instances	GA	SSA	0.819775	-	0.259
(ts225&att532)	GA	GWO	**0.000729**	s	37.024449
	ACO	ABC	**0.000359**	s	-52.795613
	ACO	SSA	**0.000355**	s	-53.041839
	ACO	GWO	**0.000490**	s	-45.164984
	SA	ABC	0.107474	-	-2.798749
	SA	SSA	0.107205	-	-2.802892
	SA	GWO	0.216172	-	-1.785087

Table 7. T-test results of all algorithms on all and large-scale instances for average solution

Instances	Algorithm 1	Algorithm 2	P-value	Significance	T-statistic
	GA	ACO	0.055936	-	-2.115957
	GA	SA	0.078385	-	1.924068
	ACO	SA	0.050874	-	2.169134
	ABC	SSA	0.846396	-	-0.197952
All instances	ABC	GWO	0.399972	-	-0.872663
	SSA	GWO	0.505295	-	-0.686749
	GA	ABC	0.254208	-	1.197562
	GA	SSA	0.289645	-	1.107834
	GA	GWO	0.482505	-	0.724739
	ACO	ABC	0.052600	-	2.150456
	ACO	SSA	0.052810	-	2.148232
	ACO	GWO	0.053769	-	2.138136
	SA	ABC	**0.026046**	s	-2.537748
	SA	SSA	**0.028856**	s	-2.481920
	SA	GWO	**0.023898**	s	-2.584516
	GA	ACO	**0.046622**	s	-4.467759
	GA	SA	0.066393	-	3.684980
	ACO	SA	**0.044302**	s	4.591675
	ABC	SSA	0.555104	-	-0.702535
	ABC	GWO	0.127446	-	-2.525964
Large-scale	SSA	GWO	0.192832	-	-1.933704
instances (rat783	GA	ABC	0.123737	-	2.571889
& dsj1000)	GA	SSA	0.136871	-	2.417203
	GA	GWO	0.202491	-	1.869440
	ACO	ABC	**0.044954**	s	4.555899
	ACO	SSA	**0.045048**	s	4.550807
	ACO	GWO	**0.045375**	s	4.533231
	SA	ABC	**0.019205**	s	-7.111666
	SA	SSA	**0.015948**	s	-7.823580
	SA	GWO	**0.015742**	s	-7.875739

Table 8. T-test results for old and new two groups on all sizes instances for best opt., avg, std (%) and time

Metric	Instances	Algo. group1	Algo. group2	P-value	Significance	T-statistic
Best opt. solution	All	old	new	0.609777	-	-0.514437
	Small-scale	old	new	0.531586	-	-0.639439
	medium-scale	old	new	0.120642	-	-1.696514
	Large-scale	old	new	0.563546	-	-0.597362
Avg	All	old	new	0.702805	-	-0.384281
	Small-scale	old	new	0.812272	-	-0.241451
	medium-scale	old	new	**0.041796**	s	-2.333548
	Large-scale	old	new	0.667024	-	-0.443244
Std(%)	All	old	new	0.498638	-	0.682849
	Small-scale	old	new	0.626244	-	0.496570
	medium-scale	old	new	0.270391	-	1.166723
	Large-scale	old	new	0.650603	-	0.466863
Time(s)	All	old	new	0.072534	-	1.844435
	Small-scale	old	new	0.226801	-	1.256978
	medium-scale	old	new	0.229646	-	1.279392
	Large-scale	old	new	1.541858	-	0.154134

3.4. Discussions

This part initiates a look into consulting the tables and figures that illustrate algorithmic contrasts in the TSP solution. It next explores the differences in algorithmic efficiency that are found among various subgroups of instances. The effects of these divergences are analyzed in order to shed light on the applicability of algorithms with regard to TSP issue sizes and complications.

According to Table 3, as the size of the TSP instances increases, GWO tends to outperform ABC and SSA in terms of finding the best optimal solution, which is depicted in the box plot in Figure 2 for three different sizes of instances. Larger cases show this tendency due to GWO's boosted exploration and exploitation in complicated and broad search environments. GWO's techniques may help it explore wider solution landscapes and find superior optimal solutions in larger TSP cases than ABC and SSA. GWO's adaptability and robustness in scaling up to increasingly complicated problem sizes in the TSP domain may explain its efficiency in handling larger instances. This suggests that GWO is more effective at handling larger TSP instances.

The standard deviation percentage metric normalizes the standard deviation relative to the best optimal solution, indicating how close the solutions are to the best. ABC and GWO consistently achieve low standard deviations because, with their specific exploration and exploitation tactics, they can converge on optimal solutions and preserve solution consistency across TSP examples. Additionally, the time taken by each algorithm to solve the TSP instances increases as the size of the instances increases. GWO is the fastest algorithm, followed by

ABC and SSA. This indicates that GWO is efficient in terms of computation time, making it a favorable choice for solving larger TSP instances. All of these convergences are illustrated in Figure 3 via the line plot approach and in Figure 4 via the box plot approach.

As shown in Figure 5 and Figure 6, ACO excels over GA and SA in various TSP scenarios due to its effective optimization approaches and adaptability. In small-scale instances, ACO surpasses GA and SA with competitive optimal solutions with lower values. ACO outperforms GA and SA in optimal and average medium-scale solutions like ts225 and att532. GA outperforms ACO and SA in optimal solutions in large-scale examples like rat783 and dsj1000, while ACO remains competitive with extended computation times, demonstrating its TSP endurance. ACO's strength to balance exploration and exploitation in slightly complicated solution domains makes it better than GA and SA in medium-scale cases. ACO's pheromone-based exploration and local search techniques usually handle medium-scale situations with diligent optimization. In these TSP situations, ACO gets to high-quality solutions faster than GA and SA because it quickly looks at a lot of different solutions and takes advantage of potential areas.

Overall, the comparison highlights the varying performance of the algorithms based on the problem instance size. GA shows promise for small and large-scale instances, while ACO consistently performs well across different scales. SA demonstrates effectiveness for small-scale instances but struggles to scale effectively for larger problems. Researchers should consider these performance differences and choose the appropriate algorithm

based on the problem size and optimization requirements. All of these convergences of small, medium, and large-scale instances are illustrated in

Figure 6 via the line plot approach as well as in Figure 7 via the box plot approach
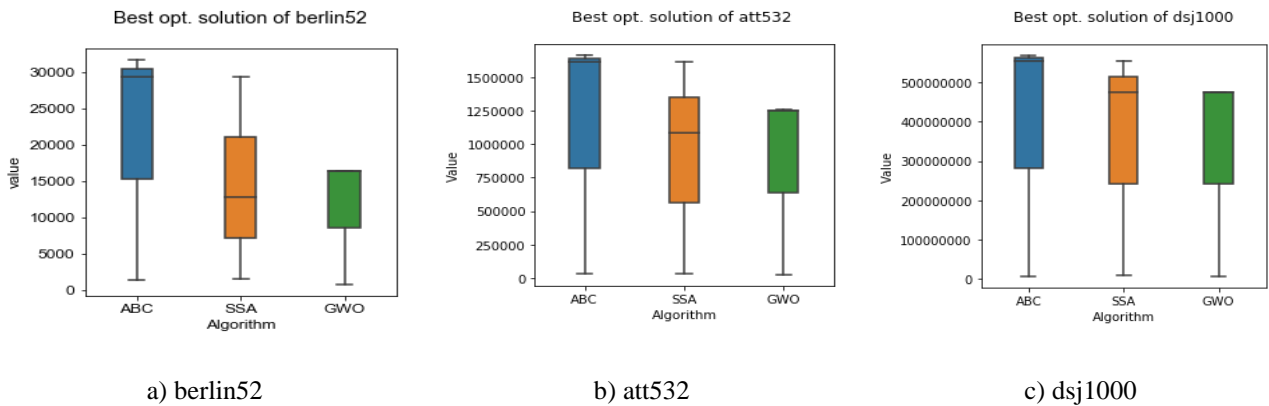

a) berlin52   b) att532   c) dsj1000

Figure 1. Box plot convergence of new algorithms on three different sizes instances for best opt. Solution.

a) berlin52   b) att532   c) dsj1000
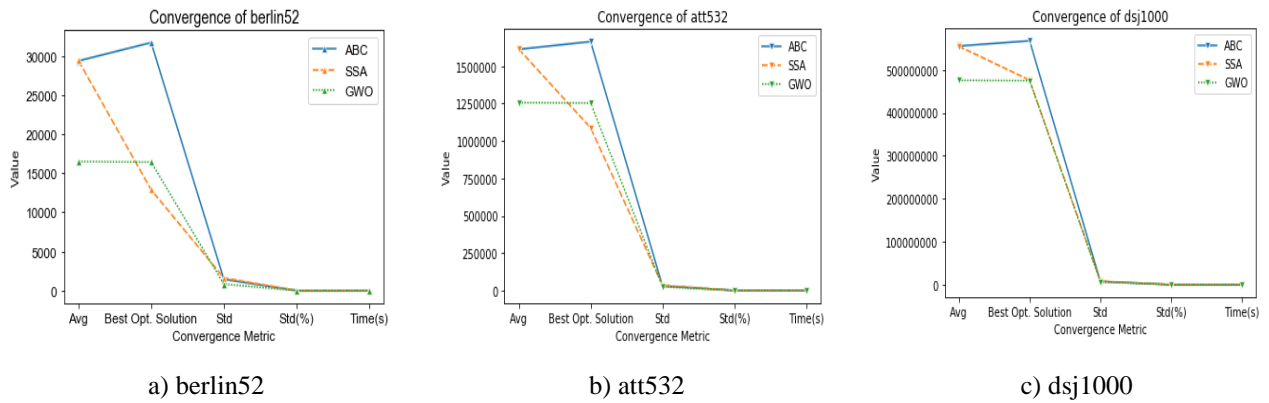
Figure 3. Line plot convergence of new algorithms on three different sizes instances for all performance metrics.

a) berlin52   b) att532   c) dsj1000
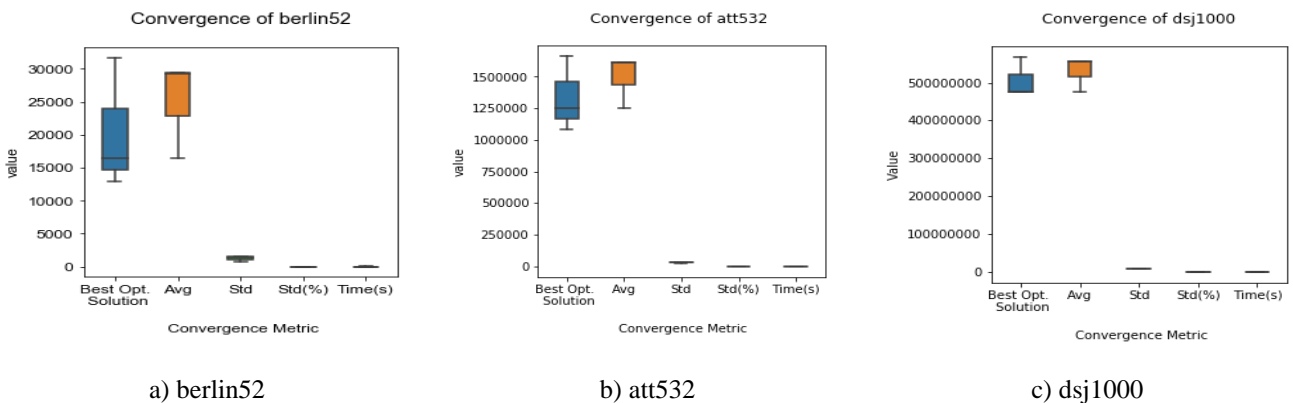
Figure 4. Box plot convergence of new algorithms on three different sizes instances for all performance metrics.

Table 6 reveals that GA and GWO outperform other algorithms in medium-sized optimization problems like TSP due to their convergence, exploration, and exploitation capabilities. GA, known for its population-based search and crossover-mutation mechanisms, is effective in exploring diverse solution

spaces but less efficient in convergence. GWO, inspired by grey wolves' hunting behaviors, utilizes promising search space areas more efficiently, improving convergence and solution quality for medium-scale instances. The t-test results for Table 7 provide some interesting findings for two groups of

instances. GA, SA, and ABC exhibit identical outcomes in the "All instances" segment, with insignificant variations in the average solution values. On the other hand, ACO performs differently from GA, SA, and ABC, showing substantive variations. Interestingly, ACO and SA show significant variances when contrasted with several algorithms in the "Large-scale instances," indicating varying effectiveness in handling larger-scale TSP situations. In both segments, ABC, SSA, and GWO show stability with each other as well as with other algorithms.

In the most significant evaluations from Table 8 for the metric "best opt. solution," there is no significant difference between the old and new algorithm groups across all instances, including small-scale, medium-scale, and large-scale cases. In terms of average performance (Avg), there is no significant difference between the old and new algorithm groups for all instances and small-scale instances. However, for medium-scale instances, the new algorithm group shows a statistically significant improvement with a lower T-statistic value.

Regarding the metric "Std(%)", which represents the standard deviation, there is no significant difference between the old and new algorithm groups for all instances and small-scale instances. However, for medium-scale instances, the new algorithm group exhibits a statistically significant improvement with a higher T-statistic value.

Lastly, in terms of the "Time(s)" metric, which measures the execution time, there is no significant difference between the old and new algorithm groups for all instances and small-scale instances. However, for medium-scale instances, the new algorithm group shows a statistically significant improvement with a higher T-statistic value. Overall, the results suggest that the new algorithm group shows promising improvements in terms of average performance, standard deviation, and execution time for medium-scale instances, and there is no significant difference between the two groups for large-scale instances. while no significant differences are observed in other instances. The overall convergence graph of all algorithms on att532 as a medium-scale instance is shown in Figure 8.

| a) berlin52 | b) att532 | c) dsj1000 |
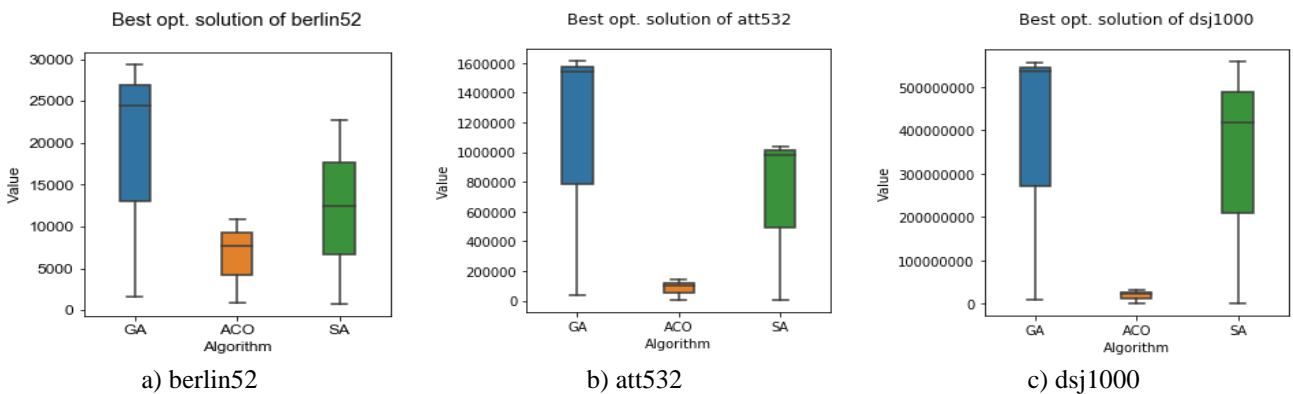
Figure 5. Box plot convergence of old algorithms on three different sizes instances for best opt. Solution.

| a) berlin52 | b) att532 | c) dsj1000 |
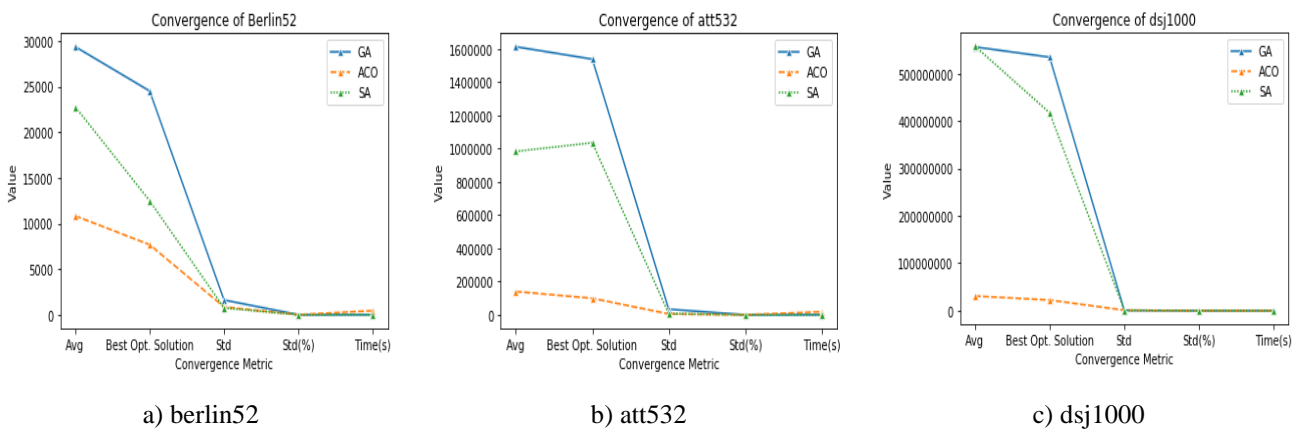
Figure 6. Plot convergence of old algorithms on three different sizes instances for all performance metrics.

a) berlin52   b) att532   c) dsj1000
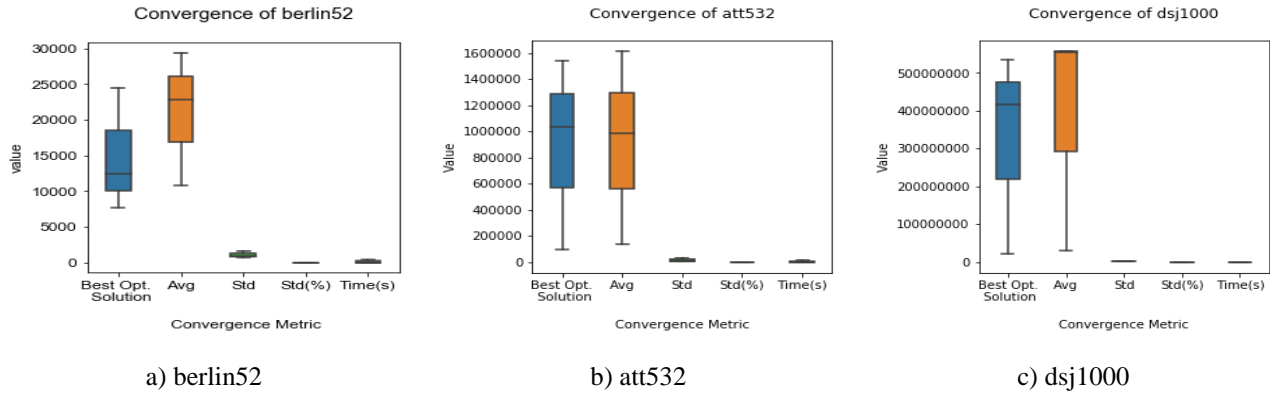
Figure 7. Box plot convergence of old algorithms on three different sizes instances for all performance metrics
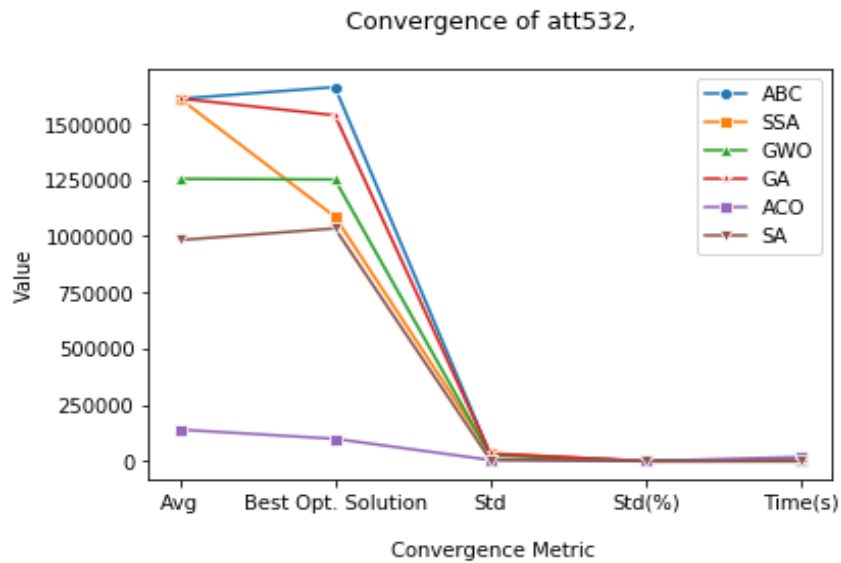
Figure 8. Overall convergence of all algorithms on att532 instances for all performance metric.

5. Conclusion

The study compared TSP optimization techniques and found significant improvements in convergence and scalability for medium-scale instances using new algorithms (ABC, SSA, and GWO). However, small and large-scale incidents did not differ significantly. The new algorithms also showed significant computational time enhancements for medium-scale instances. These findings can help researchers and practitioners choose TSP optimization techniques, but the study's limitations include a restricted collection of benchmark instances and the use of a few optimization strategies.

Future TSP optimization research should include more benchmark examples of small, medium, and large-scale scenarios, including real-world examples. There's an opportunity to refine and customize optimization algorithms for small and large-scale instances to improve efficiency and address the performance gap identified in this study. Looking into hybrid techniques that take the best parts of several algorithms and combine them may help find better solutions that take less time to compute. This is especially true for large-scale scalability.

Contributions of the authors

M.A.A.H. conducted the core research, devised the experimental setup, wrote the paper, and was vital in analyzing the findings and formulating the conclusions. Z.Y.A. contributed to the literature review, edited the paper, and provided theoretical guidance.

Conflict of Interest Statement

There is no conflict of interest between the authors.

References

[1] H. Cheng, H. Zheng, Y. Cong, W. Jiang, and S. Pu, "Select and Optimize : Learning to Solve Large-Scale Traveling Salesman Problem," in *Proceedings of The 26th International Conference on Artificial Intelligence and Statistics*, 2022, vol. 206, pp. 1219–1231.

[2] Y. Wu, T. Weise, and R. Chiong, "Local Search for the Traveling Salesman Problem: A Comparative Study," in *Proceedings of 2015 IEEE 14th International Conference on Cognitive Informatics and Cognitive Computing, ICCI*CC 2015*, 2015, pp. 213–220. doi: 10.1109/ICCI-CC.2015.7259388.

[3] M. DİRİK, "Optimization: A comparison of recent meta-heuristic optimization algorithms using benchmark function," *J. Math. Sci. Model.*, vol. 5, no. 3, pp. 113–124, 2022, doi: 10.33187/jmsm.1115792.

[4] M. ŞAHİN, "Improvement of the Bees Algorithm for Solving the Traveling Salesman Problems," *Bilişim Teknol. Derg.*, vol. 15, no. 1, pp. 65–74, 2022, doi: 10.17671/gazibtd.991866.

[5] W. Li, C. Wang, Y. Huang, and Y. ming Cheung, "Heuristic smoothing ant colony optimization with differential information for the traveling salesman problem," *Appl. Soft Comput.*, vol. 133, p. 109943, 2023, doi: 10.1016/j.asoc.2022.109943.

[6] B. A. Ajayi, M. A. Magaji, S. Musa, R. F. Olanrewaju, and A. A. Salihu, "A Comparative Analysis of Optimization Heuristics Algorithms as Optimal Solution for Travelling Salesman Problem," in *Proceedings of the 5th International Conference on Information Technology for Education and Development (ITED) 2022*, 2022, pp. 3–10. doi: 10.1109/ITED56637.2022.10051627.

[7] M. Mondal and D. Srivastava, "A Genetic Algorithm-Based Approach to Solve a New Time-Limited Travelling Salesman Problem," *Int. J. Distrib. Syst. Technol.*, vol. 14, no. 2, pp. 1–14, 2023, doi: 10.4018/IJDST.317377.

[8] L. S. Hasan, "Artificial Bee Colony Algorithm and Bat Algorithm for Solving Travel Salesman Problem," *Webology*, vol. 19, no. 1, pp. 4185–4193, 2022, doi: 10.14704/web/v19i1/web19276.

[9] M. Khajehzadeh, A. Iraji, A. Majdi, S. Keawsawasvong, and M. L. Nehdi, "Adaptive Salp Swarm Algorithm for Optimization of Geotechnical Structures," *Appl. Sci.*, vol. 12, no. 13, 2022, doi: 10.3390/app12136749.

[10] Y. Liu, L. Xu, Y. Han, X. Zeng, G. G. Yen, and H. Ishibuchi, "Evolutionary Multimodal Multiobjective Optimization for Traveling Salesman Problems," *IEEE Trans. Evol. Comput.*, pp. 1–1, 2023, doi: 10.1109/tevc.2023.3239546.

[11] I. Khan, K. Basuli, and M. K. Maiti, "Multi-objective covering salesman problem: a decomposition approach using grey wolf optimization," *Knowl. Inf. Syst.*, vol. 65, no. 1, pp. 281–339, 2023, doi: 10.1007/s10115-022-01752-y.

[12] K. Panwar and K. Deep, "Discrete Salp Swarm Algorithm for Euclidean Travelling Salesman Problem," *Appl. Intell.*, 2022, doi: 10.1007/s10489-022-03976-5.

[13] I. Khan and M. K. Maiti, "A swap sequence based Artificial Bee Colony algorithm for Traveling Salesman Problem," *Swarm Evol. Comput.*, vol. 44, no. November 2016, pp. 428–438, 2019, doi: 10.1016/j.swevo.2018.05.006.

[14] S. Sobti and P. Singla, "Solving Travelling Salesman Problem Using Artificial Bee Colony Based Approach," *Int. J. Eng. Res. Technol.*, vol. 2, no. 6, pp. 186–189, 2013, [Online]. Available: http://www.ijert.org/browse/volume-2-2013/june-2013-edition?download=3722:solving-travelling-salesman-problem-using-artificial-bee-colony-based-approach&start=20

[15] S. Sharma and V. Jain, "A Novel Approach for Solving TSP Problem Using Genetic Algorithm Problem," *IOP Conf. Ser. Mater. Sci. Eng.*, vol. 1116, no. 1, p. 012194, 2021, doi: 10.1088/1757-899x/1116/1/012194.

[16] W. Li, L. Xia, Y. Huang, and S. Mahmoodi, "An ant colony optimization algorithm with adaptive greedy strategy to optimize path problems," *J. Ambient Intell. Humaniz. Comput.*, vol. 13, no. 3, pp. 1557–1571, 2022, doi: 10.1007/s12652-021-03120-0.

[17] E. Chandomi-Castellanos *et al.*, "Modified Simulated Annealing Hybrid Algorithm to Solve the Traveling Salesman Problem," in *2022 8th International Conference on Control, Decision and Information Technologies, CoDIT 2022*, 2022, pp. 1536–1541. doi: 10.1109/CoDIT55151.2022.9804145.

[18] T. Tlili and S. Krichen, "A simulated annealing-based recommender system for solving the tourist trip

design problem," *Expert Syst. Appl.*, vol. 186, no. October 2020, p. 115723, 2021, doi: 10.1016/j.eswa.2021.115723.

[19] T. Ye, H. Wang, W. Wang, T. Zeng, L. Zhang, and Z. Huang, "Artificial bee colony algorithm with an adaptive search manner and dimension perturbation," *Neural Comput. Appl.*, vol. 34, no. 19, pp. 16239–16253, 2022, doi: 10.1007/s00521-022-06981-4.

[20] A. Ebrahimnejad, M. Enayattabr, H. Motameni, and H. Garg, "Modified artificial bee colony algorithm for solving mixed interval-valued fuzzy shortest path problem," *Complex Intell. Syst.*, vol. 7, no. 3, pp. 1527–1545, 2021, doi: 10.1007/s40747-021-00278-0.

[21] P. Chen, M. Liu, and S. Zhou, "Discrete Salp Swarm Algorithm for symmetric traveling salesman problem," *Math. Biosci. Eng.*, vol. 20, no. 5, pp. 8856–8874, 2023, doi: 10.3934/mbe.2023389.

[22] S. Kassaymeh, S. Abdullah, M. A. Al-Betar, M. Alweshah, M. Al-Laham, and Z. Othman, "Self-adaptive salp swarm algorithm for optimization problems," *Soft Comput.*, vol. 26, no. 18, pp. 9349–9368, 2022, doi: 10.1007/s00500-022-07280-9.

[23] F. Boualem, S.M., Meftah, B., Debbat, "Solving Travelling Salesman Problem Using a Modified Grey Wolf Optimizer," in *International Conference on Artificial Intelligence in Renewable Energetic Systems*, 2022, pp. 708–716. doi: https://doi.org/10.1007/978-3-030-92038-8_71.

[24] H. Liu, B. Lei, W. Wang, G. Zhong, and H. Chai, "An improved grey wolf optimization for solving TSP," in *International Conference on Computer Science and Communication Technology (ICCSCT 2022)*, 2022, no. December 2022, p. 29. doi: 10.1117/12.2661782.

[25] R. G. Revision, "TSPLIB 95 — TSPLIB 95 0.7.1 documentation," *Sphinx*, 2018. https://tsplib95.readthedocs.io/en/stable/pages/readme.html (accessed Feb. 24, 2023).

[26] N. Sultana, J. Chan, T. Sarwar, and A. K. Qin, "Learning to Optimise General TSP Instances," *Int. J. Mach. Learn. Cybern. Vol.*, vol. 13, pp. 2213–2228, 2022, doi: https://doi.org/10.1007/s13042-022-01516-8.

New Hybrid Distributed Attack Detection System for IoT

Çiğdem Bakır[1*]

[1]*Software Engineering Department, Engineering of Faculty, Dumlupinar University, Kütahya, Türkiye*

(ORCID:0000-0001-8482-2412)

Abstract

Internet of Things (IoT) is expressed as a network of physical objects with applications and various technologies that provide data connection and sharing with various devices and systems over the Internet. Security vulnerabilities in IoT devices are one of the biggest security issues in connecting devices to the internet and collecting and processing user data. These vulnerabilities can lead to increased attacks on IoT devices and malicious use of user data. In this article, we discuss these security problems that arise in IoT systems in detail in distributed systems technology. Distributed systems are increasingly used in the modern computing world. These systems are a structure where multiple independent computers communicate with each other for a common purpose. Distributed system technologies have become more common with the development of internet and cloud computing systems. However, the use of distributed systems has brought with it important security challenges such as security vulnerabilities, access controls and data integrity issues. Therefore, the security of distributed system technologies has been an important focus of work in this area. In this study, information about distributed system technologies and security for IoT is given. The all attack types were classified using Artificial Neural Network (ANN), developed Random Forest (RF) and hybrid model. In RF, all feature vectors created from all datasets (bank and two financial datasets) were also analyzed separately and the classification performance was examined. In addition, a new RF algorithm based on weight values using the Gini algorithm has been proposed. With this algorithm, the traditional RF algorithm has been developed and the success rates have been increased. In addition, a hybrid method was created by classifying the datasets obtained by RF with ANN. With the hybrid method ANN and the enhanced RF method, its accuracy in detecting normal behaviors and attack types was calculated and the success of the methods was presented comparatively. In addition, the working times of the methods were determined.

1. Introduction

The concept of the IoT is a popular technological trend that has gained increasing momentum in recent years. IoT refers to the network of devices that are connected to the internet and can communicate with each other. These devices can include all kinds of devices such as smartphones, computers, home appliances, industrial devices, vehicles, wearables, and even healthcare devices [1]. IoT devices are designed to make the world around us and people's lives easier. For example, smart home devices can enable you to remotely control your home, save energy, increase your security, and improve your quality of life at home. Industrial IoT devices, on the other hand, can increase efficiency in areas such as production and logistics, and offer new opportunities in areas such as agriculture and health [2].

Despite all these advantages, there are some security threats to IoT devices due to heterogeneous structures that communicate over different networks over the internet. In particular, it is possible to damage IoT devices and hack the system by various cyber attacks. These damages cause some irreversible problems in the future. For example, an attacker could attack an IoT device in the home, gaining access to all the devices in the home and even the personal information of the host. Another threat to IoT devices is malware infection of devices. These software can take control of devices and turn them into botnets. To deal with security threats to IoT devices, it is important to provide regular security updates to detect and fix vulnerabilities. In addition, security measures such as encryption of communication between devices and authentication must be taken in order for IoT devices to work securely. However, when these studies are evaluated as a whole at the point of detecting different types of attacks, they are often insufficient. In particular, it has shown that a stronger security mechanism is needed to detect and prevent attacks such as Denial-of-Service Attack (DoS) and Distributed Denial of Service Attack (DDoS) [3,4].

Research on data security has revealed that vulnerabilities and leaks in distributed systems in IoT devices are major problems [5,6]. For this reason, studies on solutions and measures for data security problems in distributed systems are very important. In particular, institutions and organizations need to create a strong security mechanism against important security vulnerabilities such as security vulnerabilities, access controls and data integrity problems.

In our study, security problems and precautions that arise in distributed systems related to IoT devices and networks are discussed. A method has been developed to detect and prevent possible attacks from different sources that may arise as a result of various violations such as unauthorized access, weak encryption methods, neglect of device updates, increasing attacks and threats, and management difficulties that will disrupt data confidentiality and data integrity. The developed model proposed in the study is applied on a real-life dataset to detect and prevent different attacks. In addition, short-term attacks that went undetected in the database were also observed. The working times and performance analyzes of the methods were also made. The success of the proposed new intrusion detection and prevention model is shown comparatively. When the results obtained are compared, it has been observed that the proposed model gives very successful results in preventing security problems in distributed systems IoT devices.

With the increase in the number and use of IoT devices in many areas, security problems have occurred in IoT devices. Within the scope of this study, first of all, attacks on IoT devices were mentioned and studies in the literature were mentioned. Secondly, a hybrid (RF+ANN) model was developed to detect possible attacks and the results of the proposed model were applied on three different real datasets. The success of the proposed method on all three datasets was presented by comparing it with metrics such as Accuracy, Precision, Recall and F1Score.

2. Related Works

Existing security mechanisms for distributed system technologies are insufficient due to the complexity and diversity of IoT devices [7]. Therefore, stronger and customized security mechanisms are needed for the security of IoT devices. Data privacy and security in these systems has become a major problem due to problems such as collecting, storing, processing and sharing user data. These issues include security protocols, user privacy, detection and prevention of attacks against IoT devices, scalability of IoT devices, and new security threats to IoT [8]. Therefore, stronger data privacy and security measures must be developed for IoT devices. There are many vulnerabilities in the security of IoT devices in distributed system technology and these devices are vulnerable to cyber attacks [9]. Security issues in IoT devices are due to device constraints such as low power consumption, limited processing capacity, and limited memory Many international organizations and standards organizations are developing security standards for IoT devices. Current challenges regarding the security of IoT include detection and prevention of cyber attacks, encryption of communication between devices, secure software updates. Although studies are carried out in the literature to ensure security in IoT, these studies are limited in order to solve the problems that arise. Important works done in recent years are presented below:

Table 1. Studies in the literature

Study	Technique	Attack Types	Performance	Disadvantages
Jaber et al. [10]	Autoencoder Network Model Genetic algorithm	DDoS	90.26%	the study brings reliability and computational complexity for very large data. For these reasons, the proposed model needs to be further optimized in order to increase its performance and reduce computational complexity.
Moudoud et al. [11]	Hidden Markov Model	False Data Injection (FDI)	97%	Although the performance is good, the model needs to be improved as it takes too much time to integrate into the learning process and new technologies.
Labiod et al [12]	Multi-layer sensor	DDoS	99.99% other attacks 86%	More improvements are needed to detect all types of attacks.
Habiba et.al [13]	Deep learning-based algorithm	DDos	99.99%	In this study, the efficiency of Edge AI for IoT platforms was demonstrated. Only DDos attacks are covered.
Alotaibi and Ilyas [14]	Ensemble method	TON-IoT dataset	98.63%	A multi-classification approach is required that can detect anomalies and intrusions in IoT network traffic.

Mahmoud et.al [15]	Intrusion Detection Systems based on Machine and Deep Learning (IDS_MDL)	Botnet attack dataset	99.7 %	Short-term observed attacks need to be detected
Sun et.al [16]	SVM	SCT dataset	98.71%	More features can be added to determine the physical behavior of more systems to improve the SVM method.
Elsayed et.al [17]	Secured Automatic Two-level Intrusion Detection System (SATIDS)	ToN-IoT and InSDN datasets.	96.35 %	Short-term attacks that occur during the day need to be detected and applied to the real-world IoT.
Sasikala et.al [18]	Logistic Regression	NB15 data set	97.8 %	Inaccurate missing data can be improved by using various approaches.
Jasim et.al [19]	Convolution Neural Network (CNN)	Unspecified	99.18 %	In terms of time, the proposed model works slowly
Almiani et.al [20]	Deep recurrent neural network	NSL-KDD	98.27 % (for only DoS attacks)	Probe is more susceptible to DoS attacks than detection of Remote to Local (R2L) and User to Root (U2R) attacks.
Kareem et.al [21]	Metaheuristic Algorithms	NSL-KDD, CICIDS-2017, UNSW-NB15 and BoT-IoT	95.5%, 98.7%, 81.5%, and 81.5% in the NSL-KDD,	Optimization of hypermaterials is required in solving multi-

			CICID2017, UNSW-NB, and BoT-IoT	objective problems.
			datasets, respectively	
Pehlivanoğlu et.al [22]	Gradient Boost classifier	Bot_IoT and ToN_IoT datasets	Port scanning attacks about 99%	The model proposed in the study should be tested on different data sets, especially large data sets.
Kozik et.al [23]	Deep learning	IoT-23 about 90%	(precision)	By adjusting the hyperparameter, the success and performance of the study can be increased.
Gökdemir and Çalhan [24]	Long Short-Term Memory (LSTM)	IoT dataset 99.17 %		There are some disadvantages in terms of working time.
Gökdemir and Çalhan [24]	Long Short-Term Memory (LSTM)	IoT dataset 99.17 %		There are some disadvantages in terms of working time.
Ölmez ve İnce [25]	Support Vector Machines (SVM)	Bot-IoT, CICIDS-2017, IoT-23 and N-BaIoT	99.94% for Bot-IoT dataset, 99.95% for CICIDS-2017 dataset, 99.96% for IoT-23 dataset and 99.92% for N-BaIoT dataset	Data preprocessing and converting the data into the appropriate format is a separate workload.
Yaman and Tekin [26]	XGBoost	"Brute force ftp", "brute force ssh", "dos http flood", "dos icmp flood", "dos syn flood", "syn scan" and "udp scan"	92.55%	The detection success of some attacks can be increased.

In our study, it is aimed to detect and prevent all kinds of attacks that may occur in order to ensure IoT security in distributed systems. By using artificial neural networks, proposed random forest tree and hybrid method, an attack detection system has been implemented on banks and two different financial data. Our work includes intrusion detection comprehensive and a significant contribution to

detecting different similar attacks and integrated in IoT environments. In addition, performance measurements of all models used are presented comparatively using different evaluation metrics (precision, recall, F1 Score).

3. Material and Method

Currently, intelligent environments are spreading with the IoT in all areas where computing resources are applied. However, as the techniques to exploit computer infrastructure security vulnerabilities are constantly evolving, applications and systems may inevitably be exposed to some attacks. With attacks, accessing systems, obtaining confidential information and improper use, rendering resources unusable can become unavoidable. For this reason, security becomes the most important issue for the IoT environment. Unresolved challenges regarding the security of IoT devices can be summarized as follows [34]:

Poor security practices: Unlike traditional computers, IoT devices can often have low resources and limited processing power. This can result in poor security practices being used to secure IoT devices.

Weak authentication methods: Authentication methods used in communication between IoT devices can often be insufficient or weak. This may require the development of new and more secure authentication methods for the security of IoT devices.

Hard-to-protect physical locations of IoT devices: IoT devices can be used in a variety of physical environments, and these environments can threaten the physical security of devices. Therefore, for the security of IoT devices, security issues arising from the physical location of devices that are difficult to protect may need to be addressed. Data privacy issues: IoT devices can often handle sensitive data, and it's important to protect the privacy of this data. Therefore, it may be necessary to develop new and more secure solutions to data privacy problems for the security of IoT. Some security measures taken are not sufficient to detect and prevent attacks. In order to detect attacks in IoT environments, a model that can be implemented on real platforms and in real time is needed.

Traditional pain detection systems have difficulties to cope with and implement the above-mentioned security challenges. IoT components' limited computing power, large number of interconnected devices and objects, data sharing between users, and vulnerability to security and privacy risks. Difficulty in detecting attacks such as DoS, DDoS, Man in the Middle, unsafe connections, malicious code injection

livable. In our study, a model tested on real data is presented that takes into account the context of intrusion detection and prevention in IoT-based environments. The performance of the proposed RF model and the proposed hybrid model ANN model were calculated based on different evaluation criteria

3.1. ANN

ANN have been developed by taking advantage of the working principle of the human brain. An artificial neural network consists of neurons (nodes) that make connections between input and output data, and layers that make connections between these neurons [35]. A neural network consists of a large number of neurons and layers. There are many neurons in each layer, and each neuron receives information by weighted connections that connect nerve cells. This information is passed through different activation functions and transmitted to other neurons. In addition, each neuron receives input from many nodes and passes these inputs through a function and transmits its output to other neurons. While the neurons of all layers that will form in the neural network are in series with the neurons of the previous and next layer, they are parallel among themselves. Since information will be transmitted between neurons to each layer, it contains connections between them. These links represent the weights between the layers and end at the output layer. Determining the correct weights during the training of the network is crucial for accurate and reliable output. Initially, weight values are randomly assigned. Weight values are updated in each iteration according to the neural network and learning rule to be formed. When different samples are trained according to the resulting network, the weights are changed again and the most accurate weights are tried to be determined. These processes are repeated until the optimum weights are found.

Figure 1 shows the structure of the artificial neural network. In our study, the input size was determined by the number of samples and the number of features for each data set. The N value expressed here includes the number of samples. There are 3 hidden layers for each data set. There are 150 neurons in the first layer, 120 neurons in the second layer, and 100 neurons in the last hidden layer. The learning coefficient was taken as 0.01. In each dataset, the number of output layers is determined by the general classes (5 attack types). There are also similar attacks within these classes. Since the number of similar attacks, which are subclasses, is too high, their names are not included. Classes of test samples are tried to be determined according to the training data determined in the ANN model [36]. If the classes of test data are correctly

determined, the network is considered to be properly trained. The correct determination of the ANN model depends on the activation function, the aggregation function in which the artificial nerve cells transmit information, the learning rule and the topology of the network. The aggregation function calculates the net input of the ANN model using different functions. The activation function, on the other hand, converts the information obtained as a result of the addition function to the output value by using different functions. In some cases, the created ANN model can be memorized. If this happens, training should be stopped. If there is no memorization and the network is learning, the training is not continued. The classes of test samples are determined according to the last iteration. ANN model is created by considering the following criteria [37]:
• Identifying layers
• Inputs and outputs to be used in education
• Number of neurons
• Activation functions
•The objective function used to determine whether the network is successful.
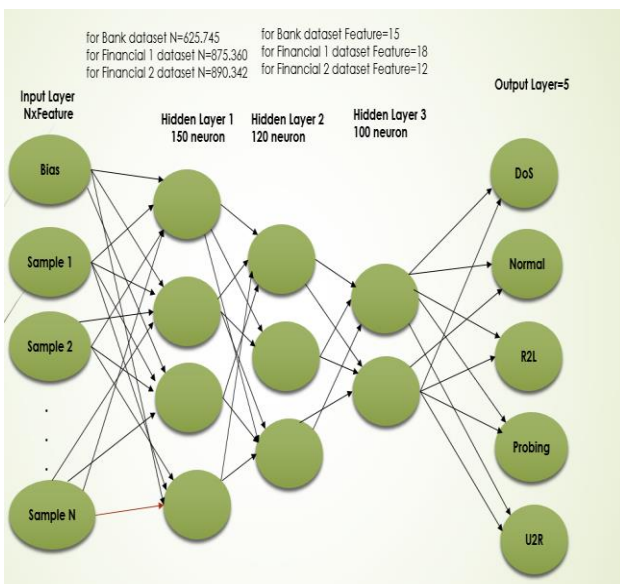
Figure 1. Proposed of ANN model

In ANN models, the structure of a pre-trained network can be used for other datasets. The purpose of transfer learning methods is to increase classification performance and training speed by using previously trained models on a new dataset [38]. If the dataset to be trained is small and insufficient, the attributes of previously trained large datasets can be directly applied to this dataset. The output layers of these trained large datasets directly form the network structure of the dataset to be trained. In addition, it can be learned in a short time and with fewer parameters

by fine-tuning it to make it more suitable for the dataset to be trained. During the training phase, the weights of the pre-trained layers are precisely adjusted and updated, and the classification layers are learned in accordance with the training. Fine-tuning the model's layers and newly added classifier layers by training them simultaneously allows the model to be improved. It is to create the local minimum value of the parameters (parameters used in activation, training and performance functions, etc.) that best suit the ANN network structure. Thus, classification success is increased by fine-tuning. This fine-tuning method can be done by backpropagation

3.2. RF

RF method is an ensemble learning method built on Decision Trees (DT) [39]. Community learning methods are popular in the field of machine learning. It can be used for classification and regression operations. As a basic principle, ensemble learning methods decide on the solution of a classification problem depending on the decisions of more than one classifier. In decision making, the highest vote (majority) or the lowest error (minimized error) approaches can be preferred.

In the RF method, there is a forest structure consisting of individual decision trees for the same problem [38]. The decision of each tree in the forest is independent of the decisions of other trees. The randomness in the method is due to the selection of variables in the creation of a decision tree. The traditional decision tree consists of root, twig (brunch) and leaves (leaf). While the root and branch structures are determined according to the variables that will determine the classification result, the leaves show the class decisions. The information gain of the variable is calculated in the selection of the variable for the roots and branches in the traditional decision tree. One of the most used calculation methods is the GINI index. Information gain is the effect of the variable on the class decision. The higher this effect, the higher the effect of the variable on the outcome. The root of the decision tree is established with the variable with the highest information gain and the branches are completed according to the gain order of the variables. In the RF method, variable selections are made randomly while creating each tree. This randomness is useful in preventing overfitting. At the same time, the samples to be selected for each tree created are selected as a subset of the whole sample with the bootstrap technique with a random approach. The RF method was developed by Breiman [40, 41]. Breiman, who previously developed the Classification and Regression Trees (CART) method,

developed the RF technique by first developing Bagging- Bootstrap Aggregating and then Random Subspace methods and combining these methods because the CART method, which has a very good learning ability, is prone to excessive learning. Our proposed RF model proposes a cloud-random forest (IoT - RF) model that combines the IoT environment and random forest for intrusion detection (Figure 2). In this model, based on traditional CART, a weight determination algorithm based on the cloud model and the decision-making trial and evaluation lab is applied to obtain the evaluation weights. The feature weight and the gain value of the smallest Gini coefficient corresponding to the same feature are weighted and summed. The weighted sum is then used to replace the original gain value. This value rule is used as a new CART node split criterion to create a new decision tree, thus creating a new random forest, i.e. IoT - RF. In the proposed RF model according to the IoT environment, the weight is determined by the following steps:

Step 1: Attack types are determined as A={a1,a2,....,aN}.

Step 2 Draw the correlation diagram between any two attack types.

Step 3 The first matrix that directly affects the attack type is created.

Step 4 The property values are determined.

Step 5 The IoT matrix of all decision makers is collected.

Step 6 The matrix of the relationship between the features is found.

Step 8 The standardized comprehensive impact matrix is measured.

Step 10 All attack types have weights.

Classification success in RF methods varies depending on hyperparameters such as the number of trees, tree depth, number of features and training rate [42]. The accuracy of the model can be increased by fine-tuning these hyperparameters manually or with optimization methods such as grid search and random search. Too many features may reduce classification performance. For this reason, the success of the model can be increased by removing features that are not related to feature reduction methods such as information gain or gain ratio. Increasing the number of trees, which affects the success of RF methods, may have a positive effect on the success of the model. Although the success of the model increases as the depth of the tree increases, the success of the model does not change when the depth of the tree reaches a certain point. Additionally, choosing the tree depth too small may cause model incompatibility. For this reason, it is very important to fine-tune these

hyperparameters that affect the classification success of RF methods.
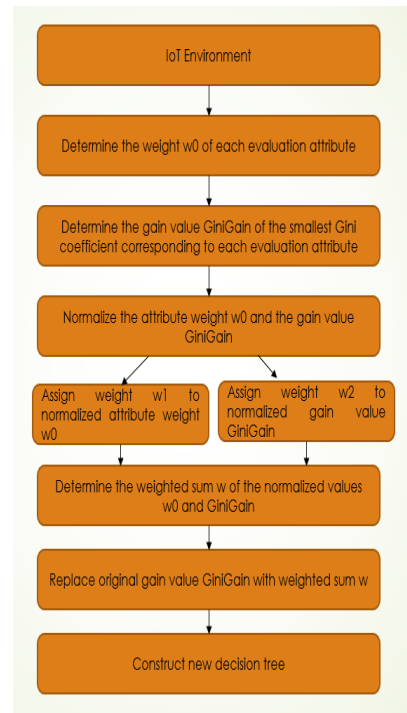
Figure 2. Proposed RF flow chart

3.3. Hybrid Model

The data sets used in the study are not open access and the study was carried out in IoT environments. Due to the confidentiality of the data, fields and features of the data set cannot be mentioned. All datasets used in the study are divided into 70% train and 30% test. Different analyzes
were also performed (60% train, 40% test or 80% training and 20% test). However, it gave the best and most optimum solution when we divided it into 70% training and 30% testing.

IoT has attracted a lot of attention in recent years in many fields such as automation, industry and smart environments. There are many different and similar types of attacks [43]. However, since IoT is a heterogeneous environment, it is also exposed to many attacks. For this reason, a hybrid model has been developed in our study to ensure IoT network security. This hybrid model is formed by combining the proposed RF and ANN model, and the flowchart is shown in Figure 3. In the hybrid model we recommend, first data with the classification model. We have classified. In studies on trained data, observed noise removal, feature extraction, and selection methods increased classification success and. These methods make the available data more useful. Therefore, the results of the studies vary

according to the situation. normalization techniques, noise removal, feature extraction and feature selection. We are at every stage determined the accuracy rate of normal and attack types, and calculated the average. Clustering of datasets is done on the basis of the variables and criteria of the proposed RF model. Then, the ANN classifier is applied sequentially to each clustered dataset. This hybrid model we propose is formed by combining the developed RF and ANN classification models. We propose a hybrid machine learning system based on RF and ANN for detecting all types of attack on bank and financial datasets. The performance evaluation and error rates of the existing models and the proposed hybrid model in the diagnosis of normal and all attack types were calculated and compared with the proposed models in terms of accuracy and time.

In the hybrid model we proposed, we first grouped the data close to each other with the proposed RF method. We performed classification process on the data we grouped with various methods. At each stage, we determined the accuracy rate of normal and preventable attack types with the model we suggested and calculated the mean. It is calculated by averaging the correct and normal behaviors found here and the types of attacks that can be prevented with the model we propose. In hybrid model we recommend, it provides data protection by better detecting attack types compared to single classification or single clustering methods. It gave more successful results. The hybrid model made more successful results than the ANN and RF method. In addition, the reason for the decrease in the success rate as the amount of data increases is due to the multidimensional and complex structure of the data. When the results are compared in all models, the hybrid model in ANN is more successful than the first hybrid model. The reason for this is that when clustering is performed first, normal behaviors and different attack types are clustered in a group as far away from each other. This ensures correct detection and prevention of attack types

Figure 3. Proposed hybrid model flow chart

4. Results and Discussion

In our study, bank and financial data were used to ensure IoT security for distributed systems. The features of the dataset we used are given in Table 2. In addition, normal and attack types and numbers are shown for all three data sets. These attacks are grouped into 4 main groups as DoS, Probing, U2R, R2L and these attacks also consist of similar attack types. Within each attack cluster, there are subclasses containing between 10 and 30 similar attack types. Similar attacks were gathered in the same cluster. Table 3 shows the number of samples in each data set according to attack types. As can be seen, the number of samples with DoS attacks is higher for all three data sets than for other types of attacks.

In data preprocessing, it was first checked whether there were null values in all three datasets. Empty values are filled by taking the average of the column. Additionally, outliers in the datasets were normalized between [0,1]. Thus, data imbalance in the datasets was eliminated. The normalization method was applied to increase the accuracy of the classical model and the proposed models. By examining the correlation matrix of the features in three datasets, the connections between the features were tried to be determined. The most important feature was chosen as the feature with the highest correlation value. These features were used in the proposed classification methods to increase the success. In addition, dimensionality reduction was performed by removing features with low correlation from the data set. The success and performance of the models used were increased by applying the min-max normalization technique to some features. Thus, the classification success of multi-class datasets has been increased by feature selection and dimensionality reduction.

Each attack occurring in these datasets is categorical. However, these categorical classes have been converted to integer data type, starting from one. In addition, the success of the models used in the study was increased by adding an extra new feature to include similar attacks in the same data set. Attacks were also investigated according to their protocol types.

In Figure 4, the accuracy results obtained in the detection of all attack types for all datasets of the artificial neural networks developed are given. In our study, unlike other studies, important results were obtained in detecting all types of attacks. In Figure 5, the values of the detection of all attack types in terms of time are given for all datasets of the artificial neural networks developed. All results are calculated based on the accuracy of the test data and the running time of the test data.

Table 2. Used Datasets

	Number of Samples	
Dataset	**Normal**	**Attack**
Bank	625.745	178.034
Financial1	875.360	279.693
Financial2	890.342	300.476

Table 3. Number of samples by attack types

Dataset	**DoS**	**Probing**	**U2R**	**R2L**
Bank	87.341	12.634	24.677	53.382
Financial1	184.302	48.072	34.974	12.345
Financial2	108.342	85.974	81.366	24.794
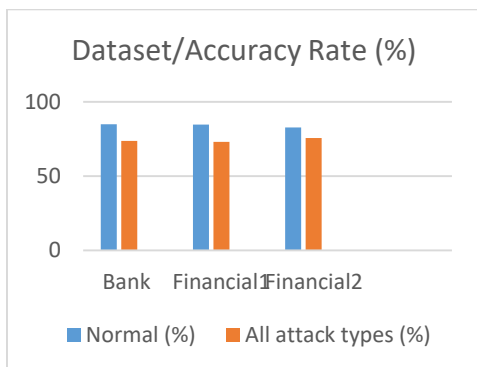
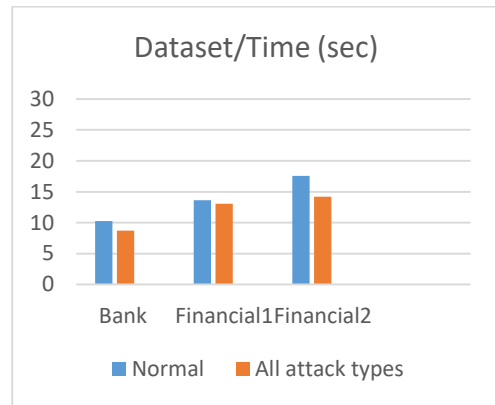

Figure 4. ANN accuracy results for all datasets
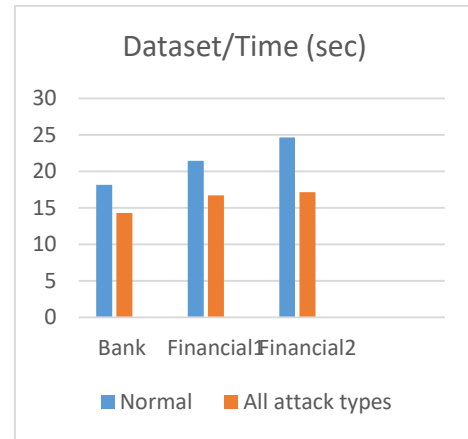
Figure 5. ANN time results for all dataset

Table 4. ANN results by different evaluation metrics

Dataset/ Performance Criteria (%)	Accuracy	Precision	Recall	F1-Score
Bank	73.64	73.50	74.42	74.10
Financial 1	73.05	72.82	72.14	72.45
Financial 2	75.64	73.64	72.42	73.02

In Table 4, the results of the ANN according to different evaluation metrics for all three data sets are given. It gave more successful results for bank data compared to all datasets. The reason for this is that the examples of DoS attacks are less than other datasets. Because the subclasses of DoS attacks are more than other attacks. In short, since there are many similar attack types, it is more difficult to detect DoS attacks when compared to other types of attacks when we look at the studies in the literature in general
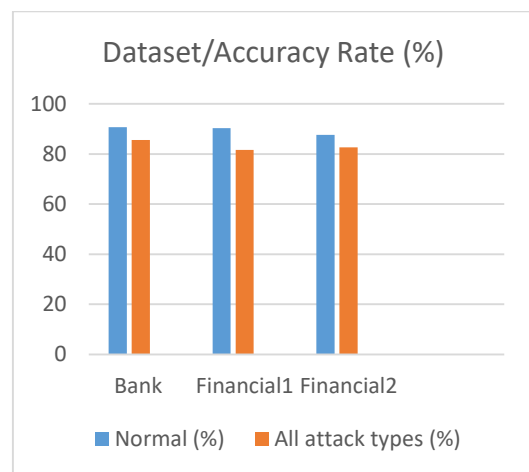
Figure 6. Proposed RF accuracy results for all datasets
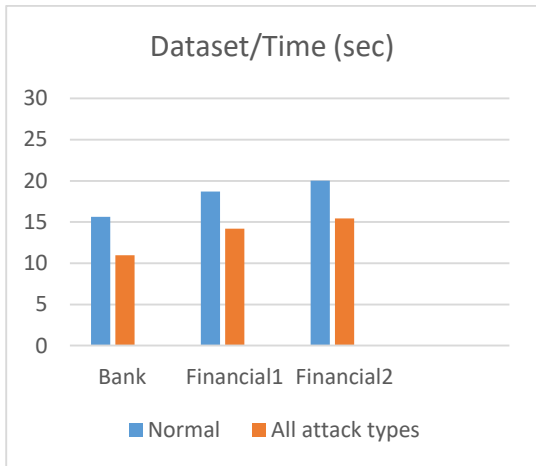
Figure 7. Proposed RF time results for all dataset

Table 5. Proposed RF results by different evaluation metrics

Dataset/ Performance Criteria (%)	Accuracy	Precision	Recall	F1-Score
Bank	85.60	86.73	84.72	84.99
Financial 1	81.67	84.60	83.15	83.01
Financial 2	82.64	82.62	85.03	85.07

In Table 5, the results of the proposed RF according to different evaluation metrics for all three data sets are given. In Figure 6, the accuracy results obtained in the detection of all attack types for all datasets of the proposed RF developed are given. In our study, unlike other studies, important results were obtained in detecting all types of attacks. In Figure 7, the values of the detection of all attack types in terms of time are given for all datasets of proposed RF developed.

In Figure 8, the accuracy results obtained in the detection of all attack types for all datasets of the Hybrid model developed are given. In our study, unlike other studies, important results were obtained in detecting all types of attacks. In our future work, we aim to increase the accuracy by using different hybrid methods and to use it in different real datasets. In Figure 9, the values of the detection of all attack types in terms of time are given for all datasets of hybrid model developed. When we compare it with other studies in terms of time, we see that it detects the attack in a short time.

Figure 8. Hybrid model accuracy results for all datasets

Figure 9. Hybrid model time results for all dataset

Table 6. Hybrid results by different evaluation metrics

Dataset/ Performance Criteria (%)	Accuracy	Precision	Recall	F1-Score
Bank	90.37	91.36	91.36	91.07
Financial 1	92.62	92.62	92.43	91.45
Financial 2	91.74	91.43	93.78	92.72

Table 6 presents the results of the proposed hybrid model according to different evaluation metrics for all three data sets. In the first stage of our study, the data trained with ANN was classified with RF. In addition, data pre-processing steps such as feature extraction and noise removal increase the success in classification. For this reason, the results of the studies vary depending on the data processing steps. We determined the accuracy rate of normal and attack types at each stage and calculated their average.

In our study, k-fold cross validation was used to ensure that the methods used, other than voting, were

resistant to the training and testing sections. 5 and 10 were chosen for the K value. While the solution is produced according to the voting technique, the ANN results for k - fold cross validation for k=5 and k=10 have been added in the accompanying Table 7. When

the results were compared, using k-fold cross validation gave more successful results than the voting technique. Additionally, in general, k=10 is more successful than k=5 in all methods used in the study.

Table 7. ANN results according to k-fold craoss validation method

Dataset/ k value	k=5	k=10
Bank	75.45	77.74
Financial 1	75.97	76.37
Financial 2	78.95	77.34

While the solution is produced according to the voting technique, the RF results for k-fold cross validation for k=5 and k=10 have been added in the accompanying Table 8.

Table 8. RF results according to k-fold craoss validation method

Dataset/ k value	k=5	k=10
Bank	88.04	88.67
Financial 1	85.34	86.72
Financial 2	85.17	87.95

While the solution is produced according to the voting technique, the hybrid model results for k-fold cross validation for k=5 and k=10 have been added in the accompanying Table 9.

Table 9. Hybrid model results according to k-fold craoss validation method

Dataset/ k value	k=5	k=10
Bank	92.32	93.01
Financial 1	93.71	92.37
Financial 2	92.82	93.54

5. Conclusion and Suggestions

Connecting IoT devices to the internet can pose a significant threat to the security of the devices. IoT devices have many different security vulnerabilities, such as malware infections, phishing attacks, and attacks through physical access. These threats can affect both consumer and industrial IoT devices and have serious consequences.

Distributed system technologies are a structure that is widely used in many areas today and allows services to be offered in a more efficient and scalable way. However, these systems have a more complex structure than central systems. In this study, we evaluated the distributed system technology for IoT and showed the distributed system architecture in detail. The security of IoT devices is very important for distributed systems technology. IoT devices, their usage areas and numbers are increasing day by day and the security of these devices is of great importance in terms of personal privacy and data security. In our study, different security methods and mechanisms that can be used in distributed system technology for the security of IoT devices are discussed. However, it was also emphasized that more research is needed to find solutions to security problems in IoT devices. Therefore, those working on the security of IoT devices need to identify different security vulnerabilities and risks and ensure the security of users by taking appropriate security measures.

The security of distributed systems is a more challenging issue than centralized systems because communication between different components has difficulty in ensuring security. Therefore, various precautions should be taken for the security of distributed systems. Among them; topics such as authentication, authorization, encryption, data integrity, confidentiality and reliability. Today, many research and development studies are carried out on the security of distributed systems. These studies provide important steps for reducing the risks of cyber security vulnerability, preventing attacks and making systems more secure. As a result, distributed system technologies and security are an increasingly important topic for IoT today. The development and security of these technologies will increase the efficiency of enterprises and enable them to provide better service. For this reason, it is very important to raise awareness about the security of distributed systems and to ensure the continuation of research studies.

In this study, a system is designed to detect and prevent different and same types of attacks that occur as a result of security vulnerabilities in distributed systems. The aim of our study is to ensure attack security in the IoT environment. The three different data sets we used were evaluated using ANN, RF and our proposed hybrid model. The results of the proposed hybrid model and the proposed RF model and the classical ANN model are shown comparatively. In addition, the operating times of all

models used in the study were calculated and compared. ANN for bank, financial 1 and financial 1 data sts are 0.7364, 0.7305, 075.64, respectively; RF 0.85, 0.8167, 0.8264; hybrid model showed success of 0.9037, 0.9262 and 0.9174. In addition, the results for all three models were analyzed with different evaluation criteria. When the results are compared, the proposed hybrid model showed approximately 10% more success than the ANN model in all three datasets. When the results are compared, it is observed that more accurate attack prediction is made in hybrid models. The effective use of hybrid models in attack detection and prevention is of great importance for future studies. Using artificial intelligence techniques at the beginning of these studies provides a greater advantage. Our study achieved very successful results in detecting different and new attack types occurring in IoT environments. In addition, the proposed hybrid model aims to address security and privacy issues that may arise in different areas in the future. Unlike previous studies, data security is ensured in all operations for IoT.

In the future, it is aimed to design attack detection and prevention systems on different and larger complex data sets with deep learning methods. It will be aimed to contribute to the studies in the literature by conducting more studies in this field. In addition, it is aimed to increase the success of the models by automatically fine-tuning the hyperparameters for the proposed models in the future using optimization algorithms.

Contributions of the Authors
All authors contributed equally to the study.

Conflict of Interest Statement
There is no conflict of interest between the authors.

Statement of Research and Publication Ethics
The study is complied with research and publication ethics

References

[1]   M. Wang, and Q. Zhang, "Optimized data storage algorithm of IoT based on cloud computing in distributed system," *Computer Communications*, vol. 157, pp.124-131, 2020.

[2]   G. Eleftherakis, D. Pappas, T. Lagkas, and K. Rousis, "Architecting the IoT paradigm: a middleware for autonomous distributed sensor networks," *International Journal of Distributed Sensor Networks*, vol. 11, no.12, pp.139735-139735, 2015.

[3]   X. Yu, J. Chu, and K. Yu, "Energy-efficiency optimization for IoT-distributed antenna systems with SWIPT over composite fading channels," *IEEE Internet of Things Journal*, vol. 7, no.1, pp. 197-207, 2019 .

[4]   A. R. Sfar, E. Natalizio, Y. Challal, and Z. Chtourou, "A roadmap for security challenges in the Internet of Things," *Digital Communications and Networks*, vol. 4, no.2, pp. 118-137, 2018.

[5]   S. Keoh, S. Kumar, and H. Tschofenig, "Securing the internet of things: A standardization perspective," *IEEE Internet of things Journal*, vol. 1, no.3, pp. 265-275, 2014.

[6]   K. Jaswal, T. Choudhury, and R. Chhokar, "Securing the Internet of Things: A proposed framework," *In 2017 International Conference on Computing, Communication and Automation (ICCCA),* 2017, pp. 1277-1281.

[7]   P. Sivaraman, C. Sharmeela, P. Sanjeevikumar, "Health Monitoring of a Transformer in a Smart Distribution System using IoT," *In IoT, Machine Learning and Blockchain Technologies for Renewable Energy and Modern Hybrid Power Systems River Publishers*, pp. 79-91, 2023.

[8]   G. Bhandari, A. Lyth, and A. Shalaginov, "Distributed Deep Neural-Network-Based Middleware for Cyber-Attacks Detection in Smart IoT Ecosystem: A Novel Framework and Performance Evaluation Approach," *Electronics*, vol. 12, no. 2, pp. 298-298, 2023.

[9]   A. Ukil, J. Sen, and S. Koilakonda, "Embedded security for Internet of Things," *In 2011 2nd National Conference on Emerging Trends and Applications in Computer Science,* 2011, pp. 1-6.

[10]   M. H. Ali, M. Jaber, and S. Abd, "Threat analysis and distributed denial of service (DDoS) attack recognition in the internet of things (IoT)," *Electronics*, vol. 11, no.3, pp. 494-494, 2022.

[11]   H. Moudoud, Z. Mlika, L. Khoukhi, and S. Cherkaoui, "Detection and prediction of fdi attacks in iot systems via hidden markov model," *IEEE Transactions on Network Science and Engineering*, vol. 9, no.5, pp. 2978-2990, 2022.

[12] Y. Labiod, Y, A. Korba, and N. Ghoualmi, "Fog computing-based intrusion detection architecture to protect iot networks," *Wireless Personal Communications,* vol. 125, no.1, pp. 231-259, 2022.

[13] M. Habiba, M.R. Islam, S.M. Muyeen, and A.S. Ali, "Edge intelligence for network intrusion prevention in IoT ecosystem," *Computers and Electrical Engineering*, vol.108, pp.108727-108727, 2023.

[14] Y. Alotaibi, and M. Ilyas, "Ensemble-Learning Framework for Intrusion Detection to Enhance Internet of Things' Devices Security," *Sensors*, vol. 23, no. 12, pp. 5568-5568, 2023.

[15] W. A. Mahmoud, M. Fathi, H. El-Badawy, and R. Sadek, R, "Performance Analysis of IDS_MDL Algorithm to Predict Intrusion Detection for IoT Applications", *In 2023 40th National Radio Science Conference (NRSC)*, vol. 1, 2023, pp. 139-149.

[16] C. Sun, D. J. Cardenas, A. Hahn, and C. Liu, "Intrusion detection for cybersecurity of smart meters", *IEEE Transactions on Smart Grid*, vol. 12, no. 1, pp. 612-622, 2020.

[17] R. A. Elsayed, and R.A.Hamada, "Securing IoT and SDN systems using deep-learning based automatic intrusion detection", *Ain Shams Engineering Journal*, vol. 14, no. 10, pp.102211- 102211, 2023.

[18] K. Sasikala, and S. Vasuhi, "Anomaly Based Intrusion Detection on IOT Devices using Logistic Regression", *In 2023 International Conference on Networking and Communications (ICNWC),* 2023, pp. 1-5.

[19] A. F. J. Jasim, and S. Kurnaz, "New automatic (IDS) in IoTs with artificial intelligence technique", *Optik*, vol. 273, pp.170417-170417, 2023.

[20] M. Almiani, A. AbuGhazleh, and A. Razaque, "Deep recurrent neural network for IoT intrusion detection system", *Simulation Modelling Practice and Theory*, 101, 102031, 2020.

[21] S. S. Kareem, R. R Mostafa, F.A. Hashim, and H. M. El-Bakry, "An effective feature selection model using hybrid metaheuristic algorithms for iot intrusion detection", *Sensors*, vol. 22, no. 4, pp. 1396-1396, 2022.

[22] M. K. Pehlivanoğlu, A.Kuyucu, K.A. Recep, "IoT Veri Kümelerinde Makine Öğrenmesi Tekniklerine Dayalı Saldırı Tespiti", *Avrupa Bilim ve Teknoloji Dergisi*, vol. 52, pp. 19-26, 2023.

[23] R. Kozik, M. Pawlicki, and M. Choraś, "A new method of hybrid time window embedding with transformer-based traffic data classification in IoT-networked environment", *Pattern Analysis and Applications,* vol. 24, no. 4, pp. 1441-1449, 2021.

[24] A. Gökdemir, and A. Calhan, "Deep learning and machine learning based anomaly detection in internet of things environments", *Journal of the Faculty of Engineering and Architecture of Gazi University*, vol. 37, no. 4, pp. 1945-1956, 2022.

[25] E.G. Ölmez, and İ. Kenan, "IoT Botnet Verisetlerinin Karşılaştırmalı Analizi", *Computer Science*, 151-164, 2022.

[26] O. Yaman, and R. Tekin, "Akıllı Ev Sistemleri için XGBoost Tabanlı Saldırı Tespit Yöntemi", *Journal of Intelligent Systems: Theory & Applications*, vol. 6, no. 2, 2023.

[27] Ş. Okul, and M. A. Aydın, "Security attacks on IoT", *In 2017 International Conference on Computer Science and Engineering (UBMK),* 2017, pp. 1-5.

[28] A. A. Ismael, and A.Varol, "IoT Sistemini Güvenliği: Yeni Bir Model", *5th National Informatics Congress,* 2018.

[29] K. İlhan, and Ş. Abdülkadir, Ş. "IoT Ağ Güvenliği için 802.1 x, DMZ ve SSL-VPN Birleştirme Tabanlı Etkili bir Güvenlik Yöntemi". *Acta Infologica*, vol. 4, no. 2, pp. 65-76, 2020.

[30] J. Azimjonov, and T. Kim, "Designing accurate lightweight intrusion detection systems for IoT networks using fine-tuned linear SVM and feature selectors", *Computers & Security,* vol. 137, no. 103598, 2024.

[31] P. Vijayan, and S. Sundar, "Original Research Article IoT intrusion detection system using ensemble classifier and hyperparameter optimization using tuna search algorithm", *Journal of Autonomous Intelligence,* vol. 7, no.2, pp. 1-10, 2024.

[32] A. Biju, and S.W. Franklin, "Evaluated bird swarm optimization based on deep belief network (EBSO-DBN) classification technique for IOT network intrusion detection", *Automatika,* vol. 65, no. 1, pp. 108-116, 2024.

[33] S. Shen, C. Cai, and S. Yu, "Deep Q-network-based heuristic intrusion detection against edge-based SIoT zero-day attacks", *Applied Soft Computing*, vol. 150, no. 111080, 2024.

[34] M. Abomhara, and G. M. Køien, "Security and privacy in the Internet of Things: Current status and open issues," In 2014 international conference on privacy and security in mobile systems (PRISMS), 2014, pp. 1-8.

[35] J. Park, and Y. S. Jeong, "Dynamic analysis for IoT malware detection with convolution neural network model," *IEEE Access*, vol. 8, pp. 96899-96911, 2020.

[36] S. Smys, H. Wang, and A. Basar, "5G network simulation in smart cities using neural network algorithm," *Journal of Artificial Intelligence*, vol. 3, no. 1, pp. 43-52, 2021.

[37] D. K. Reddy, H. S. Behera, and J. Nayak, "Deep neural network based anomaly detection in Internet of Things network traffic tracking for the applications of future smart cities," Transactions on Emerging Telecommunications Technologies, vol. 32, no. 7, 2021.

[38] W. Pannakkong, K. Thiwa-Anont, K. Singthong, K., and J. Buddhakulsomsiri, "Hyperparameter tuning of machine learning algorithms using response surface methodology: a case study of ANN, SVM, and DBN", *Mathematical problems in engineering*, 2022, 1-17, 2022.

[39] S. S. Roy, S. Dey, and S. Chatterjee, "Autocorrelation aided random forest classifier-based bearing fault detection framework", *IEEE Sensors Journal*, vol. 20, no. 18, pp. 10792-10800, 2020.

[40] Breiman, L. (2001). Random forests. Machine learning, 45, 5-32.

[41] J. Wang, C. Rao, and X. Xiao, "Risk assessment of coronary heart disease based on cloud-random forest", *Artificial Intelligence Review*, vol. 56, no. 1, pp. 203-232, 2023.

[42] H. Parmar, S. Bhanderi, S., and G. Shah, "Sentiment mining of movie reviews using Random Forest with Tuned Hyperparameters", *In International Conference on Information Science,* Kerela, 2014, pp. 1-6.

[43] F. James, "IoT cybersecurity based smart home intrusion prevention system", *In 2019 3rd Cyber Security in Networking Conference (CSNet)*, 2019, pp. 107-113.

Deep Learning Approaches for Sunflower Disease Classification: A Study of Convolutional Neural Networks with Squeeze and Excitation Attention Blocks

Yavuz ÜNAL[1*], Muhammed Nuri DUDAK[2]

[1]Computer Engineering Department, Amasya University, Amasya, Türkiye
[2]Information systems Department, Amasya University, Amasya, Türkiye
(ORCID: 0000-0002-3007-679X) (ORCID: 0000-0003-2695-8447)

Keywords: Sunflower diseases, SE-Block, Deep learning, Image processing,

Diseases in agricultural plants are one of the most important problems of agricultural production. These diseases cause decreases in production, and this poses a serious problem for food safety. One of the agricultural products is sunflower. Helianthus annuus, generally known as sunflower, is an agricultural plant with high economic value grown due to its drought-resistant and oil seeds. This study, it is aimed to classify the diseases seen in sunflower leaves and flowers by applying deep learning models. First of all, it was classified with ResNet101 and ResNext101, which are pre-trained CNN models, and then it was classified by adding squeeze and excitation blocks to these networks and the results were compared. In the study, a data set containing gray mold, downy mildew, and leaf scars diseases affecting the sunflower crop was used. In our study, original Resnet101, SE-Resnet101, ResNext101, and SE-ResNext101 deep-learning models were used to classify sunflower diseases. For the original images, the classification accuracy of 91.48% with Resnet101, 92.55% with SE-Resnet101, 92.55% with ResNext101, and 94.68% with SE-ResNext101 was achieved. The same models were also suitable for augmented images and classification accuracies of Resnet101 99.20%, SE-Resnet101 99.47%, ResNext101 98.94%, and SE-ResNext101 99.84% were achieved. The study revealed a comparative analysis of deep learning models for the classification of some diseases in the Sunflower plant. In the analysis, it was seen that SE blocks increased the classification performance for this dataset. Application of these models to real-world agricultural scenarios holds promise for early disease detection and response and may help reduce potential crop losses.

1. Introduction

Agriculture is a vital field for the nutrition and food security of large populations [1]. One of the important agricultural products is oilseeds. Oil production comes to the fore in oilseed plants used for food purposes. One of the plants grown for its oilseed is Sunflower. In many countries, sunflower is grown primarily for its vegetable oil and animal feed which is an important source of raw materials for the food industry [2]. Sunflower offers a substantial productivity advantage because of its ability to be grown under irrigated and dry farming circumstances, and appropriateness for machine use at all phases from planting to harvest [3].

Diseases seen in sunflowers cause seed yield to decrease. The agricultural economy suffers greatly from productivity losses. Preventing productivity loss is possible by diagnosing diseases in time and taking precautions [4]. Thanks to early detection, we can save plants and prevent losses. Visual detection of diseases in plants is a difficult process and diagnosis can be time-consuming. Visual detection is difficult or impossible in large agricultural areas [5].

Diagnosis of plant diseases using deep learning is becoming increasingly common nowadays [6]. This study aims to identify diseases seen in sunflower leaves and flowers using image processing and deep learning.

Sunflowers are bacteria, fungi, nematodes, parasites, viruses, etc. are exposed to many diseases [4]. The dataset includes three disease classes and one healthy sunflower leaf class. These diseases are gray mold, leaf scars, and downy mildew. Let's briefly look at these diseases.

Gray mold: A fungus known as gray mold affects the flowers, leaves, and stems of a variety of flowering plants. Small, crooked, and hidden beneath perilous areas with dark squares are sunflower leaf and fruit indicators. The botrytis blight, often known as gray mold, causes sunflower buds to decay or prevents them from opening. [7].

Leaf scars: Sunflower leaf scars from the fungus Septoria helianthi are common but do not constitute a serious concern. As a result, it can substantially impair plant growth when combined with other illnesses. The leaves wilt, and the injured tissues succumb to death [7].

Downy mildew: The plasmopara halstedii fungus, which causes downy mildew, is present in almost every nation where sunflowers are grown. The global impact on yield has been estimated to be 3.5 percent of commercial seed output [7].

The remainder of this paper is organized as follows: Section 1.1 describes related works. In section 2, the datasets and methodologies are introduced. Section 3 Results and discussion, section 4 conclusions, and future research.

1.1. Literature Review

Deep learning approaches have been proposed by researchers in recent years, and some of these have been investigated and reviewed, as stated below:

Banerjee et al. [2] used a new convolutional neural network (CNN) and support vector machine (SVM) based model to predict sunflower diseases in their study. They used three convolutional layers, three maximum pooling layers, and two fully connected layers to train the proposed model. The proposed model is trained with a dataset of different diseases affecting sunflowers. The results of the proposed research study achieved an F1 score of 83.45 and an overall classification accuracy of 83.59%. Gosh et al. [4] developed a hybrid model with transfer learning and a simple CNN to detect sunflower diseases. Of the eight models tested on a dataset consisting of four different classes, the VGG19 + CNN hybrid model achieved the best results in terms of sensitivity, recall, f1 score, and accuracy. They reached 93% classification accuracy. Dawod and Dobre [8] used ResNet interpretation methods to classify leaf diseases in sunflowers and visualization techniques were applied to explain misclassifications. Their study discovered that a classification using segmented lesions provides higher accuracy because many factors that lead to misclassification are eliminated in this way. Rajbongshi et al. [9] used 650 sunflower image datasets that they created themselves. First of all, they segmented the diseased areas in these images using the k-means clustering method. They extracted features from the segmented regions and classified them with various classifiers. They achieved the best result with Random Forest and achieved 90.68% classification success. Malik et al. [10] created a hybrid model using deep learning techniques to detect sunflower leaf diseases. They applied VGG16 and MobileNet transfer learning models on a dataset consisting of 329 sunflower images. Then, they compared these two models by applying them as a hybrid and reached 89.2% classification accuracy. In his study [11], Singh segmented sunflower leaves with the particle swarm optimization algorithm. The accuracy of the proposed system is around 98%.

Table 1 shows studies classifying sunflower diseases.

Table 1. A list of studies that were found in the literature

No	Class	Number of Data	Method	Accuracy(%)	References
1	12	3830	CNN+SVM	85.37%	[2]
2	4	838	ResNet152	98.02%	[8]
3	5	329	VGG16+MobileNet	89.2%	[10]
4	5	650	Random Forest	90.68%	[9]
5	6	149	Particle swarm	98%	[11]
6	4	467	VGG19+CNN	93%	[4]
7	4	467	Our Approach	94.68%	Our Approach
		1668		99.84%	

2. Material and Method

In this chapter, primarily the dataset, the deep learning methods, and the performance metrics used in the study will be explained.

2.1. Dataset

A publicly available dataset from mendeley data including occurrences of sunflower fruits and leaves dataset was used in this study [12]. This dataset consists of four hundred sixty-seven (467) original photographs and one thousand six hundred sixty-eight (1668) augmented images of healthy and disease-affected sunflower leaves and flowers. Sample images in the data set are given in Figure 1.
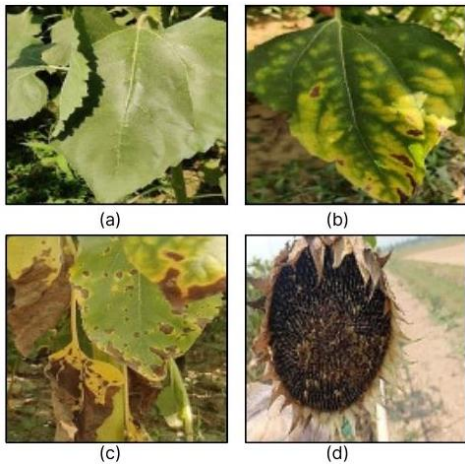
Figure 1. Sunflower plant leaf diseases dataset sample images (a) Fresh Leaf (b) downy mildew (c) Leaf scars (d) gray mold.

The dataset consists of four groups: gray mold, downy mold, leaf scars and fresh leaves. The number of classes in the data set and the number of images in each class are given in Table 2.

Table 2. Distribution of dataset by class

Class Name	Number of Original Images	Number of augmented Images
Gray Mold	72	398
Downy Mildew	120	470
Leaf Scary	141	509
Fresh Leaves	134	491
Total	467	1668

The original image is 467 in total. The number of augmented images is 1668 in total. The creators of the data set did the augmentation process. Augmentation operations include general enlargement operations in two ways, such as location and color change. All of the photos have a constant width and height of 512x512 pixels.

In the data set, there were four different classes of photos, and 80% of those images were used in the training set and 20% in the test set.

2.2. Convolutional Neural Networks

CNN is a popular deep learning technique that was created by drawing inspiration from the visual cortex of live beings. CNN architectures, which were initially employed in object recognition studies, are now employed in a wide range of applications. As with conventional artificial neural networks, CNN architectures are made up of neurons that learn to optimize themselves. The ability of CNN architectures to spot patterns in images sets them apart from traditional artificial neural networks in a big way. Even though CNN architectures can be developed in a variety of ways depending on the application, they typically start with convolution and pooling layers that are then divided up. In conventional backpropagation neural networks, they subsequently incorporate one or more fully linked layers [13].

There are many studies about CNN architecture. Layers consisting of data inputs enable CNN architectures to learn and classify features. CNN typically consists of five layers: convolution, pooling, activation, fully connected and softmax layer [14].

2.3 ResNet Neural Network

This architecture has distinguished itself in the field of computer vision, taking home first place honors in the 2015 ImageNet Large Scale Visual Recognition Challenge (ILSVRC) contests [15].

Residual blocks are used in the layers of ResNet models. These blocks help deep networks operate more effectively. The overall layout of residual blocks creates a link between the layer's input and the output of the following layers [16]. A residual block in a deep residual network is shown in Figure 2.
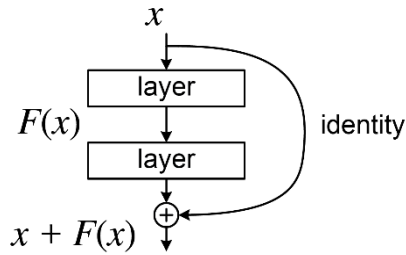
Figure 2. Residual learning: a building block [15]

The ResNet family has several versions that have been created, including ResNet-18, ResNet-34, ResNet-50, ResNet-101, and ResNet-152. The amount in the network name indicated how many levels were included in the network. In the proposed study, the classification stage is carried out using the pre-trained residual network ResNet-101 [17].

ResNet101 belongs to the ResNet (Residual Network) family and is recognized for its capability to address the vanishing gradient issue, making it suitable for training extremely deep networks. The designation "101" indicates the model's layer count. ResNet incorporates skip connections or shortcuts to streamline information flow within the network, resulting in more seamless and effective training [21].

2.4 Squeeze and Excitation (SE) Block

Squeeze-Excitation (SE) block is a channel-based attention mechanism where the network can selectively learn informative features and remove useless ones. SE performs feature recalibration to improve important features and disable less useful features. This block is independent of the network module of the specific network structure and can be embedded into the existing CNN network model with only a small increase in computational cost, thus improving the network training performance of the network model and increasing the efficiency of the network [18].

2.5 ResNext Neural Network

ResNext is a combination of ResNet and Inception. Unlike Inception v4, ResNext uses the same topology for each branch and does not require complex Inception structural details to be designed by hand. Group convolution is referred to as ResNext, and the number of groups is governed by variable cardinality. The group convolution machine strikes a balance between depth-separable convolution and regular convolution. [19] [20].

The three-layer convolutional block of the ResNet is swapped out in ResNext for a parallel stacking block with a comparable layout. ResNext employs group convolution with 3x3 filters to extract the features. The ResNext improves feature extraction capabilities while minimizing the number of network constraints by using group convolution and residual-like connections at both levels [21].

2.6 Proposed Model

In the study, classification of sunflower images was carried out with deep learning models. This process takes place in six main steps: entering images into the system, data augmentation, split data, applied classifier, performance evaluation and output. The proposed model is visualized in Figure 3.
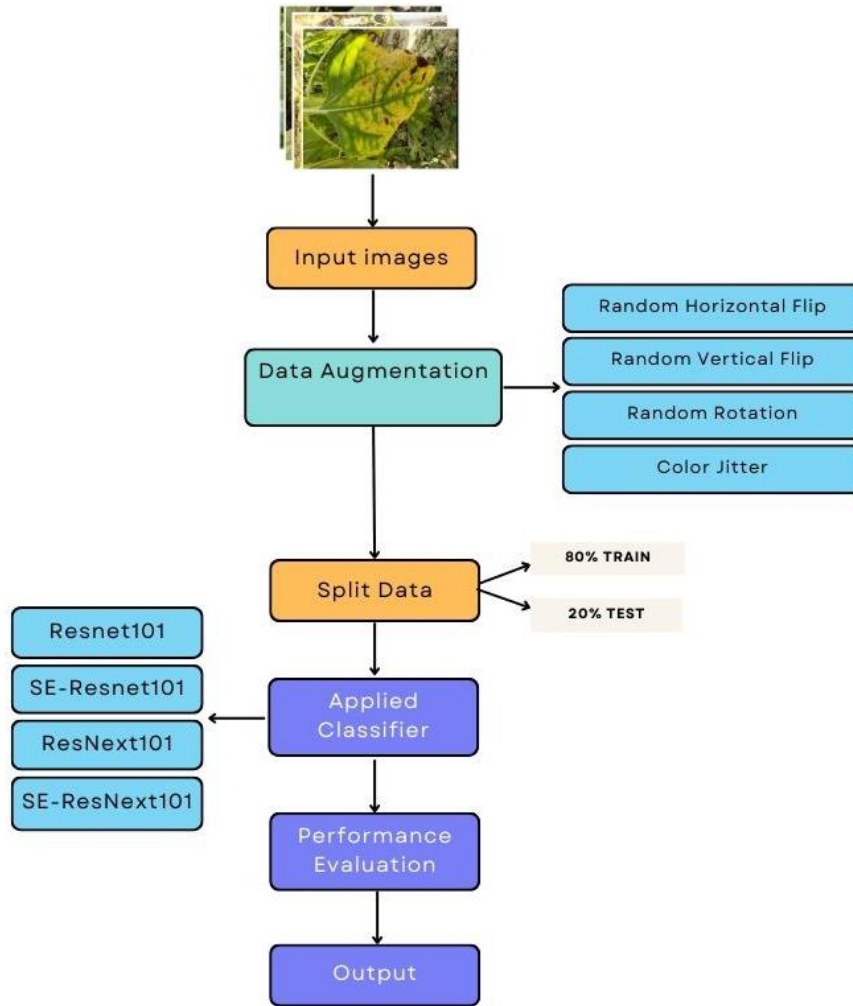
Figure 3. Flowchart of the proposed method

The number of images should be increased as we know that a large amount of data is required to train the deep learning model. Thus, model performance increases according to the increasing amount of data. During the data augmentation process of the study, a general augmentation process was performed in two ways, such as location and color change. In increasing by position, random rotation, random horizontal flip, random vertical flip methods were used. In the color enhancement process, only brightness was performed. By incorporating these augmentation techniques, the dataset used for training is effectively expanded, providing a larger and more diverse set of examples for the model to learn from. This increased variety of images helps the deep learning model to generalize better and improve its performance. The parameters used in the

augmentation process for this sunflower data set is given in Table 3.

Table 3. Augmentation parameters of deep learning models

Augmentation Type	Parameters
Random Rotation	True
Random Horizontal Flip	True
Random Vertical Flip	True
ColorJitter (brightness)	0.1

ColorJitter(brightness) value was selected as 0.1.

3. Results and Discussion

This section includes evaluation metrics and obtained results.

3.1. Evaluation Metrics

The accuracy, precision, recall, and F1-score were used to evaluate the performance of the models in the experimental data. When utilizing machine learning or deep learning techniques to solve classification problems, accuracy is a performance parameter that is used to gauge how well a model performs. This metric counts the proportion of samples that the model properly classifies. One of the basic performance criteria in classification problems is accuracy [14]. The formula is as follows.

$$Accuracy = \frac{(TP + TN)}{(TP + FP + TN + FN)} \quad (1)$$

Machine learning techniques are used to evaluate a model's performance in classification tasks using a performance parameter called precision. This metric represents the proportion of samples that the model actually classifies as positive [22]. The formula is as follows.

$$Precision = \frac{(TP)}{(TP + FP)} \quad (2)$$

Recall is a performance indicator used to assess a model's effectiveness in classifying issues when employing machine learning techniques. It gauges how well the model can predict how many genuine positive examples will be found among all positive examples [22]. The formula is as follows.

$$Recall = \frac{(TP)}{(TP + FN)} \quad (3)$$

This metric combines precision and recall measurements to produce a single performance measure. While recall evaluates how well the model can accurately predict the proportion of real positive examples out of all the actual positive cases, precision measures how well the model can accurately predict the proportion of true positive examples out of all the positive examples. The formula is as follows [22].

$$F1 - Score = \frac{(2TP)}{(2TP + FP + FN)} \quad (4)$$

Where, P = Positive class, N = Negative Class, TP = True positive, TN = True Negative, FP = False Positive, FN = False Negative.

3.2. Experimental Setup

In the first stage of the experimental study, sunflower leaf and flower images were classified with ResNet101 and ResNext101, both original images and augmented images. The selection of a ResNet variant depends on several factors, including the complexity of the task, available computational resources, and the amount of training data. Deeper networks, such as ResNet-150, are capable of capturing more complex features but require more computational power and a larger amount of data. On the other hand, shallower networks like ResNet-50 are preferred when there are limitations in computational resources. ResNet-101 architecture strikes a balance between complexity and resource requirements. It allows for the modeling of moderately complex patterns in the data without being excessively demanding to train. Through our experiments, we have determined that ResNet-101 offers a good fit for our specific problem and available resources. In order to make the results more effective, in the second stage, both the original images and the augmented images were reclassified with the Resnet101 and ResNext101 models to which Squeeze-and-Excitation Block was added. Testing of experimental studies was done through the COLAB platform. Nvidia Tesla T4 16GB graphics processor card was used in the Colab environment. The experiments were coded in Python 3 programming language.

The hyper parameters used in the study were determined by taking into account the amount of data in the dataset. The hyperparameters used in training the models are given in Table 4.

Table.4 Training parameters of deep learning models

Parameter	Value
Optimizer	Adam
Loss function	Cross-entropy
Batch Size	32
Epoch	30
Learning Rate	0.0001

The data, consisting of four classes: fresh leaf, downy mildew, leaf scars and gray mold, were classified with four different deep learning models: Resnet101, SE-Resnet101, ResNext101 and SE-ResNext101, with the parameters mentioned above, and the classification results are given in Table 5. Separate results are presented for original images and augmented images.

Table.5 Classification Results

Model	Accuracy (%)	Precision	Recall	F1-score
Resnet101 (Original images)	91.48%	0.92	0.92	0.92
SE-Resnet101 (Original images)	92.55%	0.93	0.93	0.93
ResNext101 (Original images)	92.55%	0.93	0.93	0.93
SE-ResNext101 (Original images)	94.68%	0.95	0.95	0.95
Resnet101 (Augmented images)	99.20%	1.00	0.99	0.99
SE-Resnet101 (Augmented images)	99.47%	1.00	0.99	0.99
ResNext101(Agumented images)	98.94%	0.99	0.99	0.99
SE-ResNext101 (Augmented images)	99.84%	0.99	0.99	0.99

The best classification accuracy for original images and augmented images was achieved with SE-ResNext101.

In this section, the confusion matrix obtained as a result of deep learning, Training loss and Training accuracy are given.
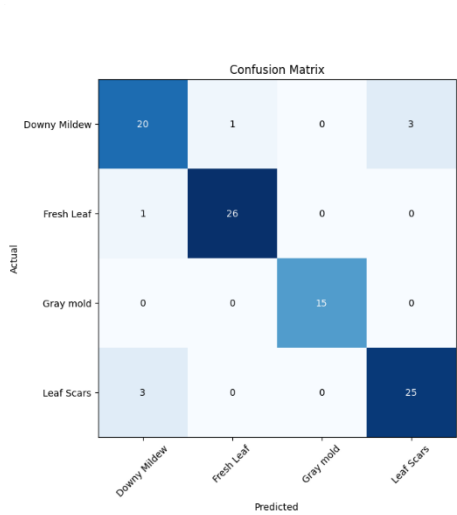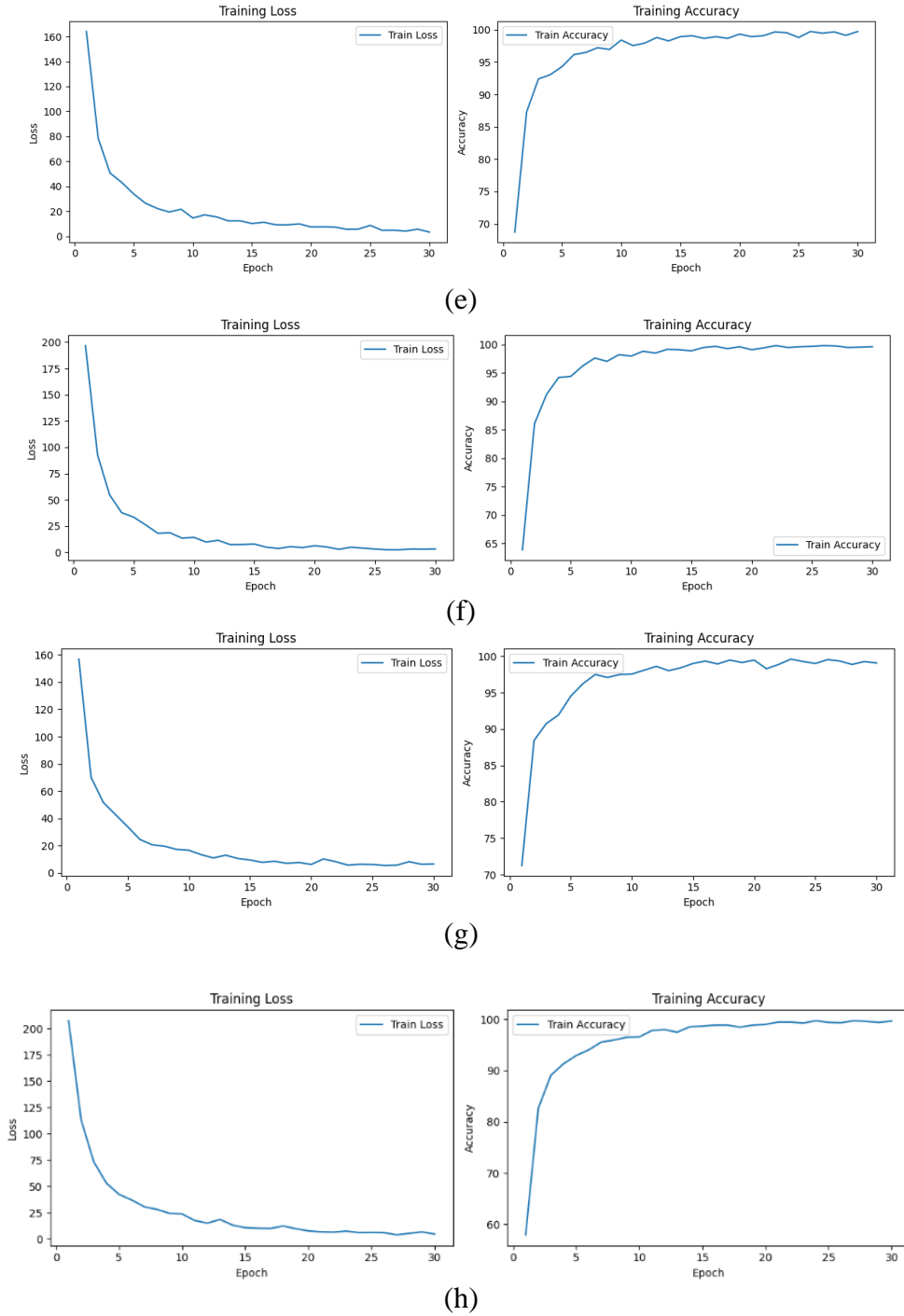

(a)Resnet101 Original

(b) Se-Resnet101 Original

(c)ResNext101 Original

(d) SE-ResNext101 Original

(e) Resnet101 Agumented

(f) SE-Resnet101 Agumented
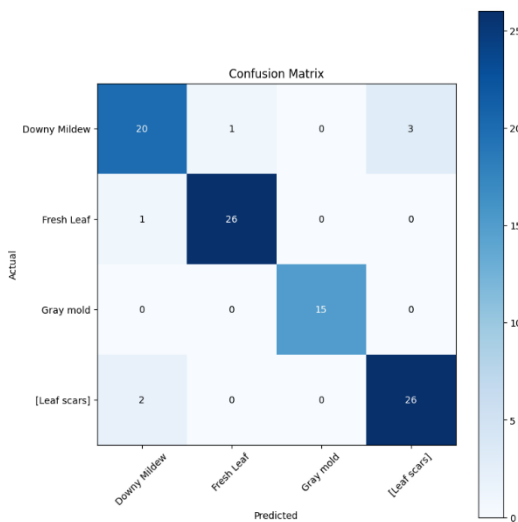
(g) ResNext101 Agumented
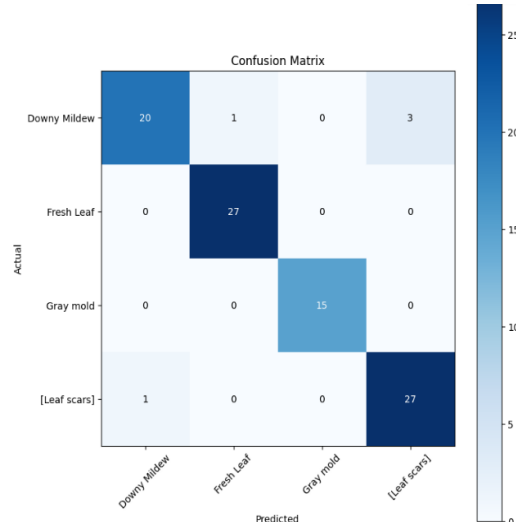
(h) SE-ResNext101 Agumented
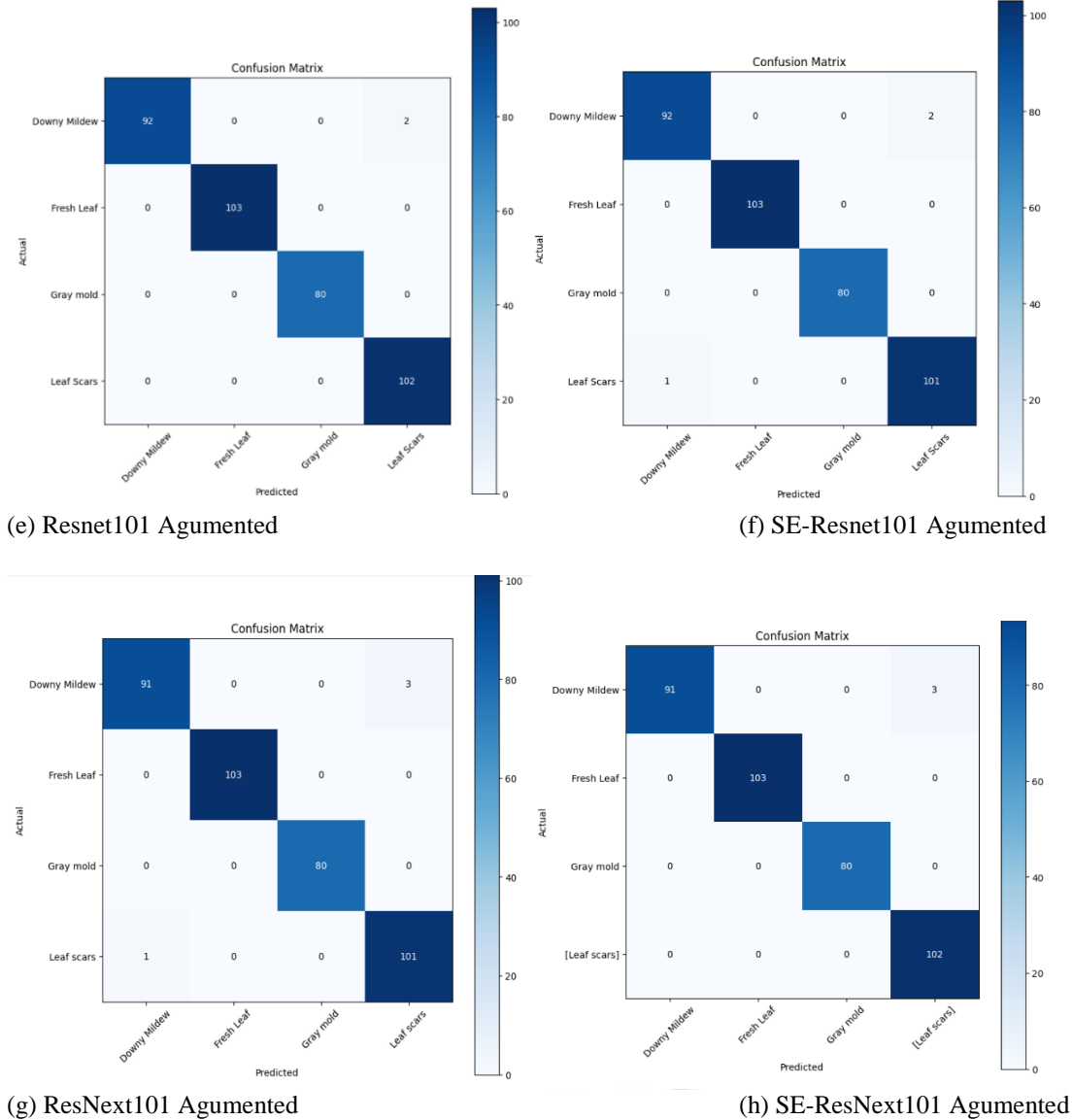
Figure 4. Confusion matrix graphics of original and augmented images (a) Resnet101 original, (b) SE-ResNet101 original, (c)ResNext101 original, (d) SE-ResNext101 original, (e) Resnet101 agumented, (f) SE-ResNet101agumented, (g) ResNext101 agumented, (h) SE-ResNext101 agumented

In Figure 4(a), the Resnet101 model was employed on original images. The confusion matrix reveals accurate classifications of 20 instances and 4 misclassifications for downy mildew. For the fresh leaf class, it correctly identified 26 and misclassified 1. The gray mold class was entirely correctly classified, while for Leaf scars, 25 were correct, and 3 were misclassified. Moving to Figure 4(b), the SE-Resnet101 model on original images showed 22 correct and 2 incorrect classifications for downy mildew. For fresh leaves, it correctly identified 27 and misclassified 1. The gray mold class had 14 correct

and 1 incorrect, and for Leaf scars, 24 were correct, with 4 misclassifications. Figure 4(c) illustrates the ResNext101 model on original images. It correctly classified 20 instances of downy mildew and misclassified 4. For fresh leaves, 26 were correct, and 1 was misclassified. Gray mold had 15 correct classifications, and Leaf scars had 26 correct and 2 incorrect. In Figure 4(d), the SE-ResNext101 model on original images correctly classified 20 instances of downy mildew and misclassified 4. Fresh leaves had 27 correct classifications, gray mold had 15 correct, and Leaf scars had 27 correct and 1 misclassification. Additionally, Figure 6 displays training loss and

accuracy curves. Moving to augmented images in Figure 4(e), the ResNet101 model classified 92 instances of downy mildew correctly and 2 incorrectly. For fresh leaves, it correctly identified 103, and for gray mold, it was correct in 80 instances. Leaf scars had 102 correct classifications. Figure 4(f) presents the SE-ResNet101 model on augmented images, classifying 92 instances of downy mildew correctly and 2 incorrectly. For fresh leaves, 103 were correct, 80 for gray mold, and 101 for Leaf scars with 1 misclassification. In Figure 4(g), the ResNext101 model on augmented images classified 91 instances

of downy mildew correctly and 3 incorrectly. Fresh leaves had 103 correct classifications, and both gray mold and Leaf scars had 80 correct, with 1 misclassification for Leaf scars. Lastly, Figure 4(h) shows the SE-ResNext101 model on augmented images, correctly classifying 91 instances of downy mildew and misclassifying 3. For fresh leaves, 103 were correct, 80 for gray mold, and 102 for Leaf scars.

The training loss and training accuracy graphs obtained as a result of the analysis are given in Figure 5.
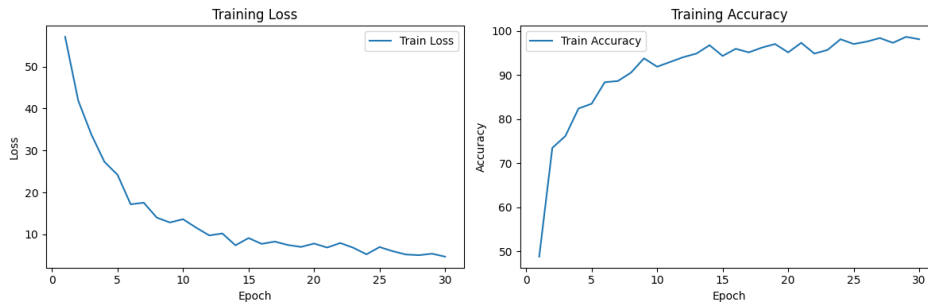
(a)
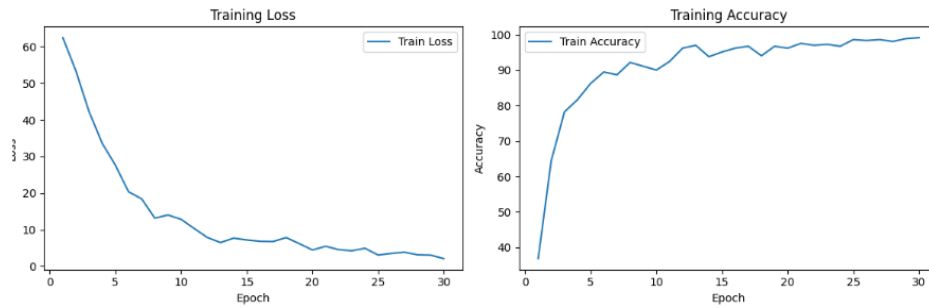
(b)
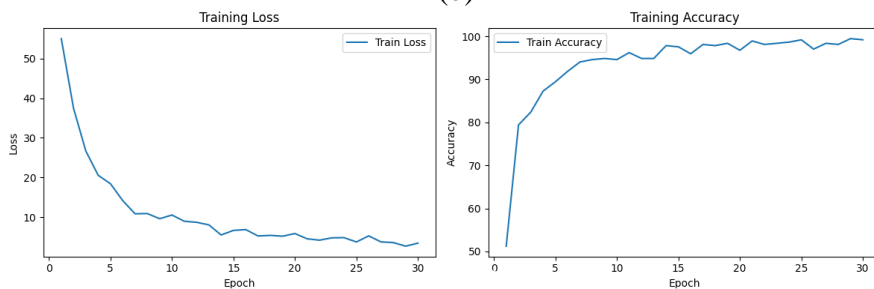
(c)
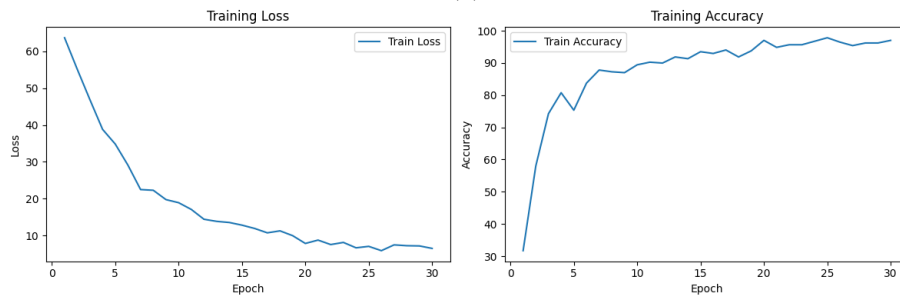
(d)

Figure 5. Training accuracy and training loss graphics. (a) Resnet101 original, (b) SE-ResNet101 original, (c)ResNext101 original, (d) SE-ResNext101 original, (e) Resnet101 agumented, (f) SE-ResNet101agumented, (g) ResNext101 agumented, (h) SE-ResNext101 agumented

Training accuracy and training loss graphs are used to monitor the performance of a deep learning model. These graphs are crucial to evaluate the model's learning performance, overfitting, and underfitting effectiveness [23]. When looking at both the training accuracy and training loss in Figure 5, neither overfitting nor underfitting seems to be observed.

4. Conclusion and Suggestions

Sunflower is one of the important food sources for the world. While its seeds are used as vegetable oil, its

stems and leaves are used as animal food. Diseases in sunflower cause significant yield losses. Traditional approaches have a lower success rate and take more time. Computerized detection of diseases, early diagnosis and prevention of these diseases are of great importance in terms of efficiency. In recent years, machine learning and deep learning algorithms have been used frequently in disease detection of various agricultural products.

In this study, some diseases seen in sunflower were classified with Resnet101 and ResNext101 models, which are pre-trained deep learning models, and by adding the SE block to these models, the classification was made separately, and the results were compared. In the analysis, it was seen that pre-trained networks with added SE blocks gave better classification results for this data set.

These proposed models may contribute to more effective classification of diseases in the sunflower industry. It may also be beneficial in the early diagnosis and treatment of diseases seen in sunflower. Identifying the diseases seen in the Sunflower plant reduces time and labor costs by enabling faster and automatic diagnosis of these diseases. As a result, productivity can be increased.

Compared to other studies, it is seen that the proposed method increases the classification success. This method can be successful not only in sunflower diseases but also in other plant diseases. As a result, higher quality and safer food products can be offered to consumers. The aim of this article is to automatically and accurately classify sunflower disease varieties based on their visual characteristics. Additionally, the resulting classification models can be used to classify diseases of other agricultural products. Additionally, mobile applications can be developed in this field.

Contributions of the authors

The authors confirm that the contribution is equally for this paper.

Conflict of Interest Statement

There is no conflict of interest between the authors.

Statement of Research and Publication Ethics

The study is complied with research and publication ethics

References

[1] M. Barrio-Conde, M. A. Zanella, J. M. Aguiar-Perez, R. Ruiz-Gonzalez, and J. Gomez-Gil, 'A Deep Learning Image System for Classifying High Oleic Sunflower Seed Varieties', *Sensors*, vol. 23, no. 5, p. 2471, Feb. 2023, doi: 10.3390/s23052471.

[2] D. Banerjee, V. Kukreja, S. Vats, V. Jain, and B. Goyal, 'AI-Driven Sunflower Disease Multiclassification: Merging Convolutional Neural Networks and Support Vector Machines', *in 2023 4th International Conference on Electronics and Sustainable Communication Systems (ICESC), Coimbatore, India: IEEE*, Jul. 2023, pp. 722–726. doi: 10.1109/ICESC57686.2023.10193473.

[3] S. Khalifani, R. Darvishzadeh, N. Azad, and R. Seyed Rahmani, 'Prediction of sunflower grain yield under normal and salinity stress by RBF, MLP and, CNN models', *Industrial Crops and Products*, vol. 189, p. 115762, Dec. 2022, doi: 10.1016/j.indcrop.2022.115762.

[4] P. Ghosh, A. K. Mondal, S. Chatterjee, M. Masud, H. Meshref, and A. K. Bairagi, 'Recognition of Sunflower Diseases Using Hybrid Deep Learning and Its Explainability with AI', *Mathematics*, vol. 11, no. 10, p. 2241, May 2023, doi: 10.3390/math11102241.

[5] A. Sirohi and A. Malik, 'A Hybrid Model for the Classification of Sunflower Diseases Using Deep Learning', *in 2021 2nd International Conference on Intelligent Engineering and Management (ICIEM), London, United Kingdom: IEEE*, Apr. 2021, pp. 58–62. doi: 10.1109/ICIEM51511.2021.9445342.

[6] S. Chen, F. Lv, and P. Huo, 'Improved detection of yolov4 sunflower leaf diseases', *in 2021 2nd International Symposium on Computer Engineering and Intelligent Communications (ISCEIC), Nanjing, China: IEEE*, Aug. 2021, pp. 56–59. doi: 10.1109/ISCEIC53685.2021.00019.

[7] U. Sara, A. Rajbongshi, R. Shakil, B. Akter, S. Sazzad, and M. S. Uddin, 'An extensive sunflower dataset representation for successful identification and classification of sunflower diseases', *Data in Brief*, vol. 42, p. 108043, Jun. 2022, doi: 10.1016/j.dib.2022.108043.

[8] R. G. Dawod and C. Dobre, 'Classification of Sunflower Foliar Diseases Using Convolutional Neural Network', *in 2021 23rd International Conference on Control Systems and Computer Science (CSCS), Bucharest, Romania: IEEE*, May 2021, pp. 476–481. doi: 10.1109/CSCS52396.2021.00084.

[9] A. Rajbongshi, A. A. Biswas, J. Biswas, R. Shakil, B. Akter, and M. R. Barman, 'Sunflower Diseases Recognition Using Computer Vision-Based Approach', *in 2021 IEEE 9th Region 10 Humanitarian Technology Conference (R10-HTC), Bangalore, India: IEEE*, Sep. 2021, pp. 1–5. doi: 10.1109/R10-HTC53172.2021.9641588.

[10] A. Malik et al., 'Design and Evaluation of a Hybrid Technique for Detecting Sunflower Leaf Disease Using Deep Learning Approach', *Journal of Food Quality*, vol. 2022, pp. 1–12, Apr. 2022, doi: 10.1155/2022/9211700.

[11] V. Singh, 'Sunflower leaf diseases detection using image segmentation based on particle swarm optimization', *Artificial Intelligence in Agriculture*, vol. 3, pp. 62–68, Sep. 2019, doi: 10.1016/j.aiia.2019.09.002.

[12] Aditya Rajbongshi, 'Sun Flower Fruits and Leaves dataset for Sunflower Disease Classification through Machine Learning and Deep Learning'. Mendeley, Jan. 18, 2022. doi: 10.17632/B83HMRZTH8.1.

[13] Ö. Arslan and S. A. Uymaz, 'Classification of Invoice Images by Using Convolutional Neural Networks', *Journal of Advanced Research in Natural and Applied Sciences*, vol. 8, no. 1, pp. 8–25, Mar. 2022, doi: 10.28979/jarnas.953634.

[14] B. Gencturk et al., 'Detection of hazelnut varieties and development of mobile application with CNN data fusion feature reduction-based models', *Eur Food Res Technol*, Sep. 2023, doi: 10.1007/s00217-023-04369-9.

[15] K. He, X. Zhang, S. Ren, and J. Sun, 'Deep Residual Learning for Image Recognition', *in 2016 IEEE Conference on Computer Vision and Pattern Recognition (CVPR), Las Vegas, NV, USA: IEEE*, Jun. 2016, pp. 770–778. doi: 10.1109/CVPR.2016.90.

[16] E. E. Kilinç, F. Aka, and S. Metlek, '3BResNet: A Novel Residual Block-Based ResNet Model Approach for COVID19 Detection', *Bitlis Eren Üniversitesi Fen Bilimleri Dergisi*, vol. 12, no. 3, pp. 925–940, Sep. 2023, doi: 10.17798/bitlisfen.1346730.

[17] K. Lin et al., 'Applying a deep residual network coupling with transfer learning for recyclable waste sorting', *Environ Sci Pollut Res*, vol. 29, no. 60, pp. 91081–91095, Dec. 2022, doi: 10.1007/s11356-022-22167-w.

[18] J. Hu, L. Shen, S. Albanie, G. Sun, and E. Wu, 'Squeeze-and-Excitation Networks', *IEEE Trans. Pattern Anal. Mach. Intell.*, vol. 42, no. 8, pp. 2011–2023, Aug. 2020, doi: 10.1109/TPAMI.2019.2913372.

[19] S. Chen, T. Wang, Z. Huang, and X. Hou, 'Detection method of Golden Chip-Free Hardware Trojan based on the combination of ResNeXt structure and attention mechanism', *Computers & Security*, vol. 134, p. 103428, Nov. 2023, doi: 10.1016/j.cose.2023.103428.

[20] S. S. Chaturvedi, J. V. Tembhurne, and T. Diwan, 'A multi-class skin Cancer classification using deep convolutional neural networks', *Multimed Tools Appl*, vol. 79, no. 39–40, pp. 28477–28498, Oct. 2020, doi: 10.1007/s11042-020-09388-2.

[21] A. Ramana Kumari, S. Nagaraja Rao, and P. Ramana Reddy, 'Design of hybrid dental caries segmentation and caries detection with meta-heuristic-based ResneXt-RNN', *Biomedical Signal Processing and Control*, vol. 78, p. 103961, Sep. 2022, doi: 10.1016/j.bspc.2022.103961.

[22] I. Naseer, S. Akram, T. Masood, A. Jaffar, M. A. Khan, and A. Mosavi, 'Performance Analysis of State-of-the-Art CNN Architectures for LUNA16', *Sensors*, vol. 22, no. 12, p. 4426, Jun. 2022, doi: 10.3390/s22124426.

[23] S. F. Ahmed et al., 'Deep learning modelling techniques: current progress, applications, advantages, and challenges', *Artif Intell Rev*, vol. 56, no. 11, pp. 13521–13617, Nov. 2023, doi: 10.1007/s10462-023-10466-8.

Investigation of Single-step Fabrication of a Cathode-supported Planar Single-chamber Solid Oxide Fuel Cell and Its Performance

Yunus SAYAN[1,2*], Jung-Sik KİM[2], Houzheng WU[2]

[1] Bitlis Eren University, Faculty of Engineering and Architecture, Department of Mechanical Engineering, Bitlis, Türkiye
[2] Loughborough University, School of Aeronautical, Automotive, Chemical and Material Engineering Loughborough, United Kingdom
(ORCID: 0000-0002-0871-6842) (ORCID: 0000-0002-3696-7251) (ORCID: 0000-0002-7628-3890)

Abstract

This study presents a cathode-supported planar solid oxide fuel cell (SOFC) fabrication made via a single step co-sintering method and investigation of its performance. The materials used are NiO-CGO, CGO and CGO-LSCF for anode, cathode, electrolyte, respectively. Our study shows that increasing the cell size has a detrimental effect on cell single step co-sinterability. Increasing cathode thickness and reducing electrolyte thickness led to curvature decrease at the edges, however these adjustments were not enough to achieve a curvature-free cathode-supported cell. Thus, three porous alumina cover plates (total mass of 49.35 g) placed on the top of the cell during sintering were utilized to suppress curvature formation, and as a result, a nearly curvature- free cathode-supported cell was obtained. Performance of the cells were investigated. The results showed that increasing cathode thickness and decreasing electrolyte thickness had negative effects on cell performance despite enhanced single step co-sinterability of the cell. The maximum power density and OCV of the final planar cell (thickness 60-40-800 μm, anode-electrolyte-cathode) were found to be 1.71 mW cm^{-2} and 0.2 V, respectively, in a fuel rich condition (R:1.6). Additionally, the maximum OCV and power density among the all cells were measured from the cell (thickness 60-40-400 μm, anode-electrolyte-cathode) as 0.56 V and 24.79 mW cm^{-2}, respectively, in a fuel rich condition (R:2.4).

1. Introduction

A new type of solid oxide fuel cell (SOFC), single chamber solid oxide fuel cells (SC-SOFCs), were introduced by researchers to reduce certain drawbacks faced in dual chamber SOFCs (DC-SOFCs), such as complex gas manifolding, flow field structures and gas-tight sealing [1]. Unlike DC-SOFCs, SC-SOFCs are composed of only one gas chamber containing a gas mixture of fuel and oxidant [1]–[4]. This distinctive characteristic of SC-SOFCs allows them to have simplified structures, resulting in less start-up and shut down time and better thermal shock resistance than DC-SOFCs [1], [3], [5]. If their

potential is released, the simplified structure could yield a considerable decrease of the total system cost. Moreover, the electrolyte layer does not have to be dense to stop gas crossover, given that there is no requirement prevent fuel mixing with oxidant gas. This property of SC-SOFCs enables utilization of less expensive manufacturing methods of the electrolyte.

For the anode supported SOFCs, potential anode re-oxidation is a serious problem which can cause cells to break after repeated cycles of cell usage [6], [7]. This is because the thicker anode (based on nickel, Ni) catalyst oxidation and reduction lead to cell to shrink and expand in time. This uncontrolled

volume shrinkage and expansion leads the cell to crack. Therefore, a new configuration of SOFCs, named as cathode-supported SOFC, were proposed by researchers to overcome this issue [1], [3]. This configuration of SOFC has showed the longest lifetime among all categories of SOFCs [8], but incurs penalties on the sluggish oxygen reduction reaction overpotentials.

Using co-sintering process for multi-layer structures leads to considerable benefits in time, energy savings and effort, and thus has been attracting growing interest in many different research areas, including SOFCs. In the production of DC-SOFCs, co-sintering has been generally applied to bi-layer structures, comprising of anode and electrolyte layers. It is because the similar sintering behavior of each layer inhibits developments of any defects such as warping, delamination and cracking during the sintering process [9]–[11].

SC-SOFCs are currently fabricated utilizing at least two sintering process: usually co-sintering anode and electrolyte, followed by a separate deposition of the cathode and its sintering [12]–[14]. The prevailing explanation for a two-step sintering is that the materials for electrolyte, cathode and anode need different sintering temperatures to obtain the required microstructures. Though possible reactions/interactions between electrolyte and cathode are reduced by a two-step sintering process [14], there are some rationales why single-step co-sintering (SSCS) of SC-SOFCs, sintering anode, cathode and electrolyte together in one step, are desired. It is primarily needed to simplify the fabrication process along with lessening the processing time and input energy [15], [16]. These advantages of single step co-sintering of SC-SOFCs decrease further the fabrication cost of SC-SOFCs and thus improve commercial viability if used in commercial scale. However, when multiple layers are sintered together, they impose stress upon each other due to the different shrinkage behavior, and thereby resulting in either curvature formation, delamination or cracks in the cell.

In this study, the SSCS of cathode-supported SC-SOFCs was investigated profoundly. The effect of layer thickness, cell size and sintering temperature on cell sinterability were analyzed. In order to achieve a curvature free cathode-supported cell, a limiting constraint was applied on the top of the cells. The fabricated cells were then tested under single chamber conditions so as to observe the functionality of the cells as working electrochemical cells and to analyze the effect of thickness and thickness ratio change on the cell performance.

2. Experimental

2.1. Preparation of the Cells

Cell green layers were procured from Maryland tape casting Ltd, USA [17]. They were all made by tape casting method, consisting of 60 wt% NiO (nickel oxide)–40 wt% $Ce_{0.8}Gd_{0.2}O_{2-\delta}$ (gadolinium doped ceria (CGO)): $Ce_{0.8}Gd_{0.2}O_{2-\delta}$ (CGO): 50 wt% $La_{0.6}Sr_{0.4}Co_{0.2}Fe_{0.8}O_{3-\delta}$(lanthanum strontium cobalt ferrite (LSCF))–50 wt% CGO (20% gadolinium(Gd)) as anode-electrolyte-cathode, (A-E-C). The slurry composition of the green tapes provided by the supplier are summarized in reference [18]. The sintering temperature of the LSCF cathode is less than that of the anode and electrolyte [19], [20]. Therefore, in order to retard the sintering behavior of the LSCF and thereby balancing the final density of materials during the process of co-sintering, the LSCF particle size was chosen to be larger than that of the anode and cathode (1 μm for the cathode green tape as opposed to 0.3 μm for the anode and electrolyte green tapes).

Multiple layers of green tapes were layered upon each other to obtain desired thickness of electrolyte and electrodes. Each component thickness was controlled by the number of individual green tape layers of each material (of around 20 μm for each tape). These layers are subsequently hot-pressed at a pressure of 2 MPa and temperature 60 °C dwelling for 5 minutes (using the Carvel Heated Bench Top Hot Press, model: 3853CE-8, USA) to allow individual layers to merge and form a complete cell. The hot pressing condition was carefully determined in order to achieve acceptable compactness and good adhesion between each layer, and also prevent over-pressing and inhomogeneous cell area distribution (detailed explanation is available in ref. [18]).

Thickness of each layer in a cell can have direct effect on as-sintered cell quality through co-sintering. In order to investigate such influence, several cells with different combinations of thicknesses were prepared. All cells were hot pressed under same conditions. Subsequently sintered at 1200 °C with a 1 hour of dwelling time under a heating and cooling rate profile as following: a 1°C min^{-1} heating rate from room temperature to 500 °C, 2 °C min^{-1} from 500 °C to 900 °C, 1 °C min^{-1} from 900 °C to 1200 °C; and a 3 °C min^{-1} cooling rate from 1200 °C to room temperature. Sintering profile of the cells were thoroughly defined with the purpose of achieving less defects during single-step co-sintering fabrication processes by carefully analyzing debinding and shrinkage properties of each green

layer (detailed information is presented in reference [18]).

In order to investigate the effect of sintering behavior of a cathode-supported cell during heating and during cooling, a cell with a thickness ratio and thickness of 3-2-10 and 60-40-200 µm, respectively, were made (anode-electrolyte-cathode), with a 40x40 mm width (W) and length (L)). In addition, two types of cells with different cathode thicknesses were made with the aim of investigating the cathode thickness and the cell size on cell SSCS. The first type of cell possessed a width and length of 40 mm and 40 mm (named cell type 1) respectively while the second type had a 30x30 mm W x L (named cell type 2). For both type of cells, cathode thickness increased from 200 µm, to 300 µm, and to 400 µm while anode and electrolyte thickness were kept constant with a thickness of 60 µm and 40 µm, respectively. Moreover, three different types of the cells were prepared to investigate the effect of electrolyte thickness and limited constraint on single step co-sinterabilty. They are named as cell 1, cell 2 and cell 3, having the same width and length (40x40 mm WxL), as listed in Table 1. Cell 3 was initially sintered without any constraint, but later iterations were sintered with either one or multiple alumina (Al$_2$O$_3$) porous cover plates (1 mm thickness, 40% porosity, ESLTM 42520-2) located on the top of the cell. This improved the ability to restrain curvature formation, and finally to achieve a curvature-free cell.

Table 1. Three different cathode-supported SC-SOFCs, their thicknesses, thickness ratio, and sintering type.

Cell Type	Thickness Ratio anode:electrolyte:cathode	Thickness / µm anode:electrolyte:cathode	Sintering Type
Cell 1	3-2-20	60-40-400	Without any constraint on the top layer of the cell
Cell 2	3-1-20	60-20-400	Without any constraint on the top layer of the cell
Cell 3	3-1-40	60-20-800	Without any constraint on the top layer of the cell
Cell 3	3-1-40	60-20-800	Sintered with a 50x50 mm LxW porous alumina cover plate on the top of the cell, with a total mass of 7.31 g
Cell 3	3-1-40	60-20-800	Sintered with a 75x75 mm LxW porous alumina cover plate on the top of the cell, with a total mass of 16.45 g
Cell 3	3-1-40	60-20-800	Sintered with two 75x75 mm LxW porous alumina cover plates on the top of the cell, with a total mass of 32.9 g
Cell 3	3-1-40	60-20-800	Sintered with three 75x75 mm LxW porous alumina cover plates on the top of the cell, with a total mass of 49.35 g

2.2. Characterizations and Tests

In order to characterize the microstructure of as-sintered cell as well as chemical element of the final planar cell, scanning electron microscopy (SEM) with energy dispersive spectroscopy (EDS) (Zeiss 1530-VP FEGSEM, Germany) was used. Acceleration voltage for imaging by backscattered electrons and secondary electrons was set to 20 kV and 5 kV, respectively. A layer of palladium-gold (Pd-Au) alloy was sputtered all examined surfaces to prevent charging during imaging. All EDS spectra were obtained as an acceleration voltage of 20 kV. Grinding and polishing were carefully applied to the final cell in order to accurately examine the grain size and pore structure of an as-sintered cell by using semi-automatic Struers LaboSystem (Germany), after the cell was mounted in Bakelite by using Struers CitoPress 5 (Germany).

The porosity of the cell was quantified by applying the ImageJ program to the obtained SEM images. The method used to estimate the mean porosity of the cathode, electrolyte and anode of the cell and can be detailed as follows: Back scatter SEM images of the anode, cathode and electrolyte cross-sectional areas of the cell were taken separately. All images possess a 10 µm scale, Mag 2.00 KX, and WD of 8.5 mm. Thereafter, obtained images were uploaded to ImageJ program and were set to 8-bit image quality for threshold analysis. Adjustment for the threshold of each images was carefully done. The percentage of the pore area were read and recorded

by measuring the percentage of black area on the images.

A potentiostat (Solarton Analytical 1280C, United Kingdom) in concert with the CorrWare®/CorrView™ electrochemical suite (Scribner Associates Inc., United States) was used to measure the open circuit voltage (OCV) and polarization of the cells. In addition, Q150T S/E/ES Turbo-Pumped Sputter Coater (Quorum Technologies, United Kingdom) was utilized to sputter gold on both electrodes as current collector. Silver paste was used to attach chromel (90% Ni,10% chromium (Cr)) wire to sputtered gold grids. A single chamber condition was applied in order to test cells. All cells were positioned in an alumina cell holder perpendicular to flow direction. Additionally, all anode electrodes of the cells were initially reduced at 600 ˚C for 1 hour in a flowing gas mixture of hydrogen and nitrogen with a flowing rate of 0.01 L min^{-1}, and 0.19 L min^{-1}, respectively. Following reduction, those cells were tested in a flowing mixture of gas with different compositions at 600 ˚C.

3. Results and Discussion

3.1. Sintering Results

3.1.1. Sintering Behavior of a Cathode-Supported Cell During Heating and During Cooling

Figure 1 depicts the picture of a cathode-supported cell taken during sintering and cooling at different temperatures (thickness ratio and thickness of the cell are 3-2-10 and 60-40-200 μm, respectively, (anode-electrolyte-cathode), with a 40x40 mm width and length. The cell was placed on a porous alumina substrate, with the cathode adjacent to it (facing downward). According to Figure 1A, there is no observable/substantial curvature formation up to 200 ˚C. However, when temperature reached 250 ˚C, there is a visible curvature formation towards the upward direction, h_1= 1.384 mm, (curvature height, h_1, from top surface of alumina substrate to the peak point of the top surface of the cell). This might be as a result of additives removal in the green body during debinding stage. Because the top surface of the cell is the drying surface and additives will be first evaporated from the top surface. This phenomenon leads to a capillary force in the top surface and cause a compressive stress in this area. Therefore, cells curved towards upward. Moreover, when the temperature reached to 300 ˚C, the cell curvature was relieved, the h_1 decreased to 0.462 mm. This could be explained by the fact that later into the drying process

(above 250 ˚C and until the end of the additive removal process (500 ˚C)), the liquid vapor interface is subjected to changes from the top surface to the interior of the green body and pores are occupied with air. This results in a reduction in compressive stress on the top surface. In addition, the lower part of the green body still contains liquid therefore it is exposed to compressive stress due to capillary forces. This brings about the tendency of the green body to warp into the opposite direction. In general, the effect of capillary force, at the lower part of the cell at the later stage of sintering was not big enough to curve cell downward. Thus, the cell curvature was still upward after the burn-out stage. Additionally, the curvature direction is still upward until 800 C˚, and the curvature height reached to 1.260 mm. It might be as a result of particle rearrangement. However, when the main densification started (after 800 ˚C), the cells edges tended to curve downward due to higher shrinkage rate of cathode which is the fact that high shrinkage of the cathode generates high compressive stress on the bottom of the cell and thus leads to more curvature formation of the cells towards the cathode side. The curvature height became 3.39 mm at 900 ˚C though the effect of additive removals on curvature formation was still at present (see Figure 1A). Moreover, in the main densification area, cell curvature directed downward, and it reached its maximum value of 6.678 mm at 1200 ˚C (see Figure 1A).

In addition, the main observation from these figures was that it was expected for the cell to crack when it reached at 1200 ˚C or after dwelling at 1200 ˚C. However, surprisingly, there was no cracking or delamination during heating and after dwelling as shown in Figure 1A. Nevertheless, when the cell was cooled down, the cell did not break until 800 ˚C. It might not even have broken at a temperature of less than 800 ˚C. However, the cell broke into many pieces during cooling owing to residual stress in the cell (see Figure 1B). It might be explained by the fact that, at elevated temperature, the ceramic cell might have possessed plastic properties and thus withstood high residual stress. However, when the temperature decreased, the cell became more brittle and the contribution of coefficient of thermal expansion (CTE) mismatch stress (due to three different layers of the cell) to sintering stress became higher at room temperature. Consequently, the cell could not withstand the amount of residual stress due to its brittle crystal structure.

A) Cell's pictures taken during sintering
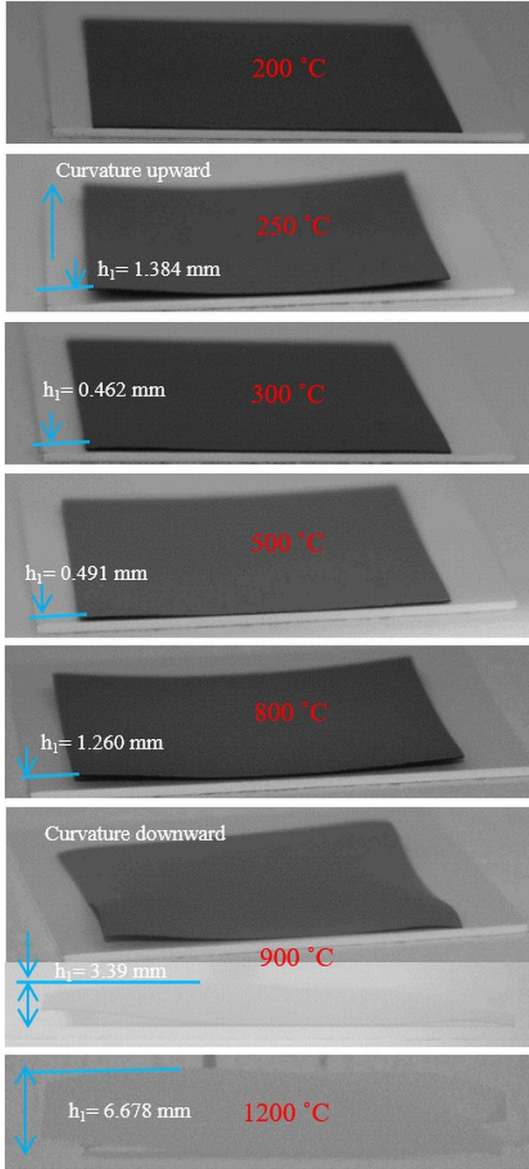
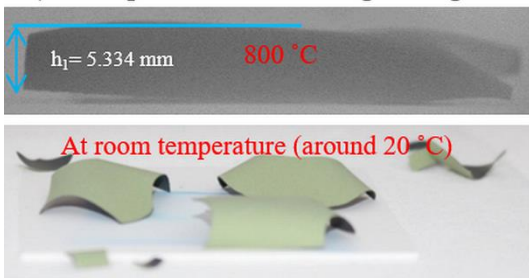**B) Cell's pictures taken during cooling**

Figure 1. The pictures of a cathode-supported cell taken A) during sintering and B) during cooling at different temperatures, thickness ratio and thickness of the cell are 3-2-10 and 60-40-200 µm, respectively, (Anode-Electrolyte-Cathode), with a 40x40 mm width and length.

3.1.2. The Influence of Cathode Thickness and Cell Size On Cell SSCS

Figure 2 shows the sintering results of type 1 and type 2 cells. It can be clearly seen from the figure as a visual inspection for both type of cells, increasing cathode thickness improved cell SSCS. The following reasons are put forth: firstly, the cathode layer became more dominant in overall cell composition, thus, the individual effects of anode and cathode become less pronounced during sintering. Secondly, increased cathode thickness improved cell resistance to deformation and fracture, therefore, the cells become more robust towards withstanding either sintering stress during heating or CTE mismatch stress during cooling as a result of increased cross-sectional area of the cathode normal to the length direction. Furthermore, it can also be seen from the Figurer 2, increasing cell size from 30x30 mm to 40x40 mm (WxL) has negative effect on SSCP. For instance, cell type 1 with a cathode thickness of 200 µm broke into numerous pieces while cell type 2 for the same cathode thickness splintered into fewer pieces. Similarly, cell type 1 with a cathode thickness of 400 µm broke into three parts whereas cell type 2 for the same cathode thickness has no carks present after sintering.
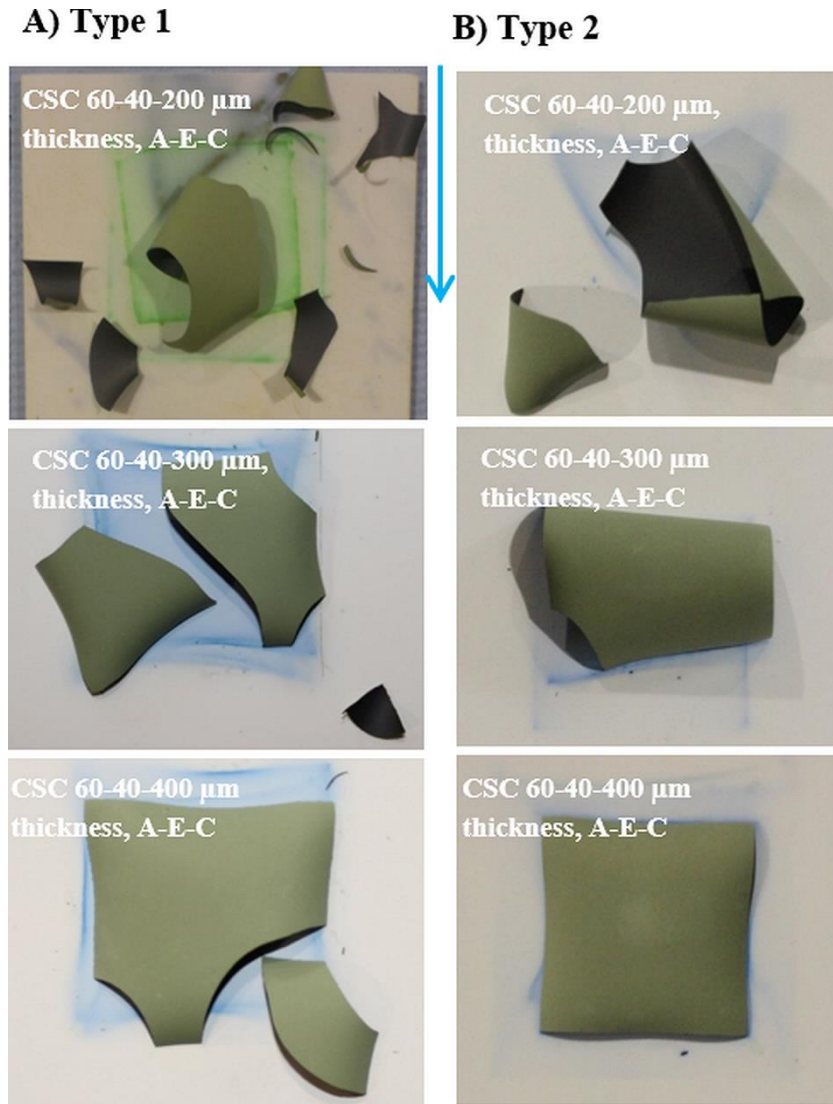
Figure 2. The influence of cathode thickness and cell size on cell sinterability, sintered at 1200 ˚C, A) Type 1: Cells` Width X Length 40x40 mm and B) Type 2: Cells` Width X Length 30x30 mm. CSC is the abbreviation of the cathode supported cell.

3.1.3. The Influence of Electrolyte Thickness On Cell SSCS

Figure 3 shows the sintering results of two different cathode-supported cells. Cell 1 and Cell 2 possess the same anode and cathode thickness (60 µm and 400 µm, respectively) while their electrolyte thickness is 40 µm and 20 µm, respectively. The figure shows that decreasing electrolyte thickness improved SSCS of the cell. The cell mean curvature height decreased from 4.29 mm to 3.87 mm and there was no crack after sintering (see Figure 3, cell 1 and cell 2). This might be as a result of the electrolyte mismatch stress contribution mitigation. The mean curvature height, h, was calculated from the cathode top surface to the peak point of curves as shown in Figure 3. The measurement was carried out from each side of the cells and the average of them was taken.

Cell 1 40 x 40 mm WxL thickness ratio 3-2-20 (A-E-C) thickness 60-40-400 µm

View from anode side   View from cathode side

Mean curvature – height: 4.29 mm
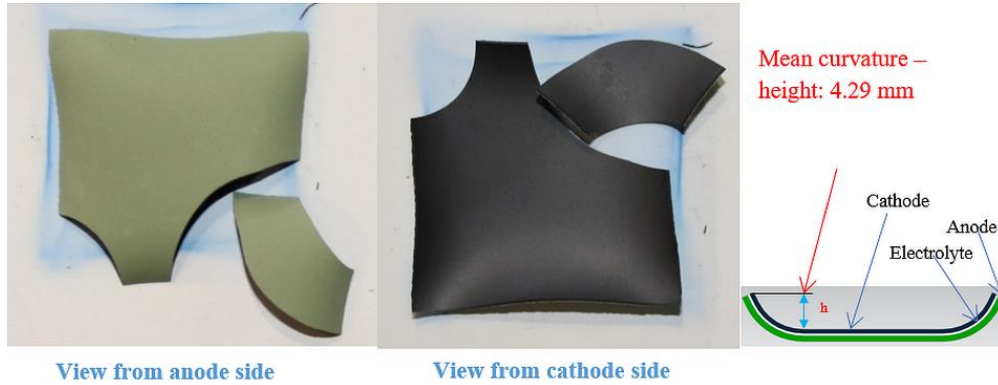
Cell 2 40 x 40 mm WxL thickness ratio 3-1-20 (A-E-C) thickness 60-20-400 µm

Mean curvature – height: 3.87 mm
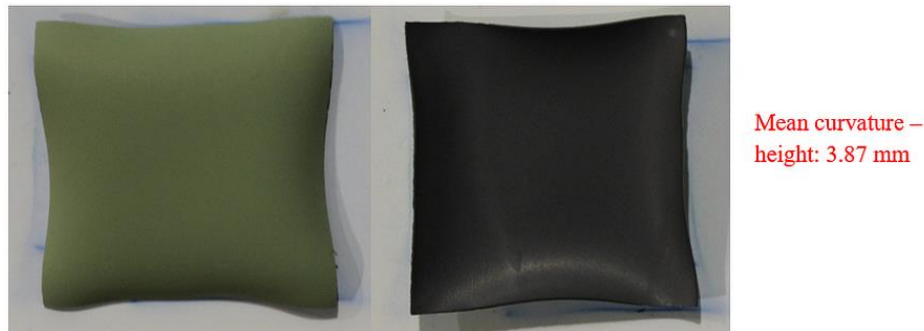
Figure 3. The influence of electrolyte thickness on cell sinterability.

3.1.4. Constrained Sintering of Cathode-Supported Cells

For the cathode-supported cell, increasing cathode thickness continuously and decreasing electrolyte thickness was not enough to obtain curvature-free cells as seen in previous sections. In addition, concentration polarization becomes a serious problem when the cathode thickness is increased too much. This is because the thicker cathode causes impediments to the gas transport from top surface of the cathode to the inner pores of the cathode-electrolyte interface and product removal from triple phase boundary (TPB). This issue becomes more vital when a cell is placed as a flow-through (perpendicular to gas flow) arrangement in the mixture. Therefore, it is important to investigate different methods to remove curvature formation rather than continuously increasing cathode thickness. Placing a limiting constraint on the top of the cell was a useful approach to obtain curvature-free cells without changing the thickness of the cell as demonstrated in [18]. Therefore, five cells with the same size, thickness and thickness ratio were made and sintered either free or with limited constraint on the top of the cells. For that purpose, either one or

multiple alumina porous cover plates were located on the top of the cells during sintering so as to investigate the effect of the limited constraint on cell sinterability, the ability to suppress curvature formation, and finally to obtain curvature free cell. The cells were made with a 40x40 mm of WxL and a thickness of 60-20-800 µm A-E-C (thickness ratio of 3-1-40). The porosity and thickness of alumina cover plate is around 40% and 1 mm, respectfully. The length and width of the alumina cover plates can be seen in the Figure 4. The cells were sintered at 1200˚C. Figure 4 depicts the sintering results of these cells.

According to Figure 4, the cell sintered with a 50x50 mm, WXL, porous alumina cover plate has less mean curvature height (h = 1.18 mm) in comparison to the cell sintered without cover plate (h = 1.93 mm). However, whilst sufficient for an anode supported cell, this mass of cover plate is not enough to suppress curvature evolution of the cathode-supported cell studied here. Furthermore, increasing cover plate mass (from 7.31 g to 16.45 g) by simply using a bigger size of porous cover plate (75x75 mm, WxL) reduced mean curvature height further (to 0.65 mm). Increasing porous cover plate mass has no linear effect on curvature reduction as can be seen

from Figure 4B. According to Figure 4B shows the relation of porous alumina cover plate mass with the mean curvature height with a possible equation, $y = 0.391 + 1.539 \times \exp(-0.089 \times x)$. It can be used to predict the mean curvature height with the change of the cover plate mass for the cathode-supported SC-SOFCs. Though the Figure 4B has limited data for its reliability, it can still give an approximate idea about required cover plate mass for curvature free cathode-supported cell for this type of cells with the same size, thickness, and thickness ratio. Figure 4 shows the mean curvature height becomes almost stable after using two or more 75x75 mm cover plates on top of the cell (around 0. 47 mm for two cover plate and 0.41 mm for three cover plates). To conclude, a cell with a low mean curvature height (0.41 mm) was obtained after using three 75x75 mm, WxL, alumina porous cover plates on the top of the cell during sintering.

Figure 4. A) Free and limited constraint sintered of cathode-supported cells having the same width, length, thickness and thickness ratio (40mm, 40mm, 3-1-40 (A-E-C) and 60-20-800 μm (A-E-C), respectively) and B) Estimated mean curvature height reduction with mass of the porous alumina cover plate used to suppress curvature formation and its possible equation.

3.1.5. Characterization of Selected Optimum Specimen of Sintered Cells

Figure 5 displays the SE image of unpolished and BSE SEM images of polished nihai cell 3 sintered with three 75x75 mm LxW porous alumina cover plates on the top of the cell. When inspecting the SE and BSE SEM images in Figure 5, there is consistently good adhesion between anode-electrolyte, and cathode-electrolyte layers across the cell. However, it has a porous electrolyte (acceptable in the SC-SOFC configuration, but needs full densification for use in conventional DC-SOFCs). Moreover, in general for the cell, there is a good connection of NiO phase on anode side and LSCF phase on cathode side. However, the CGO continuity on both sides is not as good as desired. In addition, there is normal grain growth in all section of the cells;

however, the cathode in the cell possesses coarser microstructure than the anode as a consequence of over-sintering. Furthermore, from Figure 5, the estimated porosity of the anode, electrolyte and cathode for cell 3 was measured (by using ImageJ program) to be 24.11%, 12.43% and 26.04%, respectively (see Figure 4). In addition, for the same cell, the mean particle and pore size was found to be 2.895 ± 1.864 µm and 1.267 ± 0.723 µm for anode, respectively, and that of 3.645 ± 2.27 µm and 1.603 ± 0.736 µm, respectively, for cathode. It can be generally seen that cathode has higher porosity and mean pore size compared to that of the anode. This might be as a result of coarser microstructure of cathode because the increase in mean grain size is accompanied by a rise in the mean pore size.
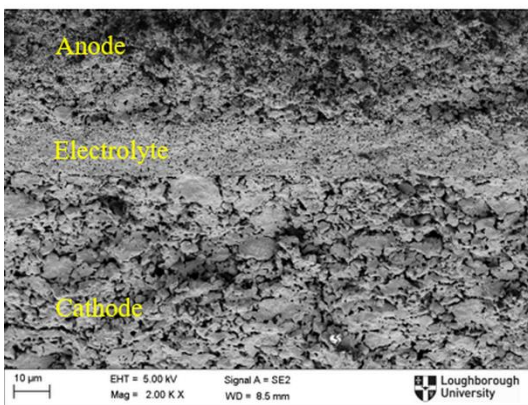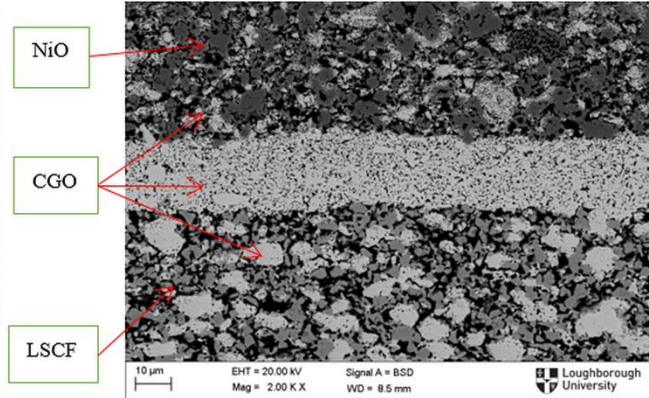

Figure 5. A) Unpolished SE SEM image of Cell 3 and BSE image of polished Cell 3, having the 40x40 mm WxL thickness ratio 3-1-40 (A-E-C), thickness 60-20-800 µm sintered with three 75x75 mm LxW porous alumina cover plates on the top of the cell.

Figure 6 depicts the EDS spectrum of cell 3 (the final obtained cell) from anode and cathode side, respectively. The purpose taking of EDS analysis of cell 3 is to investigate possible impurities introduced during fabrications process. The EDS spectrums of the cell shows all elements in the scanned region. Figure 6A shows the map sum spectrum of cell from the anode side. It can be observed that there is a small amount of gold, palladium, aluminum (Al), zirconium (Zr), silisyum or silicon (Si), strontium (Sr) and cobalt (Co). The existence of Au and Pd is due to the sputtering of these elements before SEM imaging in order to make the cell conductive. Aluminum might have been introduced during sintering either from alumina substrate or porous cover plate. Zirconium might have been introduced during ball milling by ball milling medium which is

made of yttria stabilized zirconia (YSZ). However, the existence of strontium and cobalt was due to the diffusion of these elements from cathode sides. Furthermore, silicon might be coming from different stages of the fabrication process since Si elements could be present in any of these stages. In addition, from the cathode side EDS spectrum (Figure 6B), there were also Au, Pd, Al, Zr, and Si elements on the cathode side due to the same respectively reasons mentioned for EDS spectrum analysis from the anode side. In addition to these contaminations, Ni was also detected on cathode side because of the nickel diffusion from the anode side. To conclude there were same contaminations on both sides of electrodes, and small amounts of anode- and cathode-side elements diffused from anode to cathode and cathode to anode, respectively. It is important to

avoid or to minimize this contamination to a reasonable level so as to obtain better performance from the cells, with regards to catalytic selectivity and favorable reactant concentration gradients at the respective electrodes.

Furthermore, Figure 6C displays X-Ray diffraction (XRD) patterns of the cell 3. According to this figure, there is no undesired phase formation after sintering except the required phases (NiO, CGO and LSCF) for the cell. Though there were some impurities detected from EDS analysis in the previous paragraph, their reaction with other elements which form new phases such as silisyum oxide (SiO), zirconium oxide (ZrO), cobalt oxide (CoO) and so forth were not observed in XRD patterns due to their small amount.
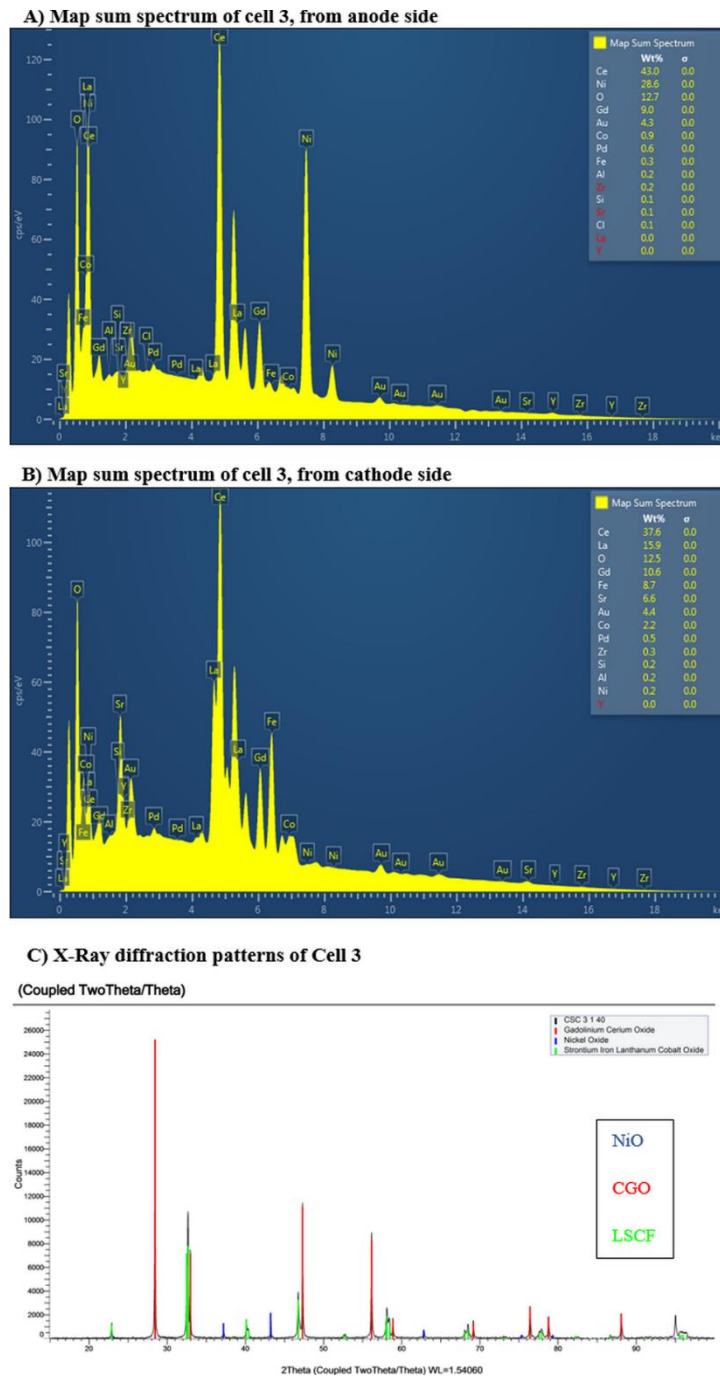

Figure 6. Map sum spectrum of cell 3 taken from A) anode side, B) cathode side and C) X-Ray diffraction patterns of Cell 3, the cell possesses a thickness of 60-20-800 µm A-E-C sintered with three 75x75 mm alumina porous cover plate

3.2. Cell Performance

Cathode-supported cells were tested in order to examine the functionality of sintered samples as working electrochemical cells, and to investigate the influence of electrolyte and cathode thickness on the cell performance. During performance testing of cells, 100 mL min^{-1} nitrogen gas was used as diluting agent at different fuel/oxygen gas (O_2) mixture (R) so as to reduce the danger of explosion, improve the diffusion and flow of the fuel and oxygen gases as well as for the reactant adsorption and product desorption processes on the anode and cathode [21]. The gas mixture was sent as a flow through (gas flow perpendicular to cathode layer). Figure 7 shows the open circuit voltages and polarization results of cell 1, cell 2 and cell 3, respectively, at different flow rates and gas mixture ratios. Additionally, Table 2 depicts the maximum OCV and power density measurements of these cells.

According to Figure 7A, the OCV of cell 1 diminishes with the increased amount of oxygen gas at both fixed amounts of 50 mL min^{-1} methane (CH_4) and 40 mL min^{-1} CH_4. Maximum OCV and power density of cell 1 were found to be 0.56 V and 25 mW cm^{-2}, respectively, in a quite fuel rich gas mixture (gas mixture 4). This can be explained as follows: a fuel rich condition is required to supply more methane to anode surface because of lack of fuel reforming on anode side due to the thin anode thickness in a cathode-supported cell. As a result of increased fuel reforming, more syngas such as hydrogen gas (H_2) and carbon monoxide (CO) were generated. These products react with oxygen ions (O^{-2}) migrating from the cathode side. Therefore, partial pressure differences between two layers increases and thus led to improved OCV and power density. Conversely, the formation of volatile nickel hydroxide Ni (OH)$_2$ due to presence of water vapor (H_2O) leads to nickel loss and it becomes severe in oxygen-rich mixture where a higher quantity of water vapor was produce [1], [7]. This could be among the reasons why cells` OCV and power density reduced with increased amount of oxygen gas (see Table 2). However, having high power density at fuel rich condition brings certain problems. For instance, coking of nickel catalyst interfaces, and chemical reactions between methane and oxygen gas or ion could occur on cathode side, and thereby resulting in cell degradation and low cell performance.

The OCV and power density of cell 1 at gas mixture 4 (R: 2.4) and gas mixture 5 (R: 1.6) is higher than that at the gas mixture 1 (R: 2.4) and gas mixture 2 (R: 1.6), respectively whereas the OCV and power density of cell 1 at gas mixture 3 (R: 1) is greater than that of at gas mixture 6 (R: 1). Therefore, the OCVs

and power densities of cell 1 at fixed methane of 40 mL min^{-1} is generally higher than that of fixed methane of 50 mL min^{-1} at the same fuel /oxygen ratio. In general, increasing gas mixture flow rate has positive effects on cell performance owing to the improved gas exchange at both electrodes which results in reduction in overpotential relating to gas diffusion at both electrodes [1], [3], [21], [22]. However, for cell 1, reduction in the amount of gas mixture by decreasing the fixed amount of CH_4 from 50 mL min^{-1} to 40 mL min^{-1} (resulting in reduced total flow rate) for the same fuel/oxygen ratio improved cell`s OCV as well as its power density (see Figure 7A and Table 2). This could be attributed to the increased residence time of reactant gases on anode electrode where the reforming was limited due to the insufficient anode thickness [22].

Furthermore, for the same anode and cathode thickness (cell 1 and cell 2), decreasing electrolyte thickness from 40 µm to 20 µm had severe effect on power density especially at rich fuel/oxygen condition. Moreover, there is a little reduction in OCV at gas mixture 1 and gas mixture 5 with comparison to cell 1 (see Figure 7 and Table 2). However, at gas mixture 3 and gas mixture 6, the OCV of cell 2 is mora than two folds higher than that of cell 1. Therefore, one can generally define that there is an OCV reduction at fuel rich gas mixture (R: 2.4 and R: 1.6) while an increase in OCV is observed at fuel lean condition when cell electrolyte thickness was reduced. In OCV conditions, the oxygen partial pressure differential between the anode-electrolyte and cathode-electrolyte boundaries is the dominant factor that develops the thermodynamic voltage. The reduction in electrolyte thickness allows a faster oxygen gas flux through to the cathode, and the lean condition provides more oxygen overall. Thus, after the partial oxidation on the anode, there is greater net flux of oxygen to the cathode side, resulting in the higher OCV. The OCV reduction could also be attributed to reduced electrolyte thickness leading to better ionic conductivity, thus enabling faster oxygen ion travel from cathode to the anode side. Consequently, oxygen reduction reaction proceeds at the fastest rate for the present condition and therefore depletes oxygen gas at the cathode membrane. The OCV decrease could also be as a result of gas cross-over. Because cells possessing porous electrolytes usually have gas cross-over problem. From the flow-through configuration, the anode reforming and fuel utilization plays a large role. Unused reformate gases generated from anode side such as H_2 and CO can diffuse to the cathode side via porous electrolyte and react parasitically with oxygen gases and thereby causing simply chemical reaction which is not beneficial for SOFC [1], [22], [23]. For the cell

possessing thinner electrolyte, the gas cross over becomes more severe due to easy diffusion of these syngas. Cell 2 possess thinner electrolyte in comparison to cell 1, thereby facilitating higher gas cross-over. In both cases, oxygen partial pressure differences between anode and cathode sides reduce, therefore decreasing OCV, and also further impeding the favorable conditions for methane reforming [1], [22]. The reason for the OCV increment with decreased electrolyte thickness at oxygen rich condition (gas mixture 3 and gas mixture 6) could be explained by the fact that the thinner and porous electrolyte could allow faster oxygen and methane gas transport from cathode side to anode side. Because the gas mixture contacts first to the cathode and pass through electrolyte to anode layer. However, the increment in the amounts of methane diffusion to the anode side will be higher than that of oxygen gas because methane possesses higher diffusivity rate than oxygen gas due to its lower molar mass comparing to O_2. This leads to more methane reforming on the anode side and thus resulting in more oxygen gas consumption. Therefore, the partial pressure of oxygen increases between two electrodes and thus OCV rises.

The gas cross-over problem does not just lead to OCV reduction but also results in lower fuel partial pressure and limits the use of these fuels for electrochemical reaction, in favor of direct chemical oxidation/reforming. This could explain why less power was obtained from cell 2 in comparison to cell 1 despite the likely lower ohmic losses due to reduction in electrolyte thickness. In addition, the general trend was that the maximum OCV and power density was obtained at fuel rich condition, similar to cell 1. The maximum OCV and power density of cell 2 was found to be 0.38 V and 3.32 mW cm^{-2}, respectively at gas mixture 2 (see Figure 7 and Table 2) (around 87% reduction in power density compared to cell 1). According to Figure 7 and Table 2, the OCV of cell 2 generally mitigates with the increased amount of oxygen gas at both fixed amount of 50 mL min^{-1} CH$_4$ and 40 mL min^{-1} CH$_4$ as cell 1. Furthermore, in both cells, the lowest OCV and power density were obtained at lean condition, R=1, and the OCVs were not stable. The oscillation of OCVs might be as a consequence of oxidation-reduction cycle of Ni-cermet anode and accompanying temperature fluctuation at rich oxygen condition [1]. Alternately, the equilibrium may be dynamically shifting between the favorability towards steam methane reforming, partial methane oxidation and the water-gas shift reactions at the anode side.

Moreover, for the same anode and electrolyte thickness (cell 2 and cell 3), increasing cathode thickness from 400 μm to 800 μm led to considerable OCV and power density reductions at all gas mixtures. Additionally, there were almost no OCV and power density at the oxygen rich gas mixtures (gas mixture 3 and gas mixture 6, see Table 2 and Figure 7). The maximum power and OCV was found to be 1.71 mW cm^{-2} and 0.2 V, respectively, at gas mixture 2 (around 51% power density reductions comparing to cell 2). Figure 7C also shows that the OCV and power density of cell 3 generally diminished with the increased amount of oxygen gas at both fixed amount of 50 mL min^{-1} CH$_4$ and 40 mL min^{-1} CH$_4$ as cell 1 and cell 2. The low OCV and power density of the cell 3 might be ascribed to the thicker cathode. Because thick cathode causes high concentration polarization on the cathode side of the cell due to increased difficulties of oxygen gas movement into the inner part of cathode and distance for oxygen ion diffusion from cathode side to anode side of the cell [24]. However, cathode thickness increment also leads to an increase in triple phase boundary for oxygen gas reduction and thus alternately could result in better cell performance. However, the results demonstrated that the benefit of increased triple phase boundary is much less than the negative effect of cathode concentration polarization (mass transport limitation). Furthermore, the LSCF cathode material can also oxidize methane (parasitic catalytic combustion)) [1], [25], [26]. Therefore, the increased cathode thickness could lead to more methane oxidation which consume oxygen gas on the cathode side and thereby resulting in low OCV due to decreased oxygen partial pressure difference between cathode and anode. In addition, the reaction product (CO and H$_2$) after methane reforming on cathode side can be adsorbed on the cathode surface and leads to a reduction in active area for oxygen gas adsorption [22].

To sum up, the reduced electrolyte thickness and increased cathode thickness selected for the benefit of obtaining planar cathode-supported cell via single step co-sintering unfortunately resulted in severe performance degradation.
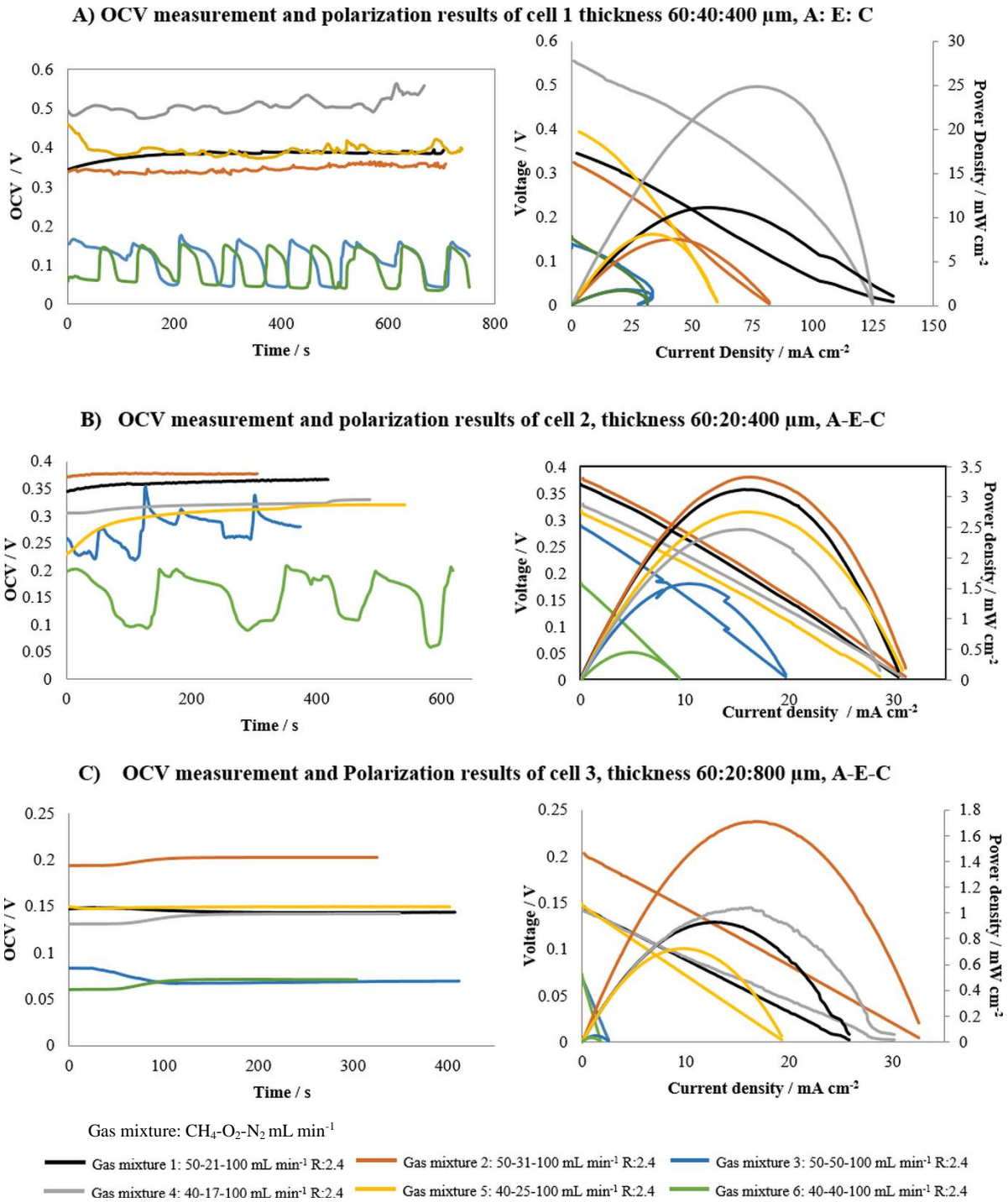
Figure 7. OCV Measurement and polarization results of A) Cell 1 thickness 60-40-400 μm A- E-C, B) Cell 2 thickness 60-20-400 μm A-E-C and C) Cell 3 thickness 60-20-800 μm A-E-C, at different flow rate and gas mixture, R, fuel to oxygen ratio.

Table 2. The maximum OCV and power density results of cell 1, cell 2 and cell 3 at different gas mixtures.

		Cell 1 *thickness 60-40-400 μm* A-E-C		Cell 2 *thickness 60-20-400 μm* A-E-C		Cell 3 *thickness 60-20-800 μm* A-E-C	
		OCV / V	Power density / mW cm^{-2}	OCV / V	Power density / mW cm^{-2}	OCV / V	Power density / mW cm^{-2}
Fixed CH$_4$ / 50 mL min^{-1}	gas mixture 1 (R:2.4)	0.4	11.1	0.37	3.11	0.143	0.93
And	gas mixture 2 (R:1.6)	0.36	7.5	0.38	3.32	0.20	1.71
Fixed N$_2$ / 100 mL min^{-1}	gas mixture 3 (R:1)	0.124	1.85	0.28	1.58	0.07	0.05
Fixed CH$_4$ / 40 mL min^{-1}	gas mixture 4 (R:2.4)	0.56	24.79	0.33	2.75	0.141	1.04
And	gas mixture 5 (R:1.6)	0.394	8.13	0.32	2.47	0.15	0.72
Fixed N$_2$ / 100 mL min^{-1}	gas mixture 6 (R:1)	0.05	1.69	0.2	0.45	0.071	0.03

In general, the performance of the cathode-supported SC-SOFCs were found comparatively low with comparison to available results presented in the literature for cathode-supported SC-SOFCs. The cells` performance could be adversely influenced by various reasons. Some were mentioned in the prior section and others could be explained as follows. Lack of fuel utilization due to low selectivity of anode and cathode towards their corresponding gases (H$_2$ and CO for anode, O$_2$ for cathode). It is a general problem for all type of SC SOFCs [1], [22]. This results in quite low cell performance and fuel utilization. Furthermore, the thick and porous electrolyte (thickness varies from 20 μm to 40 μm and porosity around 14%) result in high ohmic losses due to increased ionic transport losses. In addition, CGO electrolyte could be partially reduced at high temperature and low oxygen partial pressure since 600 ˚C working temperature is a critical temperature for CGO functionality [12], [27], as predominant on the anode side. This reduction brings about electronic conductivity in a great volume fraction of the electrolyte extending from anode side. Thus electrons flow from anode side to cathode side through electrolyte even at open circuit, and consequently resulting in low power output [1], [12], [28]. Furthermore, the reactivity of oxygen gas for a direct catalytic reaction is higher than the oxygen ion (with the electrochemical charge transfer), thus the oxygen gas easily reacts with H$_2$ or CO in comparison to O^{-2} on the anode side. This can be exacerbated by the higher thickness of the electrodes. Because the catalytic reactions can occur throughout the electrode thickness, whereas the electrochemical reactions are generally understood to occur within the TPB region, only adjacent to the electrode-electrolyte interfaces.

Another reason for low power output could be the lack of fuel reforming at 600 ˚C. Near-complete methane reforming is only achieved at temperatures above 600 ˚C. Therefore, for better cell performance, more active fuels such as higher chain hydrocarbons ethane, propane etc. should be used at low temperatures [1].

Moreover, the increased sintering temperature of composite cathode (from 1000 ˚C [29] to 1200 ˚C) caused coarse structure of cathode as well as low porosity (see Figure 5). This leads to reduction in the reaction area, and therefore a lack of oxygen reduction reactions [29], [30]. The limitation of oxygen gas transportation through cathode due to low porosity mitigate cell performance owing to increased concentration polarization [31]. Good bonding is also required between particles for better electrical conductivity [29]. However, the CGO conductivities are not as good as it should be on both electrodes (see SEM images of cell 3). This could lead to the oxygen ion interruption through the electrolytes. The weak connections between agglomerated particles escalate the resistance of oxygen ion as well as electrons transfer through the porous cathode [32].

Besides, impurities in electrolyte as well as electrodes have also adverse effect on cell performance. Si can poison the electrolyte material and thus reduce the performance. For instance, silicon can segregate at the grain boundaries of the electrolyte materials, forming insulating siliceous (SiO_2) and thus decreasing conductivity. Si has also detrimental effect on cathode electrode. It can cause serious surface exchange coefficient degradation especially in humidified atmosphere [33]–[35]. For instance, Si can react with Sr in LSCF cathode and cause cathode degradation [36]. The EDS analysis of the cell 3 shows that there was small amount of Si contamination on both electrodes (see Figure 6). Furthermore, strontium carbonate ($SrCO_3$) is formed on LSCF cathode in atmosphere of O_2-carbon dioxide (CO_2) [37], [38]. Thus oxygen activity and surface adsorption on LSCF decreases and it becomes worse with the existence of H_2O. The existence of H_2O with CO_2 also give rise to strontium oxide (SrO) on LSCF cathode [39]. Zhao et al. [37] defines that the existence of H_2O aggravates the interaction of carbon dioxide with perovskite oxide. Because the H_2O-CO_2 van der Waals complex is formed and later is transformed to bicarbonate at oxygen vacancies and it thereby reduces oxygen reduction reaction. CH_4 was used for testing of these cathode-supported cells therefore, it is highly possible the formation of CO_2 and H_2O due to the fuel reforming and electrochemical or chemical reaction of H_2 or CO with oxygen species. Consequently, the formation of $SrCO_3$ or SrO insulating layers could have caused lower power density. In addition, Ni could be poisoned by the sulfur compounds in the gas mixture (hydrocarbon fuels), even at concentration of 0.1 ppm sulfur compounds [12]. This could also have caused low performance results since the methane used in these experiments has 96% purity. Diffusion of strontium out of LSCF cathode brings about strontium depletion in the cathode and considerably mitigates performance of the cell [24]. The EDS result of cell 3 (see Figure 6) shows that there is not only diffusion of Sr out of LSCF but also Co and Fe, and they were also observed on the anode side. Similarly, Ni was also observed on cathode side. In addition to these impurities, small amount of Al and Zr was also detected on both electrodes. These impurities could also cause less performance by blocking active surface area for either fuel oxidation or oxygen reduction on anode and cathode, respectively. Finally, there was a short circuit observed during experiment of these cells due to silver and gold diffusion from one side to other sides through porous electrolyte. The magnitude of this short circuit was quite high and thereby leading to high power losses. Lastly, Ni oxidation (NiO due to

existence of O_2) increases the cell resistance [40] and thus causing low cell performance.

Although SC-SOFCs have low power density with comparison to existing results presented in the literature for cathode-supported planar SC-SOFCs, they can still be considered for Microelectromechanical systems (MEMS) applications, potential sensing functions and power recovery devices from exhaust gases.

4. Conclusions

A cathode-supported planar SOFC for single chamber conditions was made via single step co-sintering fabrication method. Our study showed that determining optimum thickness and thickness ratio of the cell with the optimized hot pressing and sintering conditions leads to better co-sintering results: no crack and delamination but limited curvature at the edge of the cell. Decreasing electrolyte thickness and increasing cathode thickness led to curvature decrease at the edges, but these adjustments were not enough to obtain curvature free cathode-supported cell. Three porous alumina cover plates with a 75x75 mm WxL and mass of 49.35 g was utilized to suppress curvature formation, and as a result, almost a curvature free cathode-supported cell was obtained (cell 3). The fabricated cells' performances were investigated with different gas mixture at 600 ˚C. The results indicated that increasing cathode thickness and reducing electrolyte thickness had detrimental effects on cell performance despite improved single step co-sinterability of the cell. The maximum power density and OCV of the final planar cell (cell 3, thickness ratio 3-1-40, thickness 60-20-800 μm, A-E-C) were found to be 1.71 mW cm^{-2} and 0.2 V, respectively, in a gas mixture of 50 mL min^{-1} of CH_4, 31 mL min^{-1} of O_2 and 100 mL min^{-1} N_2, R:1.6. Furthermore, the maximum power density and OCV among the all cells were measured from the cell 1 (thickness ratio 3-2-20, thickness 60-40-400 μm, A-E-C) as 24.79 mW cm^{-2} and 0.56 V, respectively, in a fuel rich condition (R:2.4, 40 mL min^{-1} of CH_4, 17 mL min^{-1} of O_2 and 100 mL min^{-1} N_2). In general, the performance of the cells was quite low, suggesting that additional work is required to find solutions to the problems mentioned in the previous section. The future study is to test single-step sintered cells under dual chamber conditions in order to investigate their real performance.

Conflict of Interest Statement

There is no conflict of interest between the authors.

Contributions of the authors

All contributions to this study belong to the authors.

Statement of Research and Publication Ethics

The study is complied with research and publication ethics

References

[1]   M. Kuhn and T. W. Napporn, "Single-chamber solid oxide fuel cell technology – from its origins to today's state of the art," *Energies*, vol. 3, no. 1, pp. 57–134, 2010.

[2]   T. Hibino, A. Hashimoto, T. Inoue, J. Tokuno, S. Yoshida, and M. Sano, "Single-chamber solid oxide fuel cells at ıntermediate temperatures with various hydrocarbon-air mixtures," *Journal of The Electrochemical Society*, vol. 147, no. 8, pp. 2888–2892, 2000.

[3]   M. Yano, A. Tomita, M. Sano, and T. Hibino, "Recent advances in single-chamber solid oxide fuel cells: A review," *Solid State Ionics*, vol. 177, no. 39–40, pp. 3351–3359, 2007.

[4]   T. Suzuki, P. Jasinski, V. Petrovsky, H. U. Anderson, and F. Dogan, "Anode supported single chamber solid oxide fuel cell in CH_4-air mixture," *Journal of The Electrochemical Society*, vol. 151, no. 9, pp. A1473–A1476, 2004.

[5]   M. Liu and Z. Lü, "Effect of stack configurations on single chamber solid oxide fuel cell, anode-cathode, anode-anode, and cathode-cathode configuration," *Electrochimica Acta*, vol. 104, pp. 64–68, 2013.

[6]   W. Z. Zhu and S. C. Deevi, "A review on the status of anode materials for solid oxide fuel cells," *Materials Science and Engineering A*, vol. 362, no. 1–2, pp. 228–239, 2003.

[7]   A. Faes, A. Hessler-Wyser, A. Zryd, and J. Van Herle, "A review of redox cycling of solid oxide fuel cells anode.," *Membranes*, vol. 2, no. 3, pp. 585–664, 2012.

[8]   K. Huang, A. Zampieri, and M. Ise, "Cathode polarizations of a cathode-supported solid oxide fuel cell," *Journal of The Electrochemical Society*, vol. 157, no. 10, p. B1471, 2010.

[9]   R. K. Bordia and E. A. Olevsky, *Advances in sintering science and technology*. California: John Wiley & Sons, 2009.

[10] L. C. De Jonghe and M. N. Rahaman, "Sintering of ceramics," in *Handbook of advanced ceramics*, S. Somiya, F. Aldinger, R. M. Spriggs, K. Uchino, K. Koumoto, and M. Kaneno, Eds. San Diego, California: Elsevier, 2003, pp. 187–264.

[11] M. N. Rahaman, "Sintering and microsturcture development," in *Ceramic processing*, Florida: Taylor&Francis Group, 2007, pp. 365–441.

[12] S. C. Singhal and K. Kendall, *High temperature solid oxide fuel cells:Fundementals, design and applications*. Oxford: Elsevier Advanced Technology, 2003.

[13] A. Hagen, R. B. Menon, P. V. Hendriksen, S. Ramousse, and P. H. Larsen, "Properties and performance of SOFCs produced on a pre-pilot plant scale," *Fuel Cells*, vol. 6, no. 2, pp. 146–150, 2006.

[14] H. Wang, Z. Gao, and S. A. Barnett, "Anode-supported solid oxide fuel cells fabricated by single step reduced-temperature co-firing," *Journal of The Electrochemical Society*, vol. 163, no. 3, pp. F196–

F201, 2016.

[15] J. H. Myung, H. J. Ko, C. H. Im, J. Moon, and S. H. Hyun, "Development of solid oxide fuel cells (SOFCs) by tape-casting and single-step co-firing of monolithic laminates," *International Journal of Hydrogen Energy*, vol. 39, no. 5, pp. 2313–2319, 2014.

[16] G. Ye, F. Ju, C. Lin, S. Gopalan, and U. Pal, "Single-step co-firing technique for SOFC fabrication," in *Advences in Solid Oxide Fuel Cells*, N. P. Bansal, D. Zhu, and W. M. Kriven, Eds. Florida: The American ceramic Society, 2005, pp. 25–32.

[17] "Maryland Tape Casting." [Online]. Available: http://www.marylandtapecasting.com/.

[18] Y. Sayan, V. Venkatesan, E. Guk, H. Wu, and J. S. Kim, "Single-step fabrication of an anode supported planar single-chamber solid oxide fuel cell," *International Journal of Applied Ceramic Technology*, vol. 15, no. 6, pp. 1375–1387, 2018.

[19] Y.-G. Choi *et al.*, "Ceria-based electrolyte reinforced by sol–gel technique for intermediate-temperature solid oxide fuel cells," *International Journal of Hydrogen Energy*, vol. 38, no. 23, pp. 9867–9872, 2013.

[20] C. Montgkolkachit and S. Wanakitti, "Characterization of $(La,Sr)(Co,Fe)O_{3-\delta}$ ferrite-based cathodes for ıntermediate-temperature SOFCs," *Journal of Metals, Materials and Minerals*, vol. 18, no. 2, pp. 33–36, 2008.

[21] Y. Tian *et al.*, "Effect of gas supply method on the performance of the single-chamber SOFC micro-stack and the single cells," *Journal of Solid State Electrochemistry*, vol. 17, no. 1, pp. 269–275, 2013.

[22] I. Riess, "On the single chamber solid oxide fuel cells," *Journal of Power Sources*, vol. 175, no. 1, pp. 325–337, 2008.

[23] P. Briault, M. Rieu, R. Laucournet, B. Morel, and J.-P. Viricelle, "Anode supported single chamber solid oxide fuel cells operating in exhaust gases of thermal engine," *Journal of Power Sources*, vol. 268, pp. 356–364, 2014.

[24] C. Sun, R. Hui, and J. Roller, "Cathode materials for solid oxide fuel cells: a review," *Journal of Solid State Electrochemistry*, vol. 14, no. 7, pp. 1125–1144, 2009.

[25] J. C. F. II and S. S. C. Chuang, "Investigating the CH 4 reaction pathway on a novel LSCF anode catalyst in the SOFC," *Catalysis Communications*, vol. 10, no. 6, pp. 772–776, 2009.

[26] Y. Hao, Z. Shao, J. Mederos, W. Lai, D. G. Goodwin, and S. M. Haile, "Recent advances in single-chamber fuel-cells: Experiment and modeling," *Solid State Ionics*, vol. 177, no. 19–25, pp. 2013–2021, 2006.

[27] J. Viricelle, S. Udroiu, G. Gadacz, M. Pijolat, and C. Pijolat, "Development of single chamber solid oxide fuel cells (SCFC)," no. 4, pp. 683–692, 2010.

[28] R. M. Ormerod, "Solid oxide fuel cells," *Chemical Society Reviews*, vol. 32, no. 1, pp. 17–28, 2003.

[29] Y. Leng, S. H. Chan, and Q. Liu, "Development of LSCF-GDC composite cathodes for low-temperature solid oxide fuel cells with thin film GDC electrolyte," *International Journal of Hydrogen Energy*, vol. 33, no. 14, pp. 3808–3817, 2008.

[30] C. Zhang, Y. Lin, R. Ran, and Z. Shao, "Improving single-chamber performance of an anode-supported SOFC by impregnating anode with active nickel catalyst," *International Journal of Hydrogen Energy*, vol. 35, no. 15, pp. 8171–8176, 2010.

[31] M. Liu, M. Liu, D. Ding, K. Blinn, X. Li, and L. Nie, "Enhanced performance of LSCF cathode through surface modification," *International Journal of Hydrogen Energy*, vol. 37, no. 10, pp. 8613–8620, 2012.

[32] C. Ding *et al.*, "Effect of thickness of $Gd_{0.1}Ce_{0.9}O_{1.95}$ electrolyte films on electrical performance of anode-supported solid oxide fuel cells," *Journal of Power Sources*, vol. 195, no. 17, pp. 5487–5492,

2010.

[33] E. Bucher and W. Sitte, "Long-term stability of the oxygen exchange properties of $(La,Sr)_{1-z}(Co,Fe)O_{3-\delta}$ in dry and wet atmospheres," *Solid State Ionics*, vol. 192, no. 1, pp. 480–482, 2011.

[34] E. Bucher, W. Sitte, F. Klauser, and E. Bertel, "Impact of humid atmospheres on oxygen exchange properties, surface-near elemental composition, and surface morphology of $La_{0.6}Sr_{0.4}CoO_{3-\delta}$," *Solid State Ionics*, vol. 208, pp. 43–51, 2012.

[35] E. Bucher and W. Sitte, "Defect chemical modeling of $(La, Sr)(Co, Fe)O_{3-\delta}$," *Journal of Electroceramics*, vol. 13, no. 1–3, pp. 779–784, 2004.

[36] Z. Yang, M. Guo, N. Wang, C. Ma, J. Wang, and M. Han, "A short review of cathode poisoning and corrosion in solid oxide fuel cell," *International Journal of Hydrogen Energy*, vol. 42, no. 39, pp. 24948–24959, 2017.

[37] Z. Zhao *et al.*, "High and low temperature behaviors of $La_{0.6}Sr_{0.4}Co_{0.2}Fe_{0.8}O_{3-\delta}$ cathode operating under CO_2/H_2O-containing atmosphere," *International Journal of Hydrogen Energy*, vol. 38, no. 35, pp. 15361–15370, 2013.

[38] J. Hayd, L. Dieterle, U. Guntow, D. Gerthsen, and E. Ivers-Tiffée, "Nanoscaled $La_{0.6}Sr_{0.4}CoO_{3-\delta}$ as intermediate temperature solid oxide fuel cell cathode: Microstructure and electrochemical performance," *Journal of Power Sources*, vol. 196, no. 17, pp. 7263–7270, 2011.

[39] R. R. Liu *et al.*, "Influence of water vapor on long-term performance and accelerated degradation of solid oxide fuel cell cathodes," *Journal of Power Sources*, vol. 196, no. 17, pp. 7090–7096, 2011.

[40] Z. H. Wang *et al.*, "Redox tolerance of thin and thick Ni/YSZ anodes of electrolyte-supported single-chamber solid oxide fuel cells under methane oxidation conditions," *Fuel Cells*, vol. 13, no. 6, pp. 1109–1115, 2013.

In silico Evaluation of the Potential of Natural Products from Chili Pepper as Antiviral Agents Against Dna-Directed Rna Polymerase of the Monkeypox Virus

Özkan FİDAN[1*], Somdutt MUJWAR[2]

[1]*Depertmant of Bioengineering, Faculty of Life and Natural Sciences, Abdullah Gül University, Kayseri, Türkiye, 38080*
[2]*Chitkara College of Pharmacy, Chitkara University, Rajpura-140401 Punjab, India*

(ORCID: 0000-0001-5312-4742) (ORCID: 0000-0003-4037-5475)

Abstract

This study focused on the discovery of new drug candidates effective against the monkeypox virus. Virtual screening was performed to evaluate the potential of chili pepper natural products against homology-modeled DNA-directed RNA polymerase of the monkeypox virus using molecular docking. Our findings revealed that structurally similar triterpenes such as α-amyrin, β-amyrin, and β-sitosterol had strong binding affinities towards the DNA-directed RNA polymerase and can inhibit this pivotal viral enzyme. The stability of one of the drug candidate molecules, α-amyrin with the strongest binding affinity towards the binding cavity of the enzyme was also confirmed via molecular dynamics simulation. This study showed that α-amyrin is a promising DNA-directed RNA polymerase inhibitor to treat monkeypox disease. It also paves the way for the idea of the potential dietary supplement candidate for monkeypox patients.

1. Introduction

Human monkeypox is a zoonotic disease caused by monkeypox virus. Its clinical manifestations such as fever and skin lesions are similar to smallpox disease, which devastated the humankind in the history and identified as a potential bioterrorism agent [1, 2]. Since then, mostly African countries have been affected with the monkeypox outbreaks. Nevertheless, there have also been cases reported from other countries. Indeed, it has become a public health concern over the globe [3]. Generally, two different clades of monkeypox have been described as Central African clade with the fatality rate of ∼10% and West African clade with the fatality rate of ∼3% [4, 5].

According to WHO, the main mode of transmission of monkeypox virus takes place from animal to human due to direct contact with infected animals and handling their raw meat. In fact, it can also be transmitted from human to human through respiratory droplets, direct contact with body fluids, sexual intercourse, and transplacental transfer. The infection has two periods; the first one is the incubation period during which fever, intense headache, lymphadenopathy, back pain, myalgia and intense asthenia are observed. Particularly, lymphadenopathy, which is the swelling of the lymph nodes, is a distinctive symptom of monkeypox disease as compared to similar diseases such as chickenpox and smallpox. In the second period, skin eruption is observed and the rash is more likely to be mostly seen on the face and extremities more than on the trunk.

Monkeypox virus is a double-stranded DNA virus with the genome size of about 197 kbp, which exhibits around 96% identity to the smallpox virus [6, 7]. It is

Corresponding author: ozkan.fidan@agu.edu.tr

a member of poxviruses that belong to the orthopoxvirus genus including the closely related variola, monkeypox, cowpox, and vaccinia viruses. Studies indicated that monkeypox virus is more closely related to variola than to vaccinia virus [7, 8]. Monkeypox virus cases have recently been reported in UK on 13 May 2022. Since then, multiple cases of monkeypox were reported in several non-endemic countries including the US and other European countries. They were identified as Western African clade [3, 9]. According to Centers for Disease Control and Prevention (CDC), as of 1 of November 2023, the number of monkeypox cases in the US approached to almost 31,000 confirmed cases and the total number of cases reached to more than 91,000 over the world. For this outbreak, the rate of transmission is relatively high compared to previous outbreaks and it is suspected to be due to mutations enhancing human transmission. A significant portion of cases has been reported due to sexually transmitted infections with a perianal or genital rash, which were observed among men who have sex with men [3, 10, 11].

For the treatment of monkeypox, there are no effective drugs currently available in the medicine. However, brincidofovir and tecovirimat are approved by FDA for the treatment smallpox, which is due to a potential biowarfare with smallpox [12, 13]. In animal models, these two drug molecules have also been effective against orthopoxviruses including monkeypox [14, 15]. In a recent case study in UK, out of seven monkeypox patients, three of them were orally treated with brincidofovir and one received tecovirimat, while the remaining patients were not treated with any antiviral drug. In patients treated with brincidofovir, elevated liver enzymes was observed and the therapy was ended, while for the patients treated with tecovirimat, no adverse effects were seen. This case study revealed that it is urgent to conduct the future prospective studies of these antivirals for monkeypox disease treatment [16]. With the current knowledge, a definitive conclusion cannot be drawn for these drugs to be used in the treatment of monkeypox disease [10, 17].

As WHO declared monkeypox as a global health emergency and the unavailability of approved drugs for the treatment of monkeypox, the discovery and development of new drug candidates become increasingly important. Therefore, in this study, we investigated the potential of natural products from chili pepper against monkeypox virus using *in silico* approaches. Particularly, natural products from chili pepper were docked against homology-modeled DNA-directed RNA polymerase. The articles in the literature about the chemical composition of chili pepper was used to prepare the list of chili pepper natural products including capsaicinoids, carotenoids, terpenoids, flavonoids. In specific, capsaicinoids occupy the majority of the natural product composition [18, 19]. RNA polymerases have been used as an important drug target for various viruses such as SARS-CoV-2, hepatitis C virus, cowpox virus, Zika virus, influenza viruses, and so on [20–23]. Chili extracts and one of the important constituent, capsaicin, were previously tested against some viral species including herpes simplex virus, Lassa virus, and SARS-CoV-2 [24–27]. The results clearly indicated the high potential of chili pepper natural products as antiviral agents. Considering the dietary supplement potential of chili pepper natural products, the discovery of the drug or dietary supplement candidate/s from chili pepper can extend the options for the treatment of monkeypox disease. Our docking results showed α-amyrin has the strongest affinity for DNA-directed RNA polymerase of monkeypox virus. This result was further confirmed in molecular dynamics simulations during which α-amyrin stably bound to DNA-directed RNA polymerase of monkeypox virus throughout the simulation. Thus, our study reveals that α-amyrin is a potential DNA-directed RNA polymerase inhibitor to treat monkeypox disease. It also puts forth the idea of the potential dietary supplement candidate for monkeypox patients.

2. Materials and Methods

2.1. Design and Preparation of Ligand Library

A ligand library from chili pepper, Capsicum annum, was created by exploring the literatures from various sources. 47 ligands were shortlisted for generating a ligand library. Their two-dimensional structures were obtained in isomeric SMILES from PubChem Database and subsequently converted into three-dimensional structures through energy minimization process in ChemDraw 8.0 software. All the ligands with three-dimensional structure were eventually prepared for molecular docking experiment using AutoDock Tools software, in which aromatic carbon and rotatable bonds were detected, torsion number was automatically set, non-polar hydrogens were merged, and Gasteiger charges were added for all ligand molecules [22].

2.2. Homology Modeling

DNA-directed RNA polymerase is the main physiological enzyme of monkey-pox virus and is involved in the catalysis of the viral transcription process to form RNA from DNA by utilizing the nucleotides [28–30]. DNA-directed RNA polymerase is essential for regulating the important process of

viral transcription for the synthesis of viral RNA, which is further required by the virus to biosynthesize the various structural and functional proteins. The unavailability of the three-dimensional structural model of this enzyme led us to developing a structural model by using homology modeling approach. The protein sequence of the DNA-directed RNA polymerase of monkeypox virus required for performing homology modeling was obtained from Uniprot database (Sequence ID: Q8V4V3) by using Swiss-Modeller webserver [29, 31]. The modeled macromolecular structure was validated by using Ramachandran plot [32]. Ramachandran plot depicts the position of amino acids in the 'favorable' or 'disallowed' regions based upon the analysis of the torsional phi and psi angles of the macromolecular backbone.

2.3. Molecular Docking Studies

Three-dimensional structure model of the DNA-directed RNA polymerase prepared by homology modeling was used to proceed further with molecular docking studies. Macromolecular structure of the target protein was prepared for molecular docking simulation studies by assigning autodock atom type, Gasteiger charge and its equal distribution among the macromolecular residues [33]. The utilized docking protocol was internally validated by docking the structural model of the target protein with an endogenous ligand, S-adenosylmethionine (SAM). After the validation of the docking protocol, the similar parameters were further utilized for computational screening of the ligand library against the macromolecular drug target protein used in the current study [22, 34].

2.4. Pharmacokinetic and Toxicological Evaluation

The lead molecule must possess qualities that will enable it to be therapeutically effective within the body. Therefore, assessing the ADME characteristics (absorption, distribution, metabolism, and excretion) of the chemical is a significant part of the drug development process. Computer simulations can be a suitable substitute for biological studies in predicting the pharmacokinetic profile of new ligands, leading to higher success rate, lower costs, and a decrease in the number of animals used for experimental testing. The pkCSM-pharmacokinetics server was employed to anticipate the physicochemical, pharmacokinetic, and toxicological characteristics of the lead compound identified from the docking-based screening [35–37]. Major pharmacokinetic characteristics, such as blood-brain barrier (BBB) permeability and passive human gastrointestinal absorption (HIA), may be easily estimated using pkCSM. Molecular weight (MW), topological polar surface area (TPSA), partition coefficient (LogP), rotatable bonds count, hydrogen bond acceptor/donor (HBA/HBD), and solubility (LogS) of the lead compounds were calculated. These variables control the lead candidates' ADME-T profile. The druggability of lead molecules was further determined by their gastrointestinal absorption, permeability across BBB, and the inhibitory potential of the cytochrome P450 isoenzymes [37–39]. Lipinski's rules of five, Veber's rule, and druggability were used to standardize these characteristics. pkCSM permits substances to be tested for cytochrome P450 (CYP) inhibitory action. This is an essential topic since CYP isoforms are engaged in medication excretion via metabolic biotransformation, affecting therapeutic efficiency as well as drug toxicity and side effects [37, 40].

2.5. Molecular Dynamics Simulation

The Desmond program of Schrödinger was utilized to execute MD simulations for 100 ns on the macromolecular complex of α-amyrin and a homology-modeled viral DNA-directed RNA polymerase, which were acquired from the virtual screening, to further investigate their binding strength and binding pattern [38, 39]. The TIP3P explicit water model was employed to create a simulation box with an orthorhombic shape and a 10 Å gap between the ligand-protein complex and the wall of the box. To establish an isosmotic environment, counter ions were added to neutralize the charge, with a concentration of 0.15 M NaCl. The system was optimized by carrying out 2000 iterations with a merging criterion of 1 kcal/mol. MD simulations were then conducted with the minimized energy complex system. The temperature and air pressure were monitored, with 300K and 1.013 bars respectively, for the duration of the simulation. The trajectory path was adjusted to 9.6 and the energy interval was changed to 1.2 ps, with the resulting trajectories being used to generate simulation interaction diagrams at the end of the simulation [33, 34, 40].

3. Results and Discussion

3.1. Homology Modeling

The three-dimensional structural model of the macromolecular target protein used in this study was tested against SAM to validate the docking protocol.

Table 1. The grid box used in the molecular dynamics studies.

x-D	y-D	z-D	Spacing (Å)	x center	y center	z center
40	40	40	0.581	165.852	145.231	189.106

The protein sequence of viral target protein DNA-directed RNA polymerase obtained from UniProt database consists of 1750 amino acid residues. The homology modeling of this protein sequence was performed by using crystallized structure model of DNA-dependent RNA polymerase subunit rpo132 from vaccinia virus (PDB ID: 6RID) and poxvirus (PDB ID: 7AMV) with the help of SWISS-MODEL webserver [41, 42]. The validation of the prepared structural model of viral DNA-dependent RNA polymerase was performed using a Ramachandran plot. The Ramachandran plot obtained for the structural model of DNA-directed RNA polymerase of monkeypox virus revealed that the structural model has 97.519% residues observed in the highly preferred region demonstrated in green colour, 2.195% residues were in the preferred region demonstrated in orange colour, while 0.286% residues were observed in the non-preferred region demonstrated in red colour (Figure 1).

3.2. Molecular Docking Studies

A suitable gridbox was used to conduct molecular dynamics as shown in Table 1.

Following this, the molecular ligand library was computationally screened against the homology-modelled DNA-directed RNA polymerase of the monkeypox virus. The best lead molecule was identified based on a minimum binding energy of -5 to -15 kcal/mole [33, 38]. The binding scores of the ligand molecules with high affinity to the macromolecular target protein as well as the interacting residues and chemical structures were listed in Table 2. Analysis of the docking scores obtained after the computational screening of the designed library clearly showed that the α-amyrin had the strongest binding affinity towards the DNA-

directed RNA polymerase of the monkeypox virus.

3.3. Pharmacokinetic and Toxicological Evaluation

The characteristics of a drug molecule, such as its physicochemical and pharmacokinetic properties, are essential for the evaluation of its pharmacodynamics and toxicological qualities. Lipinski's rule of five
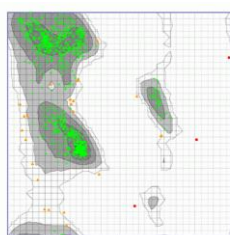

Figure 1. Ramachandran plot for the structural model of DNA-directed RNA polymerase of monkeypox virus.
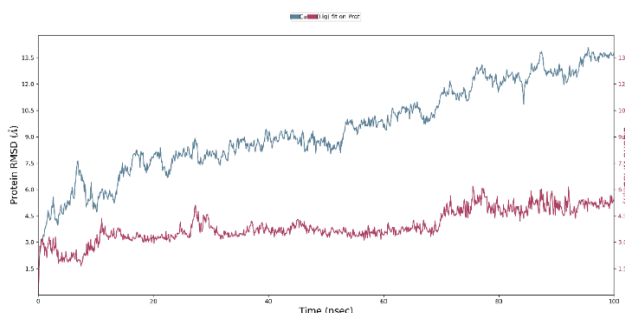

Figure 2. RMSD profiles of the Cα backbone of DNA-directed RNA polymerase of monkeypox virus and α-amyrin observed during the MD simulation for 100 ns.

states that these parameters should be within a certain range, such as a molecular weight of less than 500, fewer than 10 hydrogen bond acceptors, fewer than 5 hydrogen bond donors, and a topological polar surface area of 20-130 Å2, with the exception of the partition coefficient (LogP) value, which should be less than 0.5. The reported features of α-amyrin indicate that it has drug-like properties with improved pharmacokinetics. Additionally, P-glycoprotein serves as a natural filter for drugs, toxins, and other foreign substances. α-amyrin has not been predicted to act as a substrate for the P-glycoprotein, however, was predicted to act as a P-glycoprotein inhibitor. Similarly, α-amyrin was predicted not to act as CYP450 isoenzymes substrate, except CYP3A4. AMES, hERG-I inhibition, minnow toxicities were also investigated in the current study. Overall, based on physicochemical criteria, the projected pharmacokinetics and toxicological profile of α-amyrin matched well within the stated range, indicating that the molecule may be a good future therapeutic candidate [37, 43]. Table 3 lists the pharmacokinetic and toxicological features of shortlisted compounds.

3.4. Molecular Dynamics Simulation

MD simulation using the Schrodinger Desmond program was conducted to con-firm the long-term stability of the DNA-directed RNA polymerase of the monkeypox virus when it was associated with the proposed herbal-based inhibitor molecule, α-amyrin. The macromolecular target has 1155 amino acid residues having 9317 heavy atoms out of total 18702 atoms and the ligand is having 31 heavy atoms out of total 81 atoms with only 1 rotatable bond. The protein backbone's stability and changes in structure were monitored by calculating the RMSD over the simulation period. Results from the MD simulation of the macromolecular target and α-amyrin complex showed that it remained stable throughout the 100 ns simulation, with an average RMSD value of between 5.0-13.5 Å for the macromolecular backbone. Despite some initial fluctuations for adjusting the ligand within the enzyme's cavity, the RMSD value of the ligand molecule was maintained within the 3-5 Å range throughout the simulation run. After attaining the active binding site of the DNA-directed RNA polymerase of the monkey-pox virus, the ligand α-amyrin went through a series of vibrations to attain the most consistent affirmation within the active binding site. Figure 2 displayed that RMSD profiles of the complex, ligand, and macromolecule had only slight variations and were consistent over time.

Table 2. The binding score achieved for each ligand from the intended ligand library against the monkeypox virus's DNA-directed RNA polymerase with the identified interaction residues.
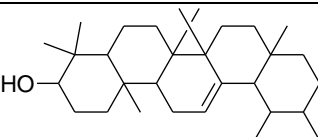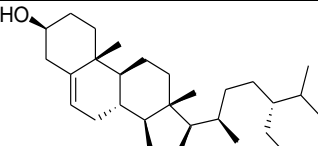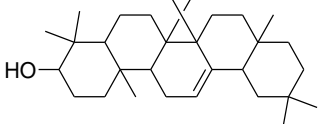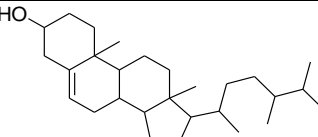
Name	Structure	BE	Interacting Residues
α-amyrin		-8.19	Arg45, Pro198, Val195, Ile174, Tyr205, Lys173, Lys421, Leu360, Glu172, Lys364, Tyr447
β-sitosterol		-7.77	His371, Ile49, Leu201, Tyr205, Val195, Glu172, Lys421, Thr368, Ile174, Lys173, Asp423, Tyr447, Lys364, Leu360
β-amyrin		-7.71	Pro198, Ser196, Val195, Tyr205, Ile174, Lys421, Tyr447, Lys173, Leu360, Glu172, Lys364
Ergost-5-en-3-ol		-7.18	Leu360, Lys421, Glu172, Thr368, Glu367, Arg45, Thr203, Val195, His207, His371, Tyr205, Ile174, Lys173
Zeaxanthin		-6.79	Arg45, His207, Lys364, Lys209, Ser224, Thr225, Thr175, Lys173, Ile174, Lys421, Ser193, Leu360, Tyr205, Glu367, Thr368
Capsanthin		-6.77	Lys364, Lys421, Lys173, Asp449, Val451, Lys179, His207, Lys420, Tyr205, Ile174, Val195, Thr368
β-carotene		-6.61	Val451, Asp449, Lys452, Glu367, His371, Thr203, Lys364, Val195, Thr368, Glu172, Leu360, Ile174, Tyr205, Lys421, Lys420, Glu450, Lys173
β-cryptoxanthin		-6.52	Ile174, Lys209, Tyr208, Ser191, Ser224, Thr225, His207, Lys226, Tyr205, Lys421, Lys173
Methyl-3-hydroxy cholestenoate		-6.40	Arg206, Thr225, Tyr208, Lys209, Ser223, His207, Tyr205, His371, Arg204, Asn314
SAM		-4.97	Lys226, Thr227, His207, Tyr205, Thr225, Lys209, Gln8
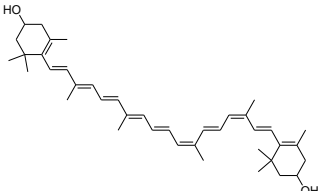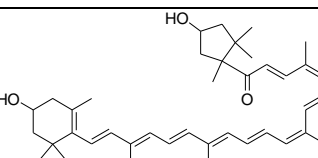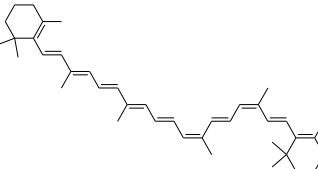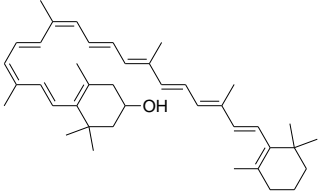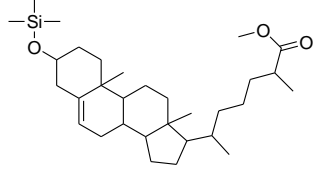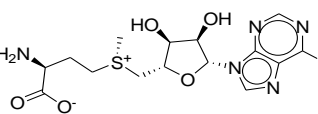
Table 3. Physicochemical, pharmacokinetics, and pharmacodynamics properties of the lead molecules (Y= Yes; N=No).

Property	Descriptor	α-amyrin	β-sitosterol	β-amyrin	Ergost-5-en-3-ol	Zeaxanthin	Capsanthin	β-carotene	β-cryptoxanthin	Methyl-3-hydroxycholestenoate	SAM
MW	(g/mol)	426.73	414.718	426.73	400.691	568.886	584.885	536.888	552.887	502.856	398.445
LogP	-	8.0248	8.0248	8.1689	7.6347	10.5474	9.8063	12.6058	11.5766	8.401	-3.257
Rotatable bond	-	0	6	0	5	10	11	10	10	8	7
HBA	-	1	1	1	1	2	3	0	1	3	11
HBD	-	1	1	1	1	2	2	0	1	0	4
TPSA	$(Å)^2$	192.398	187.039	192.398	180.674	256.963	261.814	247.375	252.169	216.868	152.263
Absorption	Water solubility (mol/L)	-6.906	-6.871	-7.001	-7.006	-6.903	-6.968	-7.314	-7.17	-7.146	-2.685
Absorption	$CaCO_2$ permeability	1.358	1.205	1.368	1.217	1.3	1.275	1.256	1.324	1.249	-0.229
Absorption	Intestinal absorption (%) (human)	97.891	94.866	97.983	94.367	88.683	89.827	91.072	89.891	96.645	14.993
Absorption	Skin Permeability (Log Kp)	-2.828	-2.794	-2.841	-2.846	-2.75	-2.771	-2.74	-2.738	-2.903	-2.735
Absorption	P-glycoprotein substrate	N	N	N	N	N	N	N	N	N	Y
Absorption	P-glycoprotein I inhibitor	Y	N	Y	N	N	N	N	N	Y	N
Absorption	P-glycoprotein II inhibitor	Y	Y	Y	Y	Y	Y	Y	Y	Y	N
Distribution	VDss (human)	0.321	0.24	0.360	0.389	-0.263	-0.314	0.229	-0.06	0.09	-0.358
Distribution	Fraction unbound (human)	0	0	0	0	0	0	0	0	0	0.551
Distribution	BBB permeability	0.713	0.797	0.719	0.774	-0.244	-0.276	0.936	0.771	-0.086	-1.341
Distribution	CNS permeability	-1.925	-1.754	-1.925	-1.765	-1.559	-1.35	-1.094	-1.292	-2.451	-3.921
Metabolism	CYP2D6 substrate	N	N	N	N	N	N	N	N	N	Y
Metabolism	CYP3A4 substrate	Y	Y	Y	Y	Y	Y	Y	Y	Y	N
Metabolism	CYP1A2 inhibitor	N	N	N	N	N	N	N	N	N	N
Metabolism	CYP2C19 inhibitor	N	N	N	N	N	N	N	N	N	N

Metabolism	CYP2C9 inhibitor	N	N	N	N	N	N	N	N	N	N
Metabolism	CYP2D6 inhibitor	N	N	N	N	N	N	N	N	N	N
Metabolism	CYP3A4 inhibitor	N	N	N	N	N	N	N	N	N	N
Excretion	Total Clearance (log ml/min/kg)	0.119	0.628	-0.044	0.572	1.039	0.868	1.061	0.923	0.378	0.491
Excretion	Renal OCT2 substrate	N	N	N	N	N	N	N	N	N	N
Toxicity	AMES toxicity	N	N	N	N	N	N	Y	N	N	N
Toxicity	Max. tolerated dose (human) (log mg/kg/day)	-0.275	-0.555	-0.086	-0.525	-1.143	-1.152	-0.423	-0.845	-0.452	0.643
Toxicity	hERG I inhibitor	N	N	N	N	N	N	N	N	N	N
Toxicity	hERG II inhibitor	Y	Y	Y	Y	Y	N	Y	Y	N	N
Toxicity	Oral Rat Acute Toxicity (LD50) (mol/kg)	2.345	2.326	2.333	2.173	2.629	2.552	2.111	2.468	2.49	2.416
Toxicity	Oral Rat Chronic Toxicity (LOAEL) (mg/kg/day)	1.031	0.829	1.041	0.876	2.596	2.402	0.64	0.658	1.954	2.291
Toxicity	Hepatotoxicity	N	N	N	N	N	N	N	N	N	N
Toxicity	Skin Sensitization	N	N	N	N	N	N	N	N	N	N
Toxicity	*T. pyriformis* toxicity (mg/L)	0.418	0.454	0.427	0.598	0.331	0.345	0.322	0.331	0.463	0.285
Toxicity	MinNw toxicity	-1.953	-2.12	-2.074	-1.888	-2.722	-2.523	-3.899	-3.25	-2.759	2.354

The movement of amino acids in the active site was evaluated by calculating the RMSF of the macromolecule's Cα atoms. This was done to identify the fluctuations of the amino acids in relation to their initial positions. The RMSF values of the residues are displayed on the y-axis of the RMSF plot, while their number is shown on the x-axis. Most of the residues of the macromolecular backbone, except the terminal ones, had RMSF values that ranged between 2 and 5 Å. It became evident that the fluctuations of the active amino acids had a mean variation of 2.0-2.5 Å, which is an acceptable range within the macromolecular active site. The MD simulation of 100 ns produced an RMSF plot for the Cα backbones of the receptor macromolecule and ligand, as shown in Figure 3.

DNA-directed RNA polymerase of the monkeypox virus was analyzed throughout the MD simulation process and it was found that ligand molecule interacts with Ile174, Leu360, and Pro198 amino acid residues of the protein by hydrophobic interaction, amino acid Ser196 via forming a hydrogen bond, and amino acids Arg45, Pro197, Val200, Thr203, and Glu367 via forming water bridges. The interactions observed between the α-amyrin and macromolecular target DNA-directed RNA polymerase of the monkeypox virus were demonstrated in residues throughout the simulation were demonstrated in Figure 5. The macromolecular target protein was found to be interacting with α-amyrin through the residues such as Arg45, Pro197, Val200, Thr203, and
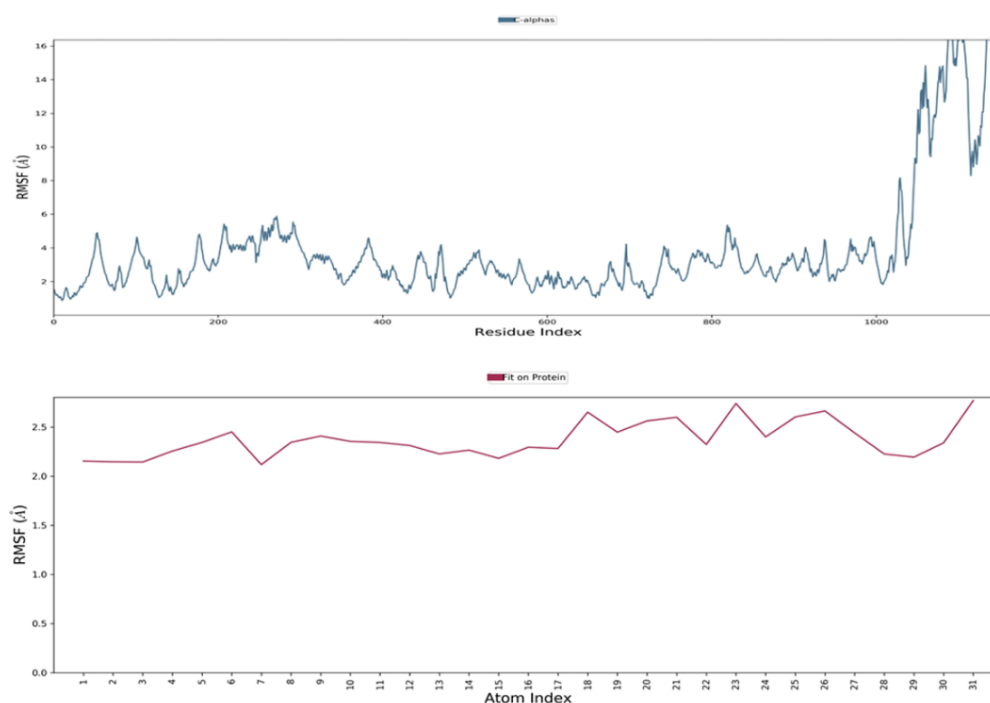

Figure 3. RMSF profiles of the DNA-directed RNA polymerase of monkeypox virus and α-amyrin observed after performing the MD simulation for 100 ns.

Macromolecular secondary structures (α-helices (21.80%) and β-sheets (19.30%)) with a total of 41.10% were conserved throughout the simulation process. The stability of the receptor-ligand complex was due to the formation of hydrogen bonds, hydrophobic contacts, and ionic interactions throughout the MD simulation. To measure the stability of α-amyrin, the intensity of these interactions was observed during MD simulation.
To measure the stability of α-amyrin, the intensity of these interactions was observed during MD simulation. The interaction of α-amyrin against the

Glu367 via water bridges, with residues Ile174 and Leu360 via hydrophobic inter-action, and with Ser196 via classical hydrogen bonding with the ligand (Figure 5).
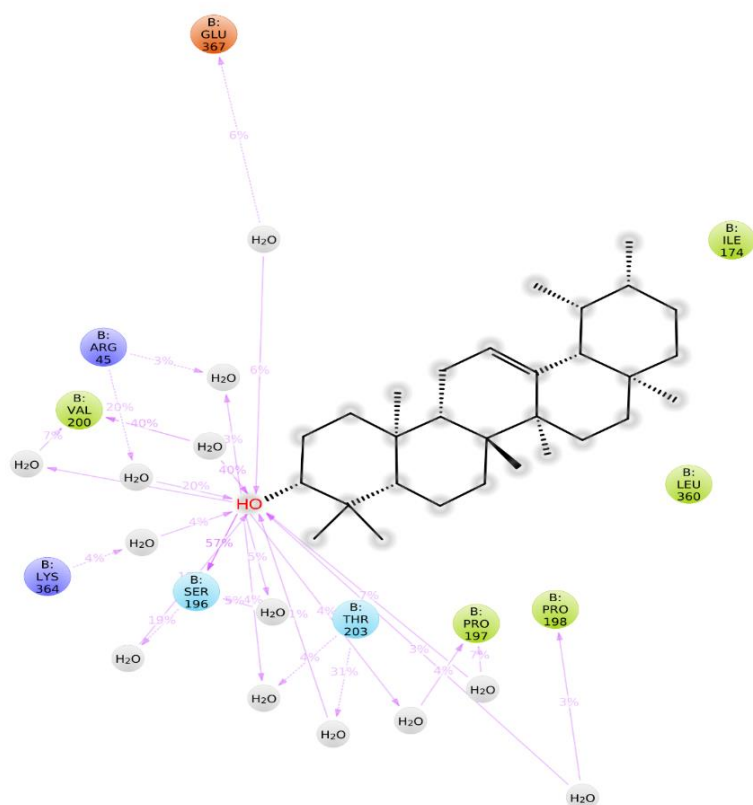
Figure 4. Analysis of the way α-amyrin interacts with viral DNA-directed RNA polymerase indicated that the macromolecular residues shown in green had hydrophobic connections, and the sky blue residues had polar connections with the complexed ligand. The orange-colored residues were negative, and the dark blue were positive.

4. Discussion

Monkeypox disease have been a public health concern in the history and humankind has occasionally faced monkeypox outbreaks [44, 45]. It is because of a smallpox-like virus, monkeypox virus, which can be transmitted via large respiratory droplets, close or direct contact with skin lesions, sexual intercourse, and possibly via contaminated fomites [46]. The most recent outbreak was declared as a global health emergency as of 24th of July, 2022. The number of monkeypox cases has been increasing around the globe and reached to around 31,000 within just three months. This number increased to more than 90,000 cases.

However, there is no currently available approved drugs specifically for monkeypox disease [17]. It is therefore urgent and essential to discover and develop novel drug candidate/s against monkeypox virus. It can also be beneficial to identify potential dietary supplement candidate/s as an alternative and easy-to-access option for the treatment of monkeypox disease, particularly in the poor regions of the world.

For the discovery of potential drug and/or dietary supplement candidate/s, this study focused on chili pepper as a medicinal plant. Chili pepper have used in the traditional medicine for the treatment of various diseases. For instance, Mayas used it for treating asthma, coughs, and sore, while the Aztecs used it to relieve toothaches [47]. In modern time, it is used in tear gas to control crowds by security agencies and has a wide range of application areas starting from culinary to pharmaceutical industry [48]. Various biological activities of chili pepper were summarized in the literature and can be listed as antioxidant, anticancer, anti-inflammatory, antiviral, antifungal, antiobesity, and antiplatelet [48–50]. Particularly for antiviral activities, chili extracts and one of the important natural products in chili pepper, capsaicin, showed promising antiviral activities against some viral species including herpes simplex virus, Lassa virus, and SARS-CoV-2 [24–27], indicating its antiviral potential for other viral species. In this study, we explored the antiviral potential of chili pepper against monkeypox virus using *in silico* techniques.
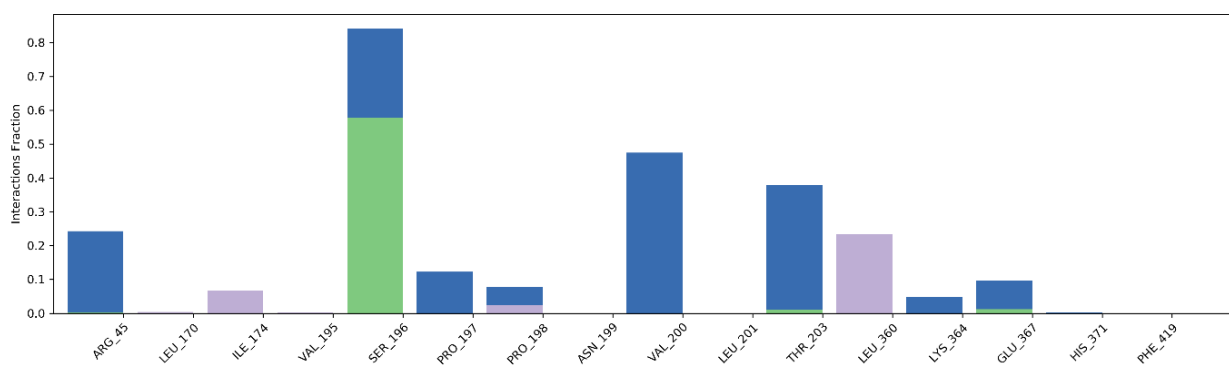
Figure 5. Protein-ligand contacts between viral RNA polymerase and complexed ligand α-amyrin. The green bars indicate H-bonds, the blue bars signify water bridges, the purple bars show hydrophobic interactions, and the dark pink bars highlight ionic interactions between the viral RNA polymerase and its complexed ligand, α-amyrin.

The molecular docking experiments in this study revealed that some of the natural products from chili pepper had strong binding affinities to the DNA-directed RNA polymerase of the monkeypox virus. The top lead molecules out of 47 ligands were tabulated in Table 2. Particularly, α-amyrin, β-sitosterol, and β-amyrin possess very low binding energy scores of -8.19, -7.77, and -7.71, respectively. Out of these hit molecules, MD simulations were conducted for α-amyrin complexed with the macromolecular target protein since it had the lowest binding energy value. Throughout the 100 ns MD simulation, α-amyrin complexed with DNA-directed RNA polymerase of the monkeypox virus was highly stable and it was interacting with some of the amino acid residues as shown in Figure 4. The structural similarity of these three lead compounds, which are pentacyclic triterpenes, might generate the expectation of having a similar profile in MD simulations for the other two lead compounds. In a recent study, Alandijany et al. also investigated potential drug candidates for monkeypox using DNA-directed RNA polymerase as well as viral core cysteine proteinase of monkeypox virus. They computationally discovered some of the tetracycline family ligands, exhibiting multi-target inhibition as a therapeutic solution for monkeypox viral infection [51]. While this study revealed that tetracyclic compounds can be potent against multi-target of monkeypox virus, our study indicated pentacyclic compounds can provide a potential solution for monkeypox outbreak. Furthermore, Akash et al. computationally investigated natural curcumin derivatives for the anti-viral drug discovery against monkeypox and smallpox infections and found that curcumin derivatives can indeed show potential for

the treatment of monkeypox and smallpox viruses with strong binding affinity toward profilin-like protein from monkeypox virus [52]. Interestingly, similar to our study and the study by Alandijany et al., curcumin derivatives with strong binding affinities indeed had multi-cyclic structures with three aromatic rings. This can unearth that multi-cyclic ligands can be potent antiviral agents in the prevention and treatment of monkeypox virus.

The pentacyclic triterpenes may be classified under four groups: oleanane, ursane, lupane and hopane. α-amyrin has an ursane skeleton, while β-amyrin has an oleanane skeleton. Amyrins are widely distributed in nature and exist in various plants and plant materials including leaves, bark, wood, and resins [53]. They exhibit various biological activities such as analgesic, anti-inflammatory, anxiolytic, anticonvulsant, anti-colitis, antidepressant, antihyperglycemic, anti-pancreatitis, and gastroprotective and hepatoprotective activities [53–55]. On the other hand, β-sitosterol is the main phytosterol found in the majority of plants and was reported to exhibit anti-inflammatory, antineoplastic, antipyretic, and immunomodulation activities [56]. However, there is not much literature showing the antiviral potential of amyrins. Glycyrrhetinic acid, a derivative of the β-amyrin, was obtained from the herb liquorice and had an inhibitory effect on various viruses including hepatitis B virus (HBV) and HIV [57]. There is also some *in silico* studies for the antiviral potential of amyrins against SARS-CoV-2. For instance, α-amyrin and β-sitosterol were listed among the top-ranked molecules with the lowest binding energies towards both the spike glycoprotein of SARS-CoV-2 and human ACE2 receptor [58]. α- and β-amyrin were

also tested against main protease of SARS-CoV-2 using *in silico* approaches and showed strong binding affinities to the main protease [59]. To our knowledge, there is no study in the current literature showing the potential of amyrins as an antiviral agent against monkeypox virus. Thus, our study paved the way for the potential of amyrins as antiviral drug and/or dietary supplement candidate/s in the treatment of monkeypox disease.

5. Conclusion

In conclusion, due to the current outbreak of the monkeypox virus and the unavailability of approved drugs, there is an urgent need for the discovery and development of drug candidates effective against the monkeypox virus. In the current study, the natural products from chili pepper were evaluated for their potential antiviral activities against the monkeypox virus through *in silico* studies. The molecular docking experiments for 47 ligand molecules from chili pepper were performed against the homology-modeled DNA-directed RNA polymerase of the monkeypox virus. α-amyrin, β-sitosterol, and β-amyrin were among the top-ranked molecules with strong binding affinities towards DNA-directed RNA polymerase of the virus. In particular, the stability of

α-amyrin complexed with the macromolecular target was also confirmed with MD simulations. Because there is no study indicating the antiviral potential of α-amyrin against the monkeypox virus, this study revealed that α-amyrin has a potential inhibitory effect on DNA-directed RNA polymerase and could therefore constitute a potential lead molecule for the design of new antiviral agents against monkeypox. It also establishes α-amyrin as a possible dietary supplement candidate for monkeypox patients because it is a natural substance present in a variety of herbal and medicinal plants, including chili pepper.

Acknowledgement

Conflict of Interest

The author declares no conflict of interest.

Statement of Research and Publication Ethics

This study complies with research and publication ethics

References

[1]   S. Riedel, "Edward Jenner and the history of smallpox and vaccination," *Proc. (Bayl. Univ. Med. Cent).*, vol. 18, no. 1, p. 21, Jan. 2005, doi: 10.1080/08998280.2005.11928028.

[2]   J. Guarner, C. del Rio, and P. N. Malani, "Monkeypox in 2022—What Clinicians Need to Know," *JAMA*, vol. 328, no. 2, pp. 139–140, Jul. 2022, doi: 10.1001/JAMA.2022.10802.

[3]   S. R. Chowdhury, P. K. Datta, and S. Maitra, "Monkeypox and its pandemic potential: what the anaesthetist should know," *Br. J. Anaesth.*, vol. 0, no. 0, Jul. 2022, doi: 10.1016/J.BJA.2022.06.007.

[4]   E. M. Bunge *et al.*, "The changing epidemiology of human monkeypox—A potential threat? A systematic review," *PLoS Negl. Trop. Dis.*, vol. 16, no. 2, p. e0010141, Feb. 2022, doi: 10.1371/JOURNAL.PNTD.0010141.

[5]   Z. Ježek, M. Szczeniowski, K. M. Paluku, and M. Mutombo, "Human monkeypox: clinical features of 282 patients," *J Infect Dis*, vol. 156, pp. 293–298, 1987.

[6]   A. L. Hughes, S. Irausquin, and R. Friedman, "The evolutionary biology of poxviruses," *Infect. Genet. Evol.*, vol. 10, no. 1, pp. 50–59, Jan. 2010, doi: 10.1016/J.MEEGID.2009.10.001.

[7]   S. N. Shchelkunov *et al.*, "Human monkeypox and smallpox viruses: genomic comparison," *FEBS Lett.*, vol. 509, no. 1, pp. 66–70, Nov. 2001, doi: 10.1016/S0014-5793(01)03144-1.

[8]   C. T. Cho and H. A. Wenner, "Monkeypox Virus," *Bacteriol. Rev.*, vol. 37, no. 1, pp. 1–13, 1973, Accessed: Jul. 20, 2022. [Online]. Available: https://journals.asm.org/journal/br

[9]   F. S. Minhaj *et al.*, "Monkeypox Outbreak — Nine States, May 2022," *Morb. Mortal. Wkly. Rep.*, vol. 71, no. 23, p. 764, Jun. 2022, doi: 10.15585/MMWR.MM7123E1.

[10]   D. Mileto *et al.*, "New challenges in human monkeypox outside Africa: A review and case report from Italy," *Travel Med. Infect. Dis.*, vol. 49, p. 102386, Sep. 2022, doi: 10.1016/J.TMAID.2022.102386.

[11]   A. Zumla *et al.*, "Monkeypox outbreaks outside endemic regions: scientific and social priorities," *Lancet. Infect. Dis.*, vol. 22, no. 7, p. 929, Jul. 2022, doi: 10.1016/S1473-3099(22)00354-1.

[12]   D. W. Grosenbach *et al.*, "Oral Tecovirimat for the Treatment of Smallpox," *N. Engl. J. Med.*, vol. 379, no. 1, pp. 44–53, Jul. 2018, doi: 10.1056/NEJMOA1705688.

[13]   G. Chittick, M. Morrison, T. Brundage, and W. G. Nichols, "Short-term clinical safety profile of brincidofovir: A favorable benefit–risk proposition in the treatment of smallpox," *Antiviral Res.*, vol. 143, pp. 269–277, Jul. 2017, doi: 10.1016/j.antiviral.2017.01.009.

[14]   C. L. Hutson *et al.*, "Pharmacokinetics and efficacy of a potential smallpox therapeutic, brincidofovir, in a lethal monkeypox virus animal model," *Am Soc Microbiol*, vol. 6, no. 1, Feb. 2022, doi: 10.1128/mSphere.00927-20.

[15]   A. T. Russo *et al.*, "Effects of treatment delay on efficacy of tecovirimat following lethal aerosol monkeypox virus challenge in cynomolgus macaques," *J. Infect. Dis.*, vol. 218, no. 9, pp. 1490–1499, Sep. 2018, doi: 10.1093/INFDIS/JIY326.

[16]   H. Adler *et al.*, "Clinical features and management of human monkeypox: a retrospective observational study in the UK," *Lancet Infect. Dis.*, vol. 22, no. 8, pp. 1153–1162, Aug. 2022, doi: 10.1016/S1473-3099(22)00228-6.

[17]   J. G. Rizk, G. Lippi, B. M. Henry, D. N. Forthal, and Y. Rizk, "Prevention and Treatment of Monkeypox.," *Drugs*, vol. 82, no. 9, pp. 957–963, Jun. 2022, doi: 10.1007/S40265-022-01742-Y.

[18]   A. M. Vera-Guzmán, E. N. Aquino-Bolaños, E. Heredia-García, J. C. Carrillo-Rodríguez, S. Hernández-Delgado, and J. L. Chávez-Servia, "Flavonoid and Capsaicinoid Contents and Consumption of Mexican Chili Pepper (Capsicum annuum L.) Landraces," *Flavonoids - From Biosynth. to Hum. Heal.*, Aug. 2017, doi: 10.5772/68076.

[19]   A. Wesołowska, D. J.-A. S. Pol., U. Hortorum, and U. 2011, "Chemical composition of the pepper fruit extracts of hot cultivars Capsicum annuum L," *Acta Sci. Pol., Hortorum Cultus*, vol. 10, no. 1, pp. 171–184, 2011, Accessed: Jul. 26, 2022. [Online]. Available: https://czasopisma.up.lublin.pl/index.php/asphc/article/view/3190.

[20]   S. E. Altmann *et al.*, "Inhibition of cowpox virus and monkeypox virus infection by mitoxantrone," *Antiviral Res.*, vol. 93, no. 2, pp. 305–308, Feb. 2012, doi: 10.1016/J.ANTIVIRAL.2011.12.001.

[21]   J. Deval, J. A. Symons, and L. Beigelman, "Inhibition of viral RNA polymerases by nucleoside and nucleotide analogs: therapeutic applications against positive-strand RNA viruses beyond hepatitis C virus," *Curr. Opin. Virol.*, vol. 9, p. 1, 2014, doi: 10.1016/J.COVIRO.2014.08.004.

[22]   S. Mujwar, L. Sun, and O. Fidan, "*In silico* evaluation of food-derived carotenoids against SARS-CoV-2 drug targets: Crocin is a promising dietary supplement candidate for COVID-19," *J. Food Biochem.*, p. e14219, 2022, doi: 10.1111/JFBC.14219.

[23]   Y. Furuta, B. B. Gowen, K. Takahashi, K. Shiraki, D. F. Smee, and D. L. Barnard, "Favipiravir (T-705), a novel viral RNA polymerase inhibitor," *Antiviral Res.*, vol. 100, no. 2, pp. 446–454, Nov. 2013, doi: 10.1016/J.ANTIVIRAL.2013.09.015.

[24]   N. Rahmattullah, E. Laras Arumingtyas, M. Hermawan Widyananda, A. N. Ahyar, and I. Tabroni, "Bioinformatics Analysis of Bioactive Compounds of Four *Capsicum* Species against SARS-CoV-2 Infection," *Int. J. Adv. Biol. Biomed. Res.*, vol. 9, no. 4, pp. 298–319, 2021, doi: 10.22034/ijabbr.2021.139183.1335.

[25]   N. Ordaz-Trinidad, L. Dorantes-Álvarez, J. Salas-Benito, B. L. Barrón-Romero, M. Salas-Benito, and M. De Nova-Ocampo, "Cytotoxicity and antiviral activity of pepper extracts (*Capsicum* spp)," *Polibotánica*, vol. 0, no. 46, Jul. 2018, doi: 10.18387/POLIBOTANICA.46.18.

[26]   K. Tang, X. Zhang, and Y. Guo, "Identification of the dietary supplement capsaicin as an inhibitor of Lassa virus entry," *Acta Pharm. Sin. B*, vol. 10, no. 5, pp. 789–798, May 2020, doi: 10.1016/J.APSB.2020.02.014.

[27]   T. A. Hafiz, M. A. Mubaraki, M. A. Dkhil, and S. Al-Quraishy, "Antiviral Activities of Capsicum annuum Methanolic Extract against Herpes Simplex Virus 1 and 2," *Pak. J. Zool.*, vol. 49, no. 1, pp. 251–255, Jan. 2017, doi: 10.17582/JOURNAL.PJZ/2017.49.1.251.255.

[28]   K. H. Choi, "Viral polymerases," *Adv. Exp. Med. Biol.*, vol. 726, pp. 267–304, 2012, doi: 10.1007/978-1-4614-0980-9_12/COVER.

[29] A. Bateman *et al.*, "UniProt: the universal protein knowledgebase in 2021," *Nucleic Acids Res.*, vol. 49, no. D1, p. D480, Jan. 2021, doi: 10.1093/NAR/GKAA1100.

[30] W. D. Arndt *et al.*, "Monkeypox virus induces the synthesis of less dsRNA than vaccinia virus, and is more resistant to the anti-poxvirus drug, IBT, than vaccinia virus," *Virology*, vol. 497, pp. 125–135, Oct. 2016, doi: 10.1016/J.VIROL.2016.07.016.

[31] A. Waterhouse *et al.*, "SWISS-MODEL: homology modelling of protein structures and complexes," *Nucleic Acids Res.*, vol. 46, no. W1, pp. W296–W303, Jul. 2018, doi: 10.1093/NAR/GKY427.

[32] K. Gopalakrishnan, G. Sowmiya, S. S. Sheik, and K. Sekar, "Ramachandran Plot on The Web (2.0)," *Protein Pept. Lett.*, vol. 14, no. 7, pp. 669–671, Aug. 2007, doi: 10.2174/092986607781483912.

[33] S. Mujwar and R. K. Harwansh, "*In silico* bioprospecting of taraxerol as a main protease inhibitor of SARS-CoV-2 to develop therapy against COVID-19," *Struct. Chem.*, vol. 1, p. 1, 2022, doi: 10.1007/S11224-022-01943-X.

[34] O. Fidan, S. Mujwar, and M. Kciuk, "Discovery of adapalene and dihydrotachysterol as antiviral agents for the Omicron variant of SARS-CoV-2 through computational drug repurposing," *Mol. Divers.*, vol. 27, no. 1, pp. 463–475, Feb. 2023, doi: 10.1007/S11030-022-10440-6.

[35] S. Mujwar, K. Shah, J. K. Gupta, and A. Gour, "Docking based screening of curcumin derivatives: A novel approach in the inhibition of tubercular DHFR," *Int. J. Comput. Biol. Drug Des.*, vol. 14, no. 4, pp. 297–314, 2021, doi: 10.1504/IJCBDD.2021.118830.

[36] S. Mujwar, "Computational bioprospecting of andrographolide derivatives as potent cyclooxygenase-2 inhibitors," *Biomed. Biotechnol. Res. J.*, vol. 5, no. 4, p. 446, Oct. 2021, doi: 10.4103/BBRJ.BBRJ_56_21.

[37] D. E. V. Pires, T. L. Blundell, and D. B. Ascher, "pkCSM: Predicting small-molecule pharmacokinetic and toxicity properties using graph-based signatures," *J. Med. Chem.*, vol. 58, no. 9, pp. 4066–4072, May 2015, doi: 10.1021/ACS.JMEDCHEM.5B00104.

[38] R. Jain and S. Mujwar, "Repurposing metocurine as main protease inhibitor to develop novel antiviral therapy for COVID-19," *Struct. Chem.*, pp. 1–13, 2020, doi: https://doi.org/10.1007/s11224-020-01605-w.

[39] S. Mujwar, "Computational repurposing of tamibarotene against triple mutant variant of SARS-CoV-2," *Comput Biol Med*, vol. 136, p. 104748, 2021, doi: https://doi.org/10.1016/j.compbiomed.2021.104748.

[40] K. Shah, S. Mujwar, G. Krishna, and J. K. Gupta, "Computational Design and Biological Depiction of Novel Naproxen Derivative," *https://home.liebertpub.com/adt*, vol. 18, no. 7, pp. 308–317, Oct. 2020, doi: 10.1089/ADT.2020.977.

[41] H. S. Hillen *et al.*, "Structural Basis of Poxvirus Transcription: Transcribing and Capping Vaccinia Complexes," *Cell*, vol. 179, no. 7, pp. 1525-1536.e12, Dec. 2019, doi: 10.1016/J.CELL.2019.11.023.

[42] C. Grimm, J. Bartuli, B. Boettcher, A. A. Szalay, and U. Fischer, "Structural basis of the complete poxvirus transcription initiation process," *Nat. Struct. Mol. Biol. 2021 2810*, vol. 28, no. 10, pp. 779–788, Sep. 2021, doi: 10.1038/s41594-021-00655-w.

[43] L. Z. Benet, C. M. Hosey, O. Ursu, and T. I. Oprea, "BDDCS, the Rule of 5 and drugability," *Adv. Drug Deliv. Rev.*, vol. 101, pp. 89–98, Jun. 2016, doi: 10.1016/J.ADDR.2016.05.007.

[44] B. L. Ligon, "Monkeypox: A review of the history and emergence in the Western hemisphere," *Semin. Pediatr. Infect. Dis.*, vol. 15, no. 4, pp. 280–287, Oct. 2004, doi: 10.1053/J.SPID.2004.09.001.

[45] J. S. Bryer, E. E. Freeman, and M. Rosenbach, "Monkeypox emerges on a global scale: a historical review and dermatological primer," *J. Am. Acad. Dermatol.*, Jul. 2022, doi: 10.1016/J.JAAD.2022.07.007.

[46] J. P. Thornhill *et al.*, "Monkeypox Virus Infection in Humans across 16 Countries - April-June 2022.," *N. Engl. J. Med.*, Jul. 2022, doi: 10.1056/NEJMOA2207323.

[47] B. K. Saleh, "Medicinal uses and health benefits of chili pepper (*Capsicum* spp.): a review Evaluation of husbandry, insect pest, diseases and management practices of vegetables cultivated in Zoba Anseba Eritrea View project Mycology isolation of fungi from sorghum pearl millet View project," 2018, doi: 10.15406/mojfpt.2018.06.00183.

[48] S. Idrees, M. A. Hanif, M. A. Ayub, A. Hanif, and T. M. Ansari, "Chili Pepper," *Med. Plants South Asia Nov. Sources Drug Discov.*, pp. 113–124, Jan. 2020, doi: 10.1016/B978-0-08-102659-5.00009-4.

[49] G. E. S. Batiha *et al.*, "Biological Properties, Bioactive Constituents, and Pharmacokinetics of Some *Capsicum* spp. and Capsaicinoids," *Int. J. Mol. Sci.*, vol. 21, no. 15, pp. 1–35, Aug. 2020, doi: 10.3390/IJMS21155179.

[50] K. Srinivasan, "Biological Activities of Red Pepper (*Capsicum annuum*) and Its Pungent Principle Capsaicin: A Review," *http://dx.doi.org/10.1080/10408398.2013.772090*, vol. 56, no. 9, pp. 1488–1500, Jul. 2015, doi: 10.1080/10408398.2013.772090.

[51] T. A. Alandijany *et al.*, "A multi-targeted computational drug discovery approach for repurposing tetracyclines against monkeypox virus," *Sci. Reports 2023 131*, vol. 13, no. 1, pp. 1–22, Sep. 2023, doi: 10.1038/s41598-023-41820-z.

[52] S. Akash *et al.*, "Anti-viral drug discovery against monkeypox and smallpox infection by natural curcumin derivatives: A Computational drug design approach," *Front. Cell. Infect. Microbiol.*, vol. 13, p. 1157627, 2023, doi: 10.3389/FCIMB.2023.1157627.

[53] A. O. Nogueira, Y. I. S. Oliveira, B. L. Adjafre, M. E. A. de Moraes, and G. F. Aragão, "Pharmacological effects of the isomeric mixture of alpha and beta amyrin from *Protium heptaphyllum*: a literature review," *Fundam. Clin. Pharmacol.*, vol. 33, no. 1, pp. 4–12, Feb. 2019, doi: 10.1111/FCP.12402.

[54] F. A. Santos *et al.*, "Antihyperglycemic and hypolipidemic effects of α,β-amyrin, a triterpenoid mixture from *Protium heptaphyllum* in mice," *Lipids Health Dis.*, vol. 11, no. 1, pp. 1–8, Aug. 2012, doi: 10.1186/1476-511X-11-98.

[55] G. F. Aragao, M. C. C. Pinheiro, P. N. Bandeira, T. L. G. Lemos, and G. S. de B. Viana, "Analgesic and Anti-Inflammatory Activities of the Isomeric Mixture of Alpha- and Beta-Amyrin from *Protium heptaphyllum*(Aubl.) March," *http://dx.doi.org/10.1080/J157v07n02_03*, vol. 7, no. 2, pp. 31–47, Jan. 2009, doi: 10.1080/J157V07N02_03.

[56] L. Fraile, E. Crisci, L. Córdoba, M. A. Navarro, J. Osada, and M. Montoya, "Immunomodulatory properties of Beta-sitosterol in pig immune responses," *Int. Immunopharmacol.*, vol. 13, no. 3, pp. 316–321, Jul. 2012, doi: 10.1016/J.INTIMP.2012.04.017.

[57] R. Pompei, O. Flore, M. A. Marccialis, A. Pani, and B. Loddo, "Glycyrrhizic acid inhibits virus growth and inactivates virus particles," *Nat. 1979 2815733*, vol. 281, no. 5733, pp. 689–690, 1979, doi: 10.1038/281689a0.

[58] V. K. Maurya, S. Kumar, M. L. B. Bhatt, and S. K. Saxena, "Antiviral activity of traditional medicinal plants from Ayurveda against SARS-CoV-2 infection," *J. Biomol. Struct. Dyn.*, vol. 40, no. 4, pp. 1719–1735, 2022, doi: 10.1080/07391102.2020.1832577.

[59] B. Kar, B. Dehury, M. K. Singh, S. Pati, and D. Bhattacharya, "Identification of phytocompounds as newer antiviral drugs against COVID-19 through molecular docking and simulation based study," *J. Mol. Graph. Model.*, vol. 114, p. 108192, Jul. 2022, doi: 10.1016/J.JMGM.2022.108192.

A Fuzzy Based Intelligent Traffic Light Control (ITLC) Method: An Implementation in Ankara City

Tuğçe İNAĞ[1*], Murat ARIKAN[1]

[1]*Gazi University, Faculty of Engineering, Industrial Engineering Department, Ankara, Turkey*

(ORCID: 0000-0002-8800-6727) (ORCID: 0000-0003-1437-8939)

Abstract

The escalating global population and increased vehicle usage have worsened traffic congestion in metropolitan areas, a significant urban challenge. Addressing this, adaptive traffic light control methods, especially at intersections, are being developed to improve traffic flow and reduce waiting times. This study significantly contributes to this field by implementing Fuzzy Logic in intelligent traffic light systems, focusing on Ankara's Polatlı Refik Cesur intersection. Using the SUMO simulation platform and Python programming, it analyzed waiting times and queue lengths. The initial phase used queue length for each intersection arm as an input. Fuzzy logic rules then determined the output, prioritizing street or phase order for optimal flow. The study further proposed an Adaptive Neuro-Fuzzy Inference System (ANFIS)-based control plan. ANFIS merges neural network capabilities with fuzzy logic, using waiting time and queue length as inputs to regulate the green light duration. Compared to existing traffic systems, this model showed a substantial improvement. It achieved a 36.5% reduction in waiting times, underlining the efficiency of the Fuzzy Logic-based method. This approach not only enhances traffic management but also contributes significantly to the literature on intelligent traffic light control systems. By addressing key urban traffic issues, the study paves the way for future advancements in traffic management technologies. The findings highlight the potential of combining advanced computational methods, like ANFIS, with traditional traffic control techniques to optimize urban traffic flow, offering a blueprint for similar challenges in other metropolitan areas.

1. Introduction

Today's population continues to grow rapidly, and this increase brings significant challenges to the transportation sector. One of the primary challenges is the traffic congestion observed in large cities and densely populated areas. The increasing demand exceeds the capacity of roads and infrastructure, leading people to spend more time commuting to work, shopping, or traveling.Furthermore, vehicle exhaust emissions contribute to air pollution, releasing greenhouse gases into the atmosphere and causing climate change.

Another issue resulting from traffic and vehicles is noise pollution High fuel consumption has adverse effects on both individual and national budgets Paragraphs following the first paragraph should begin with the paragraph indentation [1].

Building new roads to alleviate traffic congestion can be a traditional approach, but this method can create new environmental issues. In recent years, one of the approaches seen as a to alleviate traffic congestion is using intelligent traffic light control systems.

These systems regulate the lights based on road density at each traffic intersection. Roads with lower traffic density result in less waiting time, while they can manage traffic more effectively in densely populated areas. This situation can improve traffic flow and reduce congestion [2].

Intelligent traffic light control systems can continuously monitor traffic data and adjust settings to optimize traffic flow. This approach provides environmental benefits such as reduced energy consumption and decreased air pollution. Therefore, using intelligent traffic control systems is a more appealing option to create a sustainable transportation system, as opposed to traditional infrastructure development. Traffic lights, especially at intersections, are considered one of the most effective ways of managing traffic. These lights not only ensure safe and efficient traffic flow but also reduce travel times, alleviate traffic congestion, and support the more effective use of road capacity [3]. Furthermore, they assist in enhancing safety and emergency management. All of these advantages demonstrate that adaptive intelligent traffic light control systems, sensitive to real-time traffic conditions, make a significant contribution to solving the problem of traffic congestion.

This study deployed intelligent controllers, including Fuzzy Logic and the Adaptive Neuro-Fuzzy Inference System (ANFIS), to manage traffic lights at a four-way intersection. The fuzzy logic controller decides which road to prioritize for the green light based on the vehicle queue length, while ANFIS processes waiting times and queue length data to determine the optimal duration for green traffic lights. Our research addresses a significant gap in the existing literature on traffic control systems. Despite the promise shown by intelligent traffic light control systems in optimizing traffic flow, the specific application and effectiveness of ANFIS, coupled with Fuzzy Logic controllers at a four-way intersection, still need to be explored. By addressing this gap, our study contributes valuable insights to enhance the comprehension of intelligent traffic control systems and their practical implementation.

The following sections of the paper will provide an in-depth exploration of ANFIS's utilization in the literature, the methodologies applied, and the detailed outcomes of its practical implementation.

2. ANFIS (Adaptive Neuro-Fuzzy Inference System)

ANFIS is a computational model that combines the fundamental principles of fuzzy logic and artificial neural networks to solve complex problems. This model is rooted in fuzzy logic, a mathematical framework designed to address uncertainty and non-precise situations, utilizing linguistic variables, fuzzy sets, and fuzzy rules to handle such uncertainties in the data. On the other hand, artificial neural networks are computational models inspired by the structure and functioning of the human brain. They consist of interconnected nodes, or neurons, which process information and transmit it through weighted connections. Artificial neural networks are known for their ability to learn from data and can be employed for various tasks, including pattern recognition, regression, and classification.

ANFIS effectively merges the strengths of both fuzzy logic and artificial neural networks. This approach, known as neuro-fuzzy systems, provides a flexible and robust solution, particularly in complex domains where data is incomplete or imprecise. In fields such as control systems, decision support, and modeling real-world problems, these neuro-fuzzy systems are practical tools to address complex, uncertain, and non-precise scenarios [4]. In Figure 1, the general structure of our ANFIS model is illustrated.
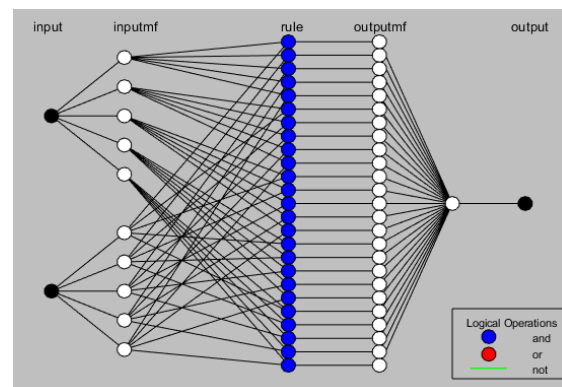

Figure 1. ANFIS model structure in Matlab

The terms "inputmf (input membership functions)" and "outputmf (output membership functions)" indicate the type of fuzzy logic membership functions associated with the input and output variables of this model.

3. Literature Review

Various studies have proposed different approaches and methods to enhance traffic light

control. Among these approaches, one prominent method is the Adaptive Neuro-Fuzzy Inference System (ANFIS). ANFIS employs a hybrid training method that can automatically generate fuzzy rules based on the dataset [5].

Araghi et al. developed a cuckoo search optimization algorithm to optimize the parameters of intelligent controllers using ANFIS. This study investigates how ANFIS can be employed in traffic light control and assesses the effectiveness of ANFIS-based traffic light controllers [6].

Walukov et al. determined the green light duration for a four-way isolated intersection using ANFIS. Traffic volume and waiting time were utilized to determine the green light duration as the output. This study demonstrates how traffic light control can be optimized using ANFIS [4].

Araghi et al. compared interval type 1 ANFIS, interval type 2 ANFIS, fixed fuzzy logic, and three different fixed-timing fuzzy logic methods for traffic light control. The comparisons revealed that fuzzy controllers outperformed traditional controllers. This study developed a distributed control system for a network comprising nine intersections. Each intersection had its controller and considered traffic density in neighboring intersections when determining signal durations for traffic phases. This approach contributes to making traffic light control more efficient and effective. It underscores the significance of fuzzy logic-based methods in traffic light control [7].

Andayani et al. applied the Adaptive Neuro-Fuzzy Inference System (ANFIS) method by using traffic density and road width data to determine the traffic light duration. This study was conducted to optimize traffic light control and adopt an approach sensitive to traffic density. ANFIS processed the data on traffic density and road width to target the most efficient determination of green light durations [8].

Abiodun et al. have adopted the Adaptive Neuro-Fuzzy Inference System (ANFIS) method with the sole aim of controlling traffic lights based on road density. This study was conducted to regulate traffic flow and effectively manage traffic density. Road density data were processed by ANFIS and used to determine the durations of traffic light signals [9]. In another study, vehicle density and road width data were the basis for determining signal durations. The manually collected data were processed using the Fuzzy

Logic method, leading to the optimization of signal durations. This study was carried out in a simulation environment, demonstrating the effectiveness of the technique [10].

George et al. employed the Internet of Things (IoT) and the Adaptive Neuro-Fuzzy Inference System (ANFIS) to enhance traffic conditions. In this study, an ANFIS traffic light controller was developed in the MATLAB SIMULINK environment, utilizing inputs such as waiting time and vehicle density. Cameras were employed to detect traffic density, and the captured images were sent to the cloud. Subsequently, these images were analyzed on a server using the ANFIS controller to ascertain the suitable signal durations [3]. Azura et al. have proposed a fuzzy logic-based traffic controller for multi-lane isolated signalized intersections. This controller, developed using MATLAB, relies on the current green light status, vehicle waiting times, traffic density, and traffic density in other intersections. Additionally, in this study, a traffic model based on queue theory and the First-In-First-Out (FIFO) principles has been developed [11].

Utomo et al. have proposed ANFIS as a controller for two adjacent intersections in Djuanda-Bandung. This system can adjust real-time traffic light phase durations for both intersections based on traffic conditions. Vehicle queue length and changes in these queues were used as inputs for ANFIS during the adjustment process. ANFIS, as a result, generates an output value such as street urgency. Through MATLAB simulations, it was revealed that this ANFIS-based control system outperformed the traditional fixed-timing traffic control method [12].

Awoyera et al. have proposed an Intelligent Traffic Control System (ITCS) based on the Adaptive Neuro-Fuzzy Inference System (ANFIS) using real-time traffic data obtained from different traffic lanes. The ANFIS-based ITCS can learn from historical traffic data and consider traffic data from side lanes to predict future traffic flow on the main road. Simulations confirmed that this intelligent traffic control system based on ANFIS provided a lower average delay for different vehicle queue lengths and waiting times at a four-lane road intersection [13].

Araghi et al. offer an optimal approach for traffic signal controllers designed by the Adaptive Neuro-Fuzzy Inference System (ANFIS). This controller aims to adjust green times at a single intersection to improve traffic

flow and reduce congestion. The ANFIS controller has the learning capability to determine suitable green times for each traffic phase. During this learning process, the Cuckoo Search (CS) algorithm has been utilized for parameter tuning. The performance of the proposed method has been compared to Fuzzy Logic Controller (FLC) and fixed-timing traffic control methods. The results demonstrate that the ANFIS controller outperforms the other comparative controllers, showcasing its effectiveness [14].

Zeynal et al. have presented an innovative approach to control traffic flow in congested areas efficiently. They introduced an innovative input-selective adaptive network-based fuzzy inference system (ANFIS) approach, enhancing the ANFIS prediction system. The proposed model has been tested at an intersection in Mashhad, Iran [15].

Mittal and Cavla highlight that traffic congestion in urban areas is one of the primary issues that can be addressed through infrastructure improvement and the construction of one-way roads. One-way roads can increase vehicle speed and reduce travel times. Since congested roads can make the control of isolated intersections inefficient, coordinated traffic intersections on the roads are beneficial. In this article, signal coordination techniques based on the distance between two intersections are proposed. This ANFIS-based system is compared with linear and decision tree regression methods, demonstrating its effectiveness. They used average delay time as the comparison parameter If necessary, subheadings can be added under the main heading [16].

4. Methodology and Implementation

The current state of the Polatlı Refik Cesur intersection in Ankara province, which experiences high traffic density, and the outcomes of applying the proposed models have been examined. The general layout of the intersection is illustrated in Figure 2. It is a four-way intersection with five phases, one of which is the pedestrian phase, comprising ten lanes. The numbers in Figure 2 represent directions. The intersection allows for straight, right, and left turns. There are eight traffic signals, and different traffic signals control right turns.

Figure 2. Polatlı Refik Cesur intersection.

The data for the Polatlı Refik Cesur intersection was obtained by the Gazi University Urban Transportation Technologies Accessibility Application and Research Center (KUTEM). This dataset includes the hourly counts of vehicles, vehicle types, weather conditions, vehicle routes, current phase information, and the existing light plan from 08:00 to 16:00. There are five types of vehicles in traffic: cars, buses, trailers, medium-duty commercial vehicles (MDCV), and trucks. An example of the dataset for cars is shown in Table 1. The table provides the counts of cars entering the intersection at one-hour intervals, heading in different directions.

In this study, the traffic light control system of an isolated four-lane traffic intersection has been examined using fuzzy logic and ANFIS-based intelligent control mechanisms. This mechanism operates under the assumption that the arrival times of vehicles follow a Poisson distribution without prior knowledge.

Table 1. Traffic flow example at Polatlı Refik Cesur intersection

Vehicle type	Time	Street 1 (Eskişehir-Ankara)			Street 2 (Ankara-Eskişehir)			Street 3 (Polatlı- Huzur evi)			Street 4 (Huzur evi- Polatlı)		
		1 - 2	1 – 3	1 - 4	2 -1	2 - 3	2 - 4	3 – 1	3 - 2	3 – 4	4 – 1	4 - 2	4 – 3
CAR	08-09	400	42	25	437	132	22	25	205	95	21	55	105
	09-10	443	38	14	401	126	20	20	190	80	20	51	95
	10-11	563	43	11	380	121	18	16	169	75	27	54	80
	11-12	505	40	13	466	116	16	15	171	60	25	50	75
	12-13	606	38	17	529	109	15	18	168	56	23	45	69
	13-14	599	29	16	571	95	25	6	251	61	42	29	146

14-15	675	32	17	630	209	29	23	242	125	25	28	85
15-16	825	26	15	697	215	48	13	265	102	35	24	91

This article presents a fuzzy logic-based intelligent control mechanism for managing traffic lights at the intersection. The primary goal is to enhance traffic flow and increase intersection capacity to reduce waiting times. Initially, the next phase allowed in traffic is determined. Subsequently, an integrated system model is created that extends the green light duration adaptively, considering vehicle density and waiting times. The model structure is depicted in Figure 3.
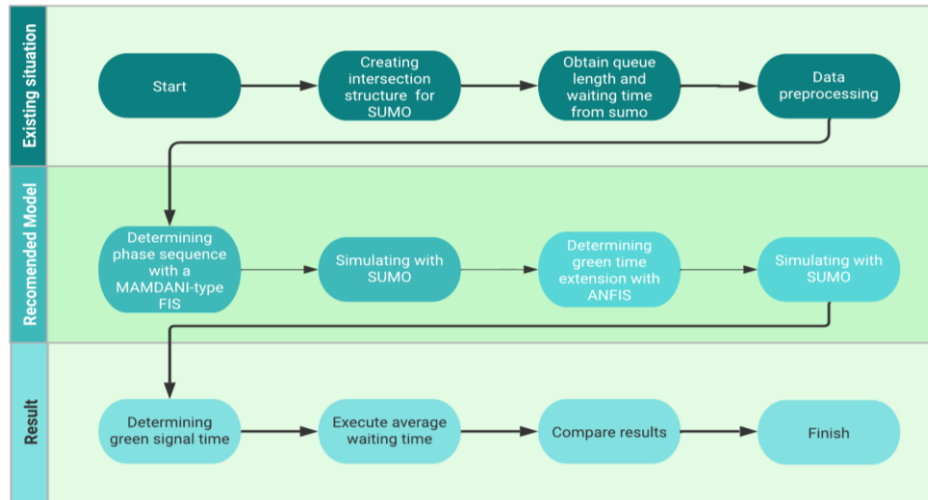
Figure 3. Traffic controller model

4.1. SUMO (Simulation of Urban Mobility)

The intersection was visualized in the SUMO (Simulation of Urban Mobility) simulator based on accurate data, and real-time data on the number of vehicles in the queue and waiting times were collected using Python programming. The SUMO simulation platform was chosen due to its open-source nature and its ability to simulate individual behaviors of vehicles in traffic, as well as handle continuous events. Additionally, SUMO is a powerful tool for dynamic time simulations [17].

These typical four-lane intersections operate based on the M/M/1 queuing theory principle. According to this theory, vehicles enter the queue to receive service, following the first-come, first-served principle. However, in this study, an intelligent control system has been used instead of fixed-time traffic light control plans.

The traffic flow of the existing intersection was visualized in the SUMO simulation platform. Figure 4 provides a visual representation of the Polatlı Refik Cesur Intersection in the SUMO simulation environment. Real-time data on the number of vehicles in the queue and waiting times were extracted from SUMO and recorded in Excel.
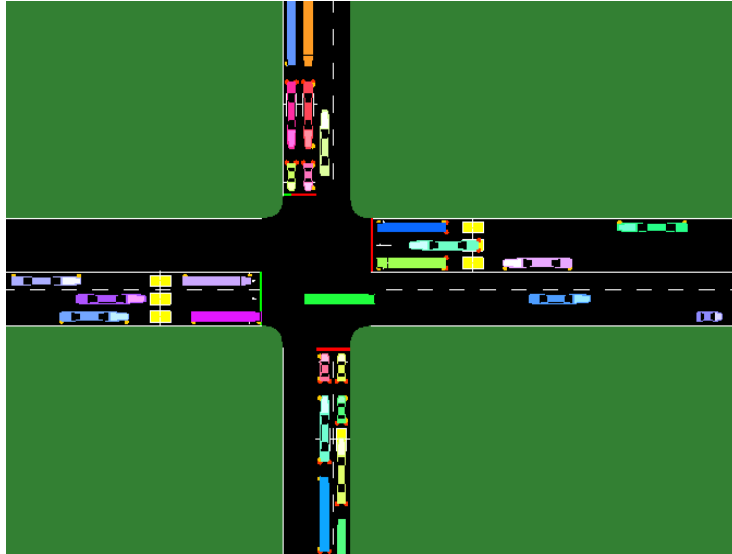
Figure 4. SUMO intersection structure image

4.2. Next Phase Modul

At this stage, a system has been developed that automates the control of the traffic intersection using fuzzy logic. Rule-based Mamdani-type fuzzy modeling technique is used to model the system [18]. At this stage, the system parameters for each street, such as vehicle density and the sequence of phases for street selection, are defined. The membership functions of these parameters are determined by fuzzy logic. Using

data extracted from SUMO, the queue length (very short, short, long, very long, extremely long) was defined for each street. The street with the longest queue is the one to receive the green light in the next phase. As a result of this process, the following traffic phase has been determined.

Firstly, the street to which the green light will be given was determined by the Mamdani fuzzy logic system, as shown in Figure 5.The results obtained should be included in this section and supported by figures and tables if necessary.
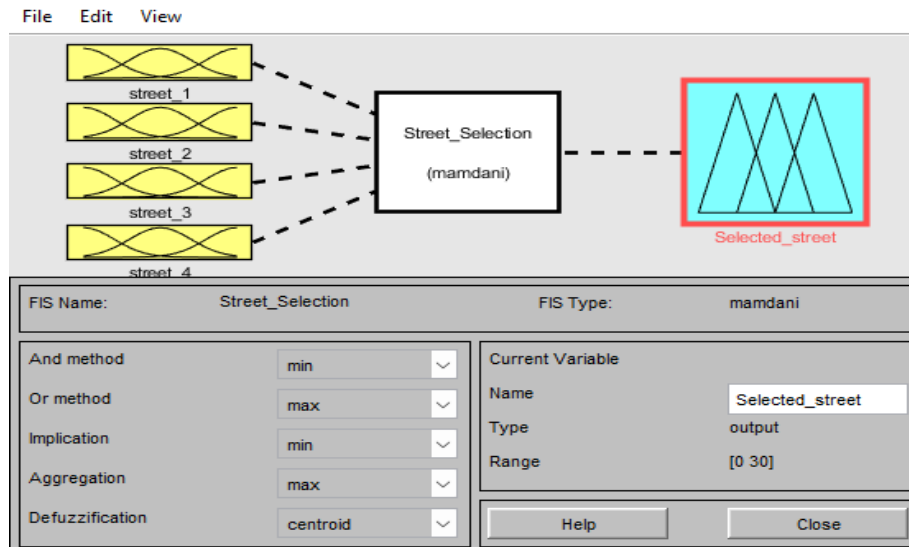

Figure 5. A Mamdani-type fuzzy logic model for street selection

In the fuzzy logic modeling process, after determining the input and output parameters, the decision is made on the number of linguistic variables for each. Then, the type of membership

function is selected. In the first section of this study, queue length is used as the input parameter, and street selection is used as the output parameter. Gaussian membership

functions were preferred. The roads at the intersection are named street_1, Street_2, Street_3, and Street_4, respectively, and for input parameters, the queue length of each road is named "very short," "short," "long," "very long," "extremely long." A different Gaussian membership function is defined for each road.

The membership function for Street_1 is shown in Figure 5. The output functions for street selection are determined as "street 1," "street 2," "street 3," and "street 4." The designed input and output membership functions are shown in Figure 6.
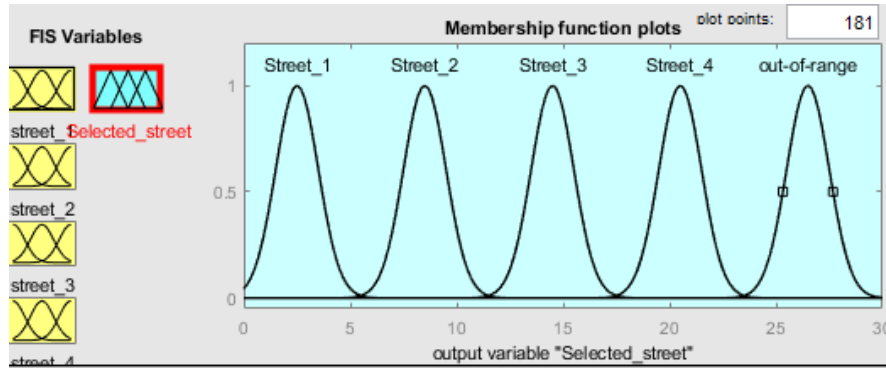

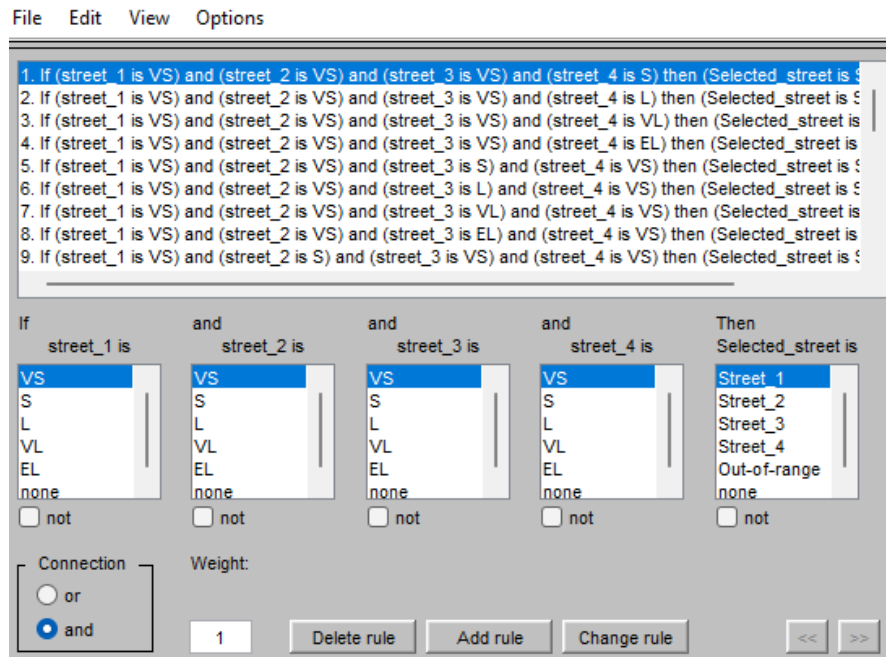**Figure 6.** The output membership functions for the selected street

Figure 7. The rules created for street selection

In this study, specific rules have been created to provide an intelligent control mechanism by the system. These rules involve the selection of a street based on the traffic density level of each road. For example, according to the second rule, if the queues of Street_1, Street_2, and Street_3 are "Very Short," and the queue of Street_4 is "Long," then Street_4 is preferred.

4.3. Green Time Extension Module

During this stage, the duration of the green light for the initially determined traffic phase is calculated to determine how much it should be extended. This duration can be adjusted based on traffic density and waiting times. ANFIS (Adaptive Neuro-Fuzzy Inference System) controls traffic lights by observing vehicle waiting times and queue lengths. As a result, the

traffic signal timing can be adjusted based on traffic density and the number of vehicles on each street, making traffic flow more smoothly [19].

This system determines the traffic signal phase sequences using Fuzzy Logic and directs traffic flow by adjusting the green light duration for each traffic phase using ANFIS technology. This approach ensures a more efficient traffic flow. The reason for using the ANFIS model is its ability to adjust this duration based on traffic conditions dynamically.

The process of assigning green light durations to phases is modeled by Fuzzy Logic or Fuzzy Inference System (FIS). In fuzzy logic, it looks at the degree of conformity to the rule's antecedent. The obtained degree of conformity is then subtracted from the consequences of each rule. All the results are combined to obtain the overall result.

ANFIS traffic signal controller uses a Sugeno-type fuzzy logic system. In the consequent part of the rules, a first-order Sugeno-Type FIS employs a linear system to model the output membership functions. This system operates based on specific rules. FIS constructs the output membership function based on the following rules.

If input_1= x and input_2=y.Then, the output_z is calculated as output_z = ax + by + c. It computes an output value using a linear combination of two inputs. The terms "a" and "b" represent the multipliers of the input values, while "c" is a constant term. The parameters a, b, and c are related to traffic light control and are used to determine the green light duration. These parameters are used to calculate the outcomes of a specific traffic signal control strategy or algorithm. "a" and "b" are the weights of the inputs used to determine the traffic light duration (e.g., queue length and waiting time). "a" represents the impact of queue length on the green light duration. A significant "a" value implies that queue length has a more significant influence on the green duration. "b" represents the impact of waiting time on the green light duration. A significant "b" value implies that waiting time has a more significant influence on the green duration. "c" represents the initial value of the traffic light, meaning it represents the initial duration of the green light. For example, a value like c = 2.4 would initiate the green light with a duration of 2.4 time units [13].

To achieve the best simulation results, we use optimal weights of a = b = 0.026 and a fixed value of c = 1. This rule employs a linear model to produce an output based on inputs and combines these outputs to obtain the overall result. As a result, the extension durations of green phases can be adjusted based on a specific logic, and it can be used to optimize traffic flow.

Input_1 (x) = Queue Length, Qt (0 - 60 vehicle)

Input_2 (y) = Waiting Time, Wt (0 - 80 second)

Output_z = Green Extension Time, Et (0 - 6 second).

Hence, the Green Light Extension Output, Et, is expressed as Et = a[Wt] + b[Qt] + c.

In the Data Preprocessing step, the available data has been analyzed, and meaningful cleaning, imputation of missing values, and correction of outliers have been carried out.

The data has been divided into two sections using MATLAB software: training data (70%) and test data (30%). The training data includes the data on which the model was trained, while the test data was used to evaluate the performance of the trained model. The ANFIS model was trained on the training set and then evaluated on the test data. The proposed Smart Traffic Control System network design is shown in Figure 8.
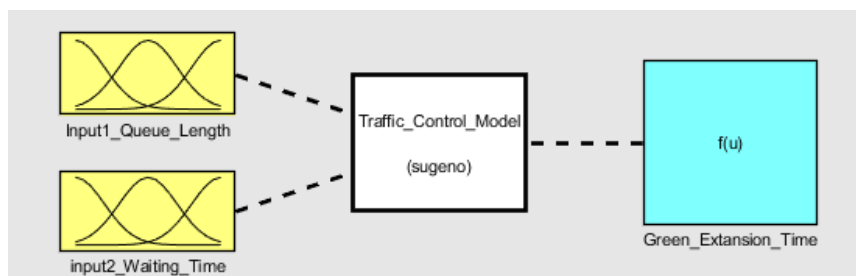

Figure 8. Fuzzy logic control for intelligent traffic

Fuzzy membership functions for all the necessary input and output variables for traffic light control have been defined separately. These inputs are queue length (Qt) and waiting time (Wt). The output variable is the extension time of the green light (Et). Based on the data, the range of input membership functions has been defined as follows: According to the data obtained from SUMO, the queue length varies between 0 to 60 vehicles, and the waiting time ranges from 0 to 80 seconds. The input membership functions are graphically represented in Figure 9 and Figure 10. Five different labels have been defined: very short (VS), short (S), long (L), very long (VL), and extremely long (EL).
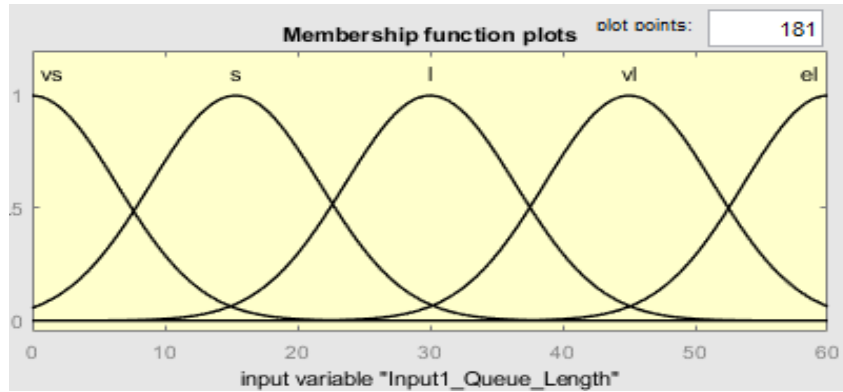

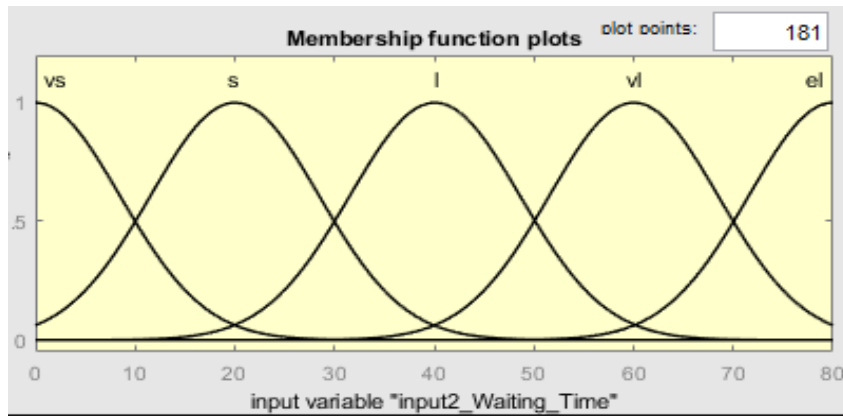**Figure 9.** Vehicle queue length 0-60 vehicles.

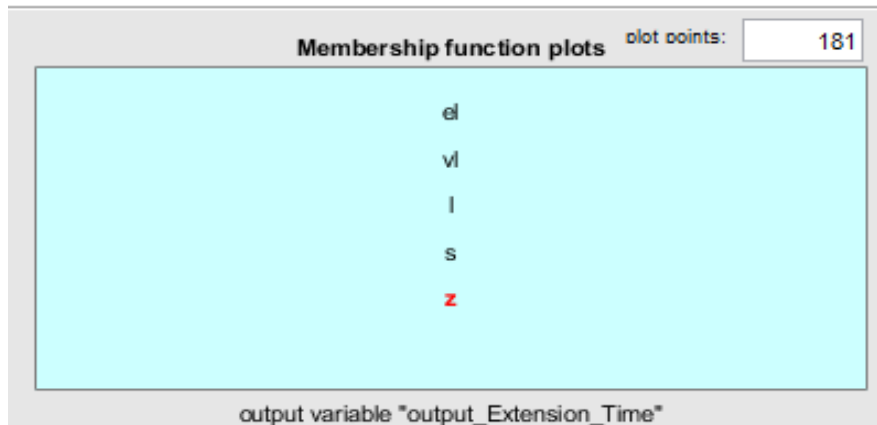**Figure 10.** Vehicle waiting time 0-80 seconds

Figure 11. Green extension time 0-6 seconds

The range of output membership functions, on the other hand, varies between 0 and 6 seconds, and these functions are presented in Figure 11. Afterward, fuzzy rules were written using IF-THEN statements. The IF part represents the condition to be met, and the THEN part indicates the action to be taken when the condition is met. The rules are shown in Figure 12.
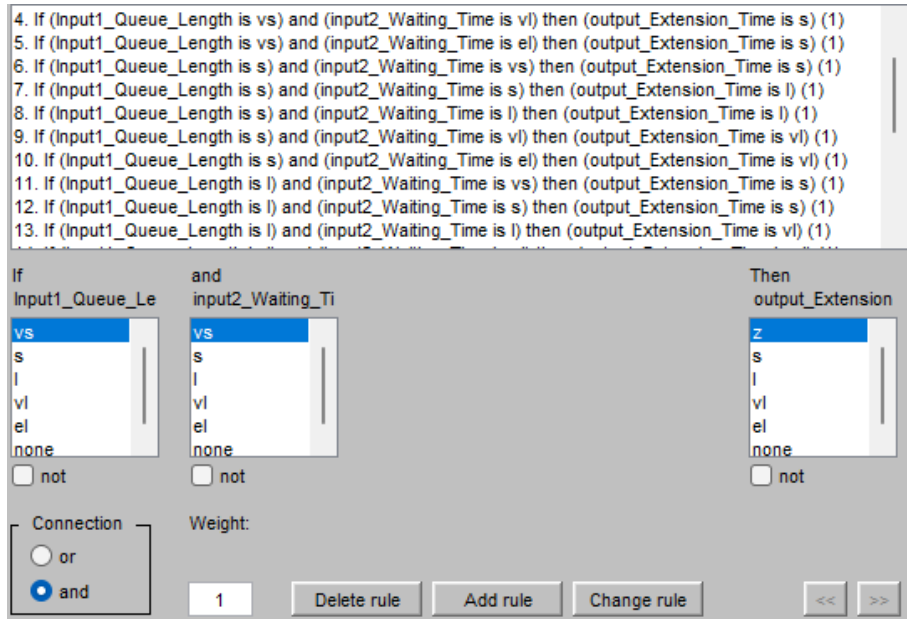

Figure 12. Fuzzy rule editor

5. RESULTS

In this study, firstly, the Polatlı Refik Cesur intersection was simulated using the SUMO simulation platform. Then, using the PYTHON programming language, the waiting times and queue lengths of vehicles obtained from this simulation platform were extracted. In the initial stage, using these data, it was determined in which phase the green light should be on using a Mamdani-type Fuzzy Logic model, as shown in Figure 6. For instance, if street_1, street_2, and street_3 have short queues, while street_4 has a long queue, the phase containing street_4 is determined as the new phase where the green light needs to be activated. After determining the phase sequence, it was decided how the green light duration should be adjusted using an ANFIS model that considers the queue length and waiting times on the street. The output of the ANFIS traffic controller is shown in Figure 13. This method presents an approach that combines simulation and fuzzy logic modeling to address complex traffic control problems and is used to adapt green light durations to make traffic flow more efficient.
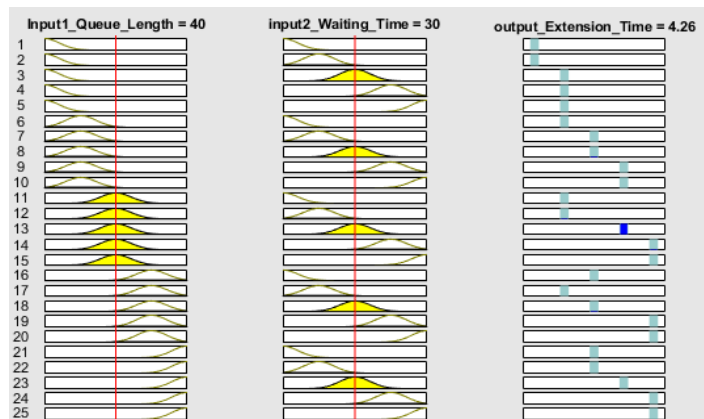

Figure 13. Fuzzy Rules ve Green Time Extension

When the queue length for any vehicle is considered 40 vehicles and the waiting time is 30 seconds, the ANFIS-based model calculates the green light duration as 4.26 seconds. Figure 14 shows a surface plot of one output function and two input variables. This graph demonstrates that as the queue length and waiting time of vehicles increase, the green light duration also increases. This duration can go up to a maximum of 6 seconds. The ANFIS controller adjusts the green light duration for different traffic densities and waiting times. Table 2 provides a detailed breakdown of the increases in green light duration for different waiting times and queue length scenarios. These results emphasize the effectiveness of ANFIS-based control in managing traffic flow.
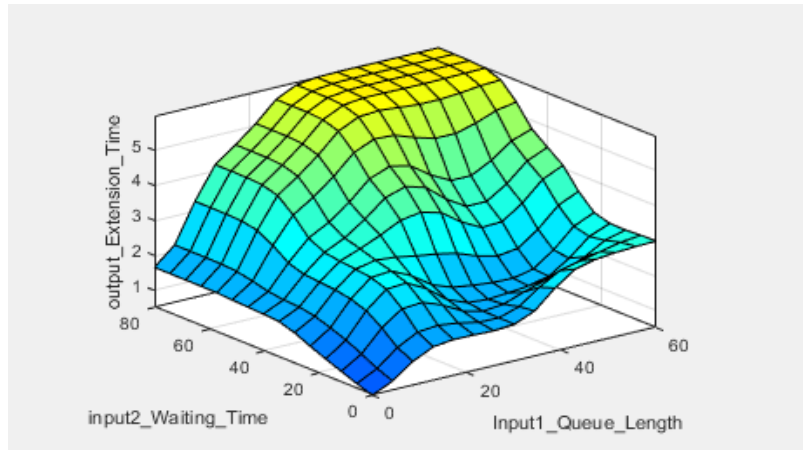

Figure 14. Surface views for ANFIS outputs

As the queue length and waiting time of vehicles increase, the green light extension time gradually increases. It has reached a maximum of 6 seconds. As shown in Table 3, the ANFIS controller effectively assigns green light extension time when different traffic volumes and waiting times are provided.

Table 2. Performance of the system

Queue Length	Waiting Time	Extension Time
5	10	1,17
10	10	1,75
15	15	2,56
20	20	2,87
25	25	2,97
30	25	3,32

The average error of the test set was calculated as 0.92648. The ANFIS method was used to optimize the green light durations. Figure 15 displays the ANFIS model created in MATLAB. This model has been successfully employed in traffic signal control. The blue dots represent the actual rules, while the red ones represent the rules of our model. The optimization model is selected as "hybrid". This means that a combination of genetic algorithm and gradient-based methods is used during the training of the ANFIS model. This can help the ANFIS model perform better. The epoch value is set to 3, indicating that the ANFIS model is trained for a maximum of 3 epochs. Each epoch represents the updating of the model on the training data and the learning process. Using more epochs means the model is trained further, but excessive epochs can lead to overfitting issues [20]. Therefore, an epoch value of 3 has been chosen.
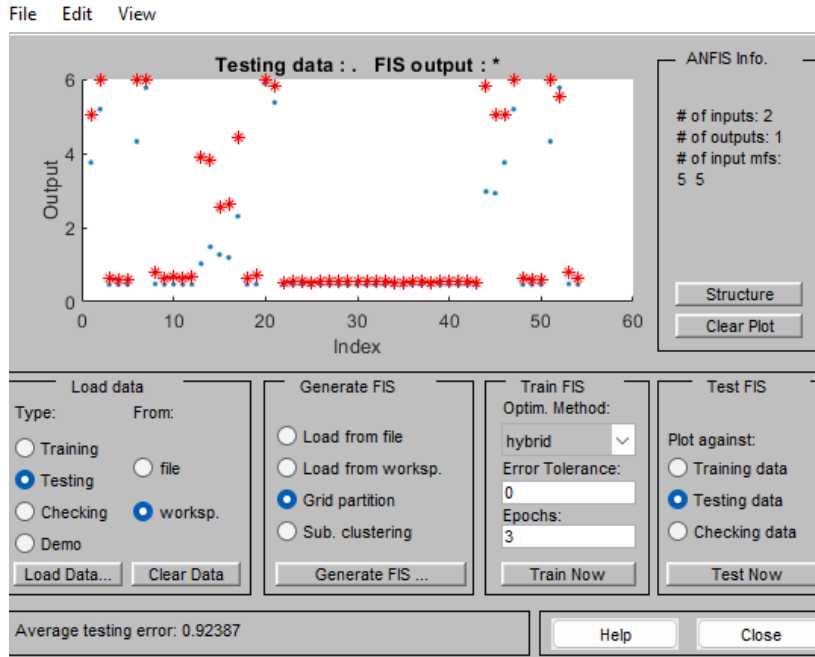
Figure 15. The simulation of ANFIS

5.1. Simulation Results

The proposed new Intelligent Traffic Control model has been integrated with the SUMO (Simulation of Urban Mobility) simulation platform, and its impact on per-vehicle waiting times has been thoroughly investigated. The research results present the observed improvements in waiting times for each street in Table 2.

Table 3. The improvement achieved in waiting time

Street Name	The waiting time per vehicle while fixed-time (sec/vehicle)	The waiting time per vehicle after the proposed model (sec/vehicle)	Improvement in waiting time (sec/vehicle)	Improvement in waiting time (%)
Street 1	80.45	38	42.45	**53**
Street 2	76.17	40.20	35.97	**47.2**
Street 3	58.14	50.21	7.93	**13.6**
Street 4	62.41	42.32	20.09	**32.2**

As seen in the table, there is a 36.5% reduction in the average waiting time at the intersection. For Street 1, which has the highest waiting time, the fixed-time traffic light plan results in a delay of 80.45 seconds per vehicle, while with our proposed model, this time is reduced to 38 seconds. The improvement in waiting time is 42.45 seconds. Proportionally, an approximate 53% improvement has been achieved.

Figure 16 provides a comparison between the proposed fuzzy logic and ANFIS-based new Intelligent Traffic Light Control (ITLC) system and the traditional fixed-time traffic light control (FTLC) system based on instantaneous waiting time data during a 500-second simulation period of vehicles following a Poisson distribution. As can be seen from the figure, the newly proposed system has significantly reduced waiting times.
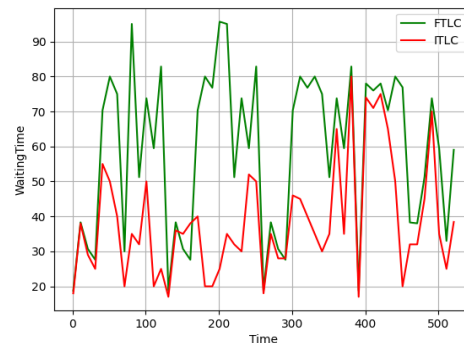

Figure 16. Simulation results for waiting time

303

Figure 17 presents a graph showing the change in the number of vehicles waiting in the queue over time, as recorded instantaneously by SUMO (Simulation of Urban Mobility). The proposed system tends to reduce the number of vehicles in the queue. This situation supports the observed decrease in waiting times.
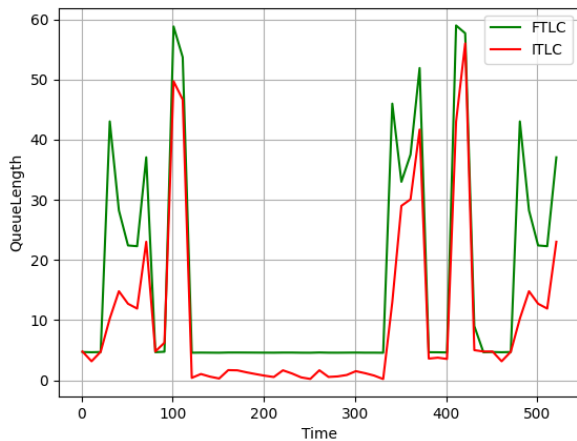

Figure 17. Simulation results for queue length

According to the data presented in Figures 16 and 17, when the queue length is low, the proposed model outperforms the fixed-time traffic light control model. However, when the queue length increases, it is observed that our model achieves relatively better results. One of the primary reasons for the improved performance of the proposed model is the more efficient utilization of intersection capacity and the faster clearance of incoming vehicles from the intersection.

6. Conclusion

This study focuses on the challenges of real-time traffic control at an isolated intersection under uncertain traffic conditions. The developed system presents an effective method for monitoring and regulating traffic flow by integrating a Mamdani-type fuzzy logic model and ANFIS-based systems. The proposed model demonstrates a performance trend of reducing

waiting times by minimizing queue lengths facilitating faster intersection clearance for entering vehicles. As a result, the intersection is utilized more efficiently, achieving reduced waiting times and queue lengths compared to the fixed-time traffic light control method.

As part of future research, the potential applications of this system involve more comprehensive studies incorporating multiple intersections and considering the traffic status of adjacent roads. Such an integrated system could extend beyond a single road, potentially optimizing traffic management in broader geographical areas. In conclusion, this study provides a solution to the complexities of traffic control and enhances traffic flow by effectively combining fuzzy logic and ANFIS technologies. To enhance the practical impact of our findings, we propose recommendations on how this system can proactively prevent congestion in real-world scenarios. Our findings, based on original datasets, emphasize the potential of the proposed system to play an influential role in traffic management and offer unprecedented solutions. In this context, the results of our study provide a valuable foundation for researchers and decision-makers aiming to understand the practical impact of the developed method and improve future traffic management strategies.

Conflict of Interest Statement
There is no conflict of interest between the authors.
Statement of Research and Publication Ethics

The study is complied with research and publication ethics

References

[1]   B. Vatchova, Y. Boneva, and A. Gegov, "Modelling and Simulation of Traffic Light Control," *Cybernetics and Information Technologies,* vol. 23, no. 3, pp. 179-191, 2023, doi: 10.2478/cait-2023-0032.

[2]   D. Jutury, N. Kumar, A. Sachan, Y. Daultani, and N. Dhakad, "Adaptive neuro-fuzzy enabled multi-mode traffic light control system for urban transport network," *Applied Intelligence,* vol. 53, no. 6, pp. 7132-7153, 2023, doi: 10.1007/s10489-022-03827-3.

[3]   A. M. George, V. I. George, and M. A. George, "IOT based Smart Traffic Light Control System," in *2018 International Conference on Control, Power, Communication and Computing Technologies, ICCPCCT 2018*, 2018, pp. 148-151, doi: 10.1109/ICCPCCT.2018.8574285. [Online].   Available: https://www.scopus.com/inward/record.uri?eid=2-s2.0-85060024823&doi=10.1109%2fICCPCCT.2018.8574285&partnerID=40&md5=c045a62856f de8f2d6192d92beb1c808

[4]   S. B. Walukow, F. J. Doringin, R. E. Katuuk, and A. S. Wauran, "Regulation of the Real Time Traffic Light at Teling Intersection in Manado City by using Fuzzy Logic and ANFIS," in *2018 International Conference on Applied Science and Technology (iCAST)*, 2018: IEEE, pp. 259-262.

[5]   K. M. Udofia, J. O. Emagbetere, and F. O. Edeko, "Dynamic traffic signal phase sequencing for an isolated intersection using ANFIS," *Automation, Control and Intelligent Systems,* vol. 2, no. 2, pp. 21-26, 2014.

[6]   S. Araghi, A. Khosravi, and D. Creighton, "Intelligent cuckoo search optimized traffic signal controllers for multi-intersection network," *Expert Systems with Applications,* vol. 42, no. 9, pp. 4422-4431, 2015, doi: 10.1016/j.eswa.2015.01.063.

[7]   S. Araghi, A. Khosravi, and D. Creighton, "Comparing the performance of different types of distributed fuzzy-based traffic signal controllers," *Journal of Intelligent and Fuzzy Systems,* vol. 36, no. 6, pp. 6155-6166, 2019, doi: 10.3233/JIFS-181993.

[8]   U. Andayani *et al.*, "Simulation of Dynamic Traffic Light Setting Using Adaptive Neuro-Fuzzy Inference System (ANFIS)," in *Journal of Physics: Conference Series*, 2019, vol. 1235, 1 ed., doi: 10.1088/1742-6596/1235/1/012058.   [Online].   Available: https://www.scopus.com/inward/record.uri?eid=2-s2.0-85070022009&doi=10.1088%2f1742-6596%2f1235%2f1%2f012058&partnerID=40&md5=ab0dba18e53025008af8a2cfe6718a0a

[9]   B. A. Abiodun, A. A. Amosa, A. O. Olayode, A. T. Morufat, and S. A. Adedayo, "Traffic Light Control Using Adaptive Network Based Fuzzy Inference System," in *Proceedings of 2014 International Conference on Artificial Intelligence & Manufacturing Engineering (ICAIME 2014), Dubai*, 2014, pp. 156-161.

[10]   C. I. Sitorus, "Perancangan Simulasi Pengatur Lampu Lalu Lintas Berdasarkan Volume Kendaraan Dan Lebar Jalan Berbasis Logika Fuzzy," *Universitas Sumatera Utara. Medan,* 2014.

[11]   A. C. Soh, L. G. Rhung, and H. M. Sarkan, "MATLAB simulation of fuzzy traffic controller for multilane isolated intersection," *International Journal on Computer Science and Engineering,* vol. 2, no. 4, pp. 924-933, 2010.

[12]   R. A. B. Utomo, D. A. Permana, and P. H. Rusmin, "Intelligent traffic light control system at two intersections using adaptive neuro-fuzzy inference system (ANFIS) method," in *Earth and Space 2018: Engineering for Extreme Environments - Proceedings of the 16th Biennial International Conference on Engineering, Science, Construction, and Operations in Challenging Environments*, 2018, pp. 976-990, doi: 10.1061/9780784481899.092. [Online]. Available: https://www.scopus.com/inward/record.uri?eid=2-s2.0-85087897263&doi=10.1061%2f9780784481899.092&partnerID=40&md5=4f5383efe750bc3 7b5c02894eed689de

[13]   O. Awoyera, O. Sacko, O. Darboe, and O. Cynthia, "Anfis-Based Intelligent Traffic Control System (ITCS) for Developing Cities," *Journal of Traffic and Logistics Engineering,* pp. 18-22, 01/01 2019, doi: 10.18178/jtle.7.1.18-22.

[14]   S. Araghi, A. Khosravi, and D. Creighton, "Design of an Optimal ANFIS Traffic Signal Controller by Using Cuckoo Search for an Isolated Intersection," in *Proceedings - 2015 IEEE International Conference on Systems, Man, and Cybernetics, SMC 2015*, 2016, pp. 2078-2083, doi: 10.1109/SMC.2015.363.   [Online].   Available: https://www.scopus.com/inward/record.uri?eid=2-s2.0-84964506090&doi=10.1109%2fSMC.2015.363&partnerID=40&md5=c7a296a6f315a302fddc 960737afb88a

[15]   H. Zeynal, Z. Zakaria, A. Kor, and H. Torkamani, "An Improved ANFIS Based Traffic Flow Control through a Novel Approach on Input Selection," in *ICPEA 2021 - 2021 IEEE International Conference in Power Engineering Application*, 2021, pp. 161-166, doi: 10.1109/ICPEA51500.2021.9417843.   [Online].   Available: https://www.scopus.com/inward/record.uri?eid=2-s2.0-85106411438&doi=10.1109%2fICPEA51500.2021.9417843&partnerID=40&md5=6840475e894b11d99817f9830a3ecc23

[16]   U. Mittal and P. Chawla, "Traffic Green Signal Optimization using Adaptive Neuro-Fuzzy Inference System on Coordinated Intersections," in *2022 10th International Conference on Reliability, Infocom Technologies and Optimization (Trends and Future Directions), ICRITO 2022*,   2022,   doi: 10.1109/ICRITO56286.2022.9964576.   [Online].   Available: https://www.scopus.com/inward/record.uri?eid=2-s2.0-85144597052&doi=10.1109%2fICRITO56286.2022.9964576&partnerID=40&md5=f2bdc95617a984ec8965835cefb828ed

[17]   M. E. M. Ali, A. Durdu, S. A. Çeltek, and A. Yilmaz, "An adaptive method for traffic signal control based on fuzzy logic with webster and modified webster formula using SUMO traffic simulator," *IEEE Access,* vol. 9, pp. 102985-102997, 2021.

[18]   A. Zade and D. Dandekar, "Simulation of adaptive traffic signal controller in MATLAB simulink based on fuzzy inference system," in *National Conference On Innovative Paradigms İn Engineering & Technology*, 2012, vol. 9, p. 13.

[19]   X. C. Vuong, R. F. Mou, T. T. Vu, and H. Van Nguyen, "An Adaptive Method for an Isolated Intersection under Mixed Traffic Conditions in Hanoi Based on ANFIS Using VISSIM-MATLAB," *IEEE Access,* Article vol. 9, pp. 166328-166338, 2021, doi: 10.1109/ACCESS.2021.3135418.

[20]   G. Noureddine, "Intelligent Controllers for Permanent Magnet Synchronous Motor Drive Systems," *AJIT,* 01/01 2004.

Symbolic Aggregate Approximation-Based Clustering of Monthly Natural Gas Consumption

Mehmet Eren NALİCİ[1], İsmet SÖYLEMEZ[1*], Ramazan ÜNLÜ[1]

[1]Abdullah Gül University, Faculty of Engineering, Industrial Engineering Department,
Kayseri Türkiye

(ORCID: 0000-0002-7954-6916) (ORCID: 0000-0002-8253-9389) (ORCID: 0000-0002-1201-195X)

Abstract

Natural gas is an indispensable non-renewable energy source for many countries. It is used in many different areas such as heating and kitchen appliances in homes, and heat treatment and electricity generation in industry. Natural gas is an essential component of the transportation sector, providing a cleaner alternative to traditional fuels in vehicles and fleets. Moreover, natural gas plays a vital role in boosting energy efficiency through the development of combined heat and power systems. These systems produce electricity and useful heat concurrently. As nations move towards more sustainable energy solutions, natural gas has gained prominence as a transitional fuel. This is due to its lower carbon emissions when compared to coal and oil, thus making it an essential component of the global energy framework. In this study, monthly natural gas consumption data of 28 different European countries between 2014 and 2022 are used. Symbolic Aggregate Approximation method is used to analyze the data. Analyses are made with different numbers of segments and numbers of alphabet sizes, and alphabet vectors of each country are created. These letter vectors are used in hierarchical clustering and dendrogram graphs are created. Furthermore, the elbow method is used to determine the appropriate number of clusters. Clusters of countries are created according to the determined number of clusters. In addition, it is interpreted according to the consumption trends of the countries in the determined clusters.

1. Introduction

For many nations, natural gas is an essential non-renewable energy source. It is utilized in a wide range of applications, including heat treatment and power production in industry, as well as heating and cooking appliances in residences. Because it offers a more environmentally friendly option to conventional fuels for automobiles and fleets, natural gas is a vital component of the transportation industry. Its adaptability also extends to the manufacture of petrochemicals, where it serves as a feedstock to produce several necessary goods including chemicals, plastics, and fertilizers. Furthermore, natural gas is essential for developing combined heat and power

(CHP) systems, which increase energy efficiency. These systems simultaneously provide usable heat and power. Natural gas has become more well-known as a transitional fuel as countries shift to more environmentally friendly energy sources. Although energy from environmentally damaging sources has been utilized for a long time, there has been a shift in trend toward lower carbon energy sources. In this situation, using natural gas has become a viable substitute for using coal [1]. Natural gas plays an important role in reducing contaminants and climate change because it emits 50% less carbon dioxide (CO_2) than coal and 30% less than oil. The International Gas Union cites three main reasons for this, including the fact that it is more affordable than

other energy sources based on fossil fuels, easier to deliver and install, and a sustainable resource. Considering these circumstances, several nations strive to enhance their natural gas production technologies, including the utilization of non-traditional production techniques, to augment the physical network components within the gas supply chain [2].

In modern economies, energy resources are becoming increasingly scarce. Therefore, it is important to obtain energy more cheaply and use it wisely. The need to use energy more wisely has arisen due to the rapid increase in energy consumption, which has occurred regardless of the world's population growth. This increase is also impacting the use of natural gas in particular [3]. The demand for natural gas has been rising globally since 2005, reaching a peak in 2019 before the coronavirus outbreak. Global natural gas consumption reached 3.9 million metric tons in 2018, up 4.6% over the previous year. The switch from coal to natural gas in the US and China, as well as the huge demand from these two nations, were the main causes of this growth. Natural gas, which has a lower carbon footprint than other non-renewable energy sources like coal and oil, is being promoted by laws in other nations as well. Specifically, compared to coal and oil, natural gas produces 20 to 50% less CO_2, making it a greener energy source [4].

The examination of predicting natural gas usage was undertaken across various scopes, encompassing global, national, gas distribution system, commercial, residential, and individual customer levels. Diverse datasets, including economic indicators, weather information, historical energy and natural gas consumption records, software simulation data, household survey data, and additional factors like days of the week, were utilized to construct forecasting models. The forecast durations spanned from a few hours to several decades ahead [5]. There are different studies in the literature regarding the estimation of natural gas consumption. Different methods have been used for natural gas consumption such as ARIMA [3,6,7], Neural Networks [6,7], Exponential Smoothing [8] and Holtz-Winter Method [8]. Moreover, artificial intelligence methods such as LASSO [9], Support Vector Regressor [9] is used for natural gas consumption prediction.

The report uses monthly data from 2014 to 2022 on natural gas usage from 28 different European nations. To analyze the data, the Symbolic Aggregate Approximation (SAX) approach is applied. Alphabet vectors for every nation are produced, and analyses are conducted using different numbers of segments and different alphabet sizes. Hierarchical clustering and the creation of dendrogram graphs require these alphabet vectors. Moreover, the elbow approach is employed to establish the proper number of clusters. Based on the number of clusters that are found, groups of nations are formed. Furthermore, the interpretation is based on the consumption patterns of the nation's inside the identified clusters.

2. Material and Method

In this section, general structure of the data will be given. also, method information will be mentioned.

2.1. Data

In this data set, monthly natural gas consumption data of 28 countries between 2014 and 2022 are used. The unit of data is determined as million cubic meters [10].

2.1. Symbolic Aggregate Approximation (SAX)

For time series clustering, the Symbolic Aggregate Approximation (SAX) approach is applied. The SAX method traditionally employs alphabetical symbols to represent and store time-series data. It is well-known for its ability to effectively represent high-dimensional time series data while maintaining the characteristics of the original data points [11]. This discretization procedure is unique because it makes use of a representation that lies between the raw time series and the symbolic characters. Initially, the normalized data is converted into a Piecewise Aggregate Approximation (PAA) model, which is a discrete string representation [12-13].

The data transformation method known as Piecewise Aggregate Approximation (PAA) reduces the data's dimensionality. PAA divides the data into segments of equal length and creates an approximation of the original sequence that is piecewise-constant, presenting the average value of each segment [14]. The SAX approach is an extension of PAA that provides a symbolic representation of time data. To reduce dimensionality, the approach calculates segment PAA values, normalizes the time series using the Z-score, and replaces the segment mean value with a symbolic code. The code is derived from a preset table of discretization intervals with mean values. The table is

Table 1. Example of Monthly Consumption of Countries in 2022

COUNTRY	2022-01	2022-02	2022-03	2022-04	2022-05	2022-06	2022-07	2022-08	2022-09	2022-10	2022-11	2022-12
Belgium	2,208	1,684	1,540	1,272	1,000	906	895	942	977	1,136	1,339	1,860
Bulgaria	384	317	349	203	202	178	187	136	140	143	221	276
Czechia	1,123	892	902	688	394	340	309	308	391	527	761	973
Denmark	301	260	267	207	160	140	114	118	126	156	200	288
Germany	12,108	9,884	9,444	6,967	4,325	3,491	3,679	3,018	4,261	5,039	7,101	9,942
Estonia	60	50	45	31	21	15	11	13	16	19	30	43
Ireland	518	403	464	461	428	416	443	445	397	380	415	519
Greece	581	503	645	303	349	427	533	485	327	246	357	467
Spain	3,741	3,098	3,047	2,403	2,329	2,607	2,779	2,538	2,525	2,507	2,507	2,525
France	5,921	4,420	4,153	3,160	2,040	1,727	1,744	1,595	1,991	2,261	3,425	5,016
Croatia	376	300	268	194	132	127	151	143	138	203	235	254
Italy	9,733	7,672	7,970	5,268	4,199	4,232	4,443	3,810	4,034	4,235	5,578	7,372
Latvia	137	103	98	61	41	19	18	41	38	27	102	158
Lithuania	198	157	198	152	141	145	95	55	90	92	112	214
Luxembourg	95	75	69	55	34	27	25	21	31	39	53	70
Hungary	1,474	1,240	1,200	848	433	440	398	345	529	545	915	1,182
Netherlands	4,492	3,601	3,423	2,818	2,223	2,040	1,848	1,743	1,822	2,208	2,759	4,015
Austria	1,156	970	1,001	705	467	374	348	318	471	559	798	963
Poland	2,390	2,071	2,076	1,798	1,332	1,148	1,103	989	1,050	1,357	1,895	2,230
Portugal	536	450	485	415	453	489	503	479	461	449	475	377
Romania	1,591	1,263	1,247	729	576	490	455	435	493	637	965	1,309
Slovenia	116	93	96	72	53	48	46	42	48	56	79	91
Slovakia	715	561	534	409	227	196	192	154	189	313	451	588
Finland	179	150	162	96	103	94	85	101	75	69	78	89
Sweden	102	82	60	55	50	37	53	54	43	55	54	82
Norway	686	618	676	640	587	1,072	922	253	916	746	902	1,148
North Macedonia	37	40	45	7	4	3	13	23	32	5	34	33
Türkiye	7,137	6,138	6,951	3,698	3,055	2,946	2,767	3,507	3,130	3,269	2,674	5,768

generated based on the observation that values for different types of normalized time-series segments follow a Gaussian distribution. To obtain the levels of discretization for the symbolic code, the Gaussian distribution of the PAA value is divided into equiprobable intervals. The number of symbols in the SAX alphabet for a given method instance is determined by the number of symbolic intervals [15]. Figure 1 shows an example of the SAX application. In this application, the number of segments is 9 and the alphabet size is 8 as SAX parameters. The blue line shows the normalized consumption data. The orange line shows the graph resulting from PAA. Since we reduced it to 9 data, it was created by taking the average of 12 consecutive months of natural gas consumption data. Finally, the PAA data was marked with the symbol of the value corresponding to the values divided into 8 equal parts of the Normal

distribution and the Alphabet vector was created. The alphabet vector of each country is created according to the alphabet value corresponding to each "PAA" value. Hierarchical clustering is done according to the "Unicode" values of the letters in these vectors and dendrogram graphics are plotted. The combinations of the number of alphabets and the number of segments are directly proportional to the size of our data set, which is 108. The divisor numbers of the number 108 are determined as the number of segments, and the alphabet number is determined as all numbers between 4 to 10. Combinations between these two values can be selected as SAX parameters. In this study, 4 different combinations are considered such as "Alphabet Size=8 Number of Segment=12", "Alphabet Size=6 Number of Segment=12", "Alphabet Size=8 Number of Segment=27", "Alphabet Size=6 Number of Segment=9".
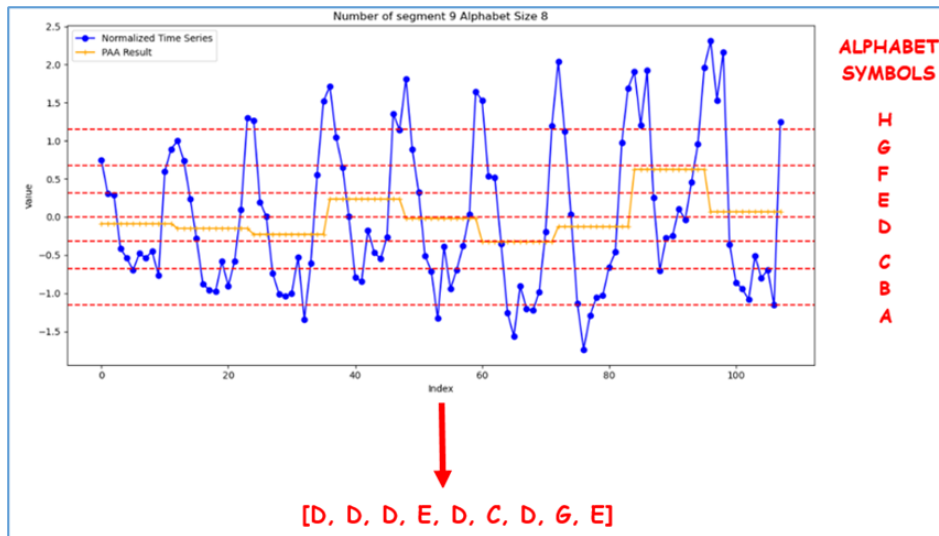
Figure 1. Example of PAA Application for Türkiye Monthly Consumption with Alphabet Size = 8
Number of Segment = 9

3. Results and Discussion

Dendrogram graphs are plotted for 4 different segment number and alphabet number combinations. Moreover, the "Elbow Method" is used to determine the ideal number of clusters. In Figure 2, the results of the elbow methods applied for Number of Segments 12 and 12, Alphabet Sizes 6 and 8 respectively. Moreover, in Figure 3, the results of the elbow methods applied for Number of Segments 27 and 9, Alphabet Sizes 8 and 6 respectively. According to these results, the appropriate cluster numbers are determined as 5, 4, 5, and 4, correspondingly. Dendrogram graphs are plotted (see figure 4 and 5) for the segment number and alphabet number combinations applied in the elbow method, and the elements in the clusters are determined according to

these dendrograms. When the dendrogram graphs are analyzed, the clusters formed according to the number of clusters determined are stated in "Table 2". The results obtained for the case where "Number of Segment = 12" and "Alphabet Size = 8" are as follows. Ireland and Portugal are in the first cluster. Greece Spain and North Macedonia are clustered at the second group. While Denmark, Estonia, Latvia, Romania, Lithuania, Netherlands, Luxemburg, and Finland are grouped together, Türkiye, Sweden, Poland, Slovakia, Belgium, Italy, Hungary, Slovenia, Austria, Czechia, France, Croatia, Bulgaria, and Germany are assigned together. Norway has not acted in concert with any country. More details are given in the next chapter.
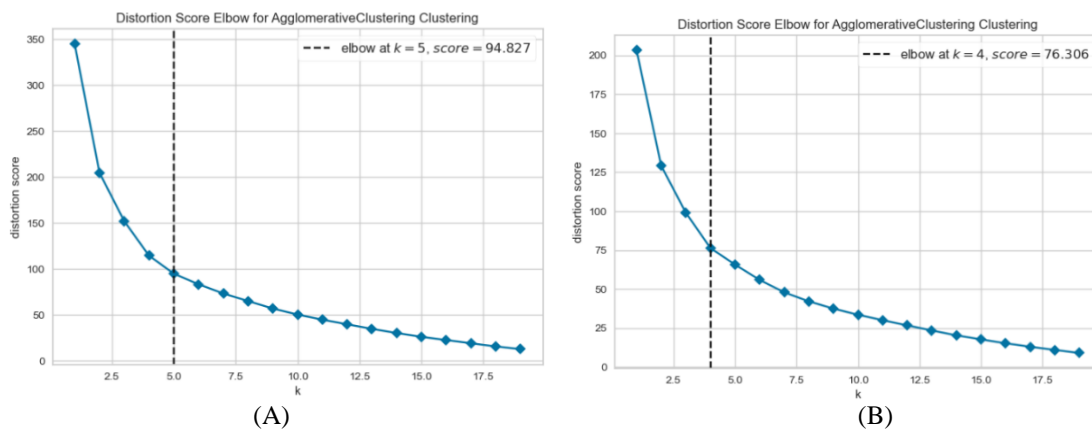

(A)   (B)

Figure 2. Application of Elbow Method for Number of Segment = 12 Alphabet Size = 6 and 8

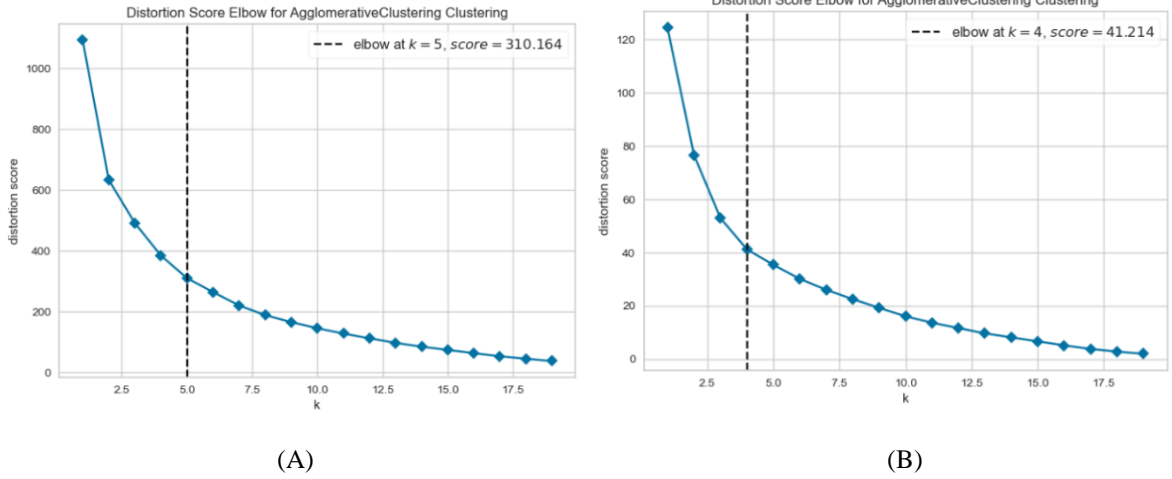(A)   (B)

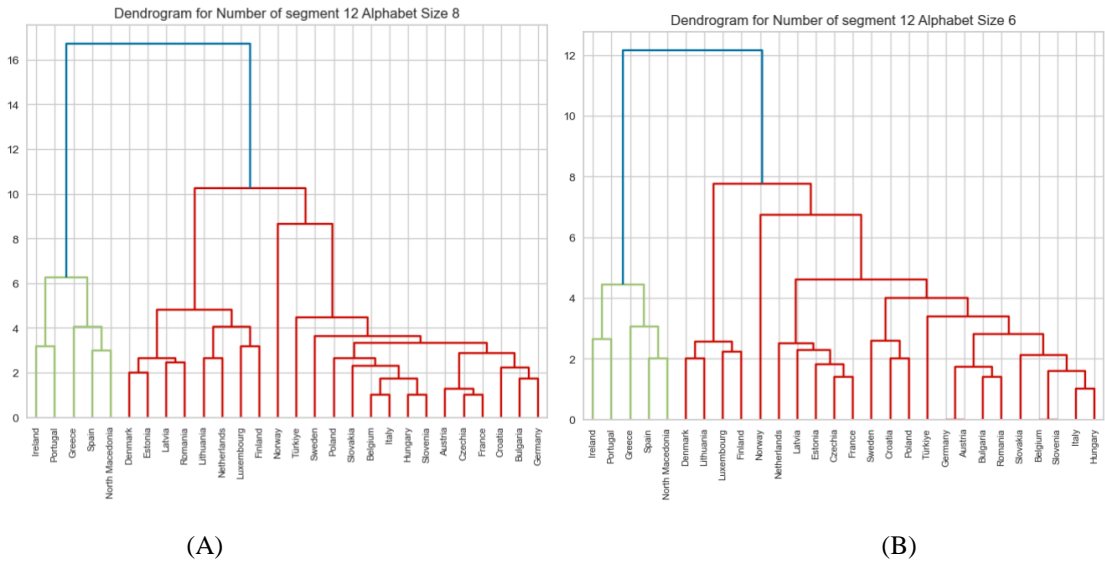**Figure 3.** Application of Elbow Method for Number of Segment = 27 and 9 Alphabet Size = 8 and 6

(A)   (B)

Figure 4. Dendrograms for Number of Segment = 12 Alphabet Size = 8 and 6

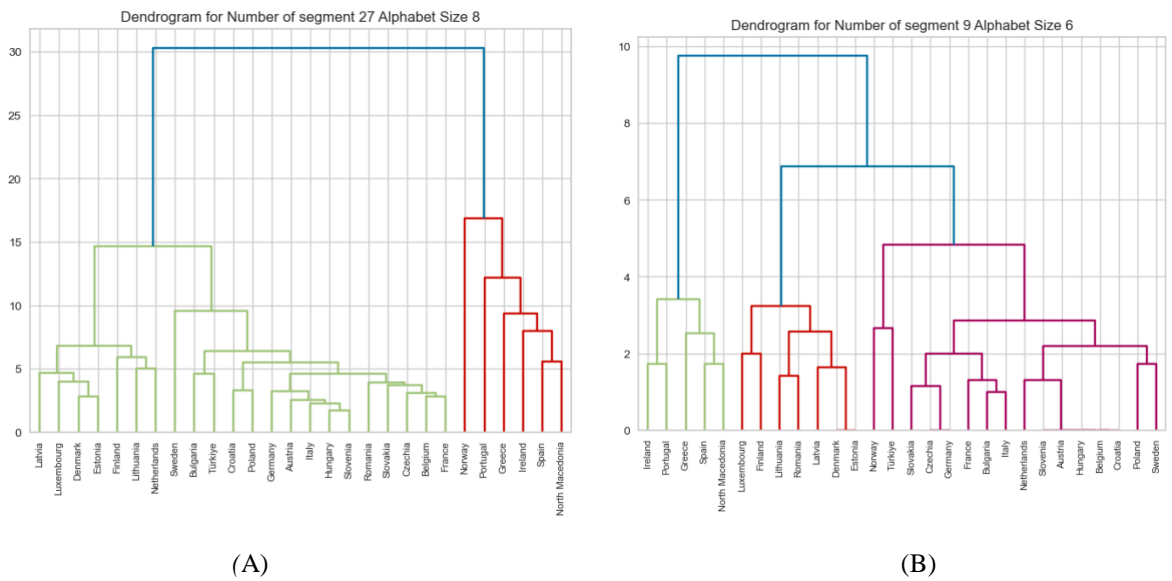*(*A)   (B)

Figure 5. Dendrograms for Number of Segment = 27 and 9 & Alphabet Size = 8 and 6

Table 2. Country Clustering in Natural Gas Consumption: Applying the Elbow Method to Segment & Alphabet Analysis

Cluster	Number of Segment = 12 Alphabet Size =8	Number of Segment = 12 Alphabet Size = 6	Number of Segment = 27 Alphabet Size = 8	Number of Segment = 9 Alphabet Size =6
1	Ireland, Portugal	Ireland, Portugal, Greece, Spain, N. Macedonia	Greece, Ireland, Spain, N. Macedonia, Portugal	Sweden, Poland, Croatia, Belgium, Hungary, Austria, Slovenia, Netherlands, Italy, Bulgaria, France, Germany, Czechia, Slovakia
2	Greece Spain, N. Macedonia	Denmark, Lithuania, Luxemburg, Finland	Portugal	Türkiye, Norway
3	Denmark, Estonia, Latvia, Romania, Lithuania, Netherlands, Luxemburg, Finland	Norway	Norway	Estonia, Denmark, Latvia, Romania, Lithuania, Finland, Luxemburg,
4	Norway	Netherlands, Latvia, Estonia, Czechia, France, Sweden, Croatia, Poland, Türkiye, Germany, Austria, Bulgaria, Romania, Slovakia, Belgium, Slovenia, Italy, Hungary	France, Belgium, Czechia, Slovakia, Romania, Slovenia, Hungary, Italy, Austria, Germany, Poland, Croatia, Türkiye, Bulgaria, Sweden	N. Macedonia, Spain, Greece, Portugal, Ireland
5	Türkiye, Sweden, Poland, Slovakia, Belgium, Italy, Hungary, Slovenia, Austria, Czechia, France, Croatia, Bulgaria, Germany	-	Netherlands, Lithuania, Finland, Estonia, Denmark, Luxemburg, Latvia	-

4. Conclusion and Suggestions

Natural gas could be an essential resource for countries around the world. As countries' policies regarding carbon footprint increase, natural gas usage may also increase. In this study, "Symbolic Aggregate Approximation" method is used for made to cluster the natural gas consumption trends of 28 countries. The tests are made on 4 different SAX combinations and countries are tried to be clustered according to the results of the "Elbow method". When the results are analyzed, the consumption trends of the countries might be in 4 groups. Norway can be considered as cluster 1. This country tends to act alone in different tests. The reason for this may be that it has a significantly different natural gas consumption pattern than other countries. The fact that Norway ranks 2nd in Europe [10] in natural gas production and uses these resources efficiently may be another

indicator that affects this. The second cluster can be considered as Southern European countries and these can be considered as the "Portugal, Greece, Spain, N. Macedonia" cluster. Warm climatic conditions can reduce natural gas consumption, especially in countries such as Spain and Greece. The impact of the tourism sector may be significant in these countries. Economic growth and energy efficiency policies can influence consumption trends. Furthermore, the reason why countries such as "Ireland" and "Portugal" act together in some tests may be that both countries have small populations, and their energy demands are generally lower. The 3rd cluster can be considered as the cluster of Northern European countries such as Denmark, Estonia, Latvia, Romania, Lithuania, Netherlands, Luxemburg, Finland. Northern European countries may have cold climates, so heating needs may be higher. Economic growth and industrial activities can also affect natural gas

demands. The last group can be Türkiye, Sweden, Poland, Slovakia, Belgium, Italy, Hungary, Slovenia, Austria, Czechia, France, Croatia, Bulgaria, Germany. The countries that make up this cluster generally have large economies and diverse climatic conditions. The level of industrialization, economic growth and population density can affect natural gas demands. Factors such as energy policies, energy security and foreign dependency may also shape this cluster. Given the fact that energy is produced with scarce resources, especially non-renewable ones, accurate forecasting allows planning for the required amount of energy production.

For the future research papers, this study also shows that the SAX method can be applied for different data sets. A comparative study can also be carried out with different forecasting time series methods.

Contributions of the authors

Each author contributed equally to the article.

Conflict of Interest Statement

There is no conflict of interest between the authors.

Statement of Research and Publication Ethics

The study has complied with research and publication ethic

References

[1]   T. S. Adebayo, M. T. Kartal, and S. Ullah, "Role of hydroelectricity and natural gas consumption on environmental sustainability in the United States: Evidence from novel time-frequency approaches," *Journal of Environmental Management*, vol. 328, no. 116987, p.116987, 2023.

[2]   M. O. Turan, T. Flamand, "Optimizing investment and transportation decisions for the European natural gas supply chain," *Applied Energy*, vol. 337, p. 120859, 2023.

[3]   S. Yildiz, "Doğal Gaz Tüketim Tahmini," *Sosyal Ve Beşeri Bilimler Dergisi*, vol. 5, no. 1, 440-452, 2013.

[4]   M. S. Shaari, T. B. Majekodunmi, N. F. Zainal, N. H. Harun, A. R Ridzuan, "The linkage between natural gas consumption and industrial output: New evidence based on time series analysis," *Energy*, vol. 284, no. 1, p. 129395, 2023.

[5]   B. Soldo, "Forecasting natural gas consumption," *Applied Energy*, vol. 92, pp. 26–37, 2012.

[6]   O. Kaynar, S. Taştan, F. Demirkoparan, "Yapay sinir ağlari ile doğalgaz tüketim tahmini," *Atatürk Üniversitesi İktisadi ve İdari Bilimler Dergisi*, vol. 25, pp. 463-474, 2012.

[7]   O. Çoban, C. C. Özcan, "Sektörel Açidan Enerjinin Artan Önemi: Konya İli İçin Bir Doğalgaz Talep Tahmini Denemesi," *Sosyal Ekonomik Araştırmalar Dergisi*, vol. 11, no. 22, pp. 85-106, 2011.

[8]   K. Oruç, K., &Ş. Çelik, "Isparta İli İçin Doğal Gaz Talep Tahmini," *Süleyman Demirel Üniversitesi İktisadi ve İdari Bilimler Fakültesi Dergisi*, vol. 22, no. 1, pp.31-42, 2017

[9]   Y. Hou, Q. Wang, & T. Tan, "A robust stacking model for predicting oil and natural gas consumption in China. Energy Sources," *Part B: Economics, Planning, and Policy*, vol. 19, no. 1, 2024.

[10]   EUROSTAT. (2023). DATABASE. Europa.eu. URL: https://ec.europa.eu/eurostat/ databrowser /view/nr g_cb_gasm/default/table?lang=en

[11]   D. H. Yang, & Y. S. Kang, "Distance- and Momentum-Based Symbolic Aggregate Approximation for Highly Imbalanced Classification," *Sensors,* vol. 22, no.14, pp. 5095–5095, 2022.

[12]   J. Lin, E. Keogh, S. Lonardi, & B. Chiu, "A symbolic representation of time series, with implications for streaming algorithms," *in Proceedings of the 8th ACM SIGMOD Workshop on Research Issues in Data Mining and Knowledge Discovery - DMKD '03*, 2003

[13]   Lin, J., Keogh, E., Wei, L., & Lonardi, S. "Experiencing SAX: a novel symbolic representation of time series," *Data Mining and Knowledge Discovery*, vol. 15, no. 2, pp.107–144, 2007.

[14]   A. Roques, & A. Zhao, "Association Rules Discovery of Deviant Events in Multivariate Time Series: An Analysis and Implementation of the SAX-ARM Algorithm," *Image Processing on Line*, 12, pp. 604–624, 2022

[15]   J. W Earnest, "Sum of Gaussian Feature-Based Symbolic Representations of Eddy Current Defect Signatures," *Research in Nondestructive Evaluation*, vol. 34, no. 3-4, pp. 136–153, 2023.

Classification of Blood Cells with Convolutional Neural Network Model

Emrah ASLAN[1*], Yıldırım ÖZÜPAK[2]

[1] Dicle University, Silvan Vocational School, Department of Computer Programming, Diyarbakır, Türkiye
[2] Dicle University, Silvan Vocational School, Department of Electricity, Diyarbakır, Türkiye
 (ORCID: 0000-0002-0181-3658) (ORCID: 0000-0001-8461-8702)

Abstract

White Blood Cells are the primary blood cells that come from the bone marrow and are essential for constructing our body's defense system. Leukopenia is a disorder where the body's capacity to fight off infections is compromised due to a low white blood cell count. White blood cell counting is a specialty procedure that is usually carried out by experts and radiologists. Thanks to recent advances, image processing techniques are frequently used in biological systems to identify a wide spectrum of illnesses. In this work, image processing techniques were applied to enhance the white blood cell deep learning models' classification accuracy. To expedite the classification process, Convolutional Neural Network models were combined with Ridge feature selection and Maximal Information Coefficient techniques. These tactics successfully determined the most important characteristics. The selected feature set was then applied to the classification procedure. ResNet-50, VGG19, and our suggested model were used as feature extractors in this study. The categorizing of white blood cells was completed with an amazing 98.27% success rate. Results from the experiments demonstrated a considerable improvement in classification accuracy using the proposed Convolutional Neural Network model.

1. Introduction

White Blood Cells (WBCs) are essential components within the circulatory system of humans [1], playing a crucial role in immune defense against bacteria, viruses, and microbes [2]. WBCs counts in people usually fall between 4000 and 10,000. These counts can act as markers for different diseases or show signs of abnormalities such as persistent infections, sudden weight loss, weakness, and exhaustion. In these situations, early diagnosis becomes crucial [3]. WBCs are classified as Eosinophil, Lymphocyte, Monocyte, and Neutrophil in microscopic pictures for expert evaluation, as shown in Figure 1. This is a common way of clinical diagnosis. WBCs types can be identified with the use of microscopic imaging, albeit the process is highly dependent on the skill of the experts. This work highlights the critical relevance of feature selection in the quick and precise identification of WBCs types utilizing a suggested method with microscopic pictures. Feature selection techniques support an intersection approach in sets, which optimizes sets generated by deep learning models.

The accurate and rapid classification of WBCs is pivotal in disease diagnosis and management, and the use of **Convolutional Neural Networks** (CNNs) based methods is recommended. While CNNs offer high accuracy, enhancing success involves developing deep features at various levels of CNN architecture. Therefore, combining feature selection methods can boost accuracy by providing more distinguishing features in a lower-dimensional space. This article introduces and evaluates such a combination, with specific goals such as assessing feature selection combinations, comparing them with simple feature combinations, and predicting the number of selected best features.

CNN models that have already been trained are now widely used as an effective method for differentiating distinct WBC kinds. CNNs were trained to perform this new task using transfer learning techniques. Fully automated systems were utilized in this manner. In this work, we concentrate on deep characteristics that are taken from various CNN architecture layers. A variety of feature selection techniques were used to extract the most pertinent information from two distinct pre-trained CNN models. We used pre-trained ResNet-50 and VGG19 models for transfer learning. The outcome is a totally automatic, reliable, and very accurate model for WBC classification.

The organization of the paper is as follows: Section 2 presents a literature review on WBCs studies, Section 3 introduces the data set and methods, Section 4 reports the experimental results and Section 5 concludes.

2. Literature Review

This section provides a summary of the literature on MDG classification, taking into account the dataset, methods and performance measures. There are many approaches to classify the WBC type in the literature. The most popular of these approaches are Machine Learning (ML), Fuzzy Logic, or a combination of all of them. Singh et al. proposed a CNN model for MDD classification [21]. We provide a thorough overview of the literature on WBCs categorization in this part, taking into account various datasets, approaches, and performance indicators. Using deep learning models, segmentation, pattern identification, form recognition, picture rotation methods, and feature extraction, Abbas et al. classified white blood cells data into three primary groups and seven sub-classes. Geometric Active Contours (GACs), level set approaches, edge and boundary detection, and thresholding techniques were all used in the segmentation process [4-5]. Zhao et al. demonstrated an automated recognition and classification method using microscopic images that determines the types of white blood cells by utilizing the correlation between RGB and intermediate colors. Granularity features, specifically binary rotation-invariant local binary patterns, were utilized with the Support Vector Machines (SVMs) classifier for certain WBCs types, while the CNN model and Random Forest (RF) were employed for others, resulting in a classification accuracy of 92.6% [6-7]. Habibzadeh et al.'s classification of white blood cells data consisted of three steps: preprocessing computations, a classification technique, and white blood cell identification utilizing hierarchical topological property subtraction using Inception and ResNet

architectures. Kurniadi et al. employed k-Nearest Neighbors (kNN) and XGBoost for classification, and the VGG16 model in conjunction with Local Binary Pattern (LBP) for property subtraction. 92.93% of reclassifications using test data and 90.16% of reclassifications utilizing data augmentation were successful [8–12].

Ma et al. created a classifier by combining ResNet and DC-GAN to increase the accuracy [22]. The CNN model was trained using two hundred iterations. In a study applying CNN to classify white blood cells, Şengür et al. proposed a BCC classification approach in which the "First Region of Interest" (ROI) is extracted from blood cell images in HSV space and then feature extraction is performed using ResNet50 [23]. In this study, feature extraction was performed using the Principal Component Analysis (PCA) method and classification was performed using the UKSB classifier. With this approach, an accuracy of 85.7% was achieved. Using the same dataset, Patil et al. used the Canonical Correlation Analysis (CCA) method to improve the accuracy [24, 25]. In this study, CNN models were combined to enrich the understanding of image content. Çınar et al., in a study, proposed a DL-based Hybrid CNN model for the classification of WBCs. The proposed model is based on pre-trained Alexnet and Googlenet architectures. The feature vector in the final pooling layer of both CNN architectures is combined and the resulting feature vector is classified by a Support Vector Machine [26]. In addition, Girdhar et al. proposed a CNN approach that is said to be able to classify the BKH type with much fewer iterations than other approaches [27]. Yu et al. used ResNet50, Inception V3, VGG16, VGG19, Xception software for MDD classification in their study and stated that the highest value with an accuracy rate of 88.5% among other classification methods was obtained with the CNN method [28]. Macawile et al. used the CNN techniques GoogleNet, Alexnet and ResNet-101 for MDD classification and obtained an average accuracy of 96.63% [29]. Zhao et al. presented an automatic detection and classification method for MDR data [30]. In the study, microscope images were examined and WBC types were identified by linking red, green, blue (RGB) and their intermediate colors. CNN model was used to generate features and the classification accuracy was limited to 92.6%. Razzak et al. performed segmentation and classification using the MDD dataset and used the Extreme Machine Learning (EML) method [30] in combination with CNN in the classification step [31]. The segmented cell images are masked before the feature extraction phase. Features were then extracted from each segmented cell and classification was performed with a 95.1% success rate. Hegde et al.

used both traditional image classification and CNN in their study and compared the results of these two approaches [32]. Although the results obtained were similar, it was stated that the traditional method relies heavily on segmentation and feature extraction, while CNN does not depend on these parameters. However, it was also mentioned that the CNN approach requires a large amount of labeled data and traditional image processing does not have such requirements. Considering the related studies, pre-trained CNN models have been shown to be a useful tool for differentiating different types of WBCs.

While some studies relied on handcrafted features, which can be labor-intensive, CNN-based approaches leveraged pretrained models for distinguishing WBCs types. Transfer learning techniques adapted CNNs to new tasks, resulting in fully automatic systems. However, this study emphasizes the extraction of deep features from various CNN architecture levels. The most pertinent characteristics were obtained from three pretrained CNN models, which were chosen using a variety of feature selection techniques.

3. Material and Method

3.1. WBCs Dataset

This work made use of a dataset that was freely accessible and was separated into four different categories: neutrophil, lymphocyte, monocyte, and eosinophil. The dataset is available as open access on kaggle (https://www.kaggle.com/datasets/paultimothymoon ey/blood-cells) [20]. The images in the dataset have been labelled by the experts who created the dataset. For a total of 12,435 photos, the WBCs dataset includes 3,120 images of neutrophils, 3,102 images of lymphocytes, 3,091 images of monocytes, and 3,120 images of eosinophils. Every image is saved in JPEG format, with 320×240 pixels of resolution and 24 bits of depth. All samples in the dataset underwent examination and labeling by experienced experts. To ensure efficiency in the study, an equal number of data samples, totaling 12,364 images, were maintained for each class, with 3,091 images from each category. In cases where a class had more than 3,091 images, image election was performed randomly. Additionally, the dataset was divided into training and test sets, with proportions of 70% for training and 30% for testing. This division aimed to facilitate the estimation of the proposed approach's performance on unseen data.
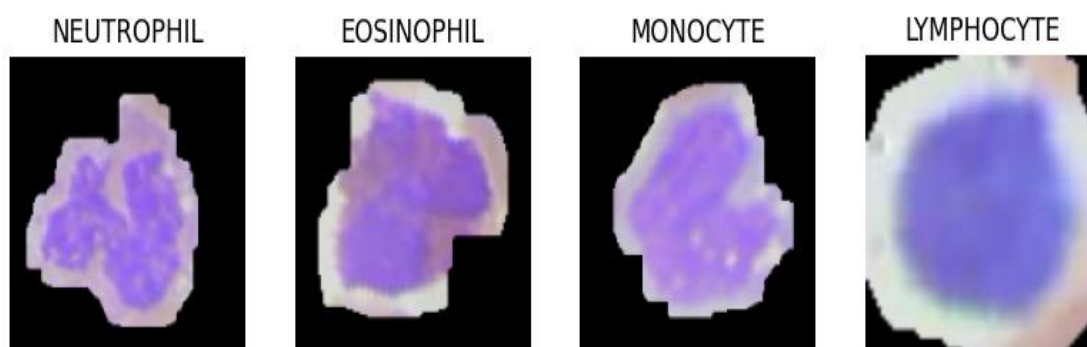

Figure 1. White Blood Cells Types [20]

3.2. Convolutional Neural Network Models

Convolutional Neural Networks (CNNs) stand out as powerful deep learning models, particularly successful in domains like image recognition. They are a specialized type of artificial neural network designed for feature identification and learning within data. What distinguishes CNNs from traditional neural networks is the inclusion of convolutional layers, which diminish the sensitivity of features to alterations like scale, translation, and rotation. Figure 2 illustrates the CNN model.

Key components of CNNs include:

- Convolutional Layers: These layers execute convolution operations on input data using filters (kernels), extracting feature maps.

- Pooling Layers: Utilized to shrink the size of feature maps while retaining salient features. Max pooling is a common method of choice.
- Fully Connected Layers: Responsible for generating the CNN's output, often applied in tasks such as classification or regression.

CNNs find extensive application, especially in realms like image recognition, object detection, and facial recognition. Notably, pre-trained networks can be

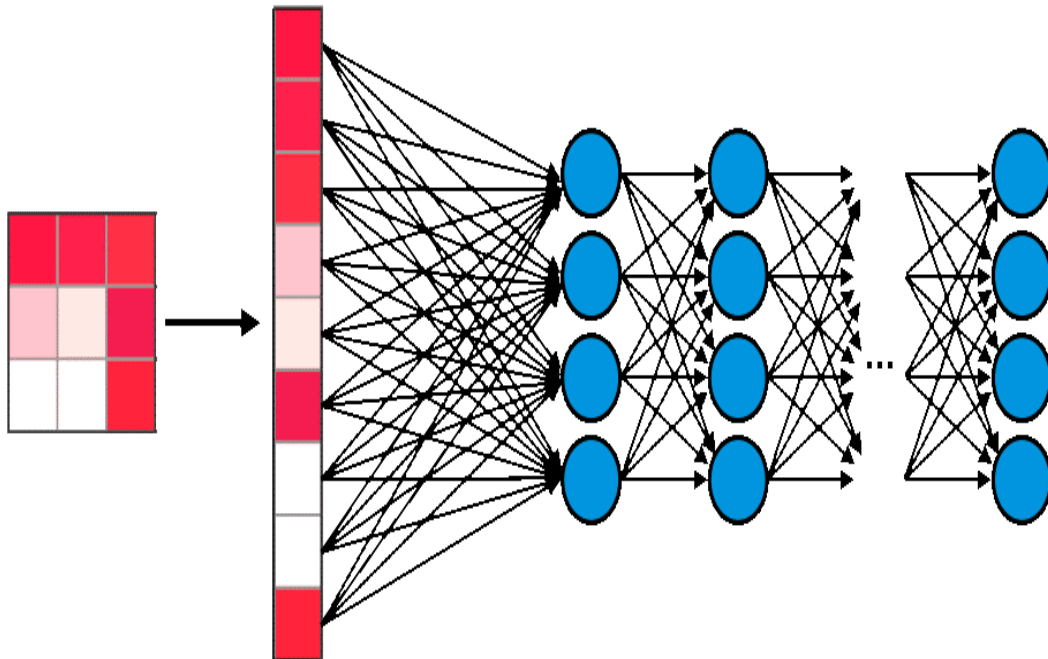repurposed effectively in various tasks through transfer learning.

Figure 2. CNNs model.

3.3. VGG19

VGG19, a CNN improved by the Visual Geometry Group (VGG) at the University of Oxford, holds a prominent place in the realm of CNNs. As part of the VGG family, it has demonstrated significant success in various applications. VGG19, specifically, is a deep CNN composed of a total of 19 layers, featuring a distinctive architecture with key characteristics:
- Layer Structure: VGG19 comprises 16 convolutional layers and 3 fully connected layers, summing up to a total of 19 layers.
- Convolution and Pooling: Between convolutional layers, 3x3-sized filters and sequential max pooling are employed. This design enhances the network's depth and augments its capability for feature extraction.

- Fully Connected Layers: Post the convolutional layers, fully connected layers are used for the classification process, making VGG19 well-suited for classification tasks.
- Activation Functions: VGG19 typically utilizes ReLU (Rectified Linear Unit) activation functions, contributing to its overall performance.
- Total Number of Parameters: VGG19 is characterized by a large model size, indicated by a high total number of parameters. This underscores the necessity for training on substantial datasets.
VGG19 has earned recognition for its exceptional performance on the ImageNet dataset and has

excelled in the ImageNet Large Scale Visual Recognition Challenge (ILSVRC). Furthermore, its efficacy extends to transfer learning applications, where pre-trained networks can be leveraged for diverse tasks.

3.4. ResNet-50

Microsoft Research created the deep learning model ResNet-50. ResNet presents "residual learning" as a way to make deep neural network training easier. This model is designed to address challenges encountered when training large and deep neural networks. Key features of ResNet-50 include:

- Residual Blocks: ResNet incorporates residual blocks, which differ from traditional CNNs. These blocks enable "residual" learning by adding the unit's output to its input, facilitating training and reducing the issue of gradient vanishing.
- First Layer: ResNet-50 includes a convolutional layer to reduce the dimension of input data.
- Layer Structure: ResNet-50 consists of a total of 50 layers, including convolutional layers, residual blocks, and fully connected layers.
- Global Average Pooling: ResNet models often use global average pooling to reduce the feature map's size from the last convolutional layer. This can help the network learn more general and scalable features.
- Activation Functions: ReLU activation functions are commonly used.

- Total Number of Parameters: ResNet-50 is a large model with millions of parameters.
ResNet-50 has achieved significant success in the ImageNet dataset's ImageNet Large Scale Visual Recognition Challenge (ILSVRC). It is commonly used in transfer learning applications, allowing the utilization of a pre-trained network for various tasks. ResNet-50 has a deep network structure with the incorporation of residual connections, effectively addressing the challenges of backpropagation in deep architectures.

3.5. Classifier using Quadratic Discriminant Analysis

Due to its ability to complete both jobs simultaneously, Linear Discriminant Analysis (LDA) is a popular option. Discriminant analysis is important for both classification and dimensionality reduction. On the other hand, Quadratic Discriminant Analysis (QDA) offers the advantage of nonlinear data analysis. By optimizing the shared probability value across classes, QDA is a machine learning technique that generates a unique covariance matrix for every class. However, it does not serve as a dimensionality reduction technique. Equations play a pivotal role in the classification process of QDA [13]. 'k' stands for a class in these calculations, while $\sum$ k indicates the total number of classes. πk modifies the prevalence ratio of observations unique to each class 'k'. The equations use the observation 'x,' and QDA is used to determine the probability that 'x' is a member of class 'k'. Equation (1) is used to calculate new points using QDA using either the discriminant function or the number of posterior probabilities (δx). The top portion of the matrix and the covariance matrix diagonal are taken into account since each class's covariance matrix is computed separately via QDA. Where μk denotes a class-specific mean vector. 'p' is the input parameter for the p class prediction, and the number of QDA parameters is quadratic in p [14]. Together, these formulas strengthen QDA's ability to handle intricate data structures and perform accurate categorization.

In this study, the reason for using the QDA classifier is that it yields more successful results compared to other classifiers.

$$\delta_x = -\frac{1}{2}\log\left|\sum_k k\right| - \frac{1}{2}(x-\mu_k)^T \sum_k{}^{-1}(x-\mu_k) + \log\pi_k \tag{1}$$

3.6. Feature Selection Method

Methods for choosing features are essential in the field of machine learning because they help create a subset of more distinguishing characteristics while lowering processing costs and improving classification accuracy. These techniques are essentially made to reduce the number of dimensions in the data, which enhances the functionality of machine learning models. Using a feature selection strategy yields a new set of features, F', and a lower dimensionality, S', if the property extracted from the dataset are represented as F and the dimensionality is indicated as S, for example. The main goal is to have F' < F and S' < S. As a result, property election is frequently used to improve machine learning algorithms' efficacy and simplify data.

The Maximum Information Coefficient (MIC) is the first. MIC looks for correlations between different variables in big datasets. A statistical metric used to assess the relationship between two variables is called mutual information. It assesses the probability of two variables occurring together, considering both linear and nonlinear relationships. The method selects variables with the maximum information content. The variables in Equation (2) are indicated by the parameters X and Y. In order to minimize any irregularities (entropy) between variables, normalization is carried out by dividing by the largest value within that set if the paired variables in the dataset disagree, as shown in Equation (3). These steps collectively contribute to the effectiveness of the MIC method in selecting informative features for improved machine learning outcomes.

$$H(X_b) = H(Y_b) = H(X_b, Y_b) \tag{2}$$

$$I(X;Y) = H(X) + H(Y) - H(X,Y) \tag{3}$$

A statistical technique for examining data based on multivariate cause-and-effect relationships is ridge regression. This method is advised as it can yield variance rates that are lower than those obtained by the Least Squares Approach. Ridge regression masks any problems by decreasing the size of the regression coordinates. That's the reason it works so well. Equation (4) contains the ridge regression formula. The constant variable "z" in this equation has values ranging from 0 to 1. Equation (4) uses the parameter 'I', the unit matrix, to represent the identity matrix. Furthermore, each feature in the dataset has plane coordinates that correlate to the

parameter's "X" and "Y". Ridge regression is particularly useful in scenarios where the least squares method may encounter issues such as multicollinearity, providing a more robust approach to regression analysis.

$$\text{Ridge} = (XX^I + zI)^{-1}X^IY \qquad (4)$$

Where, represents the Ridge regression coefficient vector, 'X' is the matrix of input features, 'Y' is the output vector, 'I' is the identity matrix, and 'z' is the regularization parameter. The use of Ridge regression is especially advantageous when dealing with datasets that exhibit multicollinearity, enhancing the stability and performance of the regression analysis. The objective was to compare these two strategies' efficacy with three other feature selection methods, namely F Regression, Recursive Feature Elimination (RFE), and Linear Regression. The objective was to determine which two of these five feature selection techniques performed the best. The BKH dataset was subjected to experimental investigations, which demonstrated that the MIC and Ridge Regression techniques performed better than the other feature selection algorithms. The reference section contains the source code for various feature selection techniques. Efficient features were extracted by applying separate applications of MIC and Ridge Regression to the merged feature sets. This strategy leveraged the agreement between the best-performing MIC and Ridge Regression techniques to improve the robustness and dependability of the chosen features.

4. Proposed Method

The proposed method comprises three main steps, as outlined below:

1. Feature Extraction using CNN Models:

- In the initial step, CNN models VGG19 and ResNet-50 are employed as property extractors.

- Features obtained from the layers of CNN models are combined, creating a comprehensive feature set.

2. Ridge Regression and MIC-Based Feature Selection:
The use of feature selection techniques, particularly Ridge Regression and MIC, is done in the second stage. The most illuminating aspects from the combined feature set are chosen and kept using these techniques.
3. Combination of Classification and Feature Selection Techniques: - A variety of feature selection techniques are used in the third phase.
- This combined feature set uses the intersecting features that were chosen using the Ridge Regression and MIC techniques.
- The selected features are then classified using the QDA.
The overall design and flow of the proposed approach are visualized in Figure 3, illustrating how the CNN models, feature selection methods, and classification steps are intricately connected to achieve an effective and robust solution. We trained VGG19 and ResNet-50 with transfer learning and combined the results with our proposed model. Table 1 shows the hyperparameters of the VGG19 and ResNet-50 models. ReLU was used as the activation function and Adam as the optimiser in the models.

Table 1. VGG19 and ResNet-50 model hyperparameters

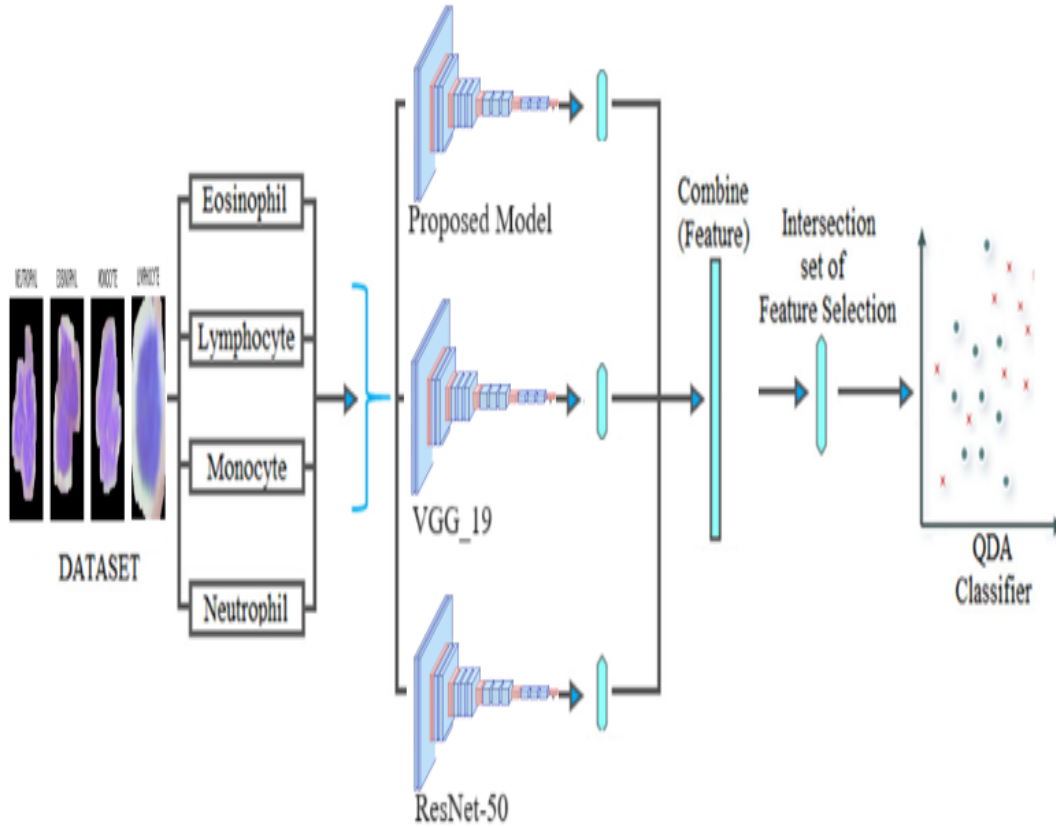| Hyperparameters	Value
Activation	ReLU
Optimizer	Adam
Loss	categorical_crossentropy
Pooling	max
Learning_Rate	0,01
Epochs	50
Batch_Size	32
Dropout	0,2

Figure 3. Model design of the proposed model

The images used to validate the proposed approach were obtained from an openly accessible dataset. The dataset was randomly divided for training, with 80% of the data used for training and 20% for test samples from each class. Additionally, the training dataset (randomly selected) was further divided into 90% for training and 10% for training validation purposes. Randomly selected cell samples from the dataset are provided in Figure 4.

The proposed approach unfolds in three key stages: data preprocessing, feature extraction, and classification. These stages are visually depicted in Table 2. For a more detailed overview and understanding of the proposed approach, the block diagram is provided in Figure 5. This diagram illustrates the interconnected flow of processes, emphasizing the progression from data preprocessing through feature extraction to the final classification step. The block diagram serves as a comprehensive visual representation of the methodology, aiding in the comprehension of the overall approach and its sequential execution of essential tasks.
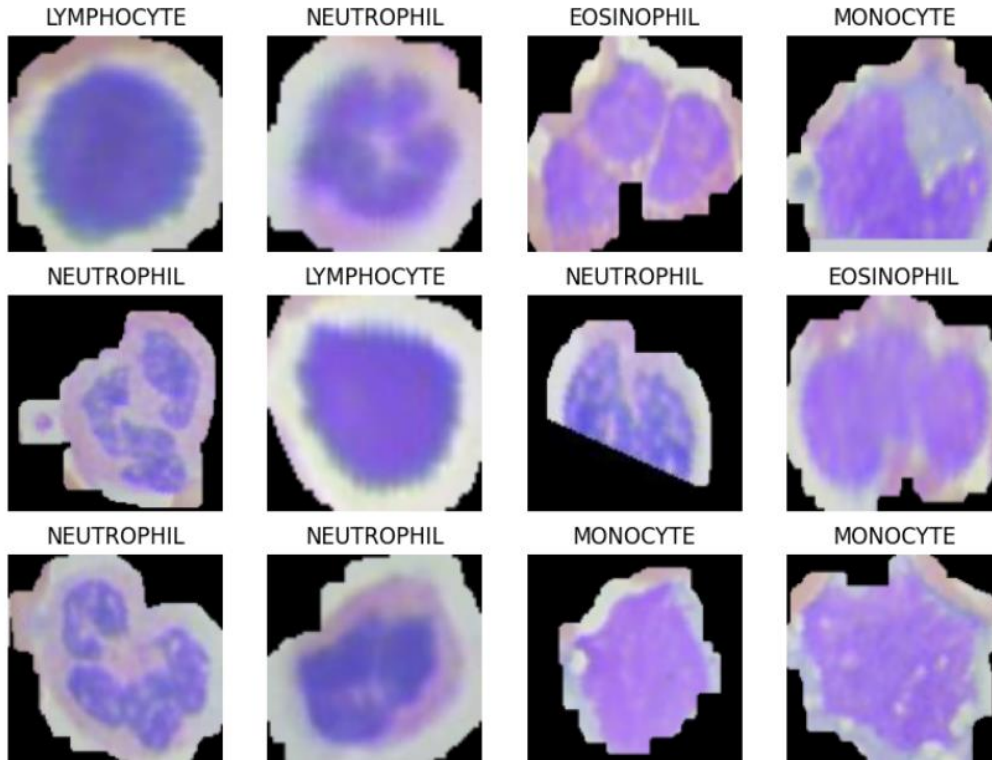
Figure 4. Dataset [20]

Table 2. Details of the proposed method

Layer	Output Shape	Parameter
Conv2d (Conv2D)	(None, 118, 118, 64)	1792
Max_pooling2d (Maxpooling2D)	(None, 59, 59, 64)	0
Dropout (Dropout)	(None, 59, 59, 64)	0
Conv2d_1 (Conv2D)	(None, 57, 57, 128)	73856
Max_pooling2d_1 (Maxpooling2D)	(None, 28, 28, 128)	0
Dropout_1 (Dropout)	(None, 28, 28, 128)	0
Conv2d_2 (Conv2D)	(None, 26, 26, 256)	295168
Max_pooling2d_2 (Maxpooling2D)	(None, 13, 13, 256)	0
Dropout_2 (Dropout)	(None, 13, 13, 256)	0
Flatten (Flatten)	(None, 43264)	0
Dense (Dense)	(None, 1024)	44303360
Dropout_3 (Dropout)	(None, 1024)	0
Dense_1 (Dense)	(None, 4)	4100

Total parameters:	44678276 (170.43 MB)
Trainable parameters:	44678276 (170.43 MB)
Non-trainable parameters:	None

conv2d_input	input:	[(None, 120, 120, 3)]
InputLayer	output:	[(None, 120, 120, 3)]

conv2d	input:	(None, 120, 120, 3)
Conv2D	output:	(None, 118, 118, 64)

max_pooling2d	input:	(None, 118, 118, 64)
MaxPooling2D	output:	(None, 59, 59, 64)

dropout	input:	(None, 59, 59, 64)
Dropout	output:	(None, 59, 59, 64)

conv2d_1	input:	(None, 59, 59, 64)
Conv2D	output:	(None, 57, 57, 128)

max_pooling2d_1	input:	(None, 57, 57, 128)
MaxPooling2D	output:	(None, 28, 28, 128)

dropout_1	input:	(None, 28, 28, 128)
Dropout	output:	(None, 28, 28, 128)

conv2d_2	input:	(None, 28, 28, 128)
Conv2D	output:	(None, 26, 26, 256)

max_pooling2d_2	input:	(None, 26, 26, 256)
MaxPooling2D	output:	(None, 13, 13, 256)

dropout_2	input:	(None, 13, 13, 256)
Dropout	output:	(None, 13, 13, 256)

flatten	input:	(None, 13, 13, 256)
Flatten	output:	(None, 43264)

dense	input:	(None, 43264)
Dense	output:	(None, 1024)

dropout_3	input:	(None, 1024)
Dropout	output:	(None, 1024)

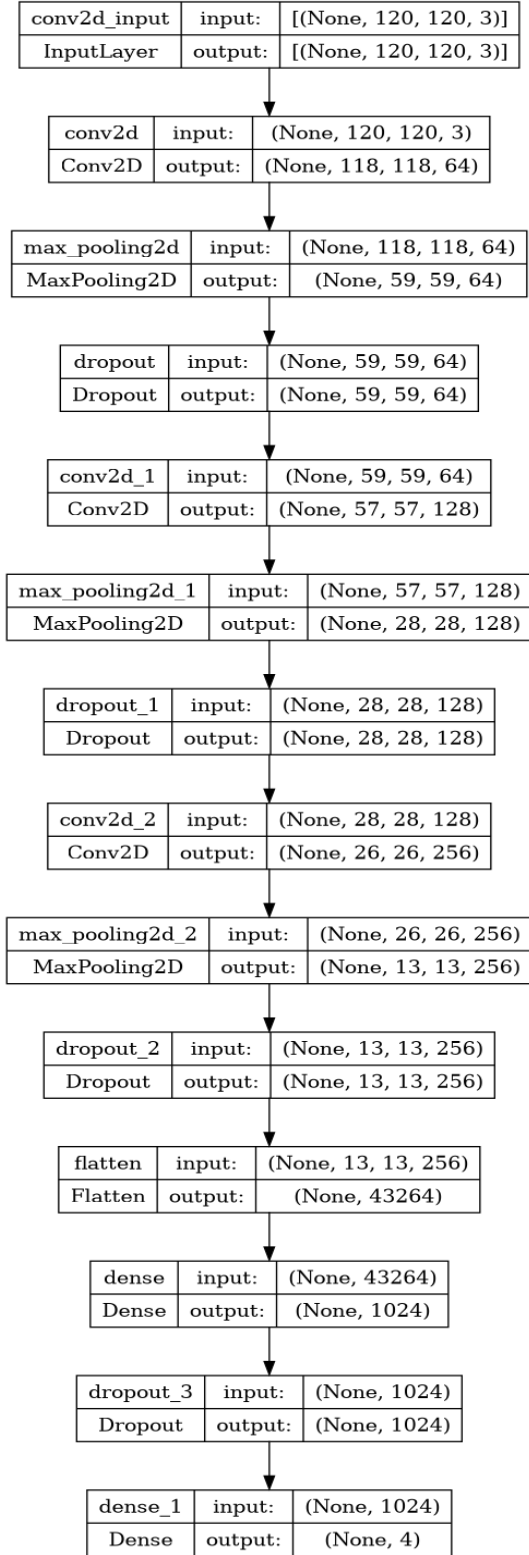| dense_1	input:	(None, 1024)
Dense	output:	(None, 4)

Figure 5. Flow diagram of the proposed method

5. Experimental Results
In this section, the outcomes derived from the materials and methods outlined in the preceding section are presented.

Important measures, such as sensitivity, specificity, F1-score, and accuracy, are used to assess the proposed model. The parameters true positive (TP), true negative (TN), false positive (FP), and false negative (FN) are the foundation of these measures.

The parameters in these equations are defined as follows:

- True Positive (TP): Instances that the model accurately classified as positive.

- True Negative (TN): Examples that the model accurately classified as negative.

- False Positive (FP): Cases that the model mistakenly classified as positive.

- False Negative (FN): Examples that the model misinterpreted as negative.

These metrics provide a comprehensive evaluation of the model's performance, considering both positive and negative classifications. The F1-score strikes a compromise between precision and recall, while sensitivity and specificity provide information about the model's capacity to properly detect positive and negative examples, respectively. The accuracy measure offers a general evaluation of how accurate the model's predictions are.

$$Accuracy = \frac{TP + TN}{(TP + TN + FP + FN)} \qquad (9)$$

$$Recall = \frac{TN}{(TP + FN)} \qquad (10)$$

$$Specificity = \frac{TN}{(TN + FP)} \qquad (11)$$

$$Precision = \frac{TP}{(TP + FP)} \qquad (12)$$

$$F_1 = 2 * \frac{Precision * Recall}{(Precision + Recall)} \qquad (13)$$

In this step, considering the classification performance metrics (sensitivity, precision, etc.), the overall accuracy rate is 98.27%. The proposed confusion matrix is presented in Figure 6, and the performance curve graph is provided in Figure 7. Additionally, intersecting features have been extracted using feature selection methods. This indicates the selection of more intersecting features. The model's ability to classify blood cells is shown in Figure 8.
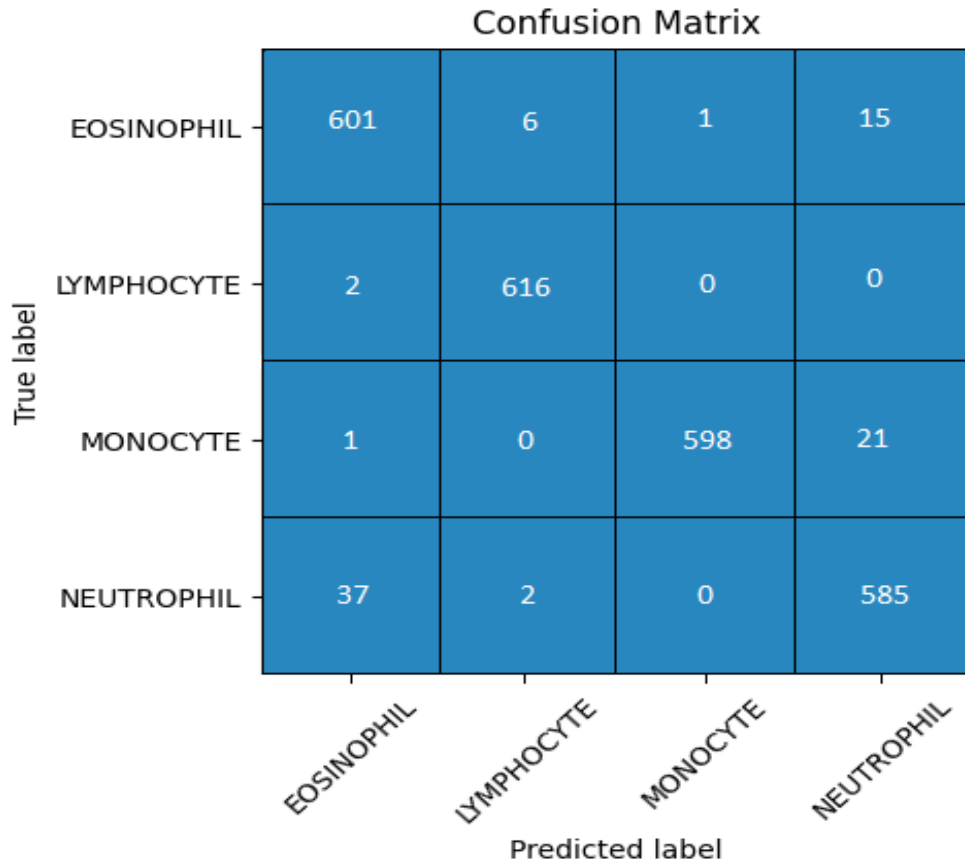
Confusion Matrix

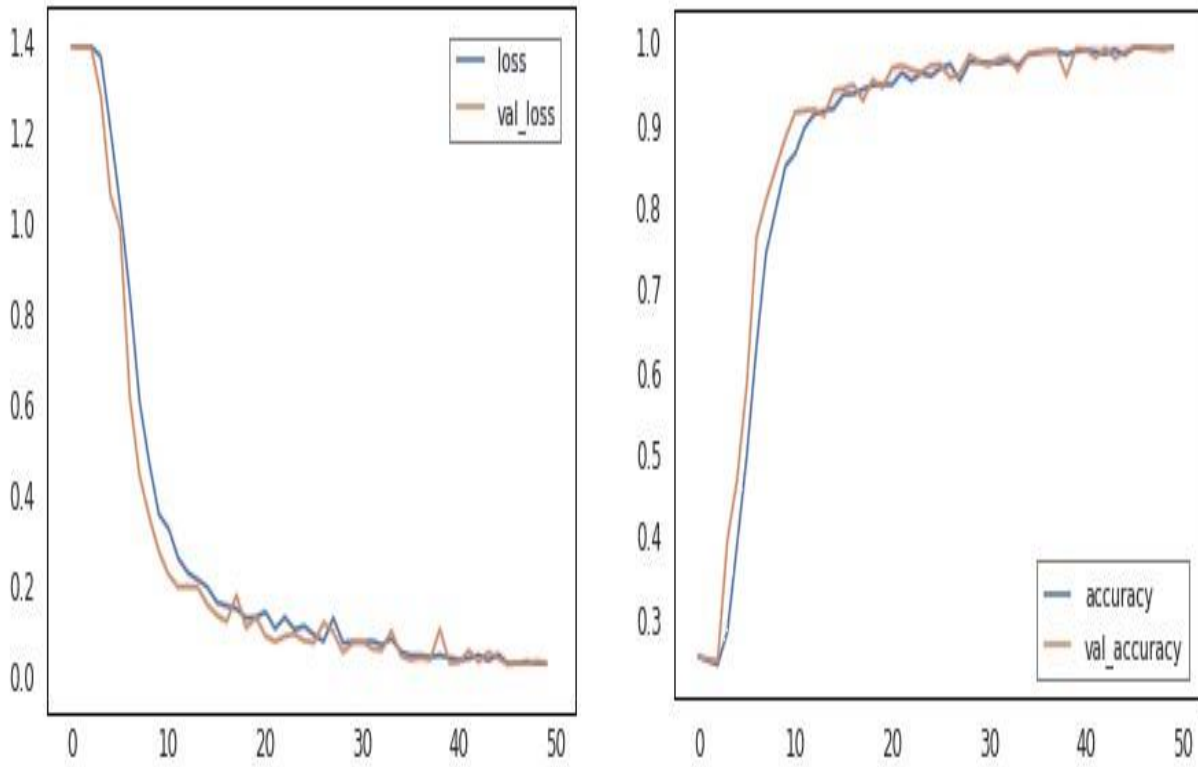**Figure 6.** Confusion matrix of the proposed model

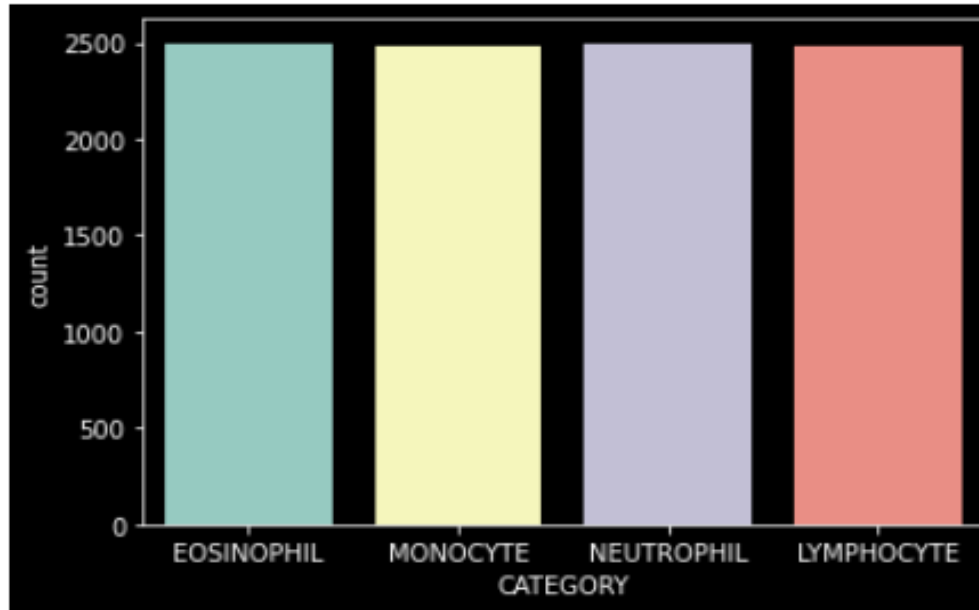**Figure 7.** Performance graph of the proposed model

Figure 8. Categorization capability of the model

According to the data presented in Table 3, our developed method can determine the features of the input image by following an adaptive learning process. This enables effective classification without being tightly dependent on cell segmentation or feature design. Traditional methods are known to often cause imbalance issues, which can hinder the classifier from accurately predicting cell abnormalities. Our method can effectively address this imbalance issue. Additionally, our model, when compared to classical neural network models like ResNet-50 and VGG-19, appears to fully utilize the spatial and temporal information of image features. In conclusion, our new method may have significant application potential in the classification of blood cell images. Overall, our study, with its proposed approach and sufficient image count in the dataset, provides reliable results, being both innovative and trustworthy.

Table 3. Comparison of the results of the model with the results in the literature.

Study	Methods	Classification Accuracy (%)
Kumar et al. [17]	Multi SVM	75.88
Sedat et al. [18]	Principal Component Analysis	95.79
Li et al. [19]	Dual-ThresholdMethod	91.20
Proposed Model	ResNet-50, VGG19, QDA	98.27

6. Conclusion

In this study evaluated the efficacy of a variety of feature selection methods for the categorization of Eosinophils, Lymphocytes, Monocytes, and Neutrophils utilizing Eosinophil-Specific Antibodies. The suggested method combines features taken from ResNet-50, VGG19's 1000-feature layers, and a specially created model. Ridge and MIC property election approaches were used to the merged feature collection. The classification results were notably improved by the intersecting features that were obtained from the MIC and Ridge approaches, indicating the additional benefit of integrating feature selection techniques. Using the Quadratic Discriminant Analysis (QDA) approach, the experimental findings demonstrated a remarkable overall accuracy rate of 98.27% for CNN classification. With 97.48% accuracy for Eosinophil, 99.58% for Lymphocyte, 99.05% for Monocyte, and 96.96% for Neutrophil, the CNN kinds' accuracy results were particular and impressive. This demonstrates the model's consistent performance in a range of cell types. Preprocessing procedures are expected to be added to the suggested technique for future research. With this evolution, the model's performance is intended to be further optimized,

which may help in the development of high-performance computer-aided systems for future medical imaging jobs. The work establishes the groundwork for future developments in automated cell categorization, especially with regard to image analysis and medical diagnostics.

Conflict of Interest Statement

There is no conflict of interest between the authors.

Statement of Research and Publication Ethics

The study is complied with research and publication ethics

References

[1] G.C. Kabat, M.Y. Kim, J.A.E. Manson, L. Lessin, J. Lin, S. Wassertheil-Smoller, T.E. Rohan, "White blood cell count and total and cause-specific mortality in the women's health initiative," *Am. J. Epidemiol.*, vol. 186, pp. 63–72, 2017. (http://dx.doi.org/10.1093/aje/kww226)

[2] A. Mbanefo and N. Kumar, "Evaluation of malaria diagnostic methods as a key for successful control and elimination programs," *Trop Med Infect Dis,* vol. 5, no. 2, p. 102, 2020.

[3] S. Nema, M. Rahi, A. Sharma, and P.K. Bharti, "Strengthening malaria microscopy using artificial intelligence-based approaches in India," *Lancet Reg Health - Southeast Asia*, vol. 5, p. 100054, 2022.

[4] World Health Organization, *Malaria microscopy quality assurance manual-version 2*, 2021.

[5] K.A.L.-D.ulaimi, I. Tomeo-Reyes, J. Banks, and V. Chandran, "Evaluation and benchmarking of level set-based three forces via geometric active contours for segmentation of white blood cell nuclei shape," *Comput. Biol. Med.*, vol. 116, p. 103568, 2020. [doi:10.1016/j.compbiomed.2019.103568](http://dx.doi.org/10.1016/j.compbiomed.2019.103568)

[6] J. Zhao, M. Zhang, Z. Zhou, J. Chu, and F. Cao, "Automatic detection and classification of leukocytes using convolutional neural networks," *Med. Biol. Eng. Comput.*, vol. 55, pp. 1287–1301, 2017. [doi:10.1007/s11517-016-1590-x](http://dx.doi.org/10.1007/s11517-016-1590-x)

[7] P. Chun, I. Ujike, K. Mishima, M. Kusumoto, and S. Okazaki, "Random forest-based evaluation technique for internal damage in reinforced concrete featuring multiple nondestructive testing results," *Constr. Build. Mater.*, vol. 253, p. 119238, 2020. [doi:10.1016/j.conbuildmat.2020.119238](http://dx.doi.org/10.1016/j.conbuildmat.2020.119238)

[8] A. Barai, M.F. Faruk, S.M. Shuvo, A.Y. Srizon, S.M. Hasan, and A. Sayeed, "A Late Fusion Deep CNN Model for the Classification of Brain Tumors from Multi-Parametric MRI Images," *in 2023 International Conference on Next-Generation Computing, IoT and Machine Learning (NCIM), Gazipur, Bangladesh*, 2023, pp:1-6. https://doi.org/10.1109/NCIM59001.2023.10212729).

[9] N. Mahajan and H. Chavan, "MRI Images Based Brain Tumor Detection Using CNN for Multiclass Classification," *in 2023 3rd Asian Conference on Innovation in Technology (ASIANCON), Ravet IN, India*, 2023, pp. 1-5.(https://doi.org/10.1109/ASIANCON58793.2023.10270492)

[10] K. Kaplan, Y. Kaya, M. Kuncan, M.R. Minaz, and H.M. Ertunç, "An improved feature extraction method using texture analysis with LBP for bearing fault diagnosis," *Appl. Soft Comput.*, vol. 87, p. 106019, 2020. [doi:10.1016/j.asoc.2019.106019](http://dx.doi.org/10.1016/j.asoc.2019.106019)

[11] R. Singh, A. Sharma, N. Sharma, and R. Gupta, "Impact of Adam, Adadelta, SGD on CNN for White Blood Cell Classification," *in 2023 5th International Conference on Smart Systems and Inventive Technology (ICSSIT), Tirunelveli, India*, 2023, pp. 1702-1709. [doi:10.1109/ICSSIT55814.2023.10061068](http://dx.doi.org/10.1109/ICSSIT55814.2023.10061068)

[12] S. Montaha, S. Azam, A. Rafid, M. Hasan, Z. Karim, and A. Islam, "TimeDistributed-CNNLSTM: A Hybrid Approach Combining CNN and LSTM to Classify Brain Tumor on 3D MRI Scans Performing Ablation Study," *IEEE Access*, vol. 10, pp. 60039-60059, 2022. [doi:10.1109/ACCESS.2022.3179577](https://doi.org/10.1109/ACCESS.2022.3179577)

[13] S. Saeedi, S. Rezayi, H. Keshavarz, and S. R Niakan Kalhori, "MRI-based brain tumor detection using convolutional deep learning methods and chosen machine learning techniques," *BMC Med Inform Decis Mak*, vol. 23, no. 1, p. 16, Jan. 23, 2023. [doi:10.1186/s12911-023-02114-6](https://doi.org/10.1186/s12911-023-02114-6)

[14] I.M. Baltruschat, H. Nickisch, M. Grass, T. Knopp, and A. Saalbach, "Comparison of deep learning approaches for multi-label chest X-ray classification," *Sci. Rep.*, vol. 9, p. 6381, 2019. [doi:10.1038/s41598-019-42294-8](http://dx.doi.org/10.1038/s41598-019-42294-8)

[15] H.P. Beck, "Digital microscopy and artificial intelligence could profoundly contribute to malaria diagnosis in elimination settings," *Front Artif Intell*, vol. 5, p. 510483, 2022.

[16] Y. Kumar, A. Koul, and S. Mahajan, "A deep learning approaches and fastai text classification to predict 25 medical diseases from medical speech utterances, transcription and intent," *Soft Comput*, vol. 26, no. 17, pp. 8253–8272, 2022.

[17] P.S. Kumar and S. Vasuki, "Automated diagnosis of acute lymphocytic leukemia and acute myeloid leukemia using multi-SV," *Journal of Biomedical Imaging and Bioengineering*, vol. 1, no. 1, pp. 20–24, 2017.

[18] S. Nazlibilek, D. Karacor, T. Ercan, M.H. Sazli, O. Kalender, and Y. Ege, "Automatic segmentation, counting, size determination and classification of white blood cells," *Measurement*, vol. 55, pp. 58–65, 2014.(https://doi.org/10.1016/j.measurement.2014.04.008)

[19] Y. Li, R. Zhu, L. Mi, Y. Cao and D. Yao, "Segmentation of White Blood Cell from Acute Lymphoblastic Leukemia Images Using Dual-Threshold Method," *Computational and Mathematical Methods in Medicine*, pp. 1–12, 2016. [doi:10.1155/2016/9514707](https://doi.org/10.1155/2016/9514707)

[20] P, Mooney., Kaggle Dataset, Blood Cell Images, 14 March 2018 [Online] Avaible: https://www.kaggle.com/datasets/paultimothymooney/blood-cells.

[21] I. Rojas, O. Valenzuela, F. Rojas, ve F. Ortuño, "Bioinformatics and Biomedical Engineering: *7th International Work-Conference. Proceedings* 2019; Part I," (11465).

[22] L. Ma, R. Shuai, X. Ran, W. Liu, ve C. Ye, "Combining DC-GAN with ResNet for blood cell image classification," *Medical & biological engineering & computing*, vol 58, no. 6, pp. 1251-1264, 2020.

[23] A. Şengür, Y. Akbulut, Ü. Budak, ve Z. Cömert, "White blood cell classification based on shape and deep features," *International Artificial Intelligence and Data Processing Symposium (IDAP)*, pp. 1-4, 2019.

[24] A. M. Patil, M. D. Patil, ve G. K. Birajdar, "White blood cells image classification using deep learning with canonical correlation analysis," *IRBM*, vol 42, no. 5, pp. 378-389, 2021.

[25] A. Çınar ve S. A. Tuncer, "Classification of lymphocytes, monocytes, eosinophils, and neutrophils on white blood cells using hybrid Alexnet-GoogleNet-SVM," *SN Applied Sciences*, vol 3, no. 4, pp. 1-11, 2021.

[26] A. Girdhar, H. Kapur, ve V. Kumar, "Classification of White blood cell using Convolution Neural Network," *Biomedical Signal Processing and Control*, vol 71, no. 103156, 2022.

[27] W. Yu, J. Chang, C. Yang, L. Zhang, H. Shen, Y. Xia, ve J. Sha, "Automatic classification of leukocytes using deep neural network," *12th international conference on ASIC (ASICON)*, pp. 1041-1044, 2017.

[28] M. J. Macawile, V. V. Quiñones, A. Ballado, J. D. Cruz, ve M. V. Caya, "White blood cell classification and counting using convolutional neural network," *3rd International conference on control and robotics engineering (ICCRE)*, pp. 259-263, 2018.

[29] J. Zhao, M. Zhang, Z. Zhou, J. Chu, ve F. Cao, "Automatic detection and classification of leukocytes using convolutional neural networks," *Medical & biological engineering & computing*, vol 55, no. 8, pp. 1287-1301, 2017.

[30] Y. Ming, E. Zhu, M. Wang, Y. Ye, X. Liu, ve J. Yin, "DMP-ELMs: Data and model parallel extreme learning machines for large-scale learning tasks," *Neurocomputing*, vol 320, pp. 85-97, 2018.

[31] M. Imran Razzak ve S. Naz, "Microscopic blood smear segmentation and classification using deep contour aware CNN and extreme machine learning," *Proceedings of the IEEE Conference on Computer Vision and Pattern Recognition Workshop*s, pp. 49-55, 2017.

[32] R. B. Hegde, K. Prasad, H. Hebbar, ve B. M. K. Singh, "Comparison of traditional image processing and deep learning approaches for classification of white blood cells in peripheral blood smear images," *Biocybernetics and Biomedical Engineering*, vol 39, no. 2, pp. 382-392, 2019.

Gamma-Ray Shielding Capacity of Bi₂O₃-SiO₂-B₂O₃ Glass Powders with Different Bi₂O₃ Contents

Aycan SENGUL[1*], İskender AKKURT[2]

[1] Akdeniz University, Health Services Vocational School, Medical Imaging Techniques, Antalya, Turkey
[2] Suleyman Demirel University, Science Faculty, Physics Department, Isparta,
(ORCID: 0000-0003-4548-5403) (ORCID: 0000-0002-5247-7850)

Abstract
The study investigated the shielding properties of Bi₂O₃-SiO₂-B₂O₃ glass powders with varying Bi₂O₃ levels (45-60 mass%) against ionizing radiation using GAMOS (version 6.2). The simulation geometry produced by GAMOS was validated by comparing the results to conventional XCOM data for mass attenuation coefficients of glass particles. The Monte Carlo simulations were used to score photons that traveled in an absorber within the energy range of 0.01 MeV to 20 MeV, depending on the parameter under study. The simulation model involved a monoenergetic point source producing a pencil beam, absorber, and detector. We have calculated the mass attenuation coefficient (MAC), Half-value layer (HVL), Tenth-value layer (TVL), and Mean Free Path (MFP). The greatest linear attenuation coefficients in the whole energy range are related to 60Bi and the lowest were to 45Bi. The obtained results were compared, and these results are in good agreement with the obtained values from the XCOM program.

1. Introduction

The use of radiation in nuclear technology, medicine, agriculture, and industry has become widespread. As a result, the significance of radiation protection and research on protective materials has increased. To minimize potential radiation exposure, the ALARA principle is applied along with three main rules: time, distance, and shielding. Time and distance are manageable parameters for individuals. However, providing maximum protection from radiation requires investigating various types of materials, compounds, and mixtures for radiation shielding. The literature contains various theoretical, experimental [1]-[10], and simulation evaluations [11]-[23] investigations on shielding materials.

To determine the amount of shielding necessary for a specific target environment, it is necessary to consider the attenuation features of radiation. An absorber's mass attenuation coefficient (MAC) (μ/ρ) indicates the likelihood of a photon undergoing scatter or absorption interactions per unit distance and unit density of the material. This information is useful in estimating the thickness of a material needed to shield a known type and energy of an ionizing photon beam [24], [25]. The attenuation of material is determined using the transmission method, which follows the Lambert-Beer law. This law is formulated as in Equation 1;

$$\frac{\mu}{\rho} = \left(-\frac{1}{x\rho}\right)\ln\left(\frac{I(x)}{I_0}\right) \qquad (1)$$

Where I_0 and I_x denote the initial and reduced photon intensity, respectively. The variable x denotes the magnitude of the attenuator material's thickness.

The choice of shielding method primarily relies on the radiation energy and charge characteristics of the shielding materials. The choice of shielding material is contingent upon several factors, such as the nature of the radiation, system specifications, resilience to radiation-induced harm,

economic circumstances, and mechanical characteristics [26]. Low-melting glass is a common binder phase in advanced electronics technology due to its low sealing temperature, heat resistance, and air tightness [27], [28]. PbO-based glasses are particularly popular due to their low glass transition temperature and excellent thermal and electrical properties [29]. Due to the negative effects of lead on health and the environment, many research projects are evaluating lead-free high-density glasses. Several studies on ternary Bi_2O_3-containing glass have been undertaken [30]-[33].

The purpose of this study is to compute the gamma-ray shielding parameters of Bi_2O_3-SiO_2-B_2O_3-ZnO-Al_2O_3 glasses. with different Bi_2O_3 contents are calculated utilizing the GAMOS simulation tool. The computations use Monte Carlo simulations for a wide range of photon energies, and the examined values are compared to XCOM results.

2. Material and Method

In problems involving the transport of photons, a Monte Carlo code uses interaction cross sections, along with the geometrical and material descriptions of the medium, to compute estimates of dosimetric quantities such as flux and dose [34], [35].

The investigation utilized the Monte Carlo software package GAMOS 6.2 to model the geometry of the source, absorber, and detector. GAMOS is a CERN-developed derivative of Geant4 commonly used by medical physicists for investigating ionizing

radiation sources in diagnostic or therapeutic contexts [36]. For each sample, representing a separate simulation, photon energies ranging from 0.01 MeV to 20 MeV were studied. All Monte Carlo runs were performed using 10^6 particle histories/tracks, resulting in statistical errors below 0.1%. The simulations did not utilize any variance reduction technique. As seen in figure 1, the simulations involved a mono-energetic photon beam emitted from a pencil beam photon source. The beam was directed towards a disk shape absorber positioned 50 cm away from the source. To prevent any photon interactions with materials other than the sample, all irradiation geometry components were enclosed within a vacuum sphere with a radius of 100 cm.
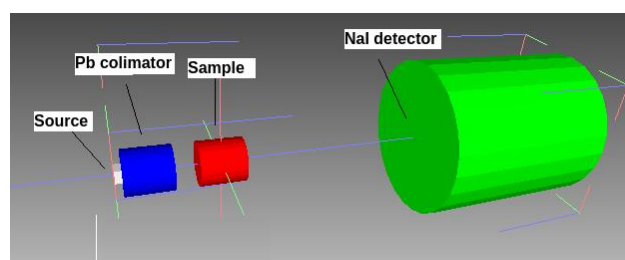

Figure 1. GAMOS Simulation geometry obtained with Paraview.

This work investigates the gamma shielding capabilities of four glasses with varying fractions of Bi_2O_3, which are significant in radiation protection. Table 1 shows the compositions and densities of each sample.

Table 1. Compositions of the Bi_2O_3-SiO_2-B_2O_3-ZnO-Al_2O_3 glasses (mass%).

Sample	ρ (g/cm^3)	Bi_2O_3	SiO_2	B_2O_3	ZnO	Al_2O_3
45Bi	5.82	45	10	35	7	3
50Bi	5.93	50	10	30	7	3
55Bi	6.16	55	10	25	7	3
60Bi	6.32	60	10	20	7	3

3. Results and Discussion

Four glass samples were performed MAC Monte Carlo tests. The simulations were conducted at twenty-eight different photon intensities, ranging from 0.01 MeV to 20 MeV. The values obtained from the Monte Carlo simulations were inputted into Equation (1) to produce GAMOS code results, which are presented in Table 2.

We calculated the LAC for each sample at different energies, ranging from 0.01 MeV to 20 MeV, using the GAMOS code and XCOM. The

results obtained from both codes were in good agreement with each other.

Figure 2 shows that 60Bi has the highest LAC across the entire energy range, while 45Bi has the lowest. Increasing the amount of Bi_2O_3 in the material increases its density and therefore its linear attenuation coefficient.

The MAC provides information about the material's performance based on its elemental makeup, regardless of its density. Figure 3 illustrates the variation in μ/ρ values in the 0.01-20 MeV energy range.
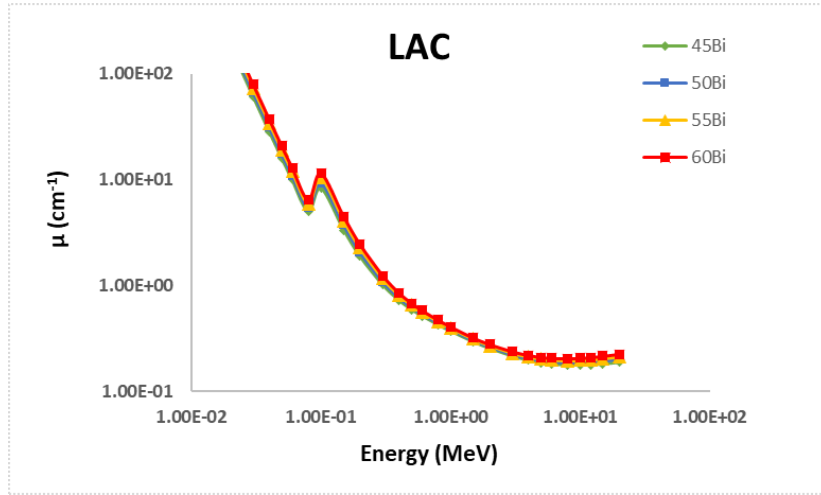
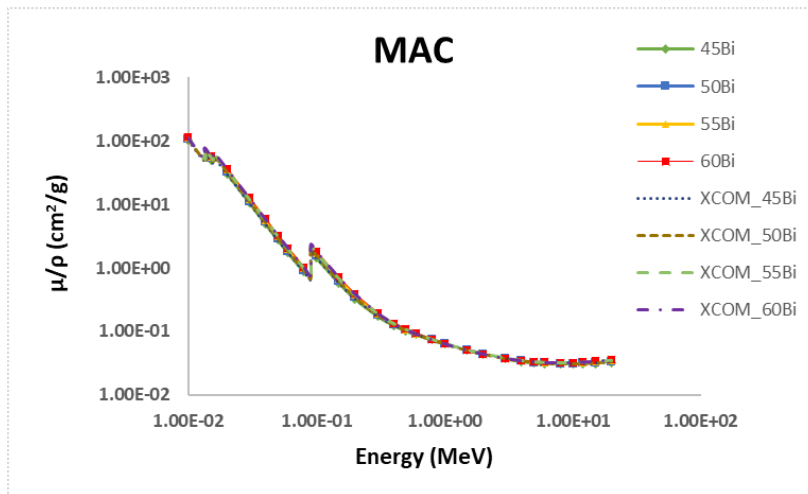**Figure 2.** LAC (cm^{-1}) in terms of photon energy for glasses.

Figure 3. MAC (cm^2/g) in terms of photon energy for glasses (GAMOS and XCOM).
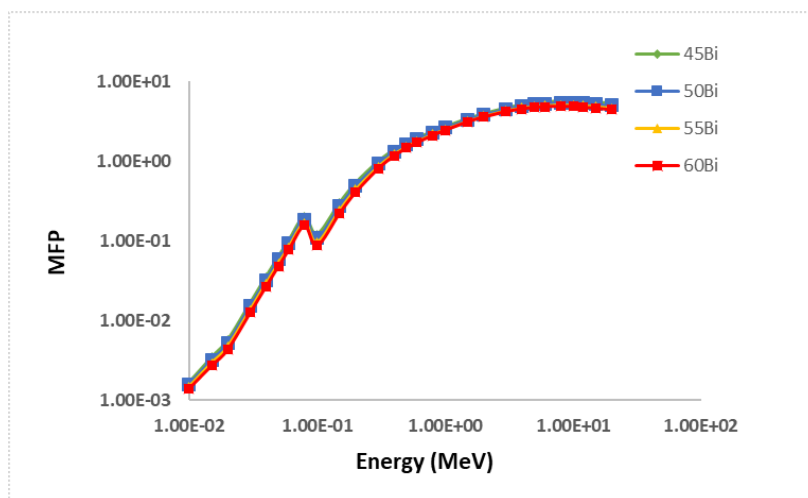

Figure 4. MFP (cm) in terms of photon energy for glasses.

The MFP is an important parameter for evaluating photon shielding characteristics. It refers to the distance that a particle travels between two consecutive collisions, which affects the direction, energy, and other properties of the particle. The MFP is calculated using Equation 2 and is determined by the photon energy, as shown in Figure 4. Increasing the gamma photon energy escalates the MFP of the material. The changes are shown in the energy range of 0.01-20 MeV. At lower energies of 1 MeV, the mean free path (MFP) increases modestly with slope, but at higher energies the slope increases more. The MFP moves relatively smoothly between 0.1 and 1 MeV. As shown in figure 4, 45Bi and 50Bi have a higher average free distance than other materials. This indicates that their materials have less interaction with atoms and may not be the best option for use in shields.

$$MFP = \left(\frac{1}{\mu}\right) \quad (2)$$

The shield thicknesses that reduce the intensity of the incident beam by 50% and 10% are referred to as HVL and TLV, respectively. Equations 3 and 4 are related to LAC.

$$HVL = \left(\frac{ln2}{\mu}\right) \quad (3)$$

$$TVL = \left(\frac{ln10}{\mu}\right) \quad (4)$$

Radiation shielding is considered adequate when the HVL value is low. Figure 5 shows that HVL and TVL values increase with energy, with 45Bi and 50Bi having the highest values compared to other materials. 60Bi has the lowest value compared to other materials due to its MFP.

Table 2. MAC (cm^2/g) of glasses at various photon energies determined by GAMOS simulation.

Energy (MeV)	45Bi		50Bi		55Bi		60Bi	
	XCOM	GAMOS	XCOM	GAMOS	XCOM	GAMOS	XCOM	GAMOS
0.01	1.03E+02	1.04E+02	1.06E+02	1.07E+02	1.09E+02	1.10E+02	1.12E+02	1.13E+02
0.015	5.02E+01	5.01E+01	5.29E+01	5.27E+01	5.56E+01	5.54E+01	5.83E+01	5.81E+01
0.02	3.07E+01	3.05E+01	3.28E+01	3.26E+01	3.49E+01	3.47E+01	3.70E+01	3.67E+01
0.03	1.05E+01	1.05E+01	1.13E+01	1.12E+01	1.20E+01	1.19E+01	1.27E+01	1.27E+01
0.04	4.93E+00	4.88E+00	5.28E+00	5.22E+00	5.63E+00	5.56E+00	5.97E+00	5.91E+00
0.05	2.76E+00	2.72E+00	2.95E+00	2.91E+00	3.14E+00	3.09E+00	3.34E+00	3.28E+00
0.06	1.74E+00	1.71E+00	1.85E+00	1.83E+00	1.97E+00	1.95E+00	2.09E+00	2.06E+00
0.08	8.69E-01	8.58E-01	9.25E-01	9.12E-01	9.80E-01	9.66E-01	1.04E+00	1.02E+00
0.1	1.44E+00	1.43E+00	1.58E+00	1.56E+00	1.71E+00	1.69E+00	1.84E+00	1.82E+00
0.15	5.78E-01	5.75E-01	6.24E-01	6.21E-01	6.70E-01	6.67E-01	7.16E-01	7.11E-01
0.2	3.28E-01	3.25E-01	3.49E-01	3.46E-01	3.71E-01	3.68E-01	3.92E-01	3.89E-01
0.3	1.74E-01	1.74E-01	1.82E-01	1.81E-01	1.89E-01	1.89E-01	1.96E-01	1.96E-01
0.4	1.25E-01	1.25E-01	1.29E-01	1.28E-01	1.32E-01	1.32E-01	1.36E-01	1.35E-01
0.5	1.03E-01	1.02E-01	1.04E-01	1.04E-01	1.06E-01	1.06E-01	1.08E-01	1.08E-01
0.6	8.90E-02	8.89E-02	9.02E-02	9.01E-02	9.13E-02	9.13E-02	9.25E-02	9.25E-02
0.8	7.32E-02	7.34E-02	7.37E-02	7.39E-02	7.42E-02	7.44E-02	7.47E-02	7.49E-02
1	6.38E-02	6.37E-02	6.40E-02	6.41E-02	6.42E-02	6.44E-02	6.45E-02	6.46E-02
1.5	5.07E-02	5.06E-02	5.07E-02	5.06E-02	5.08E-02	5.07E-02	5.08E-02	5.07E-02
2	4.41E-02	4.39E-02	4.41E-02	4.40E-02	4.42E-02	4.40E-02	4.43E-02	4.41E-02
3	3.73E-02	3.71E-02	3.75E-02	3.72E-02	3.77E-02	3.74E-02	3.79E-02	3.77E-02
4	3.41E-02	3.39E-02	3.44E-02	3.41E-02	3.47E-02	3.44E-02	3.49E-02	3.47E-02
5	3.23E-02	3.22E-02	3.27E-02	3.26E-02	3.31E-02	3.30E-02	3.35E-02	3.33E-02
6	3.13E-02	3.12E-02	3.18E-02	3.17E-02	3.22E-02	3.22E-02	3.27E-02	3.27E-02
8	3.05E-02	3.05E-02	3.11E-02	3.11E-02	3.17E-02	3.17E-02	3.23E-02	3.23E-02
10	3.04E-02	3.05E-02	3.12E-02	3.11E-02	3.19E-02	3.19E-02	3.26E-02	3.26E-02

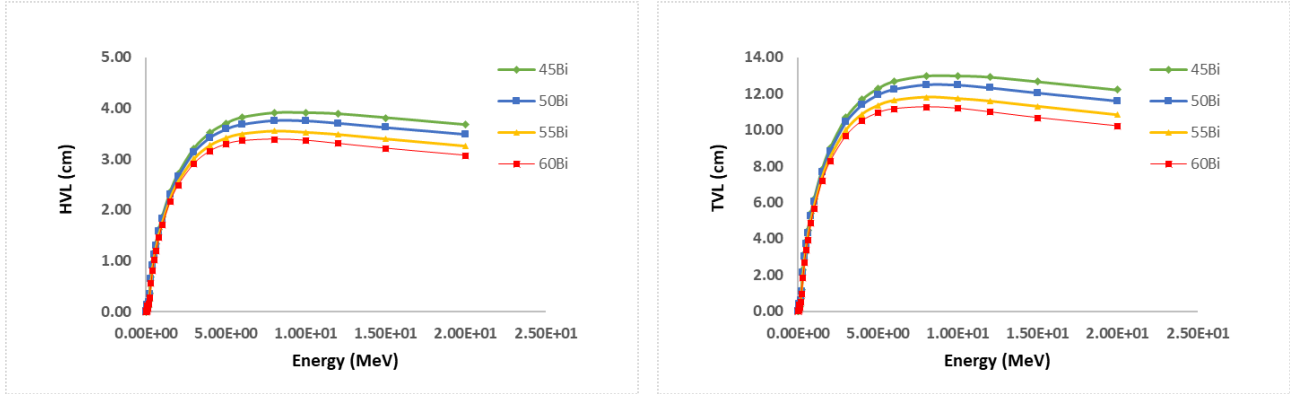| 12 | 3.07E-02 | 3.06E-02 | 3.15E-02 | 3.15E-02 | 3.23E-02 | 3.23E-02 | 3.32E-02 | 3.32E-02 |
| 15 | 3.14E-02 | 3.12E-02 | 3.23E-02 | 3.23E-02 | 3.33E-02 | 3.31E-02 | 3.42E-02 | 3.42E-02 |
| 20 | 3.27E-02 | 3.24E-02 | 3.38E-02 | 3.35E-02 | 3.49E-02 | 3.45E-02 | 3.60E-02 | 3.57E-02 |

Figure 5. HVL and TVL (cm) in terms of photon energy for glasses.

Figure 6 shows that for the four cases analyzed in this study, the results obtained from GAMOS and XCOM agree with each other by <0.5%.
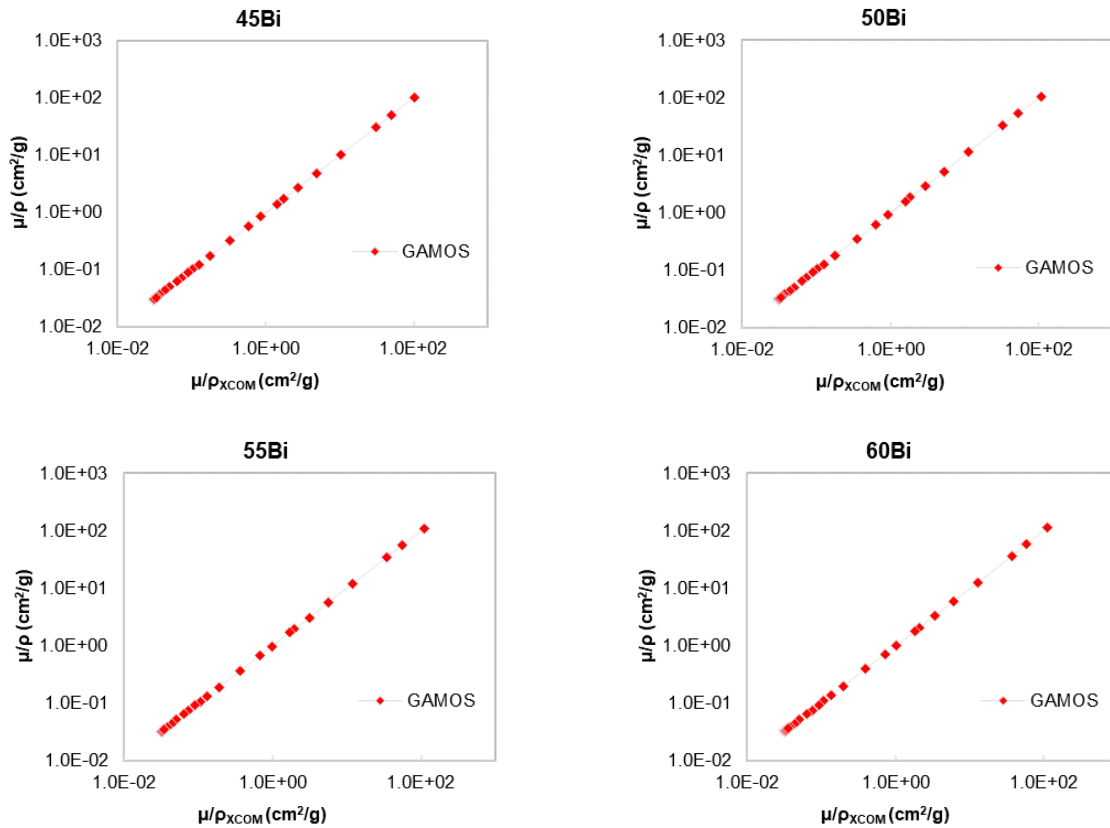

Figure 6. MAC (cm^2/g) of glasses obtained from Monte Carlo simulations (GAMOS) plotted against data from XCOM database.

4. Conclusion and Suggestions

This study presents a Monte Carlo method to calculate the MAC of Bi_2O_3-SiO_2-B_2O_3 glass with varying quantities of Bi_2O_3. The shielding properties of ionizing radiation, such as LAC, MAC, HVL, TVL and MFP, were investigated for glasses in the photon energy range of 0.01-20 MeV. The Monte Carlo simulations yielded results that are in excellent agreement with theoretical data, suggesting that this technique can be used for calculating interaction parameters for materials of interest. Increasing the Bi_2O_3, even in small amounts, had a significant effect on the attenuation of radiation performance. The attenuation coefficients of the selected materials, namely HVL, TVL, and MFP, increase with photon energy. Therefore, these materials are more effective in attenuating low-energy photons.

This approach can serve as an alternative when measuring attenuation coefficients is challenging due to the unavailability of certain gamma energies or difficulties in producing physical samples. This tool enables the generation of attenuation coefficient data for any given photon energy and material thickness.

Contributions of the Authors

The methodology was creating, findings were interpreted, and the article was written by A.S. The idea was developed, the findings were interpreted, and the article was written by İ. A.

Conflict of Interest Statement

There is no conflict of interest between the authors.

Statement of Research and Publication Ethics

The study is complied with research and publication ethics

References

[1]   M. S. Al-Buriahi, H. Arslan, and B. T. Tonguç, "Mass attenuation coefficients, water and tissue equivalence properties of some tissues by Geant4, XCOM and experimental data," *Indian Journal of Pure & Applied Physics (IJPAP),* vol. 57, no. 6, pp. 433-437, 2019, doi: 10.56042/ijpap.v57i6.22878.

[2]   M. E. Phelps, E. J. Hoffman, and M. M. Ter-Pogossian, "Attenuation coefficients of various body tissues, fluids, and lesions at photon energies of 18 to 136 keV," *Radiology,* vol. 117, no. 3, pp. 573-583, 1975, doi: 10.1148/117.3.573.

[3]   O. Gencel, A. Bozkurt, E. Kam, A. Yaras, E. Erdogmus, and M. Sutcu, "Gamma and neutron attenuation characteristics of bricks containing zinc extraction residue as a novel shielding material," *Progress in Nuclear Energy,* vol. 139, p. 103878, 2021.

[4]   J. H. Hubbell, "Review and history of photon cross section calculations," *Physics in Medicine & Biology,* vol. 51, no. 13, p. R245, 2006.

[5]   A. Sengul *et al.*, "Computation of the impact of NiO on physical and mechanical properties for lithium nickel phosphate glasses," *Journal of Radiation Research and Applied Sciences,* vol. 16, no. 4, p. 100737, 2023/12/01/ 2023, doi:

[6]   N. Karpuz, "Radiation shielding properties of glass composition," *Journal of Radiation Research and Applied Sciences,* vol. 16, no. 4, p. 100689, 2023/12/01/ 2023, doi:

[7]   O. V. Gul, N. Buyukcizmeci, and H. Basaran, "Dosimetric evaluation of three-phase adaptive radiation therapy in head and neck cancer," *Radiation Physics and Chemistry,* vol. 202, p. 110588, 2023.

[8]   O. V. Gul, "Experimental evaluation of out-of-field dose for different high-energy electron beams and applicators used in external beam radiotherapy," *Radiation Physics and Chemistry,* vol. 215, p. 111345, 2024.

[9]   G. Bayrak and H. Müştak, "The Characterization of Welded AA 5005 Alloy with AA 5356 Filler Metals According to Slow Welding Rate Using by MIG Welding Technique," *International Journal of Computational and Experimental Science and Engineering,* vol. 9, no. 4, pp. 346-353, 2023.

[10]   T. Şahmaran and T. Tuğrul, "Investigation of Shielding Parameters of Fast Neutrons for Some Chemotherapy Drugs by Different Calculation Methods," *International Journal of Computational and Experimental Science and Engineering,* vol. 9, no. 4, pp. 388-393, 2023.

[11]   E. Ermis, F. Pilicer, E. Pilicer, and C. Celiktas, "A comprehensive study for mass attenuation coefficients of different parts of the human body through Monte Carlo methods," *Nuclear Science and Techniques,* vol. 27, no. 3, p. 54, 2016, doi: 10.1007/s41365-016-0053-2.

[12]   H. O. Tekin, V. P. Singh, E. E. Altunsoy, T. Manici, and M. I. Sayyed, "Mass attenuation coefficients of human body organs using MCNPX Monte Carlo code," *Iranian Journal of Medical Physics,* vol. 14, no. 4, pp. 229-240, 2017.

[13]   A. Sahin and A. Bozkurt, "Monte Carlo Calculation of Mass Attenuation Coefficients of Some Biological Compounds," *Süleyman Demirel Üniversitesi Fen Edebiyat Fakültesi Fen Dergisi,* vol. 14, no. 2, pp. 408-417.

[14]   A. Bozkurt and A. Sahin "Monte Carlo Approach for Calculation of Mass Energy Absorption Coefficients of Some Amino Acids," *Nuclear Engineering and Technology,* 2021.

[15]   A. Şengül and A. Bozkurt, "Bazı Biyolojik Bileşiklerin Kütlesel Enerji Soğurma Katsayılarının Monte Carlo Yöntemiyle Hesaplanması," *Süleyman Demirel Üniversitesi Fen Edebiyat Fakültesi Fen Dergisi,* vol. 16, no. 2, pp. 416-423, 2021.

[16]   I. Akkurt, A. Alomari, M. Y. Imamoglu, and I. Ekmekçi, "Medical radiation shielding in terms of effective atomic numbers and electron densities of some glasses," *Radiation Physics and Chemistry,* vol. 206, p. 110767, 2023.

[17]   R. B. Malidarre, I. Akkurt, O. Kocar, and I. Ekmekci, "Analysis of radiation shielding, physical and optical qualities of various rare earth dopants on barium tellurite glasses: A comparative study," *Radiation Physics and Chemistry,* vol. 207, p. 110823, 2023.

[18]   G. ALMisned, G. Bilal, D. S. Baykal, F. T. Ali, G. Kilic, and H. O. Tekin, "Bismuth (III) oxide and boron (III) oxide substitution in bismuth-boro-zinc glasses: A focusing in nuclear radiation shielding properties," *Optik,* vol. 272, p. 170214, 2023.

[19]   A. Sengul, M. S. Akhtar, I. Akkurt, R. B. Malidarre, Z. Er, and I. Ekmekci, "Gamma-neutron shielding parameters of (S3Sb2) x (S2Ge) 100− x chalcogenide glasses nanocomposite," *Radiation Physics and Chemistry,* vol. 204, p. 110675, 2023.

[20]   A. Şengül, "Gamma-ray attenuation properties of polymer biomaterials: Experiment, XCOM and GAMOS results," *Journal of Radiation Research and Applied Sciences,* vol. 16, no. 4, p. 100702, 2023.

[21]   A. Şengül, "ZnO Katkılı Bazı Cam Örneklerinin Kütle Zayıflama Katsayılarının Monte Carlo ile Hesaplanması," *Dokuz Eylül Üniversitesi Mühendislik Fakültesi Fen ve Mühendislik Dergisi,* vol. 25, no. 75, pp. 751-759.

[22]   O. V. Gul and M. Duzova, "Effect of different CTV shrinkage and skin flash margins on skin dose for left chest wall IMRT: A dosimetric study," *Radiation Physics and Chemistry,* vol. 216, p. 111445, 2024.

[23]   A. Coşkun, B. Çetin, İ. Yiğitoğlu, and B. Canimkurbey, "Theoretical and Experimental Investigation of Gamma ShieldingProperties of TiO2 and PbO Coated Glasses," *International Journal of Computational and Experimental Science and Engineering,* vol. 9, no. 4, pp. 398-401, 2023.

[24]   M. Berger *et al.*, "XCOM: Photon Cross Sections Database. NIST, PML, Radiation Physics Division," ed, 2019.

[25]   J. K. Shultis and R. E. Faw, *Fundamentals of Nuclear Science and Engineering*. CRC Press, 2016.

[26]   H. O. Tekin, V. P. Singh, and T. Manici, "Effects of micro-sized and nano-sized WO3 on mass attenauation coefficients of concrete by using MCNPX code," *Applied Radiation and Isotopes,* vol. 121, pp. 122-125, 2017.

[27]   G. Hongwei *et al.*, "Microstructures and properties of (65-x) SiO2-xBi2O3-10B2O3-25CuO glasses," *Journal of Non-Crystalline Solids,* vol. 569, p. 120972, 2021.

[28]   H. Masai, M. Takahashi, Y. Tokuda, and T. Yoko, "Gel-melting method for preparation of organically modified siloxane low-melting glasses," *Journal of materials research,* vol. 20, pp. 1234-1241, 2005.

[29]   S. K. Hong, H. Y. Koo, Y. N. Ko, J. H. Kim, J. H. Yi, and Y. C. Kang, "Eu-doped B 2 O 3–ZnO–PbO glass phosphor powders with spherical shape and fine size prepared by spray pyrolysis," *Applied Physics A,* vol. 98, pp. 671-677, 2010.

[30]   I. Dyamant, D. Itzhak, and J. Hormadaly, "Thermal properties and glass formation in the SiO2–B2O3–Bi2O3–ZnO quaternary system," *Journal of non-crystalline solids,* vol. 351, no. 43-45, pp. 3503-3507, 2005.

[31] V. Golubkov, P. Onushchenko, and V. Stolyarova, "Studies of glass structure in the system Bi 2 O 3-B 2 O 3-SiO 2," *Glass Physics and Chemistry,* vol. 41, pp. 247-253, 2015.

[32] Y. Gao, J.-J. Ma, Y. Chen, and M.-H. Wang, "Effect of Bi2O3 on the structure and thermal properties of Bi2O3-SiO2-B2O3 glasses prepared by sol-gel method," *Journal of Sol-Gel Science and Technology,* vol. 103, no. 3, pp. 713-721, 2022.

[33] B. Oruncak, "Computation of Neutron Coefficients for B2O3 reinforced Composite," *International Journal of Computational and Experimental Science and Engineering,* vol. 9, no. 2, pp. 50-53.

[34] P. Arce, P. Rato, M. Canadas, and J. I. Lagares, "GAMOS: A Geant4-based easy and flexible framework for nuclear medicine applications," in *2008 IEEE Nuclear Science Symposium Conference Record*, 2008: IEEE, pp. 3162-3168.

[35] P. Andreo, "Monte Carlo techniques in medical radiation physics," *Physics in Medicine & Biology,* vol. 36, no. 7, p. 861, 1991.

[36] S. Agostinelli *et al.*, "GEANT4—a simulation toolkit," *Nuclear instruments and methods in physics research section A: Accelerators, Spectrometers, Detectors and Associated Equipment,* vol. 506, no. 3, pp. 250-303, 2003.

Using Machine Learning Algorithms to Analyze Customer Churn with Commissions Rate for Stocks in Brokerage Firms and Banks

Hakan KAYA*

*Istanbul Okan University, Graduate School, Banking Doctorate (PhD) Program,
34959 Tuzla / ISTANBUL / Türkiye
(ORCID: 0000-0002-0812-4839)*

Abstract

Stock commission rates of banks and brokerage firms are a critical factor for investors. These rates affect the cost of stock investments. It's crucial to highlight the significance of stock commission rates in brokerage firms and banks, as well as the factors that influence their determination. This article aims to draw attention to the study's focus on customer churn and commission rates within the financial industry. Previous research has mainly focused on identifying the key variables affecting customer churn without considering its impact on forecast accuracy. This work has two primary research goals: first one is to investigate how commission rates affect the accuracy of customer churn prediction in brokerage firms and the banking sector using machine learning models, and second one is to compare and evaluate the most effective machine learning approaches for predicting customer churn. The customer churn management approach was enhanced through the analysis of a data set obtained from a bank and brokerage firm. This data set, comprised of 7816 entries and 14 columns, reflects the firm's transactions and was sourced from a publicly accessible database. The analysis employed Decision Tree, Random Forest, K-NN, Gaussian NB, and XGBoost algorithms to evaluate performance using three accuracy measures. Two approaches are included for model creation. According to the first analysis results, the Gaussian NB, for second approach the K-NN algorithms gave the best result.

1. Introduction

Institutions can gain valuable insights by analyzing customer data and behavior to identify potential churn risks. Utilizing predictive analytics and machine learning algorithms, institutions can proactively pinpoint at-risk customers and take necessary actions to prevent churn.

Churn analysis refers to the process of identifying customers who may leave a company and implementing appropriate marketing precautions.

Brokerage firms and banks typically earns a portion of the commissions sale of stocks that the makes for an investor. Anticipating and mitigating customer churn presents a significant opportunity for additional revenue generation for both brokerage firms and banks. In the banking and brokerage sectors, various machine learning algorithms are commonly used for analyzing customer churn.

Stock commission is a fee that investors incur when they buy or sell stocks, charged by brokerage firms or banks involved in stock transactions. Typically, stock commission is calculated as a percentage of the investment amount. It's worth noting that commission rates can vary among brokerage firms, banks, and countries. Moreover, these rates may differ based on factors such as the type and amount of the transaction, as well as the investor's client status. In addition to the

commission, exchange fees and a 5% Banking and Insurance Transactions Tax (BITT) are collected based on the commission amount. Commission rates are automatically deducted from the accounts of investors engaging in stock transactions.

What are some common machine learning algorithms used to analyze customer churn in the banking and brokerage industry? Can you provide examples of successful customer churn prevention strategies implemented by businesses using predictive analytics? answers to these questions were sought. Additionally, how businesses can use predictive analytics and machine learning algorithms to identify at-risk customers and prevent customer churn is discussed.

With the rapid advancements in machine learning, it has become increasingly valuable to develop predictive models that can determine whether a customer will leave a specific bank. In this study, we aim to perform data analysis and develop a churn prediction model to forecast which customers are likely to churn based on historical data and various features. Machine learning techniques such as Decision Trees, Random Forests, K-NN, Gaussian NB, and XGBoost algorithms are utilized to identify churn patterns [1]. These ML methods are not only employed in the banking sector but also applied across various industries including insurance [2], medical systems [3], cyberbullying [4], retail marketing [5], automobile and gaming industry [3], and telecommunication [6]. Therefore, the significance of this study can be summarized in three aspects: i) gathering churn customer data from approximately 8,000 institutions, ii) overcoming class imbalance issues by using a combination of SMOTE data sampling and the K-NN classifier during the initial stage of analysis, and iii) conducting a comprehensive assessment of five models to facilitate informed model selection and evaluation [1].

Many machine learning techniques can research customer churn analysis. In this study, banking was compared with brokerage firms. Here is a brief overview of the related work on the available methods: A recent study employed [7] on utilizing methods such as stochastic gradient boosting, random forest, logistic regression, and k-nearest neighbors to predict early customer churn and develop effective retention strategies. In another study [8] developed an approach for customer churn prediction utilizing three intelligent models: AdaBoost, Random Forest (RF), and Support Vector Machine (SVM). To address the issue of an

unbalanced dataset, the team applied the Synthetic Minority Oversampling Technique (SMOTE) along with a combination of undersampling and oversampling. Another study conducted [9] the topic of customer churn prediction across various domains such as telecommunications, energy sectors, retail banking, e-banking, and insurance was explored. The modelling techniques utilized in this field include Logistic Regression, Neural Network Model, Random Forest, Decision Tree, Support Vector Machine, and Rough set approach. These methods have been implemented to detect churn among customers. Other work in the literature [10] SHapely Additive exPlanations (SHAP) values to improve the assessment and interpretability of the machine learning model. The research aimed to develop an interpretable machine learning model using authentic banking industry data and assess various machine learning models using test data. A similar study [11] explored the techniques such as k-means clustering for customer segmentation, as well as logistic regression, k-nearest neighbors, random forest, decision tree, and support vector machine algorithms to analyze the dataset. The literature [12] took a slightly different approach to customer churn management by analyzing a dataset obtained from a real-world telecommunication firm. To analyze the dataset, the researchers employed Artificial Neural Network (ANN), Support Vector Machines (SVM), and Naive Bayes (NB) algorithms. The performance of the analysis was evaluated using four accuracy measures. In the given study [13] emphasized the prediction of customer churn within the banking sector using a distinctive customer-level dataset acquired from a prominent Brazilian bank. The researchers compared various machine learning models including decision trees, elastic net, k-nearest neighbors, logistic regression, random forests and support vector machines. For example, in one study in the literature [6] provides offer readers a general understanding of the commonly used data mining methods, their results, and performance, while also highlighting the need for further research in the Telecommunication Industry. In contrast, another study [14] the analysis involved examining the customer behavior data of a real water purifier rental service within an electronics company in Korea to create and validate a churn prediction model. The model's performance was assessed using the F-measure and area under curve (AUC) metrics.

The rest of this paper is structured as follows: Section 2 outlines the research

methodology. The experimental findings are presented in Section 3. Finally, Section 4 concludes the paper and recommendations to the instutions to captures the development of a predictive model to pinpoint influential factors contributing to customer churn, encompassing the testing of different machine learning algorithms, the use of SMOTE to address class imbalance, and the subsequent repetition of the initial approach's steps.

2. Material and Method

This research focused on analyzing brokerage firms and banks in Turkey, specializing in stock commission rates. A dataset of 7816 observations was utilized. The study initially evaluated the weights of fourteen features and then proceeded to predict non-churn and churn customers using Decision Tree, Random Forest, K-NN, Gaussian NB, and XGBoost machine learning methods. The performance metrics considered in this study included Accuracy, Recall, Precision, and F1-Score.

The research was conducted using anonymous data from brokerage firms and banks, ensuring that only data from customers with permission to process data was anonymized and made available for analysis under the scope of Personal Data Protection Authority. Prior to creating and training the model, the dataset's features were extracted and formatted appropriately for model creation and prediction.

2.1. Used Algorithms

2.1.1. Decision Tree

A decision tree is a flowchart-like structure with nodes representing features, branches representing decision rules, and leaf nodes indicating the outcome or class label.

The algorithm recursively divides the data based on selected features, creating subsets with shared class labels. This process continues until a stopping condition is met, such as reaching a maximum depth or having a minimum number of instances in each leaf [18].

2.1.2. Random Forest

Random Forest is a popular machine learning algorithm that combines decision trees with an ensemble learning approach. It can handle classification and regression tasks effectively, offering high accuracy and robustness.

In Random Forest, multiple decision trees are built, each trained on a different subset of data and a random subset of features. This randomness helps prevent overfitting and improves the model's ability to generalize to new data. During training, each tree is grown similarly to traditional decision trees, but with only a random subset of features considered for splitting at each node [19]. To make predictions, the algorithm combines the individual tree predictions through voting (for classification) or averaging (for regression).

2.1.3. K-NN

K-Nearest Neighbors (K-NN) is a popular machine learning algorithm used for both classification and regression tasks. It makes predictions based on the similarity of data points.

In K-NN, the "K" represents the number of nearest neighbors considered for predictions. To determine proximity, K-NN uses distance measures like Euclidean or Manhattan distance. The algorithm calculates distances between the new data point and all others in the training set, selecting the K nearest neighbors. Choosing the right K value is crucial to avoid overfitting, where the model becomes too sensitive to noise in the data [20].

2.1.4. Gaussian NB

Gaussian Naive Bayes (GNB) is a popular machine learning algorithm for classification tasks. It assumes that features follow a Gaussian distribution and are independent of each other.

GNB estimates the mean and standard deviation of each feature for each class during training. To make predictions, it calculates the conditional probability of each class given the feature values using Bayes' theorem. GNB is computationally efficient, works well with high-dimensional data, and handles missing values effectively [21]. However, if features are strongly correlated, GNB may not perform as well as other algorithms.

2.1.5. XGBoost

XGBoost, short for Extreme Gradient Boosting, is a powerful and efficient machine learning algorithm that belongs to the gradient boosting framework. It combines weak prediction models, usually decision

trees, to create a robust and accurate model. The algorithm iteratively trains and adds new models to improve upon the errors made by the previous ones, using a technique called gradient boosting [17].

To enhance its speed and efficiency, XGBoost incorporates various optimizations. These include parallel computing, column block loading, and approximate algorithms for finding splits. These optimizations make XGBoost one of the fastest and most scalable gradient boosting frameworks available.

2.2.Used Performance Metrics

Here are the definitions of the four terms related to binary classification:

True negatives (TN): These are the instances that are correctly predicted as negatives (zeros).

True positives (TP): These are the instances that are correctly predicted as positives (ones).

False negatives (FN): These are the instances that are incorrectly predicted as negatives (zeros) when they are actually positives (ones).

False positives (FP): These are the instances that are incorrectly predicted as positives (ones) when they are actually negatives (zeros).

2.2.1.Accuracy

Accuracy can be defined as the proportion of correct predictions to the total number of predictions made by the system [15].

$$Accuracy = (TP+TN) / (TP+TN+FN+FP) \quad (1)$$

2.2.2.Precision

Precision is a measure of success when predicting positive outcomes. It is calculated as the ratio of true positives (TP) to the sum of true positives and false positives (TP + FP).

Precision represents the classifier's ability to correctly identify samples as positive and not falsely label negative samples as positive.

$$Precision = TP / (TP + FP) \quad (2)$$

2.2.3.Recall

Recall is a metric that measures the success of predicting positive outcomes [16]. It is calculated as the ratio of true positives (TP) to the sum of true positives and false negatives (TP + FN).

Recall represents the classifier's ability to identify all positive samples, capturing the proportion of positive instances correctly detected by the model.

$$Recall = TP / (TP + FN) \quad (3)$$

2.2.4.F1-Score

The F1-Score is a metric that combines the recall and precision into a single value. It is calculated as the harmonic mean of the recall and precision values.

The F1-Score provides a balanced measure of a classifier's performance, taking into account both the ability to correctly identify positive samples (recall) and the ability to avoid false positives (precision). The F1 score can be computed by using the formula: 2 * (Precision * Recall) / (Precision + Recall)

3. Results and Discussion

To gain a deeper understanding and improve our ability to predict customer attrition, our primary focus will be on the target variable "Exited." This variable serves as a vital indicator of churn and will guide our efforts in building a robust churn model.

3.1. Categorical Variables

3.1.1.Exited

The variable "Exited" serves as an important indicator, distinguishing between existing customers (0) and churned customers (1), and providing valuable insights into customer retention.

The dataset exhibits with around 80% of the data representing existing customers and the remaining 20% representing churned customers.
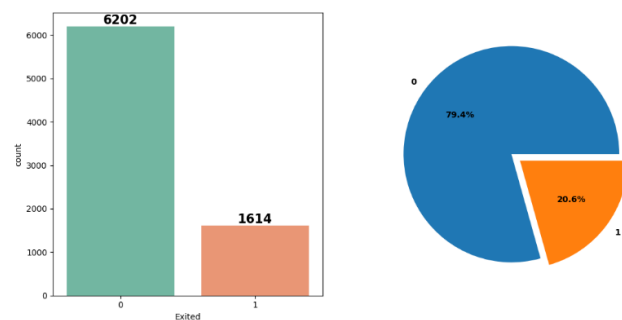

Figure 1. Customer Churned Disribution

3.1.2.Institutions

The dataset includes customer churn data from two types of institutions: Banks and Brokerage Firms, providing a comprehensive view of customer behavior within these industries.

In terms of customer distribution, banks represent 60% of the customer base, while Brokerage Firms make up the remaining 40% of institutions. This distribution allows for a well-rounded analysis and understanding of churn patterns in both banks and brokerage firms, enabling us to develop insights and strategies that cater to the specific characteristics of each type of institution.

Table 1. Distribution of Customer in Institutions

Banks	60.22262
Brokerage Firms	39.77738

Interestingly, the findings of both analyses are remarkably similar to one another on churn analysis.

Table 2. Distribution of Customer Churn in Institutions

Brokerage Firms	0	79.125121
	1	20.87487
Banks	0	79.498619
	1	20.501381
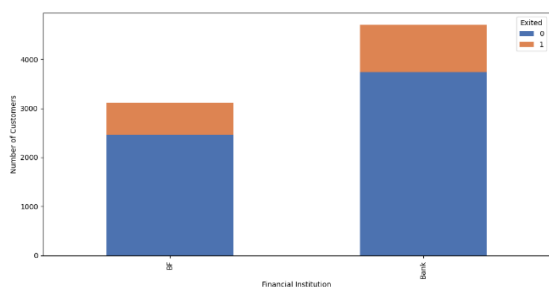
Figure 2. Financial Institutions and Customer Churn Distribution

3.1.3.Gender

The customer base is divided between male and female customers, with males representing 54% and females making up 46% of the total customer population.

Table 3. Distribution of Customer Gender

Male	54.183726
Female	45.816274

Churn rates by gender is intriguing to note that 26% of female customers have churned, indicating a higher attrition rate in this group. On the other hand, the churn rate for male customers is 16%, suggesting relatively lower customer churn within this segment.

Table 4. Distribution of Customer Churn Rates between Genders

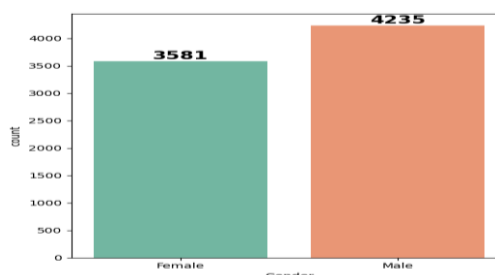|		
Female	0	74.280927
	1	25.719073
Male	0	83.636364
	1	16.363636

Figure 3. Gender and Customer Churn Distribution

3.1.4.Tenure

The duration of customer tenure ranges from 0 to 10 years, with an average tenure of 5 years. This suggests a wide spectrum of customer relationships established with the institutions over time.

Table 5. Distribution of Tenure

count	7816.000000
mean	5.013946
std	2.882681
min	0.000000
25%	3.000000
50%	5.000000
75%	7.000000
max	10.000000

The majority of customers, accounting for around 90%, maintain a tenure that spans from 1 year to 9 years. This concentration signifies a strong sense of customer loyalty within this timeframe, underscoring the importance of fostering long-term relationships with clients.

Table 6. Distribution of Concentrated Tenure Range

0	4.183726
1	10.273797
2	10.248209
3	10.158649
4	9.992323
5	10.145855

6	9.608495
7	10.427329
8	10.491300
9	9.825998
10	4.644319

3.1.5. Number of Products

Customers exhibit a diverse range of product ownership, typically ranging from 1 to 4 products. This indicates varying levels of engagement with the bank's offerings, showcasing the breadth of options available to cater to individual needs and preferences.

Table 7. Distribution of Number of Products

count	7816.000	**1**	4002	**No.**		**Exited**
	000	**2**	3551	**Of**		
mean	1.527764	**3**	215	**Prod.**		
std	0.584068	**4**	48			
min	1.000000					
25%	1.000000			1	0	71.91
50%	1.000000				1	28.09
75%	2.000000			2	0	92.59
max	4.000000				1	7.41
				3	0	83.26
					1	16.74
				4	1	100.00

Churned customers are worth mentioning that all customers who had 4 card products have churned, suggesting a strong likelihood of attrition within this particular group. Furthermore, a substantial percentage (83%) of customers with 3 card products has also churned, underscoring the significance of conducting a thorough analysis of churn patterns specific to each product.
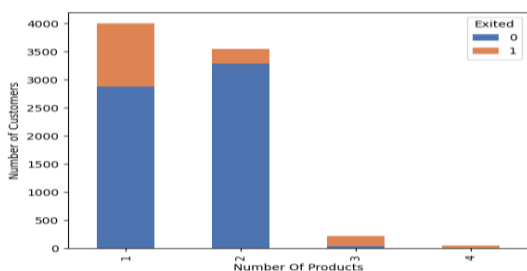
Figure 4. Number of Products and Customer Churn Distribution

3.1.6. Has Credit Cards

Around 70% of customers are found to possess a credit card, highlighting a substantial portion of the customer base actively utilizing this financial product. This demonstrates the widespread adoption and popularity of credit cards among the customer community.

Table 8. Distribution of Has Credit Cards

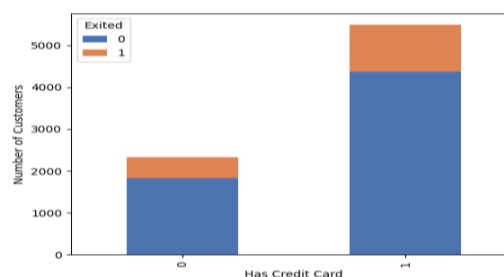| count	7816.0000	**0**	2323	**Has**		**Exited**
	00	**1**	5493	**Credit**		
mean	0.702789			**Cards**		
std	0.457059			0	0	78.82
min	0.000000				1	21.18
25%	0.000000			1	0	79.57
50%	1.000000				1	20.43
75%	1.000000					
max	1.000000					

Figure 5. Has Credit Card and Customer Churn Distribution

3.1.7. Is Active Member

Roughly 52% of customers are actively enrolled as members, indicating a significant portion of the customer base actively participating in the bank's membership program.

Within the group of active members, approximately 14% have churned, while among non-active members, the churn rate stands at around 28%. The number of active and non-active customers is approximately equal. However, it is noteworthy that the churn rate among non-active customers is nearly double compared to active customers. This suggests that customers who are not actively engaged in the institutions's offerings are more likely to deactivate their banking facilities.

Table 9. Distribution of Is Active Member

count	7816.000	**0**	3814	**IsActive**		**Exited**
	000	**1**	4002	**Member**		
mean	0.512027			0	0	72.65
std	0.499887				1	27.35
min	0.000000			1	0	85.73
25%	0.000000				1	14.27
50%	1.000000					
75%	1.000000					
max	1.000000					
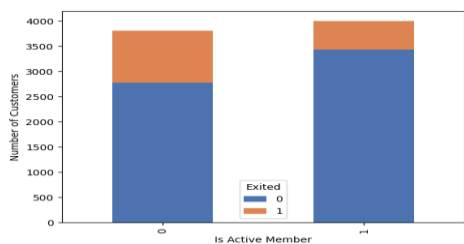
Figure 6. Is Active Member and Customer Churn Distribution

3.1.8. Credit Score

The credit scores of customers span a range from 350 to 850, indicating the diversity in their creditworthiness.

Table 10. Distribution of Credit Score

count	7816.000000
mean	650.099667
std	96.826809
min	350.000000
25%	583.000000
50%	652.000000
75%	717.000000
max	850.000000

A noteworthy observation is that all customers with credit scores below 300 have churned. This underscores the importance of credit scores as a potential factor contributing to customer attrition. It emphasizes the significance of addressing credit-related issues in order to enhance customer retention and mitigate churn risk.
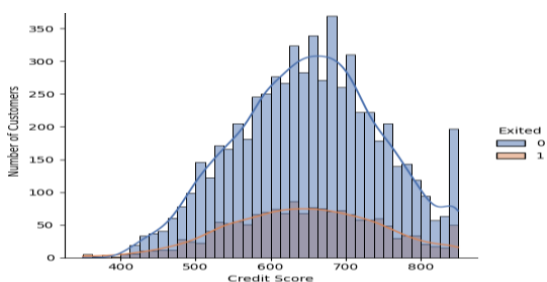
Figure 7. Credit Score and Customer Churn Distribution

3.1.9. Age

The age range of customers extends from 18 to 92, with an average age of approximately 38. This signifies a diverse customer base encompassing a wide range of age groups.

Table 11. Distribution of Age

count	7816.000000
mean	38.946392
std	10.517831
min	18.000000
25%	32.000000
50%	37.000000
75%	44.000000
max	92.000000

It has been observed that customers in the age range of 50 to 58 have shown a higher churn rate. This highlights the necessity of implementing targeted retention strategies specifically tailored for customers within this age group.

Additionally, the distribution of customer age is right-skewed (positively skewed), indicating that there are relatively fewer customers in older age groups. This skewness emphasizes the importance of considering age as a potential factor in predicting churn and underscores the need to implement suitable measures to retain customers across all age ranges.
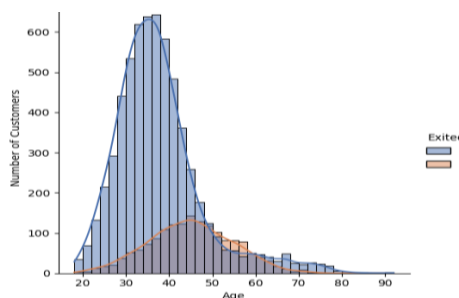

Figure 8. Age and Customer Churn Distribution

3.1.10. Balance

Currently, there are over 2300 customers who have a balance of zero in their accounts. When excluding these customers with zero balances, the distribution of account balances follows a normal distribution pattern. It is worth noting that customers with a zero balance are more prone to deactivating their accounts.

Table 12. Distribution of Balance

count	7816.000000
mean	76762.958515
std	62418.094005
min	0.000000
25%	0.000000
50%	97703.005000
75%	127811.165000
max	250898.090000

This implies that the remaining customers, who maintain a positive balance, exhibit a more typical distribution of account balances. This enables the bank to gain a clearer understanding of their financial status and effectively manage their accounts.
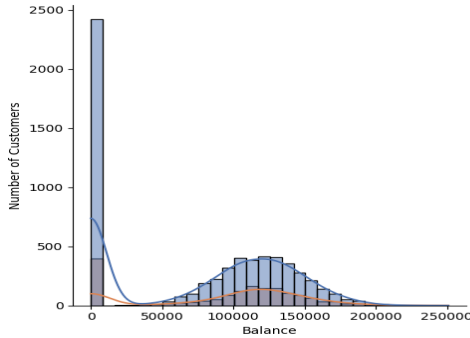

Figure 9. Balance and Customer Churn Distribution

3.1.11. Estimated Salary

The salary range of our customers is quite diverse, with estimates ranging from $11 to 199k. This indicates a significant variation in income levels among our customer base.

Table 13. Distribution of Estimated Salary

count	7816.000000
mean	100239.979496
std	57463.265346
min	11.580000
25%	51413.442500
50%	100405.680000
75%	149216.320000
max	199992.480000

The salary distribution among our customers shows a relatively equal spread across the entire range, indicating a balanced representation of customers across various income levels. Additionally, the distribution of customer churn is also evenly distributed, suggesting that salary alone is not a significant factor in customer churn.
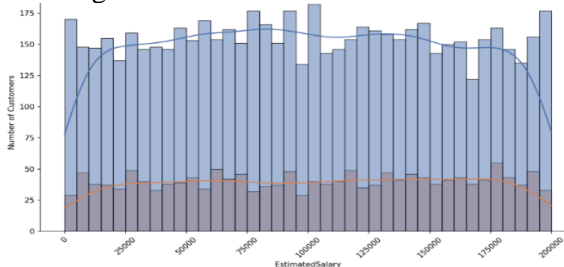
Figure 10. Estimated Salary and Customer Churn Distribution

3.2. Model Creation

This section covers two approaches, and as a result, a Predictive Model was developed to identify the key factors that have a significant impact on customer churn. The research method involves phases from data collection to data preparation and pre-processing to make it usable in the model. This includes commission rates to validate the hypothesis and addressing imbalanced data using SMOTE, a common technique for enhancing the sample size of the minority group when there is an imbalance.

Figure 11. Architecture of the Proposed Method

3.2.1 Approach 1

The dataset was split into 80% for training (6252) and 20% for testing (1564) purposes. This separation allowed us to create distinct sets for training and testing the models. To evaluate various models and determine the best performing one, cross-validation was employed.

The Gaussian NB models were utilized to generate predictions on the test data. Furthermore, it was noted that the dependent variable (Exited) exhibited an imbalance in its distribution.

Table 14. Tested Classifiers and Performance Metrics

Classifier	Average		
	Accuracy	Precision	Recall
Decision Tree	0.6731	0.5042	0.5049
Random Forest	0.6737	0.5042	0.5047
K-NN	0.7570	0.5066	0.5025
Gaussian NB	0.7935	0.3968	0.5000
XGBoost	0.7833	0.4986	0.5007

Table 15. Gaussian NB Models Evaluation using Different Metric Values

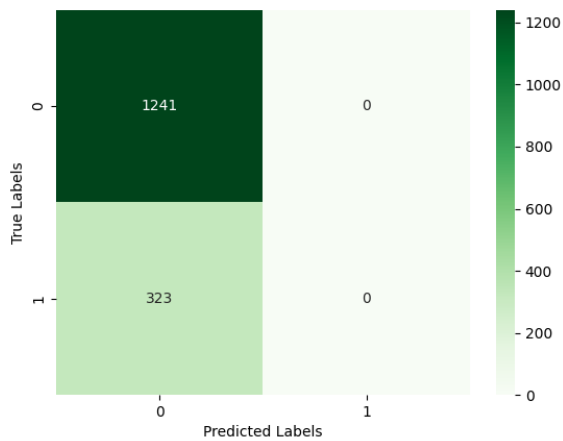|	precision	recall	f1-score	support
0	0.79	1.00	0.88	1241
1	0.00	0.00	0.00	323
accuracy			0.79	1564
macro avg	0.40	0.50	0.44	1564
weighted avg	0.63	0.79	0.70	1564

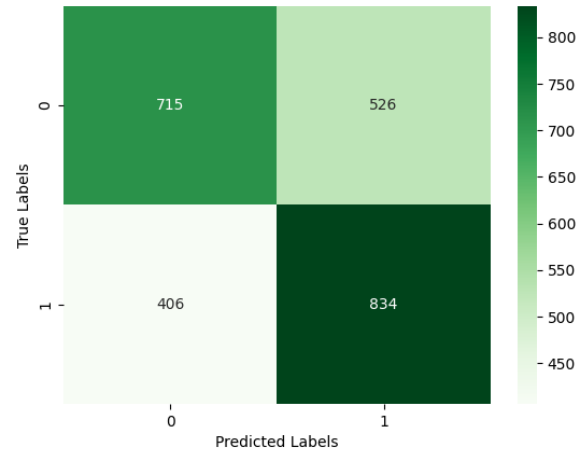**Figure 12.** Model Evaluation using Confusion Matrix of Gaussian NB

Figure 13. Model Evaluation using Confusion Matrix of K-NN

3.2.2. Approach 2

To address the issue of unbalanced datasets, the Synthetic Minority Oversampling Technique (SMOTE) was employed. SMOTE selects instances that are close in the feature space and creates synthetic samples along the line connecting those instances. By applying SMOTE, the class imbalance in the target variables was mitigated, resulting in 2481 balanced instances. Following this, the steps outlined in approach 1 were executed.

Table 16. Tested Classifiers and Performance Metrics Using the SMOTE Technique

Classifier	Average		
	Accuracy	Precision	Recall
Decision Tree	0.5557	0.5557	0.5557
Random Forest	0.5732	0.5760	0.5742
K-NN	0.6123	0.6130	0.6123
Gaussian NB	0.5060	0.5066	0.5060
XGBoost	0.6024	0.6029	0.6024

Table 17. K-NN Model Evaluation using Different Metric Values

	precision	recall	f1-score	support
0	0.64	0.58	0.61	1241
1	0.61	0.67	0.64	1240
accuracy			0.62	2481
macro avg	0.63	0.62	0.62	2481
weighted avg	0.63	0.62	0.62	2481

Several key factors have been identified as significant contributors to the deactivation of customers' facilities. These factors include institutions, gender, is active member, age and number of products.

The model used to predict customer deactivation achieved impressive results, with F1 score, recall, and precision values, all approximately 0.71. This suggests that the model has a acceptable ability to correctly identify positive cases while minimizing false positives and maximizing true positives.

Overall, the model exhibits strong performance across multiple evaluation metrics, showcasing its effectiveness in accurately predicting customer deactivation and capturing the desired outcomes.

4. Conclusion & Recommendations

The focus of the study is to draw attention to customer churn and commission rates in financial institutions. The analysis of the impact of stock commission rates on customer churn in financial institutions reveals vital insights into the dynamics of customer retention.

This article analyzes five different machine learning algorithms to identify key factors that influence customer deactivation in the brokerage firms and banks institutions. The Decision Tree, Random Forest, K-NN, Gaussian NB, and XGBoost algorithms are commonly used in churn analysis due to their ability to perform comprehensive analysis by combining different data types. While each algorithm operates differently, they excel at capturing complex relationships and interactions

within the data, making them valuable for churn analysis.

The predictive model aimed to identify the critical factors influencing customer churn. In the initial approach, five distinct machine learning algorithms were tested as classifiers using various performance metrics. The Gaussian NB model demonstrated a 0.7935% higher accuracy compared to the other models. Subsequently, in the second approach, 2481 balanced samples were generated by employing SMOTE to address the class imbalance in the target variables. The KNN model exhibited a 0.6123% higher accuracy compared to the alternative models. Following this, the steps outlined in the first approach were executed once again.

The study highlights that institutions, gender, active membership, age, and the number of products significantly impact churn rates. To address this, targeted initiatives and tailored retention strategies are recommended for specific segments, such as the 50-58 age group.

When examining the impact of stock commission rates on customer churn in financial institutions, some concepts to consider are: Proactive strategies can be implemented to identify and target customers at risk of churn. It can leverage predictive analytics and machine learning algorithms to predict customer behavior and intervene before churn occurs. To validate your findings and optimize your models, consider pilot testing your approach with a smaller group of customers before full implementation. Continuously evaluate the correlation between commission adjustments, customer retention, and revenue generation to strike an optimal balance.

Tailoring commission structures to individual customer needs is crucial for increasing satisfaction and loyalty. By offering customized pricing models that align with each customer's unique needs and behaviors, financial institution can significantly boost satisfaction and loyalty. Focus on enhancing overall customer satisfaction through personalized service, transparent communication, and value-added offerings. Invest in customer support resources and educational materials to empower customers and foster long-term relationships.

In this research presents a powerful approach to combating customer churn in financial institutions using a combination of proactively targeting, personalizing, and measuring. In research paves the way for a future-proof customer retention strategy in the financial sector.

Statement of Research and Publication Ethics

The study is complied with research and publication ethics.

References

[1] M. A. H. Farquad, V. Ravi, and S. B. Raju, "Data mining using rules extracted from SVM: An application to churn prediction in bank credit cards," in *Lecture Notes in Computer Science (including subseries Lecture Notes in Artificial Intelligence and Lecture Notes in Bioinformatics)*, vol. 5908 LNAI, pp. 390–397, 2009.

[2] N. A. Akbar, A. Sunyoto, M. Rudyanto Arief, and W. Caesarendra, "Improvement of decision tree classifier accuracy for healthcare insurance fraud prediction by using Extreme Gradient Boosting algorithm," in *Proceedings-2nd International Conference on Informatics, Multimedia, Cyber, and Information System, ICIMCIS 2020*, pp. 110–114, 2020, DOI: 10.1109/ICIMCIS51567.2020.9354286.

[3] S. M. Fati, A. Muneer, N. A. Akbar, and S. M. Taib, "A continuous cuffless blood pressure estimation using tree-based pipeline optimization tool," *Symmetry,* vol. 13, no. 4, 2021, DOI: 10.3390/sym13040686.

[4] A. Muneer and S. M. Fati, "A comparative analysis of machine learning techniques for cyberbullying detection on twitter," *Future Internet,* vol. 12, no. 11, pp. 1–21, 2020, DOI: 10.3390/fi12110187.

[5] M. Al-Ghobari, A. Muneer, and S. M. Fati, "Location-aware personalized traveler recommender system (lapta) using collaborative filtering knn," *Computers, Materials and Continua,* vol. 69, no. 2, pp. 1553–1570, 2021, DOI: 10.32604/cmc.2021.016348.

[6] F. Kayaalp, "Review of customer churn analysis studies in telecommunications industry," *Karaelmas Science & Engineering Journal*, vol. 7, no. 2, pp. 696-705 2017.

[7]   B.Prabadevi, R. Shalini, and B. R. Kavitha, "Customer churning analysis using machine learning algorithms," *International Journal of Intelligent Networks,* vol. 4, pp. 145-154, 2023, DOI: https://doi.org/10.1016/j.ijin.2023.05.005.

[8]   A. Muneer, R. F. Ali, A. Alghamdi, S. M Taib, A. Almaghthawi, and E. A Ghaleb, "Predicting customers churning in banking industry: A machine learning approach," *Indones. J. Electr. Eng. Comput. Sci,* vol.26, no.1, pp. 539-549, 2022, DOI: http://doi.org/10.11591/ijeecs.v26.i1.

[9]   J.Britto, R.Gobinath, "A detailed review for marketing decision making support system ın a customer churn prediction", *Int. J. Sci. Technol. Res,*vol. 9, no. 4, pp. 3698-3702, 2020.

[10]   H. Guliyev, T F. Y.atoğlu, "Customer churn analysis in banking sector: Evidence from explainable machine learning models," *Journal of Applied Microeconometrics,* vol. 1, no. 2, pp. 85-99, 2021, DOI: 10.53753/jame.1.2.03.

[11]   H. Tran, N. Le, and V. H.Nguyen, "Customer churn prediction in the banking sector using machine learning-based classification models," *Interdisciplinary Journal of Information, Knowledge & Management,* vol. 18, pp. 87-105, 2023, DOI: https://doi.org/10.28945/5086.

[12]   O. Kaynar, M. F. Tuna, Y. Görmez, , and M. A Deveci, "Makine öğrenmesi yöntemleriyle müşteri kaybı analizi," *Cumhuriyet Üniversitesi İktisadi ve İdari Bilimler Dergisi,* vol. 18, no. 1, pp. 1-14, 2017.

[13]   R. A. de Lima Lemos, T. C. Silva, and B. M. Tabak, "Propension to customer churn in a financial institution: a machine learning approach," *Neural Comput. Appl.*, vol. 34, no. 14, pp. 11751–11768, 2022, DOI: https://doi.org/10.1007/s00521-022-07067-x.

[14]   Y. Suh, "Machine learning based customer churn prediction in home appliance rental business," *J. Big Data*, vol. 10, no. 1, 2023., DOI: https://doi.org/10.1186/s40537-023-00721-8.

[15]   S. Naseer, S. M. Fati, A. Muneer, and R. F. Ali, "IAceS-deep: Sequence-based identification of acetyl Serine sites in proteins using PseAAC and deep neural representations," *IEEE Access*, vol. 10, pp. 12953–12965, 2022, DOI: https://doi.org/10.1109/access.2022.3144226

[16]   A. Muneer and S. M. Fati, "Efficient and automated herbs classification approach based on shape and texture features using deep learning," *IEEE Access*, vol. 8, pp. 196747–196764, 2020, DOI: https://doi.org/10.1109/access.2020.3034033

[17]   T.Chen, C. Guestrin, Xgboost: Reliable large-scale tree boosting system. In *Proceedings of the 22nd SIGKDD Conference on Knowledge Discovery and Data Mining, San Francisco, CA, USA* (pp. 13-17), 2015.

[18]   V.G. Costa, C.E Pedreira,. "Recent advances in decision trees: an updated survey," *Artif Intell Rev* 56, pp. 4765–4800, 2023. DOI: https://doi.org/10.1007/s10462-022-10275-5

[19]   L. Breiman, Random Forests. *Machine Learning,* vol. 45, no.1 pp. 5–32, 2001. DOI: https://doi.org/10.1023/A:1010933404324

[20]   S. Kiliçarslan and E. Dönmez, "Improved multi-layer hybrid adaptive particle swarm optimization based artificial bee colony for optimizing feature selection and classification of microarray data," *Multimed. Tools Appl.*, 2023, DOI: https://doi.org/10.1007/s11042-023-17234-4

[21]   N.Sahani, R. Zhu, J. H.Cho, and C. C Liu, "Machine Learning-based Intrusion Detection for Smart Grid Computing: A Survey," *ACM Transactions on Cyber-Physical Systems*, vol. 7, no. 2, pp. 1-31, 2023.

Bitlis Eren Üniversitesi Fen Bilimleri Dergisi

Explicit Formulas for Optimum Parameters of Viscoelastic-type Tuned Mass Dampers

Mehmet Ali KÖSEN [1], Gülçin TEKİN [1*]

[1]*Yıldız Technical University, Department of Civil Engineering, 34220 Istanbul, Turkey*
(ORCID: 0009-0002-8823-7944)(ORCID: 0000-0003-0207-4305)

Abstract

Tuned mass dampers (TMDs) are passive vibration control devices that are attached to a primary system to reduce the dynamic vibrations under exciting motion. The Voigt-type TMD, which is the most widely used one, is known as a standard model of dynamic vibration absorber (DVA). The purpose of this study is to improve the vibration control performance of passive control devices by using viscoelastic-type tuned mass dampers (V-TMDs). The study adopts the Zener model to represent the viscoelastic behavior of V-TMD. In this study, the fixed-point method is used to determine the optimum parameters of a V-TMD. The displacement amplification factor (DAF) of the coupled system is obtained in the frequency domain. The optimal parameters of the V-TMD system attached to an undamped single degree-of-freedom (SDOF) main system are obtained by minimizing the DAF (symbolized with β) under the effect of base excitation. The optimum parameters, such as damping ratio (ξ) and stiffness ratio (κ) of the coupled system are derived, and explicit expressions corresponding to the optimum parameters are presented for engineering design. Moreover, the change in DAF values for different mass ratios (μ) is also discussed. It is proven that V-TMD is very effective in reducing the amplitudes of vibration. The study also provides valuable insights for engineering practitioners who want to design and implement V-TMDs for vibration control applications because accurate expressions, which are simple and easy to use, are derived in order to obtain optimum parameters, and step-by-step procedures are explained.

1. Introduction

Vibration control is an important engineering field to improve the performance and safety of structural systems. To reduce the dynamic vibrations of the structure, several techniques are available. The concept of using tuned mass dampers (TMDs) is one of the several techniques, and it is a recent one. TMDs are secondary oscillators that are attached to the primary structure by parallel springs and viscous dampers. The main purpose is to transfer the vibrational energy of the primary oscillator to the secondary oscillator to increase the damping capacity of a structural system. It is usually assumed that the parameters of the primary oscillator are known. Therefore, the mathematical problem of tuning the mass damper is to select the parameters appropriately through proper calibration of the damping ratio and tuning frequency.

In the nineteenth century, the concept of the TMD was proposed by [1] which considers a vibration control device without any inherent damping. [2] extended Frahm's absorber by introducing a certain amount of damping. Details regarding the design and theory of TMDs and closed-form expressions for optimum absorber parameters are presented in [3]. The dynamic analyses of structures equipped with the conventional Voight type vibration absorber are presented in many papers in order to obtain optimum parameters. The optimum damping and tuning frequency ratios of the conventional TMD are obtained by [4] using the

*Corresponding author: gulcint@yildiz.edu.tr

numerical searching technique. Various mean square responses, such as relative displacement, velocity of the main mass, and force transmitted to the support, are minimized. Simple expressions for optimum absorber parameters are derived in [5, 6] for undamped and damped SDOF main systems under harmonic and white noise random excitations. Minimization of various response parameters is considered. The optimum tuning frequency and damping ratio of the TMD system are obtained by [7,8] using a numerical iteration searching technique. The steady-state response of damped systems is minimized to a minimum level through a curve-fitting method. [9] proposed a method for determining the optimum parameters of TMD by selecting the tuning and damping ratios that result in equal and large damping ratios in the first two modes of vibration. The responses of several single and multiple degree-of-freedom structures, with or without TMDs, subjected to different ground excitations are presented. Exact algebraic solutions are derived by [10] for the optimum tuning ratio and damping coefficient, assuming an undamped primary system and a hysterically damped primary system. Algebraic exact expressions for the resonance and antiresonance frequencies have been obtained. [11] derived the approximate optimum stiffness and a damping ratio using an extension of design formulas for H∞ optimization under the assumption of damped structures. Ground and force excitations are considered. [12] derived explicit expressions for the optimum mass ratio, damper damping, and tuning frequency of the TMD system attached to a viscously damped SDOF primary system. An algorithm for particle swarm optimization (PSO) is presented, covering both external force and base acceleration. A hybrid passive optimal control method is proposed to find the optimal damping coefficients of viscous dampers (VDs) and a TMD in shear building structures by [13]. In the optimization problem, the damping coefficients of TMD and VDs are taken as design variables. The variation of the upper limits of damping coefficients, the variation of story mass and stiffness are investigated for a six-story shear building model with VD&TMD.

The classical Maxwell or Kelvin-Voight models are the most popular DVA models, where the spring and viscous damper are arranged in series or in parallel, respectively. In recent years, various types of viscoelastically damped DVAs have attracted much attention in order to obtain a considerably reduced structural response to wind or earthquake motions. The design of structures with viscoelastic tuned mass dampers (V-TMDs) together with the optimization of parameters is an important problem from a practical viewpoint. There is little research about the optimum design of V-TMDs. [14] presented a semi-analytical iterative approach to obtain the optimal parameters of a viscoelastically damped TMD. The primary structure is assumed to be linear and undamped. It has been demonstrated that superior vibration absorption is obtained by using a viscoelastically damped TMD compared to an equivalent viscously damped TMD. [15] developed a numerical approach, which is called a generalized optimality criteria approach, to minimize the maximum amplitude magnification factor of a three-element DVA. The proposed method handles the primary system damping. Simultaneous equations for the design problem are solved using numerical computing software. As reported, the three-element DVA is more effective than a conventional DVA of twice its mass. Exact solutions for the optimum parameters of the three-element DVA are derived by [16] through numerical analysis. It has been demonstrated that the optimized three-element type of DVA is more advanced than the conventional Voigt type of DVA. Using algebraic manipulation, the optimum tuning and damping parameters are obtained for the three-element type of DVA. The H2 optimization problem for a damped and undamped primary system with a three-element type of DVA is discussed by [17]. The Newton-Raphson method is used as a numerical approach for the solution of a damped primary system. It has been proven that the three-element type of DVA is superior to the conventional Voight type of DVA. [18] studied the three-element DVA for the damped primary system. The criteria of the equivalent linearization method are utilized, and the damped structure is replaced by an equivalent undamped one. The approximate analytical solution of the DVA's parameters is obtained from the results of the undamped structure. [19] also demonstrated that the three-element TMD produces better performance than the TMD. Optimum tuning, damping, and stiffness ratios are selected as the design variables for the three-element TMD, including the damped primary system. A simulated annealing algorithm is utilized for the solution.

This study investigates the application of the fixed-point approach to the Zener type of V-TMD. The Zener model (sometimes called the standard linear solid model and/or three-element model) is more accurate than the Maxwell or Kelvin-Voight models in predicting real viscoelastic material response. The standard Voight or Maxwell models are not adequate to describe the rheological behavior of viscoelastic dampers [20]. The Zener model is a combination of a viscous damper and two springs. The objective of the present study is to consider the dynamic analysis of a structure equipped with Zener type V-TMD and the optimization analysis of the

structure, including parameter optimization. Numerous studies have been conducted on the Voigt type of TMD, and the analytical expressions for the optimum tuning and damping parameters have already been obtained. However, there are only a few papers that have been published on the viscoelastic Zener type of TMD. A literature review reveals that published works deal with the issue of parameter optimization in V-TMDs. The present study uses simplified mathematical operations, which in turn give rise to the simple analytical expressions of the optimum parameters of the V-TMD. In addition, accurate expressions that are simple and easy to use have not been derived until now for the optimum damping and stiffness ratios. The maximum DAF is efficiently minimized, and precise approximate solutions are obtained for the case where the primary oscillator is undamped. Precise expressions for the optimum parameters of a V-TMD, such as damping and stiffness ratios, are derived. In addition, the change in DAF values for different mass ratios is also discussed. The proposed procedure clearly explains the step-by-step instructions that are used to obtain optimum parameters and informs the readers associated with the process.

2. Methodology

2.1. Derivation of Equations of Motion for the Coupled System

Figure 1 shows a Zener type of V-TMD attached to an undamped SDOF main structure. It is assumed that the secondary oscillator is connected to the primary oscillator through the Zener model. By considering base excitation (y_0), the equations of motion are derived.
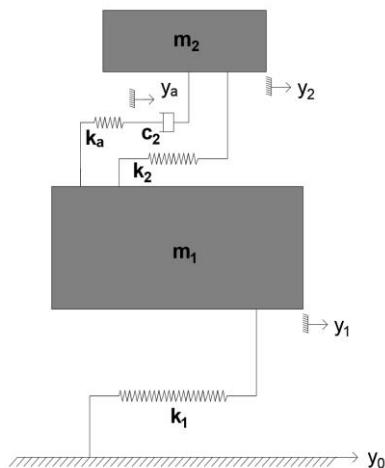
Figure 1. Zener type of V-TMD connected to an undamped structure.

The mass and stiffness parameters of the main structure are m_1 and k_1, respectively, and m_2 is the mass of the viscoelastic vibration absorber. Damping for the main structure is not considered here as it would help to reduce vibration and thus hide any additional damping that we expect to arise due to the viscoelastic damper. In order to develop and solve problems with the existence of fixed points, this assumption is a necessary condition.

The dynamic behavior of the system can be expressed by the following ordinary differential equations:

$$-y_2 k_2 - y_a k_a + y_1(k_1 + k_2 + k_a) + m_1 \frac{d^2 y_1}{dt^2} = y_0 k_1 \quad (1)$$

$$m_2 \frac{d^2 y_2}{dt^2} + c_2 \left(\frac{dy_2}{dt} - \frac{dy_a}{dt}\right) + k_2(y_2 - y_1) = 0 \quad (2)$$

$$c_2 \left(\frac{dy_a}{dt} - \frac{dy_2}{dt}\right) + k_a(y_a - y_1) = 0 \quad (3)$$

where y_1 and y_2 are the displacements of the masses of the main structure and viscoelastic vibration absorber, respectively. The viscosity of the dashpot component is c_2, k_a and k_2 are the elasticity parameters in the model. An additional internal degree of freedom y_a is introduced, connected by a spring with a coefficient k_a and by a dashpot with a coefficient c_2.

$y_a(\omega)$ and $y_2(\omega)$ are obtained after frequency domain transformation of Eqns. (1) and (3) as follows:

$$y_a(\omega) = \frac{k_2 k_a y_1(\omega) - i\omega c_2(k_1 y_0(\omega) - (k_1 + k_2 + k_a - \omega^2 m_1)y_1(\omega))}{k_2 k_a + i\omega c_2(k_2 + k_a)} \quad (4)$$

$$y_2(\omega) = \frac{k_1(-i\omega c_2 - k_a)y_0(\omega) + (k_a(k_1 + k_2 - \omega^2 m_1) + i\omega c_2(k_1 + k_2 + k_a - \omega^2 m_1))y_1(\omega)}{k_2 k_a + i\omega c_2(k_2 + k_a)} \quad (5)$$

Substituting Eqns. (4) and (5) into the Fourier transform of Eqn. (2), the DAF expression can be obtained with complex numbers as follows:

$$\beta(\omega) = \frac{k_1(k_a(k_2 - \omega^2 m_2) - i\omega c_2(-k_2 - k_a + \omega^2 m_2))}{-i(-ik_2 k_a + \omega c_2(k_2 + k_a))(-k_1 + \omega^2 m_1) + \omega^2(-k_a(k_1 + k_2 - \omega^2 m_1) - i\omega c_2(k_1 + k_2 + k_a - \omega^2 m_1))m_2} \quad (6)$$

where ω is the circular frequency. The absolute value of the equation, which is in terms of the complex numbers, is obtained as follows:

$$\beta(\omega) = \sqrt{\frac{k_1^2(k_a^2(k_2 - \omega^2 m_2)^2 + \omega^2 c_2^2(k_2 + k_a - \omega^2 m_2)^2}{k_a^2(k_2(-k_1 + \omega^2 m_1) + \omega^2(k_1 + k_2 - \omega^2 m_1)m_2)^2 + \omega^2 c_2^2((k_2 + k_a)(-k_1 + \omega^2 m_1) + \omega^2(k_1 + k_2 + k_a - \omega^2 m_1)m_2)^2}} \quad (7)$$

The following non-dimensional parameters are introduced for convenience:

Squared ratio of the excitation:

$$\Omega = \omega^2 / \omega_1^2$$

Mass ratio:

$$\mu = m_2 / m_1$$

Damping ratio:

$$\xi = c_2 / (2 m_2 \omega_2)$$

Using these notations, DAF can be expressed as follows:

$$\beta(\Omega) = \sqrt{\frac{(((-\mu\Omega k_1 + k_2)^2 k_a^2 + 4\mu\zeta^2\Omega k_1 k_2(-\mu\Omega k_1 + k_2 + k_a)^2)}{((\mu(-1+\Omega)\Omega k_1 - (-1+\Omega+\mu\Omega)k_2)^2 k_a^2 + 4\mu\zeta^2\Omega k_1 k_2(\mu(-1+\Omega)\Omega k_1 - (-1+\Omega+\mu\Omega)(k_2 + k_a))^2))}} \quad (8)$$

2.2. Derivation of Tuning Parameters

The DAF function is plotted in Figure 2 for different damping ratios. In the example, the mass ratio is 0.1, and the stiffness values are k_1=1 N/m, k_2=0.0545 N/m and k_a=0.0578 N/m.
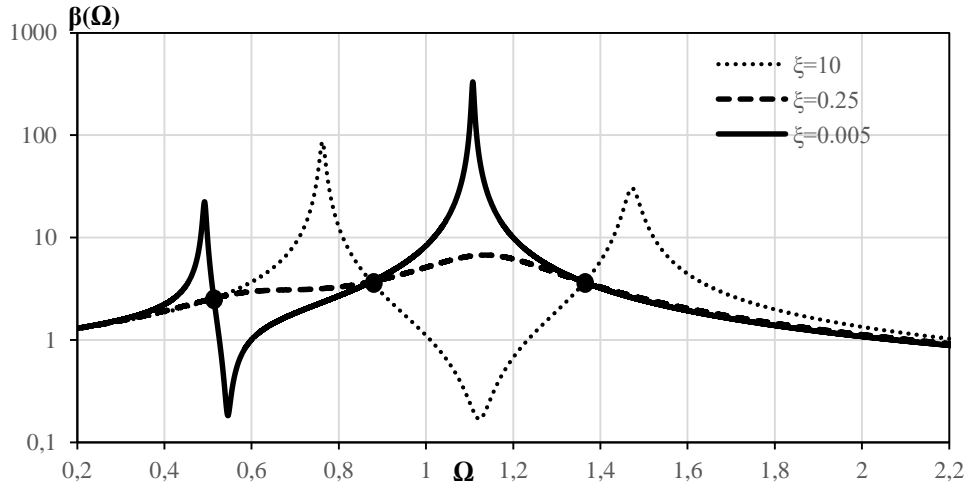
Figure 2. DAF function for different damping ratios

As can be seen from Figure 2, the response amplitude is independent of the damping ratio at three points (each one is represented by a solid circle). For classical TMDs, such fixed points have also been detected, and their number is two. For extracting the optimum parameter values of the traditional TMDs, classical methods are based on these fixed points. For the Zener type of V-TMD, there are three fixed points. The procedure for optimization is summarized through step-by-step instructions as follows:

Step 1:

Determine the optimum value for spring stiffness k_2 according to the three fixed points at which the curves intersect.

Step 2:

Determine the optimum value for spring stiffness k_a with respect to the k_2 value, which is calculated in Step 1.

Step 3:

Determine the damping ratio that gives the best symmetric DAF curve regarding the central fixed point.

2.2.1. Determination of Optimum k_2 Stiffness

In order to determine the three fixed points, the squared frequencies for which the DAF has the same values have been searched. For $\xi = 0$ and $\xi = +\infty$, the DAF yields the following equations:

$$\beta(\Omega_{\zeta_0}) = \sqrt{\frac{(-\mu\Omega k_1 + k_2)^2}{(\mu(-1+\Omega)\Omega k_1 - (-1+\Omega+\mu\Omega)k_2)^2}} \quad (9)$$

$$\beta(\Omega_{\xi_\infty}) = \sqrt{\frac{(-\mu\Omega k_1 + k_2 + k_a)^2}{(\mu(-1+\Omega)\Omega k_1 - (-1+\Omega+\mu\Omega)(k_2+k_a))^2}} \quad (10)$$

According to [16], the fixed points are settled at the same height with the following relation:

By considering the equality of Eqn. (9) and (11), the explicit expression for the optimum k_2 stiffness value is derived as follows:

$$\beta(\Omega_{l,c,r}) = \sqrt{\frac{1+\mu}{\mu}} \quad (11)$$

$$k_2 = \frac{\mu(1+\mu-\sqrt{\mu(1+\mu)})k_1}{(1+\mu)^2} \quad (12)$$

2.2.2. Determination of Optimum k_a Stiffness

The optimum k_a stiffness value is obtained by substituting the k_a stiffness value into Eqn. (10) and considering the equality with Eqn. (11). As a result, the following explicit expression is introduced:

$$k_a = \frac{2(\mu(1+\mu))^{3/2} k_1}{(1+\mu)^3} \qquad (13)$$

The ratio of stiffness of springs (k_2 / k_a) is defined as the stiffness ratio. The optimum stiffness ratios are tabulated in Table 1 for different mass ratios. As tabulated, the optimum stiffness ratio of the V-TMD increases with the increase in mass ratio of the structure.

Using the optimum k_2 and k_a stiffness values, the corresponding DAF curve is plotted in Figure 3 for 10 % mass ratio.

Table 1. Optimum stiffness ratios for different mass ratios

Mass ratio (μ)	Stiffness ratio (κ)
0.01	0.221
0.02	0.326
0.03	0.412
0.04	0.488
0.05	0.558
0.10	0.863
0.15	1.131
0.20	1.379
0.25	1.618
0.30	1.849
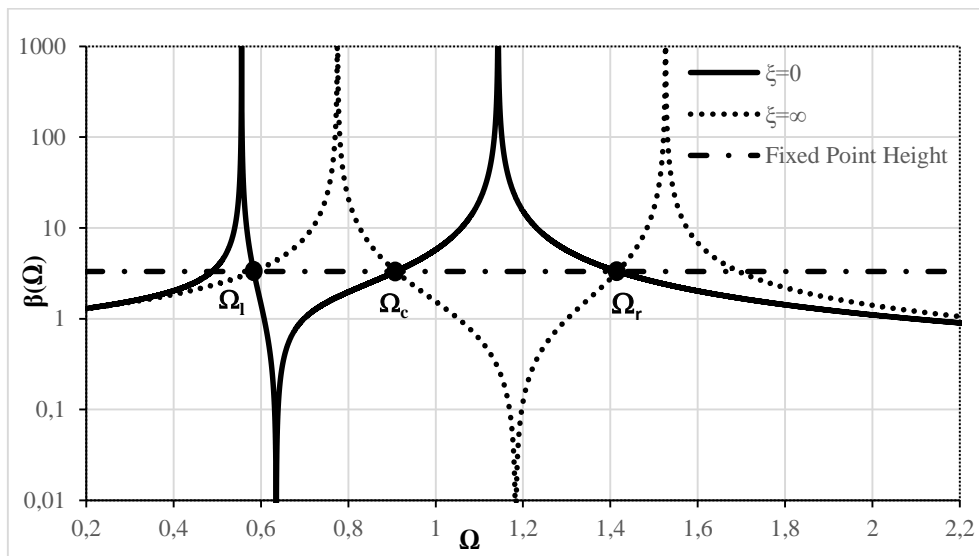
Figure 3. $\beta(\xi=0)$ and $\beta(\xi=\infty)$ curves for 10% mass ratio

It is proved that the values of the three fixed points namely the left, center, and right fixed points at which an intersection occurs satisfy Eqn. (11).

For the % 10 mass ratio, closed-form solutions of the left, center, and right fixed points' squared frequencies are derived as follows:

$$\Omega_{r,l} = 1 \pm \frac{\mu(2+\mu)}{\sqrt{\mu(1+\mu)^2(2+\mu)}}$$

$$\Omega_c = \frac{1}{1+\mu} \qquad (14)$$

Using the non-dimensional parameter, the frequencies of the three fixed points are presented in Table 2 for the cases $\mu = 0.10$, $\omega_1 = \sqrt{\frac{k_1}{m_1}}$ rad/s, $k_1 = 1$ N/m, $m_1 = 1$ kg. Results are compared with [14] and [15]. The accurate and consistent

performance of the presented approach has been indicated. As tabulated in Table 2, the calculated results are accurate to two decimal places for the frequency values of the three fixed points.

Table 2. Comparison of the left, central, and right fixed points' frequencies

Frequency values	Present Study	Reference Study [14]	Reference Study [15]
ω_{left}	0.764	~ 0.76	~ 0.76
ω_{center}	0.953	~ 0.95	~ 0.95
ω_{right}	1.190	~1.19	~ 1.18

2.2.3. Determination of the Optimum Damping Ratio (ξ)

The symmetry of the DAF curve regarding the central fixed point is directly related to the damping ratio effect. The best symmetry with regard to the central fixed point corresponds to the optimum value for the damping ratio. One way to check this symmetry is to make the slopes of the DAF curve at the left and right fixed points opposite each other. To the best of the author's knowledge, an analytical (or closed-form) expression for the optimum damping ratio has not been derived yet.

In order to get an explicit expression for the optimum value of the damping ratio, the following procedure is proposed:

The squared frequency of a central fixed point has already been calculated as $1/(1+\mu)$, so it takes a value less than 1 for any mass ratio. The square root of $1/(1+\mu)$ has a value that is less than 1. So as to obtain the optimum damping ratio, the square root of $1/(1+\mu)$ must be equal to the height values of the three fixed points (see eqn. (11)) and must satisfy the following expression:

$$\beta(\Omega_\zeta) = \beta(\Omega_{l,c,r}) = \beta(\frac{1}{1+\mu}) = \sqrt{\frac{1+\mu}{\mu}} \qquad (15)$$

Here, Ω_ξ is the squared frequency that will be used to calculate the optimal damping ratio. Thereby, the symmetry of the DAF curve is precisely satisfied. An explicit expression of the optimum damping ratio for different mass ratios is derived as follows:

$$\xi_{opt} = \sqrt{\frac{\mu(16+20\mu-3\mu\sqrt{1/(1+\mu)}-12\sqrt{\mu(1+\mu)}+\sqrt{\mu(4+5\mu)}}{16+31\mu+16\mu^2}} \qquad (16)$$

and a change in the optimal damping ratio with different mass ratios is shown in Figure 4. The optimum damping ratio of the V-TMD increases with the increase in the mass ratio of the structure, as expected.
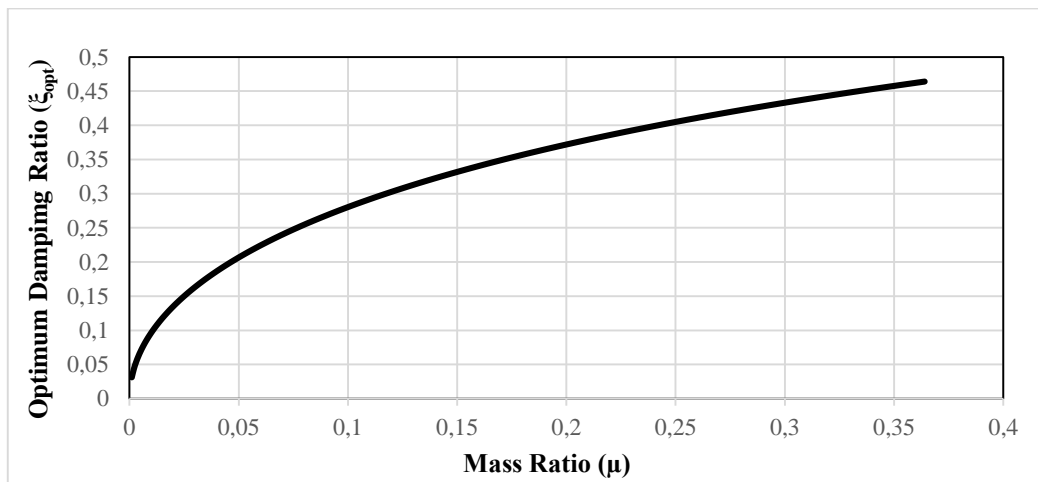

Figure 4. Change of optimum damping ratio with mass ratio considering optimum spring stiffness values

**2.2.4. Evaluation of the V-TMD Performance with Optimum Parameters**

Using the optimum values, the DAF curve is plotted in Figure 5 for different mass ratios. Noticeably, an increase in mass ratio results in a decrease in the maximum DAF values. In figure 5, the continuous line corresponds to the height values of the fixed points. It is also seen that the symmetry, which we want to investigate, is obtained using the optimum damping ratios based on the proposed algorithm for relatively large mass ratios.
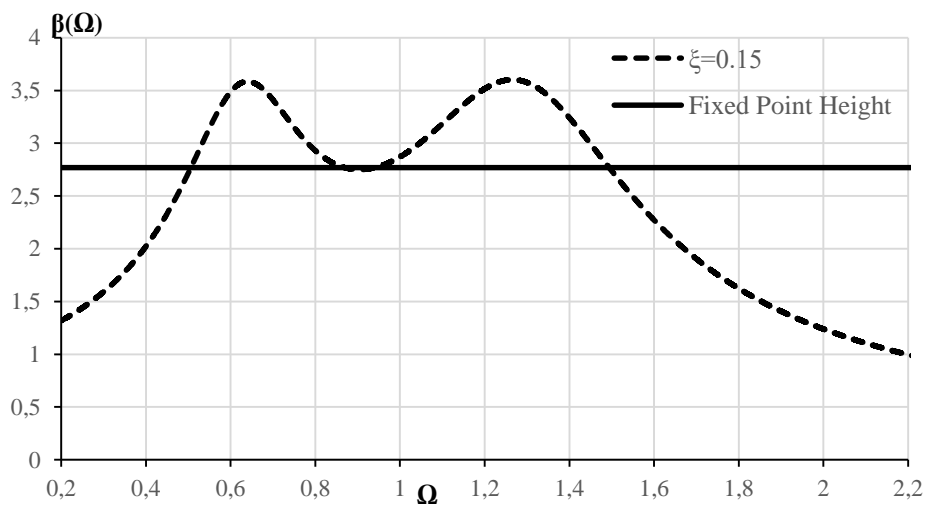

(a)

(b)

(c)

(d)

(e)
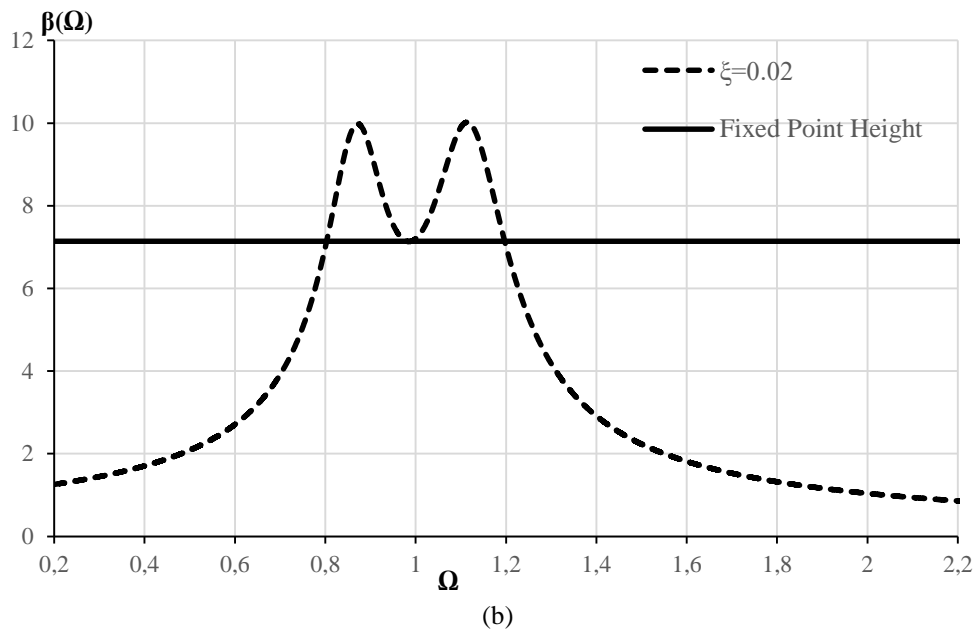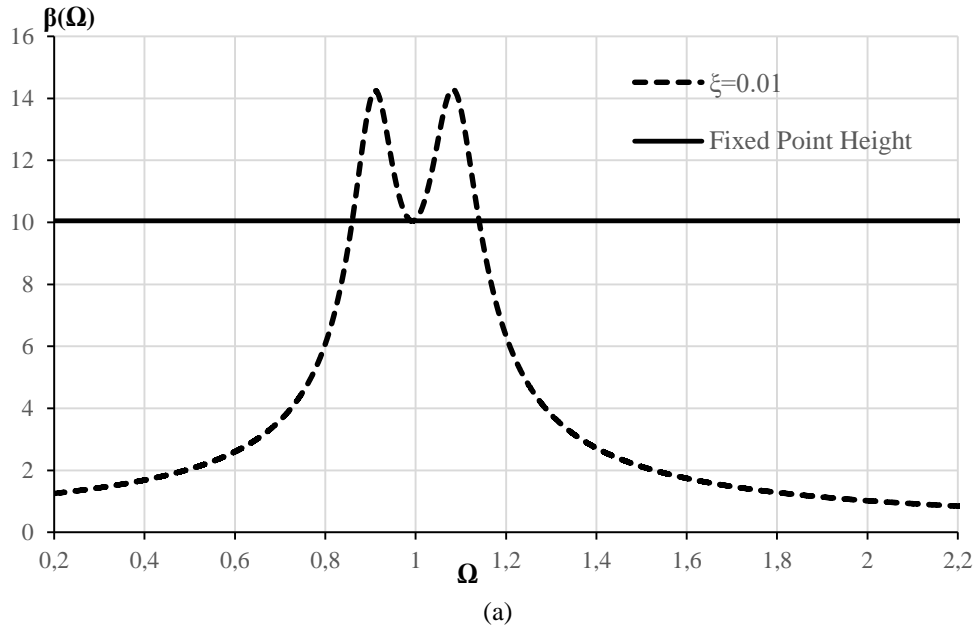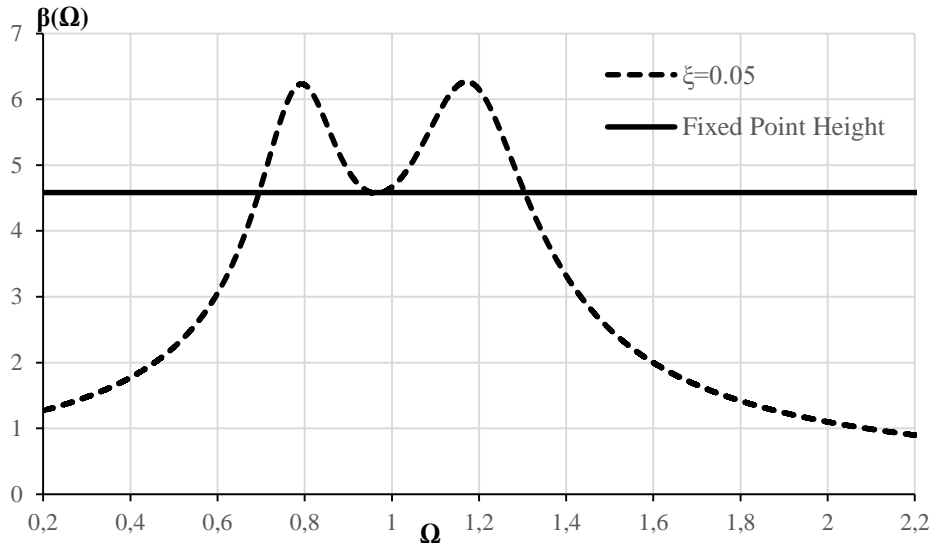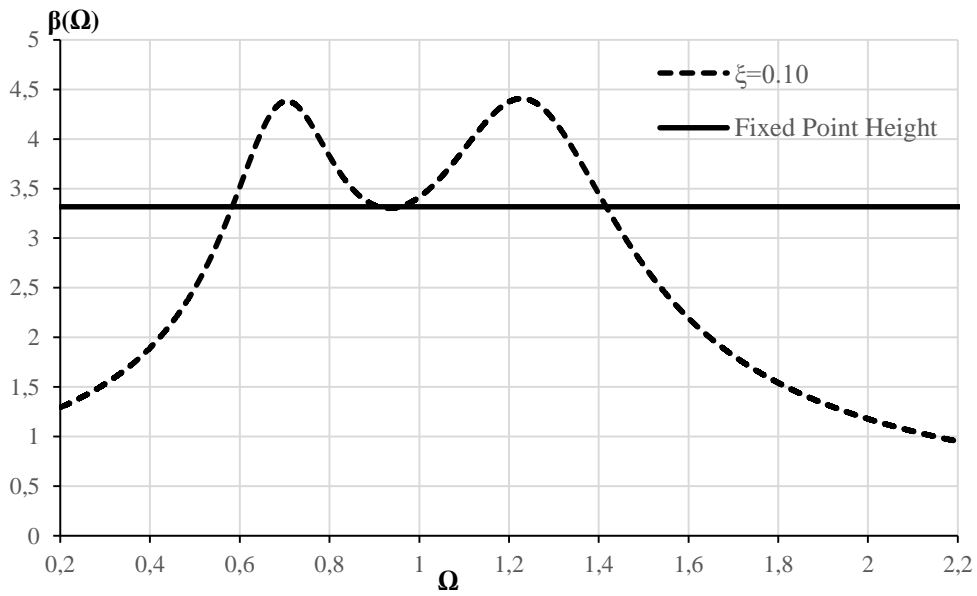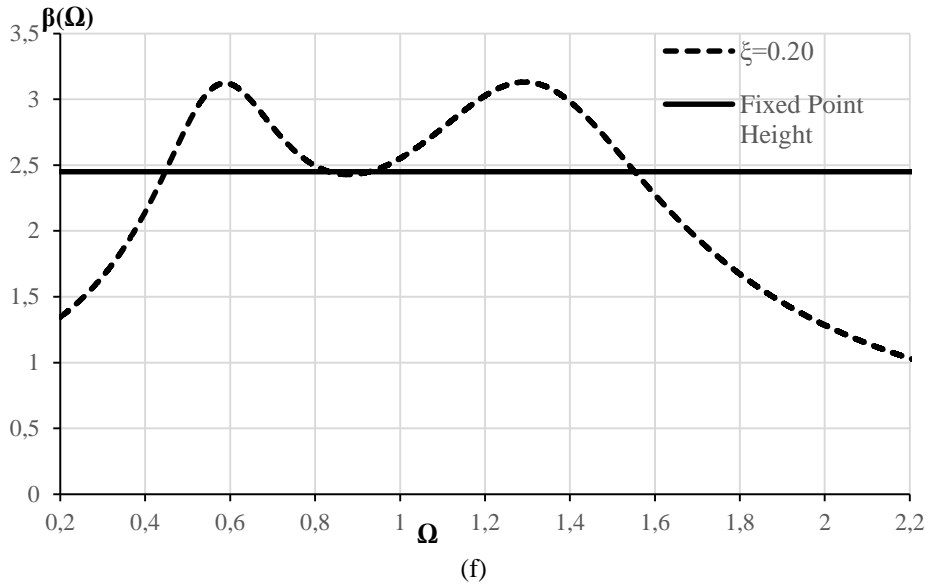
Figure 5. β(Ω) curves obtained using optimum parameters for different mass ratios (a) μ=0.01, (b) μ=0.02, (c) μ=0.05, (d) μ=0.10, (e) μ=0.15, and (f) μ=0.20

To demonstrate the efficiency of the recommended technique, the results of the V-TMD are compared to the available results in the literature and tabulated in Table 3. Additionally, the classical TMD results are given in order to make a comparison between the performance of TMD and V-TMD.

Table 3. Maximum DAFs for different mass ratios

Mass Ratio (μ)	Classical TMD Reference Study [3]	V-TMD Reference Study [15]	V-TMD Present Study
0.01	14.18	13.78	14.29
0.02	10.05	9.67	10.02
0.05	6.40	6.05	6.27
0.10	4.58	4.27	4.42
0.20	3.32	3.04	3.16

It is seen that the effectiveness of the V-TMD in diminishing the maximum DAF values is better than that of the classical TMD, as expected. Another observation from Table 3 is that the results of the present study agree well with the results of earlier research studies. Compared with the results of [15], highest error rate is nearly 4 % (when μ=0.20). This error is at an acceptable level, and symmetry disruption is inevitable for large mass ratios.

3. Conclusion

A Tuned mass damper (TMD) is a traditional passive vibration control device that is attached to a vibrating main structure. In this study, the characteristics of viscoelastically damped TMD, which is an alternative to classically damped TMD, are discussed. As a V-TMD, the Zener model is used. Some of the main points examined in this study are as follows:

- The fixed-point theory is generalized to obtain the optimal parameters of the V-TMD.

- A Zener-type TMD has three fixed points, unlike the traditional TMD with two fixed points.

- The optimal values of two stiffness parameters (k_a and k_2) are established considering the height of the DAF at three fixed points.

- An optimal damping ratio expression is developed considering the symmetry of the DAF with reference to the central fixed point.

- The change in the value of optimum stiffness parameters and damping ratio with reference to different mass ratios is also presented with representative figures and tables. It is observed that the present study results show accurate agreement with the results reported in the literature.

- Simple closed-form expressions are sufficiently accurate for practical use.

- The optimum damping ratio of the V-TMD increases with the increase in the mass ratio of the structure, as expected.

- The optimum stiffness ratio of the V-TMD increases with the increase in mass ratio of the structure, as expected.

- The authors recommend to use a viscoelastic damper model composed of multiple Maxwell and/or Voight elements for future research and searching to see if there will still be fixed points for this form of general viscoelastic model.

Contributions of the authors

The authors confirm contribution to the paper as follows: study conception and design: G. Tekin; data collection: M. A. Kösen; analysis and interpretation of results: G. Tekin and M. A. Kösen; draft manuscript preparation: G. Tekin and M. A. Kösen. All authors reviewed the results and approved the final version of the manuscript.

Conflict of Interest Statement

There is no conflict of interest between the authors.

Statement of Research and Publication Ethics

The study is in compliance with research and publication ethics.

References

[1]   H. Frahm, Device for Damping Vibrations of Bodies. US Patent No. 989, 958, 1911.
[2]   J. Ormondroyd and J. P. Den Hartog, "The Theory of Dynamic Vibration Absorber," *Journal of Applied Mechanics*, vol.50, pp. 9-22, 1928.
[3]   J. P. Den Hartog, *Mechanical Vibrations*. New York. McGraw-Hill, 1956.
[4]   S.V. Bakre and R. S. Jangid, "Optimum Parameters of Tuned Mass Damper for Damped Main System, " *Structural Control Health Monitoring*, vol. 14, no. 3, pp. 448-470, 2007.
[5]   G. B. Warburton, "Optimum Absorber Parameters for Minimizing Vibration Response," *Earthquake Engineering Structural Dynamics*, vol. 9, no. 3, pp. 251-262, 1981.
[6]   G. B. Warburton, "Optimum Absorber Parameters for Various Combinations of Response and Excitation Parameters, " *Earthquake Engineering Structural Dynamics*, vol.10, no. 3, pp. 381-401, 1982.
[7]   H-C. Tsai and G-C. Lin, "Optimum Tuned-Mass Dampers for Minimizing Steady State Response of Support-Excited and Damped Systems, " *Earthquake Engineering Structural Dynamics*, vol. 22, no. 11, pp. 957-973, 1993.
[8]   H-C. Tsai and G-C. Lin, "Explicit Formulae for Optimum Absorber Parameters for Force-Excited and Viscously Damped System, "*Journal of Sound and Vibration*, vol.176, no. 5, pp. 585-596, 1994.
[9]   F. Sadek, B. Mohraz, A. W. Taylor and R. M. Chung, "A Method of Estimating the Parameters of Tuned Mass Dampers for Seismic Applications" *Earthquake Engineering and Structural Dynamics*, vol. 26, no.6, pp. 617-635, 1997.

[10]   O. Nishihara and T. Asami, "Closed-Form Solutions to the Exact Optimizations of Dynamic Vibration Absorbers (Minimizations of the Maximum Amplitude Magnification Factors), " *Trans. ASME, Journal of Vibration and Acoustics*, vol.124, no. 4, pp.576-582, 2002.

[11]   J. Štěpánek, and J. Máca, "Optimization of Tuned Mass Dampers Attached to Damped Structures - Minimization of Maximum Displacement and Acceleration," *Acta Polytechnica CTU Proceedings*, vol.30, pp. 98-103, 2021.

[12]   A.Y.T. Leung and H. Zhang, "Particle Swarm Optimization of Tuned Mass Dampers, " *Engineering Structures*, vol.31, no.3, pp. 715-728, 2009.

[13]   H. Cetin, E. Aydin and B. Ozturk, "Optimal Damper Allocation in Shear Buildings with Tuned Mass Dampers and Viscous Dampers, " *International Journal of Earthquake and Impact Engineering (IJEIE)*, vol. 2, no.2, pp. 89-120, 2017.

[14]   A. Batou and S. Adhikari, "Optimum Parameters of Viscoelastic Tuned-Mass Dampers, " *Journal of Sound and Vibration*, vol. 445, pp. 17-28, 2019.

[15]   O. Nishihara, "Exact Optimization of a Three-Element Dynamic Vibration Absorber: Minimization of the Maximum Amplitude Magnification Factor" *Journal of Vibration and Acoustics*, vol. 141, no. 1, p.011001, 2019.

[16]   T. Asami and O. Nishihara, "Analytical and Experimental Evaluation of an Air Damped Dynamic Vibration Absorber: Design Optimizations of the Three-Element Type Model, " *Journal of Vibration and Acoustics*, vol.121, no. 3, pp. 334-342,1999.

[17]   T. Asami and O. Nishihara, "H2 Optimization of the Three-Element Type Dynamic Vibration Absorbers," *Journal of Vibration and Acoustics*, vol. 124, no. 4, pp.583-592, 2002.

[18]   N. D. Anh, N. X. Nguyen and L.T. Hoa, "Design of Three-Element Dynamic Vibration Absorber for Damped Linear Structures," *Journal of Sound and Vibration*, vol. 332, no. 19, pp. 4482-4495, 2013.

[19]   O. Araz, "Optimization of Three-Element Tuned Mass Damper for Single Degree of Freedom Structures under Ground Acceleration," *El-Cezerî Journal of Science and Engineering*, vol. 8, no. 3, pp.1264-1271, 2021.

[20]   N. W. Tschoegl, *The Phenomenological Theory of Linear Viscoelastic Behavior*. Berlin Heidelberg. Springer-Verlag ,1989.

Upper and lower extremity bone segmentation with Mask R-CNN

Ayhan AYDIN[1*], Caner ÖZCAN[2]

[1]*Computer Engineering, Ondokuz Mayıs University, 55080, Samsun, Turkiye*
[2]*Software Engineering, Karabuk University, 78050, Karabuk, Turkiye.*
(ORCID: 0000-0001-9127-0951) (ORCID: 0000-0002-2854-4005)

Abstract

Most medical image processing studies use medical images to detect and measure the structure of organs and bones. The segmentation of image data is of great importance for the determination of the area to be studied and for the reduction of the size of the data to be studied. Working with image data creates an exponentially increasing workload depending on the size and number of images and requires high computing power using machine learning methods. Our study aims to achieve high success in bone segmentation, the first step in medical object detection studies. In many situations and cases, such as fractures and age estimation, the humerus and radius of the upper extremity and the femur and tibia of the lower extremity of the human skeleton provide data. In our bone segmentation study on X-RAY images, 160 images from one hundred patients were collected using data compiled from accessible databases. A segmentation result with an average accuracy of 0.981 was obtained using the Mask R-CNN method with the resnet50 architecture.

1. Introduction

Many doctors use medical images to decide whether lesions, fractures, etc., occur in complaints that are thought to be caused by bone. With the development of medical imaging devices, a large number of high-quality medical imaging methods such as X-ray, computed tomography (CT), and magnetic resonance imaging (MRI) are widely used [1]. Visual inspection of X-ray data to determine appropriate treatments is a primary means of detecting and determining the severity of bone and bone-related phenomena [2]. An experienced physician may need to spend a lot of time checking bone integrity and health status on the X-ray image. Many hospitals today have a shortage of experienced radiologists to handle these medical images. To assist doctors in detecting bone-related disorders, computer-aided diagnosis (CAD) has been widely used to analyze medical images and has received increasing attention [3]. Deep learning applications are intensively used to classify health data and can potentially provide pioneering knowledge to domain experts [4,5]. In our study, a

segmentation application that provides the boundary information of the object with formal precision will be applied beyond visual classification and object identification within frames. Although it is translated into our language as segmentation, the process referred to as segmentation is to divide a digital image into regions or objects in the image [6]. Segmentation of four long bones in the lower and upper extremities will support experts' decision-making processes, from bone integrity to age estimation and detection of different diseases. Our study aims to show the bone structure on the image using direct radiograph images. Direct radiographs are the most intensively used diagnostic method among medical imaging methods, which is the most cost-effective diagnostic method with the highest data access. It is known that radiographs, which are examined and reported by radiologists in the first step and then by specialized physicians, create a workload for more than one physician. Today, radiologists use medical imaging methods to examine and report images in different areas and frequencies. There are systems in which

medical images are collected in a pool for interpretation and waiting for the appointment of a specialist. Automating the preliminary information in the radiographs interpreted by more than one specialist physician will save much time and labor by marking the preliminary information about different structures and presenting it to the specialist on the image. In image processing, determining the point of interest is an important stage and is one of the first steps in almost all studies. The term region of interest in the literature consists of visualizing bone and cartilage structure on direct radiographs. In addition to being a pioneering procedure, our study has an innovative aspect, with the masking success reaching 0.99 and above and possibly being integrated into radiological imaging devices. The segmentation of this region will be provided by masking produced with Mask R-CNN, as explained in the following sections.

Recently, thanks to the higher computational power of graphics processing units (GPUs), many new works on CAD based on deep learning have been presented. Current deep learning-based segmentation methods utilize some fully convolutional network (FCN) derivatives to estimate the class labels of all pixels in an image in parallel. Due to the pooling layers and up-sampling process, spatial information may be lost during the prediction, so there are some inaccuracies in the predicted segmentation map, especially in sharp regions such as boundaries. Therefore, a hopping architecture in FCN has been proposed to solve this problem [7]. Following this idea, Ronneberger et al. (2015) proposed a standard and popular medical image segmentation architecture called U-Net, which includes a symmetric encoder and decoder. The features of each encoder layer are hopingly connected to the corresponding decoder layer to recover the lost spatial information [8]. In bone structure segmentation, studies differ according to the preprocessing or masking area, and different results have been obtained with different network architectures.

Bullock et al. (2019) applied XNet architecture to segment X-ray images into bones and skin and obtained results with an overall accuracy of 0.92, which surpasses classical methods [9]. Drozdzal et al. (2018) combined Cnet with the fully connected resnet architecture (FC-ResNet) applied for CT liver images to detect lesions and obtain high-accuracy results [10]. Omar (2019) used a VGG-16-based SegNet model for CT lung image segmentation and achieved an average success rate of 0.95 [11]. Deep learning is a process that allows computational models consisting of multiple processing layers to learn representations of data with multiple levels of abstraction for the automatic segmentation of different anatomical structures. It includes automatic segmentation methods that are classified as either pre-supervised or unsupervised. For supervised methods, segmentation requires operator interaction throughout the process, while unsupervised methods usually require operator intervention only after the end of the process. Unsupervised methods are preferred to obtain a reproducible result [12]. In another study, U-net detected different human bones from computed tomography images, achieving a segmentation accuracy of 0.93 [13]. Smistad et al. (2015) applied deep learning methods to MRI tomography images to detect lung tumors and, at the same time, improve MRI image quality. The segmentation processes obtained with current methods exceed the success threshold of 0.90 based on the literature review [14]. For segmentation tasks, Mask R-CNN has several advantages over Faster R-CNN. First, it can generate more accurate and fine-grained masks for each object, better at capturing the details of shape and contour than bounding boxes. Second, it can handle overlapping and occluded objects better than semantic segmentation models, which can confuse pixels from different instances of the same class. Third, it can use the existing architecture and pre-trained weights of Faster R-CNN, which can reduce training time and data requirements. Finally, adding or modifying the mask branch can extend it to other tasks, such as key point detection, pose estimation, and panoptic segmentation.

2. Material and Method

2.1. Convolutional neural networks

It is similar to traditional artificial neural networks, consisting of neurons that self-optimize through learning. Each neuron takes one input and performs a process that is the basis of numerous ANNs. From the input raw image vectors to the final output of the class score, the entire network continues to express a single weight. The final layer contains the loss functions associated with the classes and can be used to optimize objectives such as class scores. [15]. Convolutional neural networks, also known as CNNs, are a particular type of neural network, usually consisting of the following layers.

Paragraphs following the first paragraph should begin with the paragraph indentation. The general structure of CNN layers is presented in Figure 1.
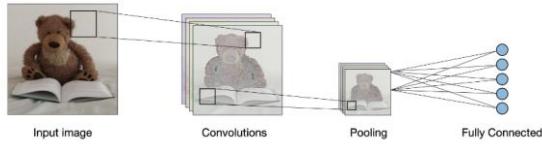
Figure 1. CNN layers [16].

When scanning images based on their size, filters perform convolution layer operations. Hyperparameters such as the filter size and step are used. The outcome of this is an activation map or feature map. This process can also be regarded as image reduction or feature extraction.
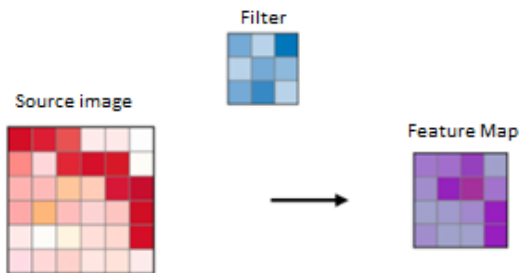

Figure 2. Convolution layer.

The full link layer represents the sampling process following the convolution layer, typically representing spatial variation. Specifically, maximum, and average co-registration represent distinct categories of co-registration, with maximum and average values taken correspondingly. Opting for maximum averaging retains the perceived features by

identifying the current matrix's highest value, constituting the most preferred method. Different methods can be employed in this layer to guarantee the selection of varied features. Convolution layer sections are presented in Figure 2.

The fully linked layer works on an input where all neurons are connected to each input. As seen in Figure 3, these layers are commonly situated towards the end of a CNN architecture and can be utilized to enhance objectives such as class scores.
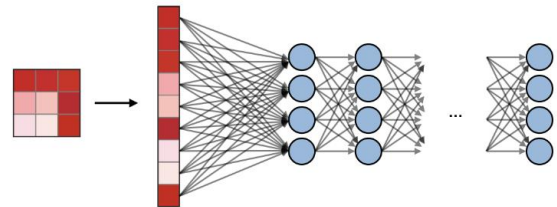

Figure 3. Fully connected layer.

2.2. Region-based CNN

The architecture used to identify objects in images and the classes of these objects was published by Girshick et al. in 2014 [17]. RCNN is run on images containing multiple objects in two different steps. The first of these steps is selective search. In this stage, the features that are candidates to be objects in the image are determined. The RCNN architecture is shown in Figure 4 below. After identifying approximately 2000 regions, each region is entered into the CNN model separately, and the boxes defining the boundaries are predicted.
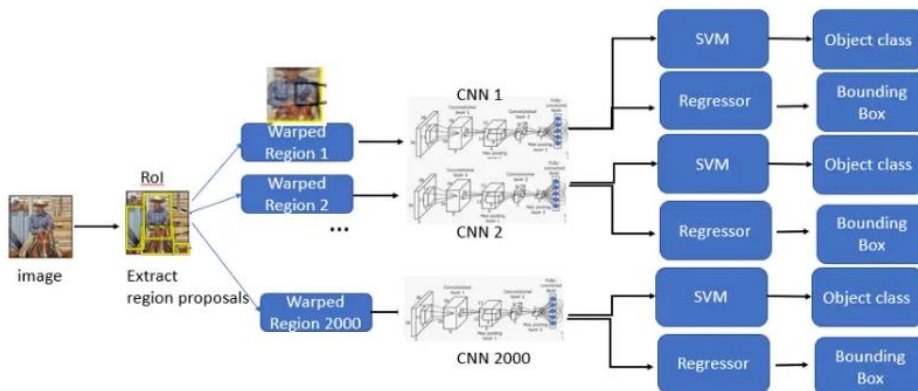

Figure 4. Region-based CNN architecture [17].

2.3. Mask R-CNN

It is a state-of-the-art example segmentation technique proposed by He et al. [18]. As shown in

Figure 5, Mask-RCNN is divided into two branches of the network: classification prediction and mask prediction. The classification prediction branch is the same as Faster-RCNN, predicts the relevant domain and produces class labels and rectangular box coordinate output. Each binary mask produced by the mask prediction branch relies on the classification prediction results to separate these objects. Mask-RCNN independently predicts a binary mask for each class to avoid competition.
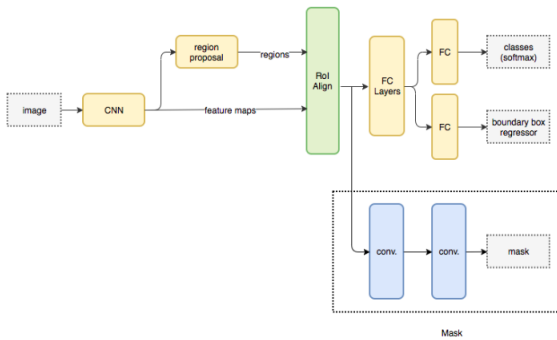

Figure 5. Mask-RCNN architecture [18].

2.3.1 Mask R-CNN Hyperparameters

Back Bone: The backbone is the Conv Net architecture. This is used in the first step of Mask R-CNN. Available backbone selection options include ResNet50, ResNet101 and ResNext 101.

Train_ROIs_Per_Image: This is the maximum number of ROIs the Region Proposal Network will generate for the image. These ROIs will be processed in the next step for classification and masking.

Detection_Min_Confidence: This is the confidence threshold above which an instance will be classified. It can be initialized by default. It can be increased or decreased depending on the model's detected instances.

Image_Min_Dim and Image_Max_Dim: These settings control the image size. The default settings resize images to 1024x1024 squares. Smaller images (512x512) can reduce memory requirements and training time.

Loss weights: Mask RCNN uses a complex loss function, calculated as the weighted sum of different losses in each model state. The hyper-parameters of the weight of the losses correspond to the weight the model should give to each state.

2.3.2 Mask R-CNN Evaluation Metric

Pixel accuracy is a common evaluation metric used in image segmentation to measure the overall accuracy of the segmentation algorithm. It is the ratio of correctly classified pixels to the total number of pixels in the image.

$$Pixel\ accuracy = \frac{Number\ of\ selected\ pixels}{Total\ number\ of\ area\ pixels} \qquad (1)$$

2.4. Resnet

In 2015, Resnet, a network structure proposed by He et al., ranked first in ILSVRC-2015 classification, ImageNet detection and localization, COCO detection, and segmentation tasks. The deepening network structure aims to solve the problem of reducing the training error by using the residual block structure. Residual blocks are added to the output by skipping one or more layers. The identity block is used if the input and output are the same [19]. If the residual block does not provide learning, it does not impose an additional load on the structure, but generally, the residual block contributes positively to the network's learning. Resnet50 architecture is presented in Figure 6 below.
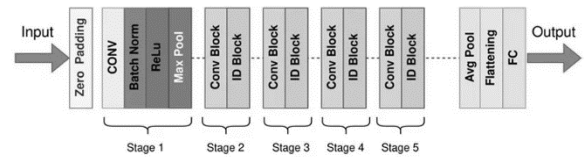

Figure 6. Resnet50 architecture [19]

With the structure shown in Figure 7, Resnet50 is used as 1x1 convolution, 3x3 convolution, and 1x1 dimensionality to recover the actual size.
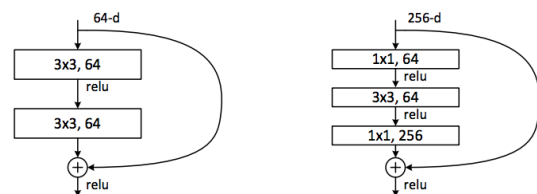

Figure 7. Resnet50 link example [19]

3. Results and discussion

LERA X-RAY images made available by Stanford University were used for educational and academic studies [20]. To compare the aims and data amounts of the studies in the literature, the information on the

publications in similar fields is presented in Table 1 below.

Study	Aim	Data
Yahalomi vd. (2019) [2]	Fracture detection	38
He vd. (2020) [21]	Tumor detection	291
Eweje vd. (2021) [22]	Tumor classification	1060
Chianca vd. (2021) [23]	Tumor classification	146
Anizusman vd. (2021) [24]	Tumor classification	50
Karthik vd. (2021) [25]	Pneumonia detection	5000
Thakur ve Kumar (2021) [26]	Pneumonia detection	3877
Felfeliyan (2022) [27]	Cartilage Segmentation	500

Images with complete bone integrity and without prosthesis were selected from the set containing different anomaly and prosthesis images. In addition, a student profile was created on the Medpix page, and appropriate images of the relevant bones made available for sharing were used [28].

The dataset consisting of 160 different images was labeled as polygons with the single class 'bone' tag in Microsoft's 'Common Objects in Contects' COCO format, which is widely used in image segmentation. Examples of labeled images are shown in Figure 8. Depending on the imaging equipment, X-rays are available in different resolutions, such as 1024*817, 2436*2966, and 2021*2021. With the Mask R-CNN architecture, these images are resized to 1024*1024.

Figure 8. Labeled image samples.

The dataset was divided randomly into training and test sections at a ratio of 120/40. Data augmentation was not applied because it would produce images outside the X-ray acquisition standards. For example,

if augmentation techniques were to be applied to the lower extremity image, the femur and tibia would be in different positions, which would differ from the real images. Train was performed on a Tesla K80 GPU provided by Google Colab. Experiments were performed with different resolutions, epochs, and parameters, and the optimal success value was obtained independently of the test images, with a resolution of 1024*1024 and a learning rate (lr) of 0.001. The process took 84 minutes, and the test results exceeded the success threshold set in the literature. Table 2 below presents some test results with Resnet101 and Resnet50 architectures using different parameters and average sensitivity values.

Table 2. Training parameters and accuracy results

mAP	Parameters			
	Validation steps	Steps per epoch	Backbone	Min. conf.
0,981	50	1000	Resnet101	0,7
0,989	50	1000	Resnet50	0,7
0,976	50	500	Resnet101	0,7
0,977	50	500	Resnet50	0,7
0,976	100	1000	Resnet101	0,7
0,977	100	1000	Resnet50	0,7

4. Conclusion and Suggestions

When diagnosing bone-related complaints, our application aims to reduce the target region by detecting the relevant area on X-ray images, which is the primary source of information for medical specialists. Our results show an average accuracy of 0.981. Figure 9 also lists the accuracy values obtained for the test radiographs, with the lowest value of 0.88. This shows that a segmentation success of 0.99 is possible by overcoming some limitations. Figure 10 shows sample images of the test set. It is important to note that this is an objective evaluation based on the resources used. The application aims to improve successful object/structure detection within the masked area. This is based on pioneering studies with Mask-RCNN in detecting anomalies, fractures, and lesions on the four long bones. The study has reached a point of success with masking and aims to create innovative software that can be added to radiological imaging devices. The Mask R-CNN architecture preferred for the study provides the segmentation function on visual data. This process provides region

of interest (ROI) extraction in fracture, implant, tumor, and anomaly detections, which are intensively included in the literature and controlled depending on the bone structure. Running deep learning models on ROI-detected images for object detection and similar operations will provide a lower workload and faster results [29]. Future studies will include images with structural differences for data augmentation and sample object detection. Additionally, they will continue to explore applications with different network and architectural structures and carry out optimization trials using the existing parameters to achieve the most optimal results for the data.
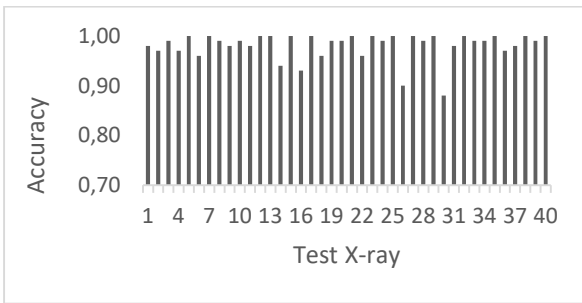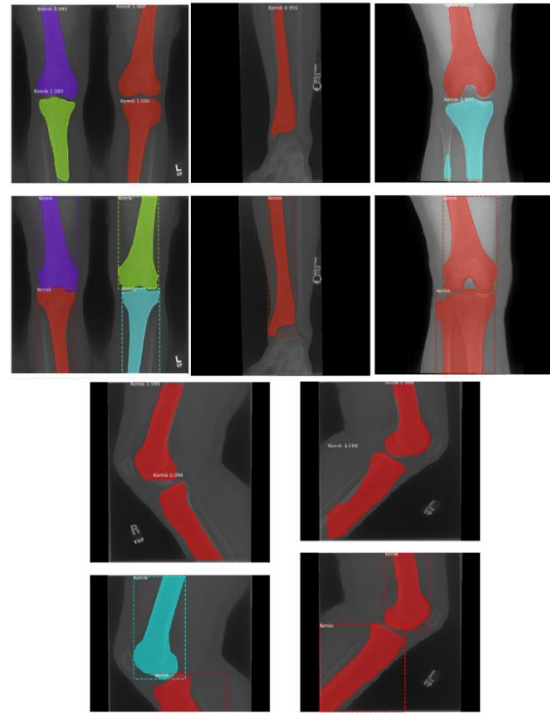

Figure 9. Test X-rays accuracy.

Figure 10. Prediction examples on test data.

Contributions of the authors

Ayhan Aydın carried out data preparation, deep learning modelled experiments and drafted the manuscript. Caner Özcan participated in the design of the study and helped to prepare the manuscript.

Conflict of Interest Statement

There is no conflict of interest between the authors.

Statement of Research and Publication Ethics

The authors of this article declare that the materials and methods used in this study do not require ethics committee approval and/or legal-special permission

References

[1]   Y. Ma and Y. Luo, "Bone fracture detection through the two-stage system of Crack-Sensitive Convolutional Neural Network," *Inform. Med. Unlocked*, vol. 22, no. 100452, p. 100452, 2021.

[2]   E. Yahalomi, M. Chernofsky, and M. Werman, "Detection of distal radius fractures trained by a small set of X-ray images and faster R-CNN," *in Advances in Intelligent Systems and Computing, Cham: Springer International Publishing*, 2019, pp. 971–981.

[3]   T. Urakawa, Y. Tanaka, S. Goto, H. Matsuzawa, K. Watanabe, and N. Endo, "Detecting intertrochanteric hip fractures with orthopedist-level accuracy using a deep convolutional neural network," *Skeletal Radiol.*, vol. 48, no. 2, pp. 239–244, 2019.

[4]   H. Çetiner, "Cataract disease classification from fundus images with transfer learning based deep learning model on two ocular disease datasets," *Gümüshane Üniversitesi Fen Bilimleri Enstitüsü Dergisi*, vol. 13, no. 2, 2023.

[5]   K. A. Y. A. Volkan and İ. Akgül, "Classification of skin cancer using VGGNet model structures," *Gümüşhane Üniversitesi Fen Bilimleri Dergisi*, vol. 13, no. 1, pp. 190–198, 2023.

[6]   R. C. Gonzalez, R. E. Woods, and S. L. Eddins, Ruan Qiuqi. *Digital Image Processing*, vol. 8. Beijing: Publishing House of Electronics Industry, 2007.

[7]   D. Wang et al., "A novel dual-network architecture for mixed-supervised medical image segmentation," *Comput. Med. Imaging Graph.*, vol. 89, no. 101841, p. 101841, 2021.

[8]   O. Ronneberger, P. Fischer, and T. Brox, "U-Net: Convolutional Networks for Biomedical Image Segmentation," arXiv [cs.CV], 2015.

[9]   J. Bullock, C. Cuesta-Lazaro, and A. Quera-Bofarull, "XNet: a convolutional neural network (CNN) implementation for medical x-ray image segmentation suitable for small datasets," *in Medical Imaging 2019: Biomedical Applications in Molecular, Structural, and Functional Imaging*, 2019.

[10]   M. Drozdzal et al., "Learning normalized inputs for iterative estimation in medical image segmentation," *Medical image analysis*, vol. 44, pp. 1–13, 2018.

[11]   A. Omar, "Lung CT Parenchyma Segmentation using VGG-16 based SegNet Model," *Int. J. Comput. Appl.*, vol. 178, no. 44, pp. 10–13, 2019.

[12]   H. Lee et al., "Fully automated deep learning system for bone age assessment," *J. Digit. Imaging*, vol. 30, no. 4, pp. 427–441, 2017.

[13]   F. La Rosa, *A deep learning approach to bone segmentation in CT scans*, Universit`a di Bologna, Alma Mater Studiorum, 2017.

[14]   E. Smistad, T. L. Falch, M. Bozorgi, A. C. Elster, and F. Lindseth, "Medical image segmentation on GPUs-A comprehensive review," *Medical image analysis*, vol. 20, no. 1, pp. 1–18, 2015.

[15]   K. O'Shea and R. Nash, "An Introduction to Convolutional Neural Networks," arXiv [cs.NE], 2015.

[16]   A. A. Shervine Amidi, *Stanford Convolutional Neural Networks Handbook. Palo Alto, CA*: Stanford University.

[17]   R. Girshick, J. Donahue, T. Darrell, and J. Malik, "Rich feature hierarchies for accurate object detection and semantic segmentation," *in 2014 IEEE Conference on Computer Vision and Pattern Recognition*, 2014.

[18]   He, K., Gkioxari, G., Dollár, P., & Girshick, R, "Mask r-cnn," *in IEEE international conference on computer vision*, 2017, pp. 2961–2969.

[19]   K. He, X. Zhang, S. Ren, and J. Sun, "Deep residual learning for image recognition," *in 2016 IEEE Conference on Computer Vision and Pattern Recognition (CVPR)*, 2016.

[20]   Stanford University, "LERA- Lower Extremity RAdiographs," Stanford Center for Artifical Intelligence in Medicine & Imaging. [Online]. Available: https://aimi.stanford.edu/lera-lower-extremity-radiographs. [Accessed: 12-Oct-2023].

[21]   Y. He et al., "Deep learning-based classification of primary bone tumors on radiographs: A preliminary study," *EBioMedicine*, vol. 62, no. 103121, p. 103121, 2020.

[22]   F. R. Eweje et al., "Deep learning for classification of bone lesions on routine MRI," *EBioMedicine*, vol. 68, no. 103402, p. 103402, 2021.

[23]   V. Chianca et al., "Radiomic machine learning classifiers in spine bone tumors: A multi-software, multi-scanner study," *Eur. J. Radiol.*, vol. 137, no. 109586, p. 109586, 2021.

[24] D. M. Anisuzzaman, H. Barzekar, L. Tong, J. Luo, and Z. Yu, "A deep learning study on osteosarcoma detection from histological images," *Biomed. Signal Process. Control*, vol. 69, no. 102931, p. 102931, 2021.

[25] R. Karthik, R. Menaka, and H. M, "Learning distinctive filters for COVID-19 detection from chest X-ray using shuffled residual CNN," *Appl. Soft Comput.*, vol. 99, no. 106744, p. 106744, 2021.

[26] S. Thakur and A. Kumar, "X-ray and CT-scan-based automated detection and classification of covid-19 using convolutional neural networks (CNN)," *Biomed. Signal Process. Control*, vol. 69, no. 102920, p. 102920, 2021.

[27] B. Felfeliyan, A. Hareendranathan, G. Kuntze, J. L. Jaremko, and J. L. Ronsky, "Improved-Mask R-CNN: Towards an accurate generic MSK MRI instance segmentation platform (data from the Osteoarthritis Initiative)," *Comput. Med. Imaging Graph.*, vol. 97, no. 102056, p. 102056, 2022.

[28] An official website of the United States government, "https://medpix.nlm.nih.gov/," MEDPIX. [Online]. Available: https://medpix.nlm.nih.gov/search?allen=true&-allt=true&alli=true&query=tibia,. [Accessed: 10-Dec-2023].

[29] A. Aslam and E. Curry, "A survey on object detection for the internet of multimedia things (IoMT) using deep learning and event-based middleware: Approaches, challenges, and future directions," *Image Vis. Comput.*, vol. 106, no. 104095, p. 104095, 2021.